ISSN 0256-1530
CN 11-1925/O4

Advances in Atmospheric Sciences

大气科学进展

Volume 39 Number 8 August 2022

Special Issue on

Carbon Neutrality: Important Roles of Renewable Energies, Carbon Sinks, NETs, and non-CO_2 GHGs

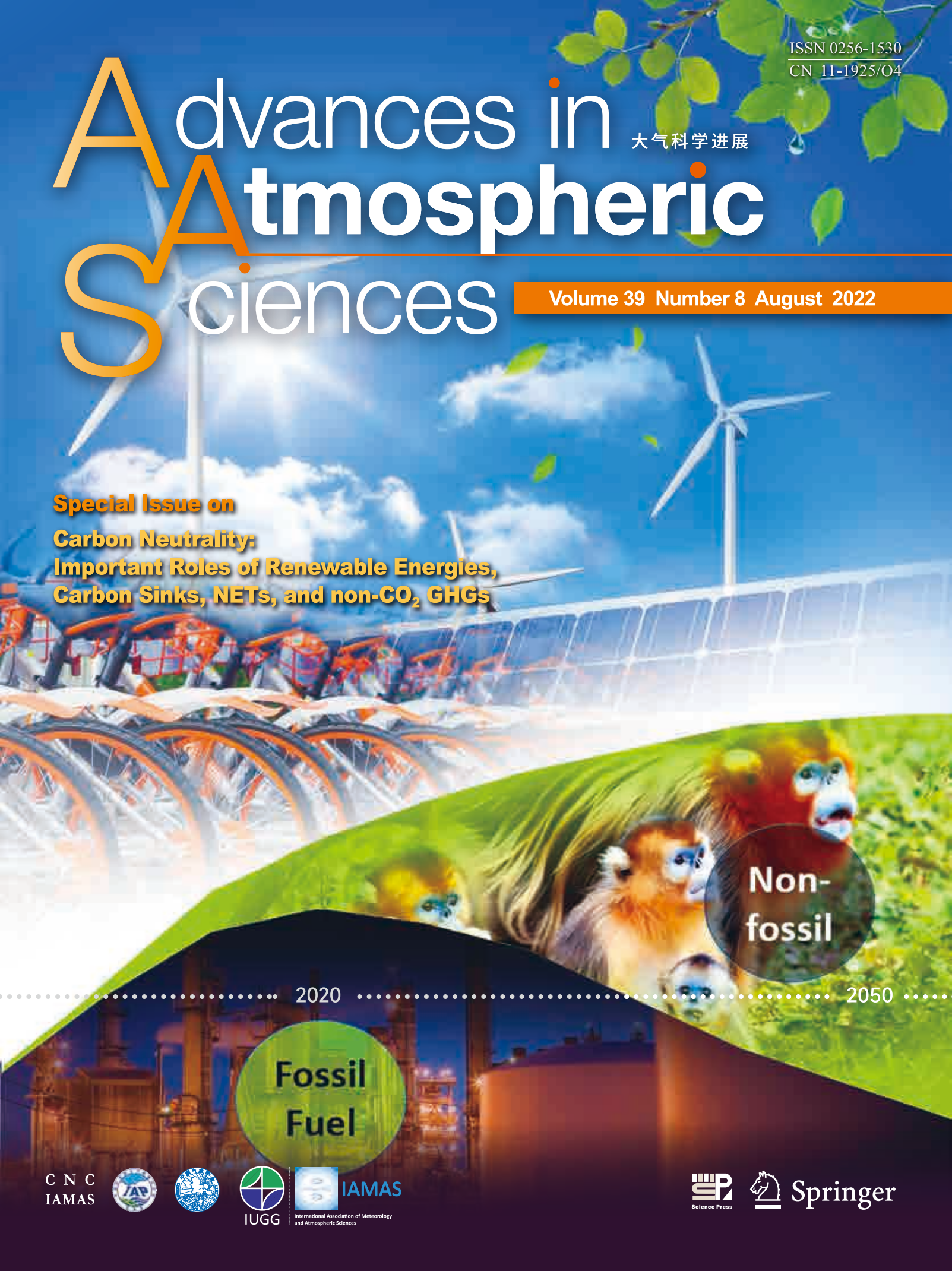

CNC
IAMAS
IUGG
IAMAS
International Association of Meteorology and Atmospheric Sciences
Science Press
Springer

Advances in Atmospheric Sciences

Vol. 39 NO. 8 August 2022

CONTENTS

EDITORIAL NOTES

1207 **Preface to the Special Issue on Carbon Neutrality: Important Roles of Renewable Energies, Carbon Sinks, NETs, and non-CO_2 GHGs**
Junji CAO, Ning ZENG, Yi LIU, Bengang LI, and Pengfei HAN

NEWS & VIEWS

1209 **COP26: Progress, Challenges, and Outlook**
Yi WANG, Yuxuan LIU, and Baihe GU

PERSPECTIVES

1217 **Climate Warming Mitigation from Nationally Determined Contributions**
Bo FU, Jingyi LI, Thomas GASSER, Philippe CIAIS, Shilong PIAO, Shu TAO, Guofeng SHEN, Yuqin LAI, Luchao HAN, and Bengang LI

1229 **The Chinese Carbon-Neutral Goal: Challenges and Prospects**
Ning ZENG, Kejun JIANG, Pengfei HAN, Zeke HAUSFATHER, Junji CAO, Daniel KIRK-DAVIDOFF, Shaukat ALI, and Sheng ZHOU

REVIEW

1239 **A Concise Overview on Solar Resource Assessment and Forecasting**
Dazhi YANG, Wenting WANG, and Xiang'ao XIA

1252 **Frontiers of CO_2 Capture and Utilization (CCU) towards Carbon Neutrality**
Lingyun ZHANG, Yanfang SONG, Jialin SHI, Qun SHEN, Deng HU, Qiang GAO, Wei CHEN, Kien-Woh KOW, Chengheng PANG, Nannan SUN, and Wei WEI

ORIGINAL PAPERS

1271 **The Variability of Air-sea O_2 Flux in CMIP6: Implications for Estimating Terrestrial and Oceanic Carbon Sinks**
Changyu LI, Jianping HUANG, Lei DING, Yu REN, Linli AN, Xiaoyue LIU, and Jiping HUANG

1285 **Changes in Global Vegetation Distribution and Carbon Fluxes in Response to Global Warming: Simulated Results from IAP-DGVM in CAS-ESM2**
Xiaofei GAO, Jiawen ZHU, Xiaodong ZENG, Minghua ZHANG, Yongjiu DAI, Duoying JI, and He ZHANG

1299 **Characterization of Regional Combustion Efficiency using ΔXCO: ΔXCO_2 Observed by a Portable Fourier-Transform Spectrometer at an Urban Site in Beijing**
Ke CHE, Yi LIU, Zhaonan CAI, Dongxu YANG, Haibo WANG, Denghui JI, Yang YANG, and Pucai WANG

1316 **Fengyun-4 Geostationary Satellite-Based Solar Energy Nowcasting System and Its Application in North China**
Chunlin HUANG, Hongrong SHI, Ling GAO, Mengqi LIU, Qixiang CHEN, Disong FU, Shu WANG, Yuan YUAN, and Xiang′ao XIA

1329 **Ocean–atmosphere Teleconnections Play a Key Role in the Interannual Variability of Seasonal Gross Primary Production in China**
Kairan YING, Jing PENG, Li DAN, and Xiaogu ZHENG

1343 **Decadal Methane Emission Trend Inferred from Proxy GOSAT XCH_4 Retrievals: Impacts of Transport Model Spatial Resolution**
Sihong ZHU, Liang FENG, Yi LIU, Jing WANG, and Dongxu YANG

1360 **Effects of Plant Community Type on Soil Methane Flux in Semiarid Loess Hilly Region, Central Gansu Province, China**
Chuanjie YANG, Guang LI, Lijuan YAN, Weiwei MA, Jiangqi WU, Yan TAN, Shuainan LIU, and Shikang ZHANG

1375 **The Synergism between Methanogens and Methanotrophs and the Nature of their Contributions to the Seasonal Variation of Methane Fluxes in a Wetland: The Case of Dajiuhu Subalpine Peatland**
Luwen WANG, Jiwen GE, Liang FENG, Yaoyao LIU, Yu LI, Jiumei WANG, Xiang XIAO, and Zhiqi ZHANG

On the cover

For China to achieve its carbon neutrality goal before 2060, a complete, but complementary (Yin-Yang) transformation from fossil fuels (bottom panel) to renewable energy (solar and wind, upper panel) must occur. Scientists believe this is attainable by promoting carbon sinks within ecosystems, such as planting trees, which will provide biodiverse habitats in the future (The inset picture in the "non-fossil" labeled section shows a golden monkey family that lives in the Shennongjia Biosphere Reserve). The special issue: "Carbon Neutrality: Important Roles of Renewable Energies, Carbon Sinks, NETs, and non-CO2 GHGs" provides highlights from carbon neutrality research.

Advances in Atmospheric Sciences
For more information:
http://www.iapjournals.ac.cn/aas
http://link.springer.com/journal/376

ADVANCES IN ATMOSPHERIC SCIENCES, VOL. 39, AUGUST 2022, 1207–1208

• **Editorial Notes** •

Preface to the Special Issue on Carbon Neutrality: Important Roles of Renewable Energies, Carbon Sinks, NETs, and non-CO_2 GHGs※

Junji CAO[1], Ning ZENG[2,3], Yi LIU[4], Bengang LI[5], and Pengfei HAN[3,4]

[1]*Institute of Atmospheric Physics*, *Chinese Academy of Sciences*, *Beijing* 100029, *China*

[2]*Department of Atmospheric and Oceanic Science*, *and Earth System Science Interdisciplinary Center*, *University of Maryland*, *College Park* 20742, *Maryland*, *USA*

[3]*State Key Laboratory of Numerical Modeling for Atmospheric Sciences and Geophysical Fluid Dynamics*, *Institute of Atmospheric Physics*, *Chinese Academy of Sciences*, *Beijing* 100029, *China*

[4]*Carbon Neutrality Research Center*, *Institute of Atmospheric Physics*, *Chinese Academy of Sciences*, *Beijing*100029, *China*

[5]*Sino-French Institute for Earth System Science*, *Laboratory for Earth Surface Processes*, *College of Urban and Environmental Sciences*, *Peking University*, *Beijing* 100871, *China*

Citation: Cao, J. J., N. Zeng, Y. Liu, B. G. Li, and P. F. Han, 2022: Preface to the special issue on Carbon Neutrality: Important Roles of Renewable Energies, Carbon Sinks, NETs, and non-CO_2 GHGs. *Adv. Atmos. Sci.*, **39**(8), 1207–1208, https://doi.org/10.1007/s00376-022-2005-6.

The year 2020 witnessed milestone commitments to carbon neutrality with the EU, China, USA, Japan, South Korea, Canada, and South Africa, each pledging to reach net-zero carbon emissions. Countries that have adopted or have considered net-zero targets now represent 63% of the total contributions to global greenhouse gas (GHG) emissions. With the efforts of all parties, the 26th Conference of the Parties (COP26) achieved a package of outcomes in the Glasgow Climate Pact. Here, a breakthrough consensus was reached on reducing coal, controlling methane, and halting deforestation (Wang et al., 2022, Page 1209). To achieve net-zero carbon, we need to take action to implement the Paris Agreement and the Glasgow Climate Pact Since the global temperature slowdown of the nationally determined contributions (NDC) scenario is only 0.6°C, all countries need to pursue stricter carbon reduction policies for a more sustainable world. (Fu et al, 2022, Page 1209).

China strives to reach peak carbon emissions before 2030 and achieve carbon neutrality before 2060. Achieving carbon neutrality is a great challenge for China as there are only 30 years from projected peak emissions to reach neutrality. However, great opportunities will arise once neutrality is reached.

To support the neutrality target, both decreasing carbon emissions and increasing the capacity of carbon sinks are vital. Power and industries are anticipated to substantially ramp up renewable energies (e.g., wind, solar, etc.), and carbon sinks will increase throughout the next few decades. A large-scale land greening campaign, ocean negative emission technology, and reductions of non-CO_2 GHGs will play a critical role.

Thus, we have organized a special issue: "Carbon Neutrality: Important Roles of Renewable Energies, Carbon Sinks, NETs, and non-CO_2 GHGs" to compile the scientific questions, technical requirements, and achievements in these fields. These efforts will provide accurate and updated scientific understanding, technical support, and possible solutions for power, industries and nations to reach carbon neutrality.

This special issue provides highlights from carbon neutrality research. The papers are categorized into four groups as follows.

(1) **Important roles of renewable energies in decreasing CO_2 emissions:** A perspective paper to show the Yin-Yang transformation from fossil fuel to renewable energies is given by Zeng et al. (2022, Page 1229), which pointed out that solar energy is a key unlimited resource while other energy resources (e.g., hydro, wind, and nuclear fission) are expected to reach their upper limits in a carbon-neutral scenario. While Yang et al. (2022, Page 1239) presented a review of solar

※ This paper is a contribution to the special issue on Carbon Neutrality: Important Roles of Renewable Energies, Carbon Sinks, NETs, and non-CO_2 GHGs.

resource assessment and forecasting and pointed out that a bridge between atmospheric sciences and solar energy engineering is needed. Furthermore, Huang et al. (2022, Page 1316) developed a solar nowcasting system based on the Fengyun-4 Geostationary Satellite, which performed well in the North China Plain. Moreover, accurate estimates of CO_2 emissions are important. By investigating regional combustion efficiency using $\Delta XCO:\Delta XCO_2$ observed by a portable Fourier-transform spectrometer in Beijing, Che et al. (2022, Page 1299) showed that the MEIC (Multi-resolution Emission Inventory for China) dataset underestimates CO_2 emissions by about 11%, and the PKU (Peking University emission inventories) dataset underestimates CO_2 emissions by 49%. These papers showcase how complex and interdisciplinary research related to carbon neutrality is.

(2) **Terrestrial carbon sinks will play an important role in offsetting the anthropogenic CO_2 in achieving a carbon-neutral goal:** Global vegetation coverage and carbon fluxes (GPP, NPP, and Ra) show an overall increase in a warmer scenario compared with the 1980–2000 period. Gao et al. (2022, Page 1285) applied the CAS-ESM2 model to investigate the response of terrestrial ecosystems to climate warming, while Ying et al. (2022, Page 1329) showed that ocean–atmosphere teleconnections mostly affect GPP over eastern China, which dominates the interannual GPP variability for China as a whole. Furthermore, Li et al. (2022, Page 1271) showed that the variability of air-sea O_2 flux in CMIP6 provides a valuable complement for estimating terrestrial and oceanic carbon sinks.

(3) **NETs (Negative Emissions Technologies) will absorb CO_2 emissions that are very difficult to reduce:** Carbon dioxide Capture and Utilization (CCU) will play an important role in the carbon-neutral goal. Zhang et al. (2022, Page 1252) summarized the frontiers of CCU, which is a new "atmosphere-to-atmosphere" carbon cycle, thus offering a huge potential for the indirect reduction of carbon. Potential cutting-edge CCU technologies during the decarbonization of energy and industrial systems include direct air capture (DAC), flexible metal-framework materials (MOFs) for CO_2 capture, integrated CO_2 capture and conversion (ICCC), and electrocatalytic CO_2 reduction (ECR).

(4) **Non-CO_2 GHGs face great challenges in emissions reductions:** Methane (CH_4) is the second most important greenhouse gas, following CO_2. Yang et al. (2022, Page 1360) showed that grassland and shrubbery are ideal vegetation types to reduce CH_4 emissions in the Loess Hilly Region. Considering that wetland ecosystems are the most important natural CH_4 sources, Wang et al. (2022, Page 1375) showed that CH_4 emissions were highest in summer and lowest in spring in the Dajiuhu subalpine peatland, which can be explained by seasonal variations of the interactions between methanogens and methanotrophs, soil temperature, and nitrogen. Furthermore, Zhu et al. (2022, Page 1343) showed two parallel GOSAT XCH4 retrievals that inverted global methane emissions from 2010 to 2019 and concluded that accelerated atmospheric methane increases over the second half of the 2010s were mainly driven by Eurasian Boreal and Tropical South American emissions.

China's carbon neutrality goal requires technological, socio-political, and economic initiatives toward clean energy to run smoothly over a short amount of time. International collaboration on scientific and technical innovation, as well as effective deployment, is essential to building a safe, fair, common, and more resilient global future. Underinternational frameworks such as the Paris Agreement, the 2030 Agenda for Sustainable Development, and the Belt and Road Initiative, China should vigorously export its renewable energy technologies and products and provide domestic and international support in achieving carbon-neutral goals.

ADVANCES IN ATMOSPHERIC SCIENCES, VOL. 39, AUGUST 2022, 1209–1216

• **News & Views** •

COP26: Progress, Challenges, and Outlook※

Yi WANG[1,2], Yuxuan LIU[1,2], and Baihe GU[*1]

[1]*Institutes of Science and Development, Chinese Academy of Sciences, Beijing* 100190, *China*

[2]*School of Public Policy and Management, University of Chinese Academy of Sciences, Beijing* 100049, *China*

(Received 2 April 2022; revised 27 April 2022; accepted 7 May 2022)

ABSTRACT

The 26th Conference of the Parties (COP26) to the United Nations Framework Convention on Climate Change (UNFCCC) was held in Glasgow a year later than scheduled, with expected outcomes achieved under a post-pandemic background. Based on the Issue-Actor-Mechanism Framework, this paper systematically evaluates the outcomes achieved at COP26 and analyzes the tendency of post-COP26 climate negotiations. Overall, with the concerted efforts of all parties, COP26 has achieved a balanced and inclusive package of outcomes and concluded six years of negotiations on the Paris Rulebook. It is fair to say that COP26 is another milestone in climate governance following the implementation of the Paris Agreement. Meanwhile, the Glasgow Climate Pact has cemented the consensus on a global commitment to accelerating climate action over the next decade and reached a breakthrough consensus on reducing coal, controlling methane, and halting deforestation. In the post-COP26 era, we still need to take concrete actions to implement the outcomes of the Paris Agreement and the Glasgow Climate Pact, innovate ways to speed up CO_2 emissions reduction, and continue to strive for breakthroughs in important issues such as finance, technology, adaptation, and collaboration. In addition to avoiding the escalation of international conflicts, we need to collectively and properly handle the relationship between energy security, carbon reduction, and development and facilitate the efforts of countries to achieve their Sustainable Development Goals (SDGs), including climate-related goals. China will continue to maintain the existing multilateral mechanisms and processes for climate governance, unremittingly take concrete actions to address climate change, promote a domestic comprehensive green transition and global cooperation on carbon neutrality, and contribute constructively to global climate governance.

Key words: COP26, Glasgow, climate change, Paris Agreement, climate governance

Citation: Wang, Y., Y. X. Liu, and B. H. Gu, 2022: COP26: Progress, challenges and outlook. *Adv. Atmos. Sci.*, **39**(8), 1209–1216, https://doi.org/10.1007/s00376-022-2097-z.

"The Summit showed the Paris Agreement is working and made progress in key areas." — COP26 World Leaders Summit –Presidency Summary, 3 November 2021

1. COP26 opened in a new development background

The 26th Conference of the Parties (COP26), originally scheduled for 2020, was postponed to 2021 at Glasgow due to the pandemic. The COVID-19 outbreak triggered a profound reflection within the international community, leading to a deeper understanding of non-traditional security issues. On 9 August 2021, the IPCC released the Working Group I Report of the Sixth Assessment Report (AR6 WG1), in which observations suggest an average temperature rise of 1.09°C between 2011 and 2020 above pre-industrial (1850–1900) levels and that climate change will further increase in all regions in the coming decades (IPCC, 2021). While the pandemic has led to short-term declines in carbon emissions in many countries, this trend is unsustainable in the long run, and a rebound in carbon emissions might occur after the pandemic (Ray et al., 2022). The new global energy crisis has also impeded the post-pandemic green recovery of economies (International Energy Agency, 2021). In this context, COP26 is of particular significance as it took place one year later than scheduled by overcoming

※ This paper is a contribution to the special issue on Carbon Neutrality: Important Roles of Renewable Energies, Carbon Sinks, NETs, and non-CO_2 GHGs.

* Corresponding author: Baihe GU
Email: gubaihe@casisd.cn

many difficulties, showing that countries have established a basic consensus on actively fulfilling international conventions and strengthening climate targets and pragmatic actions. As the first COP convened since the United States rejoined the Paris Agreement, COP26 has received considerable attention from all parties. COP26 sought to deliver on climate goals in four areas, namely mitigation, adaptation, finance, and collaboration. Specifically, first, both the global response to climate change and the sum of ambitions were still insufficient. Aside from implementation gaps, all Nationally Determined Contributions (NDCs) still cannot reach the 2°C target (UNEP, 2021a). Second, the issue of adaptation has been receiving increasing attention. Developing countries were very concerned about building infrastructure for adaptation and communicated that it was also important to enhance collaborative governance of biodiversity and climate change response as proposed in the Kunming Declaration. Third, the building capacity for climate governance remained inadequate, especially the huge gap in the widely criticized climate finance commitments. Fourth, since the Paris Agreement Rulebook has not yet been completed, it should be finalized as soon as possible to promote full implementation. The hosts of COP26 communicated extensively in the run-up to the summit and set the core goals and agenda around these four areas. In summary, COP26 had properly set the issues in key areas of global climate governance and promoted important progress in these areas during the summit.

2. COP26 achievements and outcomes

The COPs to the UNFCCC are a major part of global climate governance mechanisms. Based on the Issue-Actor-Mechanism Framework of the global governance system in a new era (Xue and Yu, 2017), this study built a framework for analyzing the achievements at COP26 (see Fig. 1). It argued that COP26 successfully introduced multiple stakeholders to discuss climate issues of common concern and established a series of implementation mechanisms, thus setting a good example of the effective functioning of the global governance system. Ahead of COP, the hosts facilitated related parties to reach a consensus on key issues of global climate governance through plenty of communication[a], paving the way for the conference to be held effectively. During COP26, the hosts set a series of agendas to actively create opportunities for full and effective multi-stakeholder discussions on specific issues. Finally, COP produced a series of governance mechanisms and solutions, including phasing down coal, curtailing deforestation, cutting methane emissions, etc.

It has been argued that the outcomes of COP26 were a step backward from the COP26 goals due to the failure to adhere to the 1.5°C target, use the specific term "phase out coal" in the coal power retirement statement, and reach a consensus on global carbon neutrality by 2050 (Arora and Mishra, 2021). However, the success of COP mainly depends on whether it preserves the existing climate governance system and vigorously advances multilateral climate processes. At COP26, the hosts promoted negotiations and consultations on key issues among various agents at different levels by organizing theme days based on previous summits, negotiations and consultations, and ministerial meetings. The parties also paid attention to driving global climate cooperation using the successful experience of the Paris Agreement, such as pushing forward multilateral processes through bilateral consultations. The U.S.—China Joint Glasgow Declaration on Enhancing Climate Action in the 2020s effectively boosted confidence in global climate governance, promoted multiple agencies, built a consensus on many key issues, and finally reached the Glasgow Climate Pact. A series of implementation alliances and agendas were reached at COP26, including the Glasgow Leaders' Declaration on Forests and Land Use, the Global Methane Pledge, the Statement on International Public Support for the Clean Energy Transition, the Declaration on Accelerating the Transition to 100% Zero-Emission Cars and Vans and the Global Energy Alliance for People and Planet (GEAPP), the Breakthrough Agenda and the Powering Past Coal Alliance, among others. Significant progress has been made in multilateral processes for global climate governance, allowing humanity's response to climate change to eventually keep pace with the worsening global climate crisis (Figueres, 2021). As stated in the COP26 world leaders summit-presidency summary, the Summit showed the Paris Agreement is working and made progress in key areas.

2.1. *COP26 set issues through extensive communication in advance of the summit and learned from the experience of the Paris Agreement in promoting international cooperation, laying a foundation for building consensus*

Stakeholders were engaged in close consultations on multiple issues of interest prior to COP26. For example, China, the US, and the EU held close consultations on bilateral climate cooperation before and during COP26 to better understand their respective positions and key issues of global climate governance, contributing to the consensus on issues. Finally, the hosts set a series of ambitious goals in four major areas based on extensive pre-COP communication. These included securing global-net-zero by mid-century and keeping 1.5°C within reach by phasing out coal, curtailing deforestation, accelerating the production of electric vehicles, making renewable investments, adapting to protect communities and natural habitats—including ecosystem protection and restoration, adaptation to investment, mobilization of finance, collaborative participation by international financial institutions to ensure developed countries receive $100 billion in climate finance

[a] The COP26 President concludes constructive discussions with China on climate action, https://www.gov.uk/government/news/cop26-president-concludes-constructive-discussions-with-china-on-climate-action

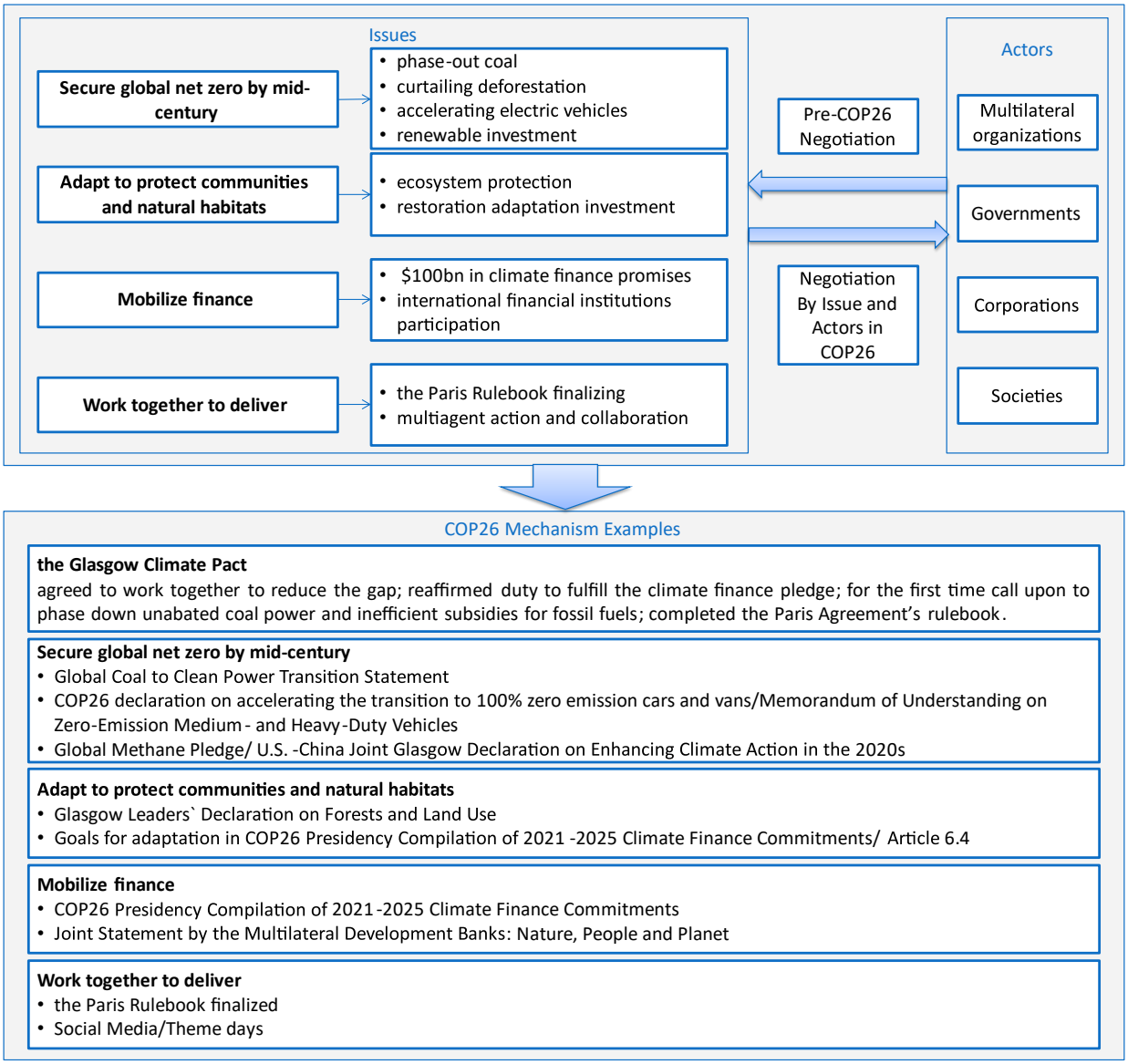

Fig. 1. A review of COP26 achievements under the Issue-Actor-Mechanism Framework.

promises, finalizing the Paris Rulebook, and facilitating multiagency action and collaboration.

2.2. *The summit is another milestone in global climate governance following the Paris Agreement; it not only upheld the goals, principles, and policy approaches of the Paris Agreement to achieve a balance between ambition and actions but also laid the institutional and capacity foundation for subsequent global climate governance*

The summit achieved certain consensus and progressed in all areas, including mitigation, adaptation, finance, technology transfer, and capacity building. Ahead of COP26, 156 countries had put forth new or updated NDCs in line with their national circumstances, among which 93 set more ambitious NDCs. At COP26, countries such as Thailand, Israel, Vietnam, Nigeria, and India came up with carbon neutrality targets. The Glasgow Climate Pact reiterated the goal of limiting global warming to well below 2°C and aiming for 1.5°C and stressed that achieving 1.5°C would require enhanced emission reduction efforts. As countries collectively launched a Decade of Action for Climate Empowerment, the mantra "actions speak louder than words" became an important trend, including raising ambition, increasing climate finance, strengthening public-private partnerships, and carrying out global stocktakes. COP26 concluded six years of negotiations on the Paris Rulebook. Pragmatic and balanced results were achieved on issues including Articles 6 and 13. A framework for building a global carbon market was established, which mandated that 5% of the revenue from transactions, as outlined in Article 6.4, would be collected and transferred to the Adaptation Foundation and that double-counting would be avoided. The transitional mechanism for the Clean Development Mechanism (CDM) was confirmed, and the enhanced transparency framework referred to in Article

13 was determined.

2.3. *COP26 finally reached a breakthrough consensus on the key issues of concern to multiple parties and produced a series of new global climate governance approaches, such as emissions reduction targets, coal phase-out, halting deforestation, methane, and climate finance*

The Glasgow Climate Pact stressed that achieving a target of 1.5°C would require a 45% decrease in global CO_2 emissions by 2030 over the 2010 level and confirmed the global stocktake in 2022 through the following steps: 1) proposed for the first time the phasing down of unabated coal power, requiring a reduction of unabated coal power and inefficient fossil fuel subsidies; 2) set a more ambitious climate finance goal despite the risk of failing again, calling for a complete review of the post-2025 new quantitative finance goal in 2024 and doubling the 2019 levels of adaptation finance to parties of developing countries by 2025; 3) decided to establish and immediately launch the 2-year Glasgow-Sharm el Sheikh Work Programme on the Global Goal on Adaptation, to start as soon as possible. Funding through the Santiago Network was arranged to support technical assistance to parties of developing countries to help address and mitigate loss and damages and, at the same time, carry out the "Glasgow Dialogue" concerning the financing mechanism for loss and damage.

Apart from the Glasgow Climate Pact, 23 countries committed to stopping coal use in the Global Coal to Clean Power Transition Statement for the first time. Over 120 countries signed the Glasgow Leaders' Declaration on Forests and Land Use, aiming to halt and reverse forest loss and land degradation by 2030, supply funds, and make 75% of forest commodity supply chains sustainable. Over 100 countries signed the Global Methane Pledge to reduce methane emissions by 30% by 2030; although China did not sign the pledge, it made a methane reduction commitment in the U.S.-China Joint Glasgow Declaration on Enhancing Climate Action in the 2020s.

2.4. *COP26 provided innovative issue-oriented discussion opportunities for multiple agencies to mobilize stakeholders and actors actively participating in global climate governance*

Before and during COP26, many businesses, industrial associations, banking institutions, and other non-governmental agents and actors were actively engaged in sectoral climate governance discussions, with clear and concrete global climate governance targets and established pathways. For example, the COP26 Declaration on Accelerating the Transition to 100% Zero-Emission Cars and Vans proposed zero emissions for all new car and van sales by 2040 globally and by 2035 in leading markets. A similar Memorandum of Understanding (MOU) was signed for medium- and heavy-duty vehicles, namely the Memorandum of Understanding on Zero-Emission Medium- and Heavy-Duty Vehicles, aiming for 30% and 100% net zero-emission vehicles by 2030 and 2040, respectively. The COP 26 Declaration—International Aviation Climate Ambition Coalition— proposed to achieve net-zero CO_2 emissions from aviation by 2050. Multilateral development banks pledged in the Joint Statement by the Multilateral Development Banks: Nature, People, and Planet to promote the mainstreaming of nature issues in policies, analyses, assessment, suggestions, investments, and operations.

As shown in Fig. 1, COP26 is a classic example of the Issue-Actor-Mechanism Framework theory for global governance, which set a series of governance issues in response to multiagency concerns, and made progress in addressing key issues referred to in the Paris Agreement, such as mitigation, adaptation, finance, technology, and capacity building. Various venues, including theme days, the world leaders summit, ministerial consultations, and negotiations provided conditions for full discussion and consensus-building on the climate governance agenda to multiple related agencies throughout the conference. Eventually, COP26 established a series of multilateral mechanisms, finalized the Paris Rulebook, left unresolved by COP25, and mentioned coal phase-down for the first time. With the aim of keeping 1.5°C alive, COP26 further clarified Global Stocktake, transparency, and other guarantee mechanisms and strengthened the scope and intensity of current climate governance (UNEP, 2021b). Therefore, COP26 successfully championed and implemented the Paris Agreement, ensuring the effectiveness of the UNFCCC-based international multilateral governance system for addressing climate change and advancing the process of global climate governance. In this way, COP26 represented another milestone in global climate governance following the Paris Agreement.

3. Post-COP26 challenges and outlook

With the pandemic still raging and the international geopolitical environment becoming more complex and even worsening, climate change is gradually affecting the socioeconomic system as a whole; thus, our climate governance requires more resilient global system thinking and reforms (D'Orazio, 2021). COPs have effectively driven consensus among countries, but there are still many disagreements and issues that need to be resolved through concerted efforts. Given the inadequate implementation of concrete actions, a lack of cooperation on tough issues, the possibility of exacerbating conflicts when tackling climate change, the dependence on fossil fuels, energy security and energy poverty, and insufficient synergies between addressing climate change and other areas, countries should adopt a pragmatic mindset, reach constructive consensus in

time and take tangible actions.

3.1. *Taking concrete actions to actively tackle the climate crisis will become a mainstream direction with an urgent need for the active and systematic multiagency engagement in climate governance*

Boosting climate ambition is important, but action is far more valuable than goals (Watts, 2021). Countries should extensively explore a wide range of issues, such as raising global climate ambitions, establishing non-CO_2 greenhouse gas (GHG) controls, and coordinating climate governance with an open mind. However, achieving the Paris Agreement goals requires more actions than words, so countries urgently need to take concrete actions (Xinhua, 2021). Developed countries, in particular, need to fulfill their climate action targets and climate finance commitments to prevent these targets and commitments from failing again (Roberts et al., 2021) while avoiding rule-of-law uncertainties in addressing climate change. Concrete actions entail active social and multiagency engagement. Countries need to mobilize the participation of multiple agencies in climate governance in the light of their national circumstances to establish green production and consumption systems, explore best practices to promote active multiagency participation in economic and social transition, and to provide a reference for developing countries to address climate change.

3.2. *Through global climate cooperation, countries should have the courage to tackle tough problems and strive to make progress in the implementation path for addressing climate change and core emission reduction issues*

The agenda for future climate cooperation should not circumvent difficulties but focus on key issues and key links. Current climate cooperation presents two easy-hard relationships: first, it is hard to reach a consensus on the implementation path and concrete actions for addressing climate change, including finance and technology, among interested parties, while it is easy for them to agree on the ambition to tackle climate change. Second, it is hard to build a consensus on core issues regarding reducing CO_2 emissions in response to climate change. At the same time, it is easy to agree on non-CO_2 emissions reduction, including methane emissions reduction and curbing deforestation. Moreover, there is an urgent need to achieve consensus on building a sustainable supply chain based on the fundamental reality of the global supply chain to clarify the goals and pathways toward a sustainable supply chain based on the premise of win-win cooperation. It is important to acknowledge that all related issues can potentially contribute to addressing climate change, but only raising ambition without clarifying the implementation path, or merely promoting non-CO_2 emissions reduction without tackling tough CO_2-related issues, will make it difficult to establish effective climate governance. Therefore, countries should strengthen communication and cooperation and tough issues.

3.3. *International cooperation and competition should not jeopardize climate change response, and the implementation of carbon pricing and financing mechanisms should avoid exacerbating international conflicts*

Considering that climate change has always been a major threat to the survival of mankind and that the international political and economic situation is becoming increasingly confrontational, promoting international political and economic cooperation is indeed conducive to the fight against climate change (Paroussos et al., 2019). Countries should take responsible actions, strengthen communication and cooperation and avoid misjudgments to ensure both competition and cooperation are beneficial rather than detrimental in addressing climate change. In the process of building a global carbon pricing mechanism, we should fully respect the differences in national circumstances and set up carbon pricing and financing mechanisms with the goal of driving the green and low-carbon structural transformation of trade and financial systems rather than setting green barriers. A one-size-fits-all approach to promoting carbon pricing, financing mechanisms, and a standards system is likely to undermine the interests of developing countries and their willingness and ability to participate in the fight against climate change (Eicke et al., 2021). Countries should work together to step up efforts to deal with the changes in carbon pricing and financing mechanisms and design an implementation mechanism, taking into account the differences unique to their national transition, to avoid further conflicts, uncertainties, and damage to international cooperation on climate change.

3.4. *While different countries are at different stages of energy transition, they should join hands to balance energy security, carbon reduction, and development*

Given different development stages and resource endowments, not every country adopts the same timeline and path for low-carbon energy transition (Safari et al., 2019). However, there is no doubt that the process of low-carbon energy transition will not be smooth for both developed and developing countries. The new global energy crisis, which began in the first half of 2021 along with soaring prices of fossil fuels like natural gas and coal, may significantly affect how governments choose policy pathways in terms of energy security and addressing climate change (Gilbert et al., 2021; Shaffer, 2021), bringing new uncertainties to the low-carbon global energy transition, while fully demonstrating how a low-carbon energy transition is an arduous and complex undertaking. While the developmental stage and transition pathways may vary from country to country based on national circumstances, balancing energy security, carbon reduction, and economic development is a common challenge for all countries. There is room for mutual learning from solutions and technical roadmaps. A successful phase-out of coal requires new development models, policy measures, and cooperative efforts (Kalkuhl et al., 2019; Cui et al.,

2021). European and American countries will have to phase down oil and gas simultaneously. Developed countries have a responsibility to work with developing countries to explore low-carbon energy development strategies for retiring coal and gas, creating an opportunity for a global response to climate change and deeper climate cooperation (Miyamoto and Takeuchi, 2019).

3.5. *Countries should enhance their adaptability to climate change and strengthen their coordinated governance of climate change in many areas, including biodiversity*

As climate risks grow, it has become increasingly necessary for countries to work together to enhance their adaptability to climate change and strive to balance mitigation and adaptation. Financial consideration is an unavoidable issue in the process. At COP26, developed countries raised their ambitions regarding financial support but might fall short again in affecting the bigger picture of global climate governance. Regarding climate finance, the developing world is showing increasingly strong demand for a higher share of adaptation finance (Chapagain et al., 2020). COP26 increased discussions on related issues such as curbing deforestation, establishing sustainable supply chains and biodiversity conservation programs, and promoting synergies among issues across multiple areas. An important direction for future multilateral climate and environmental processes is facilitating positive progress in SDGs, including climate-related ones. It is expected that discussions on the coordinated governance of climate change will be strengthened in the second part of the Convention on Biological Diversity (CBD) COP15. COP27 will be hosted by Egypt, a developing country, where issues such as adaptation to climate change and reduction of loss and damage will be priorities of discussion. Sharm el Sheikh, formerly the venue of CBD COP14, is expected to be a meeting point for the coordinated governance of biodiversity and climate change and to witness greater synergistic processes between biodiversity conservation and addressing climate change at COP27.

4. China will actively safeguard and participate in climate governance through concrete actions

As China's President XI Jinping emphasized in his remarks at the COP26 World Leaders Summit, "successful governance relies on solid action", China believes that actions speak louder than words in the global response to climate change. China has incorporated carbon dioxide peaking and carbon neutrality goals into the overall national strategy and the five-sphere integrated plan and will work unswervingly to achieve the goals and promote green transformation on all fronts. In the run-up to COP26, China issued, in succession, the Guidelines of the Central Committee of the CPC and the State Council on Working Guidance for Carbon Dioxide Peaking and Carbon Neutrality in Full and Faithful Implementation of the New Development Philosophy[b], and the Action Plan for Carbon Dioxide Peaking Before 2030[c]. A white paper entitled "Responding to Climate Change: China's Policies and Actions" submits China's Achievements, New Goals and New Measures for Nationally Determined Contributions. And a report named China's Mid-Century Long-Term Low Greenhouse Gas Development Strategy is published as well. These documents clarified the overall thinking and roadmap for China's carbon dioxide peaking before 2030 and achieving carbon neutrality before 2060 (Sun, 2022). China is now stepping up its efforts to improve the 1 + N policy system, which will eventually be a system of national and local policies and measures for both carbon dioxide peaking and carbon neutrality in all sectors and industries. The 1 + N policy system will provide comprehensive support for China to achieve carbon dioxide peaking and carbon neutrality goals by specifying the targets, pathways, and policies and finally become a Chinese solution to carbon dioxide peaking and carbon neutrality (CAS-SDG, 2021; Liu, 2021).

China firmly champions and safeguards the multilateral mechanisms and processes for climate governance and attaches importance to cooperation with the international community to tackle the global climate crisis and promote global cooperation on carbon neutrality. The UNFCCC Secretariat, UK Presidency, United States, European Union, and other countries had close consultations prior to and at COP26. As always, China supports and upholds the UNFCCC and the Paris Agreement, keeps to the goals, principles, and policy approaches of the Paris Agreement to achieve a balance between ambition and action, and stands ready to play a positive role in the cooperation on climate change and adopt systematic solutions to climate change. Meanwhile, China has pledged to cease building new coal-fired power projects abroad and pledges to step up support for other developing countries in developing green and low-carbon energy. Moving forward, China will actively engage in green BRI projects and South-South cooperation to help developing countries address climate change.

China attaches importance to inheriting the successful experience of the Paris Agreement and promoting multilateral governance processes through bilateral cooperation, with breakthroughs made in bilateral climate cooperation with the US at Glasgow. In 2021, the two countries held more than 31 intensive climate talks and communication, laying the foundation for releasing the U.S.-China Joint Glasgow Declaration on Enhancing Climate Action in the 2020s during COP26. The two reached an important consensus on four areas based on the China-U.S. Joint Statement Addressing the Climate Crisis in April 2021, including enhancing climate action, working together to make COP26 a success, actively implementing the

[b] Full Text: http://english.www.gov.cn/policies/latestreleases/202110/25/content_WS61760047c6d0df57f98e3c21.html
[c] Full Text: http://english.www.gov.cn/policies/latestreleases/202110/27/content_WS6178a47ec6d0df57f98e3dfb.html

Joint Declaration, establishing a working group on enhancing climate change in the 2020s, releasing the U.S.—China Joint Glasgow Declaration on Enhancing Climate Action in the 2020s, expediting the implementation of China—U.S. climate cooperation and contributing to the formation of consensus on the Glasgow Climate Pact. China will continue to actively engage in dialogue with the EU, US, and other economies on climate cooperation through bilateral mechanisms and achieve a series of positive results.

China will continue to work on creating synergies from the coordinated governance of climate change and promote the combination of climate governance with other issues. China places emphasis on integrating climate change response into the transformation of its economic and social systems, with a focus on expediting the development of industrial structures, production modes, living patterns, and spatial zones that will conserve resources and protect the environment, build its economic and social development upon green transition, and adhere to the coordinated promotion of carbon reduction, pollution reduction, green transition, and growth. The coordinated governance of climate and the environment will also be a priority, and the synergies between pollution abatement and carbon reduction should be further promoted. At the same time, China should combine climate and biodiversity governance and facilitate synergies to be achieved in addressing climate change in the second part of CBD COP15.

Acknowledgements. This work was jointly supported by the National Natural Science Foundation of China (Grant Nos. 72140007, 71804178) and the National Key Research and Development Program of China (Grant No. 2018YFA0606504).

REFERENCES

Arora, N. K., and I. Mishra, 2021: COP26: More challenges than achievements. *Environmental Sustainability*, **4**, 585–588, https://doi.org/10.1007/s42398-021-00212-7.

Chapagain, D., F. Baarsch, M. Schaeffer, and S. D'Haen, 2020: Climate change adaptation costs in developing countries: Insights from existing estimates. *Climate and development*, **12**, 934–942, https://doi.org/10.1080/17565529.2020.1711698.

Chinese Academy of Sciences' Sustainable Development Strategy Study Group (CAS-SDG), 2021: *China Sustainable Development Report 2020 – Exploring Pathways Towards Carbon Neutrality*. Science Press. (in Chinese)

Cui, R. Y., and Coauthors, 2021: A plant-by-plant strategy for high-ambition coal power Phase-out in China. *Nature Communications*, **12**, 1468, https://doi.org/10.1038/s41467-021-21786-0.

D'Orazio, P., 2021: Towards a post-pandemic policy framework to manage climate-related financial risks and resilience. *Climate Policy*, **21**, 1368–1382, https://doi.org/10.1080/14693062.2021.1975623.

Eicke, L., S. Weko, M. Apergi, and A. Marian, 2021: Pulling up the carbon ladder? Decarbonization, dependence, and third-country risks from the European carbon border adjustment mechanism. *Energy Research & Social Science*, **80**, 102240, https://doi.org/10.1016/j.erss.2021.102240.

Figueres, C., 2021: Cop26 took us one step closer to combating the climate crisis. The Guardian. [Available online from https://www.carbonbrief.org/daily-brief/coal-shares-lose-ground-after-glasgow-climate-deal].

Gilbert, A., M. D. Bazilian, and S. Gross, 2021: The emerging global natural gas market and the energy crisis of 2021–2022. [Available online from https://payneinstitute.mines.edu/the-emerging-global-natural-gas-market-and-the-energy-crisis-of-2021-2022/].

International Energy Agency, 2021: World Energy Outlook 2021. [Available online from https://www.iea.org/reports/world-energy-outlook-2021].

IPCC, 2021: *Climate Change 2021*: *The Physical Science Basis*. *Working Group I Contribution to the Sixth Assessment Report of the Intergovernmental Panel on Climate Change*. Cambridge University Press.

Kalkuhl, M., J. C. Steckel, L. Montrone, M. Jakob, J. Peters, and O. Edenhofer, 2019: Successful coal phase-out requires new models of development. *Nature Energy*, **4**, 897–900, https://doi.org/10.1038/s41560-019-0500-5.

Liu, H. Q., 2021: The carbon brief interview: Prof Wang Yi and Prof Wang Zhongying. Carbon Brief. [Available online from https://www.carbonbrief.org/the-carbon-brief-interview-prof-wang-yi-and-prof-wang-zhongying].

Miyamoto, M., and K. Takeuchi, 2019: Climate agreement and technology diffusion: Impact of the Kyoto Protocol on international patent applications for renewable energy technologies. *Energy Policy*, **129**, 1331–1338, https://doi.org/10.1016/j.enpol.2019.02.053.

Paroussos, L., A. Mandel, K. Fragkiadakis, P. Fragkos, J. Hinkel, and Z. Vrontisi, 2019: Climate clubs and the macro-economic benefits of international cooperation on climate policy. *Nature Climate Change*, **9**, 542–546, https://doi.org/10.1038/s41558-019-0501-1.

Ray, R. L., V. P. Singh, S. K. Singh, B. S. Acharya, and Y. P. He, 2022: What is the impact of COVID-19 pandemic on global carbon emissions. *Science of The Total Environment*, **816**, 151503, https://doi.org/10.1016/j.scitotenv.2021.151503.

Roberts, J. T., R. Weikmans, S.-A. Robinson, D. Ciplet, M. Khan, and D. Falzon, 2021: Rebooting a failed promise of climate finance. *Nature Climate Change*, **11**, 180–182, https://doi.org/10.1038/s41558-021-00990-2.

Safari, A., N. Das, O. Langhelle, J. Roy, and M. Assadi, 2019: Natural gas: A transition fuel for sustainable energy system transformation. *Energy Science & Engineering*, **7**, 1075–1094, https://doi.org/10.1002/ese3.380.

Shaffer, S., 2021: Is Europe's energy crisis a preview of America's? [Available online from https://www.realclearworld.com/2021/10/06/is_europes_energy_crisis_a_preview_of_americas_797650.html].

Sun, J., 2022: One more step forward along the long journey: On the UN climate change conference in Glasgow. [Available online from http://www.cpifa.org/en/cms/book/349].

UNEP, 2021a: Emissions gap report 2021. [Available online from https://www.unep.org/resources/emissions-gap-report-2021].

UNEP, 2021b: COP26 ends with agreement but falls short on climate action. UNEP. [Available online from https://www.unep.org/news-and-stories/story/cop26-ends-agreement-falls-short-climate-action].

Watts, J., 2021: China calls for concrete action not distant targets in last week of Cop26. The Guardian. [Available online from https://greeninstitute.ng/blog1/china-calls-for-concrete-action-not-distant-targets-in-last-week-of-cop26].

Xinhua, 2021: Interview: Cooperation, delivery crucial in tackling climate change, says head of Chinese delegation to COP26. Xinhua. [Available online from http://www.news.cn/english/2021-11/13/c_1310307725.htm].

Xue, L., and H. Z. Yu, 2017: Towards a public management paradigm for global governance: An analysis based on an issue-actor-mechanism framework. *Social Sciences in China*, **38**, 26–45, https://doi.org/10.1080/02529203.2017.1268362.

ADVANCES IN ATMOSPHERIC SCIENCES, VOL. 39, AUGUST 2022, 1217–1228

• PERSPECTIVES •

Climate Warming Mitigation from Nationally Determined Contributions※

Bo FU[1], Jingyi LI[1], Thomas GASSER[2], Philippe CIAIS[3], Shilong PIAO[1], Shu TAO[1], Guofeng SHEN[1], Yuqin LAI[1], Luchao HAN[1], and Bengang LI*[1]

[1]*Sino-French Institute for Earth System Science*, *MOE Key Laboratory for Earth Surface Processes*, *College of Urban and Environmental Sciences*, *Peking University*, *Beijing* 100871, *China*

[2]*International Institute for Applied Systems Analysis (IIASA)*, 2361 *Laxenburg*, *Austria*

[3]*Laboratoire des Sciences du Climat et de l'Environnement*, *CEA-CNRS-UVSQ*, 91191 *Gif-sur-Yvette*, *France*

(Received 26 October 2021; revised 29 March 2022; accepted 30 March 2022)

ABSTRACT

Individual countries are requested to submit nationally determined contributions (NDCs) to alleviate global warming in the Paris Agreement. However, the global climate effects and regional contributions are not explicitly considered in the countries' decision-making process. In this study, we evaluate the global temperature slowdown of the NDC scenario (ΔT = 0.6°C) and attribute the global temperature slowdown to certain regions of the world with a compact earth system model. Considering reductions in CO_2, CH_4, N_2O, BC, and SO_2, the R5OECD (the Organization for Economic Co-operation and Development in 1990) and R5ASIA (Asian countries) are the top two contributors to global warming mitigation, accounting for 39.3% and 36.8%, respectively. R5LAM (Latin America and the Caribbean) and R5MAF (the Middle East and Africa) followed behind, with contributions of 11.5% and 8.9%, respectively. The remaining 3.5% is attributed to R5REF (the Reforming Economies). Carbon Dioxide emission reduction is the decisive factor of regional contributions, but not the only one. Other greenhouse gases are also important, especially for R5MAF. The contribution of short-lived aerosols is small but significant, notably SO_2 reduction in R5ASIA. We argue that additional species beyond CO_2 need to be considered, including short-lived pollutants, when planning a route to mitigate climate change. It needs to be emphasized that there is still a gap to achieve the Paris Agreement 2-degree target with current NDC efforts, let alone the ambitious 1.5-degree target. All countries need to pursue stricter reduction policies for a more sustainable world.

Key words: climate mitigation, nationally determined contributions, attribution, regional contribution, integrated assessment models

Citation: Fu, B., and Coauthors, 2022: Climate warming mitigation from nationally determined contributions. *Adv. Atmos. Sci.*, **39**(8), 1217–1228, https://doi.org/10.1007/s00376-022-1396-8.

Article Highlights:

- Compared with a no climate policy scenario, the NDC scenario shows a slowed global warming of 0.6°C by the end of the century, although there is still a gap when considering the Paris Agreement target.
- R5OECD and R5ASIA are the top two contributors to global warming mitigation, accounting for 39.3% and 36.8% on average, respectively.
- CO_2 reduction is the decisive factor of regional contributions to climate mitigation, while non-CO_2 reductions are small but significant.

1. Introduction

Anthropogenic activities have been the main driving force behind climate change, and the impact of global warming on human society and natural systems is increasing (IPCC 2021). The Paris Climate Agreement has set a target of 2°C above the preindustrial level while also pursuing a 1.5°C target (UNFCCC 2015). Mitigating global climate change requires domestic emission reduction policies. Individual countries are supposed to submit nationally determined contributions (NDCs) to achieve these global climate goals (UNFCCC 2015).

※ This paper is a contribution to the special issue on Carbon Neutrality: Important Roles of Renewable Energies, Carbon Sinks, NETs, and non-CO_2 GHGs.

* Corresponding author: Bengang LI
Email: libengang@pku.edu.cn

NDCs are bottom-up commitments, not top-down allocations such as the Kyoto Protocol, which mainly consider their own ambitions and feasibility. Other countries' emission reductions or global climate effects are not necessarily considered. It is meaningful to quantify the regional contributions to global climate change mitigation. Previous literature has conducted some research on regional contributions. Regional carbon emission reductions are the most intuitive evaluation indicator and are widely used [e.g., (Roelfsema et al., 2020)]. Some studies also use emissions metrics (Denison et al., 2019). Historical emissions of long-lived gases remain important for future contributions to global warming and play an important role in strong mitigation scenarios (Skeie et al., 2021). Mitigating non-CO_2 emissions such as SLCFs is also critical for meeting the Paris Agreement ambitions and sustainable development goals (Lund et al., 2020). However, there is currently no literature that absolutely attributes the slowdown of temperature rise to national emission reductions. This study aims to calculate the relative contributions by region to climate mitigation, providing a perspective on the emission reduction impact of the NDC scenario compared with the no climate policy (NP) scenarios.

Thus, this study first estimates the global temperature slowdown and then attributes this response to particular world regions. Section 2 describes the data and methods, including scenario datasets, OSACR v3.1 model, simulation framework and attribution method, and uncertainty analysis. Section 3 describes the climate mitigation of the NDC scenario relative to the NP scenario. Section 4 attributes climate mitigation to regional emission reductions. Finally, section 5 presents discussions and conclusions.

2. Data and methods

2.1. *Scenario datasets*

The CD-LINKS project (Linking Climate and Development Policies - Leveraging International Networks and Knowledge Sharing) is an international collaborative project that brings together research from integrated assessment modeling and explores the complex interplay between climate action and development through global and national perspectives (http://www.cd-links.org/). This study uses emission scenario datasets from the CD-LINKS project to drive a simple climate model. We downloaded CD-LINKS scenario datasets from IMAC 1.5°C Scenario Explorer hosted by IIASA (Huppmann et al., 2018), available at http://data.ene.iiasa.ac.at/iamc-1.5c-explorer. Emissions of five species are considered in this study: carbon dioxide (CO_2), methane (CH_4), nitrous oxide (N_2O), black carbon (BC), and sulfur dioxide (SO_2). A set of consistent national and global low-carbon development pathways that take current national policies and nationally determined contributions (NDCs) is developed in the CD-LINKS project as an entry point for short-term climate action and then transition to long-term goals of 1.5°C and 2°C as defined by the Paris Agreement (Roelfsema et al., 2020). The CD-LINKS scenarios were originally developed in late 2017.

The NP scenario and NDC scenario are the two scenarios at the core of this paper. Emissions in the NDC scenario relative to the NP scenario are considered mitigation, and the differences in global mean surface temperature (GMST) and atmospheric CO_2 are the intended targets to be attributed. The 2-degree scenario (each country implements its current implemented policies until 2020 and starts with cost-effective implementation to achieve the 2-degree target between 2020 and 2030 with high probability) and the 1.5-degree scenario (each country implements current implemented policies until 2020 and starts with cost-effective implementation to achieve the 1.5-degree target between 2020 and 2030 with high probability) are also simulated as supporting data to show the mitigation gaps of climate goals and current NDC. Detailed information on the scenario definitions can be found at http://data.ene.iiasa.ac.at/iamc-1.5c-explorer. For each scenario, data from the five integrated assessment models (IAMs) are available: AIM/CGE 2.1, IMAGE 3.0.1, MESSAGEix-GLOBIOM 1.0, REMIND-MAgPIE 1.7-3.0, and WITCH-GLOBIOM 4.0. These IAMs differ at the national and sectoral integration levels, and they simulate climate policy decisions in different ways. Therefore, there are differences in the emission data calculated by these IAMs.

In this study, the world is divided into five regions, the same as the shared socioeconomic pathways (SSP) database (Riahi et al., 2017). The five regions are abbreviated as the Organization for Economic Co-operation and Development in 1990 (R5OECD), Asian countries (R5ASIA), Latin America and the Caribbean (R5LAM), the Middle East and Africa (R5MAF), and the Reforming Economies (R5REF).

2.2. *OSCAR v3.1 model*

OSCAR v3.1 is used in this study to simulate and attribute climate change mitigation from the NDCs. OSCAR v3.1 is a reduced-complexity Earth system model that contains all the components needed to simulate climate change, including modules such as the carbon cycle, tropospheric and stratospheric chemistry, aerosols, and climate response (Gasser, Ciais et al., 2017, 2018, 2020). OSCAR v3.1 is available at https://github.com/tgasser/OSCAR/tree/v3.1. In addition, OSCAR is built as an emulator with parameters calibrated by more complex models or observations, such as CMIP5, WETCHIMIP, ACCMIP, and TRENDY, making it capable of emulating the sensitivity of models of superior complexity (Gasser et al., 2017). The model is driven by emission datasets of greenhouse gases and aerosol precursors, which calculate the corresponding changes in atmospheric concentrations before predicting radiation forcing and climate change. OSCAR has widely been used in projections and attributions in climate change communities (Ciais et al., 2013; Gasser et al., 2018), especially for regional climate contributions (Li et al., 2016; Fu et al., 2021). In this study, we use OSCAR v3.1 to simulate future GMST and atmospheric CO_2 changes in different scenarios and to attribute the contributions of climate mitigation to dif-

ferent regions.

2.3. *Simulation framework and attribution method*

The temperature mitigation (ΔT) between the NDC and NP scenarios represents the objective of this study, which reflects the climate change mitigation of NDC emission reductions relative to the no climate policy scenario. The temperature difference between the experiments in the NDC and NP scenarios is regarded as warming mitigation and is attributed to various regions of the world. First, we run a base simulation to obtain the temperature mitigation. The OSCAR model is driven by the NP scenario and NDC scenario data from CD-LINKS to simulate the global temperature in the two scenarios before calculating the temperature mitigation. $\left[\Delta_{\text{base}}T = T_{\text{NP}} - T_{\text{NDC}} = \text{OSCAR}\left(E_{\text{NP,globe}}\right) - \text{OSCAR}\left(E_{\text{NDC,globe}}\right)\right]$.

To attribute the temperature slowing specific to the regions, the "normalized marginal attribution method" is used in this study. Applying the normalized marginal attribution method is advised by the United Nations Framework Convention on Climate Change (UNFCCC) to solve nonlinear climate attribution problems (UNFCCC 2002). One study discussed seven attribution methods and concluded that the normalized marginal attribution method is one of the two most suitable for climate attribution (Trudinger and Enting, 2005). The normalized marginal attribution method evaluates the contributions of individual regions proportional to their marginal effects and constrains the total of individual contributions equal to the global effect. In many early studies, this method attributed climate changes to processes or specific regions (Ciais et al., 2013; Li et al., 2016; Fu et al., 2020, 2021).

To implement the normalized marginal method in this study, we ran the basic simulation, and changed the regional emissions mitigation of each region (noted as r_i) by a small fraction ε as input for each simulation and repeatedly calculated temperature mitigation ($\Delta_{r_i}T$). The mathematical expression is $\Delta_{r_i}T = T_{\text{NP}} - T_{\text{NDC},r_i-\varepsilon} = \text{OSCAR}\left(E_{\text{NP,globe}}\right) - \text{OSCAR}\left(E_{\text{NDC,globe}} + \varepsilon\left(E_{\text{NP},r_i} - E_{\text{NDC},r_i}\right)\right)$. The purpose of these marginal experiments is to calculate the marginal effect of emission reduction in each region. Then, the marginal effects are normalized to calculate the relative contributions of each region $\alpha_i = (\Delta_{\text{base}}T - \Delta_{r_i}T)/(\sum_{i=1}^{m}\Delta_{\text{base}}T - \Delta_{r_i}T)$ and the absolute contributions are calculated by $\alpha_i\Delta_{\text{base}}T$ following the normalization marginal method. The ϵ value is 0.1%, similar to early studies that applied the OSCAR model, while several studies found that the results are insensitive to ε values (UNFCCC 2002, Trudinger and Enting, 2005).

2.4. *Uncertainty analysis*

This study considers the uncertainties from two aspects: the model parameters and the scenario data. For parameter uncertainties, all simulations are run under a Monte Carlo ensemble (n = 3000). Parameters are randomly drawn from the pool available in OSCAR v.3.1. OSCAR has approximately 200 parameters, which play a role in the carbon cycle module, tropospheric and stratospheric chemistry, aerosols, climate response, etc. They are listed in the OSACR model manual (https://github.com/tgasser/OSCAR/blob/v3.1/MANUAL.pdf). As an emulator, different configurations of OSCAR emulate different models of higher complexity, so the Monte Carlo ensemble shows the model uncertainties. For scenario data, the CD-LINKS dataset contains scenario data from five different IAMs. Data from different IAMs have large variances, so we show both the average and the standard deviation of the results as well as the results for each IAM separately.

3. Climate mitigation from NDCs

As mentioned in section 2.3, this study focuses on the difference in climate effects between NDC and NP scenarios. Their carbon dioxide emissions are shown in red and orange in Fig. 1. In the NP scenarios, R5ASIA and R5OECD emit significantly more CO_2 than other regions, followed by R5MAF, while the CO_2 emissions of R5LAM and R5REF remain low for an extended time. Compared with the NP scenario, R5ASIA and R5OECD have the most prominent contributions to CO_2 emission reduction, with cumulative emission reductions of 123.01 PgC and 106.89 PgC, respectively. The reductions of R5REF are rather small, which can also be seen in Fig. 3. The ranges of CO_2 emissions under both the NP and NDC scenarios show significant growth after 2030. Although the ranges of CO_2 emissions are affected by the simulation results of different IAMs, the ranges of CO_2 mitigation are mainly derived from the variance of the NDC scenario. The other two scenarios (the 2-degree and 1.5-degree) are also shown in Fig. 1. These two ideal scenarios are significantly different from the NP and NDC scenarios. The carbon emissions scenario shows an overall downward trend, gradually reaching carbon neutrality in the future. The 2-degree scenario achieves carbon neutrality in 2062–78, while the 1.5-degree scenario achieves carbon neutrality ten to twenty years earlier than the 2-degree scenario. This is similar to the result of (van Soest et al. 2021), who reported the realization of carbon neutrality by 2065–80 (2-degree) and 2045–60 (1.5-degree). Obviously, to achieve the climate goals of the Paris Agreement, it is not sufficient to rely solely on the existing NDCs.

In addition to CO_2, the pathways of CH_4, N_2O, BC, and SO_2 are also considered in this study and used to drive the model. The cumulative reduction (for CO_2, CH_4, and N_2O) or annual reductions (for BC and SO_2) are shown in Fig. 3**.** Their emissions can be seen in Fig. 2**.** The region with the largest N_2O emission reductions is the R5OECD, with an average of 19.59 TgN. R5OECD, R5ASIA, and R5LAM contribute significantly to CH_4 emission reductions, with average emission reductions reaching 1975.36 TgC, 1627.76 TgC, and 1309.02 TgC, respectively. The critical regions for BC emission reduction are R5ASIA and R5LAM, both reaching approximately 0.02 TgC. SO_2 is mainly reduced in R5ASIA,

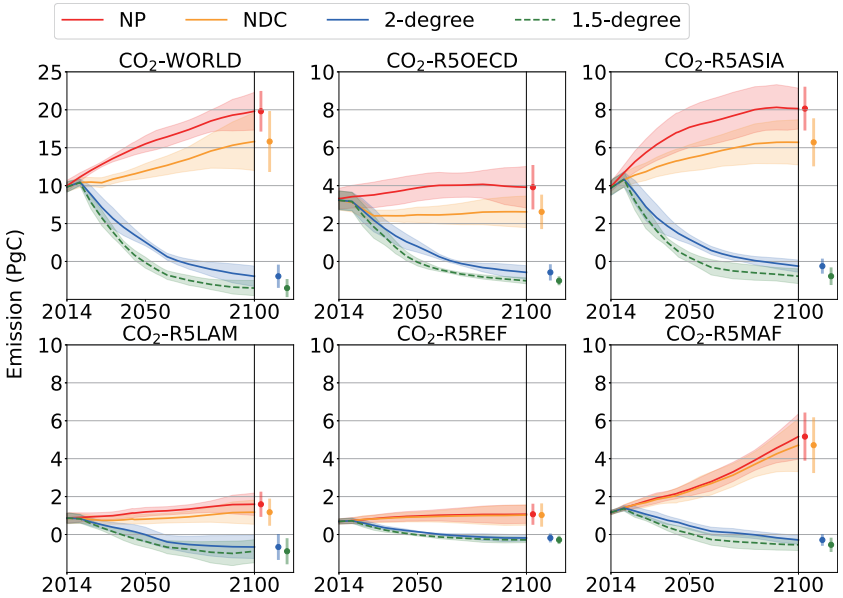

Fig. 1. CO_2 emissions of the R5 regions based on the CD-LINKS scenario dataset. Future CO_2 emissions in the R5 region under four climate scenarios. The line is the average of the results of the five emission IAMs, and the shaded areas show the range of the scenario data. "NP", "NDC", and "2-degree" scenarios are marked by red, orange, and solid blue lines. The "1.5-degree" scenario is marked by green dashed lines. Pathways of other species (CH_4, N_2O, BC, and SO_2) can be found in Fig. S1.

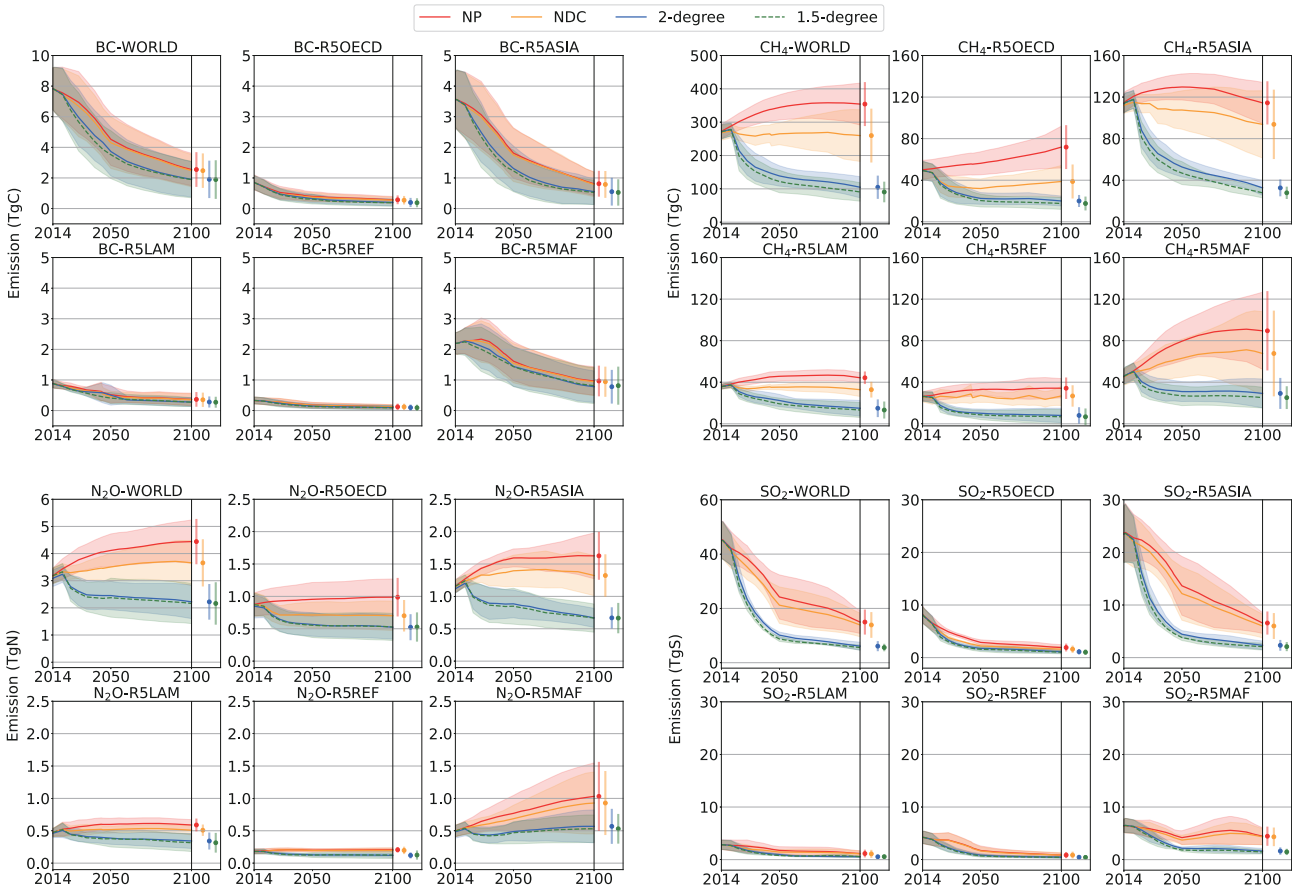

Fig. 2. CH_4, N_2O, BC, and SO_2 emissions of the R5regions based on the CD-LINKS scenario dataset. Future CH_4, N_2O, BC, and SO_2 emissions in the R5 region in four climate scenarios. The line is the average of the results of the five emission IAM and the shade shows the range of the scenario data. "NP", "NDC", and "2-degree" scenarios are marked by red, orange, and blue solid lines. "1.5-degree" scenario is marked by green dashed lines.

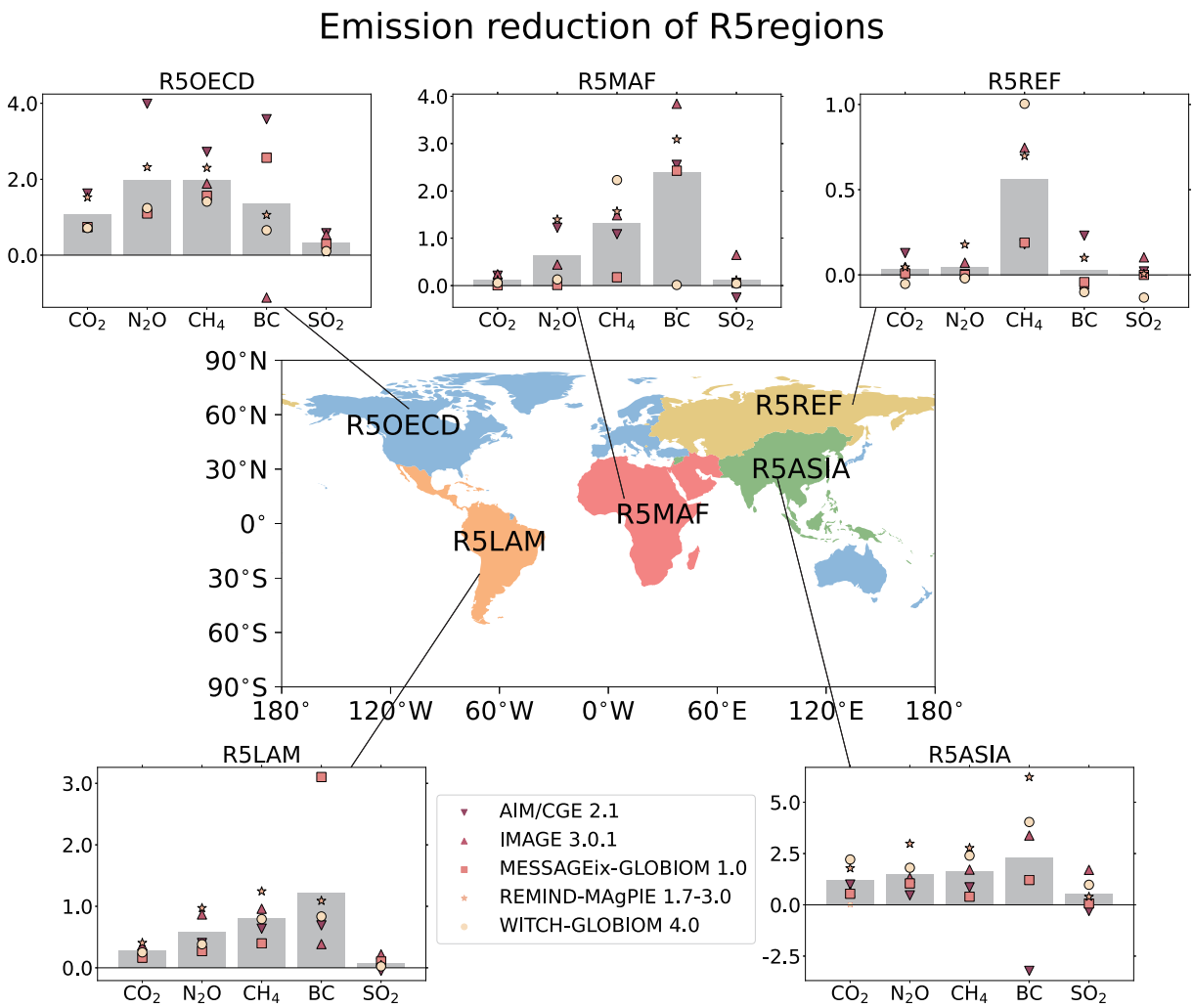

Fig. 3. The mitigation of CO_2, CH_4, N_2O, BC, and SO_2 emissions of the R5 regions based on the CD-LINKS scenario dataset. The map shows the regionalization (R5 regions) in this study. The bars around the map show emission reductions of NDC relative to NP scenarios. The cumulative reduction (for CO_2, CH_4, and N_2O) or annual reductions (for BC and SO_2) are shown here. The height of each column is a global emission difference, with the different colors representing the various R5 regions. The results are based on five IAMs are marked by different markers, and their average is shown with grey bars. The units are 100 PgC for CO_2, 10 TgN for N_2O, 1000 TgC for CH_4, 0.01 TgC for BC, and 1 TgS for SO_2 to plot the bars in one axis.

with an average of 0.57 TgS, accounting for more than 50% of global emission reductions. Notably, some data from specific IAMs show that the NDC scenario has larger regional emissions of some species than the NP scenario. For example, the emission reductions in R5REF obtained by the WITCH-GLOBIOM 4.0 simulation are small negative values except for CH_4. The emission reduction of BC in R5OECD obtained by IMAGE 3.0.1 simulation is –0.31 TgC, which is quite different from the results of other IAMs. There may be some inconsistency in how clean air policies are assumed in the IAMs. The uncertainty of IAMs is considerable, although they are less important to climate change than CO_2.

The increase in temperature and atmospheric CO_2 relative to preindustrial times (~1850) is simulated by OSCAR v3.1, driven by the CO_2, CH_4, N_2O, BC, and SO_2 scenario datasets from CD-LINKS (Fig. 4 and Table 1). The average of the five IAMs shows that the global CO_2 change relative to 1850 will reach 531.9±128.4 ppm in the NP scenario and 425.1±111.1 ppm in the NDC scenario in 2100. Adherence to NDC policy can avoid an increase of nearly 110 ppm in atmospheric CO_2. Table 1 shows the increase in atmospheric CO_2 (ΔCO_2) simulated using scenario datasets from five IAMs. For the NP scenario, AIM/CGE 2.1 and IMAGE 3.0.1 result in an increase of approximately 500 ppm, while MESSAGEix-GLOBIOM 1.0, REMIND-MAgPIE 1.7-3.0, and WITCH-GLOBIOM 4.0 result in an increase of approximately 550 ppm. For the NDC scenario, the results are also different; that is, AIM/CGE 2.1 and REMIND-MAgPIE 1.7-3.0 optimistically yield less than 400 ppm, while MESSAGEix-GLOBIOM 1.0 results are almost as high as 500 ppm. Comparing the effects of NP and NDC, the estimation of atmospheric CO_2 mitigation ranges from 56.05 ppm (MESSAGEEix-GLOBIOM 1.0) to 151.34 ppm (REMIND-

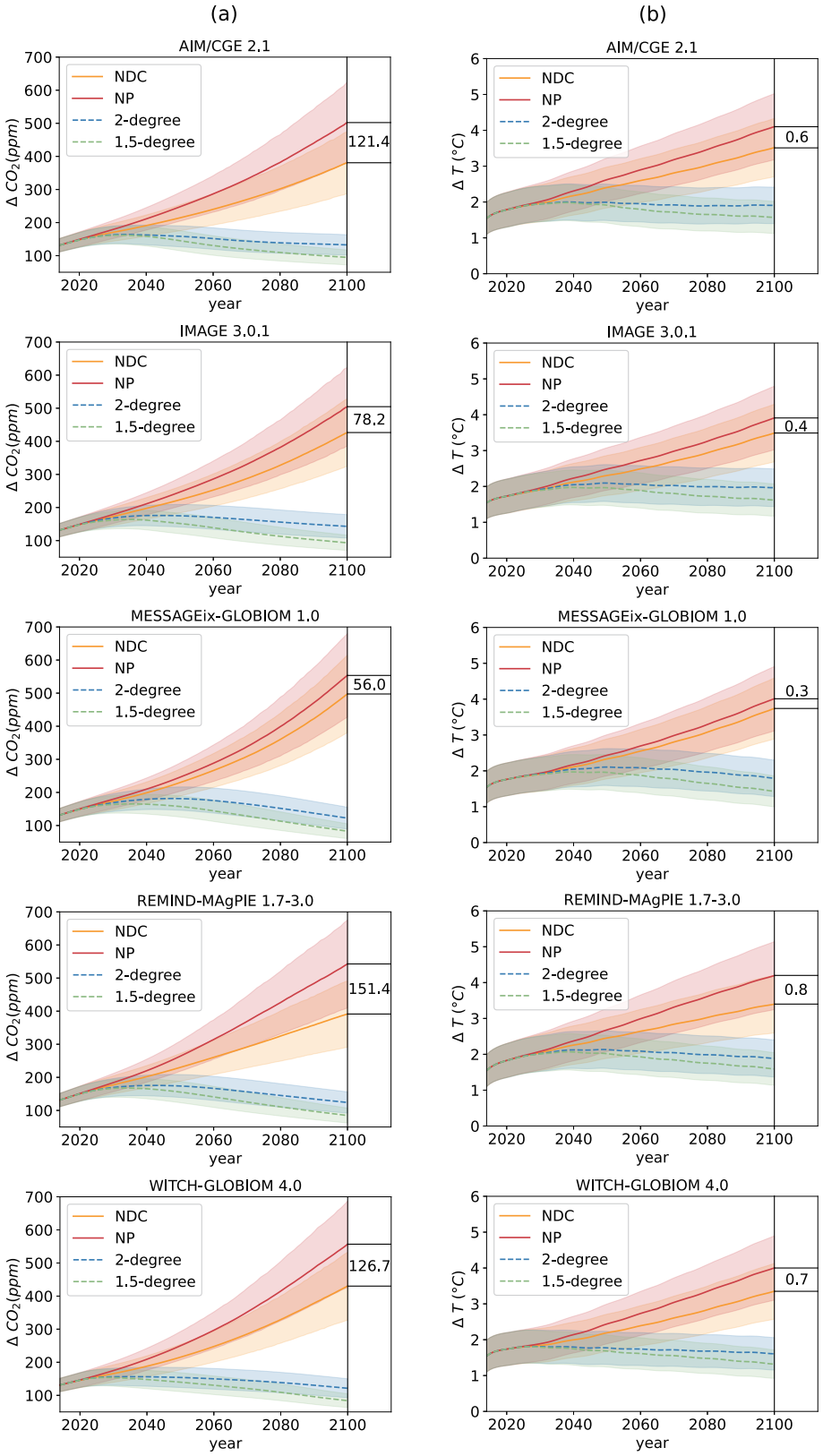

Fig. 4. Atmospheric CO_2 increase (ΔCO_2) and temperature change (ΔT) relative to preindustrial (1850) simulations for scenarios. (a) The simulation of ΔCO_2 based on emission data from the five IAMs. The mitigation of ΔCO_2 induced by NDC relative to NP is marked and valued in the figures. ΔCO_2 in the 2-degree and 1.5-degree scenarios are also shown in the figures for comparison. (b) The same as (a), but for ΔT. The mitigation of temperature increases is the core concern of this study and is attributed to regions in this study.

Table 1. Future CO_2 increase (ΔCO_2) and temperature changes (ΔT) relative to 1850 in 2100.

Model	NP	NDC	2-degree	1.5-degree
Future CO_2 increase ΔCO_2 (ppm)				
AIM/CGE 2.1	502.20±122.34	380.78±93.59	132.61±30.85	94.89±22.57
IMAGE 3.0.1	504.66±118.69	426.50±102.01	143.03±35.40	93.31±23.09
MESSAGEix-GLOBIOM 1.0	553.51±126.24	497.46±117.21	122.43±33.05	82.85±22.42
REMIND-MAgPIE 1.7-3.0	542.64±132.83	391.30±100.34	124.01±32.08	84.63±22.56
WITCH-GLOBIOM 4.0	556.76±130.53	430.10±102.42	121.36±28.68	83.96±20.79
average	531.89±128.42	425.07±111.14	128.69±33.12	87.93±22.29
Future temperature changes ΔT (°C)				
AIM/CGE 2.1	4.10±0.92	3.52±0.81	1.91±0.51	1.57±0.45
IMAGE 3.0.1	3.91±0.89	3.49±0.80	1.96±0.53	1.62±0.45
MESSAGEix-GLOBIOM 1.0	4.01±0.90	3.74±0.85	1.79±0.51	1.43±0.43
REMIND-MAgPIE 1.7-3.0	4.20±0.95	3.40±0.80	1.89±0.52	1.59±0.45
WITCH-GLOBIOM 4.0	4.00±0.90	3.35±0.78	1.61±0.45	1.32±0.40
average	4.05±0.92	3.50±0.82	1.83±0.52	1.51±0.44

MAgPIE 1.7-3.0). The range of ΔCO_2 for the NP scenario is 54.56 ppm, and that for the NDC scenario is 116.68 ppm. The range of CO_2 mitigation calculated by the five IAMs is 95.29 ppm, significantly higher than that for the NP scenario. Therefore, the range of CO_2 mitigation is mainly derived from the variance of the NDC scenario from IAMs.

The temperature increases in the four scenarios are also simulated (Fig. 4b). If no climate policy is implemented, the temperature will rise by 4.1°C±0.9°C relative to the preindustrial level. With NDC implemented, the temperature increase is controlled at 3.5°C±0.8°C. Although there is still a large gap between the NDC scenario and the goals of the Paris Agreement, significant mitigations (0.6°C on average) are achieved, which is the core focus of this article. The temperature in the NP scenario simulated by all IAMs is significantly larger than that in the NDC scenario. The temperature mitigations are calculated as the difference between the NP and NDC emission scenarios from the same IAM (Fig. 4b), ranging from 0.3°C–0.8°C. To enhance the reliability of the results, we also calculate the transient climate response to cumulative carbon emissions (TCRE) in Fig. 5, which ranges from (1.54°C–1.94°C)/PgC, close to the estimates from the existing literature (Matthews, Gillett et al., 2009, Leduc, Matthews et al., 2016).

4. The contributions to temperature mitigation

Furthermore, we attribute the temperature mitigation to regions according to the normalized marginal attribution method, in which relative contributions are proportional to the marginal climate effect of regional emission reductions. If only CO_2 reduction is considered in the attribution, R5OECD and R5ASIA are the top two contributors, each accounting for more than 40% of the temperature mitigation on average (Fig. 6). The three IAMs conclude that R5OECD is the largest contributor, while the other two IAMs are more confident about R5ASIA (Table 2). R5LAM accounts for 10.9% of the temperature mitigation, on average, and is the third-largest contributor. The remaining temperature mitigation is attributed to R5REF and R5MAF, and their contributions are very small (no more than 5% on average).

Considering additional climate forcings, the relative contribution of temperature mitigation has changed. Considering all GHG reductions, R5MAF becomes much more important, accounting for an average of 8.9%. This is because the global CH_4 and N_2O reduction proportion of R5MAF is greater than that for CO_2 (Fig. 3). Correspondingly, the share of R5ASIA dropped by approximately six percentage points, while the shares of R5OECD, R5LAM, and R5REF showed little change. In addition, we also included aerosols (BC and SO_2) in the attribution. Although there are significant changes between aerosol-included attribution ("GHGs+BC", "GHGs+SO_2", and "all" in Table 2) and aerosol-excluded attribution ("GHGs" in Table 2), they are very small. This is because GHGs have a long atmospheric lifetime, and cumulative emissions determine their climate effects. In contrast, the climate effects of short-lived aerosols are essentially determined by the current year's emissions. Since the attribution is conducted for a long period (2014–2100), GHGs are much more important than aerosols in the mitigation attribution.

Considering "all" climate forcers in this study (CO_2, CH_4, N_2O, BC, and SO_2), R5OECD and R5ASIA represent the two major contributors to global warming mitigation, accounting for 39.3% and 36.8%, respectively. R5LAM and R5MAF followed R5OECD and R5ASIA, contributing 11.5% and 8.9%, respectively. R5REF only contributed 3.5%. The relative contributions depend on regional emission reductions but are not limited solely to CO_2 emission reductions. Figure 7 shows that the regional contributions to climate mitigation are positively correlated with the CO_2 emission reductions but are not completely linear. This is attributed to non-CO_2 climate forcing and the nonlinear processes of the climate sys-

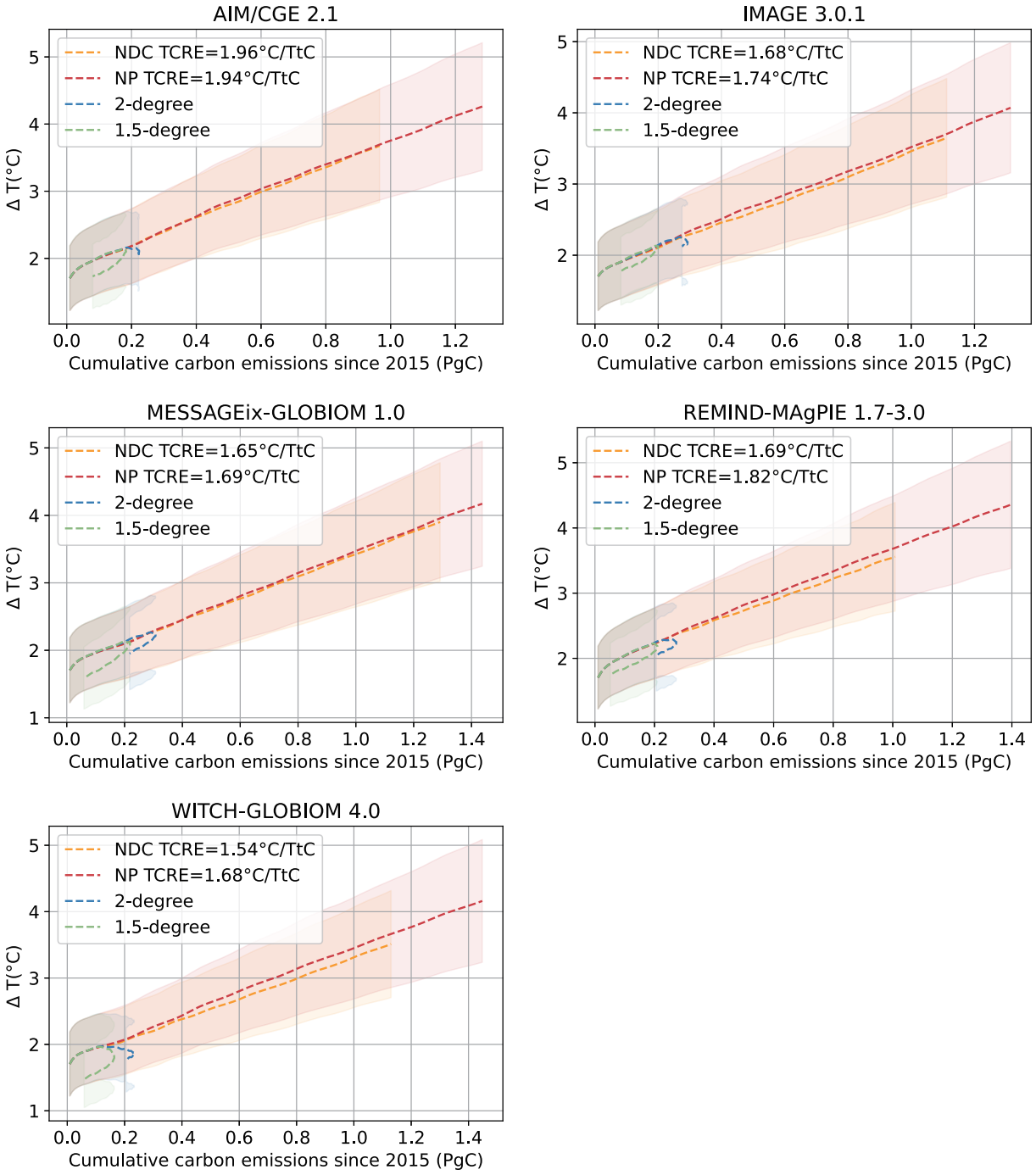

Fig. 5. The transient climate response to cumulative carbon emissions (TCRE) in this study. The lines are the average of the results of 3000 simulations and the shades show the range of the simulated data. "NP", "NDC", "2-degree" and "1.5-degree" scenarios are marked by red, orange, blue and green dashed lines. We calculate the TCRE for NDC scenario and NP scenario as the slope. Considering the negative emissions of the 2-degree and 1.5-degree scenarios, we do not calculate the TCRE for these two scenarios.

tem. The reductions in other GHGs and SO_2 are also worthy of attention, especially in certain regions, e.g., CH_4 in R5MAF and SO_2 in R5ASIA.

5. Conclusion and discussion

This study first assessed the regional contributions to the world's climate mitigation. According to our estimation, R5OECD and R5ASIA make similar contributions, covering almost three-quarters of climate change mitigation. At the same time, R5OECD and R5ASIA are the largest emitters of greenhouse gases and aerosols. The emission reduction actions of major emitters are essential to curb global climate change. R5LAM and R5MAF are of the second tier, each con-

tributing approximately 10%. R5REF is a less critical contributor to slowing down warming, only 3.5%.

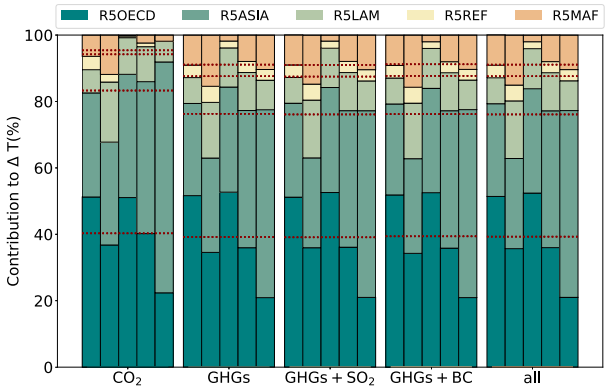

Fig. 6. The relative contributions of regions to climate mitigations with different climate forcers included. Each column represents the global climate mitigations (100%), with relative contributions from the R5 regions marked by different colors. "CO_2", "GHGs", "GHGs + SO_2", "GHGs + BC", and "all" labeled at the axis indicate which climate forcings are considered. GHGs refer to CO_2, CH_4, and N_2O, and "all" refers to GHGs, BC, and SO_2. The close-together columns represent results based on different IAMs, with the model average indicated by the red dashed lines. The five IAMs are AIM/CGE 2.1, IMAGE 3.0.1, MESSAGEix-GLOBIOM 1.0, REMIND-MAgPIE 1.7-3.0, and WITCH-GLOBIOM 4.0 (from left to right).

Our estimation of the regional contributions to climate mitigation is based on the deviation of the NP and NDC scenarios. This means that regional emission reductions determine future emission reduction contributions. Although, to a certain extent, high-emitting regions are more likely to contribute to greater emission reductions and cooling contributions, such as R5ASIA, while low-emitting regions, such as R5REF, are less likely to do so. However, this does not mean that larger emissions correspond to larger contributions. For example, the CD-LINKS dataset shows that CO_2 emissions in the R5MAF will rise in the future, becoming the world's second-largest emitter by 2100. However, the contribution of R5MAF to temperature mitigation is very small at 8.03%, a contribution that only surpasses the R5REF's contribution and is disproportionate to its emissions. Such results indicate that R5MAF has room to optimize the energy structure and develop stricter climate policies to control the climate. At the same time, technical assistance from developed countries and regions may help reduce R5MAF emissions due to historical responsibilities. It is not inappropriate to simply think that the greater the contribution in this study, the more commendable it is.

We noticed that the scenario data significantly determine the evaluation results, and the scenario data of different IAMs vary greatly. In the CD-LINKS datasets, there are significant variances in the five IAMs, with the opposite sign possibly being found in some regions and species. There is

Table 2. The contributions of regional NDC to climate change mitigation (%).

Model	Region	CO_2	GHGs	GHGs+BC	GHGs+SO_2	all
AIM/CGE 2.1	ASIA	31.3	27.8	27.4	28.3	27.9
	LAM	7.0	7.8	7.8	7.8	7.8
	REF	4.0	3.8	3.8	3.8	3.8
	OECD	51.2	51.6	51.9	51.2	51.4
	MAF	6.4	9.0	9.1	9.1	9.2
IMAGE 3.0.1	ASIA	31.0	28.4	28.5	27.1	27.2
	LAM	18.1	16.8	16.7	17.4	17.4
	REF	2.3	4.9	4.8	4.8	4.8
	OECD	36.8	34.6	34.3	36.0	35.7
	MAF	11.9	15.4	15.7	14.7	15.0
MESSAGEix-GLOBIOM 1.0	ASIA	37.1	31.7	31.4	31.6	31.4
	LAM	11.0	11.8	12.0	11.8	12.1
	REF	0.5	2.1	2.0	2.2	2.1
	OECD	51.1	52.7	52.5	52.6	52.4
	MAF	0.2	1.8	1.9	1.8	2.0
REMIND-MAgPIE 1.7-3.0	ASIA	45.8	41.3	41.4	41.1	41.2
	LAM	10.6	11.4	11.4	11.5	11.5
	REF	1.1	3.3	3.3	3.4	3.4
	OECD	40.2	36.0	35.8	36.1	36.0
	MAF	2.4	7.9	8.0	7.9	8.0
WITCH-GLOBIOM 4.0	ASIA	69.5	56.6	56.6	56.2	56.2
	LAM	7.8	8.9	8.9	9.0	9.0
	REF	−1.6	3.2	3.2	3.4	3.4
	OECD	22.4	20.9	20.9	21.0	21.0
	MAF	1.9	10.4	10.3	10.4	10.4

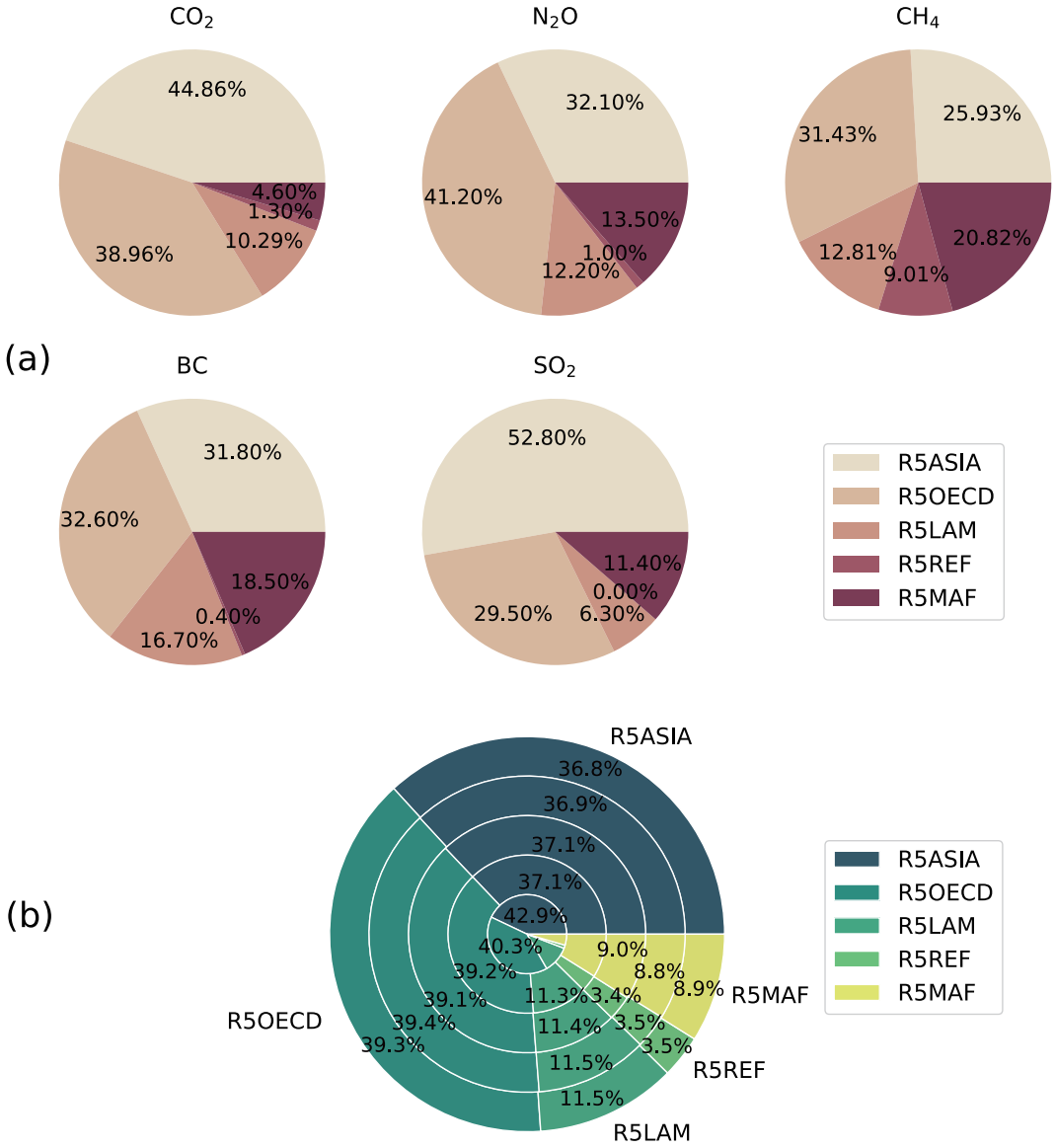

Fig. 7. Pie charts for regional emission reductions and induced climate warming mitigations. (a) Pie charts for regional reductions in CO_2, CH_4, N_2O, BC, and SO_2. (b) The nested pie chart in the center of this figure shows the regional relative contributions when calculated with different amounts of substances considered. The center part of the nested pie chart shows the relative contributions calculated with only CO_2 considered. The second layer, from the inside to the outside, considers CH_4 and N_2O in addition to CO_2 (abbreviated as GHGs in this study). The third layer considers GHGs and BC, and the fourth layer considers GHGs and SO_2. The outermost layer considers GHGs, BC, and SO_2, referred to as "all" in this study.

a great deal of uncertainty in the process of translating national policy documents into future global emission forecast data. Different possible evolutions of NDC assumptions, which have resulted in estimated emissions ranging from 47 to 63 $TgCO_2\ yr^{-1}$ in 2030, have a significant impact on the feasibility and cost of predicting future global warming (Rogelj et al., 2017). We argue that the reliability and consistency of IAM datasets are vital for future scenario projection and attribution analysis.

Apart from the data differences caused by different IAMs, the gap between NDC and climate goals should be noted. The fact is that most existing emission reduction programs exceed the 2°C target set out in the Paris Agreement. In other words, current actions are not sufficient to achieve the goals of sustainable development (Sörgel et al., 2021). In addition, even if NDCs are assumed to be achieved, there is still a wide range of future possibilities because of the definition of the long-term carbon budget (Riahi et al., 2021). However, this does not mean that NDCs cannot be evaluated. Instead, we need to assess currently proposed NDCs with a clearer picture. Only when we have a clearer understanding of the contributions, gaps, and uncertainties of NDCs, can we plan and evaluate more ambitious policies and pathways. The legacy of excessive temperatures and the

feasibility of limiting warming to 1.5°C or less are central to the post-Paris Agreement scientific agenda (Schleussner et al., 2016).

At present, 157 Paris Agreement Parties (representing 156 countries) have submitted their new or updated NDCs (Climate Watch, 2020). According to the recent NDC synthesis report released by the UNFCCC, new or updated NDCs are expected to result in 3.5% and 11.3% lower emission levels in 2025 and 2030, respectively, compared to the first NDCs, (UNFCCC, 2021). It is worth simulating the temperature mitigation and relative contributions of different regions under the updated NDC scenario. Unfortunately, the newest emission scenario pathway datasets of countries are still unavailable. We believe that the introduction of carbon-neutral policies will result in contribution increases for the current major carbon emitters, such as China (in R5ASIA), the United States, and the European Union (in R5OECD), both in absolute and relative aspects.

Meanwhile, the results of this paper can still be valuable as a reference for reflecting upon the necessary ambition to achieve the Paris goals and for discovering how countries can leverage their climate goals to achieve their sustainable development objectives. Of course, we strongly recommend evaluating the relative contributions under the updated NDCs when the newest datasets are available. Different countries give different peak carbon or carbon-neutral times, which affects their relative contributions.

We argue that all countries should introduce more ambitious emission reduction plans as soon as possible based on the current NDCs, and more international technical assistance to developing countries is needed to achieve a low-carbon world. These considerations represent important directions for climate policy research.

Acknowledgements. This study was funded by the undergraduate student research training program of the Ministry of Education, the National Natural Science Foundation of China (Grants Nos. 41771495, 41830641, and 41988101), and the Second Tibetan Plateau Scientific Expedition and Research Program Grant 2019QZKK0208. The development of OSCAR v3.1 is funded by the European Research Council Synergy project "Imbalance-P" (Grant No. ERC-2013-SyG-610028) and the European Union's Horizon 2020 research and innovation project "CONSTRAIN" (Grant No. 820829).

Author Contributions. Bengang LI designed the study and lead writing. Bo FU and Jingyi LI equally contributed to this study, who prepared the model set-up, conducted the simulations and wrote the text. Thomas GASSER, Philippe CIAIS, Shilong PIAO and Shu TAO contributed to the interpretation of the results and to the text. Guofeng SHEN, Yuqin LAI and Luchao HAN contributed to the figures and the text.

REFERENCES

Ciais, P., and Coauthors, 2013: Attributing the increase in atmospheric CO_2 to emitters and absorbers. *Nature Climate Change*, **3**(10), 926–930, https://doi.org/10.1038/nclimate1942.

Climate Watch, 2020. Washington, DC: World Resources Institute. Available from https://www.climatewatchdata.org.

Denison, S., P. M. Forster, and C. J. Smith, 2019: Guidance on emissions metrics for nationally determined contributions under the Paris Agreement. *Environmental Research Letters*, **14**(12), 124002, https://doi.org/10.1088/1748-9326/ab4df4.

Fu, B., and Coauthors, 2020: Short-lived climate forcers have long-term climate impacts via the carbon–climate feedback. *Nature Climate Change*, **10**(9), 851–855, https://doi.org/10.1038/s41558-020-0841-x.

Fu, B., and Coauthors, 2021: The contributions of individual countries and regions to the global radiative forcing. *Proceedings of the National Academy of Sciences of the United States of America*, **118**(15), e2018211118, https://doi.org/10.1073/PNAS.2018211118.

Gasser, T., L. Crepin, Y. Quilcaille, R. A. Houghton, P. Ciais, and M. Obersteiner, 2020: Historical CO_2 emissions from land use and land cover change and their uncertainty. *Biogeosciences*, **17**(15), 4075–4101, https://doi.org/10.5194/bg-17-4075-2020.

Gasser, T., P. Ciais, O. Boucher, Y. Quilcaille, M. Tortora, L. Bopp, and D. Hauglustaine, 2017: The compact Earth system model OSCAR v2.2: Description and first results. *Geoscientific Model Development*, **10**(1), 271–319, https://doi.org/10.5194/gmd-10-271-2017.

Gasser, T., and Coauthors, 2018: Path-dependent reductions in CO_2 emission budgets caused by permafrost carbon release. *Nature Geoscience*, **11**(11), 830–835, https://doi.org/10.1038/s41561-018-0227-0.

Huppmann, D., J. Rogelj, E. Kriegler, V. Krey, and K. Riahi, 2018: A new scenario resource for integrated 1.5°C research. *Nature Climate Change*, **8**(12), 1027–1030, https://doi.org/10.1038/s41558-018-0317-4.

IPCC, 2021: Summary for policymakers. *Climate Change 2021: The Physical Science Basis. Contribution of Working Group I to the Sixth Assessment Report of the Intergovernmental Panel on Climate Change*, V. Masson-Delmotte et al., Eds., Cambridge University Press.

Leduc, M., H. D. Matthews, and R. de Elía, 2016: Regional estimates of the transient climate response to cumulative CO_2 emissions. *Nature Climate Change*, **6**(5), 474–478, https://doi.org/10.1038/nclimate2913.

Li, B. G., and Coauthors, 2016: The contribution of China's emissions to global climate forcing. *Nature*, **531**(7594), 357–361, https://doi.org/10.1038/nature17165.

Lund, M. T., B. Aamaas, C. W. Stjern, Z. Klimont, T. K. Berntsen, and B. H. Samset, 2020: A continued role of short-lived climate forcers under the Shared Socioeconomic Pathways. *Earth System Dynamics*, **11**(4), 977–993, https://doi.org/10.5194/esd-11-977-2020.

Matthews, H. D., N. P. Gillett, P. A. Stott, and K. Zickfeld, 2009: The proportionality of global warming to cumulative carbon emissions. *Nature*, **459**(7248), 829–832, https://doi.org/10.1038/nature08047.

Riahi, K., and Coauthors, 2017: The Shared Socioeconomic Pathways and their energy, land use, and greenhouse gas emissions implications: An overview. *Global Environmental Change*, **42**, 153–168, https://doi.org/10.1016/j.gloenvcha.2016.05.009.

Riahi, K., and Coauthors, 2021: Cost and attainability of meeting

stringent climate targets without overshoot. *Nature Climate Change*, **11**(12), 1063–1069, https://doi.org/10.1038/s41558-021-01215-2.

Roelfsema, M., and Coauthors, 2020: Taking stock of national climate policies to evaluate implementation of the Paris Agreement. *Nature Communications*, **11**(1), 2096, https://doi.org/10.1038/s41467-020-15414-6.

Rogelj, J., O. Fricko, M. Meinshausen, V. Krey, J. J. J. Zilliacus, and K. Riahi, 2017: Understanding the origin of Paris Agreement emission uncertainties. *Nature Communications*, **8**, 15748, https://doi.org/10.1038/ncomms15748.

Schleussner, C.-F., and Coauthors, 2016: Science and policy characteristics of the Paris Agreement temperature goal. *Nature Climate Change*, **6**(9), 827–835, https://doi.org/10.1038/nclimate3096.

Skeie, R. B., G. P. Peters, J. Fuglestvedt, and R. Andrew, 2021: A future perspective of historical contributions to climate change. *Climatic Change*, **164**(1), 24, https://doi.org/10.1007/s10584-021-02982-9.

Sörgel, B., and Coauthors, 2021: A sustainable development pathway for climate action within the UN 2030 Agenda. *Nature Climate Change*, **11**(8), 656–664, https://doi.org/10.1038/s41558-021-01098-3.

Trudinger, C., and I. Enting, 2005: Comparison of formalisms for attributing responsibility for climate change: Non-linearities in the Brazilian Proposal approach. *Climatic Change*, **68**(1-2), 67–99, https://doi.org/10.1007/s10584-005-6012-2.

UNFCCC, 2002: Methodological Issues: Scientific and Methodological Assessment of Contributions to Climate Change, Report of the Expert Meeting. Available from https://unfccc.int/resource/docs/2002/sbsta/inf14.pdf.

UNFCCC, 2015: Paris Agreement. Available from https://unfccc.int/sites/default/files/english_paris_agreement.pdf.

UNFCCC, 2021: Nationally determined contributions under the Paris Agreement. Available from https://unfccc.int/sites/default/files/resource/cma2021_08_adv_1.pdf.

van Soest, H. L., M. G. J. den Elzen, and D. P. van Vuuren, 2021: Net-zero emission targets for major emitting countries consistent with the Paris Agreement. *Nature Communications*, **12**(1), 2140, https://doi.org/10.1038/s41467-021-22294-x.

ADVANCES IN ATMOSPHERIC SCIENCES, VOL. 39, AUGUST 2022, 1229–1238

• **Perspectives** •

The Chinese Carbon-Neutral Goal: Challenges and Prospects※

Ning ZENG*[1,2], Kejun JIANG[3], Pengfei HAN[4,2], Zeke HAUSFATHER[5], Junji CAO*[6], Daniel KIRK-DAVIDOFF[1], Shaukat ALI[7], and Sheng ZHOU[8]

[1]*Department of Atmospheric and Oceanic Science, and Earth System Science Interdisciplinary Center, University of Maryland, College Park* 20742, *Maryland, USA*

[2]*State Key Laboratory of Numerical Modeling for Atmospheric Sciences and Geophysical Fluid Dynamics, Institute of Atmospheric Physics, Chinese Academy of Sciences, Beijing* 100029, *China*

[3]*Energy Research Institute, National Development and Reform Commission, Beijing* 100045, *China*

[4]*Carbon Neutrality Research Center, Institute of Atmospheric Physics, Chinese Academy of Sciences, Beijing* 100029, *China*

[5]*Breakthrough Institute, Oakland* 94612, *California, USA*

[6]*Institute of Atmospheric Physics, Chinese Academy of Sciences, Beijing* 100029, *China*

[7]*Global Change Impact Study Centre, Ministry of Climate Change, Islamabad* 45250, *Pakistan*

[8]*Institute of Energy, Environment and Economy, Tsinghua University, Beijing* 100084, *China*

(Received 10 August 2021; revised 13 December 2021; accepted 21 December 2021)

ABSTRACT

On 22 September 2020, within the backdrop of the COVID-19 global pandemic, China announced its climate goal for peak carbon emissions before 2030 and to reach carbon neutrality before 2060. This carbon-neutral goal is generally considered to cover all anthropogenic greenhouse gases. The planning effort is now in full swing in China, but the pathway to decarbonization is unclear. The needed transition towards non-fossil fuel energy and its impact on China and the world may be more profound than its reform and development over the past 40 years, but the challenges are enormous. Analysis of four representative scenarios shows significant differences in achieving the carbon-neutral goal, particularly the contribution of non-fossil fuel energy sources. The high target values for nuclear, wind, and bioenergy have approached their corresponding resource limitations, with solar energy being the exception, suggesting solar's critical role. We also found that the near-term policies that allow for a gradual transition, followed by more drastic changes after 2030, can eventually reach the carbon-neutral goal and lead to less of a reduction in cumulative emissions, thus inconsistent with the IPCC 1.5°C scenario. The challenges and prospects are discussed in the historical context of China's socio-economic reform, globalization, international collaboration, and development.

Key words: carbon neutral, carbon dioxide reductions, energy system transformation, distributed energy system, model projections

Citation: Zeng, N., K. J. Jiang, P. F. Han, Z. Hausfather, J. J. Cao, D. Kirk-Davidoff, S. Ali, and S. Zhou, 2022: The Chinese carbon-neutral goal: Challenges and prospects. *Adv. Atmos. Sci.*, **39**(8), 1229−1238, https://doi.org/10.1007/s00376-021-1313-6.

Article Highlights:

- The Chinese carbon neutral goal will have profound impact but the challenges are enormous.
- Four representative scenarios show significant differences in how to achieve the carbon-neutral goal, but all agree the importance of solar energy.
- We recommend more aggressive actions on distributed solar, wind, small and modular nuclear, smart grid, and energy storage.

1. Introduction

On 22 September 2020, within the backdrop of the COVID-19 global pandemic, China announced its climate goal for peak carbon dioxide (CO_2) emissions before 2030 and reach carbon neutrality by 2060, often referred to as

※ This paper is a contribution to the special issue on Carbon Neutrality: Important Roles of Renewable Energies, Carbon Sinks, NETs, and non-CO_2 GHGs.

* Corresponding authors: Ning ZENG, Junji CAO
Emails: zeng@umd.edu, jjcao@mail.iap.ac.cn

"Shuang Tan" or "the two carbon goals" in China (Xi, 2020). After this announcement, President XI has spoken more than 30 times on important occasions and emphasized the importance of the double carbon goal. The planning efforts to reach the two goals are now in full swing in China. This announcement came as a pleasant surprise for the fight against climate change, but the pathway to decarbonization is unclear; the Climate Envoy, Zhenhua XIE, said that the carbon-neutral goal covers all greenhouse gases. The needed transition towards non-fossil fuel energy and its impact on China and the world may be more profound than its reform and development over the past 40 years, but the challenges are enormous.

2. Roadmap to carbon neutrality

Currently, China's fossil fuel CO_2 emissions are 10.2 Gt CO_2 (gigatonnes of CO_2) in 2019, which compromises 27.9% of total global emissions (Friedlingstein et al., 2020). In 2020, fossil fuels accounted for 83% of the total primary energy supply (TPES) with coal representing 57%, oil 17%, and gas 9%, while non-fossil fuel accounted for only 17% (hydro 7%, nuclear 3%, wind 3%, solar 2%, bio 2%).

To achieve the carbon-neutral goal, which ambitiously corresponds to not exceeding the 2°C target of the Paris Agreement on climate change (IPCC, 2018; Jiang et al., 2018; Project Comprehensive Report Preparation Team, 2020), the ratio of fossil fuel to non-fossil energy sources need to be completely reversed. The low carbon energy system would need to decrease to 80%–90% of the present CO_2 emissions [Fig. S1 in the Electronic Supplementary Material (ESM)]. The remainder (including the non-CO_2 emissions) would need to be offset by the terrestrial and ocean sinks and carbon capture, usage and storage (CCUS), resulting in net-zero emissions. We illustrate this with a representative scenario by running the IPAC integrated assessment model (Jiang et al., 2018). We started using the latest Chinese energy and economic statistics of 2020 and then projected them into the future at five-year intervals. The projection shows that, by 2050, the contribution of non-fossil energy would increase to 77%, while the fossil fuel portion would drop to 23% (Fig. 1 and Table 1). In particular, the contribution of coal would drop below 10%. Additionally, significant carbon sinks and negative emissions will be needed to counter the remaining fossil fuel emissions to achieve net-zero CO_2 emissions.

While the overall scenario involves detailed modeling of socio-economic and technological development, fossil fuel CO_2 emissions can be broadly understood as driven by the following key factors using the Kaya identity (Kaya and Yokoburi, 1997):

$$CO_2 = \frac{CO_2}{Energy} \times \frac{Energy}{GDP} \times \frac{GDP}{Population} \times Population, \quad (1)$$

where CO_2 is CO_2 emissions from human sources, Energy is energy consumption, and GDP is gross domestic product (GDP).

The past increases in CO_2 emissions have been mostly driven by economic development and population increases (Raupach et al., 2007). China's GDP has increased at an average rate of 9% from 1980–2019 (the 3rd factor in the Kaya Identity above). Going forward, with the annual rate of GDP expected to grow at 4%–5% and the population stabilizing, a complete decoupling of CO_2 emissions from GDP growth will be required for the carbon-neutral goal. First, CO_2 emission intensity per unit energy generation (the 1st fac-

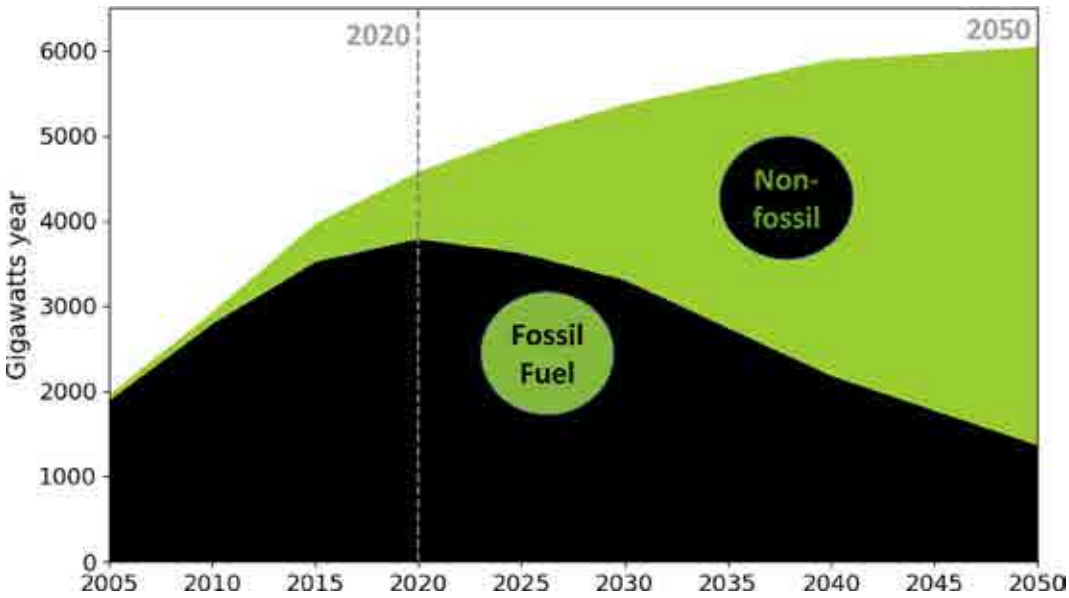

Fig. 1. The Yin and Yang of fossil vs. non-fossil fuel energy source mix. A scenario to achieve China's carbon-neutral goal before 2060 would require a complete reversal of their relative contribution to total energy supply and an unprecedented rapid increase in renewable energy plus nuclear and decrease in fossil fuel use on the timescale of 20–30 years after peak carbon.

tor) will need to be reduced drastically in a near-complete switch from fossil to non-fossil fuel energy. This can be accomplished by reducing coal and gas on the power generation side and heavy electrification and energy efficiency on the end-user side. Second, decreasing the energy intensity per GDP (the 2nd factor in the Kaya Identity) requires growth to come mostly from the service sector and non-energy intensive industries such as electronics, which is expected to occur naturally as China's rapid infrastructure build-up over the last 40 years (Zeng et al., 2008) is leveling off.

Regarding power generation specifically, this scenario calls for a 2485 Gigawatts (billion watts or GW) of installed solar capacity in 2050, a 9-fold increase from 281 GW in 2020. In the proposed mix, wind power will increase from 244 GW in 2020 to 1508 GW capacity (a 6-fold increase), while nuclear power will increase from 55 GW to 563 GW (a 10-fold increase). Such changes would require an average annual addition of 73 GW of solar-generated power, and 17 GW of nuclear power over the next 30 years, while at the same time reducing coal-fired power by 33 GW per year. In 2050, non-fossil fuel energy sources consisting of nuclear and renewables (solar, wind, hydro, bio) will provide 90% of the total power generation. After considering the differences in capacity factors, this mix of installed capacities contributes to a total TPES mix of 24% nuclear and 53% renewables (Table 1).

2.1. *Different pathways*

To further understand the assumptions and uncertainties, we compared the projections from four 1.5°C modeling synthesis scenarios: the IPAC model discussed above, GCAM-TU (Zhou et al., 2021), and ICCSD (Davidson et al., 2016; Huang et al., 2020; Project Comprehensive Report Preparation Team, 2020), and an ICCSD "transition pathway" (Project Comprehensive Report Preparation Team, 2020) (see ESM). The four scenarios all show a reversal between fossil and non-fossil fuels and similar carbon emissions. However, the energy mix differs significantly.

China submitted the updated Nationally Determined Contributions (NDC) on 28 October 2021 with several new commitments (https://www4.unfccc.int/sites/NDCStaging/pages/Party.aspx?party=CHN, accessed on 6 December 2021). China will lower its CO_2 emissions per unit of GDP by over 65 percent from 2005 levels. In the Project Comprehensive Report Preparation Team (2020) study, the projected number is 68.2%, a bit higher than the committed lower bound of 65%. For China's goal of non-fossil energy proportion (about 25% by 2030), the GCAM-TU and IPAC models predicted 36% and 30% at 2030, respectively, in the 1.5°C carbon-neutral scenarios (Fig. S2 in the ESM) (Jiang et al., 2018; Zhou et al., 2021). As for the goal of total installed wind and solar power capacity reaching over 1.2 billion kilowatts, the GCAM-TU and IPAC models predicted 1.6 and 1.4 billion kilowatts by 2030, respectively (Jiang et al., 2018; Zhou et al., 2021).

Primary energy projected by the IPAC model increases gradually and plateaus to a level that is 30% higher in 2050 than in 2020, while the other scenarios only show minor increases (Fig. 2). In 2050, fossil fuel contribution in the ICCSD scenario is 610 GWy, only half of the other two, mostly due to a much smaller coal contribution. Non-fossil energy supply ranges from 3630 to 5040 GWy, with the

Table 1. Energy sources in the total primary energy supply (TPES) mix. Future years are projected by the carbon-neutral scenario using the IPAC model. Unit is in GWy (Gigawatts year) and percentage of total in parentheses.

Year	Total	Coal	Oil	N. Gas	Nuclear	Hydro	Wind	Solar	Bio
2005	1956	1427 (72.9%)	404 (20.7%)	56 (2.9%)	18 (0.9%)	45 (2.3%)	0.8 (0.0%)	0.0 (0.0%)	4.6 (0.2%)
2020	4573	2622 (57.3%)	774 (16.9%)	390 (8.5%)	142 (3.1%)	319 (7.0%)	145 (3.2%)	103 (2.3%)	78 (1.7%)
2035	5625	1641 (29.2%)	512 (9.1%)	590 (0.5%)	818 (14.5%)	496 (8.8%)	645 (11.5%)	501 (8.9%)	423 (7.5%)
2050	6044	592 (9.8%)	211 (3.5%)	563 (9.3%)	1460 (24.2%)	535 (8.8%)	1001 (16.6%)	982 (16.2%)	702 (11.6%)

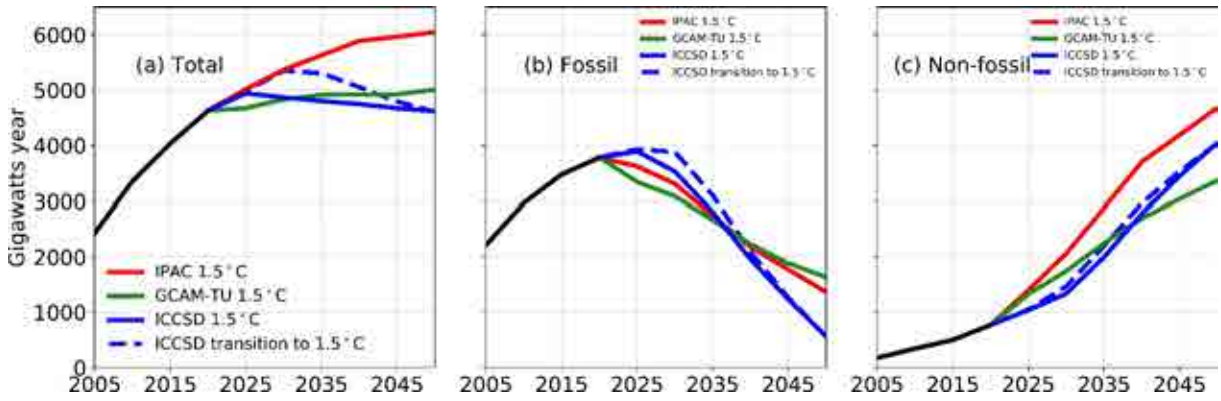

Fig. 2. Energy supply from (a) total, (b) fossil fuel, (c) non-fossil fuel sources from three 1.5°C scenarios, and a "transition pathway".

ICCSD coming in low for all fossil fuels, particularly coal, and the GCAM-TU assumes higher and longer-lasting oil use (Fig. S2 in the ESM).

Large differences exist in non-fossil energy sources (Fig. S2). For example, the IPAC model projects 1570 GWy (or Gigawatts year) nuclear energy, generated by 563 GW of installed capacity, compared to 780–850 GWy in the other two models. The ICCSD scenario projects a much higher contribution from wind energy, 1920 GWy, compared to 1010–1080 GWy, for the other two models. The IPAC and ICCSD call for 1040–1060 GWy of solar energy, compared to 430 GWy for the GCAM-TU. Hydropower is the only energy source with good agreement among the models because the development of most of the available resources has already taken place in the last 30 years.

The nearly factor-of-two differences in nuclear, wind, solar, and bioenergy in the 2050 scenarios reflect major uncertainties in the assumptions. For instance, the higher value for nuclear energy in the IPAC model, serving as crucial baseload or firm generation when coal use becomes minimal, requires the use of nearly all of the suitable sites for large-scale nuclear power plants (Jiang et al., 2018; Xiao and Jiang, 2018; Yu et al., 2020). Similarly, the higher contribution from bioenergy implies major competition with food production and other environmental goals (Zhao et al., 2015; Huang et al., 2020), and the higher wind energy scenario in the ICCSD would use much of the technically exploitable resources (Zhang et al., 2011; Yang et al., 2017). In general, the higher target values of most non-fossil fuel energy sources appear to approach resource limitation, with solar energy being the lone exception.

The IPCC 1.5°C scenario not only requires long-term commitment but also fast, near-term emissions reductions. However, because of the inertia in the energy system, a pathway is proposed to "transition" from a reinforced-policy scenario to the ICCSD 1.5°C scenario (Project Comprehensive Report Preparation Team, 2020). This scenario allows for a gradual transition in the near term, which is more consistent with China's 14th Five Year Plan (FYP) that is currently taking shape (The State Council, 2021) but requires a faster drawdown after 2030 and somewhat different cumulative carbon emissions (Fig. S3 in the ESM). Although it can eventually reach the carbon-neutral goal, this scenario leads to less cumulative emissions reduction, thus inconsistent with the IPCC 1.5°C scenario. This adds additional uncertainty to the envisioned pathways, illuminating the scale of the problem and the challenges facing the carbon-neutral goal.

2.2. *Challenges of increasing renewable energy*

Practical solar technology was developed in the US in the 1970s. The 2009 European renewable energy directive spurred its growth as Chinese manufacturers made solar panels that were sold to Germany and other countries. Over the last decade, as the technology further advanced and the scale of the economy expanded, the price of wind and solar power has achieved the stunning feat of price-parity with the Levelized Cost of Electricity (LCOE), which is now cheaper than coal and nuclear (IRENA, 2020; Lazard, 2020). China's installed solar capacity increased from 2.6 GW in 2010 to 43 GW in 2015 and 281 GW in 2020, with an annual addition rate of more than 20% in the last few years. Even during the 2020 COVID-19 pandemic, 49 GW of solar and 71 GW of wind power were added. The fact that renewable energy is now economically competitive against fossil fuels arguably provides the most important foundation for optimism on the carbon-neutral goal.

However, increasing the contribution to the energy mix of non-fossil fuel from 17% to 77%–85%, a more than 6-fold increase, in 30 years will be a daunting task. As the model scenarios show, the higher targets for nuclear, wind, and bioenergy approach their respective resource limits with the notable exception of solar energy. While the available sunlight is not a limitation, it does require vast land, mineral, and other resources. The inherent intermittency of solar and wind power due to diurnal, synoptic weather, and seasonal climate variations gives rise to load balancing and grid security problems, especially when the proportion of this intermittent source exceeds 20% of the total electricity production. The solution will require technological breakthroughs in energy storage and grid technology. Such a scaling-up investment would need to be at a comparable scale as renewable power generation itself. Such uncertainties and unforeseen costs are not necessarily fully accounted for in the model scenarios or the long-term industry outlook (Global Energy Interconnection Development and Cooperation Organization, 2021).

2.3. *Challenges of fossil fuel and coal phase-out*

To reduce fossil fuel consumption below 15%–23% of the total energy by 2050 will be equally challenging. The key to this transition is to impose end-use electrification supplied by renewable energy. China has been aggressively developing electric vehicles, and this market accounts for 50% of the world's total. Reducing oil use would require electrification of the transportation sector to at least 85%. Electrification of energy-intensive industries such as steelmaking and chemicals is in its infancy. Reducing natural gas use requires the transition of cooking and heating mechanisms from gas to electricity in residential and office buildings, a daunting task in retrofitting an urban infrastructure that is mostly complete. While energy efficiency can improve, other factors may increase demand. For example, traditionally, the Chinese cities south of the Huai River do not use indoor heating, which may eventually change. In the other direction, the demand for cooling will be higher in a warmer world. These factors would require a near doubling of electric power generation, even though the total energy consumption is projected to increase only modestly in the carbon-neutral scenarios.

Nearly 70% of China's electricity currently comes from coal. Reducing it to less than 10% in 2050 requires a fast phase-out of existing coal-fired power plants. Is this feasible? As a major baseload, the stability provided by coal will still be critical in the near to medium future. Moreover, China currently has a significant number of coal-fired power plants under construction or approved, although many of these are

cleaner Integrated Gasification Combined Cycle (IGCC) plants. Given the 30–40 years lifetime of such plants, near elimination of them in 20–30 years implies stranded assets, reduced operation hours and profit, loss of jobs, and other challenges. Recent government policy has been uncertain in coal development, which is not consistent with decisive actions needed for the carbon-neutral goal. A partial remedy during the transition period would be to gradually reduce operation hours as the Chinese coal-fired power plants generally operate at high loads. A rapid coal phase-out will also need to deal with social issues as the coal industry currently employs more than 4 million workers located in a few provinces.

Moreover, the phase-out of fossil fuels, especially coal, also brings the co-benefit of reducing methane (CH_4) emissions, an important non-CO_2 GHG, since energy activity contributed ~50% of China's anthropogenic CH_4 emissions (Lin et al., 2021). Reducing CH_4 emissions is assumed to be a cost-effective method of achieving carbon neutrality, especially in the energy sector since methane can be recovered and reused with lower costs than in the agriculture and waste treatment sectors. In the case of N_2O, the reductions would be more difficult than with CH_4 since about 60% of N_2O emissions are from agriculture (Han et al., 2021). Comprehensive evaluations on promising emission reduction measures are highly needed for both technology, maturity, and cost aspects.

2.4. *Challenges from future uncertainties: nuclear, technological bottlenecks, and geopolitics*

The carbon-neutral goal requires all variables to go in the right direction in a short amount of time: technical, socio-political, and economical. Yet, unexpected events or trends certainly can disrupt the process. Should a coal phase-out shift the lion's share of firm generation to nuclear power, a major nuclear accident becomes a worrisome possibility, despite the excellent safety record of China's nuclear fleet. In the past, society has tended to at least temporarily shift away from nuclear power after a major nuclear accident. For example, the accident at the Fukushima Daiichi nuclear power plant on 11 March 2011 caused serious environmental pollution (Povinec et al., 2013) and public alarm (Huang et al., 2013). For China, it may be prudent to ensure that rigorous safety standards are followed in conventional nuclear deployment while testing safer technology with Small Modular Reactors (SMRs) and advancing better nuclear waste management. Current carbon-neutral pathways rely heavily on conventional nuclear; the extent to which other clean energy sources may play a larger role depends on future technology costs and the extent to which challenges of intermittency and seasonal variations in generation can be solved by breakthroughs in complementary technologies such as grid storage, transmission, and hydrogen production.

With renewables and nuclear dominating the future energy mix, the remaining 15%–23% of energy from fossil fuels still needs to be offset by negative emissions technology. However, it is not clear if the leading candidates, Carbon Capture and Storage (CCS) in geological formations, Direct Air Capture (DAC), and Bioenergy with CCS (BECCS), will be technologically and commercially successful enough at the needed scale (Fuss et al., 2014; McLaren and Markusson, 2020).

Geopolitical instability remains a major threat to the Paris climate goal. Similar to the large impact of Middle East oil, demand for raw materials can lead to instability and volatility. A hostile relationship among and 'decoupling' of the major world economies will lead to more emphasis on investment in defense, leaving fewer resources for sustainable development and different technological standards that ultimately hinder the spread of renewable technology.

3. A new energy map

In 1935, geographer Huan-Yong HU drew a southwest-northeast oriented diagonal line on the map of China, later known as the 'Hu-line' (Fig. 3). He pointed out that 36% of the land southeast of this line accommodates 96% of China's population, while to the northwest, 4% of the population lives on the remaining 64% of the land. A central geo-economic reality of China is the separation of China into two regions with distinctly different climates, geography, population, and stages of economic development. This line also separates a fundamental energy "inequality". The semi-arid regions of northwestern China have much of the renewable energy resources as well as fossil fuel reserves that need to be transferred to the industrially developed central and eastern regions of China, except for development along the ancient Silk Road corridor, which is also the main continental connection to central Asia and Europe.

China is developing ultra-high voltage direct current (UHVDC) lines that can run thousands of kilometers, such as the 800 kilovolt, 2193 km-long Baihetan-Zhejiang line currently under construction. However, the current grid system is far from adequate in accommodating a pervasive distributed system at the scale envisioned for carbon neutrality. For instance, assuming 75% of the 2485 GW solar and 1508 GW wind power projected by the IPAC model for the year 2050, or 3000 GW combined, needs to be transmitted from the west to the east; such a project would require the equivalent of 300 such UHVDC transmission lines at 10 GW each, with each line occupying large amounts of contiguous land, often over difficult terrain. Yet, this still does not solve the intermittency issues inherent to wind and solar power. Energy storage such as green hydrogen, lithium-ion, solid-state, and other advanced battery technologies at very large scales will be crucial. Still, it is not yet clear they will be available in a timely fashion at a reasonable cost and needed scale.

To realize the renewable-dominated energy map, China will need to develop every possible method in a carefully balanced approach. To minimize the shortcomings of security and reliability of long-distance transmission, distributed energy systems should be widely deployed. While rooftop solar is the poster child of distributed solar, its potential on

Fig. 3. The new energy map of China with a balanced portfolio. China's carbon-neutral goal would require a stunningly large quantity of interconnected, utility-scale, and distributed non-fossil power generation, as well as carbon sinks that offset remaining fossil fuel emissions.

a per capita basis is limited in Chinese cities where high-rise buildings dominate. In contrast, the potential is much higher in rural regions. Installing solar panels on farmland and grazing land, roadside, hill slopes, and other suitable places in the open countryside (Fig. 4) has the co-benefits of generating power and enhancing plant growth under the panels (Barron-Gafford et al., 2019), providing green jobs and improving the income of farmers. Currently, China is making particular efforts by providing government-subsidized solar installations for poverty relief at local scales, but there is great potential for a nationwide expansion.

The power from individual solar panels and small wind turbines can be aggregated using micropower stations at the village level. After satisfying local power needs, a large quantity of electricity can be sent from the micro-grid to nearby towns, then to larger cities via the regional and national grids. Such a distributed system goes hand-in-hand with modularized storage systems. Together with electric and hydrogen fuel cell vehicles in the cities, a network of distributed systems with pervasive penetration across the country can catalyze a rapid price drop of energy storage technology, providing a superbly flexible and resilient energy infrastructure.

The current grid system is far from adequate in accommodating a pervasive distributed system at the scale envisioned here. Such a system will require policy and financial incentives. Because the current fossil fuel-based power system already provides a backbone grid, the micro-medium scale systems generally cover the intermediate range of linking houses and farms to the grid. Solar, wind, and small modular nuclear energy and biomass can be similarly integrated into the grid. Such a distributed system and interconnected smart grids will also offer a huge market for the internet of things (IoT) and related digital technology.

In addition to onshore wind energy, offshore wind energy is another mature technology that can significantly ramp up. This fully renewable energy source has the distinct advantage of being close to the major coastal metropolitan cities such as Tianjin, Shanghai, Shenzhen, Hong Kong, and Guangzhou. Besides building wind farms, careful planning for such a national backbone of coastal transmission cables on land or underwater will facilitate and stimulate offshore wind development (Fig. 3). In contrast to solar, the wind can blow at night and is often stronger in winter than in summer; thus, wind energy has can potentially provide an important buffer for the distributed solar system.

Reforestation and forest protection in China over the last 30 years has contributed to a significant carbon sink, estimated at 0.2 GtC yr^{-1} or larger (Fang et al., 2018; Han et al., 2021). Most of this occurred in southern China, where the climate is wet and warm. However, as these forests mature, their ability to absorb CO_2 will decline. Because China is already heavily dependent on agricultural imports, competition for land use will be a major limitation for bioenergy contribution (Zhao et al., 2015; Huang et al., 2020). Novel ways of managing forests to maintain or enhance this sink as negative emissions (Zeng, 2008) may be needed to offset hard-to-replace fossil fuel use.

To achieve the new energy map, it will be critical to strike a balance between adhering to government guidance and stimulating the market economy. In the context of renewable energy development, infrastructure build-up, and the COVID-19 response, the Chinese experience has demonstrated the importance of unified vision, concerted effort, and the willingness to sacrifice some individual interests for

Fig. 4. Top and bottom left: Distributed small solar power systems such as agrivoltaics on a micro-grid with storage embedded in a smart interconnected regional/national grid may be a key to deep decarbonization needed for China's carbon-neutral goal. Top right: end-use efficiency using smart shared bikes to connect the "last kilometer" from home to metro. Bottom right: A worker installs a solar photovoltaic panel on the rooftop of a residential building.

the community when needed. On the other hand, to ensure continued benefits from innovation and the dynamism of the market economy, greater efforts and more careful approaches will be needed both internationally and domestically. For example, the mass production of a distributed solar energy system would require government supports and even mandates for building a suitable national distributed grid that allows electricity generated by the micro solar systems to flow in, while still allowing for market mechanisms for construction and price adjustment.

4. Research, innovation, and collaboration

China's GDP has grown at an average rate of 9% annually over the last 40 years, driven by a national resolve to rise from the "hundred-year turmoil" and a focus on economic development, enabled by the vigor and dedication of 2–3 generations coming from a poverty-stricken background. However, the wealth gap has grown alarmingly large as living standards improve. As China enters a middle-wealth stage, continued development will require a deeper socio-economic transformation. The carbon-neutral goal and sustainable development, in general, provide a big opportunity for this transformation.

China's economic 'miracle' would not have been possible without the scientific knowledge, technology, and management experience in a generous international business and cultural environment. China joined the World Trade Organization (WTO) in 2001, which made the world market accessible, a crucial step leading to substantial improvement in living standards while benefiting the rest of the world. The basic technology of photovoltaics, concentrated solar power, and wind turbines was developed in the US at a commercial scale in the 1970s in response to the Middle East oil crisis. Advancements in high-speed rail have occurred in France, Germany, and Japan and within technology related to lithium-ion batteries in Japan in the 1990s. China has contributed additional developments to these technologies and achieved cost reductions and scale-up.

In the future, China's ambitious carbon-neutral goal will not be possible without continued international collaboration and a conducive international economic and political environment. A key issue is intellectual property (IP) rights. China started its patent and trademark system in 1985, and patent applications accounted for 46% of the global total in 2018. However, this number does not necessarily reflect the quality of the projects. Technical knowledge has been traditionally regarded with little value, and IP protections are weak. Working closely with other countries to improve IP protections, fair technology transfer, and market access will have the dual benefit of nurturing a productive international relationship and allowing domestic innovation to flourish. Similarly, while China's scientific research output has become number one in terms of the number of papers published, Chinese industry has benefited only modestly from such research. This is not to suggest diminishing research efforts but rather to emphasize establishing and applying multiple criteria for judging scientific output and merit. Research with real and attainable impact should be emphasized, whether basic or applied.

International collaboration sometimes starts unpleasantly and unexpectedly. In 2008, a scientific attaché at the

US embassy in Beijing set up an air quality monitor on the rooftop and started to post the $PM_{2.5}$ measurement on the Embassy's website (Kintisch, 2018). The initial reaction from the people of Beijing was to "mind-your-own-business" as the "foggy" weather is painted as natural beauty in traditional Chinese literature and arts. But it did not take long for people to recognize the health threat of air pollution. Now China has a network of thousands of monitoring stations reporting data in real time. Since 2013, the $PM_{2.5}$ has dropped by 53% (from 89.5 μg m^{-3} in 2013 to 42 μg m^{-3} in 2019) in Beijing (Beijing Municipal Ecology and Environmental Bureau, 2020). This decrease has been achieved by a combination of factors, including moving heavy polluting industries outside major cities, establishing higher emissions standards, and mandating temporary close-downs of factories during 'bad' weather conditions. While such measures have had significant impact in improving health in highly populated cities during heavy-pollution episodes, the sources of pollution largely remain unmitigated. The carbon-neutral goal provides a great opportunity to deal with air pollution and climate change from their common source—fossil fuel emissions.

The global climate change emergency is an area with high potential for international collaboration. Historically, exchange on climate science through avenues such as the Intergovernmental Panel on Climate Change (IPCC) was instrumental in transforming China from considering climate change an issue invented by the West to playing a leading role today in preventing its further development. Scientists and policymakers should continue to collaborate on the science of climate change and climate mitigation and adaptation strategies. For instance, despite a major investment, much of China's environmental data on the atmosphere and ocean and land ecosystems remain highly fragmented and often not publicly available. A concerted effort from the highest government level to individual research groups will be needed to break bureaucratic obstacles, improve data quality and availability, and create a carbon monitoring and greenhouse gas information system to realize their value for global climate efforts fully.

China's development started with little modern infrastructure so that it has had room for experimentation and competition of different technologies in a "cross-the-river-by-touching-stones" fashion, as phrased by the late Chinese leader Xiaoping DENG. A major drawback of such a trial-and-error approach is the inefficient use of material and human resources and environmental degradation on air, land, and water. For the carbon-neutral goal, China may be able to similarly scale up key technologies such as energy storage, but only with international collaboration, monitoring, and scientific exchange.

5. International development

The scale required to deploy solar, wind, and end-use electrification will have major spill-over effects to other countries, thanks to China's ability to scale up and refine a technology to make it affordable. The potential global impact of a rapid Chinese renewable development may well rival the impact on China itself, not only for its manufacturing capability, but also for the potential for technology development, and spread to developing countries or those soon to be developed where future energy demands are not foreseen.

For instance, in the Belt and Road Initiative (BRI), China plans to spend trillions of dollars in the build-up of infrastructure for developing countries in Asia, Africa, and South America (World Bank, 2018) The construction of coal-fired power plants should be switched to solar and wind farms, specifically fostering the distribution of micro solar power stations for villages and towns and rooftop and farm solar panels for rural households (Fig. 4). Efforts should not be placed solely in constructing solar installations but also directed towards expanding the capacity of human resources. Solar deployment in China will provide green jobs and infrastructure in developing countries, also helping poverty relief. China and India should collaborate because Indian energy demand is rapidly increasing with its large population and fast economic growth. India could become the "next China" in CO_2 emissions if it misses the opportunity of renewable deployment in place of coal. Novel approaches such as "debt-for-climate" swaps with developing countries (Simmons et al., 2021) can complement China's carbon goals by more efficient use of resources. Efforts in helping developing countries to sidestep fossil fuel and directly move to renewable energy, especially distributed systems, will make the world better connected and balanced.

6. Conclusions and expectations

Achieving carbon neutrality is a broad and profound economic and social systemic change in China. The significance of China's carbon-neutral goal to the Paris climate accord targets and the world's sustainable development and peace cannot be over-emphasized, but the challenges are enormous. Just like China's reform and opening up 40 years ago, China's economic development has brought new surprises to the world. In the same way, with the carbon-neutral vision that started today, China will also meet its carbon-neutral goal 40 years later, bringing confidence and providing a model for other countries in the world. The recently achieved price-parity of solar and wind with fossil fuel energy sources lays the foundation for this ambition; however, deployment at the scales needed is subject to technological and commercial bottlenecks. The envisioned pathways push resource limitations for nuclear, wind, and bio-energy. It is important to research and experiment with all possible technologies. On the deployment side, we recommend a cautious approach with conventional nuclear and a faster phase-out of coal. Still, more aggressive action is needed to distribute solar, wind, small and modular nuclear, smart grid, and energy storage. International collaboration on scientific and technical innovation and deployment will be essential to build a safe, fair, and more resilient common future globally.

Acknowledgements. This work was supported by the National Key R&D Program of China (Grant No. 2017YFB0504 000).

Electronic supplementary material: Supplementary material is available in the online version of this article at https://doi.org/10.1007/s00376-021-1313-6.

REFERENCES

Barron-Gafford, G. A., and Coauthors, 2019: Agrivoltaics provide mutual benefits across the food–energy–water nexus in drylands. *Nature Sustainability*, **2**(9), 848–855, https://doi.org/10.1038/s41893-019-0364-5.

Beijing Municipal Ecology and Environmental Bureau, 2020. 2019 Beijing Ecology and Environment Statement. Available from http://sthjj.beijing.gov.cn/bjhrb/resource/cms/article/1718882/10837172/2020073117581274300.pdf.

Davidson, M. R., D. Zhang, W. M. Xiong, X. L. Zhang, and V. J. Karplus, 2016: Modelling the potential for wind energy integration on China's coal-heavy electricity grid. *Nature Energy*, **1**(7), 16086, https://doi.org/10.1038/nenergy.2016.86.

Fang, J. Y., G. R. Yu, L. L. Liu, S. J. Hu, and F. S. Chapin III, 2018: Climate change, human impacts, and carbon sequestration in China. *Proceedings of the National Academy of Sciences of the United States of America*, **115**(16), 4015–4020, https://doi.org/10.1073/pnas.1700304115.

Friedlingstein, P., and Coauthors, 2020. Global carbon budget 2020. *Earth System Science Data*, **12**(4), 3269–3340, https://doi.org/10.5194/essd-12-3269-2020.

Fuss, S., and Coauthors, 2014: Betting on negative emissions. *Nature Climate Change*, **4**(10), 850–853, https://doi.org/10.1038/nclimate2392.

Global Energy Interconnection Development and Cooperation Organization, 2021. Research Reports on China Achieving Carbon Neutrality Before 2060. Available from https://www.geidco.org.cn/html/qqnyhlw/zt20210120_1/index.html. (in Chinese)

Han, P., and Coauthors, 2021. Decreasing Emissions and Increasing Sink Capacity to support China in achieving carbon neutrality before 2060. Available from https://arxiv.org/abs/2102.10871.

Huang, L., Y. Zhou, Y. T. Han, J. K. Hammitt, J. Bi, and Y. Liu, 2013: Effect of the Fukushima nuclear accident on the risk perception of residents near a nuclear power plant in China. *Proceedings of the National Academy of Sciences of the United States of America*, **110**(49), 19742–19747, https://doi.org/10.1073/pnas.1313825110.

Huang, X. D., S. Y. Chang, D. Q. Zheng, and X. L. Zhang, 2020: The role of BECCS in deep decarbonization of China's economy: A computable general equilibrium analysis. *Energy Economics*, **92**, 104968, https://doi.org/10.1016/j.eneco.2020.104968.

IPCC, 2018. Special Report Global Warming of 1.5 degree. Available from https://www.ipcc.ch/sr15/.

IRENA, 2020. Renewable Power Generation Costs in 2019. Available from https://www.irena.org/publications/2020/Jun/Renewable-Power-Costs-in-2019.

Jiang, K. J., C. M. He, X. Y. Xu, W. Y. Jiang, P. P. Xiang, H. Li, and J. Liu, 2018: Transition scenarios of power generation in China under global 2 °C and 1.5 °C targets. *Global Energy Interconnection*, **1**(4), 477–486, https://doi.org/10.14171/j.2096-5117.gei.2018.04.008.

Kaya, Y., and K. Yokoburi, 1997. *Environment, Energy, and Economy: Strategies for Sustainability*. United Nations University Press.

Kintisch, E., 2018. Rooftop sensors on U.S. embassies are warning the world about 'crazy bad' air pollution. *Science*, https://doi.org/10.1126/science.aat9260.

Lazard, 2020. Levelized Cost of Energy, Levelized Cost of Storage, and Levelized Cost of Hydrogen– 2020. Available from https://www.lazard.com/perspective/levelized-cost-of-energy-and-levelized-cost-of-storage-2020/.

Lin, X. H., W. Zhang, M. Crippa, S. S. Peng, P. F. Han, N. Zeng, L. J. Yu, and G. C. Wang, 2021: A comparative study of anthropogenic CH_4 emissions over China based on the ensembles of bottom-up inventories. *Earth System Science Data*, **13**(3), 1073–1088, https://doi.org/10.5194/essd-13-1073-2021.

McLaren, D., and N. Markusson, 2020: The co-evolution of technological promises, modelling, policies and climate change targets. *Nature Climate Change*, **10**(5), 392–397, https://doi.org/10.1038/s41558-020-0740-1.

Project Comprehensive Report Preparation Team, 2020. A comprehensive report on the research of China's long-term low-carbon development strategies and pathways. *China Population, Resources and Environment*, **30**(11), 1–25. (in Chinese)

Povinec, P.P. and coauthors, 2013. Cesium, iodine and tritium in NW Pacific waters – a comparison of the Fukushima impact with global fallout, Biogeosciences, **10**(8): 5481-5496. https://doi.org/10.5194/bg-10-5481-2013.

Raupach, M. R., G. Marland, P. Ciais, C. L. Quéré, J. G. Canadell, G. Klepper, and C. B. Field, 2007. Global and regional drivers of accelerating CO_2 emissions. *Proceedings of the National Academy of Sciences of the United States of America*, **104**(24), 10 288–10 293, https://doi.org/10.1073/pnas.0700609104.

Simmons, B. A., R. Ray, H. B. Yang, and K. P. Gallagher, 2021: China can help solve the debt and environmental crises. *Science*, **371**(6528), 468–470, https://doi.org/10.1126/science.abf4049.

The State Council, 2021. The Outline of 14th Five-year Plan (2021-2025) for National Economic and Social Development and the Long-Range Objectives Through the Year 2035. Available from http://www.gov.cn/xinwen/2021-03/13/content_5592681.htm. (in Chinese)

World Bank, 2018. Belt and Road Initiative. Available from https://www.worldbank.org/en/topic/regional-integration/brief/belt-and-road-initiative.

Xi, J. P., 2020. Xi Delivered an Important Speech During the General Debate of the 75th Session of the United Nations General Assembly. Available from http://www.gov.cn/xinwen/2020-09/22/content_5546168.htm. (in Chinese)

Xiao, X.-J., and K.-J. Jiang, 2018: China's nuclear power under the global 1.5 °C target: Preliminary feasibility study and prospects. *Advances in Climate Change Research*, **9**(2), 138–143, https://doi.org/10.1016/j.accre.2018.05.002.

Yang, J. B., Q. Y. Liu, X. Li, and X. D. Cui, 2017: Overview of wind power in China: Status and future. *Sustainability*, **9**(8), 1454, https://doi.org/10.3390/su9081454.

Yu, S., B. Yarlagadda, J. E. Siegel, S. Zhou, and S. Kim, 2020: The role of nuclear in China's energy future: Insights from

integrated assessment. *Energy Policy*, **139**, 111344, https://doi.org/10.1016/j.enpol.2020.111344.

Zeng, N., 2008: Carbon sequestration via wood burial. *Carbon Balance and Management*, **3**(1), 1, https://doi.org/10.1186/1750-0680-3-1.

Zeng, N., Y. H. Ding, J. H. Pan, H. J. Wang, and J. Gregg, 2008: Climate change-the Chinese challenge. *Science*, **319**, 730–731, https://doi.org/10.1126/science.1153368.

Zhang, D., X. L. Zhang, J. K. He, and Q. M. Chai, 2011: Offshore wind energy development in China: Current status and future perspective. *Renewable and Sustainable Energy Reviews*, **15**(9), 4673–4684, https://doi.org/10.1016/j.rser.2011.07.084.

Zhao, L. L., S. Y. Chang, H. L. Wang, X. L. Zhang, X. M. Ou, B. Y. Wang, and M. R. Wu, 2015: Long-term projections of liquid biofuels in China: Uncertainties and potential benefits. *Energy*, **83**, 37–54, https://doi.org/10.1016/j.energy.2015.01.060.

Zhou, S., Q. Tong, X. Z. Pan, M. Cao, H. L. Wang, J. Gao, and X. M. Ou, 2021: Research on low-carbon energy transformation of China necessary to achieve the Paris agreement goals: A global perspective. *Energy Economics*, **95**, 105137, https://doi.org/10.1016/j.eneco.2021.105137.

ADVANCES IN ATMOSPHERIC SCIENCES, VOL. 39, AUGUST 2022, 1239–1251

• **Review** •

A Concise Overview on Solar Resource Assessment and Forecasting※

Dazhi YANG*[1], Wenting WANG[1], and Xiang'ao XIA[2]

[1]*School of Electrical Engineering and Automation*, *Harbin Institute of Technology*, *Harbin* 150006, *China*
[2]*Key Laboratory for Middle Atmosphere and Global Environment Observation (LAGEO)*, *Institute of Atmospheric Physics*, *Chinese Academy of Sciences*, *Beijing* 100029, *China*

(Received 19 September 2021; revised 15 November 2021; accepted 19 November 2021)

ABSTRACT

China's recently announced directive on tackling climate change, namely, to reach carbon peak by 2030 and to achieve carbon neutrality by 2060, has led to an unprecedented nationwide response among the academia and industry. Under such a directive, a rapid increase in the grid penetration rate of solar in the near future can be fully anticipated. Although solar radiation is an atmospheric process, its utilization, as to produce electricity, has hitherto been handled by engineers. In that, it is thought important to bridge the two fields, atmospheric sciences and solar engineering, for the common good of carbon neutrality. In this überreview, all major aspects pertaining to solar resource assessment and forecasting are discussed in brief. Given the size of the topic at hand, instead of presenting technical details, which would be overly lengthy and repetitive, the overarching goal of this review is to comprehensively compile a catalog of some recent, and some not so recent, review papers, so that the interested readers can explore the details on their own.

Key words: review, solar forecasting, solar resource assessment

Citation: Yang, D., W. T. Wang, and X. A. Xia, 2022: A concise overview on solar resource assessment and forecasting. *Adv. Atmos. Sci.*, **39**(8), 1239−1251, https://doi.org/10.1007/s00376-021-1372-8.

Article Highlights:

- A review of reviews of solar resource assessment and forecasting is presented.
- An all-in-one compendium of research topics in the fields of resource assessment and forecasting is presented.
- A bridge between atmospheric sciences and solar energy engineering is needed.

1. Introduction

The field of solar energy can be broadly categorized into four parts: (1) solar resource assessment and forecasting, (2) photovoltaic (PV) technology, (3) concentrating solar power (CSP) technology, and (4) solar heating and cooling. Insofar as solar radiation is concerned, solar engineering takes a vital role in connecting atmospheric science, which deals with the atmospheric chemistry and physics governing the amount of solar radiation reaching the Earth's surface, and downstream applications, such as grid integration, daylighting, or heating, ventilation, and air conditioning (HVAC). However, unlike atmospheric science, electrical engineering, architecture, or mechanical engineering, it is not entirely clear whether or not solar engineering can be viewed as a subject on its own—very few universities offer a curriculum on that, and very few people would attain a certificate that says "Bachelor of Solar Engineering" at the end of the day. That said, as long as climate change and carbon neutrality are of interest, it is a fact that solar engineering would be involved in one way or another. On this point, one must be aware of the interdisciplinary nature when making scientific inquiries regarding the use of solar energy.

Take grid integration of solar energy, for instance, power system operators require information on future solar generation and electric load at different time scales and horizons, in order to perform unit commitment—an integer programming problem determining which thermal generator should be turned on at which instance. Clearly, the sciences and technologies involved in this task are multifaceted. First and foremost, there is atmospheric science, which is required to address the questions of when, where, and how much solar radiation is available. Next, solar engineering must be involved, since it deals with the conversion from solar radiation to solar power. Last but not least, power system engineering knowledge is needed in order to balance the (con-

※ This paper is a contribution to the special issue on Carbon Neutrality: Important Roles of Renewable Energies, Carbon Sinks, NETs, and non-CO_2 GHGs.

* Corresponding author: Dazhi YANG
Email: yangdazhi.nus@gmail.com

ventional thermal plus renewable) generation and (electric, heating, and cooling) load in an operational fashion. On top of all those, modern scientific techniques, such as statistics, machine learning, or mathematical optimization, almost always play a part.

Through the above elaboration, one can readily understand the challenge here: no one would be able to comprehensively acquire all knowledge pertaining to grid integration. And the same can be said for daylighting, HVAC, or any other application of an interdisciplinary nature. The undercurrent of resistance, as in many problems of a like form, is chiefly due to our limited time—so much has been collectively known by humankind, that a single lifetime is not sufficient to reach all frontiers of knowledge. Atmospheric science, as traditionally conceived, is the study of the Earth's atmosphere. Customarily, once theories in regard to atmospheric chemistry and physics are developed and understood, the job of atmospheric scientists is considered done. On the other hand, solar engineers are concerned with applications, hardware, and execution. During that process, little attention has been paid to the suitability and validity of scientific theories on which their engineering is based. There really is not much surprise to the reasons that have led to the status quo—people in various communities went to different schools, received training under different thinking styles, and are employed by departments of different agendas. The sheer amount of effort that would be required to convert to convert from one profession to another is monumental.

We all know it is generally beneficent to know more, but consider this question: how often do we spend time on reading relevant but secondary literature as to our own research domain? Priority is an interesting notion, in that, it is supposed to be solely internal to individuals. It is human nature to prioritize those tasks that are familiar to us and, in parallel, postpone those less familiar ones. To that end, if we are to deviate from this rule of thumb, others who hold fast to it may consequently produce more results and thus attain more recognition. This is thought to be the inquiry of interest: should we invest time and energy in things we are partially interested in but are not good at? Involution, a popular word of the Chinese urban dictionary, which refers to the situation where peer pressure forces one to take (or, not to take) certain actions that may or may not lead to a favorable outcome, is sufficient in narrating the scenario.

One remedy to counter the effect of involution is to reduce the amount of effort that is required to achieve certain goals. More formally, in line with the theory of economics, the trick is to lower the opportunity cost. One possible action of this kind is to summarize the best practices in one field to researchers and professionals in another field, e.g., through review papers. However, reading review papers is still an inefficient approach, since there are all too many of them—there are hundreds, if not thousands, of review papers published on solar resource assessment and forecasting alone—especially under today's "publish or perish" regime, which has been commonplace in most academic domains. In this regard, it is thought that überreview has now become absolutely necessary. One may interpret an überreview as a review of reviews. It is on this account that an überreview on solar resource assessment and forecasting is herein presented.

Presenting an überreview is by no means a simple task, because the literature contains many outdated, duplicated, and non-representative reviews that can be misleading or even harmful, particularly to those who are not familiar with the domain. In fact, even highly cited recent textbooks and handbooks can be outdated, and may contain questionable information. Since solar resource assessment and forecasting is a fast-advancing field with many parallel works, this überreview is composed of carefully selected and most representative reviews from credible sources that could fully reflect the state-of-the-art.

2. Solar resource assessment

The idea central to solar resource assessment resides in identifying suitable and reliable data, without which no conclusion made can be deemed valid. Data for solar resource assessment present in three main forms: (1) ground-based measurements, (2) remote-sensing retrievals, and (3) output of numerical weather prediction (NWP) models. Among these three forms, carefully calibrated ground-based measurements are most accurate, followed by remote-sensing retrievals, whereas NWP output is the least accurate.

Living in an age of data explosion, one must not forget that solar radiation data was once scarce. Before the advent of modern remote sensing and NWP, researchers used to rely on low-accuracy empirical models for the estimation of solar radiation, such as the Ångström–Prescott type of models, which are based on sunshine duration. As compared to the current data practice and ways of estimating or retrieving solar radiation, sunshine duration data are of poor and inconsistent quality, and empirical correlations obtained at one location rarely apply to another. Therefore, many researchers, such as Gueymard et al. (2009), had advocated the termination of use of such models, years ago. As of now, satellite-to-irradiance algorithms and improved parameterization of NWP models have long become mainstream, albeit numerous research issues remain. In this section, data and modeling issues related to solar resource assessment are reviewed in sections 2.1 and 2.2, respectively.

2.1. *Data for solar resource assessment*

Ground-based measurements are made using radiometers, and the respective science is known as radiometry. Whenever radiometry is of interest, the textbook by Vignola et al. (2019) always presents itself as a useful reference. In terms of instrumentation, that is, pyranometer and pyrheliometer, different radiometers are subject to different measurement uncertainties and performance. Due to the high cost of research-grade radiometers, it is exceptionally luxurious to collocate more radiometers than needed at a single site. In that, the review and intercomparison of 51 collocated radiome-

ters, as presented by Habte et al. (2016), is one of a kind. Ground-based data can be used to validate the other two forms of data. However, its own quality control (QC) must be first conducted, to ensure that the baseline for any subsequent validation is legitimate. Unfortunately, there is not any QC routine that can be deemed universal, but the basic one set forth by Long and Shi (2008) has gained most acceptance and is used by the Atmospheric Radiation Measurement (ARM) and the Baseline Surface Radiation Network (BSRN). Figure 1 shows a diagnostic visualization of potential data problems in ground-based measurements. Detailed interpretation of this plot is not within the scope of this review, nevertheless, one can see the level of complexity that is typically involved during QC of irradiance data—it is by no means just applying a few statistical filters, like what most people do, instead, much domain knowledge is required to justify the validity of the data under scrutiny.

Solar engineers are interested in four types of radiometry measurements: (1) global horizontal irradiance (GHI); (2) beam normal irradiance (BNI)[a]; (3) diffuse horizontal irradiance (DHI); and (4) global tilted irradiance (GTI). Whereas the energy production of PV systems depends on GTI, that

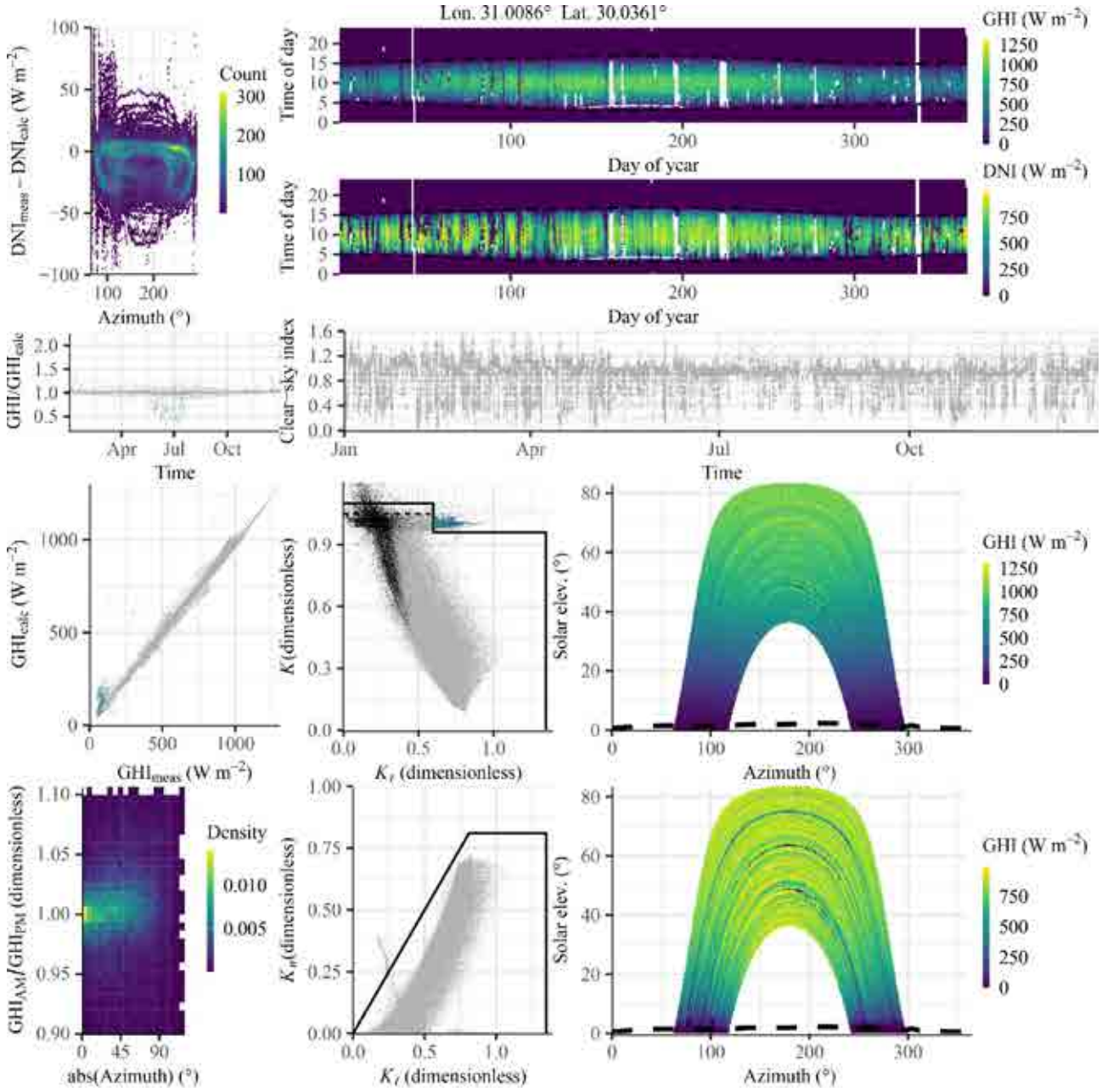

Fig. 1. Some visualization to facilitate quality control of irradiance data. See Forstinger et al. (2021) for detailed interpretation of these plots.

[a] The word "beam" is used interchangeably with "direct."

of CSP depends solely on BNI. It is well known that GHI can be split into BNI (after the modification of cosine of zenith angle) and DHI. Nonetheless, since the definition of what constitutes the beam component is a human convention, some issues regarding the circumsolar region—the vicinity of the Sun disk—exist, and a good summary of those issues can be found in Blanc et al. (2014). In fact, measuring the beam radiation component can be considered as a study domain on its own, namely, directional radiometry [see (Mishchenko, 2011), for review], which is an active research field in the area of atmospheric measurement technique, because lots of information about aerosols and clouds can be derived from circumsolar measurements. As for GTI, it is not only affected by horizontal irradiance components, albedo also plays a vital part; for albedo-related topics, the reader is referred to Gueymard et al. (2019). In any case, publicly available, research-grade, ground-based radiometry data are rare as compared to data of other meteorological variables such as temperature, humidity, or precipitation. For instance, there are about 100 radiometry stations in China, however, measurements of the aforementioned basic meteorological variables are available at more than 50 000 stations. On this point, Chapter 6 of Sengupta et al. (2021) contains a rather complete list of ground-based radiometry data sources.

In contrast to ground-based data, satellite-derived irradiance covers all locations on Earth that are between ±60° latitudes, see Fig. 2. For higher-latitude locations, satellite-derived irradiance is also available, but only comes at a lower temporal resolution. This is because satellite-derived irradiance for mid and low latitudes is retrieved from remote-sensing images taken by geostationary satellites, whereas for high-latitude irradiance estimations, they come from data of polar orbiters. Given the fields-of-view of different weather satellites, as well as the ownership of these satellites, satellite-derived irradiance products are developed by different agencies and weather centers, and thus are heterogeneous. Not only are the retrieval algorithms powering the products different, accuracy also varies greatly across products, and across locations, time periods, and sky conditions. This is precisely why a somewhat major effort has been paid to validating these satellite-derived irradiance products, among which the work by Yang and Bright (2020) can easily be regarded as most comprehensive, at the time of writing.

Satellite-to-irradiance algorithms can be broadly categorized into those that rely on radiative transfer and those that do not. Huang et al. (2019) provided a comprehensive review elaborating the pros and cons of the two categories of method. And a more detailed description regarding the treatment of clouds during the retrieval can be found in Miller et al. (2018). Notwithstanding, regardless of which algorithm is used, the satellite-derived irradiance products are always limited by the native resolutions of the original satellite imagery. Whereas previous-generation satellites have a 60-min–10-km native resolution, the native resolution of the latest-generation satellites has reduced to 10 min 1 km, offering more opportunities for operational applications of satellite data in solar engineering.

The output of NWP models is of two kinds, one forecast and the other reanalysis. Operational NWP models issue forecasts a few times a day, over forecast horizons of a few days, at a regional or global scale. From a statistics point of view, weather forecasts are multivariate time series of lattice processes, whose spatio-temporal trajectory is governed by the physical laws of the atmosphere. On this note, the textbook written by Cressie and Wikle (2015) is inspirational, in terms of linking statistics and physical science. Since atmospheric scientists are familiar with this topic, only a few notable, general, and educational reviews are suggested here: Bauer et al. (2015); Müller et al. (2021); McNeal et al. (2021). What is more important, instead, is how to parameterize NWP models such that the quality of its radiation output can be enhanced; the reader is referred to Jimenez et al. (2016) for a list of issues and challenges.

NWP produces forecasts, but the operational models are constantly undergoing changes and developments. In con-

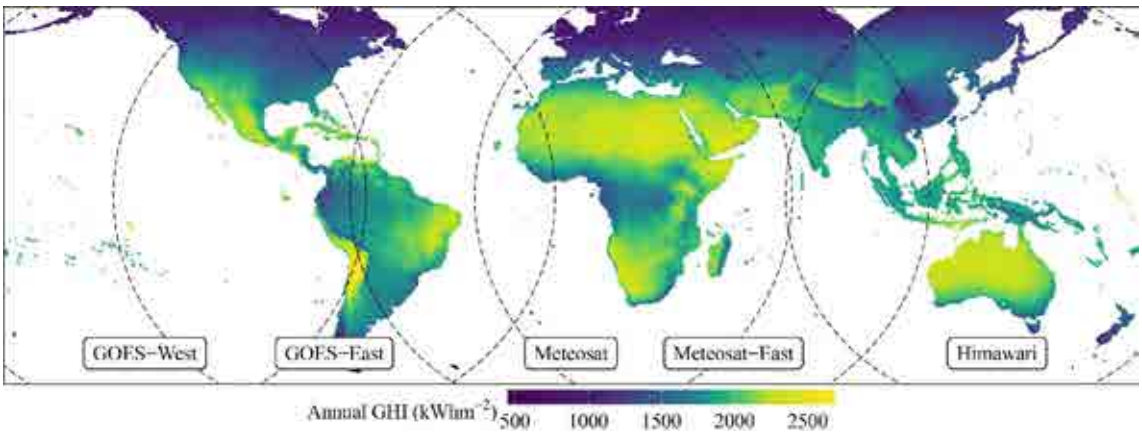

Fig. 2. Five geostationary weather satellites jointly cover all locations on Earth between ±60° latitudes. Gridded irradiance estimates can be derived from the visible- and infrared-channel images captured by these satellites. (Other meteorological satellite series, such as Fengyun, are not shown, since their field-of-views overlap with the ones in the figure.) Data source: National Solar Radiation Data Base.

trast, reanalyses use "frozen" models and produce estimates of weather variables over a period typically spanning a few decades. The most well-known global reanalyses include the ECMWF Reanalysis, Version 5 (ERA5; Hersbach et al., 2020) and Modern-Era Retrospective Analysis for Research and Applications, Version 2 (MERRA-2; Gelaro et al., 2017), which have been used in countless ways by researchers from various fields. With no exceptions, these reanalyses have been shown to be useful in solar engineering as well, particularly when measurements of atmospheric variables, such as aerosol optical depth or surface albedo, are required but are unavailable. At the moment, the literature is short of a review on how reanalysis data are involved in solar engineering.

2.2. *Models for solar resource assessment*

2.2.1. *Solar constant*

Many calculations in the field of solar engineering begin with the solar constant. The solar constant is obtained through calculating the average of total solar irradiance (TSI), which is the Sun's instantaneous output, over a long period of time, typically over a few decades. Whereas the overall concept is straightforward, the determination of the solar constant is mostly hindered by data. The pioneering work on the measurement of the solar constant was made by Samuel Pierpont Langley, who invented a precise bolometer in 1880. Spaceborne TSI observations, on the other hand, started from 1978, and are made by various instruments covering different time periods, but with some overlaps. Since the disagreement among various instruments is often non-negligible, it is generally difficult to know which instrument is trustworthy during which period. The most recent advance on this topic is put forward by Gueymard (2018), who performed an re-evaluation of the solar constant based on 42 years of TSI data. The conclusion, after careful debate and data analysis, suggests a solar constant of 1361.1 Wm^{-2}.

2.2.2. *Spectral irradiance*

A super majority of solar engineering tasks only require the broadband solar irradiance to operate. However, in some PV, photobiological, and photochemical applications, e.g., during characterization of PV materials or determination of photosynthetically active radiation, spectral irradiance is needed. For an all-inclusive compendium of applications of spectral irradiance, the reader is referred to Gueymard (2019). Just like the broadband solar irradiance, spectral irradiance data can be either measured or modeled. Given the fact that spectroradiometers are costly, spectral irradiance models are in high demand. At the moment, the Simple Model of the Atmospheric Radiative Transfer of Sunshine (SMARTS) model is arguably the most popular choice; its 25-year journey has been recently compiled by its inventor (Gueymard, 2019). One should note, however, that most spectral irradiance models, including SMARTS, are restricted to producing clear-sky spectra. In that, the accuracy of these models is highly dependent on the quality of inputs, such as aerosol, water vapor, or surface albedo.

2.2.3. *Clear-sky*

Clear-sky irradiance refers to the irradiance obtained under a cloud-free atmosphere[b]. The ratio between the irradiance (or PV power) and its clear-sky expectation is known as the clear-sky index. If not specified, clear-sky index refers to clear-sky index calculated with GHI. The models which are used to estimate the clear-sky irradiance are called clear-sky models, and they can be either physics-based or empirical. Physics-based clear-sky models leverage radiative transfer. However, owing to legacy reasons, simplified radiative transfer or look-up table are ordinarily used by the solar energy community. On the other hand, empirical clear-sky models fit irradiance observations under clear-sky conditions to some mathematical function forms, but model parameters obtained through this way are rarely general. When properly modeled, clear-sky irradiance describes the diurnal and seasonal variation in irradiance caused by all factors but clouds. Therefore, these models are very useful in terms of detrending the irradiance or PV power time series, during forecasting, satellite-to-irradiance modeling, among other data analyses pertaining to radiation modeling. A pair of recent reviews compared 75 clear-sky models for GHI (Sun et al., 2019) and 95 clear-sky models for BNI and DHI (Sun et al., 2021). It was found that the REST2 model (Gueymard, 2008) has the best overall performance, if high-quality input variables are available. REST2 is a physics-based

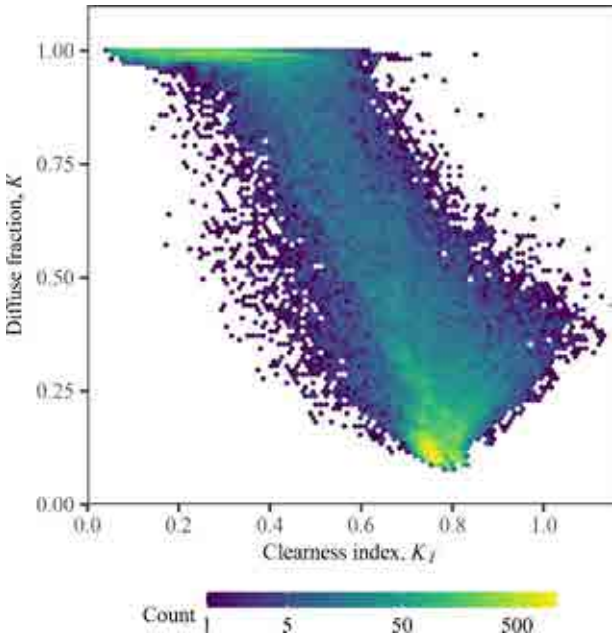

Fig. 3. A scatter plot of diffuse fraction K versus clearness index K_T. The color bar indicates the number of points in the neighborhood. Data source: Fort Peck station, Baseline Surface Radiation Network.

[b] One problem with this definition is that in situations where aerosol loading is high, the apparent clear-sky irradiance would be very low.

method that takes the effects of aerosol and other atmospheric particulates, which attenuate incoming solar radaition, into consideration. It requires several input variables, included aerosol optical depth and column ozone, which need to be sourced from reanalysis or remote-sensing databases, such as the aforementioned MERRA-2.

2.2.4. *Separation*

Also known as decomposition modeling, separation modeling aims at splitting the beam and diffuse radiation components from the global one, using parameters that are calculable, such as zenith angle or clear-sky index. More specifically, diffuse fraction (the ratio between DHI and GHI) is expressed as a function of clearness index (the ratio between GHI and extraterrestial GHI) and other variables, see Fig. 3. for an example scatter plot. The reason why solar engineers are interested in separation modeling is two-fold. Firstly, when estimating GTI, both GHI and DHI are required. If DHI measurements are unavailable, it needs to be estimated from GHI through separation modeling. Secondly, satellite-to-irradiance algorithms only estimate GHI, whereas the diffuse and beam components in most satellite-derived irradiance products need to be, and in fact are, generated using separation models. The number of separation models in the literature is numerous: there have been more than 150 models proposed so far. Besides one or two exceptions, most of these models are empirical in nature, and the performance of these models depends on the data that is used during model fitting. It is to this effect that the ranking of separation models has been controversial, until the recent review by Gueymard and Ruiz-Arias (2016), who compared 140 separation models using data from worldwide locations. In that review, the Engerer2 model (Engerer, 2015) has been identified as quasi-universal. Since then, many other models have been proposed, and Engerer2 is often used as a benchmark. Among these new proposals, the Yang2 model (Yang and Boland, 2019; Yang, 2021) is the best separation model to date, which is able to outperform Engerer2 by a significant margin (see Yang and Gueymard, 2020, for review), which is due to the fact that Yang2 uses a low-frequency diffuse fraction estimate as input that is able to capture the low-frequency variability in high-frequency diffuse fraction—Yang2 is equivalent of cascading two Engerer2 at different temporal resolutions. Traditional separation models are deterministic, in that, they do not carry any notion of uncertainty on the diffuse fraction estimates. Nonetheless, recent advances in radiation modeling have led to probabilistic separation models, albeit their widespread acceptance has not been fully evident (see Yang and Gueymard, 2020).

2.2.5. *Transposition*

Transposition models convert irradiance components on a horizontal surface to those on tilted surfaces. Since PV panels, when not restricted by topography or installation surface, should be placed on an Equator-facing surface that has a tilt angle comparable to the site's latitude (this is to maximize the annual energy production), transposition modeling is essential in PV design, simulation, and performance evaluation. The number of available transposition models is not as many as separation models, yet, there are about 25 of them. All of those models only differ in the treatment of the diffuse transposition factor, whereas the treatment for direct and reflected radiation components is shared across all models. As reported by Yang (2016), after a worldwide comparison using 18 datasets, the 1990 version of the Perez model (Perez et al., 1990) stood out from a pool of 26 models, and was found to be the most accurate model to date. The Perez model separates the sky dome into three geometrical parts, within each of which the radiance is constant: (1) the circumsolar disk, (2) the horizon band, and (3) an isotropic background. Indeed, based on a bibliometric analysis, the paper by Perez et al. (1990) is the most cited one in the history of the Solar Energy journal, which suggests the popularity of the model. Similar to the case of separation modeling, transposition has been viewed as a deterministic process, historically. Nevertheless, in the recent article by Quan and Yang (2020), probabilistic transposition models have been discussed, and two general strategies for converting traditional deterministic transposition models to probabilistic ones were explained.

2.2.6. *Angular distribution of radiance*

The three-part geometrical framework of the Perez model facilitates the determination of the sky-view factor, which is the part of the sky as seen by the tilted surface. However, in urban environment or terrain with a humpy topography, where obstruction throughout a year is complex and heterogeneous, this simple three-part division of the sky dome is no longer sufficient. Instead, one requires a more granular breakdown of the sky dome—the angular distribution of radiance—to estimate the diffuse irradiance received by a tilted surface. Beside radiance distribution, a similar concept is the angular distribution of luminance, which is essential for daylighting, as required during architectural design. Figure 4 shows the angular distribution of luminance for 15 standard sky types defined by the International Commission on Illumination (CIE, 2004). Models proposed for angular distribution of radiance/luminance are mostly empirical (see Torres and Torres, 2008, for a review), in that, the model coefficients are determined by fitting the model to measured data. The most common type of instrument measuring radiance/luminance is the sky scanner, which sequentially scans the sky dome in a patch-by-patch fashion, every few minutes.

2.2.7. *Site adaptation*

Both satellite-derived irradiance and NWP output are often found biased. To enhance the bankability of a solar energy project, may it be a PV one or a CSP one, the bias in raw data ought to be corrected—this procedure is known as site adaptation in this field, which is similar to the measure–correlate–predict procedure in wind engineering. This is, to some extent, closely related to data assimilation in NWP, in which the output field of NWP is taken as the initial state, and is adjusted by measurements using mathemati-

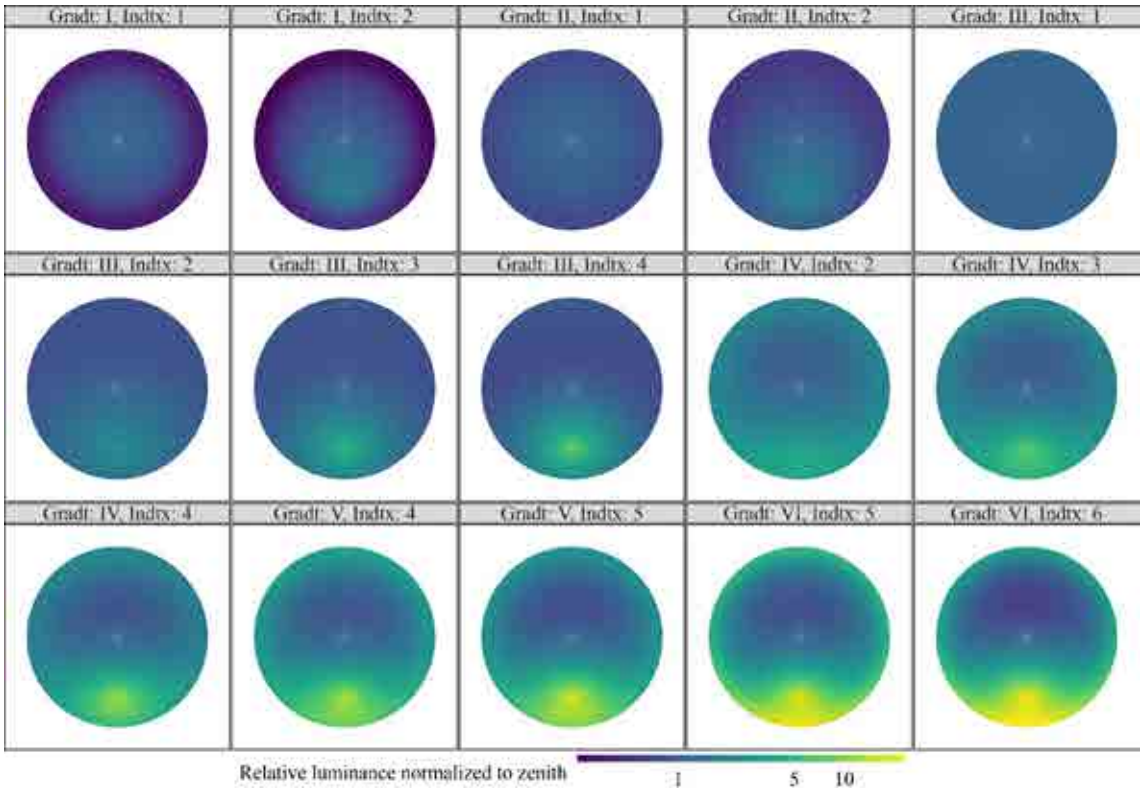

Fig. 4. Angular distribution of sky luminances for each of the 15 CIE standard sky types. A solar zenith angle of 60° and a solar azimuth angle of 180° is assumed.

cal method, such as optimal interpolation or Kalman filtering. The idea central to site adaptation is to use a short period (such as one year) of high-accuracy ground-based measurements to correct a long period (typically 10–20 years) of low-accuracy gridded data at a site collocated with the ground-based measurements. Traditionally, site adaptation has always been viewed as a deterministic regression problem, in that, various techniques have been reviewed by Polo et al. (2020). However, as uncertainty quantification slowly gains attention, probabilistic site-adaptation techniques become relevant, which are reviewed and validated by Yang and Gueymard (2021). One should note that site adaptation is a step that cannot be circumvented during solar energy system feasibility study, design, and simulation. For an overview on solar project financing and bankability, the reader is referred to Yang and Liu (2020).

3. Solar forecasting

It is customary to regard the two closely interconnected fields, namely, solar irradiance forecasting and solar power forecasting, as one—solar forecasting. At this stage, two common misconceptions must be warned. One of those is the misconception that satisfactory solar power forecasts can be produced using purely data-driven methods. As machine learning and statistical methods become widely available in software packages and tools, many novices tend to simply pass data to these packages and tools without considering the underlying physics; insofar as the methods have not been used previously, novelty can be claimed. This is in fact a very bad practice, and we shall explain why shortly after, in section 3.1. The other common misconception is that the novelty in solar forecasting should be solely revolved around forecasting methodology. Indeed, forecasting methodology is an important aspect, but it is never the only one. The field of solar forecasting has five main aspects: (1) forecasting methodology, (2) post-processing, (3) irradiance-to-power conversion, (4) verification, and (5) materialization of values. These are discussed in Section 3.2.

3.1. *Salient characteristics of solar forecasting*

It is not possible to produce good solar power forecasts without good solar irradiance forecasts. The rationale behind this argument is rather straightforward: solar power, may it be from PV or CSP, varies chiefly according to irradiance condition, in that, there does not seem to be any valid reason why solar irradiance forecasts should not be involved during solar power forecasting. Moreover, because solar irradiance is an atmospheric process, it is best forecast using physical approaches. There have been numerous works that adopt a purely data-driven approach to forecast solar power, in which historical weather and power data are used as input of machine learning and statistical methods. Forecasts generated in this way would be perpetually suboptimal, because they ignores the salient features of solar irradiance. In other words, what distinguishes solar forecasting from any other forecasting domain is not how sophisticated the data-driven methods are, instead, it is the consideration

of atmospheric physics, namely, domain knowledge, that matters.

3.1.1. *Reproducibility*

The first and foremost salient characteristic of solar forecasting is reproducibility. As methods and algorithms grow more and more complex, and their number increases exponentially, it would be very time consuming to reproduce the results of forecasting papers of interest without computer code. Statisticians are generous sharers in that respect, since publishing computer code alongside with research articles has been a common practice in their domain. Solar forecasting research, in the early days, was non-reproducible, in that, the code and data were kept proprietary. However, the situation has changed drastically now, owing to a few initiatives by field leaders (e.g., see Yang et al., 2018a). In fact, this switching of publishing regime is no coincidence, for the pitfalls of non-reproducible forecasting research have been debated elsewhere, by general-purpose forecasting experts, in the top journal of their field (Makridakis et al., 2018; Boylan et al., 2015). Moving forward, it is thought that the attention paid to non-reproducible research (or, papers do not present computer code) is going to become less and less—we do not have all day to make suppositions on the technical ambiguities, which exist almost surely in any research paper nowadays.

3.1.2. *Operational*

It is well known that NWP forecasts, when needed, can be issued at arbitrary temporal resolutions. However, most operational NWP forecasts have an hourly resolution, since otherwise, the data to be disseminated would be too big to be practical. This fact poses some challenges to solar forecasters, since the spatial and temporal scale of forecasts required for grid integration is often smaller than the synoptic- or meso-scale NWP output. Hence, to convert the raw NWP forecasts to a form that is readily usable by grid operators, downscaling and other post-processing techniques are needed. Another important aspect of operational forecasting is lead time. It is customary for researchers to design rolling forecast experiments of various sorts in academic papers.[c] Notwithstanding, in an operational sense, rolling forecasts are coupled with lead times. This fact has been largely ignored by solar forecasters. Since longer horizon is more difficult to forecast, the inclusion of lead time is of great importance for mimicking the actual operational forecasting context.

3.1.3. *Physics-based*

The third salient characteristic of solar forecasting is consisted in its physical nature. Unlike forecasting in a social setting (see Makridakis et al., 2020, for a review on that), forecasting of solar ought to pay more attention on the spatio-temporal behavior of irradiance. Information describing such behavior can be captured by sky cameras, weather satellites, or NWPs, which constitute the three most commonly used forms of exogenous data in solar forecasting. Historically, as first argued by Inman et al. (2013), sky camera, satellite, and NWP data are most suitable for intra-hour, intra-day, and day-ahead solar forecasting, respectively. Nevertheless, with the advent of high-resolution remote sensing and NWP modeling, this correspondence is no longer valid, e.g., 5-min–2-km National Solar Radiation Data Base[d] is well suited for intra-hour forecasting, or the National Oceanic and Atmospheric Administration's High-Resolution Rapid Refresh[e] updates hourly and is thus suitable for intra-day forecasting. In one way or another, utilizing physics-based approaches, as to capture the dynamics of clouds, is what distinguishes solar forecasting from any other forecasting setting.

3.1.4. *Ensemble*

Weather forecasters are fully aware of the advantages of ensemble forecasting, which issues several equally-likely trajectories of atmospheric processes, rather than just one. An ensemble forecast is a special form of probabilistic forecast, which describes the uncertainty involved in the quantity to be forecast. For probabilistic forecasting in a solar context, the review by van der Meer et al. (2018) is recommended. Reviews on probabilistic weather forecasting are numerous, and the ones by Gneiting and Katzfuss (2014); Gneiting and Raftery (2005) are among the high-quality ones. An ensemble can be constructed in different ways, a typology can be found in Roulston and Smith (2003). In the field of statistics, ensemble forecasting is known as combining forecasts, which has been widely recognized as the best forecasting practice—references and reviews on this topic are too many to list, but a few early reviews are herein enumerated (Wallis, 2011; Armstrong, 2001a; Clemen, 1989). Whereas a majority of existing works combine deterministic forecasts, combining probabilistic forecasts is now trending (Winkler et al., 2019; Clements and Harvey, 2011).

3.1.5. *Skill*

Suppose there is a world without clouds, solar forecasting would be a very straightforward calculation. This is because physics-based clear-sky models are able to attain highly accurate estimates of surface irradiance. Thus, as also mentioned earlier, clear-sky models are often employed by solar forecasters as a detrending tool, such that the variation in clear-sky index can be mostly attributed to the effects of moving and varying clouds. This argument aligns with the principle of forecasting outlined by Armstrong (2001b), which states that when seasonal component is present in the time series, it needs to be removed before forecasting. To that end, if one is to quantify the skill of a particular forecasting

[c] See https://robjhyndman.com/hyndsight/rolling-forecasts/.
[d] https://developer.nrel.gov/docs/solar/nsrdb/psm3-5min-download/.
[e] https://rapidrefresh.noaa.gov/hrrr/.

method relative to a reference method, forecasts must be first produced in terms of clear-sky index, and then back-transformed to irradiance or solar power for verification and skill computation. Otherwise, the comparison would not be fair, and the resultant skill would be futile. Most solar forecasting papers in the current literature fall victim to this pitfall, in that the reference models of poor performance are often chosen to exaggerate the skill of the proposed models. The recommended forecast verification procedures are discussed in the next section.

What we have just described, namely, reproducibility, operational, physics-based, ensemble and skill, take the acronym of ROPES, which has been recommended by Yang (2019) as the guideline to good solar forecasting research practice. Indeed, the ROPES guideline summarizes all salient characteristics of solar forecasting well. In what follows, another viewpoint on solar forecasting is presented. Instead of examining the salient characteristics, different aspects of solar forecasting, that is, the research topics, are reviewed.

3.2. *Five aspects of solar forecasting research*

3.2.1. *Forecasting methods*

Most well-cited reviews on solar forecasting, such as Antonanzas et al. (2016) or Voyant et al. (2017), have been focusing on enumerating methods. In that, a classification of forecasting techniques seems to have become an essential component of any review paper. Nevertheless, the strategy of classifying forecasting techniques has two main drawbacks. Firstly, the classification of some techniques often depends on individual viewpoints, e.g., regression can be classified into both statistics and machine learning. In other words, the border between one class of methods and another is often fuzzy, and thus rarely allows a clean-cut classification, which may in turn render the classification subjective. Secondly, the enumeration of methods would never be exhaustive. A typical review would contain at most a few hundred references, whereas the number of publications is on the order of thousands, which implies that the strategy of enumeration would always be incomplete. It is often seen sentences like "machine learning methods include A, B and C" in review papers. But why A, B, and C should be mentioned instead of D, E, and F is seldom justified. One possible defense may be that A, B, and C are more popular than D, E, and F. But if this is indeed the motivation, a more objective approach must be sought. In this regard, text mining as a bibliometric tool is useful; the reader is referred to Yang et al. (2018b) for a text-mining-based review on solar forecasting, in which most frequently appeared keywords and topics are extracted from a pool of 1000 recent papers.

3.2.2. *Post-processing*

Physics-based solar forecasting depends mainly on three types of exogenous data, they are, images captured by sky cameras, remote-sensed data by weather satellite, and output of NWP. In an early review by Inman et al. (2013), the fundamentals of physics-based solar forecasting methods have been described. However, owing to the incomplete understanding on the physical processes and the limited precision of input data, forecasts from the physics-based methods are often found to be biased or uncalibrated (or incorrectly dispersed). Post-processing of initial forecasts is hence often found to be able to improve the quality of forecasts substantially. Another important motivation for post-processing forecasts is to enable bidirectional conversion from deterministic to probabilistic forecasts, which is often required in practice. Similar to the case of base forecasting methods, there have been numerous post-processing methods proposed in the literature, and enumeration of methods would again be inefficient. Therefore, Yang and van der Meer (2021) have advocated the use of thinking tools, which can be thought of as "style" or "mechanism" of post-processing. For example, regression as a thinking tool aims to remove bias from the initial deterministic forecasts, in that, the particular choice of method does not matter, e.g., one can choose either a neural network or a polynomial regression, which, when properly set up and trained, would most likely result in similar outcomes. Other notable recent compendia on post-processing of forecasts include those from Vannitsem et al. (2021, 2018).

3.2.3. *Irradiance-to-power conversion*

The mapping between irradiance and other weather variable to solar power is closely analogous to that between wind speed and wind power; one can refer to such mapping as solar power curve. To convert irradiance to solar power, one can adopt either a direct (or data-driven) approach or an indirect (physical) one. The direct approach views the output of a solar energy system as the dependent variable (or the predictand), and irradiance and other weather variables as the independent variables (or the predictors). In this way, a regressive relationship can be established. In contrast, the indirect approach considers explicitly the physics of different steps of the conversion, which include solar positioning, separation modeling, transposition modeling, PV cell temperature modeling, soiling, shading, mismatch, degradation, among others. Since these models need to be applied sequentially, where the output of one model is the input of the next, the indirect approach is also known as model chain. The model chain concept is well described in the documentation of the pvlib library in Python (Holmgren et al., 2018). Despite the *a priori* advantage of model chain, its uptake has been stagnant, perhaps due to the complexity and effort required to master and use model chain—recall that each type of radiation model presents numerous choices. One exception is the paper by Mayer and Gróf (2021), who compared several model chains, which is likely to be the most comprehensive paper on irradiance-to-power conversion by far, and thus is highly recommended.

3.2.4. *Forecast verification*

After a solar irradiance or power forecast is issued, it is customary to validate it, so that actions can be opted as to

improve the next forecast. Good is an abstract notion, but so long as the question "what constitutes a good solar forecast" is concerned, the essay by Murphy (1993) is widely recognized as seminal, in that, consistency, quality, and value have been argued to jointly characterize the most desirable weather forecasts. Forecast verification has hitherto been a major focus of meteorology, and atmospheric scientists are expected to be familiar with, or at least aware of, the intricacy and technical depth of this topic. Whereas the book by Jolliffe and Stephenson (2012) provides an overview on forecast verification, reviews on more specific topics, such as spatial forecast verification (Gilleland et al., 2010), consistency between judgment and forecast (Gneiting, 2011), accuracy measures for deterministic forecasts (Hyndman and Koehler, 2006), are also available. Particularly worth mentioning is a pair of recent reviews, which details the verification of solar forecasts, one for deterministic forecasts (Yang et al., 2020) and the other probabilistic (Lauret et al., 2019).

3.2.5. *Materialization of values*

By "materialization of values", we mean quantifying the usefulness of forecasts. Since a forecast has no intrinsic value, its value must be materialized through its ability to influence decision-making (Murphy, 1993). At present, nor is there any work reviewing the relationship between the quality and value of solar forecasts. This is, to a large extent, due to the fact that different countries have different grid codes, under which the monetary compensation and penalty are advised; if one is to compare the economic values of two sets of forecasts in different markets, it would not be fair. In any case, the standards and challenges of using solar forecasts for grid-side operations, as described by Yang et al. (2021), are often shared by power grids worldwide. In parallel, Li and Zhang (2020); Ahmed and Khalid (2019) presented reviews on several concrete examples of how probabilistic forecasts may be used in power system operations, although in reality, given the conservative nature of the power system industry, probabilistic forecasts have yet to receive any sizable adoption. With the increasing penetration of solar energy, the value of solar forecasts would become more apparent. In the paper by Makarov et al. (2011), the basic operational practices of the California Independent System Operator (CAISO) are reviewed, from which one can understand how better forecasts can lead to higher load-following performance, less regulation and reserves, and thus higher economic values. Other notable reviews on the materialization of values of solar forecasts also exist (e.g., Emmanuel et al., 2020; Sampath Kumar et al., 2020).

4. Conclusion and outlook

In this überreview, topics related to solar resource assessment and forecasting have been listed concisely. This überreview can thus act as a catalog of research, for anyone who wishes to enter the field or stay up-to-date. Generally speaking, solar resource assessment mainly focuses on data and models. In that, ground-based, remote-sensed, and dynamically modeled radiation data play a vital part during solar energy system design, simulation, and performance evaluation. Additionally, the choice of radiation models of various sorts, such as transposition model, separation model, or site-adaptation model, also should not be viewed as trivial. Much effort has been devoted to the development and validation of these radiation models. Hence, opting the recommended radiation models during research is highly advised.

On the other hand, forecasting of solar irradiance, as a means to forecast solar power, is required during grid integration. In this regard, the value of solar forecasts solely resides in their ability to influence decision-making pertaining to power system operations. Solar forecasting research is never about which model is fancier and how much machine learning is used. Instead, understanding the salient features of solar irradiance should be emphasized. Raw solar forecasts should be generated using physics-based methods, and post-processed using statistical and machine-learning models. Moreover, irradiance-to-power conversion and forecast verification have yet to receive the attention they deserve.

In any case, solar resource assessment and forecasting can benefit from the participation of atmospheric scientists. Cloud is the critical parameter that ties atmospheric science and solar energy together. Among all cloud types, the largest uncertainty is associated with cumulus and cirrus. Further understanding of the dynamic and physical processes governing the production, maintenance, and disappearing of these clouds is necessary, as to improve the forecast skill of NWP, which would then certainly advance solar resource assessment and forecasting. Aerosol is another parameter that is key to solar engineering. Given the fact that many large solar energy systems are located in semi-arid regions, they are often affected by dust episodes. Progress in atmospheric chemistry would enhance our understanding of how natural and anthropogenic aerosols impact solar energy resources, and how to consider these effects in NWP. In this regard, developments in atmospheric science would be an important booster for solar engineering. To achieve this goal, mutual understanding is very important. First, the solar energy community should be familiar with the latest developments in atmospheric sciences. Second, the atmospheric sciences community should know the needs of solar engineers. Indeed, if we are to achieve carbon neutrality by mid of this century, a high proportion of solar energy in the energy mix is a must, and for that, interdisciplinary collaboration is absolutely vital. We should wish this review can help bridge the two communities.

REFERENCES

Ahmed, A., and M. Khalid, 2019: A review on the selected applications of forecasting models in renewable power systems. *Renewable and Sustainable Energy Reviews*, **100**, 9–21, https://doi.org/10.1016/j.rser.2018.09.046.

Antonanzas, J., N. Osorio, R. Escobar, R. Urraca, F. J. Martinez-de-Pison, and F. Antonanzas-Torres, 2016: Review of photovoltaic power forecasting. *Solar Energy*, **136**, 78–111, https://doi.org/10.1016/j.solener.2016.06.069.

Armstrong, J. S., 2001a: *Principles of Forecasting*: *A Handbook for Researchers and Practitioners*. Springer, 417–439. https://doi.org/10.1007/978-0-306-47630-3.

Armstrong, J. S., 2001b: *Principles of Forecasting*: *A Handbook for Researchers and Practitioners*. Springer, 850 pp, https://doi.org/10.1007/978-0-306-47630-3.

Bauer, P., A. Thorpe, and G. Brunet, 2015: The quiet revolution of numerical weather prediction. *Nature*, **525**, 47–55, https://doi.org/10.1038/nature14956.

Blanc P., B. Espinar, N. Geuder, C. Gueymard, R. Meyer, R. Pitz-Paal, B. Reinhardt, D. Renné, M. Sengupta, L. Wald, and S. Wilbert, 2014: Direct normal irradiance related definitions and applications: The circumsolar issue. *Solar Energy*, **110**, 561–577, https://doi.org/10.1016/j.solener.2014.10.001.

Boylan, J. E., P. Goodwin, M. Mohammadipour, and A. A. Syntetos, 2015: Reproducibility in forecasting research. *International Journal of Forecasting*, **31**, 79–90, https://doi.org/10.1016/j.ijforecast.2014.05.008.

CIE, 2004: Spatial distribution of daylight — CIE standard general sky: ISO 15469: 2004(E). International Commission on Illumination, 5 pp.

Clemen, R. T., 1989: Combining forecasts: A review and annotated bibliography. *International Journal of Forecasting*, **5**, 559–583, https://doi.org/10.1016/0169-2070(89)90012-5.

Clements, M. P., and D. I. Harvey, 2011: Combining probability forecasts. *International Journal of Forecasting*, **27**, 208–223, https://doi.org/10.1016/j.ijforecast.2009.12.016.

Cressie, N., and C. K. Wikle, 2015: *Statistics for Spatio-Temporal Data*. John Wiley & Sons, 624 pp.

Emmanuel, M., K. Doubleday, B. Cakir, M. Marković, and B.-M. Hodge, 2020: A review of power system planning and operational models for flexibility assessment in high solar energy penetration scenarios. *Solar Energy*, **210**, 169–180, https://doi.org/10.1016/j.solener.2020.07.017.

Engerer, N. A., 2015: Minute resolution estimates of the diffuse fraction of global irradiance for southeastern Australia. *Solar Energy*, **116**, 215–237, https://doi.org/10.1016/j.solener.2015.04.012.

Forstinger A., S. Wilbert, A. R. Jensen, B. Kraas, C. Fernández-Peruchena, C. A. Gueymard, D. Ronzio, D. Yang, E. Collino, J. Polo Martinez, J. A. Ruiz-Arias, N. Hanrieder, P. Blanc, and Y.-M. Saint-Drenan, 2021: Expert quality control of solar radiation ground data sets. Presentation at Solar World Congress 2021, International Solar Energy Society, Virtual conference. https://doi.org/10.18086/swc.2021.38.02.

Gelaro R., W. McCarty, M. J. Suárez, R. Todling, A. Molod, L. Takacs, C. A. Randles, A. Darmenov, M. G. Bosilovich, R. Reichle, K. Wargan, L. Coy, R. Cullather, C. Draper, S. Akella, V. Buchard, A. Conaty, A. M. da Silva, W. Gu, G. K. Kim, R. Koster, R. Lucchesi, D. Merkova, J. E. Nielsen, G. Partyka, S. Pawson, W. Putman, M. Rienecker, S.D. Schubert, M. Sienkiewicz, and B. Zhao, 2017: The modern-era retrospective analysis for research and applications, version 2 (MERRA-2). *J. Climate*, **30**, 5419–5454, https://doi.org/10.1175/JCLI-D-16-0758.1.

Gilleland, E., D. A. Ahijevych, B. G. Brown, and E. E. Ebert, 2010: Verifying forecasts spatially. *Bull. Amer. Meteor. Soc.*, **91**, 1365–1376, https://doi.org/10.1175/2010BAMS2819.1.

Gneiting, T., 2011: Making and evaluating point forecasts. *Journal of the American Statistical Association*, **106**, 746–762, https://doi.org/10.1198/jasa.2011.r10138.

Gneiting, T., and A. E. Raftery, 2005: Weather forecasting with ensemble methods. *Science*, **310**, 248–249, https://doi.org/10.1126/science.1115255.

Gneiting, T., and M. Katzfuss, 2014: Probabilistic forecasting. *Annual Review of Statistics and Its Application*, **1**, 125–151, https://doi.org/10.1146/annurev-statistics-062713-085831.

Gueymard, C. A., 2008: REST2: High-performance solar radiation model for cloudless-sky irradiance, illuminance, and photosynthetically active radiation - Validation with a benchmark dataset. *Solar Energy*, **82**, 272–285, https://doi.org/10.1016/j.solener.2007.04.008.

Gueymard, C. A., 2018: A reevaluation of the solar constant based on a 42-year total solar irradiance time series and a reconciliation of spaceborne observations. *Solar Energy*, **168**, 2–9, https://doi.org/10.1016/j.solener.2018.04.001.

Gueymard, C. A., 2019: The SMARTS spectral irradiance model after 25 years: New developments and validation of reference spectra. *Solar Energy*, **187**, 233–253, https://doi.org/10.1016/j.solener.2019.05.048.

Gueymard, C. A., and J. A. Ruiz-Arias, 2016: Extensive worldwide validation and climate sensitivity analysis of direct irradiance predictions from 1-min global irradiance. *Solar Energy*, **128**, 1–30, https://doi.org/10.1016/j.solener.2015.10.010.

Gueymard, C. A., D. Renné, and F. E. Vignola, 2009: Editorial: Journal's performance and publication criteria. *Solar Energy*, **83**, 1, https://doi.org/10.1016/j.solener.2008.07.007.

Gueymard, C. A., V. Lara-Fanego, M. Sengupta, and Y. Xie, 2019: Surface albedo and reflectance: Review of definitions, angular and spectral effects, and intercomparison of major data sources in support of advanced solar irradiance modeling over the Americas. *Solar Energy*, **182**, 194–212, https://doi.org/10.1016/j.solener.2019.02.040.

Habte, A., M. Sengupta, A. Andreas, S. Wilcox, and T. Stoffel, 2016: Intercomparison of 51 radiometers for determining global horizontal irradiance and direct normal irradiance measurements. *Solar Energy*, **133**, 372–393, https://doi.org/10.1016/j.solener.2016.03.065.

Hersbach, H., B. Bell, P. Berrisford, S. Hirahara, A. Horányi, J. Muñoz-Sabater, J. Nicolas, C. Peubey, R. Radu, D. Schepers, A. Simmons, C. Soci, S. Abdalla, X. Abellan, G. Balsamo, P. Bechtold, G. Biavati, J. Bidlot, M. Bonavita, G. De Chiara, P. Dahlgren, D. Dee, M. Diamantakis, R. Dragani, J. Flemming, R. Forbes, M. Fuentes, A. Geer, L. Haimberger, S. Healy, R. J. Hogan, E. Hólm, M. Janisková, S. Keeley, P. Laloyaux, P. Lopez, C. Lupu, G. Radnoti, P. de Rosnay, I. Rozum, F. Vamborg, S.Villaume, and J.-N. Thépaut, 2020: The ERA5 global reanalysis. *Quart. J. Roy. Meteor. Soc.*,

146, 1999–2049, https://doi.org/10.1002/qj.3803.

Holmgren, W. F., C. W. Hansen, and M. A. Mikofski, 2018: pvlib python: A python package for modeling solar energy systems. *Journal of Open Source Software*, **3**, 884, https://doi.org/10.21105/joss.00884.

Huang, G., Z. Li, X. Li, S. Liang, K. Yang, D. Wang, and Y. Zhang, 2019: Estimating surface solar irradiance from satellites: Past, present, and future perspectives. *Remote Sensing of Environment*, **233**, 111371, https://doi.org/10.1016/j.rse.2019.111371.

Hyndman, R. J., and A. B. Koehler, 2006: Another look at measures of forecast accuracy. *International Journal of Forecasting*, **22**, 679–688, https://doi.org/10.1016/j.ijforecast.2006.03.001.

Inman, R. H., H. T. C. Pedro, and C. F. M. Coimbra, 2013: Solar forecasting methods for renewable energy integration. *Progress in Energy and Combustion Science*, **39**, 535–576, https://doi.org/10.1016/j.pecs.2013.06.002.

Jimenez, P. A., J. P. Hacker, J. Dudhia, S. E. Haupt, J. A. Ruiz-Arias, C. A. Gueymard, G. Thompson, T. Eidhammer, and A. Deng, 2016: WRF-solar: Description and clear-sky assessment of an augmented NWP model for solar power prediction. *Bull. Amer. Meteor. Soc.*, **97**, 1249–1264, https://doi.org/10.1175/BAMS-D-14-00279.1.

Jolliffe, I. T., and D. B. Stephenson, 2012: *Forecast Verification: A Practitioner's Guide in Atmospheric Science*. 2nd ed. John Wiley & Sons, 274 pp, https://doi.org/10.1002/9781119960003.

Kleissl, J., 2013: *Solar Energy Forecasting and Resource Assessment*. Academic Press, 416 pp, https://doi.org/10.1016/C2011-0-07022-9.

Lauret, P., M. David, and P. Pinson, 2019: Verification of solar irradiance probabilistic forecasts. *Solar Energy*, **194**, 254–271, https://doi.org/10.1016/j.solener.2019.10.041.

Li, B., and J. Zhang, 2020: A review on the integration of probabilistic solar forecasting in power systems. *Solar Energy*, **210**, 68–86, https://doi.org/10.1016/j.solener.2020.07.066.

Long, C. N., and Y. Shi, 2008: An automated quality assessment and control algorithm for surface radiation measurements. *The Open Atmospheric Science Journal*, **2**, 23–37, https://doi.org/10.2174/1874282300802010023.

Makarov, Y. V., P. V. Etingov, J. Ma, Z. Y. Huang, and K. Subbarao, 2011: Incorporating uncertainty of wind power generation forecast into power system operation, dispatch, and unit commitment procedures. *IEEE Transactions on Sustainable Energy*, **2**, 433–442, https://doi.org/10.1109/TSTE.2011.2159254.

Makridakis, S., V. Assimakopoulos, and E. Spiliotis, 2018: Objectivity, reproducibility and replicability in forecasting research. *International Journal of Forecasting*, **34**, 835–838, https://doi.org/10.1016/j.ijforecast.2018.05.001.

Makridakis, S., R. J. Hyndman, and F. Petropoulos, 2020: Forecasting in social settings: The state of the art. *International Journal of Forecasting*, **36**, 15–28, https://doi.org/10.1016/j.ijforecast.2019.05.011.

Mayer, M. J., and G. Gróf, 2021: Extensive comparison of physical models for photovoltaic power forecasting. *Applied Energy*, **283**, 116239, https://doi.org/10.1016/j.apenergy.2020.116239.

McNeal, P., W. Flynn, C. Kirkpatrick, D. Kopacz, D. LaDue, and L. C. Maudlin, 2021: How undergraduate students learn atmospheric science: Characterizing the current body of research. *Bull. Amer. Meteor. Soc.*, 1–33, https://doi.org/10.1175/BAMS-D-20-0023.1. (in press)

Miller, S. D., M. A. Rogers, J. M. Haynes, M. Sengupta, and A. K. Heidinger, 2018: Short-term solar irradiance forecasting via satellite/model coupling. *Solar Energy*, **168**, 102–117, https://doi.org/10.1016/j.solener.2017.11.049.

Mishchenko, M. I., 2011: Directional radiometry and radiative transfer: A new paradigm. *Journal of Quantitative Spectroscopy and Radiative Transfer*, **112**, 2079–2094, https://doi.org/10.1016/j.jqsrt.2011.04.006.

Murphy, A. H., 1993: What is a good forecast? An essay on the nature of goodness in weather forecasting *Wea. Forecasting*, **8**, 281–293, https://doi.org/10.1175/1520-0434(1993)008<0281:WIAGFA>2.0.CO;2.

Müller, M., B. Kocánová, and P. Zacharov, 2021: Meteorological glossaries and dictionaries: A review of their history and current state. *Bull. Amer. Meteor. Soc.*, 1–39, https://doi.org/10.1175/BAMS-D-20-0295.1.

Perez, R., P. Ineichen, R. Seals, J. Michalsky, and R. Stewart, 1990: Modeling daylight availability and irradiance components from direct and global irradiance. *Solar Energy*, **44**, 271–289, https://doi.org/10.1016/0038-092X(90)90055-H.

Polo, J., C. Fernández-Peruchena, V. Salamalikis, L. Mazorra-Aguiar, M. Turpin, L. Martín Pomares, A. Kazantzidis, P. Blanc, and J. Remund, 2020: Benchmarking on improvement and site-adaptation techniques for modeled solar radiation datasets. *Solar Energy*, **201**, 469–479, https://doi.org/10.1016/j.solener.2020.03.040.

Quan, H., and D. Yang, 2020: Probabilistic solar irradiance transposition models. *Renewable and Sustainable Energy Reviews*, **125**, 109814, https://doi.org/10.1016/j.rser.2020.109814.

Roulston, M. S., and L. A. Smith, 2003: Combining dynamical and statistical ensembles. *Tellus A: Dynamic Meteorology and Oceanography*, **55**, 16–30, https://doi.org/10.3402/tellusa.v55i1.12082.

Sampath Kumar, D., O. Gandhi, C. D. Rodríguez-Gallegos, and D. Srinivasan, 2020: Review of power system impacts at high PV penetration Part II: Potential solutions and the way forward. *Solar Energy*, **210**, 202–221, https://doi.org/10.1016/j.solener.2020.08.047.

Sengupta, M., A. Habte, S. Wilbert, C. Gueymard, and J. Remund, 2015: Best practices handbook for the collection and use of solar resource data for solar energy applications. Tech. Rep. NREL/TP-5D00-63112, 236 pp.

Sun, X., J. M. Bright, C. A. Gueymard, B. Acord, P. Wang, and N. A. Engerer, 2019: Worldwide performance assessment of 75 global clear-sky irradiance models using Principal Component Analysis. *Renewable and Sustainable Energy Reviews*, **111**, 550–570, https://doi.org/10.1016/j.rser.2019.04.006.

Sun, X., J. M. Bright, C. A. Gueymard, X. Bai, B. Acord, and P. Wang, 2021: Worldwide performance assessment of 95 direct and diffuse clear-sky irradiance models using principal component analysis. *Renewable and Sustainable Energy Reviews*, **135**, 110087, https://doi.org/10.1016/j.rser.2020.110087.

Torres, J. L., and L. M. Torres, 2008: Angular distribution of sky diffuse radiance and luminance. *Modeling Solar Radiation at the Earth's Surface*, V. Badescu, Ed., Springer, 427–448, https://doi.org/10.1007/978-3-540-77455-6_17.

van der Meer, D. W., J. Widén, and J. Munkhammar, 2018: Review on probabilistic forecasting of photovoltaic power production and electricity consumption. *Renewable and Sustain-*

able Energy Reviews, **81**, 1484–1512, https://doi.org/10.1016/j.rser.2017.05.212.

Vannitsem, S., J. B. Bremnes, J. Demaeyer, G. R. Evans, J. Flowerdew, S. Hemri, S. Lerch, N. Roberts, S. Theis, A. Atencia, Z. B. Bouallègue, J. Bhend, M. Dabernig, L. D. Cruz, L. Hieta, O. Mestre, L. Moret, I. O. Plenković, M. Schmeits, M. Taillardat, J. V. den Bergh, B. V. Schaeybroeck, K. Whan, and J. Ylhaisi, 2021: Statistical postprocessing for weather forecasts: Review, challenges, and avenues in a big data world. *Bull. Amer. Meteor. Soc.*, **102**, E681–E699, https://doi.org/10.1175/BAMS-D-19-0308.1.

Vannitsem, S., D. S. Wilks, and J. W. Messner., 2018: *Statistical Postprocessing of Ensemble Forecasts*. Elsevier, 346 pp.

Vignola, F., J. Michalsky, and T. Stoffel, 2019: *Solar and Infrared Radiation Measurements*. 2nd ed. CRC Press, 516 pp, https://doi.org/10.1201/b22306.

Voyant, C., G. Notton, S. Kalogirou, M.-L. Nivet, C. Paoli, F. Motte, and A. Fouilloy, 2017: Machine learning methods for solar radiation forecasting: A review. *Renewable Energy*, **105**, 569–582, https://doi.org/10.1016/j.renene.2016.12.095.

Wallis, K. F., 2011: Combining forecasts - Forty years later. *Applied Financial Economics*, **21**, 33–41, https://doi.org/10.1080/09603107.2011.523179.

Winkler, R. L., Y. Grushka-Cockayne, K. C. Lichtendahl Jr., and V. R. R. Jose, 2019: Probability forecasts and their combination: A research perspective. *Decision Analysis*, **16**, 239–260, https://doi.org/10.1287/deca.2019.0391.

Yang, D., 2016: Solar radiation on inclined surfaces: Corrections and benchmarks. *Solar Energy*, **136**, 288–302, https://doi.org/10.1016/j.solener.2016.06.062.

Yang, D., 2019: A guideline to solar forecasting research practice: Reproducible, operational, probabilistic or physically-based, ensemble, and skill (ROPES). *Journal of Renewable and Sustainable Energy*, **11**, 022701, https://doi.org/10.1063/1.5087462.

Yang, D., 2021: Temporal-resolution cascade model for separation of 1-min beam and diffuse irradiance. *Journal of Renewable and Sustainable Energy*, **13**, 056101, https://doi.org/10.1063/5.0067997.

Yang, D., and J. Boland, 2019: Satellite-augmented diffuse solar radiation separation models. *Journal of Renewable and Sustainable Energy*, **11**, 023705, https://doi.org/10.1063/1.5087463.

Yang, D., and C. A. Gueymard, 2020: Ensemble model output statistics for the separation of direct and diffuse components from 1-min global irradiance. *Solar Energy*, **208**, 591–603, https://doi.org/10.1016/j.solener.2020.05.082.

Yang, D., and J. M. Bright, 2020: Worldwide validation of 8 satellite-derived and reanalysis solar radiation products: A preliminary evaluation and overall metrics for hourly data over 27 years. *Solar Energy*, **210**, 3–19, https://doi.org/10.1016/j.solener.2020.04.016.

Yang, D., and L. Liu, 2020: Solar project financing, bankability, and resource assessment. *Sustainable Energy Solutions for Remote Areas in the Tropics*, O. Gandhi and D. Srinivasan, Eds., Springer, 179–211, https://doi.org/10.1007/978-3-030-41952-3_8.

Yang, D., and C. A. Gueymard, 2021: Probabilistic post-processing of gridded atmospheric variables and its application to site adaptation of shortwave solar radiation. *Solar Energy*, **225**, 427–443, https://doi.org/10.1016/j.solener.2021.05.050.

Yang, D., and D. van der Meer, 2021: Post-processing in solar forecasting: Ten overarching thinking tools. *Renewable and Sustainable Energy Reviews*, **140**, 110735, https://doi.org/10.1016/j.rser.2021.110735.

Yang, D., C. A. Gueymard, and J. Kleissl, 2018a: Editorial: Submission of Data Article is now open. *Solar Energy*, **171**, A1–A2, https://doi.org/10.1016/j.solener.2018.07.006.

Yang, D., J. Kleissl, C. A. Gueymard, H. T. C. Pedro, and C. F. M. Coimbra, 2018b: History and trends in solar irradiance and PV power forecasting: A preliminary assessment and review using text mining. *Solar Energy*, **168**, 60–101, https://doi.org/10.1016/j.solener.2017.11.023.

Yang, D., S. Alessandrini, J. Antonanzas, F. Antonanzas-Torres, V. Badescu, H. G. Beyer, R. Blaga, J. Boland, J. M. Bright, C. F. M. Coimbra, M. David, Â. Frimane, C. A. Gueymard, T. Hong, M. J. Kay, S. Killinger, J. Kleissl, P. Lauret, E. Lorenz, D. van der Meer, M. Paulescu, R. Perez, O. Perpiñán-Lamigueiro, I.M. Peters, G. Reikard, D. Renné, Y. M. Saint-Drenan, Y. Shuai, R. Urraca, H. Verbois, F. Vignola, C. Voyant, and J. Zhang, 2020: Verification of deterministic solar forecasts. *Solar Energy*, **210**, 20–37, https://doi.org/10.1016/j.solener.2020.04.019.

Yang, D., W. Li, G. M. Yagli, and D. Srinivasan, 2021: Operational solar forecasting for grid integration: Standards, challenges, and outlook. *Solar Energy*, **224**, 930–937, https://doi.org/10.1016/j.solener.2021.04.002.

ADVANCES IN ATMOSPHERIC SCIENCES, VOL. 39, AUGUST 2022, 1252–1270

• Review •

Frontiers of CO_2 Capture and Utilization (CCU) towards Carbon Neutrality※

Lingyun ZHANG[1,2], Yanfang SONG[1], Jialin SHI[1], Qun SHEN[1], Deng HU[1], Qiang GAO[1], Wei CHEN[1], Kien-Woh KOW[2], Chengheng PANG[3,4], Nannan SUN*[1], and Wei WEI*[1,5]

[1]*CAS Key Laboratory of Low-Carbon Conversion Science & Engineering*, *Shanghai Advanced Research Institute*, *Chinese Academy of Sciences*, *Shanghai* 201210, *China*

[2]*Department of Chemical and Environmental Engineering*, *Faculty of Science and Engineering*, *University of Nottingham Ningbo China*, *Ningbo* 315100, *China*

[3]*Key Laboratory for Carbonaceous Wastes Processing and Process Intensification Research of Zhejiang Province*, *University of Nottingham Ningbo China*, *Ningbo* 315100, *China*

[4]*New Materials Institute*, *the University of Nottingham Ningbo China*, *Ningbo* 315100, *China*

[5]*School of Physical Science and Technology*, *ShanghaiTech University*, *Shanghai* 201210, *China*

(Received 6 January 2022; revised 18 March 2022; accepted 12 April 2022)

ABSTRACT

CO_2 capture, utilization, and storage (CCUS) technology is a rare option for the large-scale use of fossil fuels in a low-carbon way, which will definitely play a part in the journey towards carbon neutrality. Within the CCUS nexus, CCU is especially interesting because these processes will establish a new "atmosphere-to-atmosphere" carbon cycle and thus indirectly offer huge potential in carbon reduction. This study focuses on the new positioning of CCUS in the carbon neutrality scenario and aims to identify potential cutting-edge/disruptive CCU technologies that may find important application opportunities during the decarbonization of the energy and industrial system. To this end, direct air capture (DAC), flexible metal-framework materials (MOFs) for CO_2 capture, integrated CO_2 capture and conversion (ICCC), and electrocatalytic CO_2 reduction (ECR) were selected, and their general introduction, the importance to carbon neutrality, and most up-to-date research progress are summarized.

Key words: carbon neutrality, carbon reduction, decarbonization, CO_2, CCU

Citation: Zhang, L. Y., and Coauthors, 2022: Frontiers of CO_2 capture and utilization (CCU) towards carbon neutrality. *Adv. Atmos. Sci.*, **39**(8), 1252−1270, https://doi.org/10.1007/s00376-022-1467-x.

Article Highlights:

- CCU will play an important role for carbon neutrality by establishing a new "atmosphere-to-atmosphere" carbon cycle.
- Under the carbon neutrality scenario, several cutting-edge/disruptive CCU technologies will gain extended application opportunities.
- Progresses and future perspectives for four cutting-edge/disruptive CCU technologies are summarized.

1. Introduction

1.1. *Carbon neutrality*

The history of human civilization is accompanied by the exploration and utilization of fossil energies. Their extensive use has been an important supporting factor for the continuous progress of human society, but it also has resulted in a huge amount of CO_2 emissions, which has led to serious problems such as the greenhouse effect and climate change (IPCC, 2014). Mitigating climate change has become one of the most important themes in the world today, and CO_2 reduction is at the central part of this issue. In this context, many countries and regions have put forward "carbon neutrality" commitments, and carbon neutrality is becoming a new benchmark for evaluating countries' ambitions and actions to reduce carbon emissions (Energy & Climate Intelligence Unit, 2021).

※ This paper is a contribution to the special issue on Carbon Neutrality: Important Roles of Renewable Energies, Carbon Sinks, NETs, and non-CO_2 GHGs.

* Corresponding authors: Nannan SUN, Wei WEI
Emails: sunnn@sari.ac.cn, weiwei@sari.ac.cn

Carbon peaking and neutrality correspond to major changes in production and lifestyles, and revolutionary adjustments must be made to the existing energy structure and industrial system. In this process, a new energy system characterized by a high proportion of renewables will undoubtedly make decisive societal and economic contributions through decarbonization (IEA, 2020a). However, the reliability of renewables needs further verification due to their intermittency and high dependency on large-scale energy storage technology. Therefore, fossil energy will inevitably exist in the energy system in a certain proportion (5%–10%) for a long time (IEA, 2020a; Qu et al., 2020). On one hand, fossil energy can act as a "stabilizer" by balancing the volatility of renewable energy. At the same time, fossil energy is very important to ensure a continuous supply of high-quality energy. On the other hand, high-carbon industries such as steel, chemicals, and cement are important pillars of the modern economy, but the technological processes in these industrial sectors are relatively mature, with high technological inertia and high replacement costs. Low-carbon transformation and structural upgrading need to be carried out in an orderly manner, and the high-carbon characteristics of these industries will not change in the short term. Therefore, the use of a certain proportion of fossil energy and fossil resources will play an irreplaceable role in ensuring energy security and maintaining the integrity of the industrial chain. However, their use will inevitably lead to a certain amount of carbon emissions, which cannot be fully absorbed through the natural carbon sinks. As a result, artificial carbon sink technology, namely CO_2 capture, utilization, and storage (CCUS), will act as a safeguard towards carbon neutrality (IEA, 2020b).

1.2. *CO_2 capture, utilization, and storage (CCUS)*

CCUS is a major technological option for the end treatment of CO_2 and includes three technical steps of CO_2 capture, CO_2 utilization, and CO_2 storage. CO_2 capture is mainly used to separate and enrich CO_2 from various emission sources and even the air, and it is the beginning of the entire CCUS chain. CO_2 utilization uses CO_2 as a raw material or working medium by chemical, biological, or geological methods, and completes carbon emission reduction at the same time. CO_2 storage injects CO_2 into a certain geological environment and isolates the CO_2 from the atmosphere for a very long period during which the CO_2 may be fixed by carbonation reaction with underground minerals.

CCUS is a recognized technology that can achieve large-scale emission reductions. The International Energy Agency (IEA) predicted that to achieve global carbon neutrality by 2070, CCUS technology will not only contribute 15% of emission reductions but also provide inevitable solutions to cement, steel, chemical, and long-distance transport industries (IEA, 2020b). The IPCC special report "Global warming of 1.5°C" pointed out that by 2030 and 2050, global CCUS capacity will reach 100–400 million tons yr^{-1} and 3–6.8 billion tons yr^{-1}, respectively (IPCC, 2018).

Under the new target of carbon neutrality, the positioning of CCUS has changed significantly. CCUS technology is the only option for the low carbon utilization of fossil energies on a large scale, which is of great significance to energy security. Meanwhile, CCUS technology is a necessary solution for the decarbonization of industries that have difficulty reducing their emissions, and it is the major option to solve the problem of unavoidable "process emissions" in industries such as steel, chemical, cement, and non-ferrous metals. CCUS technology is also the main source for the necessary carbon element under the carbon neutralization scenario, which avoids the massive exploitation and utilization of fossil resources. Last but not least, the negative emission effect achieved by the coupling of CCUS and renewables is a guarantee for achieving the carbon neutrality target; which is impossible to achieve by source reduction or energy-saving approaches alone.

CCUS can be further divided into CCS and CCU according to their different approaches of CO_2 abatement. In general, CCS can provide huge capacity for direct CO_2 reduction as suitable reservoir volumes for CO_2 storage are more than enough to accommodate all the potential emissions. The CCU pathway, on the other hand, is significantly less efficient for direct reduction. This is because for most CCU technologies, any consumed CO_2 by the process will be re-released at the end of the product life-cycle (Stevenson, 2019). In fact, the importance of CCU is its great potential for indirect reduction of CO_2 emissions by avoiding the use of fossil carbon. As such, a new "atmosphere-to-atmosphere" carbon cycle can be established, while the traditional "lithosphere-to-atmosphere" mode can be largely replaced (Hepburn et al., 2019). As such, the overall CO_2 reduction capacity of CCU is high enough to apply considerable impact on carbon neutrality, and it is likely to create economic benefits as well.

Nevertheless, under the carbon-neutral scenario, routes for future CCU R&D may vary significantly, but one of the key features is that the necessity and application potential of some cutting-edge/disruptive CCUS technologies will greatly increase. In response to the above trends, this paper summarizes several cutting-edge/disruptive CCU technologies that are expected to play important roles in the carbon neutralization process from different dimensions. The latest progress and possible future trends are discussed to provide a reference for the research layout in the CCU field.

2. Direct air capture (DAC) and its indispensable carbon-negative feature for carbon neutrality

Direct air capture (DAC), as indicated by its name, is a process that captures CO_2 from the ambient air. This technology is appealing because, to some extent, it de-couples the emission source and carbon sink (i.e., the relative locations of the emission source and downstream CO_2 utilization/storage sites will not be a necessary concern). Therefore, infrastructure and expenditures for long-distance transportation of

CO_2 can be avoided, resulting in the great potential to reduce the cost of CO_2 abatement. Additionally, DAC directly uses air as the upstream source, which is a preferred technology to address mobile emission sources (such as vehicles) and micro emission sources (such as buildings) (Sanz-Pérez et al., 2016).

DAC delivers its carbon reduction capacity by coupling with either CO_2 conversion or CO_2 storage. Firstly, CO_2 obtained from DAC can be used as a raw material to replace fossil resources to produce carbon-based chemicals. In this context, the resulting products will be carbon neutral throughout their life cycles. Practically, this reshapes the existing chemical industry, leading to a disruptive impact on the entire industry and supply chain. Secondly, coupling of DAC with CO_2 storage has a significant carbon-negative effect, and its capacity is huge if large-scale deployment and application can be carried out. This offers a solution to the historical emissions and meets the demand of "reducing atmospheric CO_2 concentration" in response to climate change. Furthermore, such a carbon-negative effect may also have beneficial impacts on the energy and industrial system, promoting DAC to become an important part in the new model of carbon-neutral social and economic infrastructure (Goglio et al., 2020).

Compared with industrial emission sources, the concentration of CO_2 in the air is extremely low, only slightly higher than 400 ppm. This means that the DAC process is very unfavourable in terms of thermodynamics. Therefore, it faces great technological challenges in aspects of absorbents/adsorbents, efficiency, and energy costs. These adverse factors often cause the consumption of a large amount of materials and energy, even achieving a level that may offset the CO_2 reduction capacity of the DAC process (Deutz and Bardow, 2021). Overall, the technological maturity of DAC is still low, and its application is still in early infancy. In recent years, related studies have mainly focused on high-performance absorbents/adsorbents, prototype demonstrations, and life cycle assessments.

2.1. *Absorbents/adsorbents for DAC*

Absorbents and adsorbents are the most important components of a DAC technology system, and their performance directly dictates the overall cost and efficiency of the process. At present, most DAC studies and demonstrations have focused on solid adsorbents, and only a few experiments have used liquid absorbents with alkali metal hydroxide solution as the main component. The reason is because those solid adsorbents possess obvious advantages in terms of kinetics, stability, and environmental footprints (Shi et al., 2020).

Physical adsorbents (such as activated carbons, molecular sieves, etc.) are rarely used for DAC, mainly due to their weak interaction with the CO_2 molecules, which leads to extremely low adsorption capacity and selectivity in low CO_2 concentration environments (i.e., air). For example, Kumar et al. compared the CO_2 adsorption performance of four physical adsorbents and an immobilized organic amine sample, which is a typical chemical adsorbent. They found that although the performances of these samples only showed slight differences in 15 vol.% CO_2, the CO_2 adsorption capacities of physical adsorbents are more than one order of magnitude lower than those of chemical adsorbents in DAC conditions (Kumar et al., 2015).

Compared with physical adsorbents, chemical adsorbents are more widely used for DAC. Among them, immobilized organic amines are a kind of important CO_2 chemical adsorbent. The earliest prototype of these adsorbents comes from the "molecular basket" material proposed by Song's group (Fig. 1) (Xu et al., 2002; Ma et al., 2009). Then, Sayari's group (Franchi et al., 2005; Sayari and Belmabkhout, 2010) and Jones' group (Hicks et al., 2008; Didas et al., 2015) systematically developed the preparation method of immobilized organic amines, and in-depth studies on their adsorption behaviours and structure-performance relationship for CO_2 capture were performed. Due to the strong interaction between these adsorbents and the CO_2 molecules, their application in the DAC process has attracted extensive attention. For example, Goeppert et al. reported that fumed silica supported poly (ethyleneimine) (PEI) can effectively adsorb CO_2 from the air (Goeppert et al., 2011). In 2011, Choi et al. (2011) used 3-aminopropyl trimethoxysilane and tetraethylorthotitanate modified PEI as the adsorption components, which were loaded on porous SiO_2, and they found that this type of material exhibited great DAC performance (adsorption capacity > 2 mmol g^{-1}) and the use of modifiers can significantly improve the stability of PEI, rendering the material with excellent stability (Choi et al., 2011). Keller et

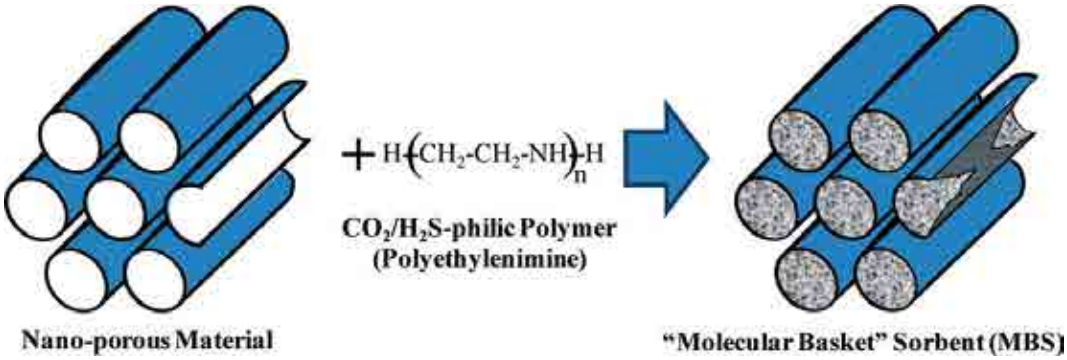

Fig. 1. "Molecular basket" sorbents [Reprinted from (Ma et al., 2009)].

al. used carbon nanotubes as a carrier for PEI to prepare a hollow fibre adsorbent. The adsorption capacity of CO_2 reached 1.07 mmol g^{-1} under DAC conditions (Keller et al., 2018). In addition to the commonly used impregnation method, immobilization of amines can also be achieved by surface grafting. Although adsorbents prepared in this way have slightly lower CO_2 uptakes under DAC conditions, their overall stability can be significantly improved (Potter et al., 2017; Sabatino et al., 2021).

Porous framework materials are a type of functional materials developed rapidly in recent years. The structure of these materials is highly ordered and can be finely characterized by various spectroscopic methods, thereby providing new dimensions for studying DAC mechanisms and performance tunning (Custelcean, 2021). For example, by the engineering of ligand for metal-organic frameworks (MOFs), Kumar et al. replaced the SiF_6^{2-} pillar in SIFSIX-3-Ni material with TiF_6^{2-}, which led to enhanced interaction between the framework and CO_2, and thus the DAC performance of the material was effectively improved (Kumar et al., 2017). Bhatt et al. further explored possible strategies by adjusting the pore size, pore shape, and surface functional groups of MOFs, and a CO_2 adsorption capacity of 1.30 mmol g^{-1} could be achieved at the condition of 400 ppm and 25°C, which is on a similar level to immobilized amine-based adsorbents (Bhatt et al., 2016). It should be noted that although the low-pressure CO_2 adsorption performance can be significantly improved through the optimization of MOFs structure, in general, its adsorption mechanism still relies on physical interactions, so it is easily affected by competitive adsorption of moisture. In fact, MOFs can also be used as carriers to prepare amine-based DAC adsorbents (Lu et al., 2013; Lee et al., 2014; Liao et al., 2016; Sen et al., 2019), and under the synergistic effect of multiple functional sites, the resulting materials may exhibit excellent DAC performance through several types of new adsorption mechanisms. For example, McDonald et al. used N, N'-dimethylethylenediamine (mmen) to functionalize Mg_2(dobpdc) (dobpdc^{4-}=4, 4'-dioxidobiphenyl-3,3'-dicarboxylate). It was found that during the adsorption of CO_2, there is a process of CO_2 insertion into the metal-amine bond, so the obtained CO_2 adsorption isotherm has step-shaped characteristics. This unique behaviour makes the material possess a higher working capacity than other chemical adsorbents (McDonald et al., 2015). Through the tunability of MOFs structure and the optimization of external amines, CO_2 adsorption capacity, kinetics, and regeneration performance under DAC, conditions can be further improved (Lee et al., 2014; Liao et al., 2016; Kim et al., 2020b; Martell et al., 2020).

In recent years, some new adsorption strategies have also been used for DAC processes. Based on the affinity difference between materials to CO_2 and water, researchers have proposed the concept of moisture-swing adsorption. In this process, the material captures CO_2 from air in a dry environment, while the competitive adsorption of moisture in a wet environment will liberate CO_2 molecules from the adsorbent surface (Shi et al., 2016; Yang et al., 2018). Inagaki et al. found that the aqueous solution of m-xylylene diamine (MXDA) can absorb CO_2 in the air and generate water-insoluble MXDA·CO_2 crystals. After simple filtration and separation, heating of MXDA·CO_2 can release CO_2 and complete the regeneration of MXDA. This process avoids the large amount of energy consumption required for the evaporation of solvent water in the traditional liquid absorption method (Inagaki et al., 2017). Based on a similar strategy, Brethomé et al. used a cheap and easily available amino acid aqueous solution to absorb CO_2, and then the CO_2 loaded solution further reacted with guanidine compounds to form insoluble carbonates, which regenerated the amino acids simultaneously, and then the separated carbonate can be decomposed under relatively mild conditions to release CO_2 (Brethomé et al., 2018).

Table 1 summarizes recent research results on DAC adsorbents. Overall, the research and development of DAC absorbents/adsorbents still face great challenges. In this study, a model was designed to estimate the cost of DAC

Table 1. Summary of research results on DAC sorbents.

Reference	Sorbents	Mechanisms	Adsorption capacity (mg-CO_2 g^{-1})	Temperature (°C)	Pressure (bar)
(Kumar et al., 2015)	TEPA-SBA-15	chemisorption	158	20	400 ppm
	Zeolite 13X	physisorption	5.8	20	
	HKUST-1	physisorption	2.1	20	
	Mg-MOF-74/	physisorption	40	20	
	SIFSIX-3-Ni	physisorption	58	20	
(Goeppert et al., 2011)	FS-PEI-33	chemisorption	75	25	400 ppm
(Choi et al., 2011)	PEI-silica	chemisorption	103	25	400 ppm
	A-PEI/silica	chemisorption	99	25	
	T-PEI/silica	chemisorption	96	25	
(Keller et al., 2018)	CNT-PEI	chemisorption	47	25	350 ppm
(Bhatt et al., 2016)	NbOFFIVE-1-Ni	chemisorption	57	25	400 ppm
(McDonald et al., 2015)	mmen-Mg_2(dobpdc)	chemisorption	154	25	1000 ppm
(Kim et al., 2020b)	Mg_2(dobpdc) (3-4-3)	chemisorption	150	90	4000 ppm

adsorbents and the corresponding relationship between adsorbent performance and its highest allowable cost was studied (Fig. 2). Based on this model, it is found that if the service life of an adsorbent is 1000 cycles, its cost must be less than \$1 kg^{-1}. Currently, there are hardly any adsorbents so low in cost. Increasing adsorbent service life can reduce its highest allowable cost; with 100 000 cycles, the allowable cost of MOF (Diamine) materials is the highest, reaching \$90 kg^{-1}. However, the price of MOF material is generally higher than \$10 000 kg^{-1}, and its stability is far from the requirements (Shi et al., 2020). This work verifies the difficulty of developing DAC adsorbents from a cost perspective, but it should be mentioned that recently, several groups have reported several CO_2 adsorbents with excellent comprehensive performance, which provides new opportunities for reducing the cost of DAC technology (Nandi et al., 2015; Yue et al., 2017; Cavalcanti et al., 2018; Mukherjee et al., 2019; Lin et al., 2021).

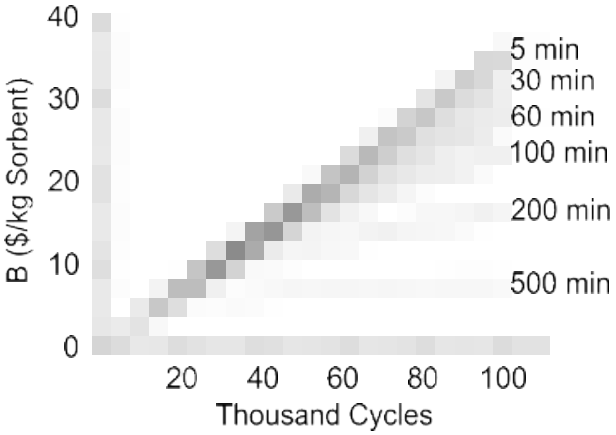

Fig. 2. Allowable price of DAC adsorbents [Reprinted from (Shi et al., 2020)].

2.2. *Prototype demonstrations of DAC*

Devices and demonstrations are also major focuses in the DAC field. This is because the concentration of CO_2 in the air is low, so the gas processing capacity of the DAC process is huge, and there is little experience in an engineering perspective to date. Over the past decade, developed countries in Europe and America have attached great importance to the development and application of DAC, and several small-scale prototypes and demonstrations have been reported, which has laid an important foundation for the future development of DAC technology.

Climeworks, a company based in Switzerland, is the first company in the world that provides customers with CO_2 captured from the air. In 2017, the company built the world's first commercial DAC device in Switzerland, which adopted modular design and used 18 adsorption units. An overall capture capacity of several hundred tons of CO_2 per year was achieved. In 2021, Climeworks built its latest Orca plant in Iceland. The Orca plant has a capture capacity of 4000 t yr^{-1} (Fig. 3) and is the largest DAC demonstration in the world to date. The captured CO_2 is injected 700 m underground for mineralization and storage (Climeworks, 2021).

DAC technology from Global Thermostat uses temperature-swing adsorption and adopts immobilized organic amine adsorbents. Global Thermostat established the first pilot plant in 2010 and the first commercial DAC plant in Alabama in 2018. It is reported that the energy consumption can be reduced to less than 6 GJ $(t\ CO_2)^{-1}$, which is around the minimum for existing DAC demonstrations (Zhu et al., 2021).

Carbon Engineering established its first DAC pilot plant by using KOH and $Ca(OH)_2$ solutions as absorbents in 2015, and in 2017, the company succeeded in the conversion of air-captured CO_2 to liquid fuels. In 2019, the company began to design and build a million-ton DAC demonstration project. Its carbon capture cost is estimated to be \$94–\$232 $(t\ CO_2)^{-1}$, with an energy consumption intensity of about 8.81 GJ $(t\ CO_2)^{-1}$ (Keith et al., 2018; Engineering, 2021).

Fig. 3. Orca plant from Climeworks [(©climeworks, 2022), used with permission].

2.3. *Life-cycle assessment (LCA) of DAC*

At present, there are still some controversies around the economic and environmental benefits of DAC. Therefore, its full life cycle assessment is also a research hotspot. By applying LCA to the actual operation data, Deutz et al. found that the DAC demonstration currently carried out by Climeworks has already achieved a carbon-negative effect. The carbon capture efficiencies of its two DAC plants reached 85.4% and 93.1%, respectively. However, the environmental benefits of the DAC process are closely related to energy sources. In an energy structure dominated by renewables, it is expected that the large-scale deployment of DAC technology (reaching 1% of global carbon emissions) will not be limited by materials and energy, and related environmental issues, if any, are relatively limited (Deutz and Bardow, 2021). According to calculations on carbon balance, Jonge et al. carried out LCA studies on a NaOH absorption DAC system, with a special focus on the life cycle carbon efficiency. Their results also showed that the energy source is very important to the emission reduction benefits of DAC. In general, the utilization of renewable energy is the simplest and most significant way to improve the carbon efficiency of DAC at this stage (de Jonge et al., 2019).

Terlouw and co-workers (2021b) proposed that it is necessary to incorporate CO_2 storage into the DAC's LCA pro-

cess in order to fully reflect the emission reduction benefits and other environmental impacts of DAC. Based on this idea, the authors compared and studied the environmental impact of direct air capture and storage (DACCS) under different power/heat sources and a variety of technology combinations. It was found that although a negative carbon effect can be achieved in several scenarios, it is necessary to select the best energy supply mode according to the energy infrastructure of different countries and regions. This is of pivotal importance to the emission reduction capability and the environmental impact of DAC (Terlouw et al., 2021a).

It should be mentioned that DAC technology is still very immature, so there are significant challenges in technology evaluation. Terlouw et al. (2021b) systematically summarized the current LCA works for carbon-negative technologies and pointed out that existing methods may induce confusion between avoided emission and negative emission, resulting in misleading conclusions. In order to better support the development of DAC technology in the future, it is necessary to strengthen the comprehensiveness of the evaluation and the transparency of the methods.

3. Flexible metal-organic frameworks (MOFs) and ultra-low cost CO_2 capture technology

3.1. *Flexible MOFs as CO_2 adsorbents*

Metal-organic frameworks (MOFs) are one of the emerging and rapidly growing focuses in material science. These materials are constructed from complexation of metal ions or metal ion clusters with bridging organic linkers, which exhibit regular crystalline lattices with high surface area and well-defined pore structures (Furukawa et al., 2013; Yuan et al., 2018). In MOFs, both the metal nodes and the organic linkers can be readily adjusted. This offers an effective approach for the customization and delicate adjusting of the materials' pore structure and functionalities. Therefore, MOFs can be widely applied in separation and catalysis science. In recent years, it was found that due to the dynamic properties of the framework component, MOFs that are responsive to external stimuli (pressure, temperature, ultraviolet light, etc.) can be synthesized (Matsuda, 2014). Based on this, construction of a reversible phase transformable CO_2 adsorption material can be realized to achieve an ultra-low cost CO_2 capture process (Schneemann et al., 2014) (Table 2). It should be noted that the energy consumption of the existing carbon capture process is relatively high, often accounting for 70% of the entire CCUS technology chain.

3.2. *Light-responsive MOFs for CO_2 adsorption*

One of the general strategies to construct flexible MOFs is to use organic linkers with light-responsive function groups as subunits for the framework. Modrow et al. constructed the first porous MOF (CAU-5) with photo-switchable linker molecules (3-azo-phenyl-4,4'-bipyridine). Under the irradiation of UV light (365 nm), the azo-functionality switches from its thermodynamically stable trans-isomer to cis-isomer (Modrow et al., 2011). Similarly, CO_2 adsorption behavior can be reversibly altered upon photochemical or thermal treatment in an MOF (PCN-123) with an azobenzene functional group, which can switch its conformation (Park et al., 2012). Sensharma et al. reported the synthesis and characterization of a photoactive MOF (TCM-15), which revealed a dynamic response upon UV irradiation, leading to instant desorption of pre-adsorbed CO_2. Based on FT-IR experiments and DFT calculations, the author verified that such release of CO_2 could be attributed to the structural flexibility of the materials (Sensharma et al., 2019). Lyndon et al. synthesized an MOF loaded with azo-type light-responsive groups. The material showed rapid response towards CO_2 adsorption during the light on-and-off switching cycles. This work directly verified the possibility of developing ultra-low energy consumption carbon capture technology based on flexible framework materials (Fig. 4) (Lyndon et al., 2013).

3.3. *Guest-responsive MOFs for CO_2 adsorption*

Interaction between MOFs and guest molecules is an important way to stimulate flexibility. As early as 2003, Kitaura et al. introduced displacement freedom during the self-assembly process of rigid motifs, and they proved experimentally that the obtained material has a "gate-opening pressure" for different gases, which caused the MOF material to transition from a crystalline "closed" form into an "open" form. The authors suggest that the reason for this flexibility is the displacement of π-π stacked moieties in the material.

Table 2. Properties before and after breathing-MOF.

Reference	Sample	Trigger of flexibility	Properties alteration upon flexibility
(Park et al., 2012)	PCN-123	UV irradiation	At 1 bar pressure, CO_2 adsorption decreased from 21 to 10 $cm^3\ g^{-1}$ after UV irradiation.
(Lyndon et al., 2013)	Zn(AzDC)(4,4'-BPE)0.5	UV irradiation	Dynamic exclusion of CO_2 during UV on-.and-off switching cycles.
(Dong et al., 2021)	NTU-65	Temperature	C_2H_4 adsorption capacity (1 bar pressure) decreased from 90 to ~0 $cm^3\ g^{-1}$ when increase temperature from 195 to 263 K.
(Marks et al., 2020)	CPL-2 and CPL-5	Rotation of the pillar ligands	Due to lattice expansion, CO_2 adsorption increased rapidly at pressure lower than 20 bar.
(Taylor et al., 2018)	Co(bdp)	Formation of CO_2 clathrate	At appropriate pressure, CH_4 can be largely excluded from the pores, leading to high CO_2/CH_4 adsorption selectivity.

At the same time, due to the different interactions between different gas molecules and materials, the gate-opening pressure also varied in different atmospheres. For CO_2, the opening and closing pressure are only 0.4 and 0.2 bar, respectively (Kitaura et al., 2003). Stavitski et al. prepared amino-modified NH_2-MIL-53(Al) and found that the modified material has excellent CO_2 adsorption properties compared with the unmodified counterpart. Very interestingly, it was found that instead of binding CO_2 chemically, the introduced amino groups actually played a role in adjusting the framework flexibility. In this way, the CO_2 adsorption capacity could be enhanced while the physical adsorption nature was not altered, and therefore, a significant increase in energy consumption for desorption was avoided (Stavitski et al., 2011). Using Cu as the metal center, 2,3-pyazinedicarboxylic acid (pzdc) as the ligand, and 4,4'-bipyridine (bpy) and 1,2-di-(4-pyridil)-ethylene (bpe) as the pillar, CPL-2 ($Cu_2(pzdc)_2$ (bpy)) and CPL-5 ($Cu_2(pzdc)_2(bpe)$) were prepared, respectively. Both samples showed excellent CO_2 adsorption capacity and selectivity, and based on in situ synchrotron X-ray diffraction experiments, the authors showed that the chemical interaction between CO_2 and the materials triggered rotation of the pillar ligands. This distortion further introduced expansion of the framework lattice, which is the key factor for the high CO_2 adsorption performance (Marks et al., 2020).

Taylor and co-workers prepared a Co (bdp) (bdp^{2-} = 1, 4 benzenedipyrazolate) MOF material with a flexible framework, which showed excellent adsorption selectivity for the separation of CO_2 and CH_4. Based on in situ X-ray Powder Diffraction (XRD) measurements, the authors suggest that the high selectivity originates from a "reversible guest templating" effect. That is, in the adsorption process, the framework expanded to form CO_2 clathrates, and the expended framework collapsed back to the non-templated phase in the subsequent desorption process. Based on such a mechanism, CH_4 was completely removed during adsorption of a 1:1 CO_2-CH_4 mixture (Fig. 5) (Taylor et al., 2018).

3.4. *Regulating the flexibility of MOFs for CO_2 adsorption*

Although flexible MOFs have shown many advantages in CO_2 adsorption, how to regulate their flexibility to match practical conditions is still a challenging question.

Based on the excellent structural flexibility and mechanical resistance of MIL-53 series materials, Chanut et al. found that when an external force is applied to the materials, they gradually change from an open-pore form to a contracted form. More importantly, the pore size of the materials can be accurately controlled by the strength of the applied force. Based on this idea and considering specific separation objects, efficient separation of CO_2/N_2 and CO_2/CH_4 could be achieved under optimized external force conditions. At the same time, when the external force is unloaded, the material structure switched back to the open form, which led to gas desorption and material regeneration (Fig. 6). Clearly, such a strategy is superior to the conventional pressure-swing or temperature-swing processes (Chanut et al., 2020).

Using NH_2-MIL-53(Al) as a parent material, Bitzer et al. introduced Sc, V, Cr, and Fe as a second metal node to prepare NH_2-MIL-53 (Al, M). Based on systematic characterizations, the authors found that the flexibility of the framework can be effectively adjusted by the presence of the second metal, which further altered the CO_2 capture performance of the resulting samples. In general, the construction of polymetallic MOFs can easily and effectively regulate the framework flexibility in a wide range, which has great potential in future applications (Bitzer et al., 2020).

Ghoufi's calculation revealed that the flexibility of MIL-53 could be affected by the existence of an electric field in addition to the stimulation of the guest molecules, heat, and external forces, with a volume change of up to 40%. At the same time, varying the electric field strength led to the regulation of the unit cell volume. This provided a ready path for adjusting gas adsorption, which resulted in the efficient separation of CO_2 and CH_4 (Ghoufi et al., 2017).

Dong et al. prepared a flexible MOF (NTU-65), and its flexibility is sensitive to temperature. Based on this character-

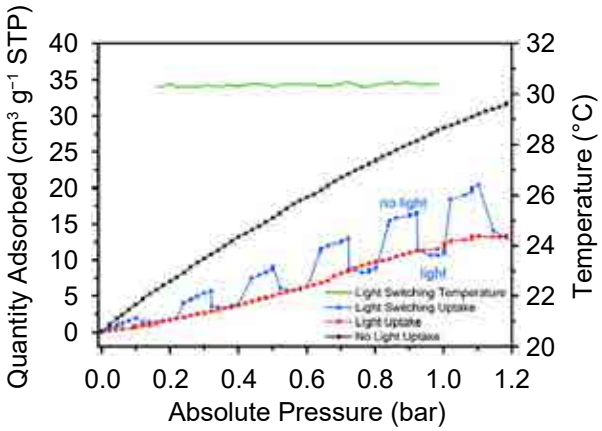

Fig. 4. Light-responsive capture of CO_2 [Reprinted from (Lyndon et al., 2013)].

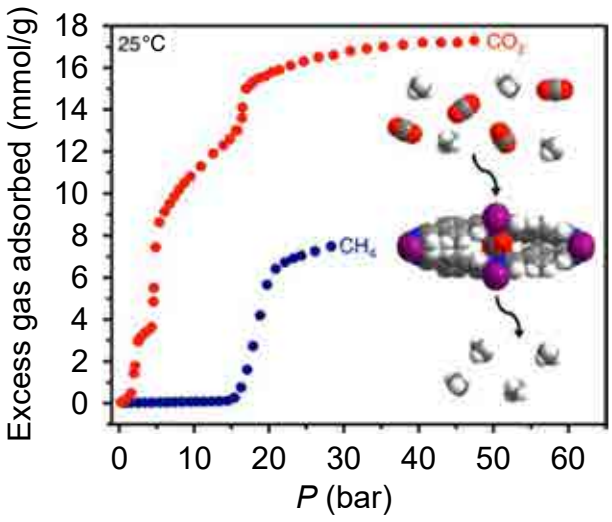

Fig. 5. Separation of CO_2 and CH_4 by flexible framework material [Reprinted from (Taylor et al., 2018)].

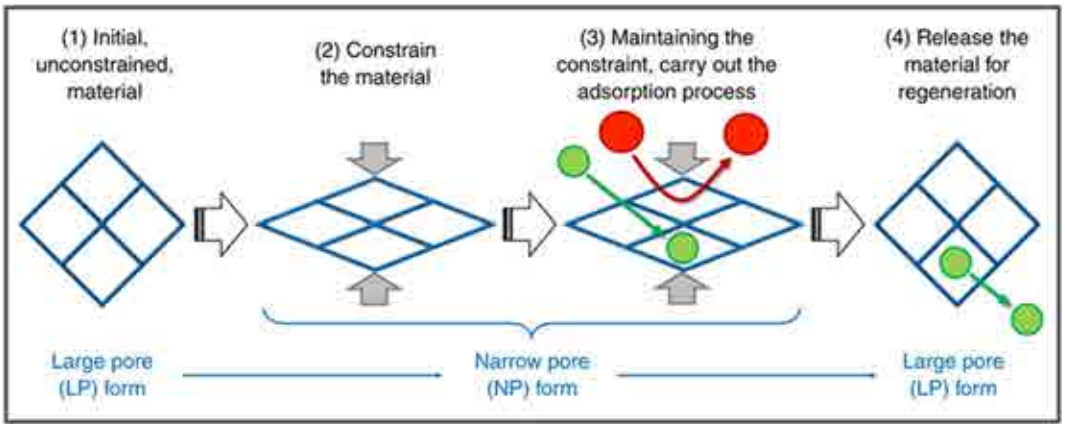

Fig. 6. Flexibility regulation by external force [Reprinted from (Chanut et al., 2020)].

istic, and together with the different gate-opening pressure of different gases, the authors successfully found a suitable operation window for the one-step separation of multi-component gases containing ethylene, ethane, and CO_2. High purity ethylene of polymerization grade was obtained by this method, which may find important potential in the petrochemical industries (Dong et al., 2021).

4. Integration of CO_2 capture and conversion (ICCC)

4.1. *General basics of ICCC*

Integration of CO_2 Capture and conversion (ICCC) refers to the connection of these two processes by their common microscopic steps, that is, the interaction between CO_2 and solid surface. During the new process, the captured CO_2 is directly converted to a value-added product without its desorption and enrichment (Fig. 7) (Zhou et al., 2020). Compared with the traditional CCUS chain, there are multiple advantages of ICCC. Firstly, it avoids the energy consumption of CO_2 desorption from absorbent/adsorbent in the traditional carbon capture process. Since this is one of the key factors causing the high cost of CCUS, it is thus expected that ICCC may significantly reduce the cost for CO_2 abatement. Besides, ICCC allows the disposal of CO_2 at close vicinity of its emission, which greatly reduces the demand for CO_2 transportation, and thus provides a solution to the source-sink matching problem. It is also possible that the products from an ICCC process can be readily used in downstream chains or even by the original emitter, leading to decarbonization of the energy and industrial system. The above advantages dictate the significant application potential of ICCC in carbon neutralization scenarios. However, this technology is still in the stage of laboratory verification, and systematic investigations are needed to clarify more approaches that are suitable for the current emission sources.

4.2. *ICCC for methanol production*

Methanol is a very important platform chemical that is widely used as a fuel and a chemical raw material. Under the background of carbon neutrality, methanol is expected to become a renewable energy carrier that can replace fossil energy. The technology of CO_2 hydrogenation to methanol has attracted more and more attention in recent years, mainly because this process can greatly reduce the consumption of fossil resources for methanol synthesis, thereby bringing a significant effect of indirect reduction of carbon emission.

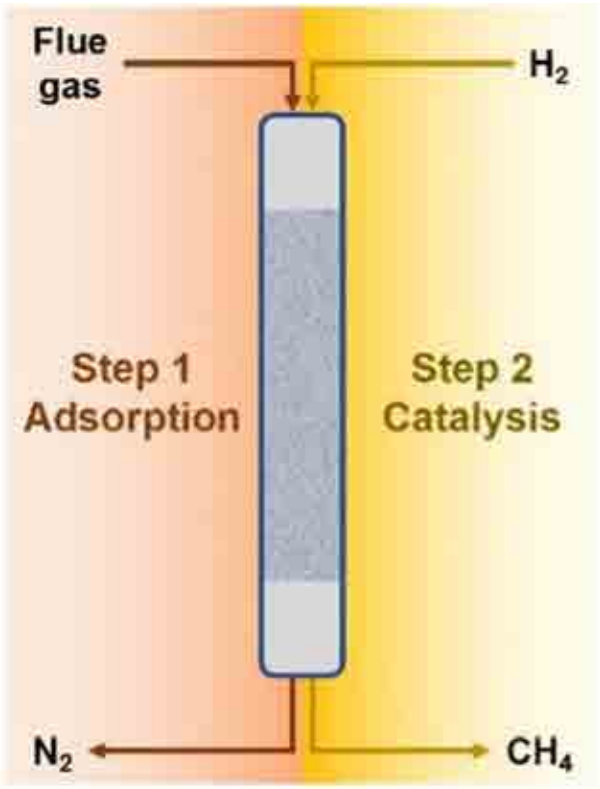

Fig. 7. Integrated CO_2 capture and conversion [Reprinted from (Zhou et al., 2020)].

Reller et al. were among the earliest who investigated methanol producing ICCC process. In their work, N, N-Diethylethanolamine (DEEA) and Cu/ZnO-Al_2O_3 catalyst were mixed, and the system was in contact with high-pressure CO_2 (10–20 bar) and H_2 (50–70 bar) consecutively. As

such, CO_2 was firstly absorbed by DEEA, and then CO_2 could be activated and converted to methanol by Cu/ZnO-Al_2O_3. This experiment used high-pressure and pure CO_2 in the CO_2 capture stage, so it cannot be strictly classified as an ICCC process, but it clearly verifies the feasibility for the conversion of captured CO_2 to value-added products (Reller et al., 2014).

In 2016, Prakash's group reported capturing CO_2 directly from the air and its conversion to methanol for the first time. They used pentaethylenehexamine as a CO_2 absorber and Ru-based Prince complex as a catalyst to convert the captured CO_2 to methanol under high-pressure H_2. With the optimal conditions, the yield of methanol reached 95% and could be recovered by distillation (Kothandaraman et al., 2016). Based on this work, a series of follow-up studies on several principal technical difficulties were performed. Firstly, in order to improve the efficiency of amine absorbent, a two-phase system was developed to simplify the separation of catalyst and amine, and thus the cycling stability of amine could be enhanced (Kar et al., 2018). Additionally, the authors also reported that either immobilized amines or metal hydroxide solutions can also be used for CO_2 capture in the process, which might provide solutions to the instability issue of amine-based absorbents (Fig. 8) (Kar et al., 2019; Sen et al., 2020).

4.3. *ICCC for CO/syngas production*

CO is the main component of coke-oven gas and a common reducing gas in the metallurgical industry. In addition, syngas composed of CO and H_2 is a widely used synthetic building block, which can be converted to a range of chemicals. At present, the preparation of CO and syngas mainly takes coal as the raw material through coking and gasification, respectively. The energy consumption of these processes is high, and an additional water-gas shift is needed to fulfill the downstream requirements on H_2/CO ratio for syngas, which further lowers the carbon efficiency by converting some CO to unusable CO_2. Therefore, carbon emission from CO/syngas production is huge, and relevant industries are facing severe pressures under the scenario of carbon neutrality. In recent years, some researchers have also studied the feasibility of preparing CO/syngas through the ICCC strategy by combining CO_2 capture with either its direct hydrogenation or reforming with alkanes.

Ni/CaO-Al_2O_3 mixed oxide was prepared by Li et al. by using CaO for high-temperature adsorption of CO_2 and Ni as the catalyst for CO_2-CH_4 reforming. This system can efficiently convert adsorbed CO_2 into syngas, but due to the sintering of CaO, the materials are gradually deactivated in prolonged cycles (Li et al., 2009). In Qiao's work, γ-Al_2O_3 was successively impregnated with K-Ca double salts and Ni species, acting as the CO_2 adsorption and catalytic component, respectively. CO_2 adsorption and subsequent reforming with ethane to prepare syngas were then performed successfully (Qiao et al., 2017).

Bobadilla et al. prepared FeCrCu/K/MgO-Al_2O_3 bi-functional materials, and an ICCC process was carried out based on reverse water gas shift to produce syngas. The process can be operated stably under simulated flue gas conditions containing oxygen and steam (Bobadilla et al., 2016). Ce doped Ni-Ca composite oxides were prepared by Sun et al., in which the oxygen vacancy on CeO_2 can significantly enhance the activation of CO_2, and thus its ICCC stability could be improved. When the Ca/Ni/Ce ratio is 1:01:0.033, the material can achieve 100% CO selectivity and 51.8% CO_2 conversion at the optimum temperature (650°C); no deactivation was observed in 20 capture-conversion cycles (Sun et al., 2019). Fe-Co-Mg-Ca multicomponent composites were prepared by Shao and co-workers. It was found that the existence of MgO can effectively lower the sintering of CaO, and the synergistic effect between MgO and CaO benefited CO_2 adsorption, whereas Fe and Co species can provide additional oxygen vacancies for CO_2 activation. Therefore, the material shows excellent ICCC performance with 90% CO_2 conversion and nearly 100% CO selectivity. The

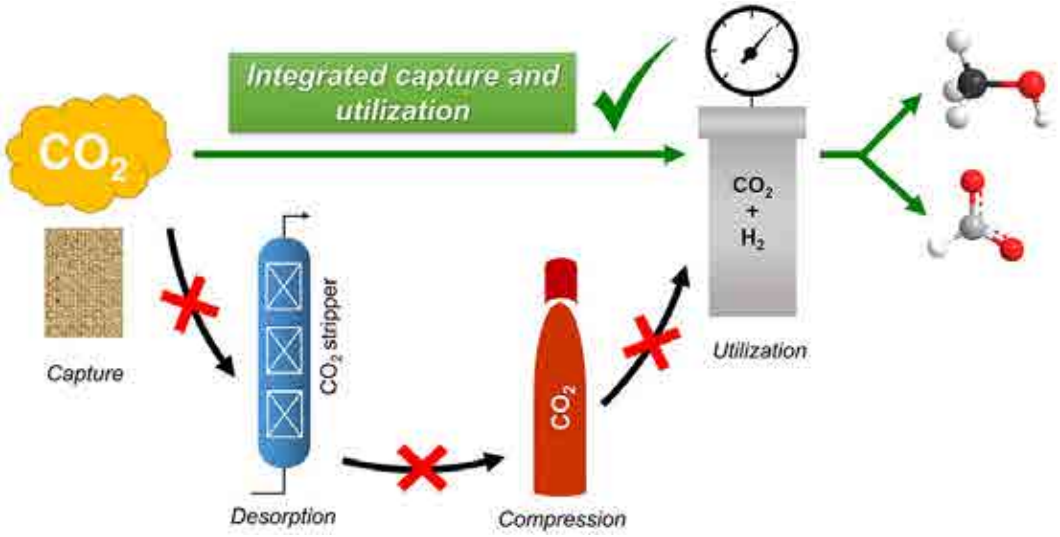

Fig. 8. Integrated CO_2 capture and conversion to methanol [Reprinted from (Kar et al., 2019)].

authors also proposed a heterojunction redox mechanism. It was considered that the newly formed Fermi level in $Fe_5Co_5Mg_{10}CaO$ significantly lowered the Fe^{3+}/Fe^{2+} redox potential. Therefore, electron transfer became easier, which is responsible for the enhanced activity of CO_2 conversion in reverse water-gas shift (RWGS) reaction (Fig. 9) (Shao et al., 2021).

4.4. *ICCC for CH_4 production*

CH_4 has a high hydrogen content, so the carbon emission during the CH_4 consumption process is relatively low. Through hydrogenation reaction, CO_2 can be directly converted to methane under atmospheric pressure, and its reaction temperature is significantly lower than that of reforming and reverse water gas. Therefore, it can be better coupled with existing industrial emission sources to realize the ICCC process. This is also the most studied direction in the ICCC field.

In the process of ICCC for CH_4 production, the adsorption step and conversion step can be coupled in several ways. For example, Veselovskaya et al. used tandem reactors, where K_2CO_3/Al_2O_3 adsorbent was loaded in a first reactor for CO_2 capture, and 4% Ru/Al_2O_3 catalyst was used in a second reactor for CO_2 conversion after it was purged out from the first reactor via H_2 (Veselovskaya et al., 2018). Alternatively, potassium-containing hydrotalcite and nickel-based catalyst were loaded in a single bed via a layer-by-layer way, and CO_2 adsorption and subsequent conversion to CH_4 were then achieved at 300°C –350°C, with a yield of 2.36 mol CH_4 kg^{-1} cat h^{-1} (Miguel et al., 2017). In Sun's work, MgO and Ru/CeO_2 were employed as adsorbent and catalyst, respectively, and their physical mixture was used for the ICCC to CH_4 process, however, the conversion rate of CO_2 in such a combination is relatively low (Sun et al., 2020).

In contrast to the above strategies, a combination of adsorption and catalysis sites in a single material is the most straightforward way. Farrauto's group reported on a range of experiments based on this idea. The performances using Na, K, Mg, and Ca oxides as adsorption sites and Rh, Ru, Ni, Pt, and Co as the catalytic sites were thoroughly investigated. Meanwhile, the influences of reaction conditions and related mechanisms were also clarified (Duyar et al., 2015, 2016; Zheng et al., 2016; Arellano-Treviño et al., 2019a, b; Proaño et al., 2019).

The process of continuous abatement of CO_2 in simulated flue gas by ICCC was reported by Zhou et al. In their work, Ni-MgO-Al_2O_3 two-dimensional nanosheets were used as a bi-functional material. Through the optimization of reaction temperature, capture, and conversion time interval, the authors realized nearly 100% CO_2 capture and conversion under isothermal conditions (Fig. 10). The overall efficiency of the process has been greatly improved compared to the traditional temperature-swing and pressure-swing adsorption (Zhou et al., 2020).

5. Electro-catalytic CO_2 reduction (ECR)

5.1. *General basics of ECR*

Electro-catalytic CO_2 reduction (ECR) represents the processes that convert CO_2 via an electro-chemical way. In sharp contrast to the conventional thermal-catalytic process where high temperature and pressure are normally needed for CO_2 activation and conversion, ECR processes can be readily carried out in much milder conditions (atmospheric pressure and room temperature). Meanwhile, as the required energy can be largely provided in the form of electrons, the ECR processes can be directly integrated with low-grade renewables, and H_2O, rather than other energized molecules,

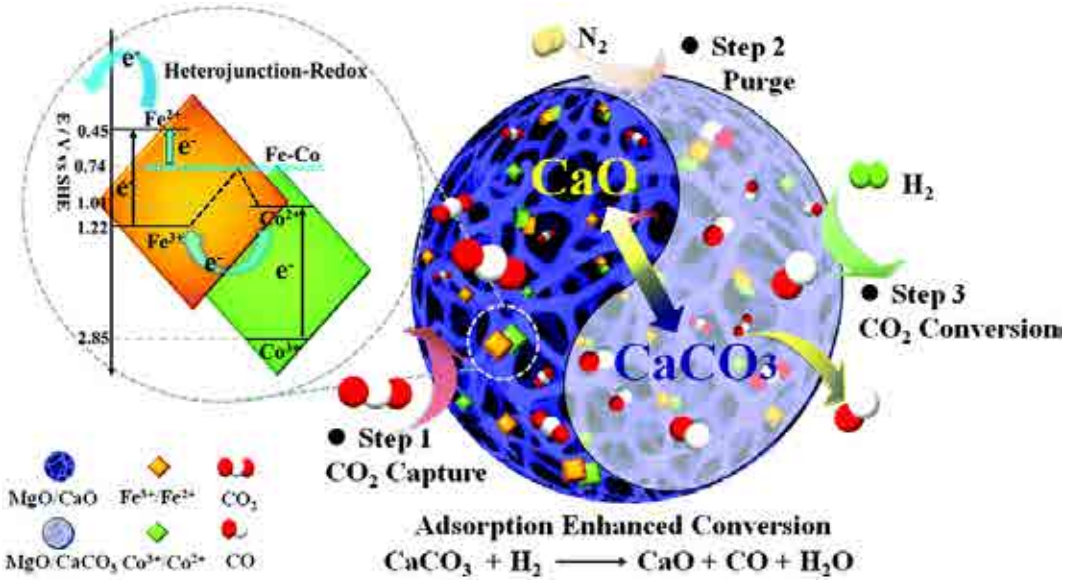

Fig. 9. Heterojunction redox mechanism for CO_2 capture and conversion to syngas [Reprinted from (Shao et al., 2021)].

can be used as a hydrogen source. As such, ECR enables the transformation of renewable energies to chemical energies in form of fuels and/or chemicals including CO, hydrocarbons (methane, ethylene), hydrocarbon oxygenates (formic acid, methanol, ethanol, etc.), or a mixture of them, and after their consumption, the released CO_2 can be recycled to close the carbon loop (Yang et al., 2016). All these merits give ECR great promise for the realization of carbon neutrality. In Table 3, we summarized several representative results from recent publications on ECR.

5.2. *ECR to CO*

Selective ECR to CO is a promising route toward industrial implementation because the produced CO can be used as a chemical feedstock to produce numerous higher-value chemicals or fuels, such as liquid fuel, low carbon olefin, and low carbon alcohol. However, direct reduction of CO_2 to $*COO^-$ involves a one-electron transfer process with a very negative redox potential (−1.9 V versus reversible hydrogen electrode (RHE)), which significantly inhibits the activation of CO_2 (Hunt et al., 2003). Therefore, suitable electrocatalysts should be developed to stabilize the $*COO^-$ intermediate, thereby reducing the activation overpotential.

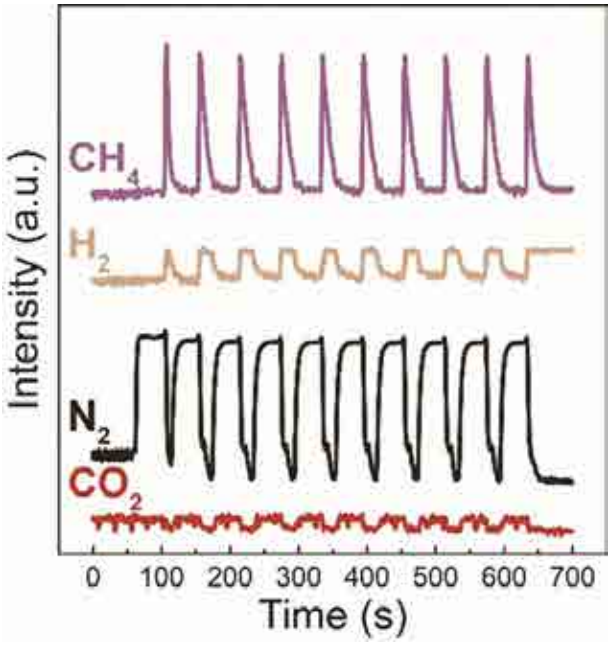

Fig. 10. Continuous capture and conversion of CO_2 to CH_4 [Reprinted from (Zhou et al., 2020)].

Metal catalysts including Au, Ag, Zn, and Cd with both weak hydrogen and oxygen adsorption (Uesaka et al., 2018) have been widely investigated for ECR to CO. Among them, Ag exhibits extraordinary ECR to CO performance. For example, Yang's group reported that when an Ag nanoparticle/ordered-ligand interlayer catalyst is applied in a gas-diffusion environment, a high FE of 92.6% for CO formation at a high current density of 400 mA cm^{-2} could be achieved. It was verified that the interlayer structure facilitated the synergistic effect between multiple components and is responsible for such excellent performance (Kim et al., 2020a). Single-atom catalysts (SACs) with individual metal atoms dispersed on solid substrates can maximize atom utilization efficiency and thereby enhance catalytic performance. In comparison with bulk Ni metal that catalyses hydrogen evolution exclusively under ECR conditions, the Ni single-atom counterpart can selectively electrochemically reduce CO_2 to CO. Zhang et al. designed a methoxy group of functionalized nickel phthalocyanine (NiPc-OMe) molecules supported on carbon nanotubes, which catalyses the ECR to CO process with >99.5% selectivity. The electron-donating OMe groups could enhance the Ni-N bond strength in the Ni-N_4 sites and accelerate CO desorption, thereby improving the catalyst stability (Zhang et al., 2020).

Metal-free carbon-based materials were also found to be effective for ECR to CO. However, the pristine, defect-free carbon materials are less effective, and incorporating heteroatoms such as nitrogen into the carbon matrix is necessary to improve activity. Su's group reported an N-doped CNT synthesized through the pyrolysis of mixtures of poly (diallyl dimethylammonium chloride) and oxidized CNTs. By adjusting types and contents of the used nitrogen dopants, a maxi-

Table 3. Summary of research results on ECR catalysts.

Reference	Sample	Potential (V vs. RHE)	j_{CO} (mA m^{-2})	Products and FE
(Kim et al., 2020a)	Ag nanoparticles	−0.82	400	CO, 92.6%
(Zhang et al., 2020)	NiPc-OMe	−0.64	300	CO, 99.5%
(Xu et al., 2016)	N-doped CNT	−0.9	5.8	CO, 90%
(Dinh et al., 2018)	Cu electrocatalyst	−0.55	100	C_2H_4, 70%
(Zhong et al., 2020)	Cu-Al alloy electrocatalyst	−1.5	400	C_2H_4, 80%
(Xiong et al., 2021)	Ag@Cu_2O	−1.2	178 ± 5	CH_4, 74% ± 2%
(Yadav et al., 2022)	N-doped GQDs	−0.85	170	CH_4, 63%
(Bai et al., 2017)	Pd-Sn alloy electrocatalyst	−0.43 V	–	HCOOH, >99%
(Yan et al., 2021)	s-SnLi	−1.2	1000	HCOOH, 92%
(Xu et al., 2020)	Cu catalyst	−0.7	1.8	C_2H_5OH, 91%
(Wang et al., 2020)	N-C/Cu	−0.68	300	C_2H_5OH, 52% ± 1%
(Song et al., 2017)	N-C	−0.56	–	C_2H_5OH, 77%

mum FE of 90% for CO formation and stable operation over 60 h with total current density and FE of 5.8 mA cm^{-2} and 85% can be achieved, respectively. During the reaction, the N-containing functionalities played an important role in stabilizing the $^{*}COO^{-}$ intermediate, and this is the key for the sample to possess high performance (Xu et al., 2016).

5.3. *ECR to hydrocarbons*

With the combination of hydrogen from water, CO_2 can be electrocatalytically converted to hydrocarbons, mainly containing methane (CH_4) and ethylene (C_2H_4), via eight electron-proton and twelve electron-proton reaction processes, respectively. Cu-based nanoparticles can produce hydrocarbons at moderate overpotentials. This is attributed to the appropriate strength of CO chemisorption on Cu, and protonation or dimerization of CO is considered to be a key step towards the formation of single- (CH_4) or multi-carbon (C_2H_4) hydrocarbons (Peterson et al., 2010) (Kortlever et al., 2015). During the above mechanism, the *CO coverage on the catalysts can significantly influence the ECR activity and selectivity. A high *CO coverage can readily trigger C-C coupling that enhances C_2H_4 formation, while less *CO on the catalyst surface might not be competitive enough over hydrogen evolution reaction (Huang et al., 2017).

In the past several years, significant progress has been made in ECR to C_2H_4 conversion, including catalysts, electrolytes, and electrodes. A typical example was reported by Sargent's group where a Cu electrocatalyst at an abrupt reaction interface in an alkaline electrolyte (7 M KOH) reduces CO_2 to C_2H_4 with 70% FE at a potential of −0.55 V vs. RHE. The remarkable performance is correlated to hydroxide ions on or near the Cu surface, which lowered the activation energy barriers of ECR and C-C coupling (Dinh et al., 2018). A graphite/carbon NPs/Cu/PTFE electrode was further constructed to prevent flooding problems and stabilize the Cu catalyst surface, thereby resulting in enhanced stability over the prolonged operation for 150 h. Afterwards, they developed a Cu-Al alloy electrocatalyst to further improve the FE of C_2H_4 to 80% at a current density of 400 mA cm^{-2} in 1 M KOH electrolyte. They suggested that the Cu-Al alloys provide multiple sites and surface orientations with near-optimal CO binding for both efficient and selective ECR (Zhong et al., 2020).

The progress on ECR to CH_4, which has the highest heating value of 55.5 MJ kg^{-1} among all the ECR products, is far behind that of C_2H_4. There is still a lack of applicable catalysts with satisfactory CH_4 selectivity. Only very recently, Xiong et al. fabricated an Ag@Cu_2O core-shell structure. By fixing the Ag core and adjusting the Cu_2O envelope size, the *CO coverage and *H adsorption at the Cu surface can be modulated to steer the ECR pathway towards CH_4. The optimal catalyst delivered a high CH_4 FE of 74% ± 2% and a partial current density of 178 ± 5 mA cm^{-2} at −1.2 V vs. RHE (Xiong et al., 2021). Yadav and co-workers reported an amine functionalized N-doped GQDs for efficient ECR to CH_4. It revealed that the CH_4 yield (partial current density) increased linearly with amino group (NH_2) content. Consequently, a maximum CH_4 FE of 63% could be obtained over the catalyst with the maximum NH_2 content of 9.07 atomic concentration (at. %) (Yadav et al., 2022).

5.4. *ECR to oxygenates*

Investigations on ECR to oxygenates mainly focus on formic acid (or formate) and ethanol via two electron-proton and twelve electron-proton reaction processes, respectively. Formic acid is an important product from ECR that has been widely explored as a hydrogen carrier. The common strategy for industrial production of formic acid is carbonylation of methanol, which, however, requires intensive energy input. It is thus highly desired to directly convert CO_2 to formic acid via the ECR process, which was predicted to have a production potential of 475 kt yr^{-1} by 2030 globally. (Contentful, 2021).

Several metals, including Sn, In, and Bi, have been investigated as electro-catalysts for selective ECR to formic acid or formate. Among these metals, Sn commands the most attention for its low toxicity and cost. Bai and some of the co-authors of this paper developed a Pd-Sn alloy electrocatalyst for exclusive formic acid formation (FE>99%) in a 0.5 M $KHCO_3$ solution. The presence of Pd modified the electronic configuration and oxygen affinity of Sn, which stabilized the HCOO* intermediate and the subsequent formic acid formation (Bai et al., 2017). Recently, Zheng's group developed a surface-Li-doped Sn (s-SnLi) catalyst, which exhibited a high FE of 92% and a partial current density of 1.0 A cm^{-2} for producing formate. The introduction of Li dopants into the Sn lattice enabled the localization of negative charges and lattice strains to their neighbouring Sn atoms; thereby, both activity and selectivity of ECR to formate were enhanced (Fig. 11) (Yan et al., 2021).

Ethanol, a kind of clean and renewable liquid fuel with a heating value of –1366.8 kJ mol^{-1}, is a preferred product from ECR. Owing to the higher energy density and ease of storage and transportation compared to gas products, ethanol has also been considered as one of the optimal candidate fuels that substitute or supplement fossils in many applications (Shih et al., 2018). Moreover, ethanol is also an important and widely used common chemical feedstock for organic chemicals and medical disinfectants. Based on the considerable market demand, direct conversion of CO_2 to ethanol using only water and driven by renewable energy is highly desired.

Cu is the only reported metal so far that can electrochemically catalyse ECR to ethanol. However, the selectivity is extremely low due to its moderate binding energy with most reaction intermediates. To promote the selectivity towards ethanol, manipulation of the binding strength of reaction intermediates on Cu is a commonly used strategy. Xu et al. reported a carbon-supported Cu catalyst via an amalgamated Cu–Li method, by which most Cu is atomically dispersed on the carbon surface. The high initial dispersion of single Cu atoms favors the selective ECR to ethanol with FE reaching ~91% at –0.7 V vs. RHE and outstanding durability of

16 h. However, the current density (around 1.8 mA cm^{-2}) is still below the industrial level (Xu et al., 2020). Based on recent investigations, the improvement of current density is at the expense of ethanol FE. For instance, Sargent's group coated a nitrogen-doped carbon (N-C) layer on a Cu surface to build a confined reaction volume, which promoted C-C coupling and suppressed the breaking of the C-O bond in HOCCH*, thereby promoting ethanol selectivity in ECR. Under a current density of 300 mA cm^{-2}, an ethanol FE of (52 ± 1) % is achieved on 34% N-C/Cu (Wang et al., 2020). Metal-free nitrogen-doped carbon materials have also been recently reported to be capable of ethanol production from ECR, which delivered comparable catalytic activities to Cu-based catalysts and even better durability. Song and co-workers developed a metal-free cylindrical mesoporous nitrogen-doped carbon as a robust catalyst for selective ECR to ethanol. The synergy of nitrogen heteroatoms and highly uniform cylindrical channel structures dramatically boosted C–C bond formation in ECR. Therefore, the catalyst enabled efficient production of ethanol with a high FE of 77% at –0.56 V vs. RHE in 0.1 M $KHCO_3$ (Song et al., 2017). Inspired by the potential of adjusting the nanostructure of

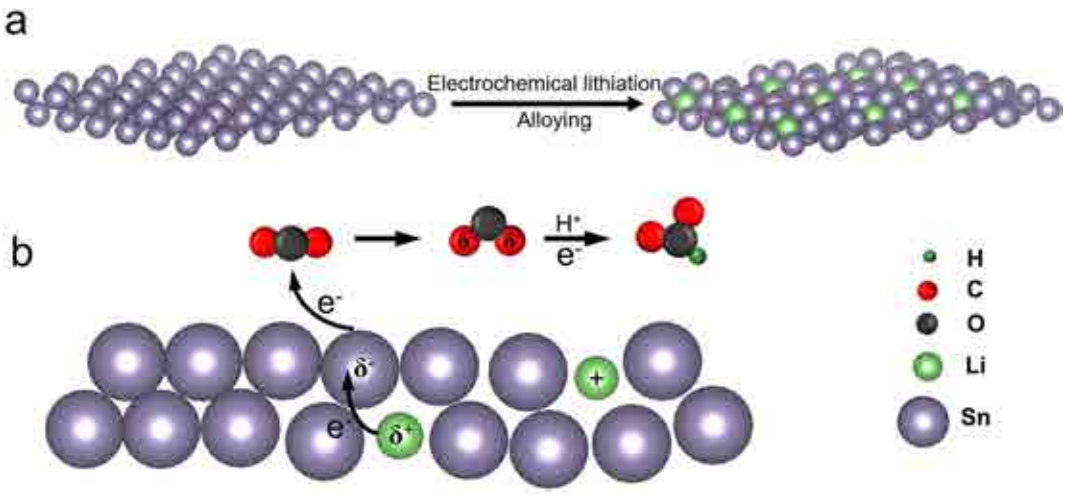

Fig. 11. Scheme illustrations of (a) electrochemical lithiation preparation of the s-SnLi catalyst, and (b) its function mechanism for ECR to formate [Reprinted from (Yan et al., 2021)].

Fig. 12. The demonstration system of CO_2 electrolysis for syngas production [Reprinted from (Carbon Energy Technology Co. LTD, 2020)].

the catalyst to acquire multi-carbon compounds, the group further developed a hierarchical porous N-doped carbon with micropores embedded in the channel walls of N-doped ordered mesoporous carbon. By controlling the micropore content, the ethanol formation rate is improved by one order of magnitude compared to that of the counterpart without medium micropores. These reports have provided new insights for designing highly efficient electrocatalysts for ECR to ethanol in the future (Song et al., 2020).

6. Summary

Clearly, CCUS will play an important role in reaching the carbon neutrality target, not just at its current stage, but more so after future development. In particular, deep decarbonization requires a considerable revolution of the current energy and industrial infrastructure. Therefore, cutting-edge /disruptive CCUS technologies are becoming increasingly important and influential.

In this paper, we reviewed four technologies that are regarded as frontiers of CCUS. In Table 4, their relevance to carbon neutrality over other low-carbon technologies, advantages over regular CCUS technologies, and difficulties for future development are summarized.

DAC is one of the rare technologies that is able to offer negative emission, and very uniquely, DAC also provides a solution to historical emissions. Both characteristics are necessary to suppress climate change. When comparing with other CCUS technologies, localization of DAC is highly flexible. Therefore, the necessity for CO_2 transportation can be minimized by deployment of DAC in close vicinity of CO_2 emitters and/or downstream utilization/storage sites. Based on such a feature, DAC is an ideal approach for distributed, mobile, and small-scale emitters. Currently, DAC is an immature technology, and the process cost is relatively high. Efficient absorbents/adsorbents, coupling with renewable energies, process engineering, and scaling-up are among the most urgent issues to be solved.

Flexible MOFs are a type of smart materials that can potentially alter the landscape of many applications. When they are used as CO_2 adsorbents, their reversible breathing behavior toward external stimuli may change the fundamental thermodynamic driving force for adsorbent regeneration and thus enable less energy-intensive strategies over traditional temperature-swing and pressure-swing processes. Lowering the cost of CO_2 capture by flexible MOFs is of particular importance to facilitate the large-scale application of CCUS, which in turn guarantees carbon neutrality to be achieved. However, the performance of the reported flexible MOFs cannot meet the requirement of practical application. Further research, including design of a suitable process, is needed.

ICCC technology represents a new way of carbon recycling, which may promote the formation of low-carbon models and processes of the industrial system. This is of promise as decarbonization of industrial departments is considerably difficult. Compared with existing CCUS technologies, ICCC has obvious advantages in terms of cost reduction, source-sink matching, and so forth. Nevertheless, ICCC is still in the laboratory verification stage. How CO_2 capture and its conversion can be efficiently combined, how value-added products can be obtained, and how the process can be adjusted to match practical application scenarios are still questionable at this stage.

Recently, ECR has been one of the most eye-catching areas in catalysis. Due to its natural connection with renewable electricity, the process manages to close the carbon loop of fuels and chemicals by storing the low-grade renewable energy. Therefore, large-scale deployment of ECR can effectively avoid consumption of fossil fuels and thus contribute carbon reduction in an indirect way. Compared with other CO_2 conversion technologies, the ECR process can be carried out under very mild conditions. Additionally, ECR can be readily modularized, which greatly facilitates its scaling up. The primary technical difficulties of ECR include the design and preparation of the catalyst with high activity and selectivity and engineering challenges related to coupling

Table 4. Summary of selected CCUS technologies.

Technology	Relevance to carbon neutrality over other low-carbon technologies	Advantages over regular CCUS technologies	Technological difficulties
DAC	• Negative emission effects • Solution to historical emissions	• Flexibility in localization • Minimize transportation demand • Solution to dispersed and small-scale emission sources	• High-performance adsorbents/ absorbents • Coupling with renewable energies • Process engineering • Scaling-up
Flexibilt MOFs	• Enable low-cost CCUS for carbon neutrality	• Lowering energy consumption for carbon capture	• High-performance materials • Process engineering
ICCC	• A new way of carbon recycling • Re-shape industrial system	• Lowering CCUS cost • Source-sink matching	• Efficient coupling of absorption and conversion process • Extension of products • Matching with application scenarios
ECR	• Avoiding fossil fuels • Storing low-grade renewable energies	• Milder conditions • Easy to scale-up	• High-performance catalysts • Coupling with low-grade renewable energy

with low-grade renewable energy.

7. Outlook

CCUS technology is the only approach that can achieve large-scale and low-carbon utilization of fossil energy and resources, which will surely play an important role in coping with climate change. However, under the new goal of carbon neutrality, the positioning of CCUS technology has changed significantly, and the application scenarios of some cutting-edge/disruptive CCUS technologies have been greatly expanded, which is expected to constitute inevitable carbon reduction solutions for the energy and industrial system.

The CCUS technologies reviewed in this paper have attracted widespread attention from both the academia and industrial sectors, and their feasibility has been well verified, with some technologies having been demonstrated on a certain scale. In the future, it will be necessary to further strengthen related investigations on materials, mechanisms, processes, and engineering. These will lead to the lowering of process costs and clarification of application scenarios, eventually promoting the practical application of the technologies. It should be noted that in recent years, research on CCUS and related fields has progressed very rapidly, and this paper is not comprehensive as it only lists a limited number of examples. Facing the future, cutting-edge/disruptive CCUS technologies will continue to emerge and develop, and we anticipate they will offer important contributions to carbon neutrality.

Acknowledgements. This work was supported by Shanghai Science and Technology Committee (Grant Nos. 21692112200 and 20DZ1207500) and Inner Mongolia Science and Technology Department (Grant No. 2021ZD0020).

REFERENCES

Arellano-Treviño, M. A., N. Kanani, C. W. Jeong-Potter, and R. J. Farrauto, 2019a: Bimetallic catalysts for CO_2 capture and hydrogenation at simulated flue gas conditions. *Chemical Engineering Journal*, **375**, 121953, https://doi.org/10.1016/j.cej.2019.121953.

Arellano-Treviño, M. A., Z. Y. He, M. C. Libby, and R. J. Farrauto, 2019b: Catalysts and adsorbents for CO_2 capture and conversion with dual function materials: Limitations of Ni-containing DFMs for flue gas applications. *Journal of CO_2 Utilization*, **31**, 143–151, https://doi.org/10.1016/j.jcou.2019.03.009.

Bai, X. F., W. Chen, C. C. Zhao, S. G. Li, Y. F. Song, R. P. Ge, W. Wei, and Y. H. Sun, 2017: Exclusive formation of formic acid from CO_2 electroreduction by a tunable Pd-Sn alloy. *Angewandte Chemie International Edition*, **56**, 12 219–12 223, https://doi.org/10.1002/anie.201707098.

Bhatt, P. M., Y. Belmabkhout, A. Cadiau, K. Adil, O. Shekhah, A. Shkurenko, L. J. Barbour, and M. Eddaoudi, 2016: A fine-tuned fluorinated MOF addresses the needs for trace CO_2 removal and air capture using physisorption. *Journal of the American Chemical Society*, **138**, 9301–9307, https://doi.org/10.1021/jacs.6b05345.

Bitzer, J., S.-L. Heck, and W. Kleist, 2020: Tailoring the breathing behavior of functionalized MIL-53(Al,M)-NH_2 materials by using the mixed-metal concept. *Microporous and Mesoporous Materials*, **308**, 110329, https://doi.org/10.1016/j.micromeso.2020.110329.

Bobadilla, L. F., J. M. Riesco-García, G. Penelás-Pérez, and A. Urakawa, 2016: Enabling continuous capture and catalytic conversion of flue gas CO_2 to syngas in one process. *Journal of CO_2 Utilization*, **14**, 106–111, https://doi.org/10.1016/j.jcou.2016.04.003.

Brethomé, F. M., N. J. Williams, C. A. Seipp, M. K. Kidder, and R. Custelcean, 2018: Direct air capture of CO_2 via aqueous-phase absorption and crystalline-phase release using concentrated solar power. *Nature Energy*, **3**, 553–559, https://doi.org/10.1038/s41560-018-0150-z.

Cavalcanti, L. P., G. N. Kalantzopoulos, J. Eckert, K. D. Knudsen, and J. O. Fossum, 2018: A nano-silicate material with exceptional capacity for CO_2 capture and storage at room temperature. *Scientific Reports*, **8**, 112827, https://doi.org/10.1038/s41598-018-30283-2.

Chanut, N., A. Ghoufi, M.-V. Coulet, S. Bourrelly, B. Kuchta, G. Maurin, and P. L. Llewellyn, 2020: Tailoring the separation properties of flexible metal-organic frameworks using mechanical pressure. *Nature Communications*, **11**, 1216, https://doi.org/10.1038/s41467-020-15036-y.

Choi, S., M. L. Gray, and C. W. Jones, 2011: Amine-tethered solid adsorbents coupling high adsorption capacity and regenerability for CO_2 capture from ambient air. *ChemSusChem*, **4**, 628–635, https://doi.org/10.1002/cssc.201000355.

Climeworks, 2021: Direct air capture: a technology to remove CO_2. Available from https://climeworks.com/co2-removal.

Custelcean, R., 2021: Direct air capture of CO_2 *via* crystal engineering. *Chemical Science*, **12**, 12 518–12 528, https://doi.org/10.1039/D1SC04097A.

de Jonge, M. M. J., J. Daemen, J. M. Loriaux, Z. J. N. Steinmann, and M. A. J. Huijbregts, 2019: Life cycle carbon efficiency of Direct Air Capture systems with strong hydroxide sorbents. *International Journal of Greenhouse Gas Control*, **80**, 25–31, https://doi.org/10.1016/j.ijggc.2018.11.011.

Deutz, S., and A. Bardow, 2021: Life-cycle assessment of an industrial direct air capture process based on temperature–vacuum swing adsorption. *Nature Energy*, **6**, 203–213, https://doi.org/10.1038/s41560-020-00771-9.

Didas, S. A., S. Choi, W. Chaikittisilp, and C. W. Jones, 2015: Amine-oxide hybrid materials for CO_2 capture from ambient air. *Accounts of Chemical Research*, **48**, 2680–2687, https://

doi.org/10.1021/acs.accounts.5b00284.

Dinh, C. T., and Coauthors, 2018: CO_2 electroreduction to ethylene via hydroxide-mediated copper catalysis at an abrupt interface. *Science*, **360**, 783–787, https://doi.org/10.1126/science.aas9100.

Dong, Q. B., and Coauthors, 2021: Corrigendum: Tunning gate-opening of a flexible metal–organic framework for ternary gas sieving separation. *Angewandte Chemie International Edition*, **60**, 3850–3850, https://doi.org/10.1002/anie.202100663.

Duyar, M. S., M. A. A. Treviño, and R. J. Farrauto, 2015: Dual function materials for CO_2 capture and conversion using renewable H_2. *Applied Catalysis B: Environmental*, **168–169**, 370–376, https://doi.org/10.1016/j.apcatb.2014.12.025.

Duyar, M. S., S. X. Wang, M. A. Arellano-Treviño, and R. J. Farrauto, 2016: CO_2 utilization with a novel dual function material (DFM) for capture and catalytic conversion to synthetic natural gas: An update. *Journal of CO_2 Utilization*, **15**, 65–71, https://doi.org/10.1016/j.jcou.2016.05.003.

Energy & Climate Intelligence Unit, 2021: Net zero emissions race. [Available from https://eciu.net/netzerotracker].

Engineering, C., 2021: Carbon engineering deployment timeline. Available from https://carbonengineering.com/our-story/.

Franchi, R. S., P. J. E. Harlick, and A. Sayari, 2005: Applications of pore-expanded mesoporous silica. 2. Development of a high-capacity, water-tolerant adsorbent for CO_2. *Industrial & Engineering Chemistry Research*, **44**, 8007–8013, https://doi.org/10.1021/ie0504194.

Furukawa, H., K. E. Cordova, M. O'Keeffe, and O. M. Yaghi, 2013: The chemistry and applications of metal-organic frameworks. *Science*, **341**, 1230444, https://doi.org/10.1126/science.1230444.

Ghoufi, A., K. Benhamed, L. Boukli-Hacene, and G. Maurin, 2017: Electrically induced breathing of the MIL-53(Cr) metal–organic framework. *ACS Central Science*, **3**, 394–398, https://doi.org/10.1021/acscentsci.6b00392.

Goeppert, A., M. Czaun, R. B. May, G. K. S. Prakash, G. A. Olah, and S. R. Narayanan, 2011: Carbon dioxide capture from the air using a polyamine based regenerable solid adsorbent. *Journal of the American Chemical Society*, **133**, 20 164–20 167, https://doi.org/10.1021/ja2100005.

Goglio, P., A. G. Williams, N. Balta-Ozkan, N. R. P. Harris, P. Williamson, D. Huisingh, Z. Zhang, and M. Tavoni, 2020: Advances and challenges of life cycle assessment (LCA) of greenhouse gas removal technologies to fight climate changes. *Journal of Cleaner Production*, **244**, 118896, https://doi.org/10.1016/j.jclepro.2019.118896.

Gong, Q., and Coauthors, 2019: Structural defects on converted bismuth oxide nanotubes enable highly active electrocatalysis of carbon dioxide reduction. *Nature Communications*, **10**, 2807, https://doi.org/10.1038/s41467-019-10819-4.

Hepburn, C., and Coauthors, 2019: The technological and economic prospects for CO_2 utilization and removal. *Nature*, **575**, 87–97, https://doi.org/10.1038/s41586-019-1681-6.

Hicks, J. C., J. H. Drese, D. J. Fauth, M. L. Gray, G. G. Qi, and C. W. Jones, 2008: Designing adsorbents for CO_2 capture from flue gas-hyperbranched aminosilicas capable of capturing CO_2 reversibly. *Journal of the American Chemical Society*, **130**, 2902–2903, https://doi.org/10.1021/ja077795v.

Huang, Y., A. D. Handoko, P. Hirunsit, and B. S. Yeo, 2017: Electrochemical reduction of CO_2 using copper single-crystal surfaces: Effects of CO* coverage on the selective formation of ethylene. *ACS Catalysis*, **7**, 1749–1756, https://doi.org/10.1021/acscatal.6b03147.

Hunt, P., D. R. Worrall, F. Wilkinson, and S. N. Batchelor, 2003: Quantitative rate constants for the reaction of dyes and alkenes with α-hydroxyalkyl radicals, measured by laser flash photolysis. *Photochemical & Photobiological Sciences*, **2**, 518–523, https://doi.org/10.1039/B212051H.

IEA, 2020a: World energy outlook 2020. 171 pp.

IEA, 2020b: Energy technology perspectives 2020. 461 pp.

Inagaki, F., C. Matsumoto, T. Iwata, and C. Mukai, 2017: CO_2-selective absorbents in air: Reverse lipid bilayer structure forming neutral carbamic acid in water without hydration. *Journal of the American Chemical Society*, **139**, 4639–4642, https://doi.org/10.1021/jacs.7b01049.

IPCC, 2014: Climate Change 2014: Synthesis Report, contribution of Working Groups I, II and III to the Fifth Assessment Report of the Intergovernmental Panel on Climate Change. IPCC, Geneva, Switzerland, 151 pp.

IPCC, 2018: Global Warming of 1.5°C. World Meteorological Organization, Geneva, Switzerland, 32 pp.

Kar, S., R. Sen, A. Goeppert, and G. K. S. Prakash, 2018: Integrative CO_2 capture and hydrogenation to methanol with reusable catalyst and amine: Toward a carbon neutral methanol economy. *Journal of the American Chemical Society*, **140**, 1580–1583, https://doi.org/10.1021/jacs.7b12183.

Kar, S., A. Goeppert, and G. K. S. Prakash, 2019: Integrated CO_2 capture and conversion to formate and methanol: Connecting two threads. *Accounts of Chemical Research*, **52**, 2892–2903, https://doi.org/10.1021/acs.accounts.9b00324.

Keith, D. W., G. Holmes, D. S. Angelo, and K. Heidel, 2018: A process for capturing CO_2 from the atmosphere. *Joule*, **2**, 1573–1594, https://doi.org/10.1016/j.joule.2018.05.006.

Keller, L., B. Ohs, J. Lenhart, L. Abduly, P. Blanke, and M. Wessling, 2018: High capacity polyethylenimine impregnated microtubes made of carbon nanotubes for CO_2 capture. *Carbon*, **126**, 338–345, https://doi.org/10.1016/j.carbon.2017.10.023.

Kim, D., and Coauthors, 2020a: Selective CO_2 electrocatalysis at the pseudocapacitive nanoparticle/ordered-ligand interlayer. *Nature Energy*, **5**, 1032–1042, https://doi.org/10.1038/s41560-020-00730-4.

Kim, E. J., and Coauthors, 2020b: Cooperative carbon capture and steam regeneration with tetraamine-appended metal-organic frameworks. *Science*, **369**, 392–396, https://doi.org/10.1126/science.abb3976.

Kitaura, R., K. Seki, G. Akiyama, and S. Kitagawa, 2003: Porous coordination-polymer crystals with gated channels specific for supercritical gases. *Angewandte Chemie International Edition*, **42**, 428–431, https://doi.org/10.1002/anie.200390130.

Kortlever, R., J. Shen, K. J. P. Schouten, F. Calle-Vallejo, and M. T. Koper, 2015: Catalysts and reaction pathways for the electrochemical reduction of carbon dioxide. *The Journal of Physical Chemistry Letters*, **6**, 4073–4082, https://doi.org/10.1021/acs.jpclett.5b01559.

Kothandaraman, J., A. Goeppert, M. Czaun, G. A. Olah, and G. K. S. Prakash, 2016: Conversion of CO_2 from air into methanol using a polyamine and a homogeneous ruthenium catalyst. *Journal of the American Chemical Society*, **138**, 778–781, https://doi.org/10.1021/jacs.5b12354.

Kumar, A., D. G. Madden, M. Lusi, K. J. Chen, E. A. Daniels, T. Curtin, J. J. Perry IV, and M. J. Zaworotko, 2015: Direct air

capture of CO_2 by physisorbent materials. *Angewandte Chemie International Edition*, **54**, 14 372–14 377, https://doi.org/10.1002/anie.201506952.

Kumar, A., C. Hua, D. G. Madden, D. O'Nolan, K.-J. Chen, L.-A. J. Keane, J. J. Perry IV, and M. J. Zaworotko, 2017: Hybrid ultramicroporous materials (HUMs) with enhanced stability and trace carbon capture performance. *Chemical Communications*, **53**, 5946–5949, https://doi.org/10.1039/C7CC02289A.

Lee, W. R., S. Y. Hwang, D. W. Ryu, K. S. Lim, S. S. Han, D. Moon, J. Choi, and C. S. Hong, 2014: Diamine-functionalized metal–organic framework: Exceptionally high CO_2 capacities from ambient air and flue gas, ultrafast CO_2 uptake rate, and adsorption mechanism. *Energy & Environmental Science*, **7**, 744–751, https://doi.org/10.1039/C3EE42328J.

Li, L. Y., D. L. King, Z. M. Nie, and C. Howard, 2009: Magnesia-stabilized calcium oxide absorbents with improved durability for high temperature CO_2 capture. *Industrial & Engineering Chemistry Research*, **48**, 10 604–10 613, https://doi.org/10.1021/ie901166b.

Liao, P.-Q., and Coauthors, 2016: Putting an ultrahigh concentration of amine groups into a metal-organic framework for CO_2 capture at low pressures. *Chemical Science*, **7**, 6528–6533, https://doi.org/10.1039/C6SC00836D.

Lin, J. B., and Coauthors, 2021: A scalable metal-organic framework as a durable physisorbent for carbon dioxide capture. *Science*, **374**, 1464–1469, https://doi.org/10.1126/science.abi7281.

Lu, W., J. P. Sculley, D. Yuan, R. Krishna, and H.-C. Zhou, 2013: Carbon dioxide capture from air using amine-grafted porous polymer networks. *The Journal of Physical Chemistry C*, **117**, 4057–4061, https://doi.org/10.1021/jp311512q.

Lyndon, R., K. Konstas, B. P. Ladewig, P. D. Southon, C. J. Kepert, and M. R. Hill, 2013: Dynamic photo-switching in metal–organic frameworks as a route to low-energy carbon dioxide capture and release. *Angewandte Chemie International Edition*, **52**, 3695–3698, https://doi.org/10.1002/anie.201206359.

Ma, X. L., X. X. Wang, and C. S. Song, 2009: "Molecular Basket" sorbents for separation of CO_2 and H_2S from various gas streams. *Journal of the American Chemical Society*, **131**, 5777–5783, https://doi.org/10.1021/ja8074105.

Marks, S. D., K. Riascos-Rodriguez, R. R. Arrieta-Pérez, A. A. Yakovenko, J. Exley, P. G. Evans, and A. J. Hernández-Maldonado, 2020: Lattice expansion and ligand twist during CO_2 adsorption in flexible Cu bipyridine metal–organic frameworks. *Journal of Materials Chemistry A*, **8**, 18 903–18 915, https://doi.org/10.1039/D0TA03298K.

Martell, J. D., P. J. Milner, R. L. Siegelman, and J. R. Long, 2020: Kinetics of cooperative CO_2 adsorption in diamine-appended variants of the metal–organic framework Mg2(dobpdc). *Chemical Science*, **11**, 6457–6471, https://doi.org/10.1039/D0SC01087A.

Matsuda, R., 2014: Selectivity from flexibility. *Nature*, **509**, 434–435, https://doi.org/10.1038/509434a.

McDonald, T. M., and Coauthors, 2015: Cooperative insertion of CO_2 in diamine-appended metal-organic frameworks. *Nature*, **519**, 303–308, https://doi.org/10.1038/nature14327.

Miguel, C. V., M. A. Soria, A. Mendes, and L. M. Madeira, 2017: A sorptive reactor for CO_2 capture and conversion to renewable methane. *Chemical Engineering Journal*, **322**, 590–602, https://doi.org/10.1016/j.cej.2017.04.024.

Modrow, A., D. Zargarani, R. Herges, and N. Stock, 2011: The first porous MOF with photoswitchable linker molecules. *Dalton Transactions*, **40**, 4217–4222, https://doi.org/10.1039/c0dt01629b.

Carbon energy technology Co., Ltd (Beijing), 2020: The pilot project of carbon dioxide electrolysis to syngas successfully passed the on-site assessment. https://www.sohu.com/a/434528697_99896823. (in Chinese)

Mukherjee, S., and Coauthors, 2019: Trace CO_2 capture by an ultramicroporous physisorbent with low water affinity. *Science Advances*, **5**, eaax9171, https://doi.org/10.1126/sciadv.aax9171.

Nandi, S., and Coauthors, 2015: A single-ligand ultra-microporous MOF for precombustion CO_2 capture and hydrogen purification. *Science Advances*, **1**, e1500421, https://doi.org/10.1126/sciadv.1500421.

Park, J., D. Q. Yuan, K. T. Pham, J.-R. Li, A. Yakovenko, and H.-C. Zhou, 2012: Reversible alteration of CO_2 adsorption upon photochemical or thermal treatment in a metal–organic framework. *Journal of the American Chemical Society*, **134**, 99–102, https://doi.org/10.1021/ja209197f.

Peterson, A. A., F. Abild-Pedersen, F. Studt, J. Rossmeisl, and J. K. Nørskov, 2010: How copper catalyzes the electroreduction of carbon dioxide into hydrocarbon fuels. *Energy & Environmental Science*, **3**, 1311–1315, https://doi.org/10.1039/C0EE00071J.

Potter, M. E., K. M. Cho, J. J. Lee, and C. W. Jones, 2017: Role of alumina basicity in CO_2 uptake in 3-aminopropylsilyl-grafted alumina adsorbents. *ChemSusChem*, **10**, 2192–2201, https://doi.org/10.1002/cssc.201700115.

Proaño, L., E. Tello, M. A. Arellano-Trevino, S. X. Wang, R. J. Farrauto, and M. Cobo, 2019: *In-situ* DRIFTS study of two-step CO_2 capture and catalytic methanation over Ru, "Na_2O" /Al_2O_3 dual functional material. *Applied Surface Science*, **479**, 25–30, https://doi.org/10.1016/j.apsusc.2019.01.281.

Qiao, Y. Q., J. Y. Wang, Y. Zhang, W. L. Gao, T. Harada, L. Huang, T. A. Hatton, and Q. Wang, 2017: Alkali nitrates molten salt modified commercial MgO for intermediate-temperature CO_2 capture: Optimization of the Li/Na/K ratio. *Industrial & Engineering Chemistry Research*, **56**, 1509–1517, https://doi.org/10.1021/acs.iecr.6b04793.

Qu, C. F., X. Yang, D. Zhang, and X. L. Zhang, 2020: Estimating health co-benefits of climate policies in China: An application of the regional emissions-air quality-climate-health (reach) FRAMEWORK. *Climate Change Economics*, **11**, 2041004, https://doi.org/10.1142/S2010007820410043.

Reller, C., M. Pöge, A. Lißner, and F. O. R. L. Mertens, 2014: Methanol from CO_2 by organo-cocatalysis: CO_2 capture and hydrogenation in one process step. *Environmental Science & Technology*, **48**, 14 799–14 804, https://doi.org/10.1021/es503914d.

Sabatino, F., A. Grimm, F. Gallucci, M. van Sint Annaland, G. J. Kramer, and M. Gazzani, 2021: A comparative energy and costs assessment and optimization for direct air capture technologies. *Joule*, **5**, 2047–2076, https://doi.org/10.1016/j.joule.2021.05.023.

Sanz-Pérez, E. S., C. R. Murdock, S. A. Didas, and C. W. Jones, 2016: Direct capture of CO_2 from ambient air. *Chemical Reviews*, **116**, 11 840–11 876, https://doi.org/10.1021/acs.chemrev.6b00173.

Sayari, A., and Y. Belmabkhout, 2010: Stabilization of amine-containing CO_2 adsorbents: Dramatic effect of water vapor. *Jour-*

nal of the American Chemical Society, **132**, 6312–6314, https://doi.org/10.1021/ja1013773.

Schneemann, A., V. Bon, I. Schwedler, I. Senkovska, S. Kaskel, and R. A. Fischer, 2014: Flexible metal–organic frameworks. *Chemical Society Reviews*, **43**, 6062–6096, https://doi.org/10.1039/C4CS00101J.

Sen, R., A. Goeppert, S. Kar, and G. K. S. Prakash, 2020: Hydroxide based integrated CO_2 capture from air and conversion to methanol. *Journal of the American Chemical Society*, **142**, 4544–4549, https://doi.org/10.1021/jacs.9b12711.

Sen, T., Y. Kawajiri, and M. J. Realff, 2019: Adsorption process intensification through structured packing: A modeling study using zeolite 13X and a mixture of propylene and propane in hollow-fiber and packed beds. *Industrial & Engineering Chemistry Research*, **58**, 5750–5767, https://doi.org/10.1021/acs.iecr.8b02189.

Sensharma, D., N. Y. Zhu, S. Tandon, S. Vaesen, G. W. Watson, and W. Schmitt, 2019: Flexible metal–organic frameworks for light-switchable CO_2 sorption using an auxiliary ligand strategy. *Inorganic Chemistry*, **58**, 9766–9772, https://doi.org/10.1021/acs.inorgchem.9b00768.

Shao, B., and Coauthors, 2021: Heterojunction-redox catalysts of $Fe_xCo_yMg_{10}CaO$ for high-temperature CO_2 capture and *in situ* conversion in the context of green manufacturing. *Energy & Environmental Science*, **14**, 2291–2301, https://doi.org/10.1039/D0EE03320K.

Shi, X. Y., H. Xiao, K. S. Lackner, and X. Chen, 2016: Capture CO_2 from ambient air using nanoconfined ion hydration. *Angewandte Chemie International Edition*, **55**, 4026–4029, https://doi.org/10.1002/anie.201507846.

Shi, X. Y., H. Xiao, H. Azarabadi, J. Z. Song, X. L. Wu, X. Chen, and K. S. Lackner, 2020: Sorbents for the direct capture of CO_2 from ambient air. *Angewandte Chemie International Edition*, **59**, 6984–7006, https://doi.org/10.1002/anie.201906756.

Shih, C. F., T. Zhang, J. H. Li, and C. L. Bai, 2018: Powering the future with liquid sunshine. *Joule*, **2**, 1925–1949, https://doi.org/10.1016/j.joule.2018.08.016.

Song, Y. F., W. Chen, C. C. Zhao, S. G. Li, W. Wei, and Y. H. Sun, 2017: Metal-free nitrogen-doped mesoporous carbon for electroreduction of CO_2 to ethanol. *Angewandte Chemie International Edition*, **56**, 10 840–10 844, https://doi.org/10.1002/anie.201706777.

Song, Y. F., S. B. Wang, W. Chen, S. G. Li, G. H. Feng, W. Wei, and Y. H. Sun, 2020: Enhanced ethanol production from CO_2 electroreduction at micropores in nitrogen-doped mesoporous carbon. *ChemSusChem*, **13**, 293–297, https://doi.org/10.1002/cssc.201902833.

Stavitski, E., and Coauthors, 2011: Complexity behind CO_2 Capture on NH_2-MIL-53(Al). *Langmuir*, **27**, 3970–3976, https://doi.org/10.1021/la1045207.

Stevenson, S. A., 2019: Thermodynamic considerations in CO_2 utilization. *AIChE Journal*, **65**, e16695, https://doi.org/10.1002/aic.16695.

Sun, H. M., J. Q. Wang, J. H. Zhao, B. X. Shen, J. Shi, J. Huang, and C. F. Wu, 2019: Dual functional catalytic materials of Ni over Ce-modified CaO sorbents for integrated CO_2 capture and conversion. *Applied Catalysis B: Environmental*, **244**, 63–75, https://doi.org/10.1016/j.apcatb.2018.11.040.

Sun, H. M., Y. Zhang, S. L. Guan, J. Huang, and C. F. Wu, 2020: Direct and highly selective conversion of captured CO_2 into methane through integrated carbon capture and utilization over dual functional materials. *Journal of CO_2 Utilization*, **38**, 262–272, https://doi.org/10.1016/j.jcou.2020.02.001.

Taylor, M. K., and Coauthors, 2018: Near-perfect CO_2/CH_4 selectivity achieved through reversible guest templating in the flexible metal–organic framework Co(bdp). *Journal of the American Chemical Society*, **140**, 10 324–10 331, https://doi.org/10.1021/jacs.8b06062.

Terlouw, T., K. Treyer, C. Bauer, and M. Mazzotti, 2021a: Life cycle assessment of direct air carbon capture and storage with low-carbon energy sources. *Environmental Science & Technology*, **55**, 11 397–11 411, https://doi.org/10.1021/ACS.EST.1C03263.

Terlouw, T., C. Bauer, L. Rosa, and M. Mazzotti, 2021b: Life cycle assessment of carbon dioxide removal technologies: A critical review. *Energy & Environmental Science*, **14**, 1701–1721, https://doi.org/10.1039/d0ee03757e.

Uesaka, M., Y. Saito, S. Yoshioka, Y. Domoto, M. Fujita, and Y. Inokuma, 2018: Oligoacetylacetones as shapable carbon chains and their transformation to oligoimines for construction of metal-organic architectures. *Communications Chemistry*, **1**, 23, https://doi.org/10.1038/s42004-018-0021-3.

Veselovskaya, J. V., P. D. Parunin, O. V. Netskina, L. S. Kibis, A. I. Lysikov, and A. G. Okunev, 2018: Catalytic methanation of carbon dioxide captured from ambient air. *Energy*, **159**, 766–773, https://doi.org/10.1016/j.energy.2018.06.180.

Wang, X., and Coauthors, 2020: Efficient electrically powered CO_2-to-ethanol via suppression of deoxygenation. *Nature Energy*, **5**, 478–486, https://doi.org/10.1038/s41560-020-0607-8.

Xiong, L. K., and Coauthors, 2021: Geometric modulation of local CO flux in $Ag@Cu_2O$ nanoreactors for steering the CO_2RR pathway toward high-efficacy methane production. *Advanced Materials*, **33**, 2101741, https://doi.org/10.1002/ADMA.202101741.

Xu, H. P., and Coauthors, 2020: Highly selective electrocatalytic CO_2 reduction to ethanol by metallic clusters dynamically formed from atomically dispersed copper. *Nature Energy*, **5**, 623–632, https://doi.org/10.1038/s41560-020-0666-x.

Xu, J. Y., and Coauthors, 2016: Revealing the origin of activity in nitrogen-doped nanocarbons towards electrocatalytic reduction of carbon dioxide. *ChemSusChem*, **9**, 1085–1089, https://doi.org/10.1002/cssc.201600202.

Xu, X. C., C. S. Song, J. M. Andresen, B. G. Miller, and A. W. Scaroni, 2002: Novel polyethylenimine-modified mesoporous molecular sieve of MCM-41 type as high-capacity adsorbent for CO_2 capture. *Energy & Fuels*, **16**, 1463–1469, https://doi.org/10.1021/ef020058u.

Yadav, R. M., and Coauthors, 2022: Amine-functionalized carbon nanodot electrocatalysts converting carbon dioxide to methane. *Advanced Materials*, **34**, 2105690, https://doi.org/10.1002/adma.202105690.

Yan, S., and Coauthors, 2021: Electron localization and lattice strain induced by surface lithium doping enable ampere-level electrosynthesis of formate from CO_2. *Angewandte Chemie International Edition*, **60**, 25 741–25 745, https://doi.org/10.1002/anie.202111351.

Yang, H., M. Singh, and J. Schaefer, 2018: Humidity-swing mechanism for CO_2 capture from ambient air. *Chemical Communications*, **54**, 4915–4918, https://doi.org/10.1039/c8cc02109k.

Yang, K. D., and Coauthors, 2016: Graphene quantum sheet catalyzed silicon photocathode for selective CO_2 conversion to CO. *Advanced Functional Materials*, **26**, 233–242, https://

doi.org/10.1002/adfm.201502751.

Yuan, S., and Coauthors, 2018: Stable metal–organic frameworks: Design, synthesis, and applications. *Advanced Materials*, **30**, 1704303, https://doi.org/10.1002/adma.201704303.

Yue, M. C, K. Imai, Y. Miura, and Y. Hoshino, 2017: Design and preparation of thermo-responsive vinylamine-containing micro-gel particles for reversible absorption of carbon dioxide. *Polymer Journal*, **49**, 601–606, https://doi.org/10.1038/pj.2017.28.

Zhang, X., and Coauthors, 2020: Molecular engineering of dispersed nickel phthalocyanines on carbon nanotubes for selective CO_2 reduction. *Nature Energy*, **5**, 684–692, https://doi.org/10.1038/s41560-020-0667-9.

Zheng, Q. H., R. Farrauto, and A. C. Nguyen, 2016: Adsorption and methanation of flue gas CO_2 with dual functional catalytic materials: A parametric study. *Industrial & Engineering Chemistry Research*, **55**, 6768–6776, https://doi.org/10.1021/acs.iecr.6b01275.

Zhong, M., and Coauthors, 2020: Accelerated discovery of CO_2 electrocatalysts using active machine learning. *Nature*, **581**, 178–183, https://doi.org/10.1038/s41586-020-2242-8.

Zhou, Z. J., and Coauthors, 2020: 2D-layered Ni-MgO-Al_2O_3 nanosheets for integrated capture and methanation of CO_2. *ChemSusChem*, **13**, 360–368, https://doi.org/10.1002/cssc.201902828.

Zhu, X. C., T. S. Ge, J. Y. Wu, F. Yang, and R. Z. Wang, 2021: Large-scale applications and challenges of adsorption-based carbon capture technologies. *Chinese Science Bulletin*, **66**, 2861–2877, https://doi.org/10.1360/TB-2021-0017.

ADVANCES IN ATMOSPHERIC SCIENCES, VOL. 39, AUGUST 2022, 1271–1284

• **Original Paper** •

The Variability of Air-sea O_2 Flux in CMIP6: Implications for Estimating Terrestrial and Oceanic Carbon Sinks※

Changyu LI[1], Jianping HUANG*[2], Lei DING[1], Yu REN[1], Linli AN[1], Xiaoyue LIU[1], and Jiping HUANG[3]

[1]*College of Atmospheric Sciences*, *Lanzhou University*, *Lanzhou* 730000, *China*

[2]*Collaborative Innovation Center for Western Ecological Safety*, *Lanzhou University*, *Lanzhou* 730000, *China*

[3]*Enlightening Bioscience Research Center*, *Mississauga*, *L4X* 2*X*7, *Canada*

(Received 27 July 2021; revised 24 September 2021; accepted 8 October 2021)

ABSTRACT

The measurement of atmospheric O_2 concentrations and related oxygen budget have been used to estimate terrestrial and oceanic carbon uptake. However, a discrepancy remains in assessments of O_2 exchange between ocean and atmosphere (i.e. air-sea O_2 flux), which is one of the major contributors to uncertainties in the O_2-based estimations of the carbon uptake. Here, we explore the variability of air-sea O_2 flux with the use of outputs from Coupled Model Intercomparison Project phase 6 (CMIP6). The simulated air-sea O_2 flux exhibits an obvious warming-induced upward trend (~1.49 Tmol yr^{-2}) since the mid-1980s, accompanied by a strong decadal variability dominated by oceanic climate modes. We subsequently revise the O_2-based carbon uptakes in response to this changing air-sea O_2 flux. Our results show that, for the 1990–2000 period, the averaged net ocean and land sinks are 2.10±0.43 and 1.14±0.52 GtC yr^{-1} respectively, overall consistent with estimates derived by the Global Carbon Project (GCP). An enhanced carbon uptake is found in both land and ocean after year 2000, reflecting the modification of carbon cycle under human activities. Results derived from CMIP5 simulations also investigated in the study allow for comparisons from which we can see the vital importance of oxygen dataset on carbon uptake estimations.

Key words: air-sea O_2 flux, carbon budget, land and ocean carbon sinks, CMIP6

Citation: Li, C. Y., J. P. Huang, L. Ding, Y. Ren, L. L. An, X. Y. Liu, and J. P. Huang, 2022: The variability of air-sea O_2 flux in CMIP6: Implications for estimating terrestrial and oceanic carbon sinks. *Adv. Atmos. Sci.*, **39**(8), 1271−1284, https://doi.org/10.1007/s00376-021-1273-x.

Article Highlights:

- CMIP6 outputs are used to systematically analyze the characteristics of air-sea O_2 flux under climate change.
- The study provides a valuable complement for global carbon sinks based on the tight relationship between oxygen and carbon cycle.
- The vital role of oceanic oxygen outgassing in O_2-based estimations of land and ocean carbon uptake is revealed in this study.

1. Introduction

Human beings are now faced with continuous growth of the climate risk in the warming world. The climate change, occurring mainly as a consequence of anthropogenic CO_2 emissions, is already wielding its influences on ecosystems, economic sectors and people's health (Bopp et al., 2013; Huang et al., 2016; Frölicher et al., 2018; Wei et al., 2021). An increasing number of evidence warns us that actions should be taken urgently to minimize dangerous anthropogenic interference with the climate system, limiting global warming to 2 degrees – a threshold laid down by the Paris Agreement (Seneviratne et al., 2016; Huang et al., 2017b). Under this circumstance, the carbon neutrality, which refers to the balance of emissions of carbon dioxide with its removal, has become one of the most essential things human society needs to achieve in the mid-late 21st century (Dhanda and Hartman, 2011; Niu et al., 2021).

The land and ocean play an important role in the storage of atmospheric CO_2 (Dai et al., 2013; DeVries et al., 2019). It has been reported that the land and ocean have sequestered approximately half of the anthropogenic CO_2

※ This paper is a contribution to the special issue on Carbon Neutrality: Important Roles of Renewable Energies, Carbon Sinks, NETs, and non-CO_2 GHGs.

* Corresponding author: Jianping HUANG
Email: hjp@lzu.edu.cn

emitted to the atmosphere in the past decades, which helps greatly buffer climate change (Friedlingstein et al., 2019; Gao et al., 2019, 2020). Thus, for a reasonable design of global warming mitigation and carbon neutrality strategies, there is a pressing need to address the effectiveness of terrestrial and oceanic carbon uptake and their susceptibility to climate change. According to this view, the measurement of atmospheric O_2 concentrations and related oxygen budget could provide us a concise and effective method to estimate carbon-uptake capacity of land and ocean on the basis of the close relationship between oxygen and carbon (Huang et al., 2018, 2021; Han et al., 2021; Li et al., 2021).

The accuracy of this O_2-based carbon uptake estimation largely depends on how the oxygen data, especially the air-sea O_2 exchange, is processed in the calculation. Early studies used to assume that there was no long-term oceanic effect of O_2 on the atmosphere (Keeling and Shertz, 1992; Battle et al., 2000). However, a number of indications have revealed the huge oceanic heat uptake under climate change (Willis et al., 2004; Cheng et al., 2018; Cheng and Zhu, 2018; Li et al., 2019), which implies the air-sea O_2 exchange could vary as a consequence of warming-induced solubility and circulation changes (Bopp et al., 2002; Li et al., 2020). Later studies have thus taken air-sea O_2 flux into consideration (Manning and Keeling, 2006; Tohjima et al., 2019), where the oceanic O_2 outgassing to the atmosphere is approximately estimated by a linear regression with ocean heat content, assuming the relationship between gas flux and heat flux bears a proportional relationship at the air–sea interface. In fact, mechanisms that control the variability of air-sea O_2 flux are rather complicated. Its temporal and spatial variations could be affected by changes in ocean primary production, ventilation and stratification, as well as oceanic internal modes such as El Niño-Southern Oscillation(ENSO) (Resplandy et al., 2015; Yang et al., 2017). The intensified ocean heat uptake in the past few decades (Trenberth et al., 2014; Cheng et al., 2017) also wields its influences in the long-term period. How to accurately quantify the air-sea O_2 flux has therefore been one of the most important questions in the field of O_2-based carbon uptake estimations.

Here, based on recent CMIP6 model simulations, we systematically investigate the characteristics of air-sea O_2 flux and from it, we subsequently calculate the terrestrial and oceanic carbon sinks. We hope to provide a better understanding of air-sea O_2 flux under ongoing climate change. We also hope the applications of process-based air-sea O_2 flux from CMIP6 model simulations can provide a more comprehensive and reliable carbon sink estimation, compared with results from previous studies where the air-sea O_2 flux is not considered or simply approximated by a linear relationship between O_2 outgassing and heat content.

The paper is arranged as follows. Section 2 describes the detailed method of O_2-based carbon sink estimations and the datasets, especially air-sea O_2 flux, used in this study. The climatology characteristics of air-sea O_2 flux and its variability under climate change in CMIP6 are shown in section 3.1. Section 3.2 provides our estimations of terrestrial and oceanic carbon sinks with the use of this air-sea O_2 flux. Discussion and conclusion are presented in section 4.

2. Data and methods

2.1. *O_2-based estimations of terrestrial and oceanic carbon sinks*

2.1.1. *Mass balanced equations for global oxygen and carbon budgets*

The assessments of land and ocean carbon sinks in this study are based on the strong relationship between oxygen and carbon, which can be written as follows (Keeling and Manning, 2014; Li et al., 2021):

$$\Delta CO_2 = F_{\text{fossil}} - S_{\text{ocean}} - S_{\text{land}}\,, \tag{1}$$

$$\Delta O_2 = -\alpha_F F_{\text{fossil}} + \alpha_B S_{\text{land}} + F_{\text{air-sea}}\,, \tag{2}$$

where ΔCO_2 and ΔO_2 represent changes in atmospheric CO_2 and O_2; F_{fossil} is the industrial CO_2 emissions, which mainly comes from fossil fuel combustion; $F_{\text{air-sea}}$ represents the air-sea O_2 flux; α_F and α_B are dimensionless parameters which represent the globally averaged O_2: CO_2 mole exchange ratios for fossil fuel burning and biological process; S_{land} and S_{ocean} represent the net land carbon sink and ocean carbon sink, respectively. These two equations briefly describe the human impacts on the oxygen and carbon cycles. All variables in the equations mentioned above use the units of mole.

2.1.2. *Observed atmospheric CO_2 and O_2 concentrations*

The concentrations of CO_2 in the atmosphere (X_{CO_2}) are measured using the unit of "ppm" (parts per million). Its change can be expressed as

$$\Delta X_{CO_2} = \frac{\Delta CO_2}{M_{\text{air}}}\,, \tag{3}$$

where M_{air} represents the global total number of moles of dry air (M_{air}=1.769×10^{20}). The change of atmospheric O_2 concentrations, however, is typically measured as the mole ratio changes of O_2/N_2 rather than the mole fraction such as ppm, due to its high abundance in the atmosphere. Following Keeling and Shertz (1992), the O_2 content of an air sample can be defined as

$$\delta(O_2/N_2) = \frac{(O_2/N_2)_{\text{sample}} - (O_2/N_2)_{\text{ref}}}{(O_2/N_2)_{\text{ref}}}\,, \tag{4}$$

where $(O_2/N_2)_{\text{sample}}$ is the mole ratio of O_2 to N_2 in the sample air and $(O_2/N_2)_{\text{ref}}$ is the ratio in an arbitrary reference gas. Note that $\delta(O_2/N_2)$ is typically multiplied by 10^6 and expressed as "per meg" unit. The observed changes of $\delta(O_2/N_2)$ in the atmosphere could thus be written as

$$\Delta(\delta(O_2/N_2)) = \left(\frac{\Delta O_2}{X_{O_2}} - \frac{\Delta N_2}{X_{N_2}}\right)\frac{1}{M_{\text{air}}}\,, \tag{5}$$

where ΔO_2 and ΔN_2 are changes in moles of atmospheric O_2

and N_2; X_{O_2} and X_{N_2} are the standard mole fraction of O_2 and N_2 in the atmosphere (X_{O_2} = 0.2094 and X_{N_2} = 0.7808).

According to Eqs. (1)–(5), the land and ocean carbon sink can be written as

$$B = \frac{1}{\alpha_B}\left[\Delta(\delta(O_2/N_2))M_{air}X_{O_2} + \alpha_F F_{fossil} - F_{eff}\right], \quad (6)$$

$$O = \frac{1}{\alpha_B}\left[(\alpha_B - \alpha_F)F_{fossil} - \left(\Delta(\delta(O_2/N_2))X_{O_2} + \alpha_B \Delta X_{CO_2}\right)M_{air} + F_{eff}\right], \quad (7)$$

$$F_{eff} = F_{air-sea} - \frac{X_{O_2}}{X_{N_2}}\Delta N_2 . \quad (8)$$

The observed timeseries of atmospheric CO_2 and O_2 concentrations [i.e. X_{CO_2} and $\delta(O_2/N_2)$] can be downloaded from Scripps O_2 Program (https://scrippso2.ucsd.edu/), which provides records of both CO_2 and O_2 concentrations at 12 stations. In this study, we choose the longest three timeseries, at Alert (82.5°N, 62.3°W), La Jolla (32.9°N, 277.3°W), and Cape Grim (40.7°S, 144.7°E), respectively, and calculate the average with weights of 0.25, 0.25, 0.5 (given the equal weight in both hemispheres).

2.1.3. *Global fossil-fuel combustion and the oxidative ratio*

The global CO_2 emissions (F_{fossil}) are derived from Carbon Dioxide Information Analysis Center (CDIAC, Andres et al., 2016), which counts the consumptions of each type of fossil fuel. It should be noted that each fuel type has its own combustion ratio (α_F), as shown in Table 1 (Liu et al., 2020). The global averaged α_F therefore slightly varies with time due to changes of global energy sources [Fig. S1 in the Electronic Supplementary Material, (ESM)]. The oxidative ratio α_B also exhibits temporal variations due to modifications to global vegetation cover by human activities, however, it is generally believed the decrease of α_B is less than 0.01 over 100 years (Randerson et al., 2006). We thus set the typical value of α_B as 1.10 according to previous studies (Keeling and Manning, 2014; Battle et al., 2019).

2.2. *The air-sea O_2 flux*

Due to the importance of O_2 flux ($F_{air\text{-}sea}$) in estimating the carbon uptake, here we discuss it in greater detail. The air-sea O_2 flux evaluated in this study builds on the process-based ocean physical and biochemical models developed as part of Coupled Model Intercomparison Project phase 6 (CMIP6), which can be downloaded from https://esgf-node.llnl.gov/search/cmip6/. The detailed descriptions of these models are presented in Table 2. Here we choose the historical experiments of these models to match the timeseries of O_2 observations. Note that the air-sea O_2 flux is calculated by the model in mol m^{-2} s^{-1}, so we convert to mol of oxygen per year (mol m^{-2} yr^{-1}). For sake of comparisons and analysis, all the model results are gridded to 1°×1° resolution.

Furthermore, it should be noted that, due to import of N_2 in the atmospheric O_2 observations, oceanic N_2 outgassing must be considered in the calculations. The total effect of the ocean on carbon sinks could thus be expressed as Eq. (8). Here we apply the tuning parameter β=0.88 to represent the negative effect of N_2 outgassing (Keeling and Manning, 2014); it can be shown that the equation can be written as

$$F_{eff} = \beta F_{air-sea} . \quad (9)$$

The related ocean physics variables such as sea temperature, salinity, and mixed layer depth in CMIP6 are also used in this study to analyze mechanisms of O_2 flux change.

2.3. *The EEMD method*

We use the ensemble empirical mode decomposition (EEMD) method to separate the human-induced long-term signals from natural decadal variability in the time series of air-sea O_2 flux. This noise-assisted method can separates scales naturally without any prior subjective criterion (Ji et al., 2014; Huang et al., 2017a). EEMD performs operations that partition a series into different "modes" (Intrinsic Mode Functions, IMFs), which are expressed by the following equation:

Table 1. Typical oxidative ratio for each fuel type.

Fuel Type	Oxidative ratio (α_F)
Solid fuel (coal)	1.17±0.03
Liquid fuel (oil)	1.44±0.03
Gas fuel (natural gas)	1.95±0.04
Cement production	0.00±0.00
Biofuel	1.07±0.03

Table 2. The CMIP6 models used in this study to obtain the air-sea O_2 flux[a].

Model Name	Institute
IPSL-CM5A2-INCA	Institut Pierre-Simon Laplace, France
GFDL-CM4	Geophysical Fluid Dynamics Laboratory, USA
GFDL-ESM4	Geophysical Fluid Dynamics Laboratory, USA
MPI-ESM-1-2-HAM	Max Planck Institute for Meteorology, Germany
NorESM2-LM	Norwegian Climate Centre, Norway
NorESM2-MM	Norwegian Climate Centre, Norway

[a] The air-sea O_2 flux was calculated by the model in mol m^{-2} s^{-1}, so we converted this value to mol of oxygen per year by converting from seconds to year (×31 536 000).

$$X(t) = \sum_{i=1}^{n} \mathrm{IMF}_i(t) + r_n(t) \ , \qquad (10)$$

where IMF_i(t) is the ith IMF, and $r_n(t)$ is the residual of data $X(t)$. The detailed descriptions of the steps on how to execute EEMD method can be found in Text S1 in the ESM. In this study, the noise added to the data has an amplitude that is 0.2 times the standard deviation of the raw data, and the ensemble number is 400. The number of IMFs is 6. A python version of EEMD is available at https://www.github.com/laszukdawid/PyEMD (Laszuk, 2017).

3. Results

3.1. *The characteristics of air-sea O_2 exchange in CMIP6*

3.1.1. *Climatological status of air-sea O_2 flux in 1985–2014 and evaluation against available studies*

The transfer of gases across the air-sea interface is controlled by several physical, biological and chemical processes in the atmosphere and ocean, which could influence not only the partial pressure differences but also the efficiency of transfer processes (Wanninkhof, 1992; Liang et al., 2013). The air-sea O_2 flux thus varies considerably among the ocean regions. Figure 1a presents the model-ensemble-mean of annual air-sea O_2 flux averaged from 1985 to 2014 in CMIP6 historical experiments (positive means a flux to the atmosphere). Spatial distributions of O_2 flux in each individual model can be found in Fig. S2 in the ESM. The results show an overall net O_2 outgassing from ocean to the atmosphere at low latitudes, while a significant influx of O_2 occurs at high latitudes. The tropical and subtropical ocean (30°S–30°N) emits approximately 250.8±38.4 Tmol O_2 per year (1 Tmol = 10^{12} mol), which is partly compensated by O_2 absorption in the high-latitude ocean, about −105.2±24.8 and −87.2±41.4 Tmol yr^{-1} in the Northern (>30°N) and Southern Hemisphere (>30°S), respectively, eventually leading to a net O_2 outgassing of ~58.5±9.6 Tmol yr^{-1} over the global ocean. This pattern highlights the solubility effect driven by meridional temperature gradients, as well as combinations of the dynamical and biological effects, which lead to a surplus of oceanic O_2 production in low latitudes (Bopp et al., 2002).

Furthermore, the simulated O_2 flux is evaluated against results derived from previous studies (Gruber et al., 2001; Resplandy et al., 2015), which are found in Fig. 1b . The ocean is divided into 13 regions for sake of comparison (Fig. S3 in the ESM). The patterns presented by the ensemble-mean of the suite of models in CMIP6 correspond well with estimations based on ocean inversions (Gruber et al., 2001), except for the Sothern Ocean. The results derived from Gruber et al. (2001) exhibit a much stronger O_2 outgassing in the subpolar South Atlantic [95.0 Tmol yr^{-1} differences between this study and Gruber et al. (2001)]. However, this difference could roughly cancel out when we integrate the whole Southern Ocean regions, as it also exists a larger O_2 influx in subpolar Indian-Pacific Ocean and Oceans >58°S (differences of −58.1 and −26.2 Tmol yr^{-1}, respectively). Besides, the spatial distribution shows a remarkable consistency with preindustrial experiments presented by Resplandy et al. (2015), indicating the robust of models in simulating O_2 flux.

3.1.2. *Modifications of air-sea O_2 flux under global warming*

Temporal evolution of the air-sea O_2 flux reveals that significant modifications have been occurring in response to ongoing climate change (Fig. 2). In Fig. 2a, we can see sizable oscillations of air-sea O_2 flux during the period 1950–85. Also obvious is the increase of oceanic O_2 outgassing found since the mid-1980s, with an upward trend of ~1.49 Tmol yr^{-2} (significant at 0.01 level). Based on EEMD method, here we split the evolution of air-sea O_2 flux into decadal variability (i.e. sum of IMFs 2–5 from EEMD) and the long-term trend (i.e. IMF 6). As shown in Fig. 2b, the time series of air-sea O_2 flux from 1950 to 1985 is primarily dominated by natural decadal variability, while the human-induced long-term changes gradually wields its influence after 1985. The combination of the two terms eventually lead to an overall upward trend since the 1980s, with natural variability modulating the long-term trend.

The EOF analysis was applied to the de-trended global air-sea O_2 flux over the 1985–2014 period to explore the spatio-temporal distributions of decadal variability (Fig. 3). The first two modes explain approximately 58% of the total variance. The highest decadal variability of O_2 flux is found in the North Pacific, the North Atlantic and the Southern Ocean (Figs. 3a, 3b). The most significant changes in the Atlantic are mainly in the high-latitude areas where the sinking branch of the Atlantic Meridional Overturning Circulation (AMOC) is located, the changes of which could significantly influence climate (Yang et al., 2016; Wen et al., 2018; Yang and Wen, 2020). In the Southern Ocean, the spatial pattern exhibits opposite phase between 40°S and 65°S, suggesting the potential relationship with the Southern Annular Mode (SAM). Time series associated with EOF modes reveal a cycle of ~15 years with different phases in PC1 and PC2 (Fig. 3c). The standard deviation of the decadal variability derived from EEMD also shows a similar spatial distribution compared with the EOF analysis (Fig. S4 in the ESM).

The long-term changes of air-sea O_2 flux, which are generally considered as modifications to anthropogenic forcing, is presented in Fig. 4. Positive values are mainly found in the high latitude areas (Fig. 4a), where strong O_2 uptake in the climatological state is seen (Fig. 1a), revealing the weakening of the oceanic O_2 absorption capacity from the atmosphere. The maximum increase of the flux occurs in the Southern Ocean (SO>58°S), where it reaches 5.39±0.34 Tmol yr^{-1}. The next two highest increases occur in the North Pacific (Temp NPac) and North Atlantic (N NAtl), with an increase about 4.39±0.17 and 3.25±0.11 Tmol yr^{-1}, respectively (Fig. 4b). This long-term change could be attributed to human-induced solubility and circulation changes. The sol-

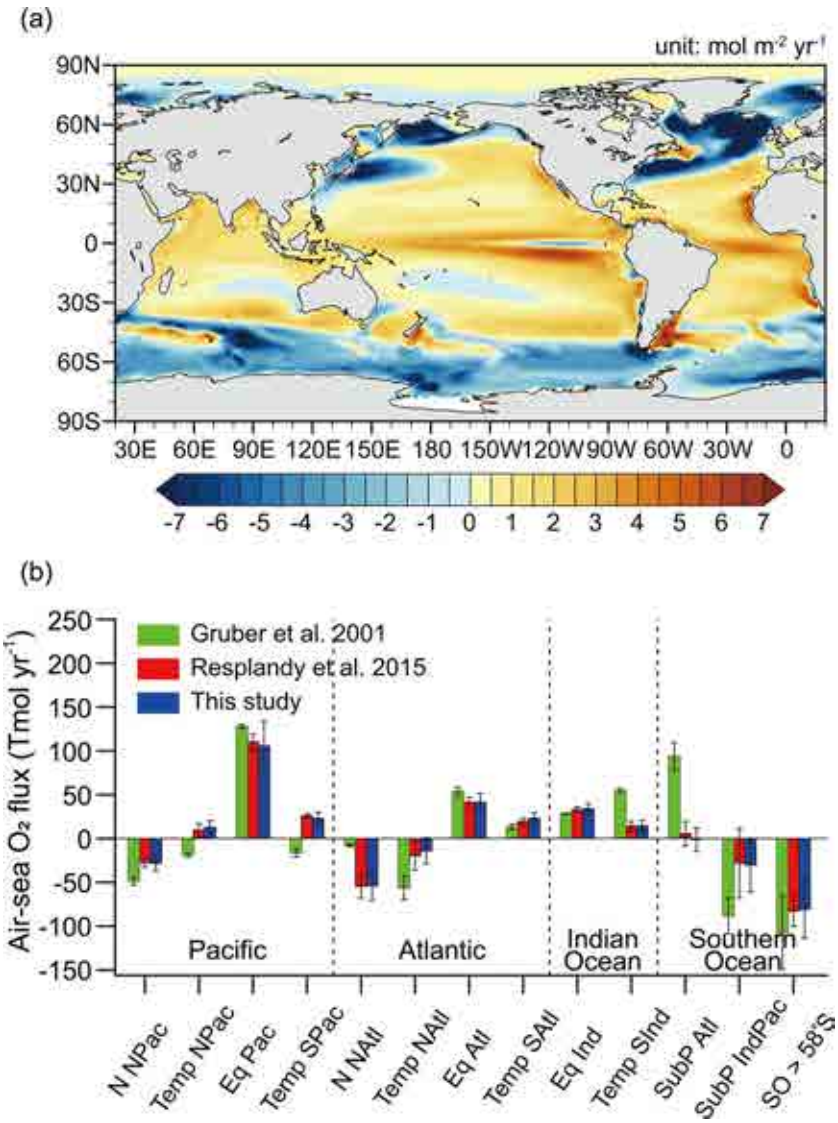

Fig. 1. The spatial distributions of annual mean air-sea O_2 flux (a) averaged from 1985 to 2014 in CMIP6 historical simulations, and (b) compared with two other studies. Positive flux in Fig. 1a means O_2 outgassing from ocean to the atmosphere. For sake of comparisons, the ocean is partitioned into 13 regions as shown in Fig. S3 in the ESM. The results from Li et al (2020) are similar with Resplandy et al 2015, which are not shown here.

ubility of dissolved O_2 has been decreasing in the warming ocean. This effect could be written as:

$$F_{\text{them,air-sea}} = -\frac{Q}{C_p}\frac{\partial O_2}{\partial T}, \tag{11}$$

where Q is the total sea-surface downward heat flux; C_p represents the heat capacity of sea water; $\partial O_2/\partial T$ is the temperature dependence of O_2 solubility which could be derived from Garcia and Gordon (1992). Our calculations reveal that roughly one quarter of the increase is directly associated with reduced solubility in the warming ocean, which is consistent with results found by Li et al. (2020) and Plattner et al. (2002). Warming-induced ocean stratification also plays an important role in the modifications of air-sea O_2 flux. Strong shoaling of the mixed layer is found in the North Atlantic and widespread areas in the Southern Ocean (Fig. S5 in the ESM), which prevents oxygen supplies from reaching the deeper layers and eventually result in a positive contribution to the air-sea O_2 flux.

3.1.3. *Comparisons with CMIP5: What's new about the air-sea O_2 flux we can learn in CMIP6*

In Li et al. (2020), the air-sea O_2 flux derived from CMIP5 is applied to investigate the terrestrial and oceanic carbon sinks. It is therefore necessary to clarify the difference of the flux between the CMIP5 and CMIP6 as well as its influences on carbon sink estimations.

For a simulated historical period from 1975 to 2005, the comparisons between CMIP6 (this study) and CMIP5

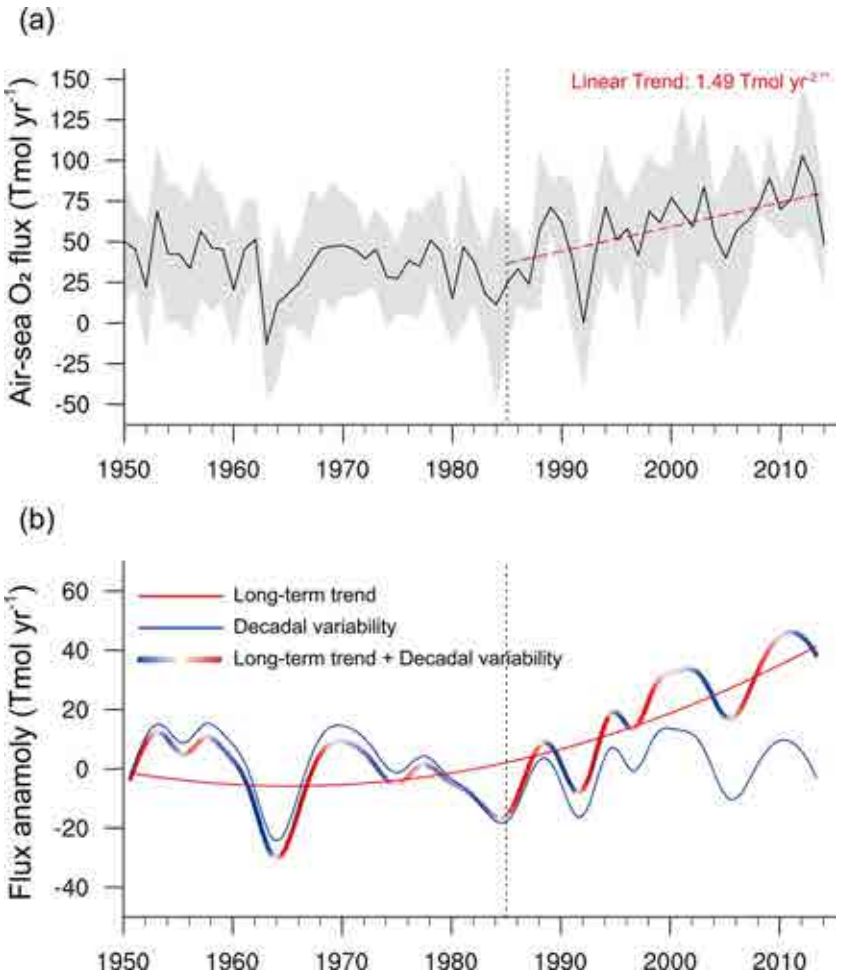

Fig. 2. Time series in the historical period (1950–2014) of (a) air-sea O_2 flux and (b) its EEMD decomposition. The red dashed line in (a) represents linear regression from 1980 to 2014, significant at the 0.01 level. Shaded area is the uncertainty of the flux represented by the standard deviation of these models. The decadal variability in (b) (the blue solid line) is the sum of IMF2-5 from the EEMD and the long-term trend (the red solid line) is the IMF6. Positive values in both panels indicate oceanic O_2 outgassing to the atmosphere.

[derived from Li et al. (2021)] reveal pronounced temporally varying differences of air-sea O_2 flux (Fig. 5). Except for a short period of time around year 1990, the ocean in CMIP6 exhibits an overall smaller oceanic O_2 outgassing, up to –22 Tmol yr^{-1}, than in CMIP5. Spatial patterns shown in Fig. 5b reveal that this difference is mainly caused by the intensified high-latitude oceanic O_2 uptake in CMIP6, especially in the North Atlantic and Southern Ocean. Although there still exists relatively large uncertainties, this intensified uptake in CMIP6 is more consistent with the regional observations in the Southern Ocean (Bushinsky et al., 2017), reflecting the improvement of simulations in CMIP6. Furthermore, slight difference also exists in the long-term trend of air-sea O_2 flux. An upward linear trend of ~1.52 Tmol yr^{-2} has been found in CMIP6 during the period 1985 to 2005, while the trend is approximately 1.12 Tmol yr^{-2} in CMIP5. This indicates an accelerated oceanic O_2 outgassing in CMIP6, which is tightly associated with ocean deoxygenation (Bopp et al., 2013; Palter and Trossman, 2018; Li et al., 2020).

According to Eqs. (6)–(8), this difference in O_2 flux could lead to a total fluctuation as large as 0.4 GtC yr^{-1} in the estimated carbon sink. It should be noted that, besides the air-sea O_2 flux, the estimated carbon sink could also be influenced by the choice of other oxygen datasets in the study, which is therefore rather complicated. Comparisons of O_2-based carbon sinks between this study and Li et al. (2021), as well as other previous studies, will be discussed in detail in the following section.

3.2. *Estimates of terrestrial and oceanic carbon sinks*

3.2.1. *O_2-CO_2 diagram from 1990 to 2014*

Simulations of the air-sea O_2 flux in CMIP6 provide a valuable complement for the O_2-based carbon uptake estimations. With the use of air-sea O_2 flux as well as other O_2-

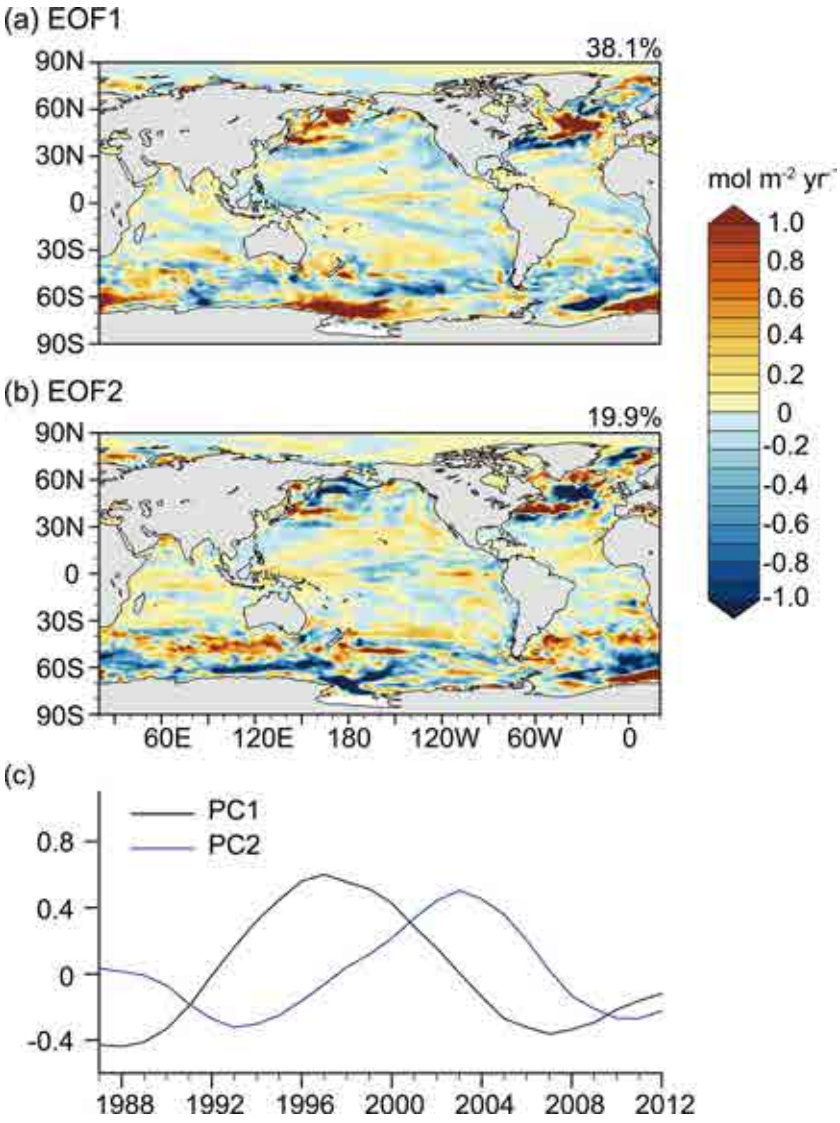

Fig. 3. EOF analysis of de-trended global air-sea O_2 flux over the 1985–2014 period. The spatial patterns of the first and second EOF mode are presented in panel (a) and (b), respectively. The black and blue lines in (a) represent the temporal coefficient of the two modes. Note that the original timeseries is pre-processed with a pentad running average to remove the influence of the high-frequency oscillations.

related variables, the global terrestrial and oceanic carbon sinks could be calculated based on Eqs. (1)–(9). The processes are briefly diagrammed in Fig. 6.

The dots in Fig. 6 are the observed anomalies of global atmospheric CO_2 (horizontal axis) and O_2/N_2 concentrations (vertical axis) from 1990 to 2014. Here we set the concentrations in year 1990 as the base point (0 ppm, 0 per meg). These dots show an increase of CO_2 concentration and a simultaneous decline in O_2/N_2 concentration with time. For example, the concentrations in 2014 could be written as (44 ppm, −465 per meg) in this coordinate system, which means a 44 ppm increase of CO_2 concentration and a 465 per meg decrease of O_2/N_2 concentration in the atmosphere since year 1990. The arrows in Fig. 6 reveal the effect of related processes on atmospheric CO_2 and O_2/N_2 concentration changes. For example, the fossil fuel combustion is marked by the black arrow in Fig. 6, starting at (0, 0) and ending at (89.0, −584.7), meaning that the fossil fuel burning would have contributed to a total 89.0 ppm increase of CO_2 (that is, a release of 189.0 GtC CO_2, 1 Gt = 10^{15} g, 1 ppm = 2.12 GtC) and 584.7 per meg decrease of O_2/N_2 concentration during 1990–2014, if no other processes were involved. This is to say, the observed decline of O_2/N_2 (~465.1 per meg) is a bit smaller compared with the decline directly derived from fossil fuel combustion (584.7 per meg) during 1990–2014. More importantly, the observed atmospheric CO_2 concentration only increases by about half of the value derived from fossil fuel combustion (that is, ~44 ppm, as shown in Fig. 6 and Fig. 7), from which we can thus infer huge land and ocean carbon sinks, absorbing a total of 96.6 GtC carbon. The projections of these arrows on the *x*- axis are also drawn in Fig. 6, which reflect how the atmospheric CO_2 con-

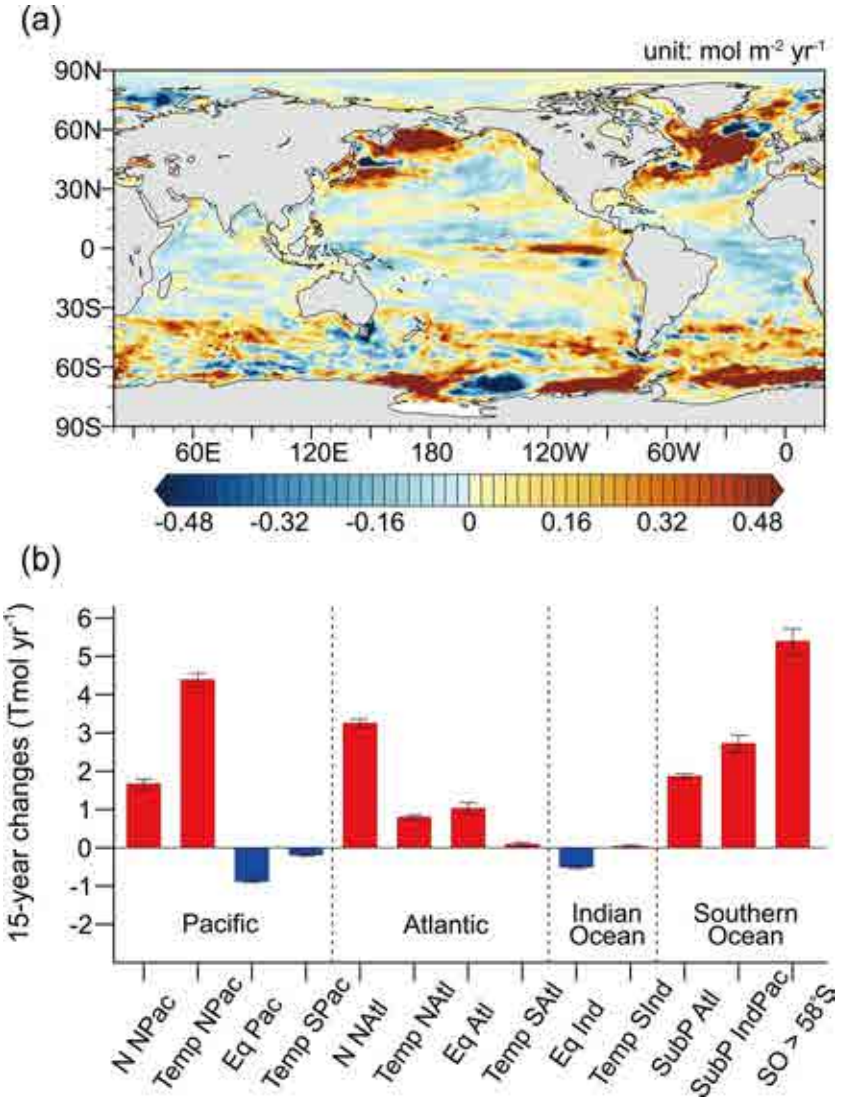

Fig. 4. 15-year changes in the long-term trend of air-sea O_2 flux since 1985. The error bars in panel (b) represent the uncertainty of flux change.

centrations are influenced by the related processes. The land and ocean carbon sinks can be separated from the total carbon uptake according to Eq. (6) and Eq. (7), as 33.5 GtC and 63.2 GtC, respectively, during this period.

It should be especially noted that the air-sea O_2 flux plays an important role in the carbon uptake estimations. The ocean emits ~1.54 Pmol O_2 (1 Pmol = 10^{15} mol) to the atmosphere (sum of the air-sea O_2 flux from 1990 to 2014 in Fig. 2a), making a positive contribution of about 36.7 per meg to the atmospheric O_2/N_2 concentration (red vector in Fig. 6). Despite this air-sea O_2 flux being relatively small, it plays an important role in the estimation of land and ocean carbon sinks. Figure 8 describes the situation assuming that the air-sea O_2 flux is negligible on a multiannual-to-decadal timescale, as proposed in the early studies (Bender and Battle, 1999; Battle et al., 2000). If the air-sea O_2 flux is not considered in the O_2 budget, the ocean carbon sink would be apparently underestimated by approximately 14.8 GtC during 1990–2014, while the land carbon uptake would be largely overestimated (bar charts in the top right of Fig. 8).

3.2.2. *Averaged terrestrial and oceanic carbon sinks in different periods*

We subsequently calculated the averaged terrestrial and oceanic carbon uptake over several different periods and compared them with previous O_2-based carbon uptake estimations (Table 3). Here, we use the linear trend of atmospheric O_2/N_2 and CO_2 concentrations in the period to represent the O_2/N_2 and CO_2 changes in Eqs. (6)–(7) ($\Delta\delta(O_2/N_2)$ and ΔCO_2). For observed atmospheric concentration changes and fossil fuel consumption (F_{fossil}), our results are relatively consistent with Keeling et al. (2014) (differences less than 0.06 ppm yr^{-1} in ΔCO_2 and 0.12 GtC yr^{-1} in F_{fossil}). The effect of air-sea flux in our study (which are derived from process-based CMIP6 model simulations, as described above) shows a relatively large discrepancy with that in Keeling et al. (2014) (which is calculated based on the linear regression between O_2 flux and net changes of ocean heat content). Our results

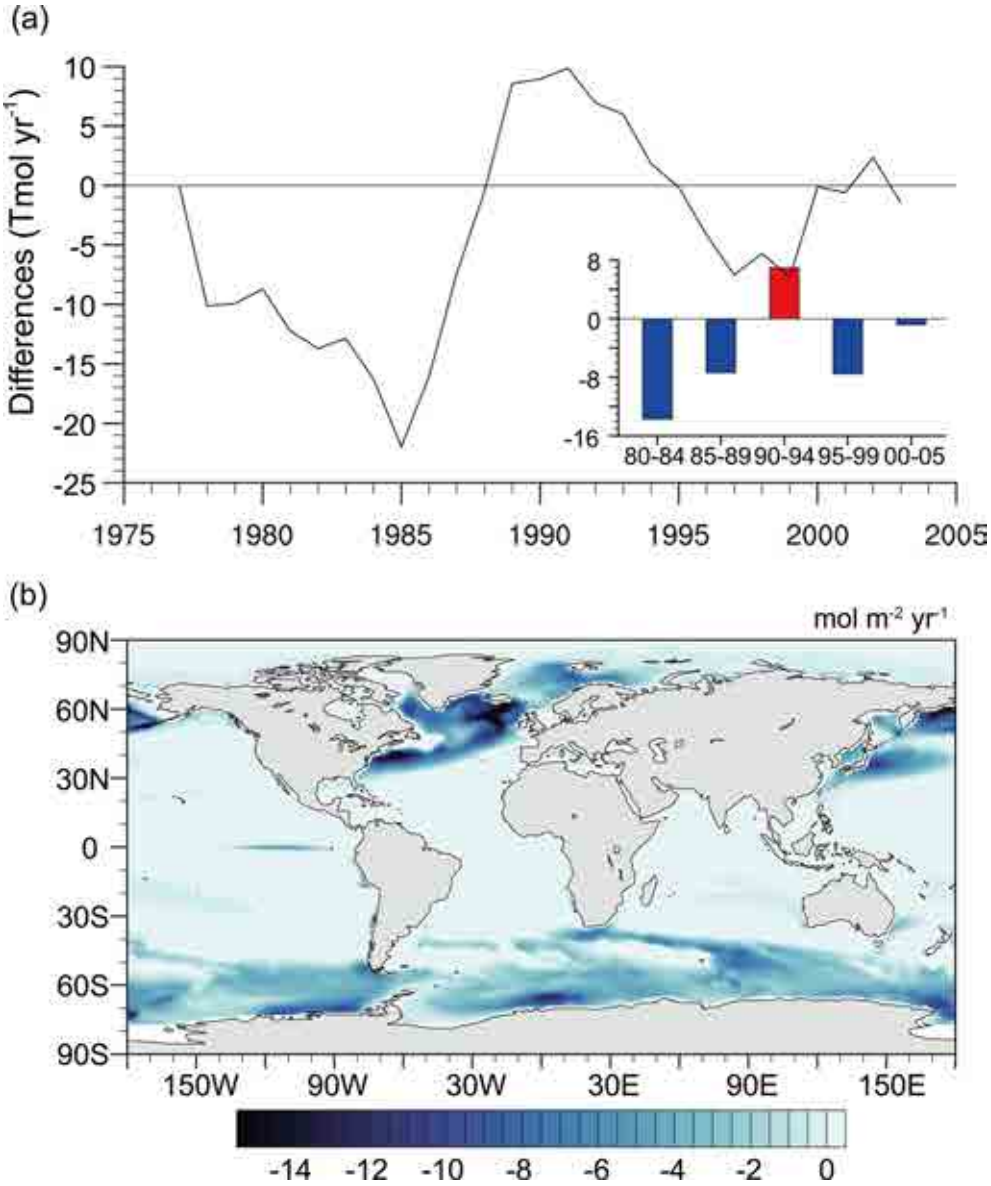

Fig. 5. Differences of air-sea O_2 flux between CMIP6 and CMIP5 during period 1975–2005 (i.e. $FLUX_{CMIP6}$ minus $FLUX_{CMIP5}$). The black line in (a) is the time series of the difference and (b) shows the spatial distribution of the difference averaged from 1975–2005.

show an averaged ocean and land carbon sink of 2.10±0.43 and 1.14±0.52 GtC yr^{-1}, respectively, during 1990–2000. An increase is found in both ocean and land carbon sinks during 2000–10, while results from Keeling et al. (2014) show an increase in ocean sink but a decline in land sink. Furthermore, the averaged carbon sinks from 2004 to 2008 in our study (2.64±0.66 GtC yr^{-1} for ocean and 1.84±0.79 GtC yr^{-1} for land) are generally larger than that in Tohjima et al. (2019) (1.97±0.62 GtC yr^{-1} for ocean and 2.17±0.82 GtC yr^{-1} for land), which could also be partly attributed to the discrepancy in the air-sea flux (Table 3).

To further explore the temporal changes of ocean and land carbon sinks over the past two decades, the averaged ocean and land carbon sinks were calculated for several representative periods: 1991–97, 1994–2000 and 2004–10 were selected for the estimates of averaged ocean sinks; meanwhile, 1994–2000, 2002–08 and 2008–14 were selected for the estimates of averaged land sinks. These results are shown as the asterisks in Fig. 9, accompanied by time-continuous estimations from the Global Carbon Project (GCP, Friedlingstein et al., 2019), Landschützer et al 2016 and Carbon Tracker (CT, Jacobson et al., 2020). The estimates by GCP clearly show a quasi-monotonous increase of the oceanic carbon sink over the past few decades (Fig. 9a, red line). However, the oceanic uptake in our results show a decline from 2.04±0.47 GtC yr^{-1} in 1991–97 to 1.85±0.45 GtC yr^{-1} in 1994–2000. A significant upward trend is subsequently found in the 21st century, with ocean uptake increasing to 2.87±0.47 GtC yr^{-1} in 2004–10. This temporal pattern is generally consistent with results derived from observed sur-

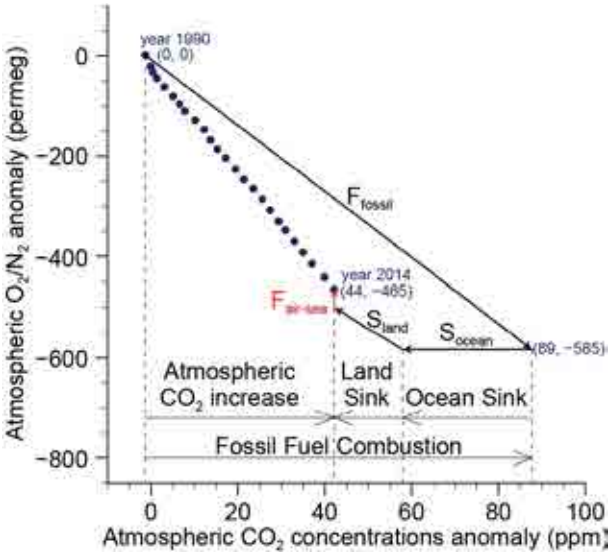

Fig. 6. Changes in observed atmospheric concentrations of O_2/N_2 and CO_2 from 1990 to 2014. The blue dots represent the annual averaged O_2 and CO_2 anomaly (here we choose the concentrations in 1990 as the reference value). The vectors in the diagram schematically illustrate the contribution of each process related to the changes in O_2 (vertical axis) and CO_2 (horizontal axis) during this period. The effect of air-sea O_2 flux is highlighted in red.

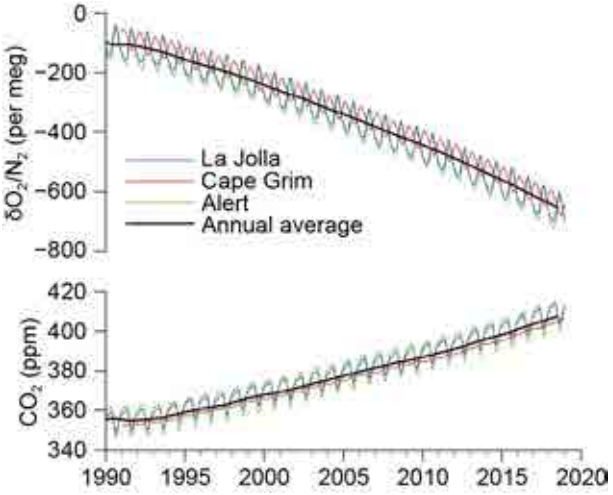

Fig. 7. The observed time series of atmospheric O_2/N_2 and CO_2 concentrations. The blue, green and red lines represents observations in La Jolla (32.9°N, 277.3°W), Alert (82.5°N, 62.3°W), and Cape Grim (40.7°S, 144.7°E), respectively. The black line is the annual mean concentrations averaged among the three stations with a weight of 0.25, 0.25 and 0.5.

face partial pressure of CO_2 in Landschützer et al. (2016) (Fig. 9a, green line), which may occur as consequences of the combined influence of anthropogenic forcing and oceanic internal modes. The net terrestrial carbon uptake estimated in this study corresponds well with the results derived from GCP. An increase of land carbon uptake (from 1.23±0.60 GtC yr^{-1} to 1.91±0.50 GtC yr^{-1} according to our estimations) could be found in the 2000s (Fig. 9b) which

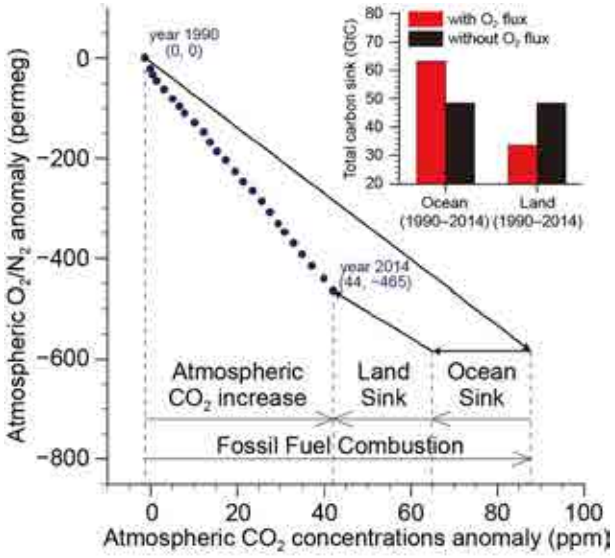

Fig. 8. Role of air-sea O_2 flux in O_2-based carbon sinks estimations. The diagram is same as Fig. 6, except for no air-sea O_2 flux considered in the calculation. The bar charts in the top right show the comparisons between estimated ocean/land carbon sink with and without O_2 flux correction.

has been reported by several atmospheric inversion and model-based studies (Keenan et al., 2016; Ballantyne et al., 2017; Piao et al., 2018). Despite the fact that the mechanisms behind this increase are still under discussion, it is generally believed that the changes in land use, modifications of terrestrial productivity and respiration, as well as climatic variations of temperature and moisture are responsible for changes in terrestrial carbon uptake (Chen et al., 2020; Piao et al., 2020a, b; Yue et al., 2020).

3.2.3. *Influence of oxygen datasets on estimated carbon uptake*

In this section, we specifically investigate the differences of the carbon sinks from that in Li et al. (2021). As mentioned in section 3.1.3, the air-sea O_2 flux used in Li et al. (2021) is derived from CMIP5, while CMIP6 simulation of the flux is used in this study. Meanwhile, the other O_2-related variables (such as atmospheric O_2 decline) in Li et al. (2021) are derived from the oxygen budget proposed by Huang et al. (2018), which is also different from this study. Terrestrial and oceanic carbon uptakes estimated by Li et al. (2021) are depicted by the triangles in Fig. 9. From the comparisons between this study and Li et al. (2021), we can discern the role of oxygen data in carbon sink estimations.

For the terrestrial carbon sink, both of the two studies corresponds well with GCP in the 21st century, which exhibit an enhanced uptake mentioned in section 3.2.2. However, the result from Li et al. (2021) seems to present an unrealistically high land carbon uptake (1.50 GtC yr^{-1}) in the 1990s, while the current study behaves in good agreement with GCP during this period (1.06 GtC yr^{-1}). The oceanic carbon uptake in both this study and Li et al. (2021) exhibits a similar variability with that in Landschützer et al. (2016) (that is, a

Table 3. Estimations of O_2-based carbon sinks in different periods.

	Period	$\Delta\delta\,(O_2/N_2)^{a,b}$ (per meg yr^{-1})	$\Delta CO_2^{a,b}$ (ppm yr^{-1})	$F_{eff}^{a,c}$ (Tmol yr^{-1})	F_{fossil}^{a} (GtC yr^{-1})	Ocean sink[a] (GtC yr^{-1})	Land sink[a] (GtC yr^{-1})
Our results	1990–00	−15.81 (0.52)	1.46 (0.08)	45.7 (30.6)	6.37 (0.24)	2.10 (0.43)	1.14 (0.52)
	2000–10	−20.14 (0.34)	1.94 (0.07)	58.7 (31.3)	7.93 (0.83)	2.66 (0.41)	1.15 (0.50)
	2004–08	−19.62 (1.33)	1.79 (0.27)	50.4 (30.1)	8.28 (0.40)	2.64 (0.66)	1.84 (0.79)
Keeling et al., 2014	1990–2000	−15.77	1.52 (0.02)	44 (45)	6.39 (0.38)	1.94 (0.62)	1.22 (0.80)
	2000–10	−20.39	1.90 (0.02)	44 (45)	7.81 (0.47)	2.72 (0.60)	1.05 (0.84)
Tohjima et al., 2019	2004–08	−19.29	1.92 (0.09)	27.5 (27.5)	8.21 (0.41)	1.97 (0.62)	2.17 (0.82)

[a] Estimated uncertainties are shown in parentheses. These uncertainties are propagated to the ocean and land sink uncertainties during calculation. [b] The linear trend of the observations during the selected period. Uncertainties shown in parentheses are the standard error of the regression coefficient. [c] Ensemble mean of the CMIP6 models. Uncertainties shown in parentheses are standard deviation among the models.

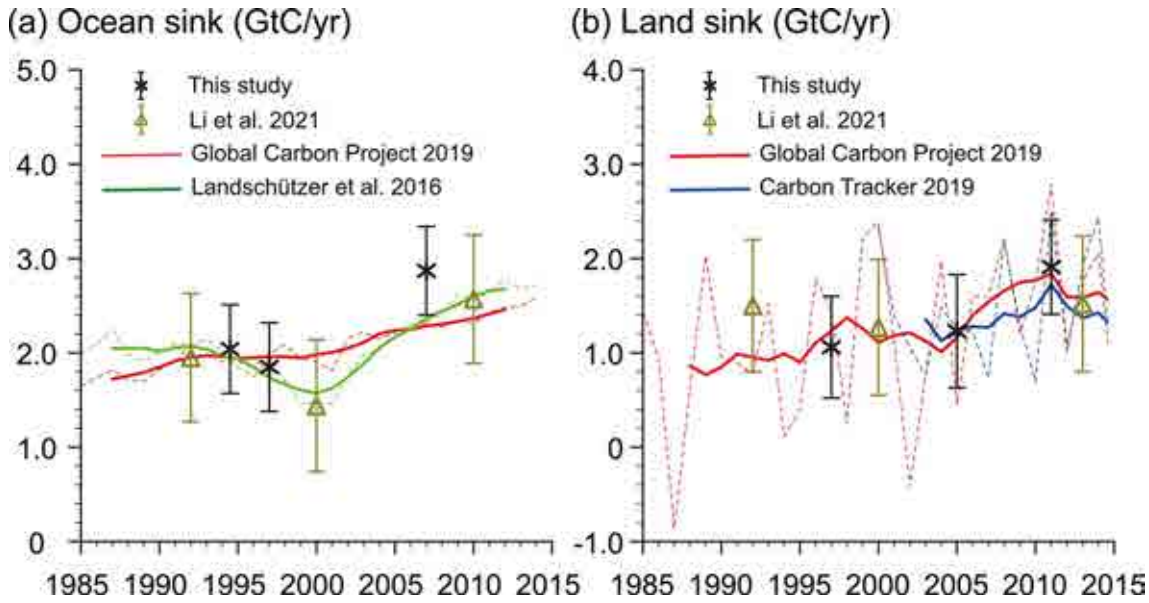

Fig. 9. Estimated ocean and land carbon sinks in different studies. The asterisks and triangles are seven-year averaged carbon sinks in this study and Li et al 2021, with error bars representing uncertainties of the estimations. The time series of carbon sinks derived from Global Carbon Project 2019, Landschützer et al 2016 and Carbon Tracker 2019 are colored in red, green and blue, respectively. The thin dashed lines and the thick solid lines are annual and seven-year running averaged carbon sinks, respectively.

downward trend in the 1990s subsequently followed by an upward trend in the 2000s). Despite this, discrepancy occurs around year 2010, as shown in Fig. 9a. The estimated oceanic carbon uptake in this study (2.87 GtC yr^{-1}) is relatively larger than it in Li et al. (2021) (2.45 GtC yr^{-1}) and GCP (2.36 GtC yr^{-1}).

Overall, both of the two studies reveal an enhanced carbon uptake in the 21st century. This study provides a more reliable estimate of the terrestrial carbon uptake in the 1990s, while the oceanic carbon sink in Li et al. (2021) is more consistent with the Global Carbon Project after year 2010. Our calculations show that the differences in air-sea O_2 flux ($F_{air-sea}$) and atmospheric O_2 change (ΔO_2) are the main contributors to the discrepancies. If the difference in O_2 flux is expressed as $\Delta F_{air-sea}$ (the other variables remain unchanged), its influence on the terrestrial and oceanic carbon uptake could then be respectively expressed as $\Delta B = -\beta/\alpha_B \Delta F_{air-sea}$ and $\Delta O = \beta/\alpha_B \Delta F_{air-sea,}$ according to Equations 6–8. This implies that a weakened oceanic O_2 outgassing, approximately −22 Tmol O_2 yr^{-1}, would lead to an increase of 0.21 GtC yr^{-1} land carbon sink and a simultaneous opposite effect on ocean carbon sink. For the period 1990–95, Li et al. (2021) shows a smaller declining trend of atmospheric O_2 and oceanic outgassing in 1990–95, which could eventually lead to a larger land uptake in Li et al. (2021) during this period. These results highlight the vital importance of oxygen datasets on carbon sink estimations.

4. Summary and discussion

We use the coupled ocean biogeochemistry models in CMIP6 to investigate the modifications of air-sea O_2 flux under climate change and its influences on the estimations of global terrestrial and ocean carbon uptake. Our results show an enhanced global oceanic O_2 outgassing to the atmosphere since the 1980s, accompanied by a strong decadal vari-

ability dominated by oceanic internal modes. Consistent with Li et al. (2020), this study shows maximum changes of flux mainly occurring in the high latitudes, with roughly one quarter of the outgassing directly associated with reduced solubility in the warming ocean, and the rest mainly linked with circulation changes and ocean stratification. This modification of air-sea O_2 flux plays an important role in estimating carbon uptake, as described in section 3.2.

The application of air-sea O_2 flux in CMIP6 provides a valuable complement for studies of O_2-based global carbon sinks estimations under climate change. Our results reveal the significant increases of terrestrial and oceanic carbon sinks in the 21st century, reflecting the human impacts on the carbon cycle and Earth's environments. The model biases of air-sea O_2 flux between CMIP5 and CMIP6 are also investigated in this study, which could lead to a total discrepancy up to 0.4 GtC yr^{-1} in the estimations, indicating the importance of improvement of air-sea O_2 flux parameterizations in the model.

Some limitations should also be acknowledged. Our estimation of carbon sinks still suffers from relatively large uncertainties (0.4–0.8 GtC yr^{-1}) due to the accumulations of uncertainty of each term in the calculations. Furthermore, the earliest observations of O_2/N_2 we could obtain are from the late 1980s, which greatly limits the lengths of estimated time series. The comparisons between this study and Li et al. (2021) also reveal the importance of the accuracy of oxygen datasets on the carbon uptake estimations. Presently, we are working on structuring the global oxygen budget (Huang et al., 2018) under the constrain of O_2/N_2 observations, from which we hope to extend the time series of atmospheric O_2 changes back to the 1900s as well as provide a more reliable oxygen dataset. Further explorations and investigations of the O_2-based carbon uptake estimations should be done in the future.

Acknowledgements. The authors acknowledge the Scripps O_2 Program for providing the observations of atmospheric O_2 and CO_2 data. The authors also acknowledge the World Climate Recruitment Programme's (WCRP) Working Group on Coupled Modelling (WGCM), and the Global Organization for Earth System Science Portals (GO-ESSP) for producing outputs of CMIP6 model simulations. This work was jointly supported by the National Science Foundation of China (Grant Nos. 41991231, 91937302) and the China 111 project (Grant No. B13045). The data processes and analysis are supported by Supercomputing Center of Lanzhou University.

Electronic supplementary material: Supplementary material is available in the online version of this article at https://doi.org/10.1007/s00376-021-1273-x.

REFERENCES

Andres, R. J., Boden, T. A. & Marland, G. (2016). Annual fossil-fuel CO2 emissions: Mass of emissions gridded by one degree latitude by one degree longitude. Carbon Dioxide Information Analysis Center, Oak Ridge National Laboratory, U. S. Department of Energy. https://doi.org/10.3334/CDIAC/ffe.ndp058.2016.

Ballantyne, A., and Coauthors, 2017: Accelerating net terrestrial carbon uptake during the warming hiatus due to reduced respiration. *Nature Climate Change*, **7**, 148–152, https://doi.org/10.1038/nclimate3204.

Battle, M., M. L. Bender, P. P. Tans, J. W. C. White, J. T. Ellis, T. Conway, and R. J. Francey, 2000: Global carbon sinks and their variability inferred from atmospheric O_2 and $\delta^{13}C$. *Science*, **287**, 2467–2470, https://doi.org/10.1126/SCIENCE.287.5462.2467.

Battle, M. O., and Coauthors, 2019: Atmospheric measurements of the terrestrial O_2: CO_2 exchange ratio of a midlatitude forest. *Atmospheric Chemistry and Physics*, **19**, 8687–8701, https://doi.org/10.5194/acp-19-8687-2019.

Bender, M. L., and M. O. Battle, 1999: Carbon cycle studies based on the distribution of O_2 in air. *Tellus*, **51**, 165–169, https://doi.org/10.3402/TELLUSB.V51I2.16268.

Bopp, L., C. Le Quéré, M. Heimann, A. C. Manning, and P. Monfray, 2002: Climate-induced oceanic oxygen fluxes: Implications for the contemporary carbon budget. *Global Biogeochemical Cycles*, **16**, 6-1–6-13, https://doi.org/10.1029/2001GB001445.

Bopp, L., and Coauthors, 2013: Multiple stressors of ocean ecosystems in the 21st century: Projections with CMIP5 models. *Biogeosciences*, **10**, 6225–6245, https://doi.org/10.5194/bg-10-6225-2013.

Bushinsky, S. M., A. R. Gray, K. S. Johnson, and J. L. Sarmiento, 2017: Oxygen in the southern ocean from argo floats: Determination of processes driving air-sea fluxes. *J. Geophys. Res.: Oceans*, **122**, 8661–8682, https://doi.org/10.1002/2017JC012923.

Chen, G., and Coauthors, 2020: Global projections of future urban land expansion under shared socioeconomic pathways. *Nature Communications*, **11**, 537, https://doi.org/10.1038/s41467-020-14386-x.

Cheng, L. J., and J. Zhu, 2018: 2017 was the warmest year on record for the global ocean. *Adv. Atmos. Sci.*, **35**, 261–263, https://doi.org/10.1007/s00376-018-8011-z.

Cheng, L. J., G. J. Wang, J. P. Abraham, and G. Huang, 2018: Decadal ocean heat redistribution since the late 1990s and its association with key climate modes. *Climate*, **6**, 91, https://doi.org/10.3390/cli6040091.

Cheng, L. J., K. E. Trenberth, J. Fasullo, T. Boyer, J. Abraham, and J. Zhu, 2017: Improved estimates of ocean heat content from 1960 to 2015. *Science Advances*, **3**, e1601545, https://doi.org/10.1126/SCIADV.1601545.

Dai, M., and Coauthors, 2013: Why are some marginal seas sources of atmospheric CO_2? *Geophys. Res. Lett.*, **40**, 2154–2158, https://doi.org/10.1002/grl.50390.

DeVries, T., and Coauthors, 2019: Decadal trends in the ocean carbon sink. *Proceedings of the National Academy of Sciences of the United States of America*, **116**, 11 646–11 651, https://doi.org/10.1073/PNAS.1900371116.

Dhanda, K. K., and L. P. Hartman, 2011: The ethics of carbon neutrality: A critical examination of voluntary carbon offset providers. *Journal of Business Ethics*, **100**, 119–149, https://doi.org/10.1007/s10551-011-0766-4.

Friedlingstein, P., and Coauthors, 2019: Global carbon budget 2019. *Earth System Science Data*, **11**, 1783–1838, https://doi.org/10.5194/essd-11-1783-2019.

Frölicher, T. L., E. M. Fischer, and N. Gruber, 2018: Marine heatwaves under global warming. *Nature*, **560**, 360–364, https://doi.org/10.1038/s41586-018-0383-9.

Gao, Z. M., H. P. Liu, E. Arntzen, D. P. Mcfarland, X. Y. Chen, and M. Y. Huang, 2020: Uncertainties in turbulent statistics and fluxes of CO_2 associated with density effect corrections. *Geophys. Res. Lett.*, **47**, e2020GL088859, https://doi.org/10.1029/2020GL088859.

Gao, Z. M., H. P. Liu, J. E. C. Missik, J. Y. Yao, M. Y. Huang, X. Y. Chen, E. Arntzen, and D. P. McFarland, 2019: Mechanistic links between underestimated CO_2 fluxes and non-closure of the surface energy balance in a semi-arid sagebrush ecosystem. *Environmental Research Letters*, **14**, 044016, https://doi.org/10.1088/1748-9326/ab082d.

Garcia, H. E., and L. I. Gordon, 1992: Oxygen solubility in seawater: Better fitting equations. *Limnology and Oceanography*, **37**, 1307–1312, https://doi.org/10.4319/lo.1992.37.6.1307.

Gruber, N., M. Gloor, S. M. Fan, and J. L. Sarmiento, 2001: Air-sea flux of oxygen estimated from bulk data: Implications for the marine and atmospheric oxygen cycles. *Global Biogeochemical Cycles*, **15**, 783–803, https://doi.org/10.1029/2000GB001302.

Han, D. L., J. P. Huang, L. Ding, X. Y. Liu, C. Y. Li, and F. Yang, 2021: Oxygen footprint: An indicator of the anthropogenic ecosystem changes. *Catena*, **206**, 105501, https://doi.org/10.1016/j.catena.2021.105501.

Huang, J. P., H. P. Yu, X. D. Guan, G. Y. Wang, and R. X. Guo, 2016: Accelerated dryland expansion under climate change. *Nature Climate Change*, **6**, 166–171, https://doi.org/10.1038/NCLIMATE2837.

Huang, J. P., Y. K. Xie, X. D. Guan, D. D. Li, and F. Ji, 2017a: The dynamics of the warming hiatus over the Northern Hemisphere. *Climate Dyn.*, **48**, 429–446, https://doi.org/10.1007/s00382-016-3085-8.

Huang, J. P., H. P. Yu, A. G. Dai, Y. Wei, and L. T. Kang, 2017b: Drylands face potential threat under 2°C global warming target. *Nature Climate Change*, **7**, 417–422, https://doi.org/10.1038/NCLIMATE3275.

Huang, J. P., J. P. Huang, X. Y. Liu, C. Y. Li, L. Ding, and H. P. Yu, 2018: The global oxygen budget and its future projection. *Science Bulletin*, **63**, 1180–1186, https://doi.org/10.1016/j.scib.2018.07.023.

Huang, J. P., and Coauthors, 2021: The oxygen cycle and a habitable Earth. *Science China Earth Sciences*, **64**, 511–528, https://doi.org/10.1007/s11430-020-9747-1.

Jacobson, A. R., and Coauthors, 2020: CarbonTracker CT2019. Available from https://doi.org/10.25925/39m3-6069.

Ji, F., Z. H. Wu, J. P. Huang, and E. P. Chassignet, 2014: Evolution of land surface air temperature trend. *Nature Climate Change*, **4**, 462–466, https://doi.org/10.1038/nclimate2223.

Keeling, R. F., and S. R. Shertz, 1992: Seasonal and interannual variations in atmospheric oxygen and implications for the global carbon cycle. *Nature*, **358**, 723–727, https://doi.org/10.1038/358723a0.

Keeling, R. F., and A. C. Manning, 2014: Studies of recent changes in atmospheric O_2 content. *Treatise on Geochemistry*. vol 5. 2nd ed., H. D. Holland and K. K. Turekian, Eds., Elsevier, 385–404, https://doi.org/10.1016/B978-0-08-095975-7.00420-4.

Keenan, T. F., I. C. Prentice, J. G. Canadell, C. A. Williams, H. Wang, M. Raupach, and G. J. Collatz, 2016: Recent pause in the growth rate of atmospheric CO_2 due to enhanced terrestrial carbon uptake. *Nature Communications*, **7**, 13428, https://doi.org/10.1038/ncomms13428.

Landschützer, P., N. Gruber, and D. C. E. Bakker, 2016: Decadal variations and trends of the global ocean carbon sink. *Global Biogeochemical Cycles*, **30**, 1396–1417, https://doi.org/10.1002/2015GB005359.

Laszuk, D., 2017. Python implementation of Empirical Mode Decomposition algorithm.GitHub. https://github.com/laszukdawid/PyEMD. GitHub Repository

Li, C. Y., J. P. Huang, Y. L. He, D. D. Li, and L. Ding, 2019: Atmospheric warming slowdown during 1998–2013 associated with increasing ocean heat content. *Adv. Atmos. Sci.*, **36**, 1188–1202, https://doi.org/10.1007/s00376-019-8281-0.

Li, C. Y., J. P. Huang, L. Ding, X. Y. Liu, H. P. Yu, and J. P. Huang, 2020: Increasing escape of oxygen from oceans under climate change. *Geophys. Res. Lett.*, **47**, e2019GL086345, https://doi.org/10.1029/2019GL086345.

Li, C. Y., J. P. Huang, L. Ding, X. Y. Liu, D. L. Han, and J. P. Huang, 2021: Estimation of oceanic and land carbon sinks based on the most recent oxygen budget. *Earth's Future*, **9**, e2021EF002124, https://doi.org/10.1029/2021ef002124.

Liang, J. H., C. Deutsch, J. C. McWilliams, B. Baschek, P. P. Sullivan, and D. Chiba, 2013: Parameterizing bubble-mediated air-sea gas exchange and its effect on ocean ventilation. *Global Biogeochemical Cycles*, **27**, 894–905, https://doi.org/10.1002/gbc.20080.

Liu, X. Y., J. P. Huang, J. P. Huang, C. Y. Li, L. Ding, and W. J. Meng, 2020: Estimation of gridded atmospheric oxygen consumption from 1975 to 2018. *Journal of Meteorological Research*, **34**, 646–658, https://doi.org/10.1007/S13351-020-9133-7.

Manning, A., and R. F. Keeling, 2006: Global oceanic and land biotic carbon sinks from the scripps atmospheric oxygen flask sampling network. *Tellus*, **58**, 95–116, https://doi.org/10.1111/J.1600-0889.2006.00175.X.

Niu, D. X., G. Q. Wu, Z. S. Ji, D. Y. Wang, Y. Y. Li, and T. Gao, 2021: Evaluation of provincial carbon neutrality capacity of china based on combined weight and improved topsis model. *Sustainability*, **13**, 2777, https://doi.org/10.3390/su13052777.

Palter, J. B., and D. S. Trossman, 2018: The sensitivity of future ocean oxygen to changes in ocean circulation. *Global Biogeochemical Cycles*, **32**, 738–751, https://doi.org/10.1002/2017GB005777.

Piao, S., and Coauthors, 2018: Lower land-use emissions responsible for increased net land carbon sink during the slow warming period. *Nature Geoscience*, **11**, 739–743, https://doi.org/10.1038/s41561-018-0204-7.

Piao, S. L., and Coauthors, 2020a: Characteristics, drivers and feedbacks of global greening. *Nature Reviews Earth & Environment*, **1**, 14–27, https://doi.org/10.1038/s43017-019-0001-x.

Piao, S. L., and Coauthors, 2020b: Interannual variation of terrestrial carbon cycle: Issues and perspectives. *Global Change Biology*, **26**, 300–318, https://doi.org/10.1111/gcb.14884.

Plattner, G. K., F. Joos, and T. F. Stocker, 2002: Revision of the global carbon budget due to changing air-sea oxygen fluxes. *Global Biogeochemical Cycles*, **16**, 1096, https://doi.org/10.1029/2001GB001746.

Randerson, J. T., C. A. Masiello, C. J. Still, T. Rahn, H. Poorter, and C. B. Field, 2006: Is carbon within the global terrestrial biosphere becoming more oxidized. *Implications for trends in atmospheric O_2. Global Change Biology*, **12**, 260–271, https://doi.org/10.1111/j.1365-2486.2006.01099.x.

Resplandy, L., R. Séférian, and L. Bopp, 2015: Natural variability of CO_2 and O_2 fluxes: What can we learn from centuries-long climate models simulations? *J. Geophys. Res.: Oceans*, **120**, 384–404, https://doi.org/10.1002/2014jc010463.

Seneviratne, S. I., M. G. Donat, A. J. Pitman, R. Knutti, and R. L. Wilby, 2016: Allowable CO_2 emissions based on regional and impact-related climate targets. *Nature*, **529**, 477–483, https://doi.org/10.1038/nature16542.

Tohjima, Y., H. Mukai, T. MacHida, Y. Hoshina, and S. I. Nakaoka, 2019: Global carbon budgets estimated from atmospheric O_2N_2 and CO_2 observations in the western Pacific region over a 15-year period. *Atmospheric Chemistry and Physics*, **19**, 9269–9285, https://doi.org/10.5194/acp-19-9269-2019.

Trenberth, K. E., J. T. Fasullo, and M. A. Balmaseda, 2014: Earth' s energy imbalance. *J. Climate*, **27**, 3129–3144, https://doi.org/10.1175/JCLI-D-13-00294.1.

Wanninkhof, R., 1992: Relationship between wind speed and gas exchange over the ocean. *J. Geophys. Res.: Oceans*, **97**, 7373–7382, https://doi.org/10.1029/92JC00188.

Wei, Y., J. G. Wu, J. P. Huang, X. Y. Liu, D. L. Han, L. L. An, H. P. Yu, and J. P. Huang, 2021: Declining oxygen level as an emerging concern to global cities. *Environ. Sci. Technol.*, **55**, 7808–7817, https://doi.org/10.1021/acs.est.1c00553.

Wen, Q., J. Yao, K. Döös, and H. J. Yang, 2018: Decoding hosing and heating effects on global temperature and meridional circulations in a warming climate. *J. Climate*, **31**, 9605–9623, https://doi.org/10.1175/JCLI-D-18-0297.1.

Willis, J. K., D. Roemmich, and B. Cornuelle, 2004: Interannual variability in upper ocean heat content, temperature, and thermosteric expansion on global scales. *J. Geophys. Res.: Oceans*, **109**, C12036, https://doi.org/10.1029/2003JC002260.

Yang, B., S. R. Emerson, and S. M. Bushinsky, 2017: Annual net community production in the subtropical Pacific Ocean from in situ oxygen measurements on profiling floats. *Global Biogeochemical Cycles*, **31**, 728–744, https://doi.org/10.1002/2016GB005545.

Yang, H. J., and Q. Wen, 2020: Investigating the role of the Tibetan Plateau in the formation of atlantic meridional overturning circulation. *J. Climate*, **33**, 3585–3601, https://doi.org/10.1175/JCLI-D-19-0205.1.

Yang, H. J., K. Wang, H. J. Dai, Y. X. Wang, and Q. Li, 2016: Wind effect on the Atlantic meridional overturning circulation via sea ice and vertical diffusion. *Climate Dyn.*, **46**, 3387–3403, https://doi.org/10.1007/s00382-015-2774-z.

Yue, C., P. Ciais, R. A. Houghton, and A. A. Nassikas, 2020: Contribution of land use to the interannual variability of the land carbon cycle. *Nature Communications*, **11**, 3170, https://doi.org/10.1038/s41467-020-16953-8.

ADVANCES IN ATMOSPHERIC SCIENCES, VOL. 39, AUGUST 2022, 1285–1298

• **Original Paper** •

Changes in Global Vegetation Distribution and Carbon Fluxes in Response to Global Warming: Simulated Results from IAP-DGVM in CAS-ESM2※

Xiaofei GAO[1,2], Jiawen ZHU[*1], Xiaodong ZENG[1,2,3], Minghua ZHANG[4], Yongjiu DAI[5], Duoying JI[6], and He ZHANG[1]

[1]*International Center for Climate and Environment Sciences*, *Institute of Atmospheric Physics*, *Chinese Academy of Sciences*, *Beijing* 100029, *China*

[2]*University of Chinese Academy of Sciences*, *Beijing* 100049, *China*

[3]*Collaborative Innovation Center on Forecast and Evaluation of Meteorological Disasters*, *Nanjing University of Information Science and Technology*, *Nanjing* 210044, *China*

[4]*School of Marine and Atmospheric Sciences*, *Stony Brook University*, *NY* 11790, *USA*

[5]*School of Atmospheric Sciences*, *Sun Yat-Sen University*, *Guangzhou* 510275, *China*

[6]*College of Global Change and Earth System Science*, *Beijing Normal University*, *Beijing* 100875, *China*

(Received 12 April 2021; revised 5 August 2021; accepted 14 September 2021)

ABSTRACT

Terrestrial ecosystems are an important part of Earth systems, and they are undergoing remarkable changes in response to global warming. This study investigates the response of the terrestrial vegetation distribution and carbon fluxes to global warming by using the new dynamic global vegetation model in the second version of the Chinese Academy of Sciences (CAS) Earth System Model (CAS-ESM2). We conducted two sets of simulations, a present-day simulation and a future simulation, which were forced by the present-day climate during 1981–2000 and the future climate during 2081–2100, respectively, as derived from RCP8.5 outputs in CMIP5. CO_2 concentration is kept constant in all simulations to isolate CO_2-fertilization effects. The results show an overall increase in vegetation coverage in response to global warming, which is the net result of the greening in the mid-high latitudes and the browning in the tropics. The results also show an enhancement in carbon fluxes in response to global warming, including gross primary productivity, net primary productivity, and autotrophic respiration. We found that the changes in vegetation coverage were significantly correlated with changes in surface air temperature, reflecting the dominant role of temperature, while the changes in carbon fluxes were caused by the combined effects of leaf area index, temperature, and precipitation. This study applies the CAS-ESM2 to investigate the response of terrestrial ecosystems to climate warming. Even though the interpretation of the results is limited by isolating CO_2-fertilization effects, this application is still beneficial for adding to our understanding of vegetation processes and to further improve upon model parameterizations.

Key words: global warming, vegetation distribution, carbon flux, leaf area index, surface air temperature

Citation: Gao, X. F., J. W. Zhu, X. D. Zeng, M. H. Zhang, Y. J. Dai, D. Y. Ji, and H. Zhang, 2022: Changes in global vegetation distribution and carbon fluxes in response to global warming: Simulated results from IAP-DGVM in CAS-ESM2. *Adv. Atmos. Sci.*, **39**(8), 1285−1298, https://doi.org/10.1007/s00376-021-1138-3.

Article Highlights:

- The projected vegetation coverage and carbon fluxes show an overall increase under global warming.
- Surface air temperature is the dominant driver of changes in vegetation distribution.
- Changes in carbon fluxes are caused by the combined effects of leaf area index, temperature, and precipitation.

1. Introduction

Terrestrial ecosystems are an important part of Earth systems. They regulate the exchanges of energy and water mass between the land surface and atmosphere via evapotran-

※ This paper is a contribution to the special issue on Carbon Neutrality: Important Roles of Renewable Energies, Carbon Sinks, NETs, and non-CO_2 GHGs.

* Corresponding author: Jiawen ZHU
Email: zhujw@mail.iap.ac.cn

spiration and provide organic carbon via photosynthesis. The change in terrestrial ecosystems is tightly coupled with climate, which is undergoing significant warming (Diffenbaugh and Field, 2013; Zhu et al., 2016; Yin et al., 2018; Liu et al., 2019). How terrestrial ecosystems respond to global warming has been a hot research topic as the responses are of great significance for accurately projecting future vegetation dynamics and climate change (Woodward and Williams, 1987; Nemani et al., 2003; Schaphoff et al., 2016; Eric Dusenge et al., 2019; Fan and Fan, 2019).

In response to global warming, land vegetation distribution and productivity have shown considerable changes over the past few decades (Cramer et al., 2001; Fraser et al., 2011; Cao et al., 2019). One of the significant changes is a poleward "greening" expansion in the middle and high latitudes (Sturm et al., 2001; Walker et al., 2006; Bi et al., 2013; Mao et al., 2016; Zhu et al., 2016; Piao et al., 2020; Tømmervik and Forbes, 2020). For example, forests in Europe were projected to expand northward and contribute to a shrinkage of the tundra area (Shiyatov et al., 2005; Frost and Epstein, 2014; Kreplin et al., 2021), with a similar expansion found in North America (Field et al., 2007, Yu et al., 2014). In Northeast China, Hu et al. (2021) found obvious vegetation greening. The results shown by Madani et al. (2020) indicated an increasing trend in annual gross primary productivity (GPP) in the northern tundra and boreal ecosystems. The greening of Arctic ecosystems has shown increased biomass and abundance in boreal shrubs (Myers-Smith et al., 2011, 2020; Mekonnen et al., 2021). Several studies have reported that warming is a key factor that accelerates the "greening" by enhancing vegetation photosynthesis and extending the length of the growing season (Piao et al., 2007; Andreu-Hayles et al., 2011; Keenan and Riley, 2018). In the tropics, the response of vegetation to warming is different from that found in mid-high latitudes (Corlett, 2011). Several studies have shown a decrease in the tropical forest growth rate and productivity in response to warming, which could be the consequence of a reduction in leaf photosynthesis under higher temperatures (Clark et al., 2003; Doughty and Goulden, 2008; Gao et al., 2019; Huang et al., 2019). The decrease in the availability of water associated with higher temperatures is reported to result in a decrease in leaf area index (LAI) and net primary productivity (NPP) in the Amazon and South Africa and a decrease in forest coverage in central and southern Mexico (Mackay, 2008; Yu et al., 2014; Gang et al., 2017). These studies all indicate that terrestrial ecosystems have undergone remarkable changes in vegetation distribution and productivity due to global warming, and these changes will continue should global warming continue in the future.

Dynamic Global Vegetation Models (DGVMs) have recently become widely used tools to investigate and predict the responses of terrestrial ecosystems to future climate change. They can simulate and project the patterns, dynamics and structure, and biogeochemical cycles of vegetation under past, present, and future climatic conditions (Scheiter et al., 2013; Smith et al., 2014). Many DGVMs have been used to run offline simulations with different climatic scenarios to predict the responses of vegetation to changes in climate or atmospheric CO_2 (Woodward and Lomas, 2004; Shafer et al., 2015; Zhang et al., 2015). In addition, some DGVMs are coupled with general circulation models (GCMs) to investigate interactions between vegetation dynamics and climate change (Raddatz et al., 2007; Brovkin et al., 2009; Quillet et al., 2010; Hawkins et al., 2019; Wu et al., 2019; Arora et al., 2020; Yu et al., 2021).

However, the simulated vegetation responses to climate change by DGVMs remain uncertain (Prentice et al., 2007; Sitch et al., 2008; Liu et al., 2018; Sulman et al., 2019; Scheiter et al., 2020; Horvath et al., 2021). Falloon et al. (2012) reported that DGVMs simulated different, and even opposite, vegetation changes in the northern high latitudes in response to climate change. In the North China Plain, the predicted potential vegetation is bare ground, whereas, in fact, it is dominated by irrigated cropland (Kang and Eltahir, 2018). South Asian savanna ecosystems are often misinterpreted by DGVMs as degraded forests (Kumar and Scheiter, 2019). In addition, the estimation of GPP often differed among DGVMs (McGuire et al., 2001; Jung et al., 2007; Piao et al., 2013; Anav et al., 2015) due to different representations of ecological processes and parameter uncertainties (Knorr and Heimann, 2001; Gurney et al., 2004; De Kauwe et al., 2014). Gang et al. (2017) argued that large uncertainties among DGVMs may relate to the differences in recognition of the vegetation types and the land surface processes that evolved. These reported uncertainties reflect the complexity of the vegetation response to climate change, and thus more investigation is needed to better understand vegetation processes and parameterizations in DGVMs.

A new DGVM developed at the Institute of Atmospheric Physics (IAP-DGVM; Zeng et al., 2014) was coupled with the second version of the Chinese Academy of Sciences Earth System Model (CAS-ESM2). The coupled results showed a good performance in reproducing the present-day vegetation distribution and carbon fluxes (Zhu et al., 2018b). In addition, the IAP-DGVM simulated a positive trend in LAI over northern mid-high latitudes during the period 1972–2004, which was consistent with that of LAI3g, with a significant correlation coefficient of 0.48 ($Prob<0.05$, where Prob is the probability of statistical significance of the linear correlation coefficient) (Fig. S1 in the Electronic Supplementary Materials). This consistency illustrates that the IAP-DGVM has a good ability to reproduce the greening trend of vegetation over northern mid-high latitudes in response to climate change during the historical period. Thus, this study focuses on the IAP-DGVM projections of vegetation distribution and carbon fluxes in response to global warming in the future. To narrow down the uncertainties in the forcing datasets, we present a method (see section 2) that is used to produce the forcing datasets based on multi-model outputs from the Coupled Model Intercomparison Project Phase 5 (CMIP5) instead of using them directly. Here, we report the simulated changes in vegetation distribution and carbon fluxes in response to global warming, and

more importantly, we further investigate the dominant driver of the changes and discuss the underlying causes. The investigation will support a better understanding of vegetation processes, and in doing so, contribute to future improvements of the model parameterizations. Moreover, the results provide a valuable sample for comparison not only for the CAS-ESM2 community but also for other model communities.

The remainder of this paper is organized as follows. Section 2 describes the model physics and experimental design, section 3 presents the results of the experiment, section 4 provides a discussion and interpretation of results, and section 5 provides a brief summary.

2. Model description and experimental design

2.1. *Model description*

The IAP-DGVM, which was first released in 2014 (Zeng et al., 2014), was used in this study. The IAP-DGVM classifies natural plants into 14 plant functional types (PFTs) and does not currently simulate crops (Table S1 in the ESM). The vegetation model has made significant developments that mainly include the shrub sub-model (Zeng et al., 2008; Zeng, 2010), the process-based fire parameterization of intermediate complexity (Li et al., 2012), and the new establishment and competition parameterization schemes (Song et al., 2016). These characteristics improve the performance of the IAP-DGVM in simulating the fractional coverage of present-day vegetation and land carbon fluxes (Zeng, 2010; Zeng et al., 2014; Zhu et al., 2018b). Thus, the IAP-DGVM has been coupled with the CAS-ESM2 to investigate vegetation-climate interactions (Zhu et al., 2018a; Zhang et al., 2020).

2.2. *Experimental design*

This study aims to investigate the possible changes in vegetation distribution and carbon fluxes under global warming. The scenario corresponding to the Representative Concentration Pathway 8.5 (RCP8.5) was selected to represent a possible scenario of future global warming and the climate for the period 2081–2100 to represent the future climate. We downloaded atmospheric forcing variables, six-hourly precipitation and solar radiation, three-hourly surface air temperature, surface pressure, specific humidity, and wind, from outputs of historical and RCP8.5 simulations of the 16 models that are participating in the Coupled Model Intercomparison Project Phase 5 (CMIP5) (Table S2 in the ESM). We recalculated the RCP8.5 outputs as the following.

$$V_1(i) = \overline{\mathrm{RCP8.5}}_{2081-2100} - \overline{\mathrm{Hist}}_{1981-2000} + V_0(i),$$
$$i = 1981, 1982, \cdots, 2000$$

where $\overline{\mathrm{RCP8.5}}_{2081-2100}$ and $\overline{\mathrm{Hist}}_{1981-2000}$ are the 20-year averages for the period 2081-–2100 in CMIP5 RCP8.5 simulations and the period 1981–2000 in CMIP5 historical simulations, respectively. Their differences indicate the future climate changes predicted by each CMIP5 model. By adding these differences to the present-day forcing data ($V_0(i)$), we finally derived the new future forcing datasets ($V_1(i)$). This method can reduce the dependence on CMIP5 models and the uncertainties in future forcing datasets and is comparable to the present-day forcing data from Qian et al. (2006).

This study conducted a few simulations, including the spin-up simulation (Fig. S2). We first ran a global spin-up simulation by driving the IAP-DGVM from a bare ground condition for 660 model years to approach an equilibrium state by cycling the atmospheric forcing data during the period 1972–2004 from Qian et al. (2006). Then, we further conducted two sets of simulations, the present-day simulation (hereafter Pre) and the future simulation (hereafter RCP8.5). The Pre simulation was forced by the atmospheric data during 1972–2004 from Qian et al. (2006) and ran for 33 model years, while the RCP8.5 simulations were forced by the recalculated datasets described above and ran for 600 model years to approach another equilibrium state. We compared the results between the Pre simulation for the period 1981–2000 and the RCP8.5 simulations for the period 2081–2100. To investigate the effects of climate factors on vegetation dynamics, we fixed atmospheric CO_2 concentration at a constant value of 367.00 ppm in all simulations to isolate the effects of CO_2 fertilization. All the simulations were run with a T85 resolution (128 × 256 grid cells). Finally, we obtained future changes in vegetation distribution and carbon fluxes from the differences between the results of one present-day simulation and 16 RCP8.5 simulations. To reduce the effects of cropland, we weighted the vegetation coverage by a factor of (100% – FC_{crop}) in each grid cell, where FC_{crop} represents the fractional coverage of crops in CLM surface dataset (Zeng et al., 2014).

3. Results

3.1. *Surface climate change*

The projected future land surface shows an overall warm and wet change relative to the present day (Fig. 1). Globally, the annual mean surface air temperature in the future is 4.87±1.14 K higher than that in the present day. The positive temperature anomalies are stronger over northern high latitudes than in other regions and are projected by all 16 selected models (Fig. 1a). Meanwhile, the projected global mean precipitation is 0.45±0.07 mm d^{-1} higher than that in the present day. The positive precipitation anomalies are more pronounced in several regions, such as western and eastern North America, Europe, northeast and southeast Asia, equatorial Africa, and southern South America. In contrast, negative precipitation anomalies are seen over the Amazon, however, it is worth noting that the Amazon region shows larger uncertainties for projected precipitation among the models than do other regions (Fig. 1b). These climate anomalies are qualitatively consistent with a large body of published studies that reported future predictions of global

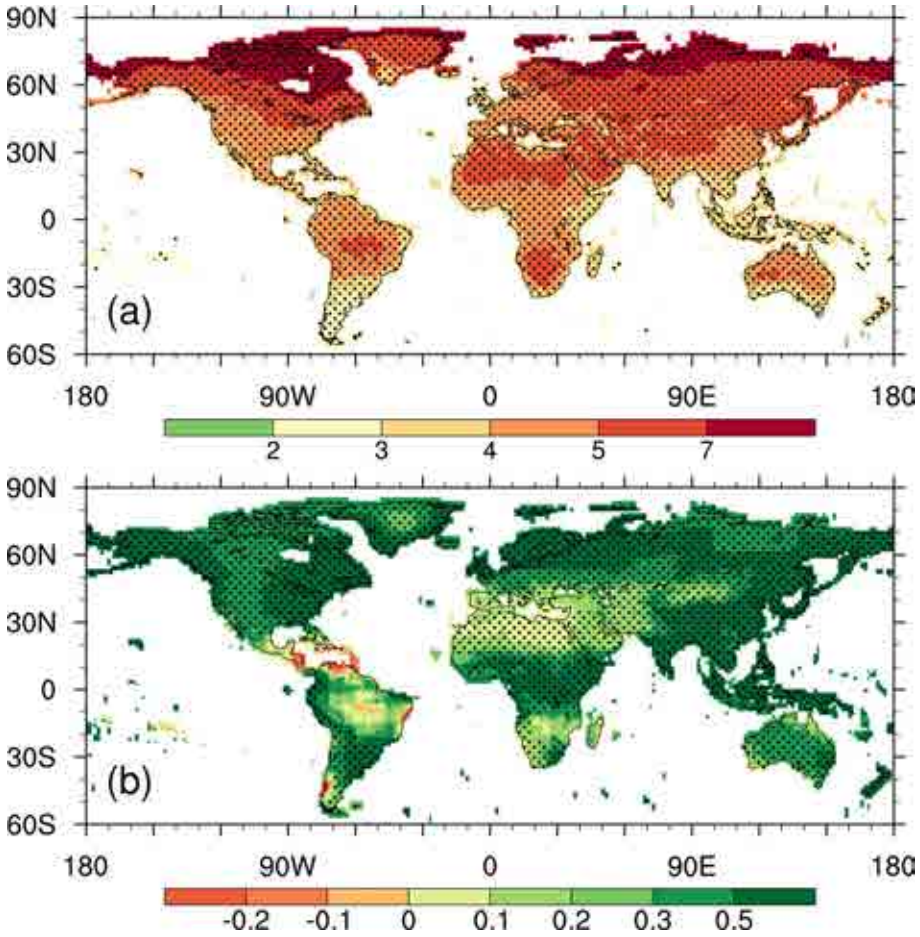

Fig. 1. Projected future changes of (a) annual surface air temperature (K) and (b) precipitation (mm d^{-1}) based on the 16 CMIP5 models. The stippled regions represent grids where at least 14 of 16 models agree with the multi-model ensemble mean.

warming and the possible drying of tropical regions in the future (Yu et al., 2014; Yin et al., 2018; Tømmervik and Forbes, 2020; Wibowo et al., 2020).

3.2. *Vegetation distribution*

We first analyzed the changes in vegetation distributions for the four aggregated vegetation types (trees, shrubs, grasses, and bare ground) between the RCP8.5 experiments and the present-day experiment. In general, there is a greening anomaly in the middle and high latitudes of the northern hemisphere (30°N–90°N) with 10.10% more projected vegetation. Trees and grasses contribute the most to the positive anomaly, while shrubs show a negative anomaly (Table 1). In contrast, there is a slight negative anomaly in the tropics (30°S–30°N) with 3.72% less projected vegetation. Grasses and shrubs contribute the most to the negative anomaly, while trees show almost no changes (Table 1).

Figure 2 shows a poleward expansion of the projected vegetation. The vegetation-growing regions in the RCP8.5 experiments are farther north than those in the present-day experiment, with 10°, 5°, and 7° for trees, shrubs, and grasses, respectively. The spatial distribution shows that the poleward expansion mainly occurred in northern Canada and Siberia for trees and grasses, and in northeastern Canada for shrubs (Fig. S3 in the ESM). These results are qualitatively consistent with previous studies based on other multiple GCMs (Alo and Wang, 2008; Yu et al., 2014; Gang et al., 2017) and with some observational-based studies (Speed et al., 2010; Vickers et al., 2016), indicating a poleward expansion of vegetation over mid-high latitudes in the future.

Table 1. The changes of trees, shrubs, and grasses between RCP8.5 experiments and the present-day experiment in 30°–90°N and 30°S–30°N, respectively.

	FC_{trees}	FC_{shrubs}	$FC_{grasses}$	FC_{total}
30°–90°N	6.39%	−11.60%	15.31%	10.10%
30°S–30°N	0.002%	−1.26%	−2.46%	−3.72%

The changes in vegetation distribution can be seen more directly by an estimation of the differences in the four aggregated vegetation types between the two scenarios (Fig. 2). Over northern mid-high latitudes, the increase in trees in the RCP8.5 experiments occurs mainly in Alaska, eastern Canada, and Siberia. However, a decrease in trees is also seen in central Canada, Western Siberia, and Northeast

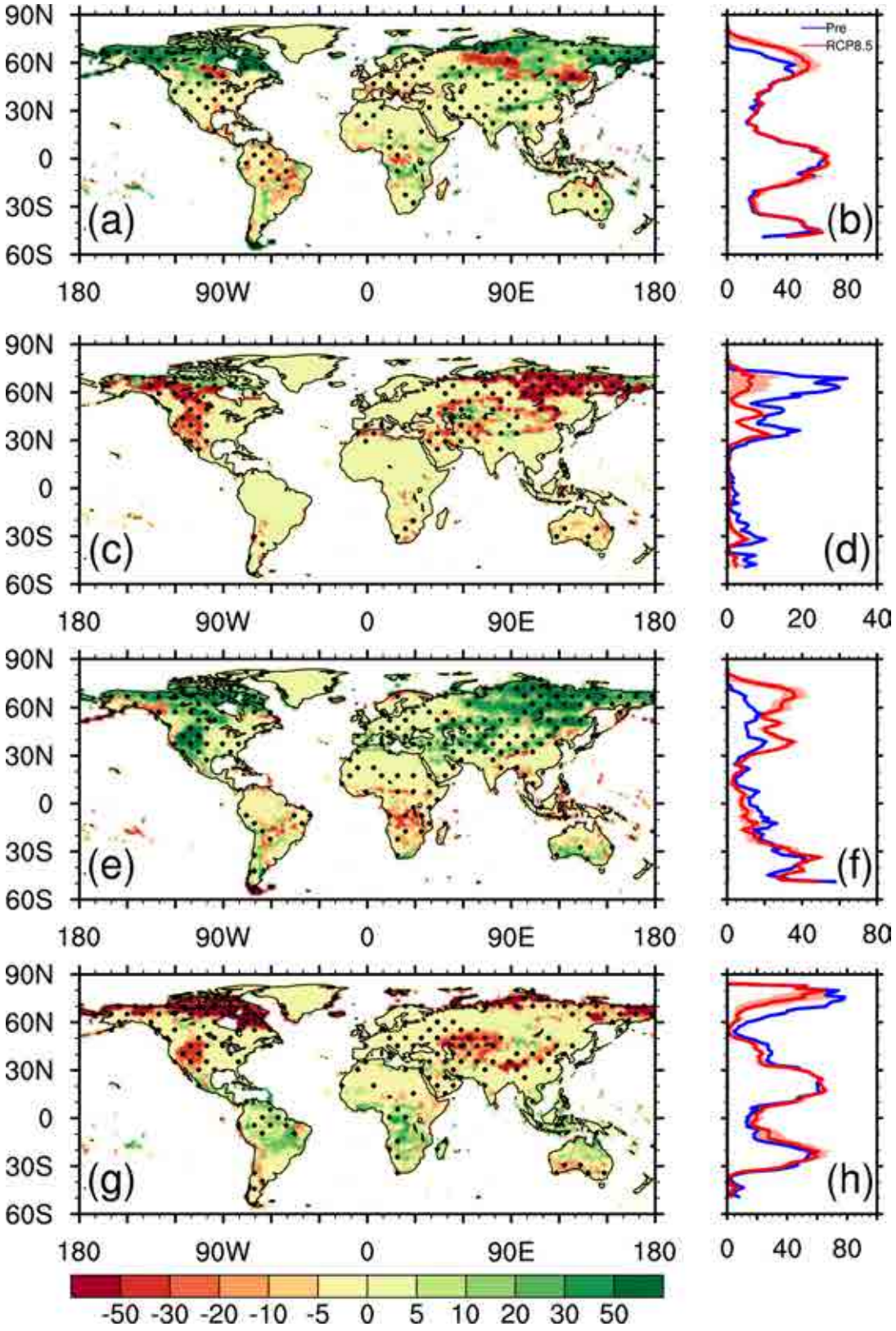

Fig. 2. Differences in fractional coverage (units: %) of (a) trees, (c) shrubs, (e) grasses, and (g) bare ground between the present-day experiment (Pre) and the RCP8.5 experiments (RCP8.5) (RCP8.5 minus Pre). The stippled regions represent grids where at least 14 of 16 models agree with the multi-model ensemble mean. (b), (d), (f), and (h) are the zonal average fractional coverage (units: %) of trees, shrubs, grasses, and bare ground in Pre (blue) and RCP8.5 (red). The shaded red areas represent one standard deviation.

China. The decreased shrubs mainly occurred in northwestern Canada, western America, and eastern Siberia; these areas are replaced by increased grasses. Over the tropics, grasses and shrubs decreased mainly in tropical Africa and Australia, with reductions of 8.57% and 3.00%, respectively (Fig. 2). Trees in tropical America decreased by 4.89%, even though, on the whole, tropical trees showed almost no changes. Figure 2 also illustrates that the changes in the projected vegetation in the above-mentioned regions are consistent among the selected 16 models.

To figure out the contribution of each PFT to the four aggregated vegetation types, we further compared the fractional coverage of vegetation at the PFT level in the two scenarios (Fig. 3). The increased trees are shown in Fig. 2. The dominant contribution of these trees comes from the category of "broadleaf deciduous temperate tree" (BDM; 3.37%), while the "needleleaf evergreen boreal tree" (NEB) makes the largest negative contribution of –1.13%. The decreased shrubs in the future are dominated by reductions in "broadleaf deciduous boreal shrub" (BDBsh; –5.18%). For the increased grasses, positive contributions are mainly from "C3 arctic grass" (C3Ar; 3.74%) and "C3 non-arctic grass" (C3NA; 4.17%), but "C4 grass" (C4) makes a negative contribution of –2.01%. The six mentioned PFTs show the largest sensitivities to global warming and are the main contributors to the global vegetation changes.

3.3. *LAI*

Over the whole globe, the projected LAI in the RCP8.5 experiments increased by 0.65±0.30 m^2 m^{-2}, relative to the present-day experiment. This increase is seen over most latitudes, especially in the middle and high latitudes (Fig. 4b). Figure 4a shows the spatial pattern of the differences in LAI between the RCP8.5 experiments and the present-day experiment. Over the northern mid-high latitudes, the increased LAI mainly occurred in Alaska, eastern Canada, central North America, and eastern Siberia, with more than 2.00 m^2 m^{-2}. However, a strong decrease in LAI is also seen in central Canada, Western Siberia, and Northeast China, which correspond to the regions that show a projected replacement of trees and shrubs by grasses (Fig. 2). Over the tropics, the projected LAI decreased in the Amazon and equatorial Africa by values that exceeded 1.00 m^2 m^{-2}, while southeastern Asia showed an increase in the projected LAI by more than 1.00 m^2 m^{-2}.

3.4. *Carbon fluxes*

The analysis here focuses on the changes of carbon fluxes for the GPP, NPP, and autotrophic respiration (Ra) between the RCP8.5 experiments and the present-day experiment. Globally, positive anomalies were observed for all three carbon fluxes (Fig. 5). GPP shows the largest anomaly with 18.36%±5.52%, which is followed by Ra and NPP, with 12.32%±3.24% and 6.04%±2.42%, respectively. Considering that the CO_2 concentration is the same in all simulations, the overall positive anomalies in GPP and NPP are caused by the warmer and wetter climate in the future, a favorable climatic condition that can enhance photosynthesis by lengthening the growing season or by reducing water limitation. Further analysis is shown in section 4.

Figure 6 clearly shows that positive anomalies occurred over most of the latitudes, while negative anomalies were only seen over a few tropical latitudes. The spatial patterns further show that the positive anomalies are more globally widespread than the negative anomalies (Figs. 6a, c, e). Over middle and high latitudes, the regions with remarkable positive anomalies are mainly in Alaska, eastern North America, Europe, eastern Siberia, and southern South America. Regions with negative or slightly positive anomalies are seen in Northeast China and Western Siberia. Over the tropics, the negative anomalies for the three carbon fluxes are observed mainly in the Amazon, while tropical Asia shows

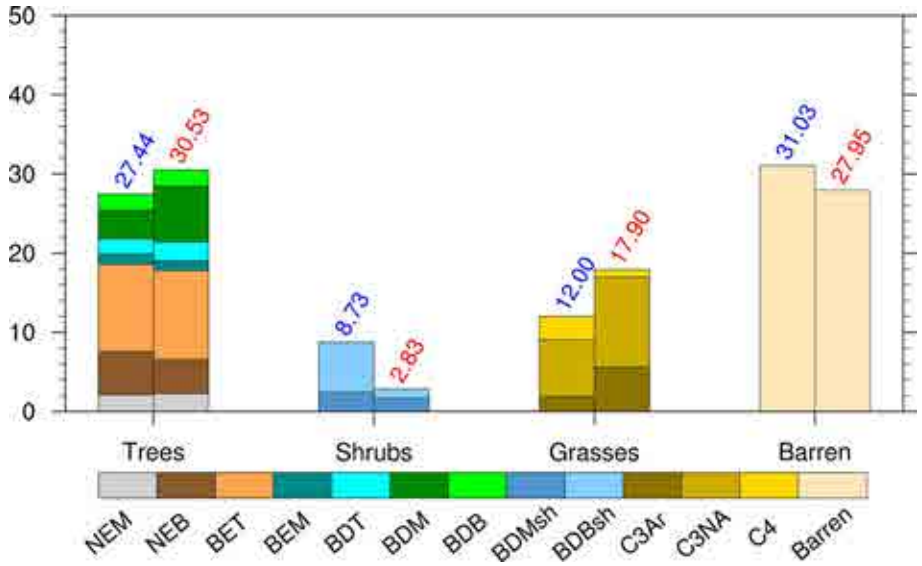

Fig. 3. Global weighted average fractional coverage (%) of each PFT for Pre (blue) and RCP8.5 (red). The abbreviations of the PFT correspond to the information in Table S1.

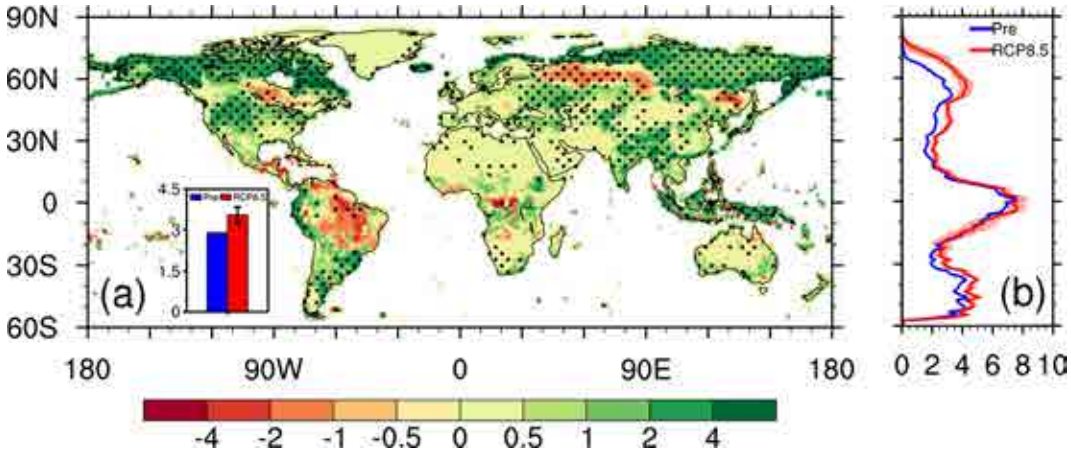

Fig. 4. (a) Spatial distribution of differences in leaf area index (LAI) between Pre and RCP8.5 (RCP8.5 minus Pre). The stippled regions represent grids where at least 14 of 16 models agree with the multi-model ensemble mean and the bars in the left bottom represent the global means of LAI in Pre (blue) and RCP8.5 (red). (b) The zonal average of LAI in the present-day experiment (Pre; blue) and the RCP8.5 experiments (RCP8.5; red), respectively. The shaded red areas represent one standard deviation. All units are m^2 m^{-2}.

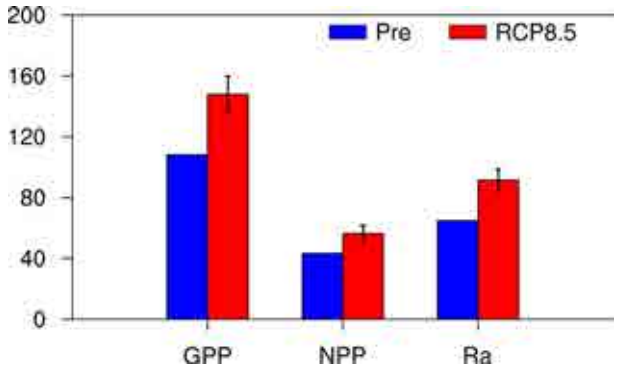

Fig. 5. Global means of carbon fluxes in Pre (blue) and RCP8.5 (red). The bars represent one standard deviation. All units are PgC yr^{-1}.

remarkable positive anomalies. Figure 6 also illustrates that the projected positive anomalies are more consistent than the projected negative anomalies among the 16 RCP8.5 experiments, which reflects more uncertainty for the projected carbon fluxes over regions with negative changes.

4. Discussion

4.1. *Linkage between climate and vegetation anomalies*

To investigate drivers of the changes in vegetation distribution, we further analyzed the relationships between the changes in fractional coverage (FC) of the above-mentioned six PFTs and the temperature and precipitation, respectively (Fig. 7). The temperature changes exhibit significant negative correlations with the changes in the PFT categories of "needleleaf evergreen boreal tree" (NEB), "broadleaf deciduous boreal shrub" (BDBsh), and "C4 grass" (C4), with correlation coefficients (cc) of –0.89, –0.65, and –0.51, respectively. In contrast, significantly positive correlations are seen between the changes in temperature and "broadleaf deciduous temperate tree" (BDM; cc= 0.88), "C3 arctic grass" (C3Ar; cc= 0.85), and "C3 non-arctic grass" (C3NA; cc= 0.64). Figure 7b shows that the changes in precipitation are significantly correlated with the changes in NEB (cc= –0.48), BDBsh (cc= –0.60), and C3Ar (cc= 0.63), while the correlations for the other three PFTs are not significant. Together with the partial correlation coefficients (Table S3), the stronger correlations between fractional coverage of vegetation and surface air temperature indicate that temperature is the dominant driver of the changes in vegetation distribution as opposed to precipitation.

The dominant role of surface air temperature in driving vegetation distribution strongly suggests that temperature is a key limiting factor for vegetation growth. The warmer climate in the future can lead to an expansion of the growing season and increased photosynthesis rates in the boreal and temperate regions. High temperatures also lead to higher mortality rates for boreal woods (NEB and BDBsh) due to heat stress and thus a decrease in FC. However, the heat stress is neglected in DGVMs, because temperate vegetation adjusts to the warmer climate and thus results in an increase in FC for BDM and C3 grasses. For C4 grass that grows in the tropics (Fig. S4), warming has little or even a negative impact on the rate of photosynthesis but significantly increases the rate of respiration, thus suppressing productivity and leading to decreased FC.

We next investigate the relationship between the projected changes in the three categories of carbon fluxes and changes in LAI, surface air temperature, and precipitation. The three carbon fluxes are known to be impacted greatly by LAI, temperature, and precipitation. Their net effects can be very different in different ecosystems, so the changes in the three carbon fluxes show large differences. Thus, we selected six regions (Table S4 in the ESM) to discuss these differences by using regional boundaries defined in previous studies (Giorgi and Francisco, 2000; Xue et al., 2010). In

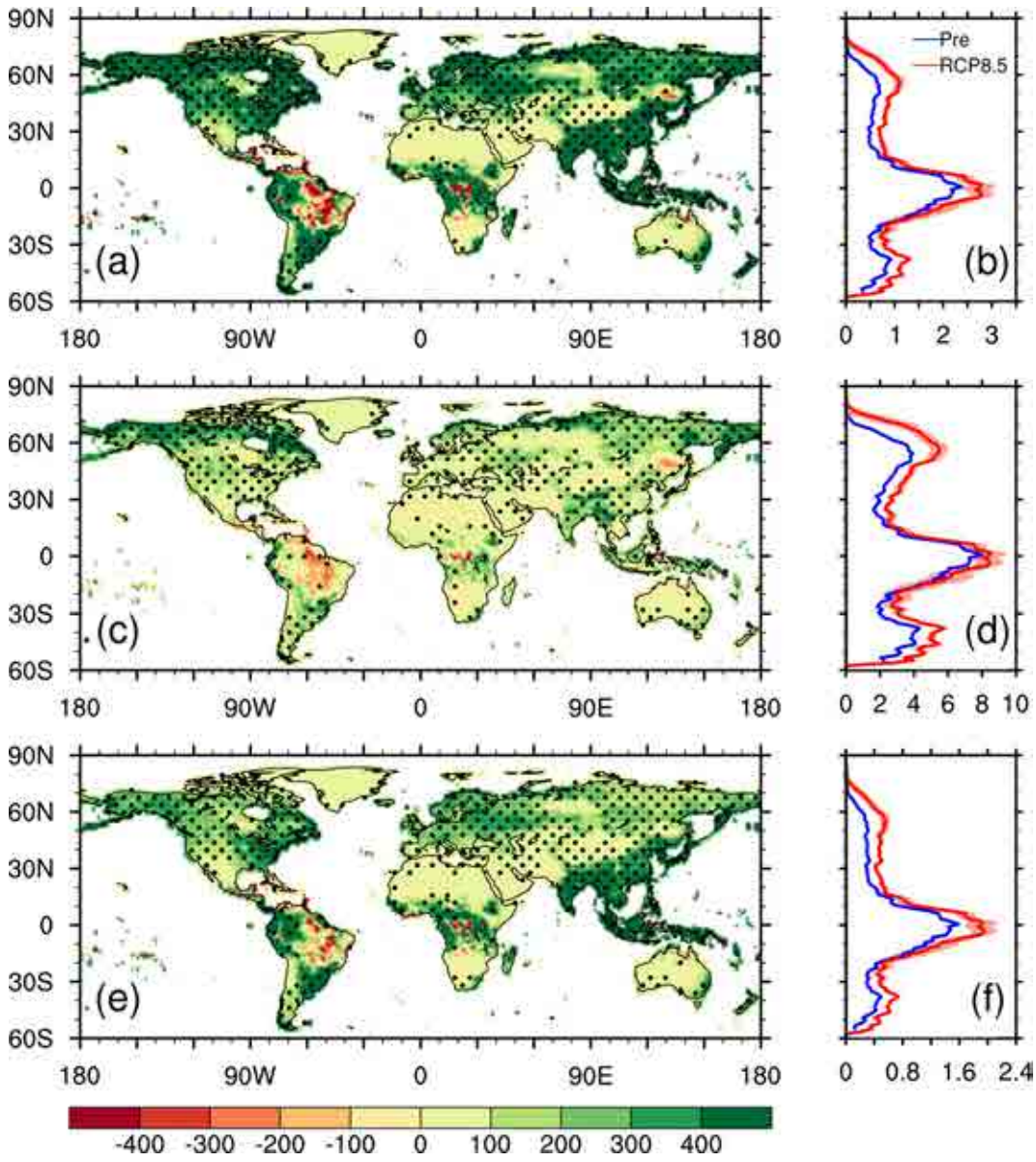

Fig. 6. Spatial distribution of differences between the present-day experiment (Pre) and the RCP8.5 experiments (RCP8.5) (RCP8.5 minus Pre) in (a) GPP, (c) NPP, and (e) Ra. (units: gC m^{-2} yr^{-1}). The stippled regions represent grids where at least 14 of 16 models agree with the multi-model ensemble mean. (b), (d), and (f) are the zonal average (units: kgC m^{-2} yr^{-1}) of GPP, NPP, and Ra in Pre (blue) and RCP8.5 (red). The shaded red areas represent one standard deviation.

these regions, the projected changes for the three carbon fluxes have either remarkably increased, slightly increased, or decreased (Fig. S5 in the ESM).

Over northern mid-high latitudes, it is known that an increase in LAI, temperature, and precipitation is generally favorable for an increase in GPP, NPP, and Ra. Figure 8 shows a remarkable increase in the projected carbon fluxes in Alaska (ALA), Northern Europe (NEU), and eastern North America (ENA) due to the combined effects of LAI, temperature, and precipitation. However, in Western Siberia (WSI), the replacement of trees and shrubs by grasses (Fig. S6 in the ESM) leads to a decrease in LAI and in the carbon fluxes, which partly offsets the increase in the carbon fluxes caused by the increased temperature and precipitation. The net result ultimately leads to a slight incremental increase of the carbon fluxes by no more than 0.50 PgC yr^{-1} in WSI.

Over the tropics, warmer climate anomalies may reduce vegetation productivity due to a suppression of photosynthesis caused by a higher vapor pressure deficit, while wetter climate anomalies can enhance vegetation productivity by reducing water stress. Figure 8 shows weaker positive anomalies for the projected temperature and stronger positive anomalies for the projected precipitation in Southeast Asia (SEA) than for the Amazon Basin (AMZ). These differences, on one hand, explain the opposite responses regarding the carbon fluxes for the two regions. On the other hand, the increased

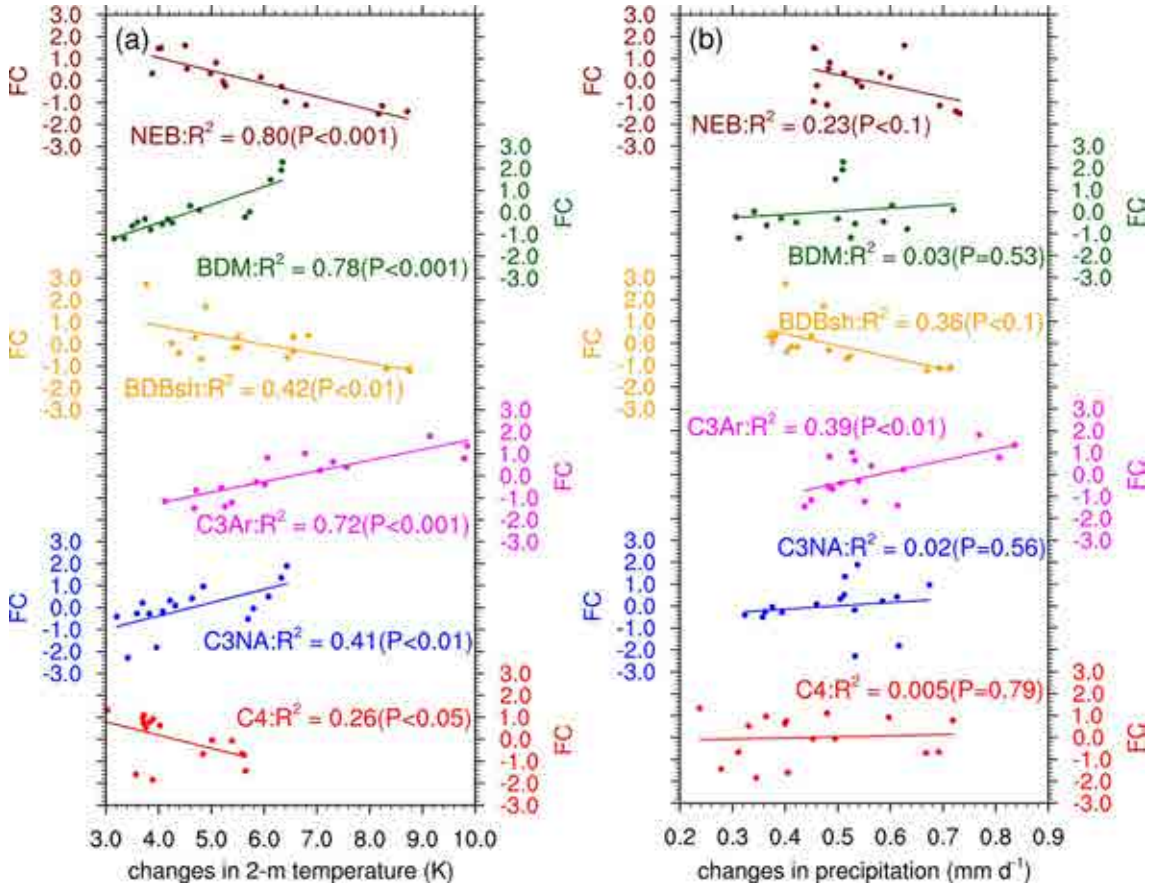

Fig. 7. Relationship between the changes in fractional coverage (FC, %) of the six PFTs (NEB, BDM, BDBsh, C3Ar, C3NA, C4) with (a) annual mean surface 2-m temperature (K), and (b) precipitation (mm d^{-1}) among the 16 ensembles. The changes in fractional coverage have been standardized. The lines represent the corresponding regression lines. The abbreviations of the PFT correspond to the information in Table S1.

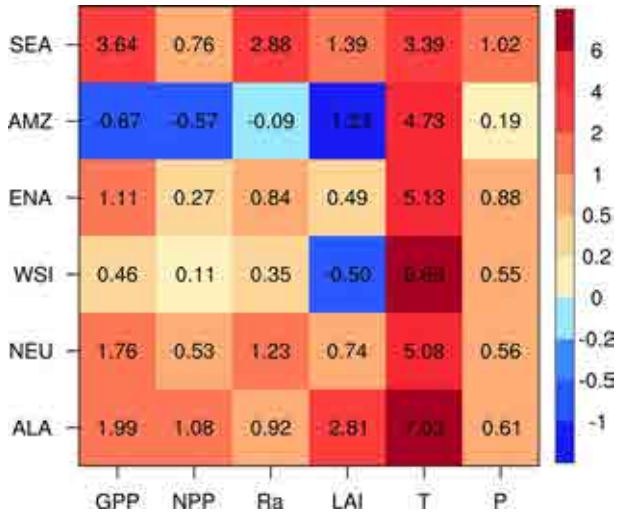

Fig. 8. Changes in carbon fluxes (GPP, NPP, and Ra; PgC yr^{-1}), LAI (m^2 m^{-2}), temperature (*T*; K), and precipitation (*P*; mm d^{-1}) over the six selected regions. The abbreviations of these regions correspond to the information in Table S4.

LAI caused by increased trees in SEA also makes large contributions to the enhanced carbon fluxes, while the decreased LAI, caused by decreased trees in the AMZ, makes large contributions to the decreased carbon fluxes. Overall, the combination of the effects caused by LAI, temperature, and precipitation result in opposite behaviors between SEA and the AMZ regarding the response to carbon fluxes.

4.2. *Uncertainties and significance*

This work mainly focuses on the impact of climate warming on vegetation dynamics and carbon fluxes, so the atmospheric CO_2 concentration is kept at a constant value in all simulations to isolate the CO_2 fertilization effects. This set of our simulations may add to our full understanding of vegetation responses. Thus, we further conducted a simulation with an elevated CO_2 of 850 ppm (hereafter eCO_2) by referring to Yu et al. (2014). We compared the results with the above results to discuss the differences in the effects of global warming and CO_2 fertilization on vegetation dynamics and carbon fluxes.

The results show that the eCO_2 simulation also produced more vegetation than the Pre simulation. The value of the greening anomaly is comparable to that of the RCP8.5 simulation (Fig. S7 in the ESM). However, there is no poleward expansion of vegetation in the eCO_2 simulation over the north-

ern high latitudes (Fig. S8 in the ESM). The three carbon fluxes are also enhanced in the eCO_2 simulation relative to the Pre simulation. Their global annual totals are comparable to those in the RCP8.5 simulation (Fig. S9 in the ESM). The spatial distribution shows that the enhancement of the three carbon fluxes of the eCO_2 simulation is seen over almost all vegetated land grids (Fig. S10 in the ESM), while the RCP8.5 simulation shows a negative anomaly in the three carbon fluxes over more vegetated grids (Fig. 6). The comparable results between the RCP8.5 and eCO_2 simulations illustrate that the effects of global warming on vegetation dynamics and carbon fluxes are just as important as those of CO_2 fertilization.

Furthermore, in our study, the projected results were based on the forcing from the RCP8.5 scenario, which corresponds to a very high baseline emission scenario to maximize the climate signal (Taylor et al., 2012). Liu et al. (2020) assessed the future changes in the climate-vegetation system over East Asia under different emission scenarios. They found a slight increase in vegetation cover over most of the region and the magnitude of these changes increased gradually from low to high RCPs. Thus, more simulations and analyses are needed to investigate the dependence of the results on the scenarios at the global scale.

Despite the uncertainties mentioned above, our study makes a valuable contribution to the development of the model and the understanding of the responses of vegetation to global warming. First, the results show opposite responses to warming between the PFT categories, "needleleaf evergreen boreal tree" (NEB) and "broadleaf deciduous temperate tree" (BDM) due to the different values for heat stress threshold in the model. This phenomenon reveals that the differences in parameters assigned to PFTs have significantly different effects on the vegetation in response to future climate changes. Meanwhile, this result also reminds us that it is necessary to further improve the parameterization of heat stress in IAP-DGVM because of the limitation of the different heat stress threshold settings for different PFT categories Thus, optimizing the parameterization of vegetation processes in the model is crucial for simulating a more realistic vegetation change. Second, this study demonstrates an application of the CAS-ESM2 for studying the response of vegetation dynamics to climate change. In the process of developing the IAP-DGVM, this application represents a new frontier after the successful coupling of IAP-DGVM with CAS-ESM2, and provides a valuable sample for comparison with both the CAS-ESM2 community and other model communities. We have coupled IAP-DGVM with the atmospheric general circulation model (IAP-AGCM; Zhang et al., 2013), so CAS-ESM2 can be used to investigate interactions between vegetation dynamics and climate. We now are able to use this coupled version of CAS-ESM2 to run the Diagnostic, Evaluation, and Characterization of Klima (DECK) experiments of phase 6 of the Coupled Model Intercomparison Project (CMIP6). Third, the poleward expansion of vegetation in northern mid-high latitudes simulated in our work is consistent with numerous studies on future projections (Mahowald et al., 2016; Yu et al., 2016; Gang et al., 2017; Tharammal et al., 2019) and with recent observations (Zhu et al., 2016; Zeng et al., 2018; Yao et al., 2019), indicating that the "greening" trend may continue in the future. This greening can provide critical feedback to the local climate by shading, changing surface albedo, and regulating the partitioning of evapotranspiration between evaporation and transpiration (Blok et al., 2010; Zhu and Zeng, 2015, 2017). Our investigation further shows the dominant role of surface air temperature in the greening phenomenon. The investigation provides for a better understanding of vegetation processes and expands upon our knowledge of model behavior in response to global warming, which favors projections of changes in terrestrial ecosystems and climate in the future. Overall, this work evaluates the responses of vegetation to global warming and shows the tight linkage between vegetation and climate changes, which is a necessary step for model development and a significant foundation for further study of vegetation-climate interactions.

5. Summary

This study investigated the changes in the distribution of vegetation and carbon fluxes in response to global warming by using IAP-DGVM in CAS-ESM2. The results, based on the present-day simulation and RCP8.5 simulations, showed a greening in the northern middle- and high-latitudes and a slight browning in the tropics. The results also showed positive anomalies in GPP, NPP, and Ra over most latitudes, while negative anomalies occurred, with higher uncertainty, in the Amazon. We argue that surface air temperature is the dominant driver in changing the vegetation distribution, as opposed to precipitation, and that the changes in GPP, NPP, and Ra can be explained by the combined effects of LAI, temperature, and precipitation.

The results of this investigation not only remind us that optimizing the parameterization of vegetation processes in the model is crucial, but also provides a better understanding of vegetation processes that could prove beneficial in the design and improvement of model parameterizations for simulating a more realistic vegetation change.

Acknowledgements. This work was supported by the National Natural Science Foundation of China (Grant No. 41705070), the Major Program of the National Natural Science Foundation of China (Grant No. 41991282) and the National Key Scientific and Technological Infrastructure project "Earth System Science Numerical Simulator Facility" (EarthLab).

Electronic supplementary material: Supplementary material is available in the online version of this article at https://doi.org/10.1007/s00376-021-1138-3.

REFERENCES

Alo, C. A., and G. L. Wang, 2008: Potential future changes of the terrestrial ecosystem based on climate projections by eight

general circulation models. *J. Geophys. Res.*, **113**, G01004, https://doi.org/10.1029/2007JG000528.

Anav, A., and Coauthors, 2015: Spatiotemporal patterns of terrestrial gross primary production: A review. *Rev. Geophys.*, **53**(3), 785–818, https://doi.org/10.1002/2015RG000483.

Andreu-Hayles, L., R. D'Arrigo, K. J. Anchukaitis, P. S. A. Beck, D. Frank, and S. Goetz, 2011: Varying boreal forest response to arctic environmental change at the Firth River, Alaska. *Environmental Research Letters*, **6**(4), 045503, https://doi.org/10.1088/1748-9326/6/4/045503.

Arora, V. K., and Coauthors, 2020: Carbon-concentration and carbon-climate feedbacks in CMIP6 models and their comparison to CMIP5 models. *Biogeosciences*, **17**(16), 4173–4222, https://doi.org/10.5194/bg-17-4173-2020.

Bi, J., L. Xu, A. Samanta, Z. C. Zhu, and R. Myneni, 2013: Divergent Arctic-boreal vegetation changes between North America and Eurasia over the past 30 years. *Remote Sensing*, **5**(5), 2093–2112, https://doi.org/10.3390/rs5052093.

Blok, D., M. M. P. D. Heijmans, G. Schaepman-Strub, A. V. Kononov, T. C. Maximov, and F. Berendse, 2010: Shrub expansion may reduce summer permafrost thaw in Siberian tundra. *Global Change Biology*, **16**(4), 1296–1305, https://doi.org/10.1111/j.1365-2486.2009.02110.x.

Brovkin, V., T. Raddatz, C. H. Reick, M. Claussen, and V. Gayler, 2009: Global biogeophysical interactions between forest and climate. *Geophys. Res. Lett.*, **36**(7), L07405, https://doi.org/10.1029/2009GL037543.

Cao, X. Y., F. Tian, A. Dallmeyer, and U. Herzschuh, 2019: Northern hemisphere biome changes (>30°N) since 40 cal ka BP and their driving factors inferred from model-data comparisons. *Quaternary Science Reviews*, **220**, 291–309, https://doi.org/10.1016/j.quascirev.2019.07.034.

Clark, D. A., S. C. Piper, C. D. Keeling, and D. B. Clark, 2003: Tropical rain forest tree growth and atmospheric carbon dynamics linked to interannual temperature variation during 1984-2000. *Proceedings of the National Academy of Sciences of the United States of America*, **100**(10), 5852–5857, https://doi.org/10.1073/pnas.0935903100.

Corlett, R. T., 2011: Impacts of warming on tropical lowland rainforests. *Trends in Ecology & Evolution*, **26**(11), 606–613, https://doi.org/10.1016/j.tree.2011.06.015.

Cramer, W., and Coauthors, 2001: Global response of terrestrial ecosystem structure and function to CO_2 and climate change: Results from six dynamic global vegetation models. *Global Change Biology*, **7**(4), 357–373, https://doi.org/10.1046/j.1365-2486.2001.00383.x.

De Kauwe, M. G., and Coauthors, 2014: Where does the carbon go? A model-data intercomparison of vegetation carbon allocation and turnover processes at two temperate forest free-air CO_2 enrichment sites *New Phytologist*, **203**(3), 883–899, https://doi.org/10.1111/nph.12847.

Diffenbaugh, N. S., and C. B. Field, 2013: Changes in ecologically critical terrestrial climate conditions. *Science*, **341**(6145), 486–492, https://doi.org/10.1126/science.1237123.

Doughty, C. E., and M. L. Goulden, 2008: Are tropical forests near a high temperature threshold. *J. Geophys. Res.*, **113**, G00B07, https://doi.org/10.1029/2007JG000632.

Eric Dusenge, M., D. Galvao Duarte, and D. A. Way, 2019: Plant carbon metabolism and climate change: Elevated CO_2 and temperature impacts on photosynthesis, photorespiration and respiration. *New Phytologist*, **221**, 32–49, https://doi.org/10.1111/nph.15283.

Falloon, P. D., R. Dankers, R. A. Betts, C. D. Jones, B. B. B. Booth, and F. H. Lambert, 2012: Role of vegetation change in future climate under the A1B scenario and a climate stabilisation scenario, using the HadCM3C Earth system model. *Biogeosciences*, **9**(11), 4739–4756, https://doi.org/10.5194/bg-9-4739-2012.

Fan, Z. M., and B. Fan, 2019: Shifts of the mean centers of potential vegetation ecosystems under future climate change in Eurasia. *Forests*, **10**(10), 873, https://doi.org/10.3390/f10100873.

Field, C. B., L. D. Mortsch, M. Brklacich, D. L. Forbes, P. Kovacs, J. A. Patz, S. W. Running, and M. J. Scott, 2007: North America. *Climate Change 2007*: *Impacts*, *Adaptation and Vulnerability*. *Contribution of Working Group II to the Fourth Assessment Report of the Intergovernmental Panel on Climate Change*, M. L. Parry et al., Eds., Cambridge University Press.

Fraser, R. H., I. Olthof, M. Carrière, A. Deschamps, and D. Pouliot, 2011: Detecting long-term changes to vegetation in northern Canada using the Landsat satellite image archive. *Environmental Research Letters*, **6**, 045502, https://doi.org/10.1088/1748-9326/6/4/045502.

Frost, G. V., and H. E. Epstein, 2014: Tall shrub and tree expansion in Siberian tundra ecotones since the 1960s. *Global Change Biology*, **20**(4), 1264–1277, https://doi.org/10.1111/gcb.12406.

Gang, C. C., and Coauthors, 2017: Modeling the dynamics of distribution, extent, and NPP of global terrestrial ecosystems in response to future climate change. *Global and Planetary Change*, **148**, 153–165, https://doi.org/10.1016/j.gloplacha.2016.12.007.

Gao, D. D., L. Dan, G. Z. Fan, J. Peng, X. J. Yang, F. Q. Yang, and Y. Y. Li, 2019: Spatial and temporal variations of net primary productivity at century scale in earth system models and its relationship with climate. *Climatic and Environmental Research*, **24**(6), 663–677, https://doi.org/10.3878/j.issn.1006-9585.2018.18052.

Giorgi, F., and R. Francisco, 2000: Uncertainties in regional climate change prediction: A regional analysis of ensemble simulations with the HADCM2 coupled AOGCM. *Climate Dyn.*, **16**(2), 169–182, https://doi.org/10.1007/PL00013733.

Gurney, K. R., and Coauthors, 2004: Transcom 3 inversion intercomparison: Model mean results for the estimation of seasonal carbon sources and sinks. *Global Biogeochemical Cycles*, **18**, GB1010, https://doi.org/10.1029/2003GB002111.

Hawkins, L. R., and Coauthors, 2019: Parametric sensitivity of vegetation dynamics in the TRIFFID model and the associated uncertainty in projected climate change impacts on Western U. *S. forests. Journal of Advances in Modeling Earth Systems*, **11**(8), 2787–2813, https://doi.org/10.1029/2018MS001577.

Horvath, P., H. Tang, R. Halvorsen, F. Stordal, L. M. Tallaksen, T. K. Berntsen, and A. Bryn, 2021: Improving the representation of high-latitude vegetation distribution in dynamic global vegetation models. *Biogeosciences*, **18**(1), 95–112, https://doi.org/10.5194/bg-18-95-2021.

Hu, L., W. J. Fan, W. P. Yuan, H. Z. Ren, and Y. K. Cui, 2021: Spatiotemporal variation of vegetation productivity and its feedback to climate change in northeast china over the last 30 years. *Remote Sensing*, **13**(5), 951, https://doi.org/10.3390/rs13050951.

Huang, M. T., and Coauthors, 2019: Air temperature optima of vegetation productivity across global biomes. *Nature Ecology &*

Evolution, **3**(5), 772–779, https://doi.org/10.1038/s41559-019-0838-x.

Jung, M., and Coauthors, 2007: Uncertainties of modeling gross primary productivity over Europe: A systematic study on the effects of using different drivers and terrestrial biosphere models. *Global Biogeochemical Cycles*, **21**(4), https://doi.org/10.1029/2006GB002915.

Kang, S., and E. A. B. Eltahir, 2018: North China plain threatened by deadly heatwaves due to climate change and irrigation. *Nature Communications*, **9**, 2894, https://doi.org/10.1038/s41467-018-05252-y.

Keenan, T. F., and W. J. Riley, 2018: Greening of the land surface in the world's cold regions consistent with recent warming. *Nature Climate Change*, **8**, 825–828, https://doi.org/10.1038/s41558-018-0258-y.

Knorr, W., and M. Heimann, 2001: Uncertainties in global terrestrial biosphere modeling: 1. *A comprehensive sensitivity analysis with a new photosynthesis and energy balance scheme. Global Biogeochemical Cycles*, **15**(1), 207–225, https://doi.org/10.1029/1998GB001059.

Kreplin, H. N., C. S. S. Ferreira, G. Destouni, S. D. Keesstra, L. Salvati, and Z. Kalantari, 2021: Arctic wetland system dynamics under climate warming. *Wiley Interdisciplinary Reviews*, **8**(4), e1526, https://doi.org/10.1002/wat2.1526.

Kumar, D., and S. Scheiter, 2019: Biome diversity in South Asia-How can we improve vegetation models to understand global change impact at regional level. *Science of the Total Environment*, **671**, 1001–1016, https://doi.org/10.1016/j.scitotenv.2019.03.251.

Li, F., X. D. Zeng, and S. Levis, 2012: A process-based fire parameterization of intermediate complexity in a Dynamic Global Vegetation Model. *Biogeosciences*, **9**(11), 2761–2780, https://doi.org/10.5194/bg-9-2761-2012.

Liu, L. B., S. S. Peng, A. Aghakouchak, Y. Y. Huang, Y. Li, D. H. Qin, A. L. Xie, and S. C. Li, 2018: Broad consistency between satellite and vegetation model estimates of net primary productivity across global and regional scales. *J. Geophys. Res.*, **123**(12), 3603–3616, https://doi.org/10.1029/2018JG004760.

Liu, W. G., G. L. Wang, M. Yu, H. S. Chen, Y. L. Jiang, M. J. Yang, and Y. Shi, 2020: Projecting the future vegetation-climate system over East Asia and its RCP-dependence. *Climate Dyn.*, **55**(9), 2725–2742, https://doi.org/10.1007/s00382-020-05411-2.

Liu, Y., Y. K. Xue, G. MacDonald, P. Cox, and Z. Q. Zhang, 2019: Global vegetation variability and its response to elevated CO_2, global warming, and climate variability-a study using the offline SSiB4/TRIFFID model and satellite data. *Earth System Dynamics*, **10**(1), 9–29, https://doi.org/10.5194/esd-10-9-2019.

Mackay, A., 2008: Climate change 2007: Impacts, adaptation and vulnerability. contribution of working group II to the fourth assessment report of the intergovernmental panel on climate change. *Journal of Environmental Quality*, **37**(6), 2407, https://doi.org/10.2134/jeq2008.0015br.

Madani, N., and Coauthors, 2020: Recent amplified global gross primary productivity due to temperature increase is offset by reduced productivity due to water constraints. *AGU Advances*, **1**(4), e2020AV000180, https://doi.org/10.1029/2020AV000180.

Mahowald, N., F. Lo, Y. Zheng, L. Harrison, C. Funk, D. Lombardozzi, and C. Goodale, 2016: Projections of leaf area index in earth system models. *Earth System Dynamics*, **7**(1), 211–229, https://doi.org/10.5194/esd-7-211-2016.

Mao, J. F., and Coauthors, 2016: Human-induced greening of the northern extratropical land surface. *Nature Climate Change*, **6**(10), 959–963, https://doi.org/10.1038/nclimate3056.

McGuire, A. D., and Coauthors, 2001: Carbon balance of the terrestrial biosphere in the twentieth century: Analyses of CO_2, climate and land use effects with four process-based ecosystem models. *Global Biogeochemical Cycles*, **15**(1), 183–206, https://doi.org/10.1029/2000gb001298.

Mekonnen, Z. A., and Coauthors, 2021: Arctic tundra shrubification: A review of mechanisms and impacts on ecosystem carbon balance. *Environmental Research Letters*, **16**(5), 053001, https://doi.org/10.1088/1748-9326/abf28b.

Myers-Smith, I. H., and Coauthors, 2011: Shrub expansion in tundra ecosystems: Dynamics, impacts and research priorities. *Environmental Research Letters*, **6**(4), 045509, https://doi.org/10.1088/1748-9326/6/4/045509.

Myers-Smith, I. H., and Coauthors, 2020: Complexity revealed in the greening of the Arctic. *Nature Climate Change*, **10**(2), 106–117, https://doi.org/10.1038/s41558-019-0688-1.

Nemani, R. R., C. D. Keeling, H. Hashimoto, W. M. Jolly, S. C. Piper, C. J. Tucker, R. B. Myneni, and S. W. Running, 2003: Climate-driven increases in global terrestrial net primary production from 1982 to 1999. *Science*, **300**(5625), 1560–1563, https://doi.org/10.1126/science.1082750.

Piao, S. L., P. Friedlingstein, P. Ciais, N. Viovy, and J. Demarty, 2007: Growing season extension and its impact on terrestrial carbon cycle in the Northern Hemisphere over the past 2 decades. *Global Biogeochemical Cycles*, **21**(3), https://doi.org/10.1029/2006GB002888.

Piao, S. L., and Coauthors, 2013: Evaluation of terrestrial carbon cycle models for their response to climate variability and to CO_2 trends. *Global Change Biology*, **19**(7), 2117–2132, https://doi.org/10.1111/gcb.12187.

Piao, S. L., and Coauthors, 2020: Characteristics, drivers and feedbacks of global greening. *Nature Reviews Earth & Environment*, **1**, 14–27, https://doi.org/10.1038/s43017-019-0001-x.

Prentice, I. C., and Coauthors, 2007: Dynamic global vegetation modeling: Quantifying terrestrial ecosystem responses to large-scale environmental change. *Terrestrial Ecosystems in a Changing World*, J. G. Canadell et al., Eds., Springer, 175–192.

Qian, T. T., A. G. Dai, K. E. Trenberth, and K. W. Oleson, 2006: Simulation of global land surface conditions from 1948 to 2004. *Part I: Forcing data and evaluations. Journal of Hydrometeorology*, **7**(5), 953–975, https://doi.org/10.1175/JHM540.1.

Quillet, A., C. H. Peng, and M. Garneau, 2010: Toward dynamic global vegetation models for simulating vegetation-climate interactions and feedbacks: Recent developments, limitations, and future challenges. *Environmental Reviews*, **18**, 333–353, https://doi.org/10.1139/A10-016.

Raddatz, T. J., and Coauthors, 2007: Will the tropical land biosphere dominate the climate-carbon cycle feedback during the twenty-first century. *Climate Dyn.*, **29**(6), 565–574, https://doi.org/10.1007/s00382-007-0247-8.

Schaphoff, S., C. P. O. Reyer, D. Schepaschenko, D. Gerten, and A. Shvidenko, 2016: Tamm review: Observed and projected climate change impacts on Russia's forests and its carbon balance. *Forest Ecology and Management*, **361**, 432–444, https://doi.org/10.1016/j.foreco.2015.11.043.

Scheiter, S., L. Langan, and S. L. Higgins, 2013: Next-generation dynamic global vegetation models: Learning from community ecology. *New Phytologist*, **198**(3), 957–969, https://doi.org/10.1111/nph.12210.

Scheiter, S., and Coauthors, 2020: Climate change promotes transitions to tall evergreen vegetation in tropical Asia. *Global Change Biology*, **26**(9), 5106–5124, https://doi.org/10.1111/gcb.15217.

Shafer, S. L., P. J. Bartlein, E. M. Gray, and R. T. Pelltier, 2015: Projected future vegetation changes for the Northwest United States and Southwest Canada at a fine spatial resolution using a dynamic global vegetation model. *PLoS One*, **10**(10), e0138759, https://doi.org/10.1371/journal.pone.0138759.

Shiyatov, S. G., M. M. Terent'ev, and V. V. Fomin, 2005: Spatiotemporal dynamics of forest-tundra communities in the polar urals. *Russian Journal of Ecology*, **36**(2), 69–75, https://doi.org/10.1007/s11184-005-0051-9.

Sitch, S., and Coauthors, 2008: Evaluation of the terrestrial carbon cycle, future plant geography and climate-carbon cycle feedbacks using five dynamic global vegetation models (DGVMs). *Global Change Biology*, **14**(9), 2015–2039, https://doi.org/10.1111/j.1365-2486.2008.01626.x.

Smith, B., D. Wårlind, A. Arneth, T. Hickler, P. Leadley, J. Siltberg, and S. Zaehle, 2014: Implications of incorporating N cycling and N limitations on primary production in an individual-based dynamic vegetation model. *Biogeosciences*, **11**(7), 2027–2054, https://doi.org/10.5194/bg-11-2027-2014.

Song, X., X. D. Zeng, J. W. Zhu, and P. Shao, 2016: Development of an establishment scheme for a DGVM. *Adv. Atmos. Sci.*, **33**, 829–840, https://doi.org/10.1007/s00376-016-5284-y.

Speed, J. D. M., S. J. Woodin, H. Tømmervik, and R. Van Der Wal, 2010: Extrapolating herbivore-induced carbon loss across an arctic landscape. *Polar Biology*, **33**(6), 789–797, https://doi.org/10.1007/s00300-009-0756-5.

Sturm, M., C. Racine, and K. Tape, 2001: Increasing shrub abundance in the Arctic. *Nature*, **411**(6837), 546–547, https://doi.org/10.1038/35079180.

Sulman, B. N., E. Shevliakova, E. R. Brzostek, S. N. Kivlin, S. Malyshev, D. N. L. Menge, and X. Zhang, 2019: Diverse mycorrhizal associations enhance terrestrial C storage in a global model. *Global Biogeochemical Cycles*, **33**(4), 501–523, https://doi.org/10.1029/2018GB005973.

Taylor, K. E., R. J. Stouffer, and G. A. Meehl, 2012: An overview of CMIP5 and the experiment design. *Bull. Amer. Meteor. Soc.*, **93**(4), 485–498, https://doi.org/10.1175/BAMS-D-11-00094.1.

Tharammal, T., G. Bala, D. Narayanappa, and R. Nemani, 2019: Potential roles of CO_2 fertilization, nitrogen deposition, climate change, and land use and land cover change on the global terrestrial carbon uptake in the twenty-first century. *Climate Dyn.*, **52**, 4393–4406, https://doi.org/10.1007/s00382-018-4388-8.

Tømmervik, H., and B. C. Forbes, 2020: Focus on recent, present and future Arctic and boreal productivity and biomass changes. *Environmental Research Letters*, **15**(8), 080201, https://doi.org/10.1088/1748-9326/ab79e3.

Vickers, H., K. A. Høgda, S. Solbø, S. R. Karlsen, H. Tømmervik, R. Aanes, and B. B. Hansen, 2016: Changes in greening in the high arctic: Insights from a 30 year AVHRR max NDVI dataset for Svalbard. *Environmental Research Letters*, **11**(10), 105004, https://doi.org/10.1088/1748-9326/11/10/105004.

Walker, M. D., and Coauthors, 2006: Plant community responses to experimental warming across the tundra biome. *Proceedings of the National Academy of Sciences of the United States of America*, **103**(5), 1342–1346, https://doi.org/10.1073/pnas.0503198103.

Wibowo, A., M. M. Yusoff, T. A. Adura, A. Wibowo, Supriatna, and L. H. Zaini, 2020: Spatial model of air surface temperature using Landsat 8 TIRS. *IOP Conference Series: Earth and Environmental Science*, **500**, 012009, https://doi.org/10.1088/1755-1315/500/1/012009.

Woodward, F. I., and B. G. Williams, 1987: Climate and plant distribution at global and local scales. *Vegetatio*, **69**, 189–197, https://doi.org/10.1007/BF00038700.

Woodward, F. I., and M. R. Lomas, 2004: Vegetation dynamics-simulating responses to climatic change. *Biological Reviews*, **79**(3), 643–670, https://doi.org/10.1017/S1464793103006419.

Wu, L., T. Kato, H. Sato, T. Hirano, and T. Yazaki, 2019: Sensitivity analysis of the typhoon disturbance effect on forest dynamics and carbon balance in the future in a cool-temperate forest in northern Japan by using SEIB-DGVM. *Forest Ecology and Management*, **451**, 117529, https://doi.org/10.1016/j.foreco.2019.117529.

Xue, Y. K., F. De Sales, R. Vasic, C. R. Mechoso, A. Arakawa, and S. Prince, 2010: Global and seasonal assessment of interactions between climate and vegetation biophysical processes: A GCM study with different land-vegetation representations. *J. Climate*, **23**(6), 1411–1433, https://doi.org/10.1175/2009JCLI3054.1.

Yao, R., L. C. Wang, X. Huang, X. X. Chen, and Z. J. Liu, 2019: Increased spatial heterogeneity in vegetation greenness due to vegetation greening in mainland China. *Ecological Indicators*, **99**, 240–250, https://doi.org/10.1016/j.ecolind.2018.12.039.

Yin, Y. H., D. Y. Ma, and S. H. Wu, 2018: Climate change risk to forests in China associated with warming. *Scientific Reports*, **8**, 493, https://doi.org/10.1038/s41598-017-18798-6.

Yu, J. J., P. Berry, B. P. Guillod, and T. Hickler, 2021: Climate change impacts on the future of forests in Great Britain. *Frontiers in Environmental Science*, **9**, 640530, https://doi.org/10.3389/fenvs.2021.640530.

Yu, M., G. L. Wang, D. Parr, and K. F. Ahmed, 2014: Future changes of the terrestrial ecosystem based on a dynamic vegetation model driven with RCP8.5 climate projections from 19 GCMs. *Climatic Change*, **127**(2), 257–271, https://doi.org/10.1007/s10584-014-1249-2.

Yu, M., G. L. Wang, and H. S. Chen, 2016: Quantifying the impacts of land surface schemes and dynamic vegetation on the model dependency of projected changes in surface energy and water budgets. *Journal of Advances in Modeling Earth Systems*, **8**(1), 370–386, https://doi.org/10.1002/2015MS000492.

Zeng, X. D., 2010: Evaluating the dependence of vegetation on climate in an improved dynamic global vegetation model. *Adv. Atmos. Sci.*, **27**(5), 977–991, https://doi.org/10.1007/s00376-009-9186-0.

Zeng, X. D., X. B. Zeng, and M. Barlage, 2008: Growing temperate shrubs over arid and semiarid regions in the community land model-dynamic global vegetation model. *Global Biogeochemical Cycles*, **22**, GB3003, https://doi.org/10.1029/2007GB003014.

Zeng, X. D., F. Li, and X. Song, 2014: Development of the IAP dynamic global vegetation model. *Adv. Atmos. Sci.*, **31**, 505–514, https://doi.org/10.1007/s00376-013-3155-3.

Zeng, Z. Z., and Coauthors, 2018: Global terrestrial stilling: Does Earth's greening play a role. *Environmental Research Letters*, **13**(12), 124013, https://doi.org/10.1088/1748-9326/aaea84.

Zhang, H., M. H. Zhang, and Q.-C. Zeng, 2013: Sensitivity of simulated climate to two atmospheric models: Interpretation of differences between dry models and moist models. *Mon. Wea. Rev.*, **141**(5), 1558–1576, https://doi.org/10.1175/MWR-D-11-00367.1.

Zhang, H., and Coauthors, 2020: Description and climate simulation performance of CAS-ESM Version 2. *Journal of Advances in Modeling Earth Systems*, **12**(12), e2020MS002210, https://doi.org/10.1029/2020MS002210.

Zhang, K., and Coauthors, 2015: The fate of Amazonian ecosystems over the coming century arising from changes in climate, atmospheric CO_2, and land use. *Global Change Biology*, **21**(7), 2569–2587, https://doi.org/10.1111/gcb.12903.

Zhu, J. W., and X. D. Zeng, 2015: Comprehensive study on the influence of evapotranspiration and albedo on surface temperature related to changes in the leaf area index. *Adv. Atmos. Sci.*, **32**(7), 935–942, https://doi.org/10.1007/s00376-014-4045-z.

Zhu, J. W., and X. D. Zeng, 2017: Influences of the seasonal growth of vegetation on surface energy budgets over middle to high latitudes. *International Journal of Climatology*, **37**(12), 4251–4260, https://doi.org/10.1002/joc.5068.

Zhu, J. W., M. H. Zhang, Y. Zhang, X. D. Zeng, and X. M. Xiao, 2018a: Response of tropical terrestrial gross primary production to the super El Niño event in 2015. *J. Geophys. Res.*, **123**(10), 3193–3203, https://doi.org/10.1029/2018JG004571.

Zhu, J. W., and Coauthors, 2018b: Evaluation of the new dynamic global vegetation model in CAS-ESM. *Adv. Atmos. Sci.*, **35**(6), 659–670, https://doi.org/10.1007/s00376-017-7154-7.

Zhu, Z. C., and Coauthors, 2016: Greening of the Earth and its drivers. *Nature Climate Change*, **6**(8), 791–795, https://doi.org/10.1038/nclimate3004.

ADVANCES IN ATMOSPHERIC SCIENCES, VOL. 39, AUGUST 2022, 1299–1315

• **Original Paper** •

Characterization of Regional Combustion Efficiency using ΔXCO: ΔXCO_2 Observed by a Portable Fourier-Transform Spectrometer at an Urban Site in Beijing※

Ke CHE[1,2,3], Yi LIU[2,3], Zhaonan CAI[*2], Dongxu YANG[2], Haibo WANG[1,3], Denghui JI[1,3], Yang YANG[1,3], and Pucai WANG[2,3]

[1]*Key Laboratory of Middle Atmosphere and Global Environment Observation*, *Institute of Atmospheric Physics*, *Chinese Academy of Science*, *Beijing* 100029, *China*

[2]*Carbon Neutrality Research Center*, *Institute of Atmospheric Physics*, *Chinese Academy of Science*, *Beijing* 100029, *China*

[3]*University of Chinese Academy of Science*, *Beijing* 100049, *China*

(Received 22 June 2021; revised 17 December 2021; accepted 5 January 2022)

ABSTRACT

Measurements of column-averaged dry-air mole fractions of carbon dioxide and carbon monoxide, CO_2 (XCO_2) and CO (XCO), were performed throughout 2019 at an urban site in Beijing using a compact Fourier Transform Spectrometer (FTS) EM27/SUN. This data set is used to assess the characteristics of combustion-related CO_2 emissions of urban Beijing by analyzing the correlated daily anomalies of XCO and XCO_2 (e.g., ΔXCO and ΔXCO_2). The EM27/SUN measurements were calibrated to a 125HR-FTS at the Xianghe station by an extra EM27/SUN instrument transferred between two sites. The ratio of ΔXCO over ΔXCO_2 ($\Delta XCO{:}\Delta XCO_2$) is used to estimate the combustion efficiency in the Beijing region. A high correlation coefficient (0.86) between ΔXCO and ΔXCO_2 is observed. The $CO{:}CO_2$ emission ratio estimated from inventories is higher than the observed $\Delta XCO{:}\Delta XCO_2$ (10.46 ± 0.11 ppb ppm^{-1}) by 42.54%–101.15%, indicating an underestimation in combustion efficiency in the inventories. Daily $\Delta XCO{:}\Delta XCO_2$ are influenced by transportation governed by weather conditions, except for days in summer when the correlation is low due to the terrestrial biotic activity. By convolving the column footprint [ppm (μmol m^{-2} $s^{-1})^{-1}$] generated by the Weather Research and Forecasting-X-Stochastic Time-Inverted Lagrangian Transport models (WRF-X-STILT) with two fossil-fuel emission inventories (the Multi-resolution Emission Inventory for China (MEIC) and the Peking University (PKU) inventory), the observed enhancements of CO_2 and CO were used to evaluate the regional emissions. The CO_2 emissions appear to be underestimated by 11% and 49% for the MEIC and PKU inventories, respectively, while CO emissions were overestimated by MEIC (30%) and PKU (35%) in the Beijing area.

Key words: FTS, remote sensing, $\Delta XCO{:}\Delta XCO_2$, combustion efficiency, megacity

Citation: Che, K., Y. Liu, Z. N. Cai, D. X. Yang, H. B. Wang, D. H. Ji, Y. Yang, and P. C. Wang, 2022: Characterization of regional combustion efficiency using $\Delta XCO{:}\Delta XCO_2$ observed by a portable Fourier-Transform Spectrometer at an urban site in Beijing. *Adv. Atmos. Sci.*, **39**(8), 1299–1315, https://doi.org/10.1007/s00376-022-1247-7.

Article Highlights:

- Daytime column-averaged dry-air mole fractions of atmospheric CO_2 and CO are provided in urban Beijing based on a portable FTS since 2019.
- The $CO{:}CO_2$ emission ratio estimated by MEIC and PKU is 42.54% and 101.15% higher than the observed $\Delta XCO{:}\Delta XCO_2$ (10.46 ppb ppm^{-1}), indicating an underestimation of the combustion efficiency in inventories.
- The MEIC underestimates CO_2 emissions by about 11% and overestimates 30% CO emissions by 30%; PKU underestimates CO_2 emissions by 49% and overestimates CO emissions by 35%.

※ This paper is a contribution to the special issue on Carbon Neutrality: Important Roles of Renewable Energies, Carbon Sinks, NETs, and non-CO_2 GHGs.

* Corresponding author: Zhaonan CAI
Email: caizhaonan@mail.iap.ac.cn

1. Introduction

The increasing anthropogenic emissions of CO_2 are the main driving force behind global warming induced by greenhouse gases (GHG) (Stocker et al., 2013). Due to increased energy consumption, global fossil CO_2 emissions reached 9.4 ± 0.5 GtC yr^{-1} over the last decade (2007–17) (Le Quéré et al., 2020). The mitigation of anthropogenic GHG emissions is often accompanied by strengthened air pollution controls (West et al., 2013). The toxic air pollutant CO is an indirect greenhouse gas because it produces positive radiative forcing (0.2 W m^{-2}) through its oxidation reaction with hydroxyl radicals (OH) in the troposphere (Myhre et al., 2013). There was a declining trend of 2% yr^{-1} in CO emissions over East Asia during 2005–16, which mainly resulted from the active clean air policies implemented in China (Zheng et al., 2018a), the largest developing and energy-consuming nation in the world with a very high contribution from megacities.

Urban areas account for 2 % of the world's land but are responsible for 40%–70% of the global anthropogenic CO_2 emissions (Satterthwaite, 2008, 2010; Ye et al., 2020). Carbon monoxide (CO) in the urban atmosphere is a product of incomplete combustion alongside the formation of CO_2 during household combustion, industrial activities, and motor transportation, which results in a general positive correlation between CO and CO_2 in urban areas. Due to the relatively short lifetime for CO of only a few weeks, it can serve as an unique tracer for atmospheric fossil-fuel CO_2 emissions and combustion efficiency by analyzing the ratio of CO:CO_2. The estimates of combustion efficiency at the urban scale could be calculated from the CO_2 and CO statistical emission inventories; such an approach is called the "bottom-up" method. Different inventories display significantly different CO_2 and CO emissions in China, especially at regional and city scales (Zhao et al., 2012; Dai et al., 2020). Accurate measurements of GHG and pollutants in cities are essential to yield significant information about the regional carbon budget and to propose strategies to control these emissions ("top-down" method). The correlation between CO and CO_2 could be assessed by directly calculating the slopes of observed CO and CO_2 volume mixing ratios (Wang et al., 2010; Worden et al., 2012). However, the slopes of CO and CO_2 are easily affected by annual background growth and biogenic sources. Thus, regression fits of excess CO (ΔCO) and excess CO_2 (ΔCO_2) from continuous observations have been extensively studied to quantify the anthropogenic contribution to carbon variation and source combustion efficiency (Wunch et al., 2009; Silva et al., 2013; Popa et al., 2014; Feng et al., 2019a; Shan et al., 2019; Cai et al., 2021; Park et al., 2021). Megacities in China show a lower combustion efficiency with a higher $\Delta CO:\Delta CO_2$ ratio than in developed countries (Silva et al., 2013; Silva and Arellano, 2017; Park et al., 2021). Studies in Hefei, China have found the Emissions Database for Global Atmospheric Research (EDGAR) and the Peking University (PKU) emission inventories overestimated $\Delta CO:\Delta CO_2$ in central China during 2015–16 (Shan et al., 2019).

Beijing is located in the northern part of China (Fig. 1). It is in a representative fast-growing economic cycle and is a heavily populated and developed region. The air pollution control policies in Beijing are directly related to the country's overall goals. The total fossil-fuel CO_2 emissions of Beijing shows high uncertainty with ranges from 1 to 8 Mt in 2012 according to different emission inventories and urban regions (~17% relative to the overall land area of Beijing) contributes about 64% CO_2 emissions to the total emissions for Beijing (Han et al., 2020). Satellite observations found the XCO:XCO_2 ratio in Beijing/Tianjin region to be one of the highest in the northern hemisphere due to its rapid economic development (Park et al., 2021). Anthropogenic emissions have been estimated to make a 75.2% contribution to the annual CO_2 enhancement in Beijing in 2014 based on isotopic analysis (Niu et al., 2016). Long-term, highly accurate in situ measurements of CO_2 and CO near the surface have been developed in rural and urban regions of Beijing. The Shangdianzi (SDZ) and Miyun sites are used for rural areas, and the Peking University site is used for urban areas (Han et al., 2009; Wang et al., 2010; Feng et al., 2019a; Dayalu et al., 2020). The ratio, $\Delta CO:\Delta CO_2$, at the Miyun site shows a significant decrease during 2005 to 2008 (Wang et al., 2010). The observation of CO at the SDZ site shows a fast downward trend in 2006–08, is stable in 2009–13, then shows another continuous downward trend after 2013, suggestive of improved combustion efficiencies in response to the Air Pollution Prevention and Control Action Plan implemented in 2013 (Li et al., 2020). The short-term pollution reduction associated with the 2008 summer Olympics and 2020 COVID-19 lockdowns result in a decrease of $\Delta CO:\Delta CO_2$, suggesting increases in combustion efficiency (Wang et al., 2010; Cai et al., 2021).

The "top-down" analysis of combustion efficiency in Beijing comes mostly from satellite and in situ observations. However, in situ surface monitoring measurements are greatly influenced by vertical mixing. The column-averaged dry-air mole fraction (X_{gas}) represents the vertically integrated concentration per dry air and is less affected by the vertical motion than in situ measurements. Therefore, the horizontal gradients of X_{gas} have a more direct relationship with the regional-scale flux (Yang et al., 2007; Wunch et al., 2011; Chen et al., 2016). Satellite observations of XCO_2 combined with XCO show obvious superiority in global coverage and have been used to quantify the correlation between CO_2 and CO for Beijing. However, satellite observation is limited by sampling size and temporal resolution to these specific megacities. Satellites make infrequent visits over cities and are easily affected by cloud, aerosol, and topography issues (Lei et al., 2021), leading to insufficient data for urban emissions studies. The Total Carbon Column Observing Network (TCCON) is an international Fourier-transform spectrometer (FTS) network that was originally used for satellite validation and mainly uses ground-based high-resolution Fourier-transform infrared (FTIR) measurements to record information

about the GHG column. High-resolution FTIR stations in China have been built at Hefei, Xianghe, and Beijing (Wang et al., 2017; Bi et al., 2018; Yang et al., 2020b). Given the poor transportability of TCCON FTS stations, portable, low-cost FTS is useful as a component in long-term urban column measurements. The EM27/SUN instrument (hereafter, EM27) is a compact FTS with its own solar tracker, which is easy to set up and transport anywhere. FTS measurements in or near urban Beijing have mainly focused on satellite validation (Bi et al., 2018; Yang et al., 2020b). To date, few pub-

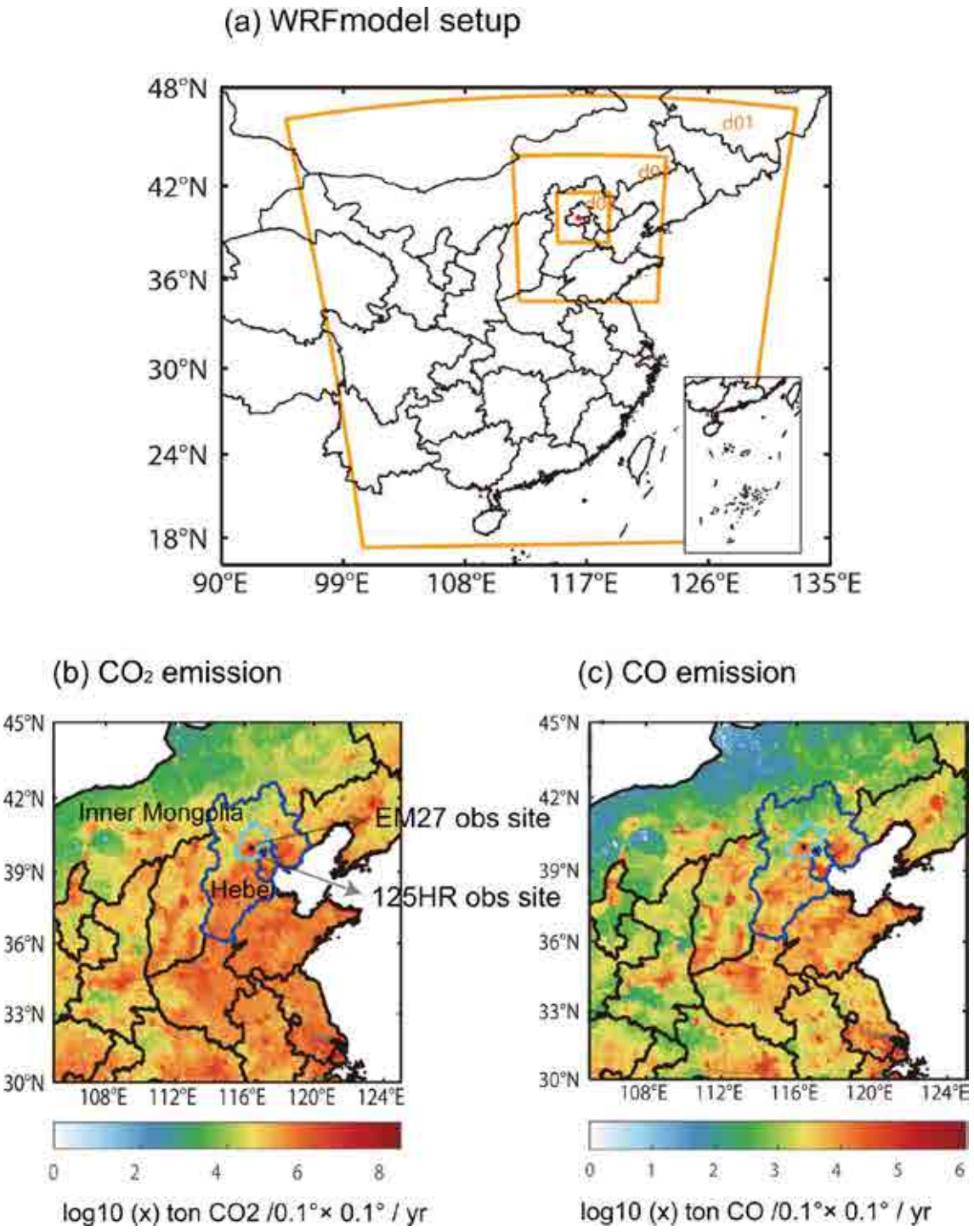

Fig. 1. (a) WRF simulation domains for three grids (27 km, 9 km, 3 km); the red point is the EM27 observation site. The map was taken from a Google satellite image (https://maps.googleapis.com/). Maps of CO_2 (b) and CO (c) emissions in 2014 are based on the PKU fossil-fuel emission dataset. Location of the EM27 site (marked by a star) in the center of Beijing (indicated by the closed turquoise line)–Tianjin–Hebei (BTH) area (indicated by the closed blue line) and 125 HR (marked by a star) in Xianghe, Inner Mongolia, Beijing, Tianjin, Hebei are also shown.

lished studies have rigorously quantified the combustion efficiency in the urban region of Beijing.

In this study, one year of XCO and XCO_2 measurements based on EM27 were collected at an urban site in Beijing. The objectives of this study were to (1) analyze the correlational relationship between observed enhancements of XCO and XCO_2 in urban Beijing, (2) reconcile the differences between top-down estimates of combustion efficiency with bottom-up estimates of combustion efficiency, and (3) evaluate the regional CO_2 and CO emissions estimated from bottom-up inventories using a remote sensing data set. The remainder of this paper is organized as follows. A description of the instrument and method is given in section 2. Section 3 presents the results and discusses their implications and section 4 concludes.

2. Data and methods

2.1. *Instrumentation*

An EM27 has been set up on the roof of the Institute of Atmospheric Physics (IAP) building in Beijing since 2019. The IAP observation site (highlighted in Fig. 1b) is located between the north 3rd and 4th ring road, with heavy traffic and high CO_2 and CO emissions. The EM27 spectral resolution is less than 0.5 cm^{-1}, corresponding to a maximum optical path difference of 1.8 cm. The compound InGaAs (indium gallium arsenide) and an extended InGaAs detector are used to stably detect 3800–14 000 cm^{-1} spectral information for accurate column concentrations of CO_2 and CO (Gisi et al., 2012; Hase et al., 2016). It takes about 60 s to record one individual spectrum with 10 interferograms averaged. The EM27 is equipped with an automated protective case with a rain sensor and a solar irradiation sensor. The cover only opens under cloudless daytime conditions (0000–0900 UTC), protecting the instrument from rain or snow and achieving automated EM27 observations. A WS500 weather station located immediately next to EM27 was used to measure surface temperature and surface pressure with accuracies of 0.2°C and 0.5 hPa, respectively, which were used to correct the a priori temperature profile needed for the XCO_2 and XCO retrievals. The Bruker Optical™ Infrared Fourier Transform Spectrometer (IFS) 125 HR used by TCCON is a high-resolution spectrometer (< 0.02 cm^{-1}) that is tied to the World Meteorological Organization (WMO) scale through numerous aircraft campaigns (Wunch et al., 2010). To ensure data quality, the EM27 has been calibrated in side-by-side experiments with 125 HR (Gisi et al., 2012; Klappenbach et al., 2015; Hedelius et al., 2017; Frey et al., 2019). High-resolution FTIR stations have been built near Beijing and are located in Xianghe, 50 km east-southeast of Beijing (highlighted in Fig. 1a) (Yang et al., 2020b). The 125 HR at the Xianghe site complies with the TCCON specifications and is used as a calibration reference for the EM27 at Beijing in this study.

A portable EM27 could act as a transfer standard between two FTIR stations (Jacobs et al., 2020). In this study, another EM27 (EM27#2) was used as a mobile transfer standard instrument for 125 HR in Xianghe and the EM27 in Beijing. The EM27#2 took measurements side-by-side with IFS 125 HR during the entire month of November 2019. To ensure stability during the shipment of EM27#2 across Beijing to Xianghe, we examined the ratio between EM27s before and after the shipment. Figures 2a and 2b show the biases between 125 HR and EM27#2. The correction equations are also shown in the figure. Figures 2c and 2d show that the ratio was consistent before and after the shipments (detailed in section 2.2), indicating that the calibration of EM27#2 and 125 HR in Xianghe could be applied to the EM27 retrieval in Beijing. The IFS 125 HR retrievals apply the TCCON standard retrieval code (GGG2014), and the EM27 uses PROFFAST, with the same meteorological data and preliminary profiles input. The results for EM27#2 show a systematic bias with 125 HR, which could be corrected by applying a linear fitting correction function (Figs. 2a and 2b). The biases between EM27 and 125HR are 0.28% and 5.3% for XCO_2 and XCO, respectively.

2.2. *EM27 data processing*

A non-linear least-squares fitting retrieval algorithm (PROFFAST) (Hase et al., 2004) is used to analyze the spectra recorded by EM27. The algorithm has been officially used in the EM27 network, COCCON (the COllaborative Carbon Column Observing Network) (Frey et al., 2019). To obtain a high-quality spectrum, the pre-processing steps involve a direct current (DC) correction (Keppel-Aleks et al., 2007), a Norton–Beer medium apodization (Naylor and Tahic, 2007), a fast Fourier transform (Bergland, 1969), and a phase correction (Mertz, 1967). The a priori profiles obtained by TCCON are the official a priori profiles (Toon and Wunch, 2015). The inverse algorithm obtains the scaled target gas column by iteratively updating the state variables to best fit the simulated and measured spectra. Finally, the gas column (C_{gas}) is converted to a dry-air column-averaged mole fraction (denoted X_{gas}) by dividing the gas column by the simultaneously retrieved column-averaged dry-air mole fractions (C_{air}) Columnair, where C_{air} could be calculated from the O_2 column combined with the volume fraction of O_2 in the air (20.95%):

$$X_{gas} = \frac{C_{gas}}{C_{air}}. \quad (1)$$

In the post-processing process, column averaging kernels (AK) describe the altitude-dependent sensitivity of the retrieved state to the true state. As shown in Fig. 3, AK differs among instruments with different spectral resolutions. EM27 is more sensitive to changes at lower levels than 125 HR, especially for high solar zenith angles (SZAs). A pressure weighting function (PW) is used to weight the pressure thicknesses of each level (ΔP) relative to the surface pressure (P_{surf}) :

$$PW = \frac{\Delta P}{P_{surf}}. \quad (2)$$

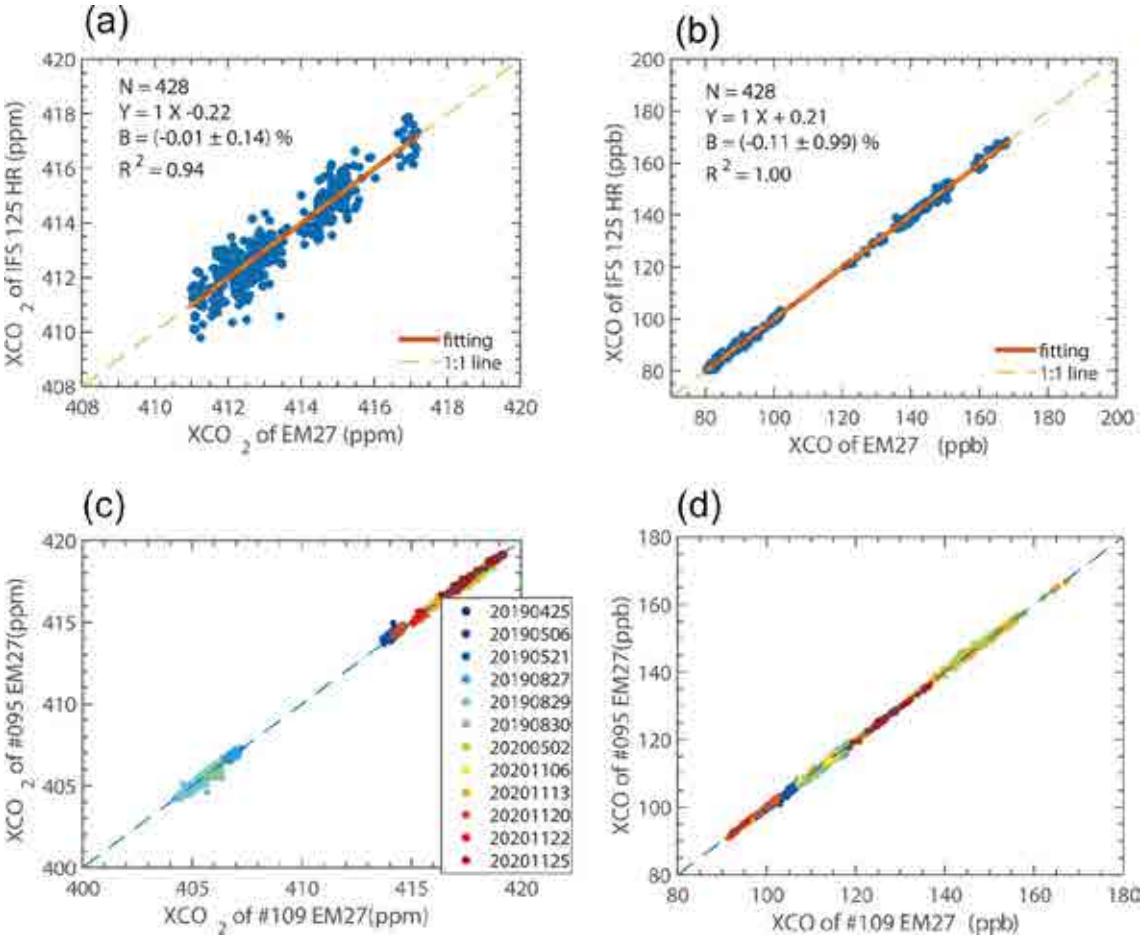

Fig. 2. (a–b) Scatter plots of XCO_2 and XCO from 125 HR and EM27#2 side-by-side measurements over the Xianghe Observatory. N is the number of comparison points, B is the bias between the two instruments, R^2 is the correlation coefficient, and the equation has the linear fit. (c–d) Scatter plots of EM27 against EM27#2 for different days before and after the EM27#2 transfer calibration campaign. The ratio is the proportional coefficient of EM27 (the result for EM27#2 has been taken as a reference).

2.3. *WRF - XSTILT model*

A Lagrangian particle dispersion model (LPDM) models a plume of atmospheric tracers from a cluster of particles. It can determine the footprint (also called an influence function or adjoint sensitivity) of multiple air parcels released from an observation site (receptor). The WRF-XSTILT, an LPDM model, is adopted to analyze the meteorologically-induced gas concentration variation by a regional column footprint simulation (Lin et al., 2003; Fasoli et al., 2018; Wu et al., 2018). The footprint is used to establish the source–receptor relationship and determine the distribution spread of entire plumes in adjacent cells over the receptor by calculating the sensitivity of the surrounding region (source) to the receptor. The column footprint (X_{foot}) is essential for tracking the air masses for column measurements. The parameter X_{foot} is the sensitivity of the column measurements to the upstream and downstream surface-atmosphere fluxes. The formula to calculate X_{foot}, with units of ppm (μmol $(m^2\ s)^{-1})^{-1}$, for each receptor is as follows:

$$X_{\text{foot}}(x_r,t_r|x_i,y_i,t_{\text{m}}) = \frac{m_{\text{air}}}{h\overline{\rho}(x_i,y_i,t_{\text{m}})}\times \frac{1}{N}\sum_{i=1}^{N}\Delta t_i(x_i,y_i,t_{\text{m}})\text{AK}(r)\text{PW}(r)\,, \quad (3)$$

where (x_r,t_r) is the receptor (r) location, (x_i,y_i,t_{m}) is the model's initial time set, denoted by the model grid coordinates of location and time, m_{air} is the mean molar mass of dry air (29 g mol^{-1}), h is the atmospheric column height (in XSTILT h is set at half the planetary boundary layer (PBL) depth), $\overline{\rho}$ is the mean density of the air below h, N is the total number of released particles, Δt_i is the residence time of particle i spent in the grid cell (x_i,y_i,t_{m}). The total column footprint X_{foot} is the integrated footprint from different vertical altitudes convolved with a pressure weighting function PW(r) and averaging kernel AK(r) at the receptor, which links the emission sensitivity to the observations. In the model setup, we applied the WRF model configurations verified by Dayalu et al. (2020) for the same study domains (Fig. 1a). The receptor site of X-STILT was set up at IAP

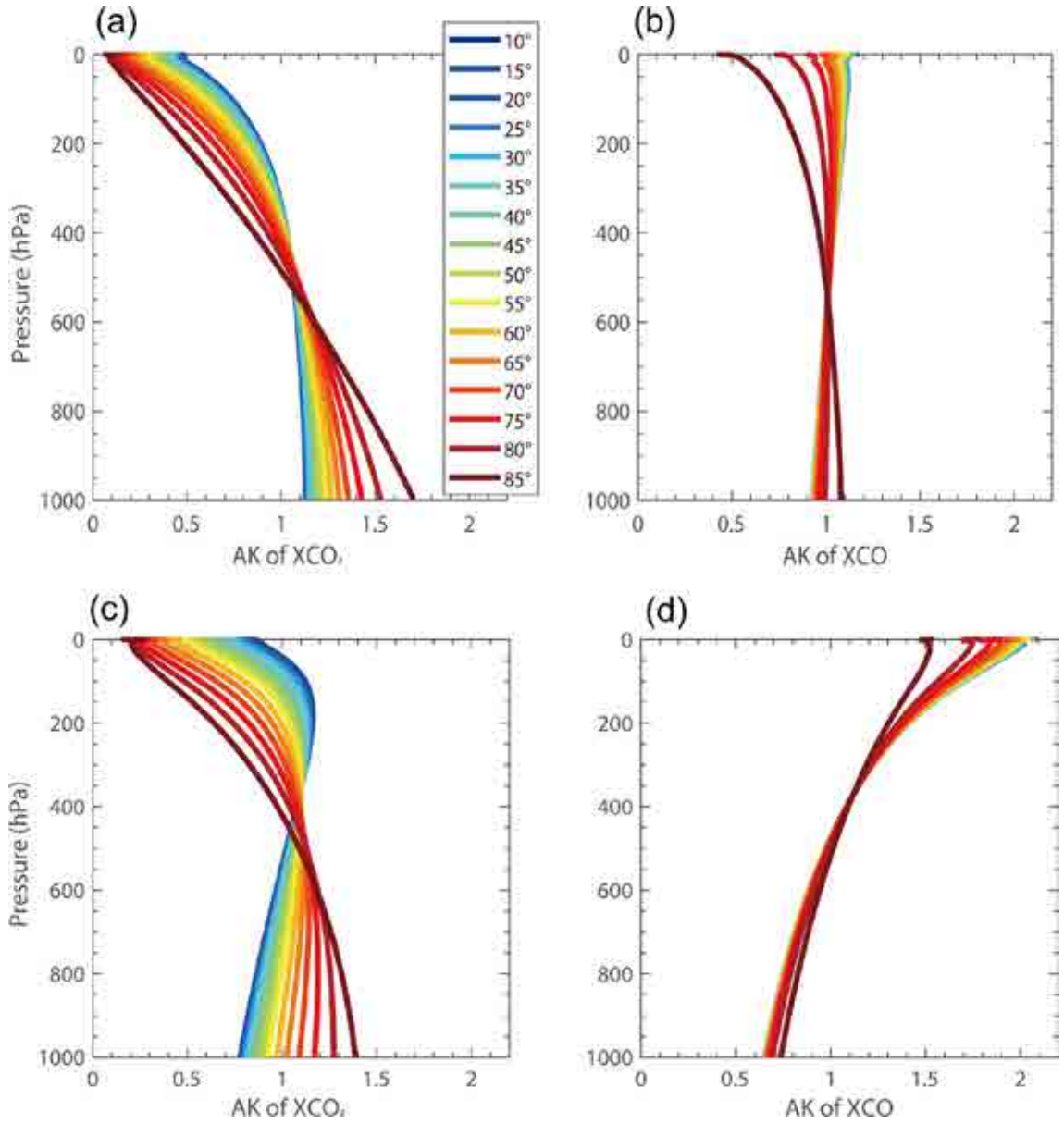

Fig. 3. A comparison of the column-averaged kernels at different SZAs for EM27 (a–b) and 125 HR (c–d).

and was run backward for seven days at a 0.25° × 0.25° spatial resolution to generate hourly column footprints. In each simulation, 100 air parcels are released every 100 m within 3 km and every 500 m from 3 to 6 km relative to the observation level, which tends to be denser near the surface. Higher altitudes are not used since only the lower atmosphere interacts with local emissions in the region (Hedelius et al., 2018). The AK and PW (detailed in section 2.2) of EM27 are used to weight and integrate the footprints of all levels to the column footprint and could be directly obtained from the output of the EM27 retrieval.

2.4. *The ΔXCO:ΔXCO$_2$ calculation method*

2.4.1. *Calculation of ΔXCO and ΔXCO$_2$ from measurements*

The observed regression slope of ΔXCO against ΔXCO_2 denotes the amount of CO per CO_2 emissions in the atmosphere that has been captured by the FTS, signifying the emission ratio or combustion efficiency. A larger slope of the regression line reveals greater combustion efficiency in the observed XCO_2. Wunch et al. (2009) proposed that the X_{gas} anomaly (ΔX_{gas}) could be calculated by subtracting X_{gas} in the morning from the afternoon value at the same SZA. The anomalies are divided by the AK at the surface to account for the sensitivity of the column measurement to surface variations because diurnal changes are assumed to be confined to the boundary layer. This method could minimize the atmospheric effects from background or natural sources and the SZA-dependent error. The ΔXCO:ΔXCO_2 ratio, calculated from the diurnal enhancement, is denoted as $(\Delta XCO:\Delta XCO_2)_d$.

Apart from the method based on diurnal variation,

ΔXCO and ΔXCO_2 could be estimated from the regional change relative to the background. The observation site at urban Beijing records the pollution-related signal of XCO and XCO_2. The quantification of background XCO_2 concentration is the sum of the boundary and biogenic XCO_2 values.

The boundary XCO_2 value was obtained from trajectory endpoint of the Copernicus Atmosphere Monitoring Service (CAMS) satellite-derived global inversion-optimized mean column concentrations data (http://atmosphere.copernicus.eu/, version: v20r3, last access: 7 June 2021) (Chevallier et al., 2005; Chevallier et al., 2010; Chevallier et al., 2019). These trajectories were derived from the Weather Research and Forecasting-Column Stochastic Time Inverted Lagrangian Transport (WRF-XSTILT). According to the validation report for the CAMS v19r1 data by Chevallier et al. (2020), the biases of modeled XCO_2 data show less bias (less than 1 ppm) in a non-urban area when compared to the TCCON retrieval results. The background XCO_2 values obtained from CAMS were mostly from the region less affected by human activities, so the CAMS background values were considered to be plausible. Biogenic XCO_2 values were from the convolution of the column footprint generated by WRF-XSTILT and the CO_2 vegetation flux. The CO_2 vegetation flux comes from a global gridded terrestrial carbon flux product developed by Zeng et al. (2020). Due to unavailable XCO background data, XCO background values were simply obtained from the lowest observed XCO. Similar to the diurnal method described above, the AK at the surface was also taken into account in calculating the anomalies. The ratio $\Delta XCO{:}\Delta XCO_2$ calculated from regional enhancement is denoted as $(\Delta XCO{:}\Delta XCO_2)_r$.

2.4.2. *Calculation of ΔXCO and ΔXCO$_2$ from bottom-up inventories*

The simulated regression slope of ΔXCO against ΔXCO_2 represents the regional XCO enhancement per XCO_2 enhancement contributed from different sources transported to the observation site. A simple way to simulate $\Delta XCO{:}\Delta XCO_2$ directly from the emission inventories in a specific geometrical shape is as follows (Wunch et al., 2009; Hu et al., 2019; Shan et al., 2019)

$$\left(\frac{\Delta XCO}{\Delta XCO_2}\right)_{sim} = \frac{\frac{E_{CO}}{E_{CO_2}}}{\frac{M_{CO}}{M_{CO_2}}}. \quad (4)$$

Here, E_{CO} and E_{CO_2} are the CO and CO_2 emissions in the specific area, M_{CO} and M_{CO_2} are the molecular masses of CO and CO_2, and $(\Delta XCO/\Delta XCO_2)_{sim}$is the simulated correlation slope of XCO to XCO_2.

The parameters ΔXCO and ΔXCO_2 can be simulated by the convolution of the source footprint function (modeled by the Lagrangian atmospheric transport model) and the anthropogenic flux inventories defined as follows:

$$\left(\frac{\Delta XCO}{\Delta XCO_2}\right)_{sim} = \frac{X_{foot,co} \times E_{CO}}{X_{foot,co_2} \times E_{CO_2}}, \quad (5)$$

where the simulated ΔXCO and ΔXCO_2 are the modeled hourly anthropogenic enhancement from different sources. The E_{CO_2} (E_{CO}) and is represented by the CO_2 (CO) surface anthropogenic emissions. The footprint quantifies the sensitivity of the measurements to emissions in terms of unit concentration per unit flux. Simulated ΔXCO and ΔXCO_2 values based on this method are divided by AK at the surface to account for the sensitivities of column measurements near the surface. We focused on simulations from 1100–1600 local standard time (LST, UTC + 8 h) consistent with the time that the atmosphere is well-mixed and the depth of planetary boundary layer (PBL) grow to approach its maximum in the late morning due to the solar heating of the surface. The PBL, in turn, collapses at sunset due to surface cooling, which increases the difficulty of simulation. We selected this period so that the footprint generated by X-STILT would be less susceptible to modeled PBL uncertainties (Sargent et al., 2018).

E_{CO_2} (E_{CO}) is obtained from monthly gridded fossil-fuel emission databases. Fossil-fuel emission products come from Peking University (PKU) and the Multi-resolution Emission Inventory for China (MEIC). The PKU product provides global CO and CO_2 grid emission maps up to 2014 with 0.1° spatial resolution according to a sub-national disaggregation of fuel data (Wang et al., 2013). The MEIC product provides China's CO and CO_2 grid emission maps up to 2017 with 0.25° spatial resolution, including the local emission information for each power plant and industrial operation (Zheng et al., 2020). The Temporal Improvements for Modeling Emissions by Scaling (TIMES) developed by Nassar et al. (2013) is applied to the MEIC and PKU products to derive diurnal CO_2 emissions. Due to unavailable temporal variations for CO, we simply averaged the monthly CO emissions and assigned them to each hour. The MEIC and PKU products provide gridded regional emissions up to 2017 and 2014, respectively. Owing to the lack of an emission trend in Beijing, we apply the inter-annual variation of CO_2 emissions in China until 2019, as concluded from Crippa et al. (2020). Due to the unavailability of CO emissions up to 2019, a mean decreasing rate in East Asia of 2% was applied, estimated from the top-down inversion method based on MOPITT data from 2005 to 2016 (Zheng et al., 2018a).

3. Results and discussion

3.1. *Time series of XCO and XCO$_2$*

The monthly means and standard deviation of XCO_2 and XCO at mid-latitude stations in the northern hemisphere are displayed in Fig. 4. These include FTIR stations in Beijing, Pasadena (34.14°N) (Wennberg et al., 2017), Xianghe (39.75°N) (Yang et al., 2020b), Karlsruhe (49.10°N) (Hase et al., 2017), Tsukuba (36.05°N) (Morino et al., 2018), and Paris (48.97°N) (Té et al., 2017). Table 1 summarizes the sea-

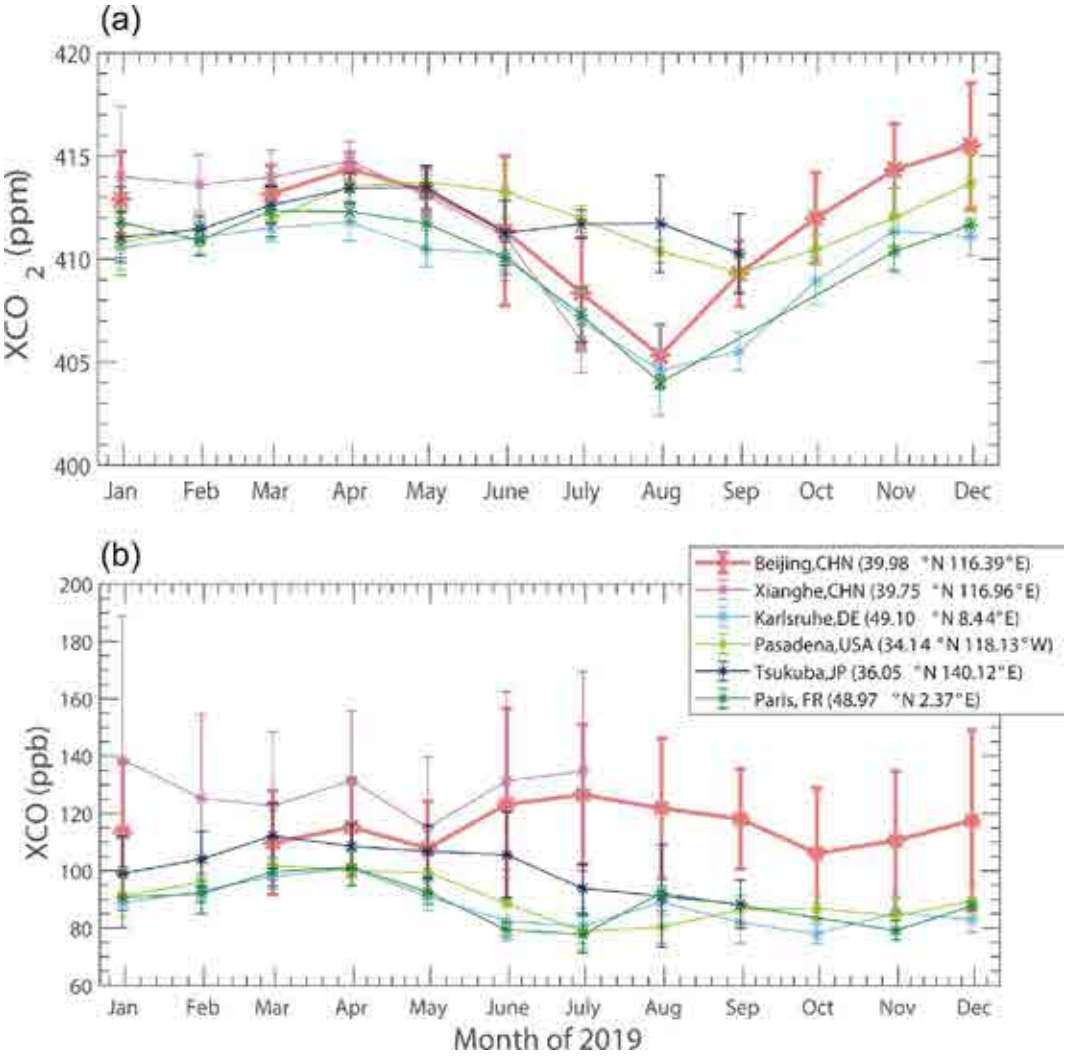

Fig. 4. Monthly variations in (a) XCO_2 and (b) XCO observed at Beijing, Xianghe, Karlsruhe, Pasadena, Tsukuba, and Paris during 2019. The geographical coordinates of each site are shown in the figure legend. The error bars are the monthly standard deviation of XCO_2 and XCO.

sonal mean and standard deviation of XCO_2 and XCO. There is no data recorded in February, which may cause a bias because anthropogenic XCO_2 enhancements during the Spring Festival should be significantly lower than normal. The XCO_2 values in Beijing ranged from 402 ppm to 423 ppm in 2019. The seasonal variation in XCO_2 achieves its peak in winter (414.33 ± 2.65 ppm), followed by spring (413.58 ± 1.25 ppm) and autumn (412.09 ± 2.88 ppm), and is lowest in summer (407.87 ± 3.34 ppm). The features of the XCO_2 seasonal variation in Beijing are similar to observations from other FTIR observation sites in the mid-latitude northern hemisphere. Intensity of photosynthesis, which is related to the latitude of the observation site, is the main reason for the seasonality in XCO_2 variation. The peak and trough of monthly XCO_2 means were found in December (415.72 ± 3.18 ppm) and August (404.87 ± 1.47 ppm), respectively, which differ slightly from other FTIR stations. The monthly XCO_2 in Paris, Park Falls, Karlsruhe, and Xianghe stations reach a peak in March to April, whereas Pasadena and Beijing stations reach a peak in December. The monthly XCO_2 of Beijing, Xianghe, Paris, Park Falls, Karlsruhe reach a trough in August, whereas Pasadena reaches a trough in September.

Table 1. Seasonal variability of average XCO_2 and XCO in 2019 observed by EM27.

Season	XCO_2 (ppm)	XCO (ppb)
Spring (March to May)	413.58 ± 1.25	109.58 ± 5.49
Summer (June to August)	407.87 ± 3.34	120.50 ± 4.28
Autumn (September to November)	412.09 ± 2.88	112.37 ± 5.58
Winter (December to February)	414.33 ± 2.65	115.78 ± 3.36

Values of XCO ranging from 85 to 192 ppb are observed in Beijing. The XCO in Beijing was higher than the values from other cities in the northern hemisphere and

lower than that of the Xianghe station (Fig. 4b), implying the presence of high regional emissions in the Beijing–Xianghe region. As can be concluded from Table 1, XCO is highest in summer (120.50 ± 4.28 ppb), followed by winter (115.78 ± 3.36 ppb) and autumn (112.37 ± 5.58 ppb), and is lowest in spring (109.58 ± 5.49 ppb). The seasonal variation in Beijing is similar to the variation in Xianghe. The increase of CO during winter in Beijing could be from the increased heating time of vehicle catalysts at low temperatures (Han et al., 2009) and domestic heating. The seasonal variations in Karlsruhe, Pasadena, and Paris show XCO values that are highest in spring and lowest in summer and autumn. The XCO in summer for the Beijing-Xianghe region presents a seasonal variation opposite of the other three urban sites. Carbon monoxide (CO) reaches a minimum during summer at those sites due to strong ultraviolet radiation and high humidity, facilitating the formation of OH, which consumes more CO in the atmosphere (Té et al., 2016; Li et al., 2020). Carbon monoxide (CO) concentration was also found to be lowest in summer from 2006 to 2018 at the Shangdianzi (SDZ) in situ site, a rural region near Beijing (Li et al., 2020). This result is consistent with the Karlsruhe, Pasadena, and Paris sites. The high XCO values in summer observed in urban Beijing and Xianghe could be associated with strong anthropogenic emissions.

3.2. *ΔXCO:ΔXCO$_2$ correlation observed by the FTS*

Carbon monoxide (CO) is co-emitted and co-transported to the observation site with CO_2. The slopes of ΔXCO to ΔXCO_2 reflect the overall combustion efficiency of the observed airmass. Figure 5 shows the daily regression slope and the Pearson correlation coefficients (R^2) of ΔXCO and ΔXCO_2 based on the diurnal variation method. Daily regression slopes are mostly around 10 ppb ppm^{-1}. Daily correlation coefficients are generally larger than 0.5 on 78% of the observation days. Significant positive correlations between ΔXCO to ΔXCO_2 in winter, spring, and autumn indicate that most air parcels originate from combustion sources. Approximately 61% of the daily correlation coefficients in summer (grey shaded region in Fig. 5) are small (< 0.1) and even negative, and the regression slope shows large uncertainties. This suggests that CO_2 emissions are dominated by non-CO-related sources in summer. In situ observations near Beijing also captured the low correlation in summer (Wang et al., 2010). The main reason is that the CO_2 signals were significantly mixed with enhanced biospheric CO_2 uptake during the growing season, which could offset the anthropogenic emissions in urban areas. It is necessary for CO and CO_2 to

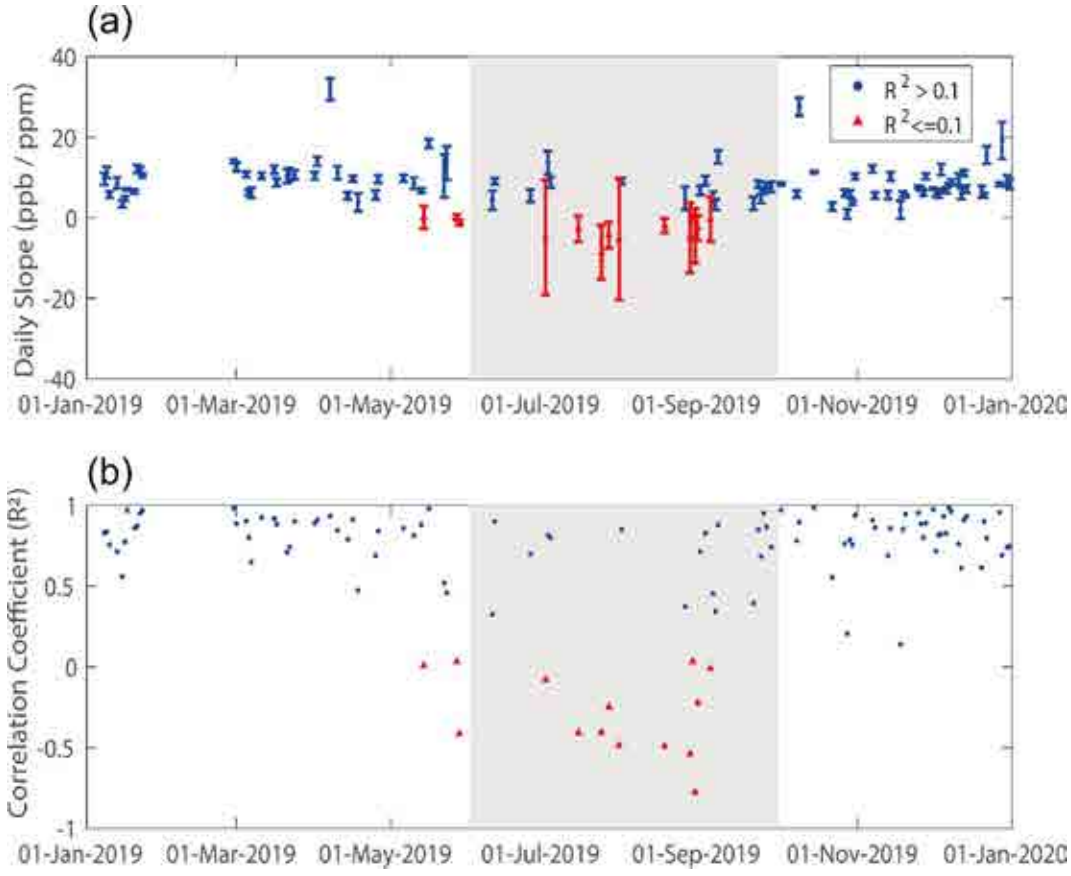

Fig. 5. (a) The time series of the daily slope of ΔXCO and ΔXCO_2 observed by EM27 over IAP. The error bar represents the confidence bounds for the slope estimates. (b) The time series of correlation coefficient (R^2) of ΔXCO and ΔXCO_2. The red triangles represent observations with R^2 less than 0.1, and the blue circles represent R^2 larger than 0.1. Summertime is indicated by grey shading.

share a common combustion process when using CO as the anthropogenic tracer for CO_2 to investigate regional combustion efficiency. One straightforward approach is to remove the observations in the growing season (Wang et al., 2010; Shan et al., 2019). Still, we found some strong correlation days in summer (Fig. 5b), so we excluded the non-CO-related observations ($R^2 \leqslant 0.1$). Before filtering the data, $(\Delta XCO{:}\Delta XCO_2)_d$ observed for urban Beijing is 8.94 ± 0.13 ppb ppm^{-1} with an R^2 of 0.80. Removal of the strong biologically-affected days contributed to the elevated $(\Delta XCO{:}\Delta XCO_2)_d$ of 10.46 ± 0.11 ppb ppm^{-1} and an R^2 of 0.86.

We extended our analysis to comparisons of $(\Delta XCO{:}\Delta XCO_2)_d$ based on other FTS station datasets of the mid-latitude northern hemisphere in and around 2019 (Table 2). The FTS stations are set up in either an urban or suburban environment with varied emissions sources: the Pasadena site is located on the southern coastal air basin of California with a population of nearly 17 million, the Tsukuba site is located in a highly urbanized city near Tokyo with a population of 2.28 million, the Paris site is in the most populous city in France (2.24 million), the Karlsruhe site is a smaller urban region surrounded by forest, which has a population of nearly 0.3 million. Stronger correlations between ΔXCO and ΔXCO_2 exist with high regression slope values in the densely populated urban regions (Beijing, Pasadena, Tsukuba, Paris, and Karlsruhe). The values of $(\Delta XCO{:}\Delta XCO_2)_d$ observed in Chinese cities (10.46 ppb ppm^{-1} in Beijing, 6.76 ppb ppm^{-1} in Xianghe) are significantly higher than stations in other nations. In addition, $(\Delta XCO{:}\Delta XCO_2)_d$ in Beijing is the highest among all the cities we included, implying a high pollution per amount of CO_2 emissions and relatively lower combustion efficiency over Beijing.

According to the in situ observations, Wang et al. (2010) found a $\Delta CO{:}\Delta CO_2$ value of 41.7 ppb ppm^{-1} at the Miyun background site in Beijing from 2007 to 2008. Han et al. (2009) derived a $\Delta CO{:}\Delta CO_2$ value of 43.4 ppb ppm^{-1} during the 2006 winter at an urban site in Beijing. Using XCO retrievals from NASA/Terra Measurement of Pollution in the Troposphere (MOPITT) and XCO_2 retrievals from the Japan Aerospace Exploration Agency Greenhouse gases Observing Satellite (GOSAT), Silva et al. (2013) estimated $\Delta XCO{:}\Delta XCO_2$ in Beijing/Tianjin to be 43.5 ppb ppm^{-1} from 2009 to 2010. These values are significantly larger than our estimated value (10.46 ppb ppm^{-1}). The reason could be that China has implemented pollution control policies since 2013. As a result, the combustion efficiency significantly increased as CO emissions decreased (Zheng et al., 2018b; Feng et al., 2019b; Li et al., 2020). Shan et al. (2019) estimated $\Delta CO{:}\Delta CO_2$ to be 15.99, 8.02, and 5.67 ppb ppm^{-1} based on in situ, ground-based FTS, and satellite measurements (GOSAT, MOPITT), respectively, at Hefei from 2015 to 2016. Li et al. (2020) estimated $\Delta CO{:}\Delta CO_2$ to be 25.5 ppb ppm^{-1} at the SDZ site near Beijing in 2018. The $\Delta XCO{:}\Delta XCO_2$ value we calculated (10.46 ppb ppm^{-1}) is close to the value estimated from ground-based FTS at Hefei in 2015–16 (8.02 ppb ppm^{-1}) and is about 60% lower than the near-surface observed value at SDZ (25.5 ppb ppm^{-1}). The value of $\Delta CO{:}\Delta CO_2$ based on FTS (8.02 ppb ppm^{-1}) at Hefei is about 50% lower than in situ observations (15.99 ppb ppm^{-1}) (Shan et al., 2019). In situ observations only capture the near-surface signal of a small sampling area in the local planetary boundary layer. In contrast, the FTS observations detect the whole layer of the atmosphere, which may weaken the near-surface signal. The FTS observations have larger footprint compared to in situ observations and could be more representative to the regional flux (Wunch et al., 2016)

3.3. *Effect of regional transportation on ΔXCO:ΔXCO$_2$*

Transportation governed by weather conditions plays an important role in the day-to-day variations in CO and CO_2 in Beijing (Feng et al., 2019a; Panagi et al., 2020). Air pollution is concentrated in Beijing's southern and eastern parts (Feng et al., 2019a). We identified source regions for each observation based on X-STILT footprints. Pathways are characterized by sources in the northwest (NW) and north China plain (NCP) according to the year-round average 24-hour backward footprints (Figs. 6c and 6e), which share 62.93% and 26.72% of the observation days, respectively. Higher XCO_2 and XCO occurred when air masses originated from the NCP region. Clean air masses originating from the NW are less affected by human activities, which may cause the observed decrease in XCO_2 and XCO.

When an air mass passes over different source regions, the correlation between CO and CO_2 shows different patterns. As shown in Figs. 6b and 6d, $(\Delta XCO{:}\Delta XCO_2)_d$ originating from the clean region is 8.23 ± 0.1 ppb ppm^{-1} and from the polluted region is 11.46 ± 0.2 ppb ppm^{-1}. Advection that brings air masses containing emissions from the NCP contributed to an elevated proportion of $(\Delta XCO{:}\Delta XCO_2)_d$,

Table 2. Comparison of $\Delta XCO{:}\Delta XCO_2$ in different FTS stations close or within the urban area in the northern hemisphere.

FTS station (longitude, latitude)	Time period	$\Delta XCO{:}\Delta XCO_2$ (ppb ppm^{-1})	R^2
Beijing, CHN (39.98°N, 116.39°E)	2019.1–2019.12	10.46 ± 0.11	0.86
Xianghe, CHN (39.75°N, 116.96°E)	2018.7–2019.7	6.76 ± 0.70	0.52
Karlsruhe, DE (49.10°N, 8.44°E)	2018.1–2019.12	1.84 ± 0.21	0.52
Pasadena, US (34.14°N, 118.13°E)	2019.1–2019.12	4.06 ± 0.18	0.61
Tsukuba, JP (36.05°N, 140.12°E)	2018.1–2019.9	4.68 ± 0.22	0.58
Paris, FR (48.97°N, 2.37°E)	2019.1–2019.12	3.06 ± 0.06	0.76

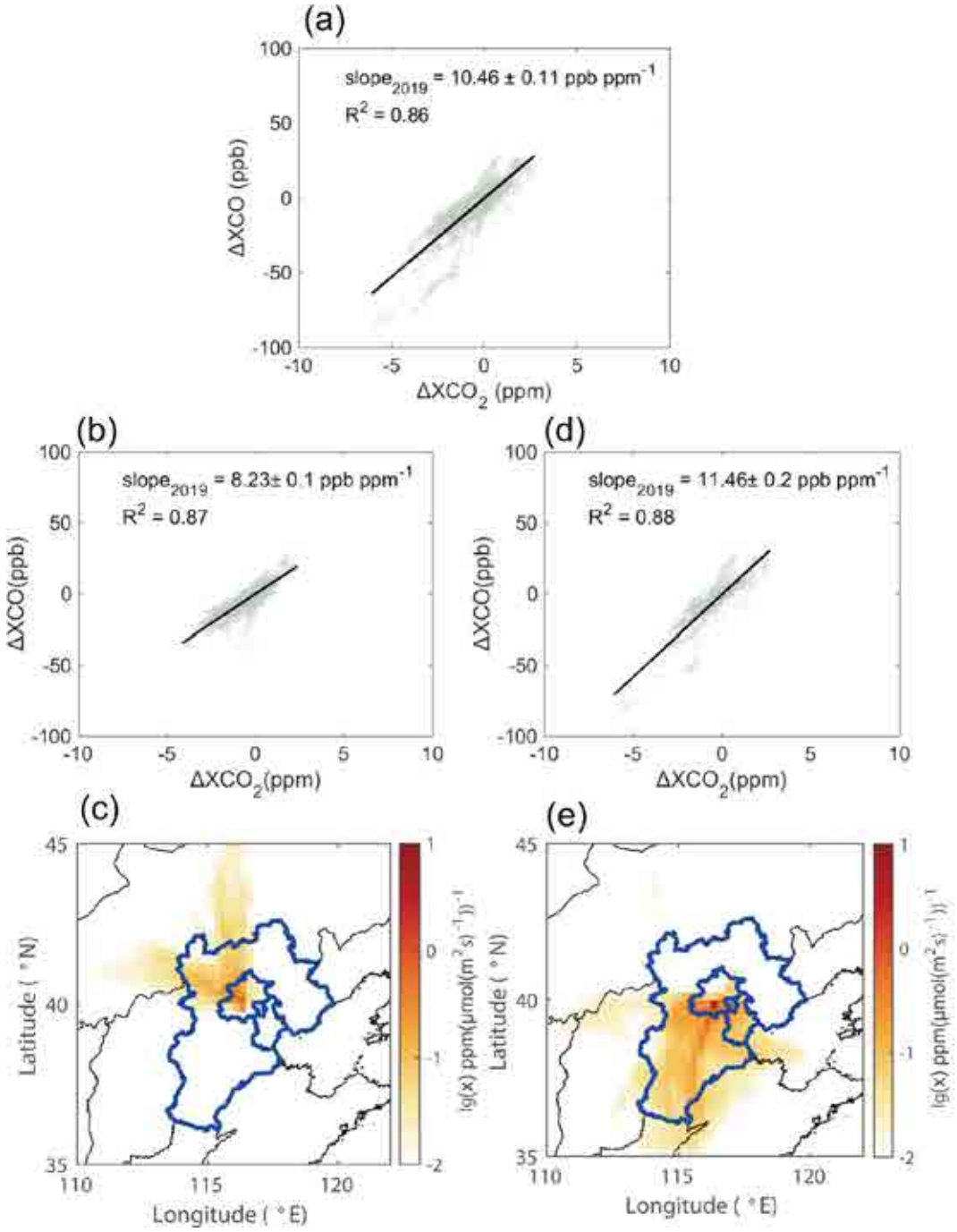

Fig. 6. (a) Correlations of ΔXCO and ΔXCO_2 in 2019. (b, d) Correlations of ΔXCO and ΔXCO_2 in 2019 originating from the NW and NCP upwind sources. R^2 is the correlation coefficient of ΔXCO and ΔXCO_2. $slope_{2019}$ is the regression slope of ΔXCO and ΔXCO_2. (c, e) Maps of mean 24-hour backward footprint [ppm / (μmol m^{-2} s^{-1}), lg(*x*)] with 0.25° resolution at IAP, Beijing, starting at 1200 LST in 2019, originating from the NW (c) and NCP (e). The closed blue line indicates the BTH area. Only footprint values larger 10^{-2} ppm / (μmol m^{-2} s^{-1}) are displayed.

which exceeded the annual slope (10.46 ± 0.11 ppb ppm^{-1}).

3.4. *Comparison of the observed and modeled regional XCO_2 and XCO enhancement*

The regression slope of $\Delta XCO{:}\Delta XCO_2$, based on the regional enhancement method $(\Delta XCO{:}\Delta XCO_2)_r$, is estimated to be 9.06 ± 1.89 ppb ppm^{-1}, which is consistent with the value of $(\Delta XCO{:}\Delta XCO_2)_d$ (10.46 ± 0.11 ppb ppm^{-1}). The ratio $(\Delta XCO{:}\Delta XCO_2)_d$ is calculated solely based on the diurnal variation observed by EM27. In contrast, $(\Delta XCO{:}\Delta XCO_2)_r$ is estimated by subtracting the background value from the observations. Uncertainty in background value yields more uncertainty for $(\Delta XCO{:}\Delta XCO_2)_r$ compared to $(\Delta XCO{:}\Delta XCO_2)_d$.

The estimated values for ΔXCO and ΔXCO_2 from regional enhancement versus the background were used for comparison with the model simulation at hourly timescales (Figs. 7 and 8). The modeled ΔXCO_2 (hereafter $\Delta XCO_{2,sim}$) was simulated from the MEIC and PKU anthropogenic emission inventories ($\Delta XCO_{2,\ MEIC}$ and $\Delta XCO_{2,\ PKU}$). The observed enhancement ΔXCO_2 (hereafter $\Delta XCO_{2,obs}$) was the difference between the observed urban XCO_2 ($XCO_{2,obs}$) and the XCO_2 background ($XCO_{2,back}$) from model. Summer data is excluded due to the unavailable background data for CO (detailed in the next paragraph). The same trend is shared by $XCO_{2,back}$ and $XCO_{2,obs}$ as shown in Fig. 7a.

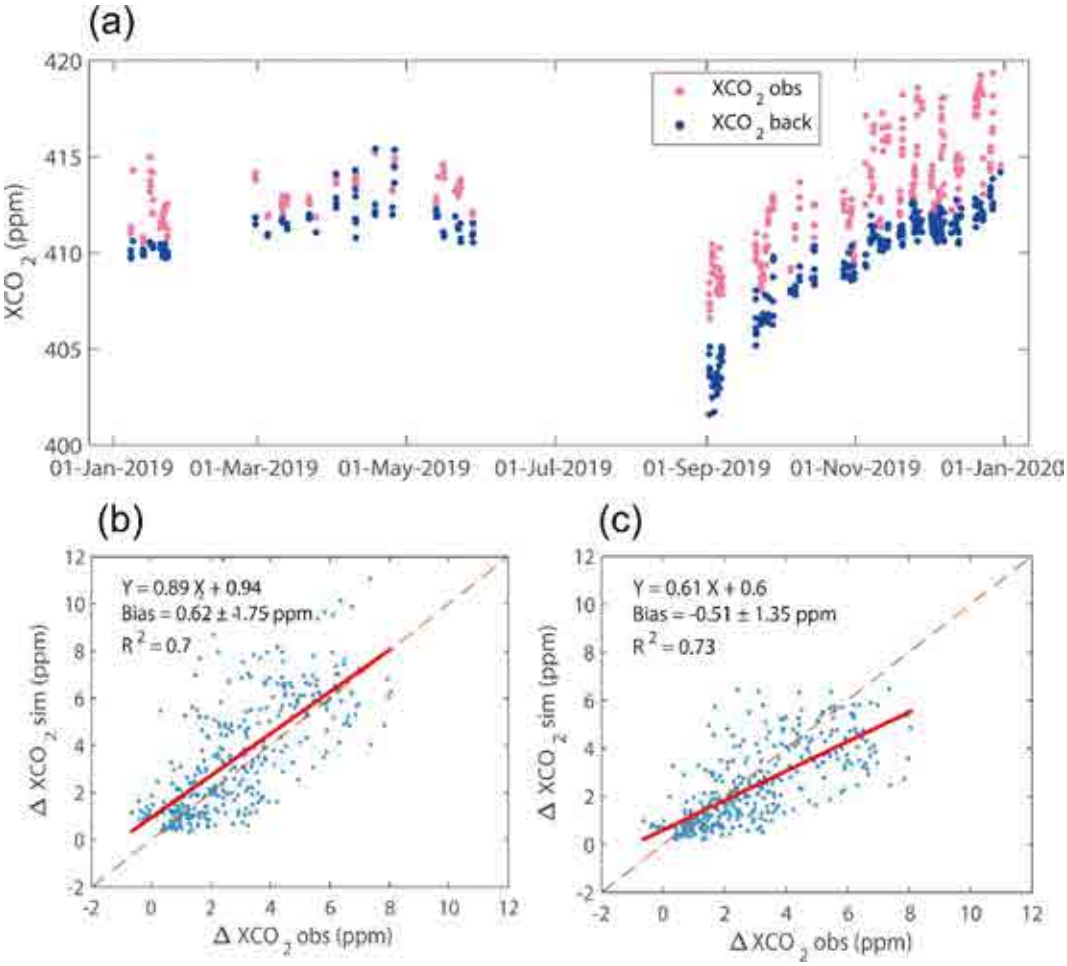

Fig. 7. (a) Measured XCO_2 and CAMS background concentration. (Only 1100 to 1600 LST periods are displayed). (b–c) Hourly measured and modeled regional enhancement ΔXCO_2 for each fossil-fuel emission inventory (b for MEIC, c for PKU).

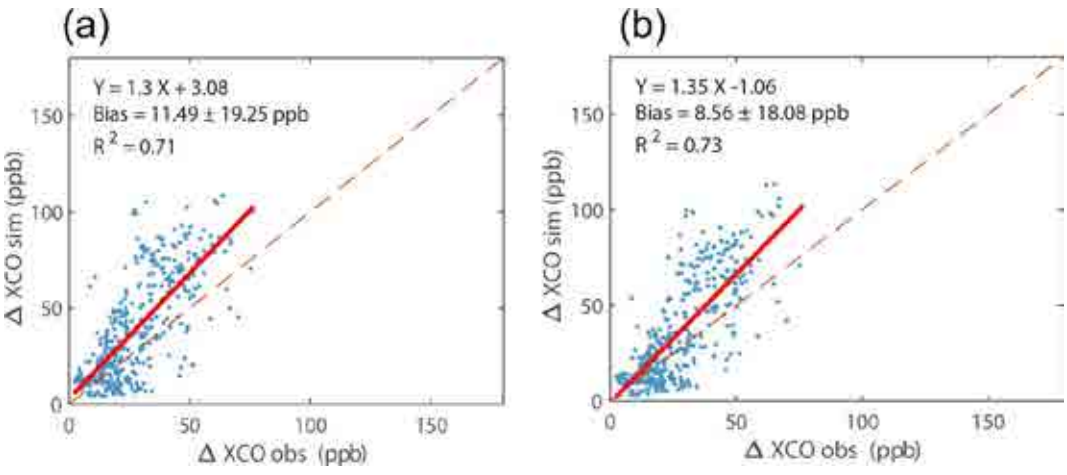

Fig. 8. Hourly measured and modeled XCO for (a) MEIC and (b) PKU.

Figures 7b and 7c show the correlation between $\Delta XCO_{2,obs}$ and $\Delta XCO_{2,sim}$. The x-intercept of the linear fitting equation of (~1 ppm for MEIC and PKU) represents the $\Delta XCO_{2,obs}$ value with no anthropogenic effect. The bias of $\Delta XCO_{2,obs}$ and $\Delta XCO_{2,sim}$ was mainly attributed to the error from emission inventories, background XCO_2 values, and transport simulation. Both the observed and modeled ΔXCO_2 are in good agreement, with correlation coefficients (R^2) of 0.70 and 0.73 for MEIC and PKU, respectively. The slope of the fitting equation denotes the ratio of the observed ΔXCO_2 change to the modeled ΔXCO_2 change. Many previous studies attempted to use the slope value as a scale factor to evaluate and constrain regional CO_2 emissions (Sargent et al., 2018; Shekhar et al., 2020; Yang et al., 2020a). The slope for MEIC (0.89 ppm ppm^{-1}) is closer to the 1:1 line than PKU (0.61 ppm ppm^{-1}). According to the regression slope value, MEIC underestimates approximately 11% of CO_2 emissions surrounding Beijing and PKU underestimates approximately 49%.

Figure 8 denotes the correlation plots of observed ΔXCO (ΔXCO_{obs}) and modeled ΔXCO (ΔXCO_{sim}). The ΔXCO_{obs} data is correlated to ΔXCO_{sim} with R^2 of 0.71 and 0.73 for MEIC and PKU, respectively. The minimum of the observed XCO (80.0 ppb) was taken as a constant XCO background value. The x-intercepts for MEIC (77.63 ppb) and PKU (80.79 ppb) show consistency and agree with the minimum of observed XCO. However, the constant background value could not capture the variation of the true XCO background, especially for summer with strong biological-influenced (detailed in section 3.1). Therefore, the ΔXCO data in Summer are excluded. The slopes for MEIC (1.3 ppb ppb^{-1}) and PKU (1.35 ppb ppb^{-1}) indicate an overestimation of approximately 30% and 35%, respectively, for CO emissions surrounding Beijing.

3.5. *Comparison the observed and simulated ΔXCO: ΔXCO_2*

Many studies have compared the observed $\Delta CO:\Delta CO_2$ with emission inventories (Turnbull et al., 2011; Tohjima et al., 2014; Shan et al., 2019). To calculate the simulated $\Delta CO:\Delta CO_2$ with emission inventories on a regional scale, it is essential to know that the observational site is representative of the region. A few studies roughly specified a geometric bounding box outlining the region which influences the observed value (Wunch et al., 2009; Hu et al., 2019; Shan et al., 2019). However, $\Delta CO:\Delta CO_2$ calculated based on the geometric bounding method is sensitive to the specified size of the enclosed area. A circle centered upon the EM27 observation site was specified as the influencing region. As the source area radius ranges from 50 to 500 km, $\Delta CO:\Delta CO_2$ varies from 17.00 to 19.77 ppb ppm^{-1} for MEIC, 32.28 to 53.74 ppb ppm^{-1} for PKU, respectively. The results show great uncertainty among different inventories and influencing areas. This method is based on the assumption that each grid in the specific geometric region of the emission map contributes equally to the observed concentration.

The region of influence and the sensitivity of each influencing grid to the observations vary over time. Using surface hourly backward column footprints for each measurement is a common and robust way to quantify the sensitivity of the atmospheric concentration changes at the receptor to upwind source regions using units of concentration per unit flux (Turnbull et al., 2011; Tohjima et al., 2014). Each footprint is convolved with the corresponding hourly gridded emission inventories (PKU, MEIC). The modeled anthropogenic enhancement of CO and CO_2 at the receptor site is the sum of contributions from the sensitive emission grid flux (detailed in section 2.3). The linear regression slopes of the modeled $\Delta XCO:\Delta XCO_2$ based on PKU, MEIC, and observations are shown in Table 3. The outliers are excluded according to the three standard deviations criterion. Modeled ΔXCO shows a good relationship with ΔXCO_2 with R^2 of 0.97 for MEIC and 0.96 for PKU. The modeled data displays a slightly greater correlation than the observed ΔXCO and ΔXCO_2 (R^2 = 0.86 for the diurnal variation method, R^2 = 0.83 for the regional enhancement method). The reason is that modeled values only take the anthropogenic influence of CO into account, ignoring the CO_2-related but not the CO-related signal, such as the resident respiration of CO_2. The observed ΔXCO and ΔXCO_2 values based on regional background enhancement display the weakest correlation (R^2 = 0.83) due to the uncertainty of the modeled background value. The simulated regression slope of ΔXCO and ΔXCO_2 in 2019 is 14.91 ± 0.36 ppb ppm^{-1} for MEIC and 21.04 ± 0.70 ppb ppm^{-1} for PKU. The MEIC and PKU inventories are 42.54% and 101.15% higher than the observed value (10.46 ± 0.11 ppb ppm^{-1}), respectively.

In recent studies, $\Delta XCO:\Delta XCO_2$ based on EDGAR (PKU) emission inventories are about 256.59% (219.39%) larger than the values calculated from the FTS in Hefei 2015–16, and 207.86% (173.31%) larger than those in 2016–17 (Shan et al., 2019). Silva and Arellano (2017) found that $\Delta CO:\Delta CO_2$ based on the EDGAR inventory was 50% higher than the value estimated by satellites in the megacities of China. Wang et al. (2010) found that the bottom-up estimate of $\Delta CO:\Delta CO_2$ was 19.2% larger than the

Table 3. Comparison of the observed and simulated $\Delta XCO:\Delta XCO_2$.

Dataset			$\Delta XCO:\Delta XCO_2$ (ppb ppm^{-1})	R^2
Emission inventories	MEIC	2019	14.91 ± 0.36	0.97
	PKU	2019	21.04 ± 0.70	0.96
Observations	FTS (diurnal variation)	2019	10.46 ± 0.11	0.86
	FTS (regional enhancement versus background)	2019	9.06 ± 1.89	0.83

observations at Miyun, Beijing, during winter 2006. Despite the observation and comparative methods, the emission inventories in urban China might overestimate $\Delta CO{:}\Delta CO_2$. The lack of consideration of CO_2 emissions from the respiration of the residents in dense urban regions may lead to the overestimation of bottom-up-based $\Delta CO{:}\Delta CO_2$ (Wang et al., 2010). Either the overestimation of CO anthropogenic flux or under-consideration of CO sinks are possible reasons for the elevated bottom-up estimates of $\Delta CO{:}\Delta CO_2$ (Vardag et al., 2015; Shan et al., 2019).

The main reason why MEIC and PKU overestimated $\Delta XCO{:}\Delta XCO_2$ surrounding Beijing is likely due to the overestimation of the regional CO emissions and underestimation of CO_2 emission. The ΔXCO and ΔXCO_2 discussed in section 3.4 are directly linked to the regional emission. The difference between the modeled and observed ΔX_{gas} is directly proportional to the difference between the emission inventories and the actual emission. The deviation of the regression fitting equation with the 1:1 line shows the model-observed difference. The slope value of modeled ΔXCO to observed is less than one, suggestive of typical overestimations of CO emissions of 30% and 35% for MEIC and PKU, respectively. The underestimation of CO_2 emissions magnifies the effects of overestimated CO emission, which contributes to the larger difference between the modeled $\Delta XCO{:}\Delta XCO_2$ and the observed ratio. For MEIC, a relatively smaller underestimation of CO_2 emissions makes the modeled $\Delta XCO{:}\Delta XCO_2$ closer to observations.

4. Conclusions

Data was collected for clear days over one year for XCO and XCO_2 using the portable FTS EM27 in the urban area of metropolitan Beijing. The overall variation in XCO_2 typical variations in anthropogenic emissions (traced by the XCO variation) which are overlaid upon the biogenic and meteorological field effects. Correlation analyses between the XCO and XCO_2 enhancements provided useful information to identify the characteristic of combustion efficiency in Beijing. The $(\Delta XCO{:}\Delta XCO_2)_d$ observed in urban Beijing (10.46 ± 0.11 ppb ppm^{-1}) is higher than other FTS urban stations (Karlsruhe, Pasadena, Tsukuba, and Paris), suggesting a high anthropogenic proportion of CO_2 emissions and lower combustion efficiency in Beijing. Daily $\Delta XCO{:}\Delta XCO_2$ varies remarkably with seasonality and weather conditions. The $\Delta XCO{:}\Delta XCO_2$ in summer shows large uncertainty, and the correlation of ΔXCO and ΔXCO_2 is weaker than the other three seasons. According to the air mass pathways arriving in Beijing tracked by the WRF-XSTILT model, the observation site had upwind sources from the NW and NCP of 62.93% and 26.72% of overall observation days, respectively. Air masses passing over the NCP region increased the proportion of ΔXCO to ΔXCO_2 (11.46 ± 0.20 ppb ppm^{-1}), which exceeded the slope with a clean upwind source (8.23 ± 0.10 ppb ppm^{-1}). When backward column footprints were combined with emission inventories, observations could be quantitatively compared with the emission inventories. The MEIC and PKU inventories are 42.54% and 101.15% higher than the observed values, respectively. After comparing the observed regional enhancement with the modeled ΔXCO and ΔXCO_2, the main reason for the difference is the overestimation of the regional CO emissions and underestimation of CO_2 emission. The less drastic underestimation of CO_2 emissions for the MEIC results in the improved modeling of $\Delta XCO{:}\Delta XCO_2$ compared to PKU. This work highlights the necessity for long-term column measurements in the heavily CO-emitting Beijing region. However, one station could only capture limited information on a regional scale within a larger urban signal. The background value obtained from the model contains a degree of uncertainty. Compared to in situ surface observations, FTS stations only record the X_{gas} in clear-sky days, which can potentially lead to bias from a less homogeneous sampling. An intensive experimental FTS station combined with WRF-XSTILT could open up additional potential pathways for regional emissions studies.

Acknowledgements. We want to thank the TCCON community for providing the FTIR observations of Pasadena, Karlsruhe, Tsukuba, and Paris. This study is supported by grants from the National Key Research and Development Program of China (Grant No. 2017YFB0504000), National Natural Science Foundation of China (Grant No. 41875043), the Strategic Priority Research 275 Program of the Chinese Academy of Sciences (Grant No. XDA17010102), External Cooperation Program of the Chinese Academy of Science (Grant No. GJHZ1802), Youth Innovation Promotion Association, CAS.

REFERENCES

Bergland, G., 1969: A radix-eight fast Fourier transform subroutine for real-valued series. *IEEE Trans. Audio Electroacoust.*, **17**, 138–144, https://doi.org/10.1109/TAU.1969.1162043.

Bi, Y., Q. Wang, Z. Yang, J. Chen, and W. Bai, 2018: Validation of Column-Averaged Dry-Air Mole Fraction of CO_2 Retrieved from OCO-2 Using Ground-Based FTS Measurements. *J. Meteorolog. Res.*, **32**, 433–443, https://doi.org/10.1007/s13351-018-7118-6.

Cai, Z., K. Che, Y. Liu, D. Yang, and X. Yue, 2021: Decreased Anthropogenic CO_2 Emissions during the COVID-19 Pandemic Estimated from FTS and MAX-DOAS Measurements at Urban Beijing. *Remote Sens.*, **13**, 517, https://doi.org/10.3390/rs13030517.

Chevallier, F., and Coauthors, 2005: Inferring CO_2 sources and sinks from satellite observations: Method and application to TOVS data. *J. Geophys. Res. Atmos.*, 110, https://doi.org/10.1029/2005JD006390.

Chevallier, F., and Coauthors, 2010: CO_2 surface fluxes at grid point scale estimated from a global 21 year reanalysis of atmospheric measurements. *J. Geophys. Res. Atmos.*, 115, https://doi.org/10.1029/2010JD013887.

Chevallier, F., M. Remaud, C. W. O'Dell, D. Baker, P. Peylin, and A. Cozic, 2019: Objective evaluation of surface- and satellite-driven carbon dioxide atmospheric inversions. Atmos. Chem. Phys., **19**, 14233-14251, doi: 10.5194/acp-19-14233-

2019. https://doi.org/10.5194/acp-19-14233-2019.

Chevallier, F.: Evaluation and Quality control document for the OCO-2-driven CO_2 inversion FT19r1, available at: https:// https://atmosphere.copernicus.eu/sites/default/files/2020-05/CAMS73_2018SC2_D73.4.3.1-2020-v1_202004_v1.pdf. (last access: 17 October 2021), 2020.

Chen, J., and Coauthors, 2016: Differential column measurements using compact solar-tracking spectrometers. *Atmos. Chem. Phys.*, **16**, 8479–8498, https://doi.org/10.5194/acp-16-8479-2016.

Crippa, M., and Coauthors, 2020: Fossil CO_2 emissions of all world countries–2020 report, doi: 10.2760/143674. https://doi.org/10.2760/143674.

Dai, S., Y. Ren, S. Zuo, C. Lai, and B. Chen, 2020: Investigating the Uncertainties Propagation Analysis of CO_2 Emissions Gridded Maps at the Urban Scale: A Case Study of Jinjiang City, China. *Remote Sens.*, **12**, 3932, https://doi.org/10.3390/rs12233932.

Dayalu, A., and Coauthors, 2020: Evaluating China's anthropogenic CO_2 emissions inventories: a northern China case study using continuous surface observations from 2005 to 2009,. *Atmos. Chem. Phys.*, **20**, 3569–3588, https://doi.org/10.5194/acp-20-3569-2020.

Fasoli, B., and Coauthors, 2018: Simulating atmospheric tracer concentrations for spatially distributed receptors: updates to the Stochastic Time-Inverted Lagrangian Transport model's R interface (STILT-R version 2). *Geosci. Model Dev.*, **11**, 2813–2824, https://doi.org/10.5194/gmd-11-2813-2018.

Feng, T., W. Zhou, S. Wu, Z. Niu, P. Cheng, X. Xiong, and G. Li, 2019a: High-resolution simulation of wintertime fossil fuel CO_2 in Beijing, China: Characteristics, sources, and regional transport. *Atmos. Environ.*, **198**, 226–235, https://doi.org/10.1016/j.atmosenv.2018.10.054.

Feng, Y., M. Ning, Y. Lei, Y. Sun, W. Liu, and J. Wang, 2019b: Defending blue sky in China: Effectiveness of the "Air Pollution Prevention and Control Action Plan " on air quality improvements from 2013 to 2017,. *J. Environ. Manage.*, **252**, 109603, https://doi.org/10.1016/j.jenvman.2019.109603.

Frey, M., and Coauthors, 2019: Building the COllaborative Carbon Column Observing Network (COCCON): long-term stability and ensemble performance of the EM27/SUN Fourier transform spectrometer. *Atmos. Meas. Tech.*, **12**, 1513–1530, https://doi.org/10.5194/amt-12-1513-2019.

Gisi, M., F. Hase, S. Dohe, T. Blumenstock, A. Simon, and A. Keens, 2012: XCO_2-measurements with a tabletop FTS using solar absorption spectroscopy. *Atmos. Meas. Tech.*, **5**, 2969–2980, https://doi.org/10.5194/amt-5-2969-2012.

Han, P., and Coauthors, 2020: A city-level comparison of fossil-fuel and industry processes-induced CO_2 emissions over the Beijing-Tianjin-Hebei region from eight emission inventories. *Carbon Balance Manage.*, **15**, 1–16, https://doi.org/10.1186/s13021-020-00163-2.

Han, S., and Coauthors, 2009: Temporal variations of elemental carbon in Beijing. *J. Geophys. Res. Atmos.*, 114, https://doi.org/10.1029/2009JD012027.

Hase, F., and Coauthors, 2004: Intercomparison of retrieval codes used for the analysis of high-resolution, ground-based FTIR measurements. *J. Quant. Spectrosc. Radiat. Transfer*, **87**, 25–52, https://doi.org/10.1016/j.jqsrt.2003.12.008.

Hase, F., T. Blumenstock, S. Dohe, J. Groß, and M. Kiel, 2017: TCCON data from Karlsruhe, Germany, Release GGG2014R1. TCCON data archive, hosted by CaltechDATA, California Institute of Technology, Pasadena, CA, U. S.A.. https://doi.org/10.14291/tccon.ggg2014.karlsruhe01.R1/1182416.

Hase, F., M. Frey, M. Kiel, T. Blumenstock, R. Harig, A. Keens, and J. Orphal, 2016: Addition of a channel for XCO observations to a portable FTIR spectrometer for greenhouse gas measurements. *Atmos. Meas. Tech.*, **9**, 2303–2313, https://doi.org/10.5194/amt-9-2303-2016.

Hedelius, J. K., and Coauthors, 2017: Intercomparability of XCO_2 and XCH_4 from the United States TCCON sites. *Atmos. Meas. Tech.*, **10**, 1481–1493, https://doi.org/10.5194/amt-10-1481-2017.

Hedelius, J. K., J. Liu, T. Oda, S. Maksyutov, and P. O. Wennberg, 2018: Southern California megacity CO_2, CH_4, and CO flux estimates using ground- and space-based remote sensing and a Lagrangian model. *Atmos. Chem. Phys.*, **18**, 16271–16291, https://doi.org/10.5194/acp-18-16271-2018.

Hu, C., and Coauthors, 2019: Anthropogenic Methane Emission and Its Partitioning for the Yangtze River Delta Region of China. *J. Geophys. Res. Biogeosci.*, **124**, 1148–1170, https://doi.org/10.1029/2018JG004850.

Jacobs, N., and Coauthors, 2020: Quality controls, bias, and seasonality of CO_2 columns in the boreal forest with Orbiting Carbon Observatory-2, Total Carbon Column Observing Network, and EM27/SUN measurements. *Atmos. Meas. Tech.*, **13**, 5033–5063, https://doi.org/10.5194/amt-13-5033-2020.

Keppel-Aleks, G., G. C. Toon, P. O. Wennberg, and N. M. Deutscher, 2007: Reducing the impact of source brightness fluctuations on spectra obtained by Fourier-transform spectrometry. *Appl. Opt.*, **46**, 4774–4779, https://doi.org/10.1364/AO.46.004774.

Klappenbach, F., and Coauthors, 2015: Accurate mobile remote sensing of XCO_2 and XCH_4 latitudinal transects from aboard a research vessel. *Atmos. Meas. Tech.*, **8**, 5023–5038, https://doi.org/10.5194/amt-8-5023-2015.

Le Quéré, C., and Coauthors, 2020: Temporary reduction in daily global CO_2 emissions during the COVID-19 forced confinement. *Nat. Clim. Change*, **10**, 647–653, https://doi.org/10.1038/s41558-020-0797-x.

Lei, R., and Coauthors, 2021: Fossil fuel CO_2 emissions over metropolitan areas from space: A multi-model analysis of OCO-2 data over Lahore, Pakistan. *Remote Sens. Environ.*, **264**, 112625, https://doi.org/10.1016/j.rse.2021.112625.

Li, Y., and Coauthors, 2020: Long-term declining in carbon monoxide (CO) at a rural site of Beijing during 2006–2018 implies the improved combustion efficiency and effective emission control. *J. Environ. Sci.*, https://doi.org/10.1016/j.jes.2020.11.011.

Lin, J. C., C. Gerbig, S. C. Wofsy, A. E. Andrews, B. C. Daube, K. J. Davis, and C. A. Grainger, 2003: A near-field tool for simulating the upstream influence of atmospheric observations: The Stochastic Time-Inverted Lagrangian Transport (STILT) model. *J. Geophys. Res. Atmos.*, **108**, https://doi.org/10.1029/2002JD003161.

Mertz, L., 1967: Auxiliary computation for Fourier spectrometry. *Infrared Phys*, **7**, 17–23, https://doi.org/10.1016/0020-0891(67)90026-7.

Morino, I., T. Matsuzaki, and M. Horikawa, 2018: TCCON data from Tsukuba (JP), 125HR, Release GGG2014.R2, https://doi.org/10.14291/TCCON.GGG2014.TSUKUBA02.R2.

Myhre, G., and Coauthors, 2013: Radiative forcing of the direct

aerosol effect from AeroCom Phase II simulations. *Atmos. Chem. Phys*, **13**, 1853–1877, https://doi.org/10.5194/acp-13-1853-2013.

Nassar, R., L. Napier-Linton, K. R. Gurney, R. J. Andres, T. Oda, F. R. Vogel, and F. Deng, 2013: Improving the temporal and spatial distribution of CO_2 emissions from global fossil fuel emission data sets. *J. Geophys. Res. Atmos.*, **118**, 917–933, https://doi.org/10.1029/2012JD018196.

Naylor, D. A., and M. K. Tahic, 2007: Apodizing functions for Fourier transform spectroscopy. *Journal of the Optical Society of America A*, **24**, 3644–3648, https://doi.org/10.1364/FTS.2005.FTuD3.

Niu, Z., and Coauthors, 2016: Atmospheric Fossil Fuel CO_2 Traced by $\Delta^{14}C$ in Beijing and Xiamen, China: Temporal Variations, Inland/Coastal Differences and Influencing Factors. *Environ. Sci. Technol.*, **50**, 5474–5480, https://doi.org/10.1021/acs.est.5b02591.

Panagi, M., and Coauthors, 2020: Investigating the regional contributions to air pollution in Beijing: a dispersion modelling study using CO as a tracer. *Atmospheric Chemistry and Physics*, **20**, 2825–2838, https://doi.org/10.5194/acp-20-2825-2020.

Park, H., S. Jeong, H. Park, L. Labzovskii, and K. Bowman, 2021: An assessment of emission characteristics of Northern Hemisphere cities using spaceborne observations of CO_2 , CO, and NO_2. *Remote Sens. Environ.*, **254**, 112246, https://doi.org/10.1016/j.rse.2020.112246.

Popa, M. E., M. K. Vollmer, A. Jordan, W. A. Brand, S. Pathirana, M. Rothe, and T. Röckmann, 2014: Vehicle emissions of greenhouse gases and related tracers from a tunnel study: CO: CO_2, N_2O: CO_2, CH_4: CO_2, O_2: CO_2 ratios, and the stable isotopes ^{13}C and ^{18}O in CO_2 and CO. *Atmos. Chem. Phys.*, **14**, 2105–2123, https://doi.org/10.5194/acp-14-2105-2014.

Sargent, M., and Coauthors, 2018: Anthropogenic and biogenic CO_2 fluxes in the Boston urban region. *Proc. Nat. Acad. Sci.*, **115**, 7491, https://doi.org/10.1073/pnas.1803715115.

Satterthwaite, D., 2008: Cities' contribution to global warming: notes on the allocation of greenhouse gas emissions. *Environ. & Urban*, **20**, 539–550, https://doi.org/10.1177/0956247808096127.

Satterthwaite, D., 2010: The Contribution of Cities to Global Warming and their Potential Contributions to Solutions. *Environ. Urban. ASIA*, **1**, 1–12, https://doi.org/10.1177/097542530900100102.

Shan, C., and Coauthors, 2019: Regional CO emission estimated from ground-based remote sensing at Hefei site, China. *Atmos. Res.*, 222, https://doi.org/10.1016/j.atmosres.2019.02.005.

Shekhar, A., and Coauthors, 2020: Anthropogenic CO_2 emissions assessment of Nile Delta using XCO_2 and SIF data from OCO-2 satellite. *Environ. Res. Lett.*, 15, https://doi.org/10.1088/1748-9326/ab9cfe.

Silva, S. J., and A. F. Arellano, 2017: Characterizing Regional-Scale Combustion Using Satellite Retrievals of CO, NO_2 and CO_2. *Remote Sens.*, **9**, 744, https://doi.org/10.3390/rs9070744.

Silva, S. J., A. F. Arellano, and H. M. Worden, 2013: Toward anthropogenic combustion emission constraints from space - based analysis of urban CO_2/CO sensitivity. *Geophys. Res. Lett.*, **40**, 4971–4976, https://doi.org/10.1002/grl.50954.

Stocker, T. F., 2013: The closing door of climate targets. *Science,*, **339**, 280–282, https://doi.org/10.1126/science.1232468.

Té, Y., and Coauthors, 2016: Seasonal variability of surface and column carbon monoxide over the megacity Paris, high-altitude Jungfraujoch and Southern Hemispheric Wollongong stations. *Atmos. Chem. Phys.*, **16**, 10911–10925, https://doi.org/10.5194/acp-16-10911-2016.

Té, Y., P. Jeseck, and C. Janssen, 2017: TCCON data from Paris, France, Release GGG2014R0. TCCON data archive, hosted by CaltechDATA, California Institute of Technology, Pasadena, CA, U.S.A. . https://doi.org/10.14291/tccon.ggg2014.paris01.R0/1149279.

Toon, G. C. and Wunch, D., 2015: A stand-alone a priori profile generation tool for GGG2014 release, CaltechDATA, https://doi.org/10.14291/tccon.ggg2014.priors.r0/1221661,2015.

Tohjima, Y., and Coauthors, 2014: Temporal changes in the emissions of CH_4 and CO from China estimated from CH_4/CO_2 and CO/CO_2 correlations observed at Hateruma Island. *Atmos. Chem. Phys.*, **14**, 1663–1677, https://doi.org/10.5194/acp-14-1663-2014.

Turnbull, J. C., and Coauthors, 2011: Atmospheric observations of carbon monoxide and fossil fuel CO_2 emissions from East Asia. *J. Geophys. Res. Atmos.*, 116, https://doi.org/10.1029/2011JD016691.

Vardag, S. N., C. Gerbig, G. Janssens-Maenhout, and I. Levin, 2015: Estimation of continuous anthropogenic CO_2: model-based evaluation of CO_2, CO, $\delta^{13}C(CO_2)$ and $\Delta^{14}C(CO_2)$ tracer methods. *Atmos. Chem. Phys.*, **15**, 12705–12729, https://doi.org/10.5194/acp-15-12705-2015.

Wang, R., and Coauthors, 2013: High-resolution mapping of combustion processes and implications for CO_2 emissions. *Atmos. Chem. Phys.*, **13**, 5189–5203, https://doi.org/10.5194/acpd-12-21211-2012.

Wang, W., and Coauthors, 2017: Investigating the performance of a greenhouse gas observatory in Hefei, China. *Atmos. Meas. Tech.*, **10**, 2627–2643, https://doi.org/10.5194/amt-2016-296.

Wang, Y., J. W. Munger, S. Xu, M. B. Mcelroy, J. Hao, C. P. Nielsen, and H. Ma, 2010: CO_2 and its correlation with CO at a rural site near Beijing: implications for combustion efficiency in China. *Atmos. Chem. Phys.*, **10**, 8881–8897, https://doi.org/10.5194/acp-10-8881-2010.

Wennberg, P. O., D. Wunch, C. Roehl, J.-F. Blavier, G. C. Toon, and N. Allen, 2017: TCCON data from California Institute of Technology, Pasadena, California, USA, Release GGG2014R1, TCCON data archive, hosted by CaltechDATA, California Institute of Technology, Pasadena, CA, U.S.A. . https://doi.org/10.14291/tccon.ggg2014.pasadena01.R1/1182415.

West, J. J., and Coauthors, 2013: Co-benefits of mitigating global greenhouse gas emissions for future air quality and human health. *Nat. Clim. Change*, **3**, 885–889, https://doi.org/10.1038/NCLIMATE2009.

Worden, H. M., and Coauthors, 2012: Satellite-based estimates of reduced CO and CO_2 emissions due to traffic restrictions during the 2008 Beijing Olympics. *Geophys. Res. Lett.*, **39**, https://doi.org/10.1029/2012GL052395.

Wu, D., and Coauthors, 2018: A Lagrangian approach towards extracting signals of urban CO_2 emissions from satellite observations of atmospheric column CO_2 (XCO_2): X-Stochastic Time-Inverted Lagrangian Transport model ("X-STILT v1"). *Geosci. Model Dev.*, **11**, 4843–4871, https://doi.org/10.5194/gmd-11-4843-2018.

Wunch, D., P. O. Wennberg, G. C. Toon, G. Keppel-Aleks, and

Y. G. Yavin, 2009: Emissions of greenhouse gases from a North American megacity. *Geophys. Res. Lett.*, **36**, https://doi.org/10.1029/2009GL039825.

Wunch, D., and Coauthors, 2016: Quantifying the loss of processed natural gas within California's South Coast Air Basin using long-term measurements of ethane and methane. *Atmos. Chem. Phys.*, **16**, 14091–14105, https://doi.org/10.5194/acp-16-14091-2016.

Wunch, D., and Coauthors, 2011: A method for evaluating bias in global measurements of CO_2 total columns from space. *Atmos. Chem. Phys.*, **11**, 12317–12337, https://doi.org/10.5194/acp-11-12317-2011.

Wunch, D., and Coauthors, 2010: Calibration of the Total Carbon Column Observing Network using aircraft profile data. *Atmos. Meas. Tech.*, **3**, 1351–1362, https://doi.org/10.5194/amtd-3-2603-2010.

Yang, E. G., E. A. Kort, D. Wu, J. C. Lin, T. Oda, X. Ye, and T. Lauvaux, 2020a: Using Space-Based Observations and Lagrangian Modeling to Evaluate Urban Carbon Dioxide Emissions in the Middle East. *J. Geophys. Res. Atmos.*, **125**, e2019JD031922, https://doi.org/10.1029/2019JD031922.

Yang, Y., and Coauthors, 2020b: New ground-based Fourier-transform near-infrared solar absorption measurements of XCO_2, XCH_4 and XCO at Xianghe, China. *Earth Syst. Sci. Data*, **12**, 1679–1696, https://doi.org/10.5194/essd-12-1679-2020.

Yang, Z., and Coauthors, 2007: New constraints on Northern Hemisphere growing season net flux. *Geophys. Res. Lett.*, **34**, https://doi.org/10.1029/2007GL029742.

Ye, X., and Coauthors, 2020: Constraining Fossil Fuel CO_2 Emissions From Urban Area Using OCO-2 Observations of Total Column CO_2. *J. Geophys. Res. Atmos.*, **125**, e2019JD030528, https://doi.org/10.1029/2019JD030528.

Zeng, J., and Coauthors, 2020: Global terrestrial carbon fluxes of 1999–2019 estimated by upscaling eddy covariance data with a random forest. *Sci. Data*, **7**, 313, https://doi.org/10.1038/s41597-020-00653-5.

Zhao, Y., C. P. Nielsen, M. B. McElroy, L. Zhang, and J. Zhang, 2012: CO emissions in China: Uncertainties and implications of improved energy efficiency and emission control. *Atmos. Environ.*, **49**, 103–113, https://doi.org/10.1016/j.atmosenv.2011.12.015.

Zheng, B., F. Chevallier, P. Ciais, G. Broquet, Y. Wang, J. Lian, and Y. Zhao, 2020: Observing carbon dioxide emissions over China's cities and industrial areas with the Orbiting Carbon Observatory-2,. *Atmos. Chem. Phys.*, **20**, 8501–8510, https://doi.org/10.5194/acp-20-8501-2020.

Zheng, B., and Coauthors, 2018a: Rapid decline in carbon monoxide emissions and export from East Asia between years 2005 and 2016,. *Environ. Res. Lett.*, **13**, 044007, https://doi.org/10.1088/1748-9326/aab2b3.

Zheng, B., and Coauthors, 2018b: Trends in China's anthropogenic emissions since 2010 as the consequence of clean air actions. *Atmos. Chem. Phys.*, **18**, 14095–14111, https://doi.org/10.5194/acp-18-14095-2018.

ADVANCES IN ATMOSPHERIC SCIENCES, VOL. 39, AUGUST 2022, 1316–1328

• **Original Paper** •

Fengyun-4 Geostationary Satellite-Based Solar Energy Nowcasting System and Its Application in North China※

Chunlin HUANG[1,2], Hongrong SHI[2,7], Ling GAO[4], Mengqi LIU[5], Qixiang CHEN[1], Disong FU[2], Shu WANG[6], Yuan YUAN[*1], and Xiang′ao XIA[*2,3]

[1]*Key Laboratory of Aerospace Thermophysics*, *Ministry of Industry and Information Technology*, *Harbin Institute of Technology*, *Harbin* 150001, *China*

[2]*Key Laboratory of Middle Atmosphere and Global Environment Observation*, *Institute of Atmospheric Physics*, *Chinese Academy of Sciences*, *Beijing* 100029, *China*

[3]*Collaborative Innovation Center on Forecast and Evaluation of Meteorological Disasters*, *Nanjing University of Information Science & Technology*, *Nanjing* 210044, *China*

[4]*National Satellite Meteorological Center*, *China Meteorological Administration*, *Beijing* 100192, *China*

[5]*Key Laboratory of Atmospheric Sounding*, *Chengdu University of Information Technology*, *Chengdu* 610225, *China*

[6]*State Key Laboratory of Operation and Control of Renewable Energy & Storage Systems*, *China Electric Power Research Institute (CEPRI)*, *Beijing* 100192, *China*

[7]*Key Laboratory of Cloud-Precipitation Physics and Severe Storms*, *Institute of Atmospheric Physics*, *Chinese Academy of Sciences*, *Beijing* 100029, *China*

(Received 20 December 2021; revised 4 March 2022; accepted 17 March 2022)

ABSTRACT

Surface solar irradiance (SSI) nowcasting (0–3 h) is an effective way to overcome the intermittency of solar energy and to ensure the safe operation of grid-connected solar power plants. In this study, an SSI estimate and nowcasting system was established using the near-infrared channel of Fengyun-4A (FY-4A) geostationary satellite. The system is composed of two key components: The first is a hybrid SSI estimation method combining a physical clear-sky model and an empirical cloudy-sky model. The second component is the SSI nowcasting model, the core of which is the derivation of the cloud motion vector (CMV) using the block-matching method. The goal of simultaneous estimation and nowcasting of global horizontal irradiance (GHI) and direct normal irradiance (DNI) is fulfilled. The system was evaluated under different sky conditions using SSI measurements at Xianghe, a radiation station in the North China Plain. The results show that the accuracy of GHI estimation is higher than that of DNI estimation, with a normalized root-mean-square error (nRMSE) of 22.4% relative to 45.4%. The nRMSE of forecasting GHI and DNI at 30–180 min ahead varied within 25.1%–30.8% and 48.1%–53.4%, respectively. The discrepancy of SSI estimation depends on cloud occurrence frequency and shows a seasonal pattern, being lower in spring–summer and higher in autumn–winter. The FY-4A has great potential in supporting SSI nowcasting, which promotes the development of photovoltaic energy and the reduction of carbon emissions in China. The system can be improved further if calibration of the empirical method is improved.

Key words: Fengyun-4A, surface solar irradiance, estimates and forecasting, cloud motion, block-matching

Citation: Huang, C. L., and Coauthors, 2022: Fengyun-4 Geostationary satellite-based solar energy nowcasting system and its application in North China. *Adv. Atmos. Sci.*, **39**(8), 1316−1328, https://doi.org/10.1007/s00376-022-1464-0.

Article Highlights:

- A Fengyun-4A-based solar energy estimate and forecasting system is established.
- A hybrid method with the capability of simultaneous estimation of GHI and DNI is developed.
- The application of this system in the North China Plain shows good performance in forecasting solar energy.

1. Introduction

To achieve carbon peak and neutrality goals, China will increase the share of renewable energy in its energy structure

※ This paper is a contribution to the special issue on Carbon Neutrality: Important Roles of Renewable Energies, Carbon Sinks, NETs, and non-CO_2 GHGs.

* Corresponding authors: Xiang′ao XIA, Yuan YUAN
Emails: xxa@mail.iap.ac.cn, yuanyuan83@hit.edu.cn

to reduce carbon emissions (Shi et al., 2021; Li et al., 2022). China has the world's largest installed photovoltaic (PV) capacity and growth rate (IRENA, 2020). Until August 2021, China had an installed capacity of 275.1 GW and had surpassed its 2016 capacity by 255.4%. The ratio of installed capacity to China's full-caliber installed capacity has increased from 4.7% (2016) to 12.0% (August 2021)[a]. The share of PV energy in China's energy structure will undoubtedly increase significantly in the coming decades (Burandt et al., 2019; Prăvălie et al., 2019; Li et al., 2020; Bai et al., 2021). The intermittence and instability of solar energy, however, pose a major challenge for the integration of solar PV into the energy grid. Solar energy mainly depends on the availability of surface solar irradiance (SSI), which is highly susceptible to variations in atmospheric components (clouds, aerosols, water vapor, etc.). This results in significant fluctuations in the PV output power. Therefore, accurate forecasting of SSI fluctuations is of great importance for utilizing and developing solar PV and reducing carbon emissions (Lamsal et al., 2018; Senatla and Bansal, 2018).

The forecast method for SSI is generally divided into three categories. Years- and decades-ahead predictions are mainly made using climate models that are commonly used for solar PV plant deployment and planning (Wild et al., 2015; Zou et al., 2019). For short-term (day/hour-scale) forecasts, regional numerical weather prediction (NWP) simulations are advantageous; the results obtained through these are useful for scheduling and optimizing microgrids and grid-connected power allocation for the next 24–48 hours (Antonanzas et al., 2016; Razagui et al., 2021). For nowcasting (0–3 h ahead), satellite-based methods are widely used, which is important for the safe operation, control, and management of PV plants and is also a prerequisite for grid connection of PV plants (Zhu et al., 2019).

The satellite-based SSI nowcasting method consists of two components. The first is to estimate SSI as accurately as possible using satellite reflectance measurements. The second is to forecast SSI at the next target time, which requires estimation of the cloud motion vector (CMV). The diverse methods used to estimate SSI from satellites can be divided broadly into physical and semi-empirical methods; both have been widely used for different satellites (e.g., NOAA series, Meteosat Second Generation (MSG), and Himawari-8) (Kallio-Myers et al., 2020; Peng et al., 2020; Letu et al., 2021). The physical method uses atmospheric and surface properties retrieved from satellite measurements and other sources, such as reanalysis products, to drive a radiative transfer model to calculate SSI. This method is based on solid physical foundations, and its uncertainty depends heavily on the availability and accuracy of the input variables. Additionally, this method requires more computing power than empirical methods. The semi-empirical method estimates SSI directly from satellite observations using a simple but effective method. One representative method of this kind in the solar energy community is the semi-empirical method for MSG, called the Heliosat method. This method was originally developed in the last century and has greatly facilitated research and application of solar energy in Europe (Cros et al., 2004; Rigollier et al., 2004). The basic principle is very simple, but its operational implementation is delicate and requires a fair amount of site-specific accounting (Kleissl, 2013). In recent years, machine learning, which can be classified as an empirical method, has developed rapidly for SSI estimation (Damiani et al., 2018; Peng et al., 2020). Empirical methods mainly use satellite observation and generally do not need atmospheric and surface properties. Therefore, they can be extremely useful when atmospheric and surface properties are not reliably available or have large uncertainties (Huang et al., 2019). Another advantage of this method is that SSI estimations can be obtained in the native spatial resolutions of the original satellite measurements. This is very useful for solar energy forecasting because the higher the spatial resolution, the better is the application.

With regard to CMV derivation, three methods are widely used: phase correlation, optical flow, and block-matching (Amillo et al., 2014; Kallio-Myers et al., 2020; Yang et al., 2020). The phase correlation method obtains motion information from the phase difference of consecutive fields. The basic principle is the shift property of the Fourier transform, which states that translation of pixels in the spatial domain produces proportional phase shifts in the frequency domain (Wang et al., 2018). The optical flow method derives the CMV based on the image gradient in which three assumptions are made. First, the pixel brightness of the image is constant between the two frames. Second, the motion in the image varies little over time. Third, the same or similar motion is shared by the target pixel and its neighboring pixels, i.e., the spatial smoothing is constrained (Nonnenmacher and Coimbra, 2014). The block-matching method assumes that cloud structures are constant along motion trajectories over a short time period. The CMV is calculated through the cloud structure displacement obtained from consecutive images (Hammer et al., 1999). CMV is generally obtained by directly using 2–3 images from geostationary satellites taken within a short period of time. Retrievals of cloud physical properties, such as cloud optical thickness, cloud top height, and cloud effective radius, have been shown to improve the CMV derivation (Wang et al., 2019).

SSI nowcasting can be achieved using a combination of CMV information and SSI estimates. Numerous SSI nowcasting studies have been conducted based on satellite sensors (e.g., Spinning Enhanced Visible and Infrared Imager (SEVIRI)) (Arbizu-Barrena et al., 2017; Gallucci et al., 2018; Mouhamet et al., 2018; Wang et al., 2019). Fengyun-4A (FY-4A), launched by China in 2016, is a new generation geostationary meteorological satellite. The advanced geosynchronous radiation imager (AGRI) on board the FY-4A can provide images with much higher spatial, temporal, and spectral resolutions than previous imagers. It has great potential

[a] http://www.nea.gov.cn/2021-09/18/c_1310196220.htm. (in Chinese)

for SSI nowcasting, which still needs to be explored (Zhang et al., 2020; Xian et al., 2021). There have been a few attempts, but all were limited in their spatial and temporal coverage and satellite-based detection of cloud motion (Yang et al., 2019; Chen et al., 2020; Yang et al., 2020). More importantly, many issues still require further investigation.

In this study, we explore the potential of FY-4A in SSI nowcasting. We attempt to answer the following three scientific questions: 1) Can the clear-sky model be used to accurately estimate clear-sky SSI even under heavy pollution conditions. 2) what is the accuracy of SSI estimation expected by using an empirical method to the AGRI onboard the FY-4A, and how can its accuracy be improved. and 3) Can the empirical method be extended to DNI estimation, and what is the expected accuracy. China has a vast absolute area of DNI superb potential [>200 000 km^2, (Prăvălie et al., 2019)], which means that accurate estimates and nowcasting of DNI fluctuations are extremely important for the development of solar PV energy in China. Therefore, it is of great significance to explore FY-based DNI estimates and the nowcasting method.

This paper is organized as follows: Section 2 describes the clear-sky model, SSI estimates model, nowcasting algorithm, and data used in the study. Section 3 presents the results of the evaluation of FY-4A SSI estimates and forecast products. The discussion and conclusions are presented in sections 4 and 5.

2. Data and methodology

2.1. *Data*

FY-4A is located over the equator at a longitude of 104.7°E. The AGRI onboard the FY-4A takes satellite images of China and its surrounding areas with varying spatial (from 0.5 km to 16 km) and temporal (from 15 min to 2 h) resolutions. To simplify the method and thereby fulfill the operational usage of the method, we only used Level 1 spectral reflectance at the near-infrared channel (0.83 μm) with a spatial resolution of 1 km to calculate the cloud index (CI) and CMV information. The data are available online (http://satellite.nsmc.org.cn/portalsite/default.aspx).

The Modern-Era Retrospective Analysis for Research and Applications version 2 (MERRA-2) uses the Goddard Earth Observing System Version 5 data assimilation system. MERRA-2 provides long-term (from 1980 to the present) radiation, meteorological, and atmospheric aerosol products, which have been widely used to study atmospheric environments, climate change, and solar energy (Randles et al., 2017). The hourly MERRA-2 aerosol optical depth at 550 nm (AOD_{550}), Ångström exponent (AE), precipitable water vapor, ozone amount, and surface albedo products (http://disc.sci.gsfc.nasa.gov) are used to drive a parametrization radiative transfer model to calculate clear-sky SSI.

The SSI measurements at Xianghe (39.75°N, 116.95°E, Fig. 1) in 2018 were used for the evaluation. GHI and DNI were measured using a Kipp and Zonen CM21 pyranometer and CHPI pyrheliometer, respectively (Liu et al., 2021). The SSI measurements were quality controlled through procedures recommended by the Baseline Surface Radiation Network, with uncertainties of approximately 6% and 3% for GHI and DNI, respectively. Only quality-assured measurements were used for the evaluation, which led to different sample numbers of GHI and DNI. Xianghe is located in the Beijing–Tianjin–Hebei region, which is a typical polluted region in China. This region has been gradually increasing the share of solar PV energy in its total energy consumption to balance energy requirements with environmental protection.

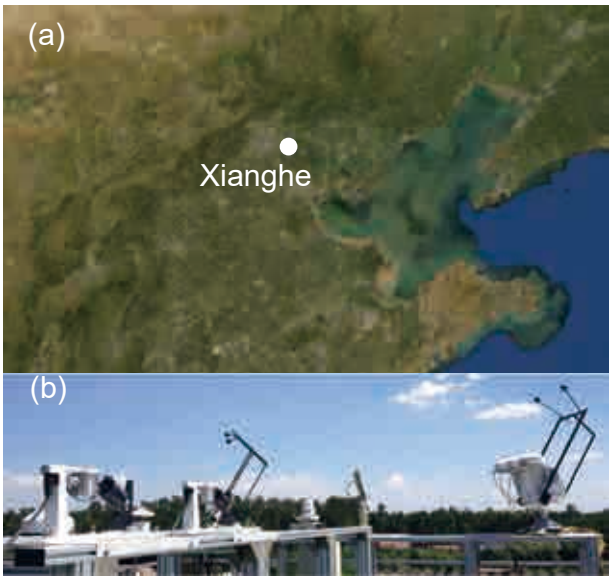

Fig. 1. (a) Geographical location of Xianghe observation site, and (b) the instrument.

1-minute SSI measurements were used to detect cloud occurrence using a random forest method (Liu et al., 2021). Daily cloud occurrences were used to classify each day into four distinct categories: C1: 0%–10%; C2: 10%–50%; C3: 50%–90%; C4: 90%–100%, roughly corresponding to clear, moderately clear, cloudy, and overcast conditions, respectively. The SSI estimates and nowcasting were evaluated under these four sky conditions to investigate their potential different performances.

Figure 2 presents the monthly occurrence frequency of these four sky types in 2018. The cloud occurrence frequency showed a seasonal pattern. Skies were much clearer in winter than in other seasons, while overcast skies dominated in summer, especially in July when 27 days were overcast.

2.2. *Methodology*

2.2.1. *Clear-sky model*

Clear-sky SSI estimation is a critical step in empirical SSI algorithms. In this work, clear-sky SSI was calculated using the REST2v5 model because of its excellent performance for supporting SSI estimates and nowcasting in a worldwide test under various conditions (Antonanzas-Torres et al., 2019; Sun et al., 2021). REST2 splits the shortwave

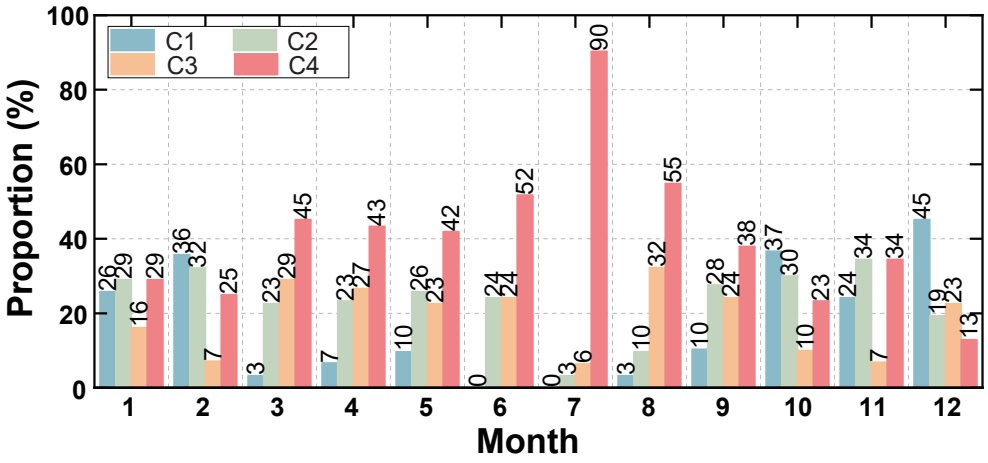

Fig. 2. Monthly proportion of four sky conditions at Xianghe in 2018.

spectrum into two bands (290–700 nm and 700–4000 nm), and DNI and diffuse horizontal irradiance (DHI) are parameterized for each band (Gueymard, 2008). The GHI is calculated as the summation of the DNI multiplied by the cosine of the solar zenith angle and DHI.

2.2.2. *All-sky SSI calculation*

The all-sky SSI values were obtained by multiplying the REST2 clear-sky SSI calculation and the clear sky index (K_c: the ratio of observed all-sky SSI to the expected clear-sky SSI). K_c is parameterized as a function of the CI:

$$\begin{cases} n_t(i,j) < -0.2;\ K_c = 1.2 \\ -0.2 \le n_t(i,j) < 0.3;\ K_c = 1 - n_t(i,j) \\ 0.3 \le n_t(i,j) < 1.1;\ K_c = 1.279 - 2.234 n_t(i,j) + 1.016 (n_t(i,j))^2 \\ 1.1 \le n_t(i,j);\ K_c = 0.05 \end{cases}, \tag{1}$$

where $n_t(i,j)$ denotes the CI derived from FY-4A reflectance measurements. The relationship between CI and K_c is determined based on the historical data of Xianghe station.

The CI at a given pixel (i,j) and time t is calculated using Eq. (2):

$$n_t(i,j) = \frac{\rho_t(i,j) - \rho_{t,g}(i,j)}{\rho_{t,c}(i,j) - \rho_{t,g}(i,j)}, \tag{2}$$

where $\rho_t(i,j)$ is the FY-4A observed reflectance, and $\rho_{t,c}(i,j)$ and $\rho_{t,g}(i,j)$ represent the reflectance associated with the brightest clouds and clear skies within a given period, respectively. The operational advantage of this all-sky SSI estimation method is that it does not require precise satellite calibration information. As the method is self-calibrating, the upper and lower bounds of the dynamic range at the target pixel are established from the data history (Kleissl, 2013). The upper bound of the dynamic range, $\rho_{t,c}(i,j)$, represents the overcast condition with the brightest clouds. We defined $\rho_{t,c}(i,j)$ as the 95th percentile of all reflectance values throughout the year in the target region (latitude 36°N to 44°N and longitude 112°E to 120°E), which considers potential measurement uncertainty. Given $\rho_{t,g}(i,j)$, the lower bound of the dynamic range is highly dependent on surface reflectance, which shows remarkable temporal variation ; it is estimated by an iteration procedure for each month. First, all satellite measurements of reflectance for each pixel in a given month are averaged as an initial threshold value (ρ_{thres}). The new average is then calculated from the reflectance smaller than the sum of the initial threshold and a specified bias ε, which is defined as 0.035 $\rho_{t,c}(i,j)$ here. This new average is used for the next iteration. Then, the iteration proceeds until no reflectance exceeds the threshold by a magnitude of ε, and the last-iterated $\rho_{t,g}(i,j)$ is used as the lower bound.

Note that the FY-4A-measured clear-sky reflectance shows a convex parabolic variation with the solar zenith angle (SZA) over the daytime. This means that $\rho_t(i,j)$ at local solar noon would exceed $\rho_{t,g}(i,j)$. Then, the $n_t(i,j)$ obtained based on Eq. (2) would tend to identify the clear-sky pixels at local solar noon as cloud pixels, eventually leading to much lower calculated clear-sky SSI values than actual SSI values. Therefore, this issue was addressed by introducing a parameterization of the FY-4A clear-sky reflectance to SZA, as follows:

$$\rho_c = \rho_0 \Big/ \left(0.35(\cos(\theta))^{1.4}\right), \tag{3}$$

where ρ_c denotes corrected reflectance, ρ_0 denotes FY-4A clear-sky reflectance, θ represents SZA.

The corrected reflectance and corresponding dynamic range are given in Fig. 3b.

The GHI is given by Eq. (4):

$$\mathrm{GHI} = \mathrm{GHI}_{cs} K_c, \tag{4}$$

where GHI_{cs} represents the GHI under clear sky calculated by the REST2 model.

The DNI is given by Eq. (5) (Pfeifroth et al., 2019), which is determined based on the historical data of Xianghe station:

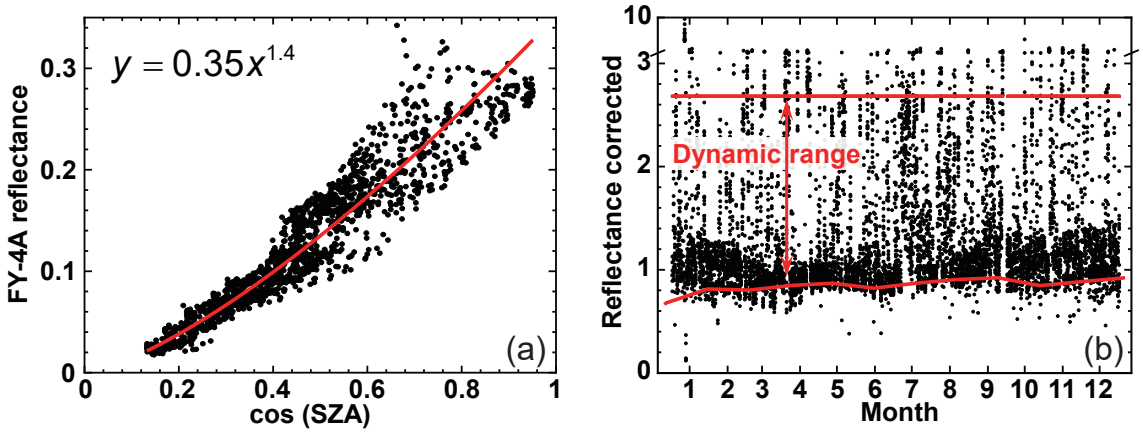

Fig. 3. (a) The function relation between FY-4A reflectance and the cosine of SZA under the clear-sky condition, and (b) the dynamic range for Xianghe station from the near infrared channel of the FY-4A satellite in 2018.

$$\begin{cases} 0.8 \leqslant K_c; & \mathrm{DNI} = \mathrm{DNI}_{cs} K_c \\ 0.35 \leqslant K_c < 0.8; & \mathrm{DNI} = \mathrm{DNI}_{cs}[K_c - 0.53(1 - K_c)]^3 \\ K_c \leqslant 0.35; & \mathrm{DNI} = 0 \end{cases}, \quad (5)$$

where DNI_{cs} represents the DNI under clear sky, which is also calculated using the REST-2 model.

2.2.3. *SSI short-term forecast method*

The forecast method includes two operational steps: forecasting clear-sky SSI background at the target horizons, and superimposing cloud attenuation (K_c) on the background. We assumed that all parameters, except the SZA, are held constant with a forecast horizon up to 6 h. The present values (0 min ahead) provided by MERRA-2 are used as the input predicted values for the prediction of the clear-sky SSI background. The SZA is the main cause of the alteration of clear-sky SSI background. The SZA values at target horizons are obtained according to the time and geographical location information. The FY-4A satellite images were first converted to CI images using the abovementioned empirical method. The CMV was subsequently calculated using the block-matching method and consecutive CI images with time intervals of 20 min. Based on the CMV information, the CI and K_c of the forecast horizon were obtained, and the SSI nowcasting was finally completed.

The development of clouds is not determined by dissipation and formation for the forecast time of several hours, and cloud tracking methods (e.g., the block-matching method) using images from geostationary satellite show good performance. As a demonstration, we used a rectangular area [112°–120°E, 36°–44°N] as our research subject. The images were divided into multiple square boxes (0.5° × 0.5°), and the motion vectors for each square region were derived using the following procedures. The block-matching method identifies cloud structures according to the pixel intensities in consecutive CI images. Assuming that pixel intensities are constant along motion trajectories over a short time period, the CMV of each square area was subsequently calculated using the cloud structure displacement (Hammer et al., 1999).

According to the assumption of constant pixel intensities, the vector $\boldsymbol{v}$ used to describe the motion is given by:

$$n_1\{\boldsymbol{x}_0 + [(t_1 - t_0)\boldsymbol{v}(\boldsymbol{x}_0)]\} \approx n_0(\boldsymbol{x}_0) , \quad (6)$$

where n_i denotes the CI at position x of the image at time t_i. The actual and past images were subscribed with 1 and 0, respectively.

The best vector describing the cloud motion was determined using the displacement vector with the minimum mean square pixel difference (MSE):

$$\mathrm{MSE} = \frac{1}{N}\sum_i [n_1(\boldsymbol{x}_i + [(t_1 - t_0)\boldsymbol{v}(\boldsymbol{x}_i)]) - n_0(\boldsymbol{x}_i)]^2 . \quad (7)$$

2.2.4. *Error metrics*

The accuracy of the SSI estimates and nowcasting with 20-min temporal resolution was evaluated for the Xianghe observations. For spatial matching, we used the SSI estimates and nowcasting for the closest pixel to the Xianghe station. The FY-4A SSI estimates and nowcasting performance were evaluated using the following statistical indices: root-mean-square error (RMSE), mean bias error (MBE), and their normalized counterparts (nRMSE and nMBE).

3. Results

In this section, we first evaluate the performance of the REST2 model, then the accuracy of the estimated GHI and DNI, and finally, the forecast accuracies for time horizons between 30–180 min. All evaluations are detailed under the four sky conditions.

3.1. *Clear-sky GHI and DNI evaluation*

Figure 4 shows the scatter statistics of the clear-sky GHI and DNI estimates based on the REST2 model. The GHI estimates were very close to the ground-based measurements, with nRMSE and nMBE of 4.93% and 1.68%, respectively. The REST2 model tended to slightly overestimate GHI on clear-sky days, and it tended to overestimate DNI

by a larger magnitude compared to GHI, with an nMBE value of 8.67%. Large overestimations of DNI were observed in low and moderate DNI conditions. One explanation is that a lower DNI is associated with a high aerosol loading, which is generally underestimated by the MERRA-2 reanalysis (Huang et al., 2021). Notably, the model estimates were very close to the surface measurements when DNI was high. The high output power of solar PV plants depends on high DNI values. Compared to the low and moderate DNI values, the fluctuations of high DNI values will induce heavier impact on the safe operation, control, and management of solar PV plants. Therefore, the accurate calculation of high DNI values is crucial for the utilization of solar PV and is the focus of DNI calculations. Overall, the REST2 model performed well in supporting the GHI and DNI estimates and nowcasting evaluations at the Xianghe station under different conditions.

3.2. *All-sky GHI and DNI evaluation*

Figure 5 presents the density plot of FY-4A GHI and DNI under all-sky conditions against surface observations at Xianghe. The estimated GHIs show good correlation with the surface measurements, with nRMSE and nMBE of 22.4% and 5.9%, respectively. The percentage of the estimated GHI values exceeding the measurements by 100 W m^{-2} was approximately 15.9%. These overestimated GHI values were concentrated at 200–500 W m^{-2}, comprising the dominant contribution to GHI overestimation. Accurate calculation of high GHI values is crucial for solar energy estimation and forecasting. The good performance of the FY-4A GHI estimation model when the GHI is high indicates that the model can support FY-4A GHI estimation and nowcasting under all-sky conditions. Compared with the estimated GHI, the performance of the estimated DNI is worse, and the model needs to be improved in this aspect. In general, the

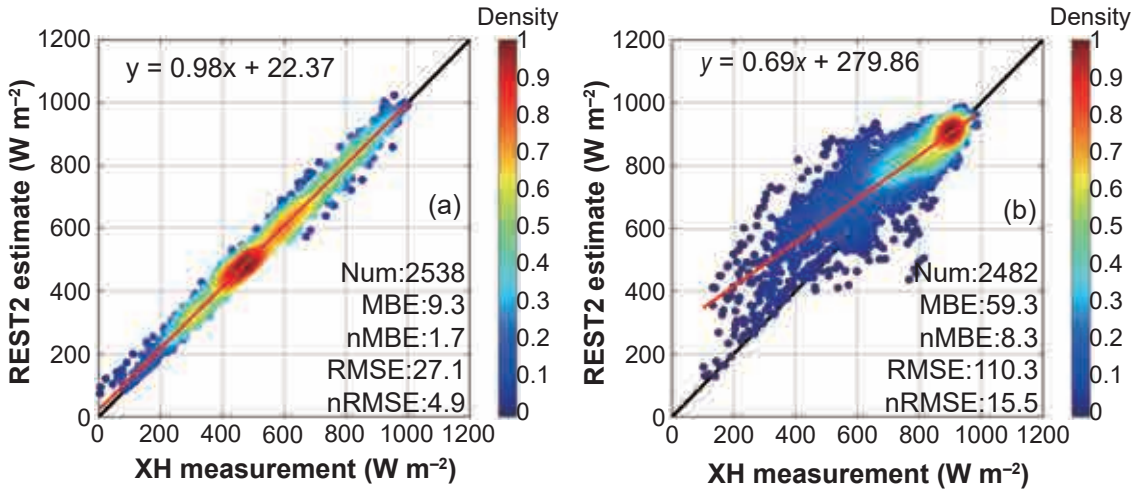

Fig. 4. Density plot of REST2 model GHI (a) and DNI (b) versus surface measurements under clear-sky conditions. The black line denotes a 1:1 line. The red lines indicates linear regression results.

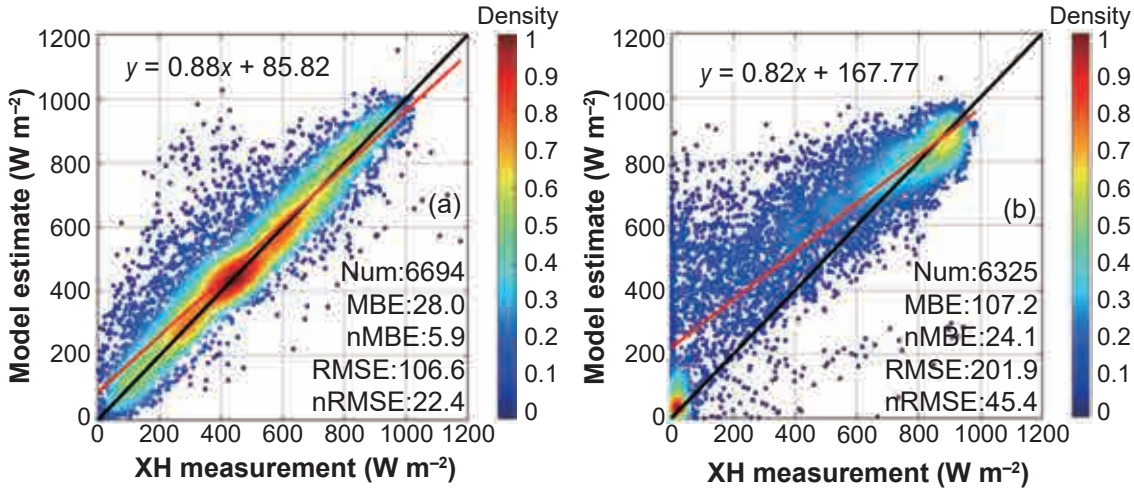

Fig. 5. Density plot of the SSI estimation model GHI (a) and DNI (b) versus SSI measurements under all-sky conditions in 2018. The black line denotes a 1:1 line. The red lines indicate liner regression results.

FY-4A DNI was overestimated with an nMBE value of 24.1% (Fig. 5b). The empirical-cloudy model performs well with a high DNI condition and tends to largely overestimate DNI when DNI values are lower than 700 W m^{-2}. One explanation is that if the ground station is covered by the shadows of clouds or surrounding features (namely, the 3D effect), its real-time measured DNI will be lower than that of other locations within the matching pixel in satellite images, thus the measured DNI values will be lower than satellite-derived values (Huang et al., 2019; Jiang et al., 2019). The deviation of clear-sky DNI background and CI is also a contributor to the overestimation.

Table 1 shows the statistical indices of the estimated GHI and DNI in this study compared with those in previous studies based on empirical methods. The nRMSE and nMBE of the GHI estimates in Shanghai obtained by Chen et al. (2020) were 34.7% and 11.4%, respectively, which were higher than those obtained in our work by 12.3% and 5.5%. The nRMSE values of the estimated GHI and DNI in our study were lower by 3.5% and 3.9%, respectively, compared to those obtained by Jia et al. (2021) in their study of northern China. The improvement of our estimation model eliminates the bias related to SZA variation by introducing a parameterization of the FY-4A clear-sky reflectance to SZA.

The evaluation of the estimated GHI and DNI for different sky conditions is shown in Fig. 6. The accuracies of GHI and DNI estimations declined with an increase in cloud occurrence (from clear-sky C1 to overcast C4). GHI estimates feature less deviation under clear, moderately clear, and cloudy conditions. The MBE values of GHI varied from –22.4 W m^{-2} to 23.5 W m^{-2}, and the RMSE values increased from 41.1 W m^{-2} to 90.5 W m^{-2} as the sky conditions varied from C1 to C3. The estimation accuracy declined sharply under C4 conditions, with the MBE and RMSE reaching 62.6 W m^{-2} and 144.5 W m^{-2}, respectively. The performance of the estimated DNI was significantly worse than that of the GHI estimation, featuring larger deviations under all four conditions. The MBE values varied from –9.1 W m^{-2} to 173.1 W m^{-2}, while the RMSE values increased from 94.2 W m^{-2} to 253.7 W m^{-2}. The poor performance under the C4 condition had a limited impact on the PV plants because the grid-connected power allocation can be adjusted to suit C4 conditions based on regional numerical models. Therefore, the performance of the GHI and DNI estimates under other sky conditions, especially C1 and C2, is the focus of GHI and DNI estimation and nowcasting and is crucial in the utilization of solar PV.

To characterize seasonal variations in model accuracy, the monthly mean estimated GHI and DNI and surface measurements were compared in Fig. 7. The monthly mean estimations of GHI and DNI were larger than the surface measurements. The difference between model and observation presented a seasonal pattern with a large discrepancy in spring–summer and a small difference in autumn–winter. The seasonal pattern of the GHI and DNI model discrepancy is related to the seasonal variation in cloud occurrence. In spring and summer, the proportion of days with the C4 condition was higher than 40%, especially in July, with the proportion reaching 90% (as shown in Fig. 2). High cloud occurrence reduces the accuracy of the estimated GHI and DNI. With the decrease in cloud occurrence, the discrepancy between estimated GHI and DNI and their respective measurements was reduced in autumn and winter.

3.3. *Forecast evaluation*

A case of forecasted and observed CI, GHI, and DNI is presented in Fig. 8, with a 60-min forecast horizon at 0140 UTC 1 December 2018. The CI at 0240 UTC was forecasted from the CI observations and CMV information at 0140 UTC. The estimated GHI and DNI and the CI forecast were used to obtain the GHI and DNI nowcasts at 0240 UTC. The FY-4A-based GHI and DNI nowcasts and the observations had similar spatial distribution patterns. An apparent divergence between forecasts and observations occurred in the red rectangular area with broken clouds (Figs. 8a and 8d) because the CMV derivation using the block-matching method does not consider the formation and dissipation of clouds. Therefore, the CMV forecast method has relatively low predictability under the broken-cloud situation.

The quality of GHI and DNI nowcasting within 0–3 h ahead, under all-sky conditions, is summarized in Table 2. The statistical indices for 0 min ahead were taken as deviations between the GHI and DNI estimations and the surface measurements. For 0–3-h forecast horizons, the nRMSE values of the GHI and DNI nowcasts increased slowly to 30.8% and 53.4%, respectively, surpassing those at 0 min ahead only by 8.4% and 8.0%, respectively. The nMBE values of GHI and DNI decreased with increasing forecast horizon from 5.9% and 24.1% at 0 min ahead to 0.8% and 18.6% at 3 h ahead, respectively. The GHI and DNI nowcasting methods offset the overestimation of the hybrid estimation method.

In the FY-4A satellite-based study conducted for

Table 1. Statistical indexes of instantaneous FY-4A SSI in the present study and previous studies.

No.	Reference	Site	SSI	RMSE	nRMSE	MBE	nMBE
1	Present study	Xianghe, China	GHI	106.6	22.4	28.0	5.9
			DNI	201.9	45.4	107.2	24.1
2	Chen et al. (2020)	Shanghai, China	GHI	–	34.7	–	11.4
3	Jia et al. (2021)	Chengde, China	GHI	120.1	25.9	–4.7	–1.0
			DNI	230.5	49.3%	–97.3	–20.8

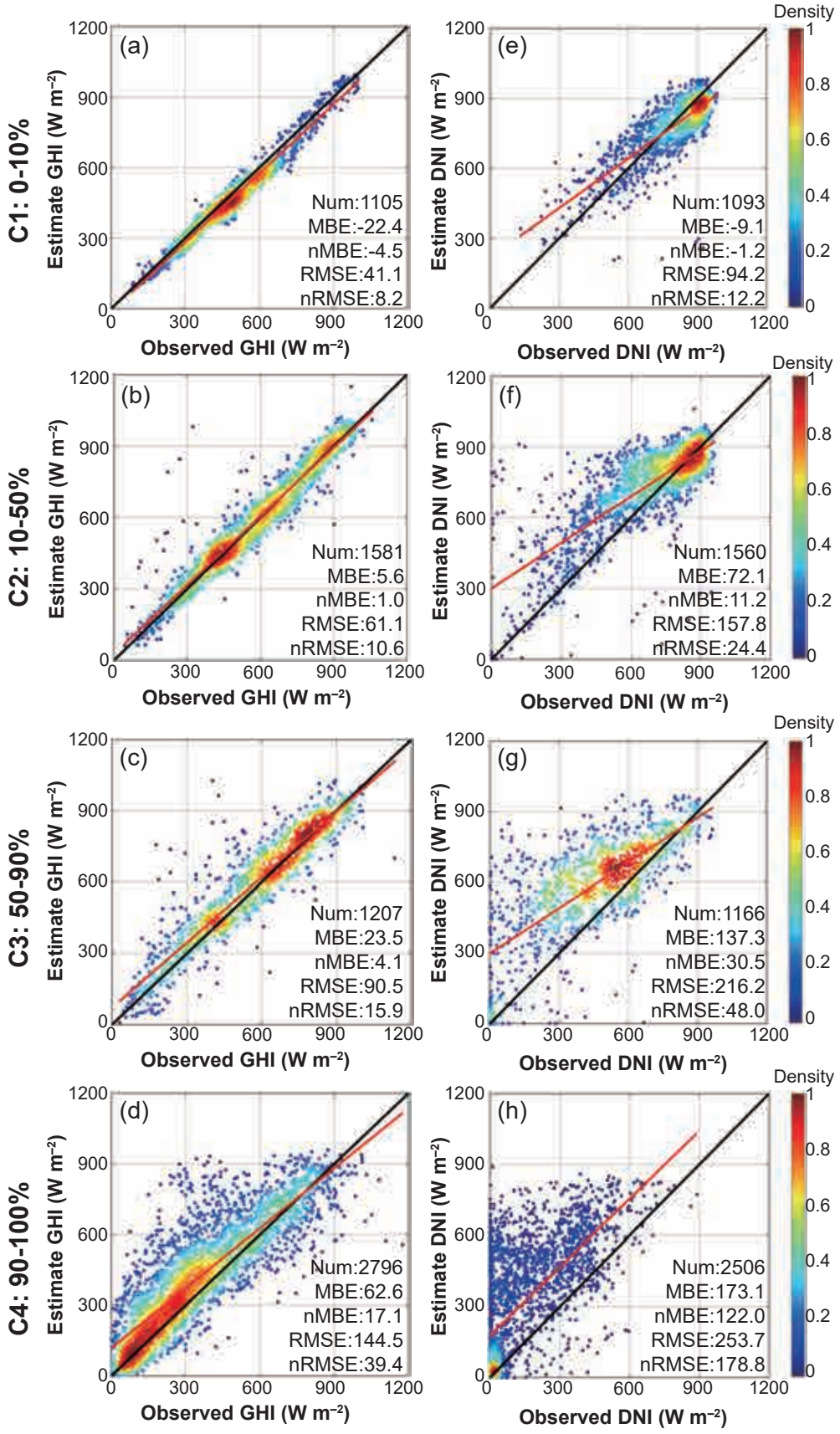

Fig. 6. Density plot of the SSI estimation model GHI (a–d) and DNI (e–h) versus observed SSI under different sky conditions. The black line denotes a 1:1 line. The red lines indicate linear regression results.

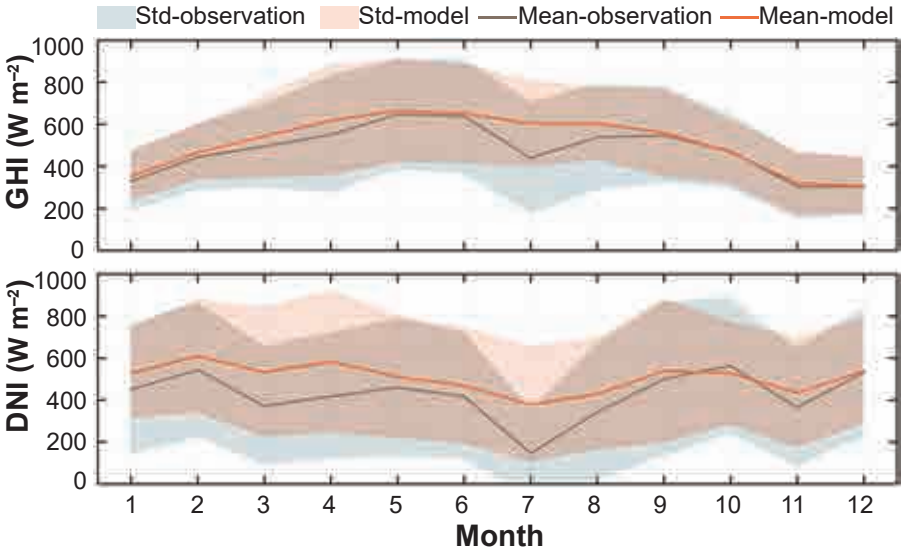

Fig. 7. Monthly mean of observed (grey line) and model (orange line) surface solar irradiance GHI (a) and DNI (b) in 2018. Shaded regions indicate one standard error of the mean.

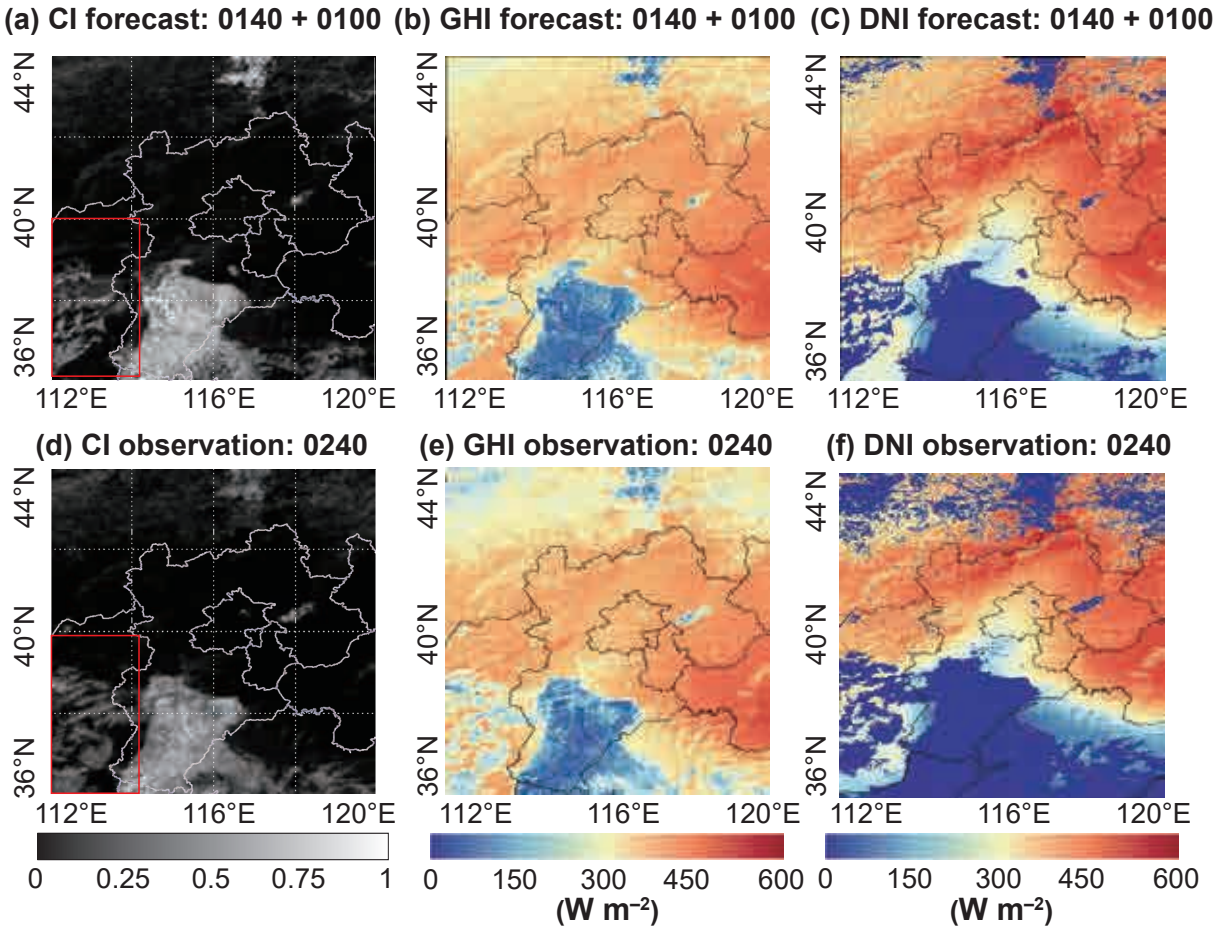

Fig. 8. An example of FY-4A-based (a–c) nowcasting and (d–f) observation for CI, GHI, and DNI at 0240 UTC on 1 December 2018.

Chengde by Yang et al. (2020), the nRMSE values of the GHI and DNI forecasts at 3 h ahead were 36.8% and 58.8%, respectively. The nRMSE of the FY-4A GHI forecasts for Shanghai calculated by Chen et al. (2020) was nearly 60% with a forecast horizon of 3 h. Both of these studies presented higher nRMSE values than the present study, suggesting

that the GHI and DNI nowcasting system in this study performed better for forecast horizons up to 3 h. The CMV derivation algorithm used in the reference and our work has a similar performance (Cros et al., 2014). In this study, the correction (the parameterization of FY-4A clear-sky reflectance to SZA before CI calculation) decreases the deviations of the estimations and further improves the performance of the GHI and DNI nowcasting systems.

Figure 9 shows the nRMSE and nMBE values of GHI and DNI nowcasting under four sky conditions with forecast horizons of 0–3 h. The nRMSE values of GHI nowcasting are between 8% and 22% at 30–180 min ahead, and the

Table 2. Statistical indexes (the mean value, RMSE, nRMSE, MBE, and nMBE) under all-sky conditions with forecast horizons from 0–180 min (units: W m^{-2}).

SSI	Metric	0 min	30 min	60 min	90 min	120 min	150 min	180 min
GHI	mean	475.9	469.4	479.9	510.9	500.9	494.8	485.6
	RMSE	106.6	117.8	125.5	138.5	144.4	143.2	149.5
	nRMSE	22.4	25.1	26.2	27.1	28.8	28.9	30.8
	MBE	28.0	34.5	28.3	27.2	14.9	18.9	3.7
	nMBE	5.9	7.3	5.9	5.3	3.0	3.8	0.8
DNI	mean	444.7	430.3	438.0	452.7	447.2	441.7	419.4
	RMSE	201.9	207.3	208.3	220.2	222.0	228.3	232.6
	nRMSE	45.4	48.1	47.6	48.6	49.6	51.7	53.4
	MBE	107.2	105.0	98.5	99.2	87.8	90.8	81.1
	nMBE	24.1	24.4	22.5	21.9	19.6	20.6	18.6

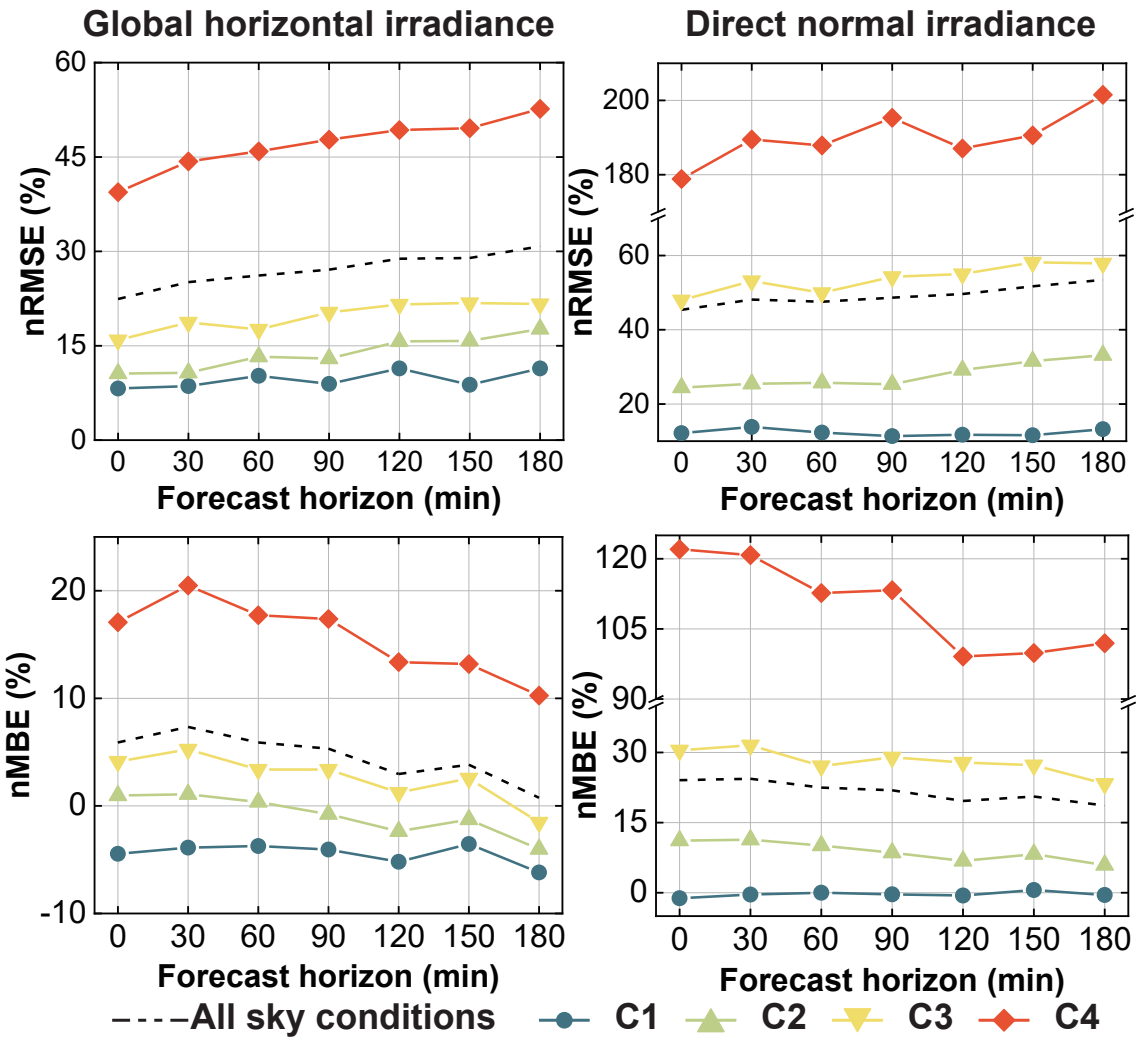

Fig. 9. The nRMSE (%) and nMBE (%) of SSI under different sky conditions with forecast horizons from 30–180 min.

increase with growing forecast horizon is relatively small under C1, C2, and C3 conditions. The nRMSE values under C4 increased rapidly as the forecast horizon increased—from 44.3% at 30 min ahead to 52.6% at 180 min. The nRMSE of DNI nowcasting exhibits similar trends, but the values are larger. The nRMSE is about 12%–13% under C1 conditions, with the 150-min forecast horizon having the smallest value. For C2 and C3 conditions, the nRMSE values increased with increasing forecast horizons—from 25.4% and 53.1% at the 30-min horizon to 33.1% and 57.9% at the 180-min horizon, respectively. Under the C4 condition, the nRMSE values of DNI show big changes over the forecast horizons of 30–180 min, ranging from 189.5% to 201.5%.

The nowcasting system tends to overestimate DNI. The most severe overestimations were under C4, followed by under the C3, C2, and C1 conditions. The nMBE values of DNI showed small changes under all sky conditions, except under C4. The highest nMBE value of DNI was 31.6% at 30 min ahead under cloudy conditions. Note that the nRMSE and nMBE values of DNI nowcasting are significantly higher under C4 conditions than under other sky conditions due to the low DNI.

4. Discussion

The benchmarks of nRMSE for GHI and DNI forecasts given by the University of Geneva are 15%–70% and 30%–160%, respectively (Beyer et al., 2009). The nRMSE values of GHI and DNI nowcasts in our study were within these ranges under all-sky conditions, except for C4. The SSI nowcasting system established in this work performed well for forecast horizons up to 180 min. The GHI nowcasting outperformed the DNI nowcasting for all forecast horizons. Furthermore, the new generation geostationary satellite FY-4A is promising for application in SSI nowcasting, but its accuracy still needs to be improved. Improving the SSI nowcasting system consists of two steps: revising the hybrid SSI estimation method and upgrading the CMV derivation algorithms.

The REST2 model performs well in estimating the clear-sky GHI in heavily polluted areas (e.g., North China). The AOD input quality in the REST2 model was key to clear-sky DNI estimation because DNI is especially sensitive to AOD compared to GHI (Gueymard and George, 2005). The empirical cloudy-sky model was first developed for MSG and is applicable to European regions (Yang et al., 2019), but it requires further revisions for it to be applicable in China using FY-4A data. The empirical coefficients of the cloudy-sky model have been calibrated based on the historical data of Xianghe station and lead to satisfactory results under clear and moderately clear conditions. The further revisions should focus on promoting the performance of the DNI estimation method under cloudy and overcast conditions. More attention should be paid to the calculation of the CI and the empirical coefficient of Eqs. (1) and (5). Long-term clear-sky DNI estimation and surface measurements should be used to fit the most suitable coefficients under different sky conditions. The empirical coefficients can be refined if high-quality SSI measurements are available across the country. Furthermore, the applicability and revision of these empirical coefficients in different regions and seasons in China is also a problem worthy of in-depth study.

The accuracy of the SSI forecast method depends on the CMV derivation algorithm. In this work, we calculated the CMV using FY-4A single-channel data. Subsequent research can develop multichannel-based CMV derivation algorithms to more accurately characterize the cloud motion. The cloud physical properties, the formation and dissipation of broken clouds, and the alteration of direction and speed in cloud motion should also be considered in future CMV derivation algorithms. For example, the square boxes used to obtain CMV fields are further divided into multiple square sub-boxes, and then intensity vectors for each sub-box, which are used to reflect the formation and dissipation process of clouds, are calculated using the alteration of pixel intensities in consecutive CI images.

5. Conclusions

A preliminary but effective SSI nowcasting system was developed based on FY-4A Level 1 reflectance data at 0.83 μm. This system was composed of an SSI estimation and forecasting method. A semiphysical SSI estimation method was developed, in which the REST2 model was first used to calculate clear-sky SSI. Subsequently, all-sky SSI was estimated according to the clear-sky SSI and the CI derived from FY-4A reflectance measurements. SSI nowcasting was developed using the CMV obtained using the block-matching method. The main conclusions are as follows:

The REST2 model performed well in supporting GHI and DNI estimates and nowcasts at Xianghe under different sky conditions. The FY-4A GHI estimates show good correlation with the surface measurements, with nRMSE and nMBE of 22.4% and 5.9%, respectively. The calibrated empirical method can be extended to DNI estimation under clear and moderately clear conditions, but it must be further improved under cloudy and overcast conditions. The FY-4A DNI estimation method tends to severely overestimate DNI when the actual DNI values are lower than 700 W m^{-2}. The difference between the model results and observations presents a seasonal pattern, with a large discrepancy in spring–summer and a small difference in autumn–winter. The seasonal pattern of the GHI and DNI model discrepancy is related to seasonal variations in cloud occurrences.

The nRMSE values of GHI and DNI nowcasts under all-sky conditions varied within 25.1%–30.8% and 48.1%–55.3%, respectively. The SSI nowcasting system performs well for forecast horizons up to 180 min, but its accuracy still needs improvement. The FY-4A has great potential for supporting SSI nowcasting, which would certainly enable the promotion of PV energy development and carbon emissions reduction in China.

Further enhancements to the SSI nowcasting system should focus on the calibration of the SSI estimation model and improving its applicability for China and FY-4A. More

specifically, the coefficients of the empirical method can be refined if high-quality SSI measurements are available across the country.

Acknowledgements. This work was supported by the National Natural Science Foundation of China (Grant Nos. 42030608, 41805021, and 51776051), the Beijing Natural Science Foundation (Grant No. 8204072), and Beijing Nova Program (Grant No. Z211100002121077). We would like to thank the National Satellite Meteorological Center and the MERRA-2 teams for providing the data used in this study. The FY-4A data were collected from http://satellite.nsmc.org.cn/portalsite/default.aspx (accessed on 20 June 2021). The MERRA-2 data were collected from http://disc.sci.gsfc.nasa.gov/ (accessed on 12 September 2021).

REFERENCES

Amillo, A. G., T. Huld, and R. Müller, 2014: A new database of global and direct aolar radiation using the eastern meteosat satellite, models and validation. *Remote Sensing*, **6**, 8165–8189, https://doi.org/10.3390/rs6098165.

Antonanzas, J., N. Osorio, R. Escobar, R. Urraca, F. J. Martinez-de-Pison, and F. Antonanzas-Torres, 2016: Review of photovoltaic power forecasting. *Solar Energy*, **136**, 78–111, https://doi.org/10.1016/j.solener.2016.06.069.

Antonanzas-Torres, F., R. Urraca, J. Polo, O. Perpiñán-Lamigueiro, and R. Escobar, 2019: Clear sky solar irradiance models: A review of seventy models. *Renewable and Sustainable Energy Reviews*, **107**, 374–387, https://doi.org/10.1016/j.rser.2019.02.032.

Arbizu-Barrena, C., J. A. Ruiz-Arias, F. J. Rodríguez-Benítez, D. Pozo-Vázquez, and J. Tovar-Pescador, 2017: Short-term solar radiation forecasting by advecting and diffusing MSG cloud index. *Solar Energy*, **155**, 1092–1103, https://doi.org/10.1016/j.solener.2017.07.045.

Bai, B., Y. H. Wang, C. Fang, S. Q. Xiong, and X. M. Ma, 2021: Efficient deployment of solar photovoltaic stations in China: An economic and environmental perspective. *Energy*, **221**, 119834, https://doi.org/10.1016/j.energy.2021.119834.

Beyer, H. G., J. P. Martinez, M. Suri, J. L. Torres, E. Lorenz, S. C. Müller, C. Hoyer-Klick, and P. Ineichen, 2009: D 1.1.3 Report on Benchmarking of Radiation Products. Management and Exploitation of Solar Resource Knowledge. Available from http://www.mesor.org/docs/MESoR_Benchmarking_of_radiation_products.pdf.

Burandt, T., B. Xiong, K. Löffler, and P.-Y. Oei, 2019: Decarbonizing China's energy system – Modeling the transformation of the electricity, transportation, heat, and industrial sectors. *Applied Energy*, **255**, 113820, https://doi.org/10.1016/j.apenergy.2019.113820.

Chen, X. M., Y. Li, and R. Z. Wang, 2020: Performance study of affine transformation and the advanced clear-sky model to improve intra-day solar forecasts. *Journal of Renewable and Sustainable Energy*, **12**, 043703, https://doi.org/10.1063/5.0009155.

Cros, S., M. Albuisson, M. Lefèvre, C. Rigollier, and L. Wald, 2004: HelioClim: A long-term database on solar radiation for Europe and Africa. *Proceedings of Eurosun 2004*, Freiburg, Germany, PSE GmbH.

Cros, S., N. Sébastien, O. Liandrat, and N. Schmutz, 2014: Cloud pattern prediction from geostationary meteorological satellite images for solar energy forecasting. *Proceedings of SPIE 9242, Remote Sensing of Clouds and the Atmosphere XIX; and Optics in Atmospheric Propagation and Adaptive Systems XVII*, Amsterdam, Netherlands, SPIE, https://doi.org/10.1117/12.2066853.

Damiani, A., and Coauthors, 2018: Evaluation of Himawari-8 surface downwelling solar radiation by ground-based measurements. *Atmospheric Measurement Techniques*, **11**, 2501–2521, https://doi.org/10.5194/amt-11-2501-2018.

Gallucci, D., and Coauthors,, 2018: Nowcasting surface solar irradiance with AMESIS via motion vector fields of MSG-SEVIRI Data. *Remote Sensing*, **10**, 845, https://doi.org/10.3390/rs10060845.

Gueymard, C. A., 2008: REST2: High-performance solar radiation model for cloudless-sky irradiance, illuminance, and photosynthetically active radiation – Validation with a benchmark dataset. *Solar Energy*, **82**, 272–285, https://doi.org/10.1016/j.solener.2007.04.008.

Gueymard, C. A., and R. George, 2005: Gridded aerosol optical depth climatological datasets over continents for solar radiation modeling. *Proceedings of Solar World Congress*, Orlando, USA, International Solar Energy Society. [Available online from https://www.semanticscholar.org/paper/GRIDDED-AEROSOL-OPTICAL-DEPTH-CLIMATOLOGICAL-OVER-Gueymard-George/a3e7dad6035e6a35afdccf9bf4b98319436c3014]

Hammer, A., D. Heinemann, E. Lorenz, and B. Lückehe, 1999: Short-term forecasting of solar radiation: A statistical approach using satellite data. *Solar Energy*, **67**, 139–150, https://doi.org/10.1016/S0038-092X(00)00038-4.

Huang, C. L., J. Z. Li, W. W. Sun, Q. X. Chen, Q.-J. Mao, and Y. Yuan, 2021: Long-term variation assessment of aerosol load and dominant types over Asia for air quality studies using multi-sources aerosol datasets. *Remote Sensing*, **13**, 3116, https://doi.org/10.3390/rs13163116.

Huang, G. H., Z. Q. Li, X. Li, S. L. Liang, K. Yang, D. D. Wang, and Y. Zhang, 2019: Estimating surface solar irradiance from satellites: Past, present, and future perspectives. *Remote Sensing of Environment*, **233**, 111371, https://doi.org/10.1016/j.rse.2019.111371.

IRENA, 2020: Renewable Capacity Statistics 2020: International Renewable Energy Agency (IRENA), Abu Dhabi. [Available online from https://irena.org/publications/2020/Mar/Renewable-Capacity-Statistics-2020]

Jia, D. Y., J. J. Hua, L. P. Wang, Y. T. Guo, H. Guo, P. P. Wu, M. Liu, and L. W. Yang, 2021: Estimations of global horizontal irradiance and direct normal irradiance by using Fengyun-4A satellite data in northern China. *Remote Sensing*, **13**, 790, https://doi.org/10.3390/rs13040790.

Jiang, H., N. Lu, J. Qin, W. J. Tang, and L. Yao, 2019: A deep learning algorithm to estimate hourly global solar radiation from geostationary satellite data. *Renewable and Sustainable Energy Reviews*, **114**, 109327, https://doi.org/10.1016/j.rser.2019.109327.

Kallio-Myers, V., A. Riihelä, P. Lahtinen, and A. Lindfors, 2020: Global horizontal irradiance forecast for Finland based on geostationary weather satellite data. *Solar Energy*, **198**, 68–80, https://doi.org/10.1016/j.solener.2020.01.008.

Kleissl, J., 2013: *Solar Energy Forecasting and Resource Assess-*

ment. Academic Press, https://doi.org/10.1016/C2011-0-07022-9.

Lamsal, D., V. Sreeram, Y. Mishra, and D. Kumar, 2018: Kalman filter approach for dispatching and attenuating the power fluctuation of wind and photovoltaic power generating systems. *IET Generation, Transmission & Distribution*, **12**, 1501–1508, https://doi.org/10.1049/iet-gtd.2017.0663.

Letu, H., T. Y. Nakajima, T.X. Wang, H. Z. Shang, R. Ma, K. Yang, A. J. Baran, J. Riedi, H. Ishimoto, M. Yoshida, C. Shi, P. Khatri, Y. H. Du, L. f. Chen, and J. C Shi, 2021: A new benchmark for surface radiation products over the East Asia-Pacific region retrieved from the Himawari-8/AHI next-generation geostationary satellite. *Bull. Amer. Meteor. Soc*, **103**, E873–888, https://doi.org/10.1175/BAMS-D-20-0148.1.

Li, M. Q., E. Virguez, R. Shan, J. L. Tian, S. Gao, and D. Patiño-Echeverri, 2022: High-resolution data shows China's wind and solar energy resources are enough to support a 2050 decarbonized electricity system. *Applied Energy*, **306**, 117996, https://doi.org/10.1016/j.apenergy.2021.117996.

Li, T., A. Li, and X. P. Guo, 2020: The sustainable development-oriented development and utilization of renewable energy industry-A comprehensive analysis of MCDM methods. *Energy*, **212**, 118694, https://doi.org/10.1016/j.energy.2020.118694.

Liu, M. Q., X. A. Xia, D. S. Fu, and J. Q. Zhang, 2021: Development and validation of machine-learning clear-sky detection method using 1-min irradiance data and sky imagers at a polluted suburban site, Xianghe. *Remote Sensing*, **13**, 3763, https://doi.org/10.3390/rs13183763.

Mouhamet, D., A. Tommy, A. Primerose, and L. Laurent, 2018: Improving the Heliosat-2 method for surface solar irradiation estimation under cloudy sky areas. *Solar Energy*, **169**, 565–576, https://doi.org/10.1016/j.solener.2018.05.032.

Nonnenmacher, L., and C. F. M. Coimbra, 2014: Streamline-based method for intra-day solar forecasting through remote sensing. *Solar Energy*, **108**, 447–459, https://doi.org/10.1016/j.solener.2014.07.026.

Peng, Z., and Coauthors, 2020: Estimation of shortwave solar radiation using the artificial neural network from Himawari-8 satellite imagery over China. *Journal of Quantitative Spectroscopy and Radiative Transfer*, **240**, 106672, https://doi.org/10.1016/j.jqsrt.2019.106672.

Pfeifroth, U., S. Kothe, J. Trentmann, R. Hollmann, P. Fuchs, J. Kaiser, and M. Werscheck, 2019: Surface Radiation Data Set - Heliosat (SARAH) - Edition 2.1. Available from https://doi.org/10.5676/EUM_SAF_CM/SARAH/V002_01.

Prăvălie, R., C. Patriche, and G. Bandoc, 2019: Spatial assessment of solar energy potential at global scale. A geographical approach. *Journal of Cleaner Production*, **209**, 692–721, https://doi.org/10.1016/j.jclepro.2018.10.239.

Randles, C. A., and Coauthors, 2017: The MERRA-2 aerosol reanalysis, 1980 Onward. Part I: System description and data assimilation evaluation. *J. Climate*, **30**, 6823–6850, https://doi.org/10.1175/JCLI-D-16-0609.1.

Razagui, A., K. Abdeladim, K. Bouchouicha, N. Bachari, S. Semaoui, and A. Hadj Arab, 2021: A new approach to forecast solar irradiances using WRF and libRadtran models, validated with MERRA-2 reanalysis data and pyranometer measures. *Solar Energy*, **221**, 148–161, https://doi.org/10.1016/j.solener.2021.04.024.

Rigollier, C., M. Lefèvre, and L. Wald, 2004: The method Heliosat-2 for deriving shortwave solar radiation from satellite images. *Solar Energy*, **77**, 159–169, https://doi.org/10.1016/j.solener.2004.04.017.

Senatla, M., and R. C. Bansal, 2018: Review of planning methodologies used for determination of optimal generation capacity mix: The cases of high shares of PV and wind. *IET Renewable Power Generation*, **12**, 1222–1233, https://doi.org/10.1049/iet-rpg.2017.0380.

Shi, H. R., and Coauthors, 2021: Surface brightening in eastern and central China since the implementation of the clean air action in 2013: Causes and implications. *Geophys. Res. Lett.*, **48**, e2020GL091105, https://doi.org/10.1029/2020GL091105.

Sun, X. X., J. M. Bright, C. A. Gueymard, X. Y. Bai, B. Acord, and P. Wang, 2021: Worldwide performance assessment of 95 direct and diffuse clear-sky irradiance models using principal component analysis. *Renewable and Sustainable Energy Reviews*, **135**, 110087, https://doi.org/10.1016/j.rser.2020.110087.

Wang, F., Z. Zhen, C. Liu, Z. Q. Mi, B.-M. Hodge, M. Shafie-Khah, and J. P. S. Catalão, 2018: Image phase shift invariance based cloud motion displacement vector calculation method for ultra-short-term solar PV power forecasting. *Energy Conversion and Management*, **157**, 123–135, https://doi.org/10.1016/j.enconman.2017.11.080.

Wang, P., R. van Westrhenen, J. F. Meirink, S. van der Veen, and W. Knap, 2019: Surface solar radiation forecasts by advecting cloud physical properties derived from Meteosat Second Generation observations. *Solar Energy*, **177**, 47–58, https://doi.org/10.1016/j.solener.2018.10.073.

Wild, M., D. Folini, F. Henschel, N. Fischer, and B. Müller, 2015: Projections of long-term changes in solar radiation based on CMIP5 climate models and their influence on energy yields of photovoltaic systems. *Solar Energy*, **116**, 12–24, https://doi.org/10.1016/j.solener.2015.03.039.

Xian, D., P. Zhang, L. Gao, R. J. Sun, H. Z. Zhang, and X. Jia, 2021: Fengyun meteorological satellite products for earth system science applications. *Adv. Atmos. Sci.*, **38**, 1267–1284, https://doi.org/10.1007/s00376-021-0425-3.

Yang, L. W., X. Q. Gao, Z. C. Li, D. Y. Jia, and J. X. Jiang, 2019: Nowcasting of surface solar irradiance using Fengyun-4 satellite observations over China. *Remote Sensing*, **11**, 1984, https://doi.org/10.3390/rs11171984.

Yang, L. W., X. Q. Gao, J. J. Hua, P. P. Wu, Z. C. Li, and D. Y. Jia, 2020: Very short-term surface solar irradiance forecasting based on Fengyun-4 geostationary satellite. *Sensors*, **20**, 2606, https://doi.org/10.3390/s20092606.

Zhang, J. Q., X. A. Xia, H. R. Shi, X. M. Zong, and J. Li, 2020: Radiation and aerosol measurements over the Tibetan Plateau during the Asian summer monsoon period. *Atmospheric Pollution Research*, **11**, 1543–1551, https://doi.org/10.1016/j.apr.2020.06.017.

Zhu, T. T., H. Zhou, H. K. Wei, X. Zhao, K. J. Zhang, and J. X. Zhang, 2019: Inter-hour direct normal irradiance forecast with multiple data types and time-series. *Journal of Modern Power Systems and Clean Energy*, **7**, 1319–1327, https://doi.org/10.1007/s40565-019-0551-4.

Zou, L., L. C. Wang, J. R. Li, Y. B. Lu, E. Gong, and Y. Niu, 2019: Global surface solar radiation and photovoltaic power from Coupled Model Intercomparison Project Phase 5 climate models. *Journal of Cleaner Production*, **224**, 304–324, https://doi.org/10.1016/j.jclepro.2019.03.268.

ADVANCES IN ATMOSPHERIC SCIENCES, VOL. 39, AUGUST 2022, 1329–1342

• **Original Paper** •

Ocean–atmosphere Teleconnections Play a Key Role in the Interannual Variability of Seasonal Gross Primary Production in China※

Kairan YING, Jing PENG*, Li DAN, and Xiaogu ZHENG

Key Laboratory of Regional Climate-Environment for Temperate East Asia, Institute of Atmospheric Physics, Chinese Academy of Sciences, Beijing 100029, *China*

(Received 11 June 2021; revised 29 November 2021; accepted 6 December 2021)

ABSTRACT

Since the 1950s, the terrestrial carbon uptake has been characterized by interannual variations, which are mainly determined by interannual variations in gross primary production (GPP). Using an ensemble of seven-member TRENDY (Trends in Net Land–Atmosphere Carbon Exchanges) simulations during 1951–2010, the relationships of the interannual variability of seasonal GPP in China with the sea surface temperature (SST) and atmospheric circulations were investigated. The GPP signals that mostly relate to the climate forcing in terms of Residual Principal Component analysis (hereafter, R-PC) were identified by separating out the significant impact from the linear trend and the GPP memory. Results showed that the seasonal GPP over China associated with the first R-PC1 (the second R-PC2) during spring to autumn show a monopole (dipole or tripole) spatial structure, with a clear seasonal evolution for their maximum centers from springtime to summertime. The dominant two GPP R-PC are significantly related to Sea Surface Temperature (SST) variability in the eastern tropical Pacific Ocean and the North Pacific Ocean during spring to autumn, implying influences from the El Niño–Southern Oscillation (ENSO) and the Pacific Decadal Oscillation (PDO). The identified SST and circulation factors explain 13%, 23% and 19% of the total variance for seasonal GPP in spring, summer and autumn, respectively. A clearer understanding of the relationships of China's GPP with ocean–atmosphere teleconnections over the Pacific and Atlantic Ocean should provide scientific support for achieving carbon neutrality targets.

Key words: interannual variation, seasonal gross primary production, ENSO, PDO, AO

Citation: Ying, K. R., J. Peng, L. Dan, and X. G. Zheng, 2022: Ocean-atmosphere teleconnections play a key role in the interannual variability of seasonal gross primary production in China. *Adv. Atmos. Sci.*, **39**(8), 1329−1342, https://doi.org/10.1007/s00376-021-1226-4.

Article Highlights:

- At regional scales, the interannual variability of seasonal GPP in the Chinese mainland is closely related to ocean–atmosphere teleconnections over the Pacific and Atlantic Ocean.
- From spring to autumn, there are considerable seasonal differences in GPP–teleconnection relationships, corresponding to local hydrothermal conditions.
- Ocean–atmosphere teleconnections mostly affect the GPP over eastern China (> 30% explained variance), which dominates the interannual GPP variability for China as a whole.

1. Introduction

Over the past six decades, China's terrestrial ecosystem has played an important role in the global carbon sink (Piao et al., 2009a; Peng et al., 2014; Le Quéré et al., 2018; Friedlingstein et al., 2020), with considerable interannual variance in response to climate changes (Zhang et al., 2019; Peng et al., 2021). Gross primary production (GPP) is one of the largest carbon fluxes and is strongly associated with the annual variance of the terrestrial carbon sink (Houghton, 2000; Piao et al., 2020). Previous studies have shown that ocean–atmosphere teleconnections exert important influences on the interannual variabilities and predictabilities of various climate variables, such as precipitation and temperature, on global and regional scales (e.g., Ying et al., 2015, 2017; Nian et al., 2020). However, in China, as one of the regions with the fastest increase in carbon emissions, such an impact of these teleconnections on the interannual vari-

※ This paper is a contribution to the special issue on Carbon Neutrality: Important Roles of Renewable Energies, Carbon Sinks, NETs, and non-CO_2 GHGs.

* Corresponding author: Jing PENG
Email: pengjing@tea.ac.cn

ances of GPP has not been well clarified. Furthermore, knowledge gaps in climate–carbon linkages may further contribute to conflicting model results concerning the future terrestrial carbon uptake in earth system models (Tharammal et al., 2019). Therefore, developing a better understanding of the relationships between the interannual variation of GPP in China and ocean–atmosphere teleconnections will not only offer the opportunity to better understand climate–carbon cycle relationships, but also increase the confidence in future projections of the carbon cycle under different carbon emission scenarios.

As indicated by various climatological studies, external forcing and low-frequency (interannual to supra-annual) internal atmospheric dynamics are influential climatic factors governing the interannual variations of seasonal mean anomalies in China's precipitation, temperature and soil moisture (e.g., Wang et al., 2008, 2015; Wu et al., 2009; Gong et al., 2011; Ying et al., 2016, 2017; Nian et al., 2020), including, for instance, global sea surface temperature (SST) anomalies and large-scale atmospheric oscillations. Because of the close relationships between GPP and local hydrothermal conditions of precipitation, temperature and soil moisture, as revealed by many previous studies (Nemani et al., 2003; Richardson et al., 2007; Beer et al., 2010; Barman et al., 2014; Zhang et al., 2019; Peng et al., 2020), the interannual variability of China's GPP should also arise from these distant ocean–atmosphere teleconnection processes. It has long been noted that the well-known climatic modes, such as El Niño–Southern Oscillation (ENSO) and Arctic Oscillation (AO), can influence the global terrestrial carbon cycle (Reimer et al., 2015; Dannenberg et al., 2018). For instance, hot and dry climate conditions in El Niño years are the primary reasons for a lower carbon sink and even a carbon source at regional scales, particularly in the tropics (Nemani et al., 2003; Ahlström et al., 2015; Zhang and Jia, 2020). In addition, Schaefer et al. (2005) and Cho et al. (2014) found a close relationship among the winter AO and the vegetation activity and carbon fluxes in the following spring over the Northern Hemisphere. However, at regional scales, due to the different intensities of the ocean–land–atmosphere coupling, the response of the regional carbon flux to natural cyclic climatic phenomena varies substantially (Dannenberg et al., 2018; Betts et al., 2021). At present, in China, how and to what extent the interannual variability of GPP responds to these impacts from sea temperature and large-scale atmospheric circulation is not yet clear. Therefore, it is important to better understand the relationship between the interannual changes in China's GPP and ocean–atmosphere teleconnection. This is a key process towards elucidating the carbon sequestration mechanisms of terrestrial ecosystems on regional scales, especially over China (Zhu et al., 2017).

Considering the sources of interannual variability of China's GPP, the significant trend in China's GPP, owing to the effects of human activities and climate change, has been extensively examined (Piao et al., 2009b; Peng and Dan, 2015; Forkel et al., 2016; Chen et al., 2017; Yao et al., 2018; Ma et al., 2019; Piao et al., 2020). This long-term trend provides an important source of interannual variability for GPP in China. Furthermore, in the same way that the oceans can store heat and soil moisture can store water, vegetation is a carbon pool, with associated "memory" features (inertia of a climate variable that persists from the past conditions). This is reflected by the close relationship between the current and prior GPP anomalies. As the GPP can "remember" the anomalous status long after those anomalies are "forgotten" by the atmosphere, it possesses larger potential predictabilities [Fig. S1 in the Electronic Supplementary Materials, (ESM)] than atmospheric variables such as precipitation (Ying et al., 2017) and temperature (Nian et al., 2020). Thus, the memory of GPP also provides a source of its annual variance. However, this study is mostly interested in the linkage of China's GPP with ocean–atmosphere teleconnections. Consequently, we separated out the significant effects from the linear trend and GPP memory as the first step.

The objective of the present study is to better understand the sources of the interannual variability of spring-to-autumn GPP in China that derive from ocean–atmosphere teleconnections. To achieve this, using monthly GPP data obtained from a seven-member TRENDY (Trends in Net Land–Atmosphere Carbon Exchanges) simulation over China, we focus on the dominant GPP signals that are mostly related to the SST and circulations, by separating out the significant effects from the linear trend and GPP memory. This study aims to explore (1) the main ocean–atmosphere teleconnections related to the interannual variability of the seasonal mean GPP in the Chinese mainland from spring to autumn; and (2) to what extent the year-to-year fluctuations of China's GPP are dominated by the identified key ocean–atmosphere teleconnection factors. The data and methods employed in the study are described in section 2. Analyses of seasonal contribution characteristics of China's GPP interannual variabilities are reported in section 3.1. The GPP interannual variability arising from the trend, GPP memory and climate forcing are presented in section 3.2 and the main sources of the interannual variability from ocean–atmosphere teleconnections are discussed in section 3.3. The fractions of variance explained by the key ocean–atmosphere teleconnection factors are evaluated in section 3.4. The conclusions and some further discussion are presented in section 4.

2. Data and methods

2.1. *Data*

To further assess the responses of China's GPP to ocean–atmosphere teleconnections, TRENDY models that participated in the Global Carbon Project (Le Quéré et al., 2018) were prepared to simulate the monthly GPP from 1951 to 2010. The seven models included in this study were CABLE, CLM4C, CLM4CN, LPJ, LPJ_GUESS, SDGVM and TRI (Table 1). The TRENDY project includes datasets of offline experiments driven by constant or varying inputs

Table 1. Seven trendy models used in this study.

Model name	Abbreviation	Spatial resolution (lat × lon)	Land surface model	Full nitrogen cycle	Fire simulation	Harve flux	Source
Community Land	CLM4C	0.5° × 0.5°	Yes	No	Yes	No	Oleson et al. (2010)
Community Land	CLM4CN	0.5° × 0.5°	Yes	Yes	Yes	No	Oleson et al. (2010)
Lund–Potsdam–Jena	LPJ	0.5° × 0.5°	No	No	Yes	Yes	Sitch et al. (2003)
LPJ-GUESS	LPJ-GUESS	0.5° × 0.5°	No	No	Yes	No	Smith et al. (2001)
Sheffield-DGVM	SDGVM	3.75° × 2.5°	No	No	Yes	No	Woodward et al. (1995)
TRIFFID	TRI	3.75° × 2.5°	Yes	No	No	No	Hughes et al. (2006)
CABLE	CABLE	0.5° × 0.5°	No	Yes	No	No	Wang et al. (2011)

(i.e., climate variables, atmospheric CO_2, and land use/cover forcing). Its purpose was to distinguish between the effects of CO_2, climate, and land use. We mainly evaluated the results of the S2 experiment, which only considers varying climate variables and CO_2, without varying land use. Further details about the S2 TRENDY simulation protocol can be found in Piao et al. (2013). Importantly, models from TRENDY are broadly considered to be the world's most advanced terrestrial ecosystem models. Through comparison with satellite remote sensing data, previous studies have demonstrated that carbon fluxes from TRENDY are simulated well in China (Zhang et al., 2016; Peng et al., 2021).

In order to better understand the air–ocean teleconnections associated with GPP in China, we used monthly mean datasets of (1) 500-hPa geopotential height from the National Centers for Environmental Prediction–National Center for Atmospheric Research Reanalysis 1 project (Kalnay et al., 1996), with a spatial grid resolution of 2.5°; (2) SST (on a 1° × 1° grid) from the UK Met Office Hadley Centre Sea Ice and Sea Surface Temperature dataset, version 1 (Rayner et al., 2003); (3) precipitation and temperature (on a 0.5° × 0.5° grid) from the Climate Research Unit time series datasets, version 4.03 (Harris et al., 2020); (4) soil moisture (on a 1° × 1° grid) from TRENDY simulations in China; and (5) climate indices from the National Oceanic and Atmospheric Administration's Climate Prediction Center (available at https://psl.noaa.gov/data/climateindices/list/).

2.2. *Methods*

Firstly, the climatological mean was removed from the monthly data. Then, by separating out the significant influences from the prolonged trend and GPP memory, the following procedure was followed to derive the GPP signals that were mostly associated with the climate forcing component:

(1) An empirical orthogonal function (EOF) analysis (Lorenz, 1956) was applied to the sample covariance matrix of the seasonal GPP field $x_{y,o}$ in year y (y = 1, 2, ..., Y; Y is the total number of years) and season o (a three-month season) to derive the EOF modes and their associated principal component (PC) time series t_y.

(2) For each PC time series t_y, the dependence on a linear trend and a red noise process was modelled as

$$t_y = \lambda[y-(Y+1)/2]+\varepsilon_y+\mu\,. \tag{1}$$

Here, λ is the linear trend (consecutive years from 1 to Y) within total Y years, μ is an intercept/mean term, and ε_y is an autoregressive process of order 1 (AR1), i.e.,

$$\varepsilon_y = \alpha\varepsilon_{y-1}+\eta_y\,, \tag{2}$$

where α is the yearly autocorrelation coefficient and η_y is the white noise [following Eq. (1) of Zheng and Basher, 1999].

In this case, by removing those effects from the trend λ and GPP memory component $\alpha\varepsilon_{y-1}$ that were statistically significant (the Autoregressive Integrated Moving Average Model in R-code was used for calculations), the climate information was included in the residual component of the PC time series η_y. For convenience, the total and residual component of the PC time series are denoted by T-PC (t_y) and R-PC (η_y), respectively.

(3) With R-PC η_y derived, the main SST and circulation factors related to the GPP in China could then be identified by calculating the correlation coefficients of the SST or circulations associated with the GPP R-PC.

Following Wilks (1995), the fractional variance was applied to evaluate the relative importance of the identified SST or circulation factors associated with the dominant GPP R-PC. Let $\boldsymbol{e}_j$ be the jth (j = 1,…., J, where J is the total number of EOF) EOF, and $\hat{\boldsymbol{p}}_{j,y}$ be the linear regression for the jth R-PC time series in year y based on its associated key ocean–atmosphere teleconnection factors. Then, the fractional variance of the seasonal mean anomalies explained by the key SST or circulation factors is

$$\mathrm{FV} = 100\left(1-\sum_{y}\left\|\boldsymbol{r}_y-\sum_{j=1}^{\mathrm{J}}\hat{\boldsymbol{p}}_{j,y}\boldsymbol{e}_j\right\|^2\Big/\sum_{y}\left\|\boldsymbol{r}_y-\bar{\boldsymbol{r}}\right\|^2\right), \tag{3}$$

where FV is the fractional variance of the seasonal mean anomalies explained by the key SST or circulation factors, $\boldsymbol{r}_y$ is the yth-year seasonal GPP, $\bar{\boldsymbol{r}} = [\bar{r}(1),...,\bar{r}(N)]$ is the climatology of $\boldsymbol{r}_y$, and $\|\|$ is the Euclidean distance operator; for example,

$$\left\|\boldsymbol{r}_y-\bar{\boldsymbol{r}}\right\|^2 = \sum_{n=1}^{\mathrm{N}}\left(r_y(n)-\bar{r}(n)\right)^2. \tag{4}$$

Here, n (= 1,…., N) denotes a specific location.

3. Results

3.1. *Seasonal contribution characteristics*

The interannual variation of the seasonal mean GPP exhibits considerable differences among seasons. In general, the interannual variability of China's GPP from spring to autumn (March to November) – covering the whole growing season – dominates the variations for all seasons (Fig. 1a), accounting for 91% of total interannual variations. Particularly, the largest interannual variations are observed in June–July–August (summer) over most of the Chinese mainland, and the second largest are in September–October–November (autumn), followed by March–April–May (spring) (Table 2; Figs. 1b–d). A similar east–west gradient in terms of spatial distribution is apparent in all these three seasons, with larger values mainly located over eastern China, where the influence of the East Asian monsoon is greatest (Figs. 1b–d). With the development of the East Asian monsoon, the maximum centers show a clear seasonal migration from spring to autumn, with the largest values over central China and southwestern China in spring [larger than 0.002 (KgC m^{-2} $month^{-1})^2$], central China and northeastern China in summer [larger than 0.004 (KgC m^{-2} $month^{-1})^2$], and southeastern China in autumn [larger than 0.004 (KgC m^{-2} $month^{-1})^2$]. Also, there are remarkable differences in the mean state and principal modes of SST and atmospheric circulations during different seasons (Frederiksen and Zheng, 2004; Zheng et al., 2008). Therefore, it is important to investigate the relationships of the interannual variability of the GPP in China associated with the SST and atmospheric circulation patterns in separate seasons. The discussions below will focus on the seasons from spring to autumn, which comprise the growing seasons and have the largest interannual variabilities.

3.2. *Variability arising from the trend, GPP memory and climate forcings*

First, the T-PC and R-PC of China's GPP are estimated using Eq. (1). As shown in Fig. 2, apparent upward trends, which are statistically significant at the 95% confidence level based on the Student's *t*-test, can be seen for the GPP T-PC1 during spring to autumn (black lines in Figs. 2b, d and f). Meanwhile, there is a statistically significant (at the 95% confidence level) memory signal in the GPP T-PC2 of summer (black line in Fig. 2j). Thus, to focus on the GPP signals that are mostly related to the climate forcing component, the R-PC needed to be extracted by removing the significant effects from the trend and GPP memory (red lines in right-hand panel of Fig. 2; only the two most dominant PC with the largest explained variances are displayed).

To explore the relative importance of the trend, memory and climate forcing on the interannual variability of seasonal GPP in China, the total variance and the residual variance from the linear trend and the GPP memory of the GPP were then obtained. Overall, the average residual-to-total percentage variance is high for the GPP in China, with values of 64%, 60% and 65% from spring to autumn, respectively (Table 2). This indicates that there is still a large amount of the GPP interannual variance that cannot have originated from the prolonged trend and the GPP memory; that is, the GPP interannual variance may be largely affected by the lagged and simultaneous conditions of the climate forcing component.

Compared to the spatial distributions of the total variance (Figs. 1b–d), the residual variance from the trend and the GPP memory (Figs. 1e–g) show similar distribution features, with the largest values over central China and southwestern China in spring, central China and northeastern China in summer, and southeastern China in autumn. In particular, the maximum centers of the residual-to-total ratio (Figs. 1h–j), which contain over 50% of the percentage, include the above particular areas that possess the largest interannual variations (Figs. 1b–g). Thus, it was necessary to identify the key ocean–atmosphere teleconnections associated with the seasonal GPP over China to further understand the main sources of the interannual variability of China's GPP.

3.3. *Sources of annual variance from SST and atmospheric teleconnections*

The focus in this section is the GPP signals that are mostly related to the climate forcing factors (R-PC), as determined by separating out the influences from the long-term trends and the GPP memory [Eq. (1)]. The spatial characteristics of the seasonal GPP in China associated with the dominant R-PC from spring to autumn are discussed. The main ocean–atmosphere teleconnections associated with the seasonal GPP in China from the SST and circulations were identified by calculating the correlation between the GPP R-PC and the seasonal mean SST or circulation anomalies. To strengthen the physical explanation of the GPP signals, we also examined the conditions of soil moisture, precipitation and temperature associated with the GPP R-PC (GPP interannual variations are strongly associated with those of the atmosphere and land).

3.3.1. *Sources from the North Pacific Ocean and North Atlantic Ocean*

The seasonal GPP field associated with the R-PC1 for spring, summer and autumn are displayed in Figs. 3a, d and g, respectively. In the phase shown here, positive loadings correspond to larger-than-normal GPP conditions in China for all three seasons. Meanwhile, the anomalous maximum centers demonstrate a clear seasonal migration. In particular, during spring, the amplitude center is situated over southern China and northeastern China, with the largest values along the Yangtze River (Fig. 3a). During boreal summer (summer), accompanied by the development of the East Asian summer monsoon and the movement of the monsoon rainfall belt, the local maximum is mainly located in the regions of the Yangtze–Huaihe River Valley and northeastern China (Fig. 3d). During autumn, as the East Asian monsoon retreats, the maximum GPP center is situated in southeastern China (Fig. 3g). In addition, similar maximum centers can

be seen for the spatial patterns of the GPP associated with the R-PC1 (Figs. 3a, d and g), as well as those with the corresponding T-PC1 (Figs. 2a, c and e), while the latter has a hybrid structure associated with the trend and climate forcing. This implies that the climate forcing component may dominate the GPP's interannual variabilities in the above

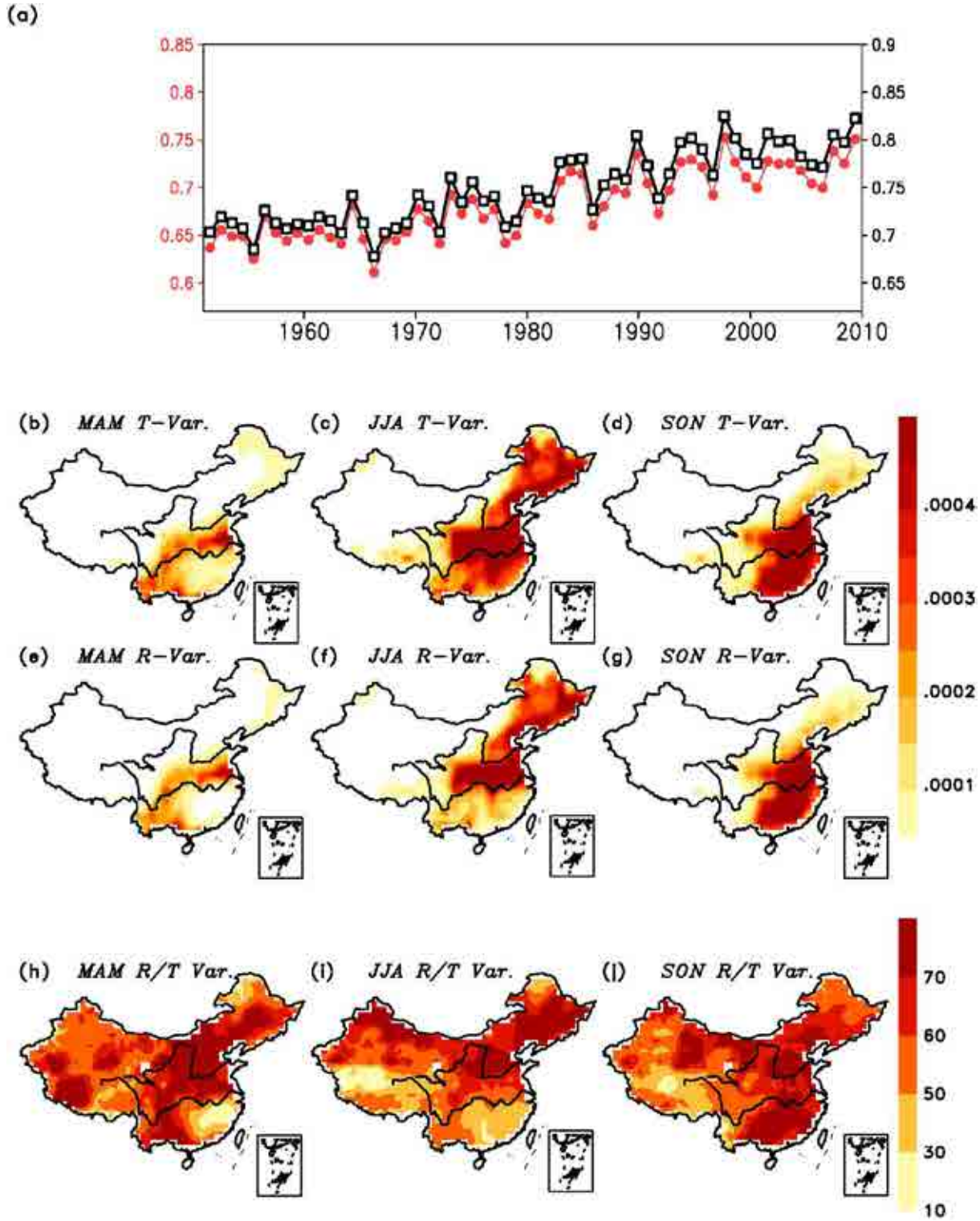

Fig. 1. (a) Temporal variations of China's GPP for all the four seasons (black) and the total of the three seasons of spring-summer-autumn (red) (units: KgC m^{-2}); and spatial distributions of the (b–d) total variance [units: (KgC m^{-2} $month^{-1})^2$] of the seasonal mean GPP over China (e–g) residual variance [units: (KgC m^{-2} $month^{-1})^2$] of the seasonal mean GPP from the trend and GPP memory, and (h–j) ratio of the residual variance to the total variance of GPP over China (units: %) for spring (left), summer (middle) and autumn (right), respectively.

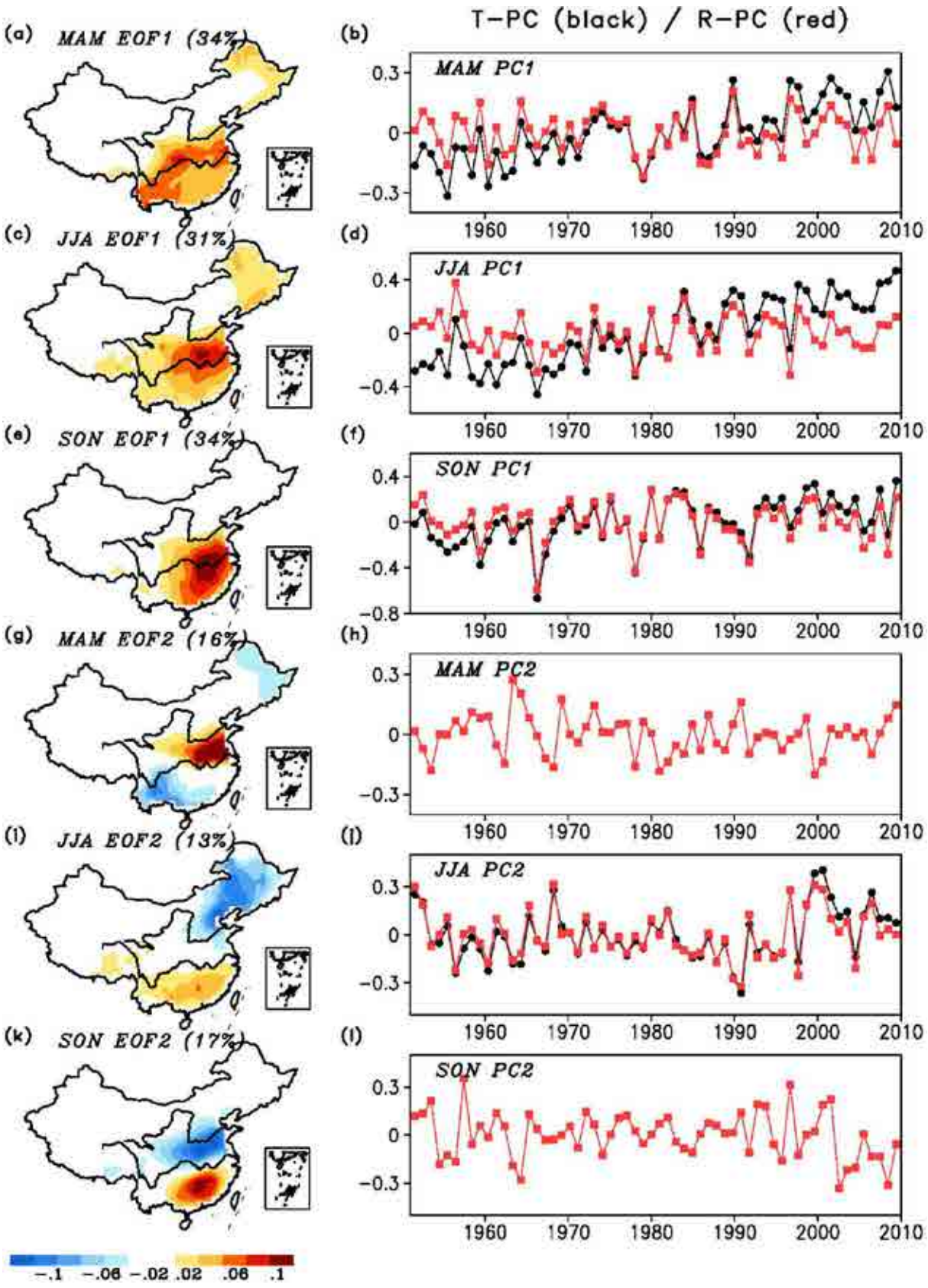

Fig. 2. Spatial distributions of the two dominant EOF modes of the total seasonal mean GPP field (with explained variance in brackets) for (a, g) spring, (c, i) summer, and (e, k) autumn, respectively; and temporal variations of the total PC time series (T-PC; black) and the residual PC time series from the trend and GPP memory (R-PC; red) for (b, h) spring, (d, j) summer, and (f, l) autumn, respectively. Noted the R-PC2 coincide with the T-PC2 in spring and autumn.

Table 2. Total variability of the mean seasonal variations in GPP pattern [leftmost column; (KgC m^{-2} $month^{-1})^2$], the residual variability from the trend and the GPP memory of the seasonal mean GPP pattern [second column; (KgC m^{-2} $month^{-1})^2$], and the percentage of the residual to total variability (third column; %).

Season	T- variability	R- variability	R/T variability
spring	0.061	0.039	64
summer	0.195	0.117	60
autumn	0.120	0.078	65

areas.

The one-point correlation maps of the simultaneous SSTs associated with the GPP R-PC1 during spring–autumn display similar spatial characteristics, as shown in Figs. 3b, e, and h. The most remarkable feature of the SST correlation is a horseshoe-shaped PDO-like pattern [PDO: Pacific Decadal Oscillation; see, for example, Fig. 3c of Ying et al. (2018)] over the North Pacific Ocean, and a sandwich-like tripole structure — with significant positive loadings in latitudes between 20°N and 40°N and negative anomalies in its north and south — over the North Atlantic Ocean. The simultaneous 500-hPa height correlation maps associated with the leading modes of spring to autumn (Figs. 3c, f and i) all show an AO-like zonal structure over the mid-to-high latitudes of the Northern Hemisphere; this is characterized by opposite anomalies over Greenland and the North Atlantic Ocean/northern Europe [see, for example, S-REOF1 in Fig. 4 of Frederiksen and Zheng (2004)], and is closely linked to the North Atlantic tripolar SSTs. These suggest that the AO and PDO may be important factors influencing China's GPP from spring to autumn. Consistently, the temporal correlation coefficients of the AO/PDO indices associated with the GPP R-PC1 in spring, summer and autumn are 0.45/−0.36, 0.26/−0.34 and 0.25/−0.28 when calculated simultaneously, and 0.43/−0.33, 0.30/−0.31 and 0.25/−0.28 when calculated at the lead time (Table 3), respectively, and are statistically significant at the 95% confidence level. Furthermore, the relationship between China's GPP and the combined effects of the PDO and AO was further examined using correlation maps of the GPP in China associated with the simultaneous and lagged PDO and AO indices in Table 3 during the seasons from spring to autumn (figures not shown), and the results were found to be consistent.

Figures 4a–i show the correlation maps of simultaneous soil moisture, precipitation and temperature associated with the GPP R-PC1 during spring to autumn. Anomalously wetter conditions of precipitation and soil moisture observed over southern China in spring (Figs. 4a and b), the Yangtze–Huaihe River Valley and northeastern China in summer (Figs. 4d and e), and southeastern China in autumn (Figs. 4g and h) are responsible for the positive anomaly of GPP in those areas (Figs. 3a, d and g). Locally, the significantly wetter conditions are a response to an anomalous anticyclone centered over the northwestern Pacific around Japan (Figs. 3c, f and i), which brings moist air from the northwestern Pacific to eastern China. This anomalous high is consistent with the significant positive SST anomalies situated over the northwestern Pacific (Figs. 3b, e and h) – one of the major features of negative PDO phases (Muller et al., 2008), and known to be closely associated with the AO variability (Gong et al., 2011). Meanwhile, significantly higher-than-normal temperature anomalies are observed in northeastern China during spring (Fig. 4c). As the temperature has a generally positive feedback to GPP in northeastern China during spring (Peng et al., 2021), the GPP there is enhanced (Fig. 3a). The temperature associated with the leading GPP mode of summer shows cooler-than-normal conditions in central-eastern China (Fig. 4f), which increases the GPP there (Fig. 3d) via its water deficit effects (Kim et al., 2017; Li et al., 2021; Peng et al., 2021). The above results are generally consistent with many previous studies (e.g., Gong et al., 2011; Yang et al., 2017; Ying et al., 2017, 2018) in which relationships between both the PDO and AO with the East Asian monsoon and climate in China have been found during different seasons.

3.3.2. *Sources from the eastern tropical Pacific Ocean*

The GPP fields associated with the R-PC2 during spring, summer and autumn are displayed in Figs. 3j, m and p, respectively. Associated with the spring R-PC2, the GPP fields have a tripolar spatial structure, with negative anomalies in southeastern and northeastern China and positive anomalies between the lower reaches of the Yangtze and Yellow rivers (Fig. 3j) in the phase shown here. Corresponding to the summer R-PC2, meanwhile, there is a dipole pattern, with higher-than-normal conditions in southern China and lower-than-normal conditions in northeastern China (Fig. 3m). For the autumn R-PC2's related GPP, there are negative loadings in central-eastern China and positive loadings in southeastern China (Fig. 3p). Again, there are large similarities between the spatial distributions of the GPP associated with the R-PC2 (Figs. 3j, m and p) and those with the T-PC2 (Figs. 2g, i and k), suggesting dominant effects from the climate forcing component in these regions.

The most notable features that appear in the simultaneous SST correlation maps associated with the R-PC2 of GPP during spring to autumn (Figs. 3k, n and q) are the significant positive values over the eastern tropical Pacific Ocean, indicating that ENSO is the possible source of the interannual variability for China's GPP during these seasons. The results are consistent with the correlation maps of China's GPP associated with the Niño3.4 index (figures not shown), which also indicate a close linkage between ENSO and China's GPP from spring to autumn. Previous studies have revealed that ENSO is one of the major factors affecting the interannual variations of China's soil moisture (Ying et al., 2016) and temperature (Nian et al., 2020), as well as the East Asian summer monsoon and monsoonal rainfall (Wu et al., 2009; Wang et al., 2015; Ying et al., 2016, 2017), via its regulation of air–sea interactions over the Pacific–Eurasia region. However, there are much stronger ENSO–GPP correlations for autumn (autumn; Fig. 3q) than in the warm seasons

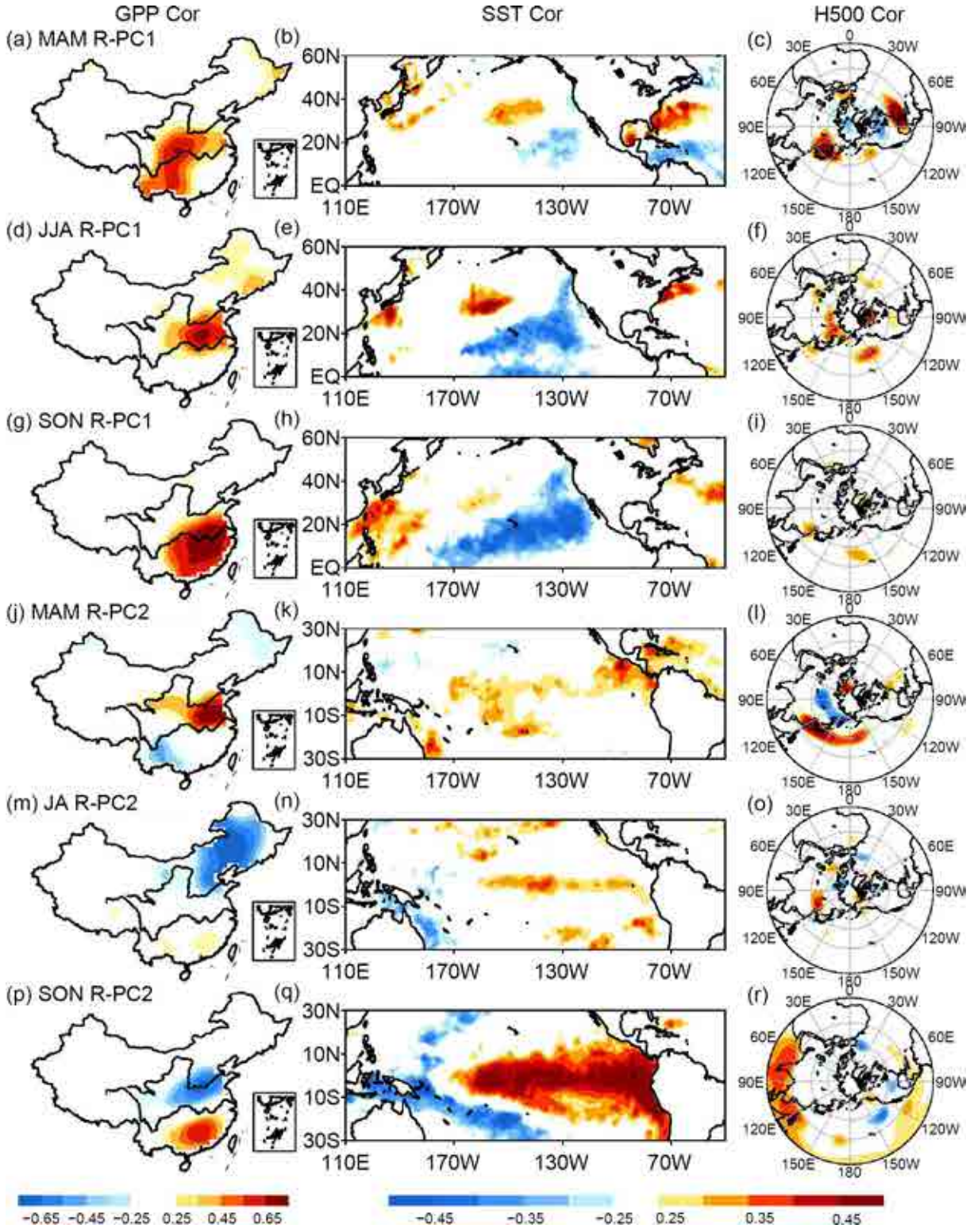

Fig. 3. Correlation maps of contemporary GPP (left-hand column), SST (middle column) and 500-hPa geopotential height (right-hand column) associated with the (a–c) spring R-PC1, (d–f) summer R-PC1, (g–i) autumn R-PC1, (j–l) spring R-PC2, (m–o) summer R-PC2 and (p–r) autumn R-PC2, respectively. The shaded areas in the correlation maps are significant at the 95% confidence level, using the Student's *t*-test.

(spring and summer; Figs. 3k and n). In particular, the temporal correlations of the Niño3.4 index associated with the second R-PC in spring, summer and autumn are 0.28, 0.28 and 0.47 when calculated simultaneously, and 0.32, −0.34 and 0.49 when calculated at the lead time (statistically significant at the 95% confidence level), respectively. Consistent with

Table 3. Correlation coefficients between the GPP R-PC and the contemporary (third column) and lead-time (fifth column) climate indices. The years used in the climate indices are denoted by (1) for the preceding year.

GPP R-PC	Climate indices	Correlation (contemporary)	Climate indices	Correlation (lead-lag)
spring R-PC1	spring AO	0.45***	Feb AO	0.43***
	spring PDO	−0.36**	spring(1) PDO	−0.33**
spring R-PC2	spring Niño-3.4	0.28*	Feb Niño-3.4	0.32*
summer R-PC1	summer AO	0.26*	May AO	0.30*
	summer PDO	−0.34**	spring PDO	−0.31*
summer R-PC2	summer Niño-3.4	0.28*	D(1)JF Niño-3.4	−0.34**
autumn R-PC1	autumn AO	0.25**	Aug AO	0.25*
	autumn PDO	−0.28*	summer PDO	−0.28*
autumn R-PC2	autumn Niño-3.4	0.47***	summer Niño-3.4	0.49***

*0.05, **0.01, *** 0.001

this, a previous study by Ying et al. (2017) reported a similar seasonality in the lead–lag and simultaneous relationship between ENSO and precipitation in eastern China from spring to autumn, based on precipitation observations, in which stronger ENSO–precipitation correlations were seen in autumn [Fig. 8b of Ying et al. (2017)] than that in spring and summer [Fig. 3j of Ying et al. (2017)]. Other studies have indicated that this seasonality in the behavior of ENSO–precipitation correlations might be due to the ENSO signal in autumn persisting throughout the entire period, whereas the signal in spring and summer has an apparent interdecadal change around the late 1970s (Wu and Wang, 2002; Wang et al., 2008; Ying et al., 2015). Explanations for the seasonality in the GPP–ENSO relationship is still an interesting and open question that needs further examination.

When examining the atmospheric circulation anomalies, the simultaneous 500-hPa geopotential height associated with the spring R-PC2 (Fig. 3l) displays a distinct meridional dipole in the western Pacific, resembling the western Pacific Oscillation (WPO) pattern of Frederiksen and Zheng (2004; their S-REOF3 in Fig. 4; pattern correlation with canonical WPO for spring is 0.66), which is closely related to ENSO. Corresponding to this anomalous circulation in spring, the soil moisture and the precipitation show negative anomalies in southern China and positive anomalies in the area between the Yangtze and Yellow rivers (Figs. 4j and k); plus, the temperature displays warmer-than-normal conditions in southern China and cooler conditions in central eastern China (Fig. 4l), which is responsible for the anomaly centers of the GPP EOF2 in these regions (Fig. 3j). Based on in-situ observations, Ying et al. (2017; their Fig. 7e) concluded that El Niño and positive WPO are significantly related to drier (wetter) rainfall patterns in the south (north) over eastern China in spring, which is consistent with our results above.

For the summer GPP R-PC2, the most noticeable feature in the associated 500-hPa height field is an anomalous positive center located around Lake Baikal (Fig. 3o). Previous studies have found that this dual blocking high condition over Lake Baikal is favorable for suppressed rainfall in northeastern China (Shen et al., 2011; Ying et al., 2018), which is consistent with our results. In particular, an increase (decrease) in soil moisture and rainfall (Figs. 4m and n), and decrease (increase) in temperature (Fig. 4o) over southern China (northeastern China), facilitate this particular GPP spatial pattern (Fig. 3m).

Associated with the GPP R-PC2 of autumn, the simultaneous 500-hPa height shows significant positive anomalies over the northwestern Pacific Ocean (Fig. 3r), which is the region most influenced by the western Pacific subtropical high (WPSH), suggesting the WPSH is an important factor affecting the GPP anomalies over China during autumn. The anomalously drier conditions in central-eastern China (Figs. 4p and q), as well as the anomalously wetter (Figs. 4p and q) and cooler conditions (Fig. 4r) in southern China, correspond to the anomalous GPP dipole structure as shown in Fig. 3p. The results agree with Ying et al. (2017), in which ENSO and the WPSH were identified as the most important factors affecting the interannual variability of autumn seasonal mean rainfall in eastern China, and an ENSO-related precipitation pattern in autumn similar to our GPP EOF2 was observed.

3.4. *Fractions of variance explained by the SST and circulation teleconnections*

Based on the above results, we calculated the fraction of variance of seasonal GPP explained by the key SST and circulation factors, using Eq. (3), in order to further evaluate the relative contributions of the identified ocean–atmosphere teleconnections of the interannual variability of China's GPP. Here, the key SST and circulation factors are represented by a projection of seasonal mean SST and height fields on their corresponding correlation maps with the GPP R-PC. In general, the key SST and circulation teleconnection factors can produce a large amount of GPP interannual variance, with an average percentage explained variance of 13%, 23% and 19% over China during spring, summer and autumn, respectively. The spatial distributions of the fraction of variance explained by the key SST and circulation factors (Fig. 5) display maximum centers (more than 30%) over central-eastern China and southwestern China in spring (Fig. 5a), central-eastern China and northeastern China in summer

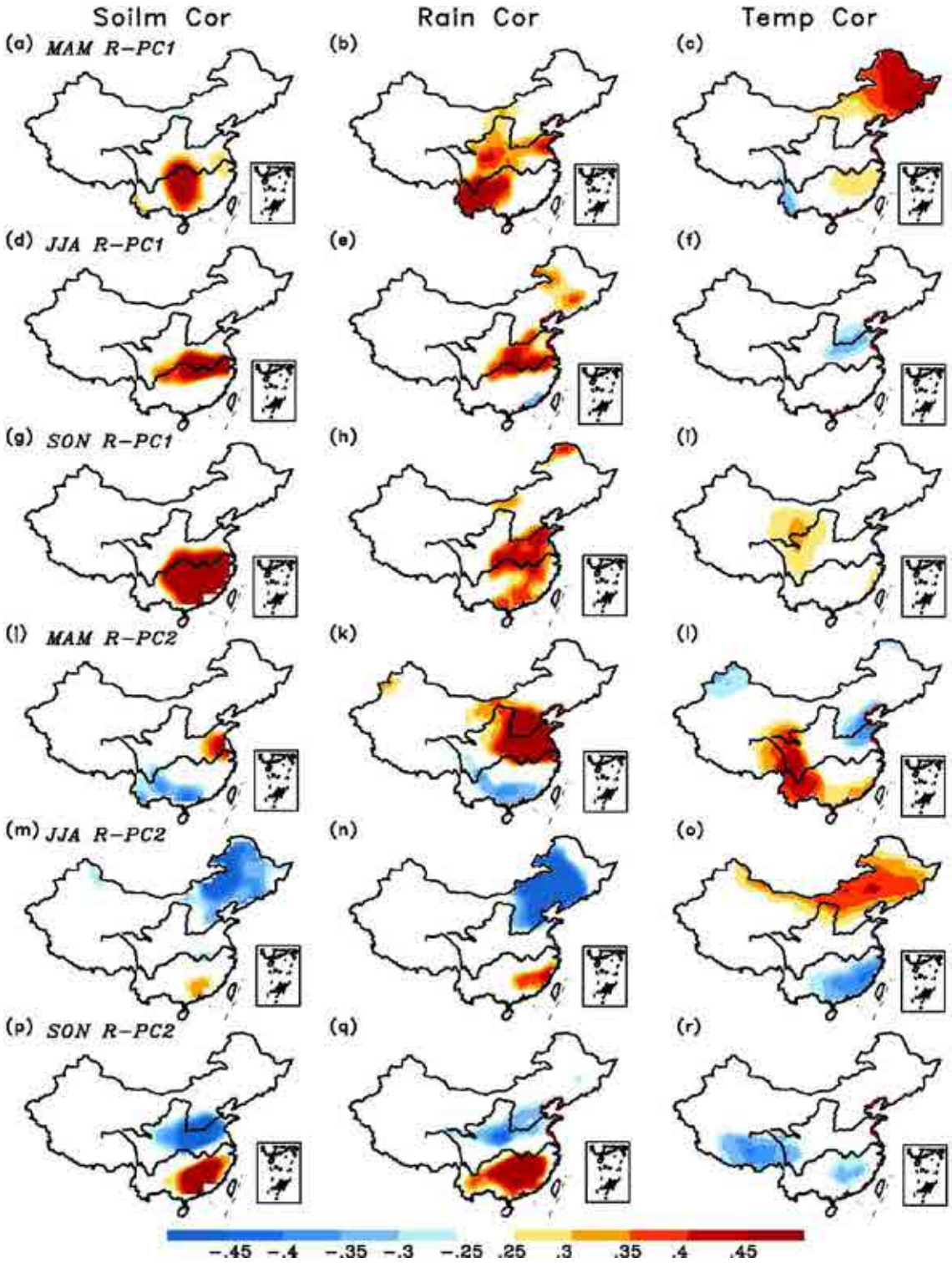

Fig. 4. Correlation maps of contemporary soil moisture (left-hand column), precipitation (middle column) and temperature (right-hand column) associated with the (a–c) spring R-PC1, (d–f) summer R-PC1, (g– i) autumn R-PC1, (j– l) spring R-PC2, (m–o) summer R-PC2 and (p–r) autumn R-PC2, respectively. The shaded areas in the correlation maps are significant at the 95% confidence level, using the Student's *t*-test.

(Fig. 5b), and southeastern China in autumn (Fig. 5c). Meanwhile, these regions make substantial absolute contributions to the carbon cycle for China, as they have the largest interannual variabilities (Figs. 1b–d) and climatological means (figure not shown) in GPP across the country as a whole. Thus, aside from the prolonged trend and the GPP memory, the SST and atmospheric teleconnections are also crucial to the interannual variance of China's GPP.

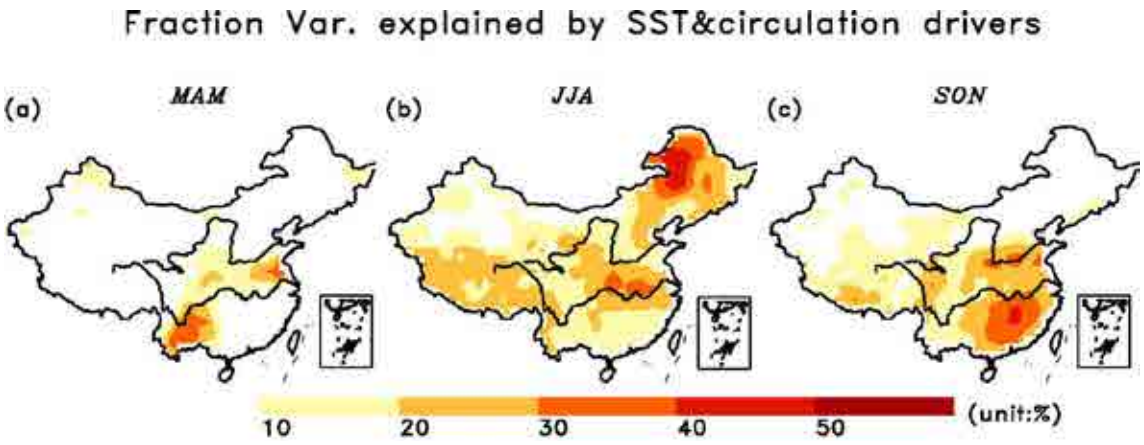

Fig. 5. Spatial distributions of the fraction of variance of GPP explained by the SST and circulation factors, for (a) spring, (b) summer and (c) autumn, respectively.

4. Summary and discussion

A seven-member TRENDY simulation was used to estimate the GPP field over China for the period 1951–2010. By separating out the significant effects from the linear trend and GPP memory, the dominant GPP signals (R-PC) that are most related to climate forcing factors were derived, for the seasons of spring to autumn. The key sources of interannual variability from the SST and atmospheric circulations for the seasonal GPP in China were then identified. In this paper, we have gained a more quantitative understanding of the sources of interannual variability of China's GPP from the ocean–atmosphere teleconnections. The main results can be summarized as follows:

(1) The seasonal GPP over China associated with the R-PC1 (R-PC2) during spring to autumn show a monopole (dipole or tripolar) spatial structure, with a clear seasonal evolution for their maximum centers from spring to autumn.

(2) The PDO and AO are closely linked with the GPP R-PC1 from spring to autumn. This combined impact on GPP in China is accompanied by a significant anomalous anticyclone or cyclone centered around Japan. ENSO is possibly the source of the interannual variability of the GPP R-PC2 of spring to autumn. In response, a WPO-like circulation, Lake Baikal blocking, and an anomalous WPSH are closely related to the GPP R-PC2 of spring, summer and autumn, respectively. Further analysis indicated that these remote relationships between GPP and both SST and large-scale circulation are regulated by the local hydrothermal conditions of rainfall, temperature, soil moisture, and so on.

(3) The fractions of variance of seasonal GPP explained by the key SST and circulation factors are large, with an average of 13%, 23% and 19% over China during spring, summer and autumn, respectively. The spatial distributions of the fractions of variance explained by the key SST and circulation factors show maximum centers (larger than 30%) over central-eastern and southwestern China in spring, central-eastern and northeastern China in summer, and southern China in autumn. Meanwhile, these are the key regions that dominate the interannual GPP variability for the country as a whole.

Our findings above are based on analyses of multi-model ensemble datasets from TRENDY. A critical question is whether the GPP–teleconnection relationships exist in each individual model. To address this question, we performed the same analysis for the seven individual models as those that were done for the multi-model ensemble from TRENDY. Based on the seven individual model outputs, the spatial structures of the contemporary GPP correlations associated with the two dominant R-PC from spring to autumn (Figs. S2 and S3 in the ESM) are quite similar to that for the multi-model ensemble from TRENDY (left column of Fig. 3). In addition, when examining the correlation coefficients between the GPP R-PC based on the seven individual model outputs and the simultaneous (or lagged) climate indices, the significant GPP–teleconnection relationships observed in the multi-model ensemble from TRENDY could also be seen for the seven individual models (Tables S1 and S2 in the ESM) in most cases. Although as expected, the GPP–teleconnection correlation values for the multi-model ensemble from TRENDY are in-between those for the individual models, this nevertheless indicates that the GPP–teleconnection relationships in TRENDY are generally robust for certain individual models.

Our work suggests that the AO, PDO, ENSO, WPO, Lake Baikal blocking and WPSH are worthy of attention in terms of the interannual variability of the seasonal mean GPP in the Chinese mainland during spring–summer–autumn, spring–summer–autumn, spring–summer–autumn, spring, summer and autumn, respectively. Also, we suggest that there are considerable seasonal differences in GPP–teleconnection relationships from spring to autumn, corresponding to local hydrothermal conditions. These findings help improve understanding of the interannual variability of China's GPP. Also, identifying the SST and large-scale circulation factors are key for improving the seasonal forecasting of GPP, as these slowly varying external forcing factors and internal dynamics could have persistent influences on China's climate (see Table 3 and Text S1 in the ESM). Thus, it provides an excellent way to estimate and project changes

in the carbon cycle across China and would also provide scientific support for achieving carbon neutrality targets.

It is important to acknowledge that our finding of an effect of external forcing and internal dynamics on GPP has been reached without consideration of land-use change. If land-use change and field irrigation are included, it is possible that the effects of ocean–atmosphere teleconnections may prove to be smaller than found in our study. Nonetheless, our results highlight the effect of ocean–atmosphere teleconnections on national-scale GPP in natural ecosystems, leading to a recommendation for a more substantial focus on understanding this process in the biosphere. In particular, it should be noted that five out seven models did not include nitrogen (N) cycle in this study. In addition, the TRENDY S2 simulation in this study did not include the phosphorus (P) cycle. Thus, our simulation did not consider the effects of N and P limitations on GPP. Ignoring these limitations may have resulted in an overestimation of GPP (Peng et al., 2020; Wieder et al., 2015). Therefore, in future work, to further verify the present reported results, we plan to carry out a similar analysis of the simulations but with due consideration paid to P limitation.

Acknowledgements. This work was supported by National Natural Science Foundation of China (Grant No. 42141017), National Basic Research Program of China (Grant No. 2020YFA0608904) and the National Natural Science Foundation of China (Grant Nos. 41975112, 42175142, 42175013, and 41630532).

Electronic supplementary material: Supplementary material is available in the online version of this article at https://doi.org/10.1007/s00376-021-1226-4.

REFERENCES

Ahlström, A., and Coauthors, 2015: The dominant role of semi-arid ecosystems in the trend and variability of the land CO_2 sink. *Science*, **348**, 895–899, https://doi.org/10.1126/science.aaa1668.

Barman, R., A. K. Jain, and M. L. Liang, 2014: Climate-driven uncertainties in modeling terrestrial gross primary production: A site level to global-scale analysis. *Global Change Biology*, **20**, 1394–1411, https://doi.org/10.1111/gcb.12474.

Beer, C., and Coauthors, 2010: Terrestrial gross carbon dioxide uptake: Global distribution and Covariation with climate. *Science*, **329**, 834–838, https://doi.org/10.1126/science.1184984.

Betts, R. A., C. A. Burton, R. A. Feely, M. Collins, C. D. Jones, and A. J. Wiltshire, 2021: ENSO and the carbon cycle. *El Niño Southern Oscillation in a Changing Climate*, M. J. McPhaden et al., Eds., John Wiley & Sons, Inc.

Chen, X. J., X. G. Mo, S. Hu, and S. X. Liu, 2017: Contributions of climate change and human activities to ET and GPP trends over North China Plain from 2000 to 2014. *Journal of Geographical Sciences*, **27**, 661–680, https://doi.org/10.1007/s11442-017-1399-z.

Cho, M.-H., G.-H. Lim, and H.-J. Song, 2014: The effect of the wintertime arctic oscillation on springtime vegetation over the northern high latitude region. *Asia-Pacific Journal of Atmospheric Sciences*, **50**, 567–573, https://doi.org/10.1007/s13143-014-0046-1.

Dannenberg, M. P., E. K. Wise, M. Janko, T. Hwang, and W. K. Smith, 2018: Atmospheric teleconnection influence on North American land surface phenology. *Environmental Research Letters*, **13**, 034029, https://doi.org/10.1088/1748-9326/aaa85a.

Forkel, M., N. Carvalhais, C. Rödenbeck, R. Keeling, M. Heimann, K. Thonicke, S. Zaehle, and M. Reichstein, 2016: Enhanced seasonal CO_2 exchange caused by amplified plant productivity in northern ecosystems. *Science*, **351**, 696–699, https://doi.org/10.1126/science.aac4971.

Frederiksen, C. S., and X. Zheng, 2004: Variability of seasonal-mean fields arising from intraseasonal variability. Part 2, application to nh winter circulations. *Climate Dyn.*, **23**, 193–206, https://doi.org/10.1007/s00382-004-0429-6.

Friedlingstein, P., and Coauthors, 2020: Global carbon budget 2020. *Earth System Science Data*, **12**, 3269–3340, https://doi.org/10.5194/essd-12-3269-2020.

Gong, D.-Y., J. Yang, S.-J. Kim, Y. Q. Gao, D. Guo, T. J. Zhou, and M. Hu, 2011: Spring Arctic Oscillation-East Asian summer monsoon connection through circulation changes over the western North Pacific. *Climate Dyn.*, **37**, 2199–2216, https://doi.org/10.1007/s00382-011-1041-1.

Harris, I., T. J. Osborn, P. Jones, and D. Lister, 2020: Version 4 of the CRU TS monthly high-resolution gridded multivariate climate dataset. *Scientific Data*, **7**, 109, https://doi.org/10.6084/m9.figshare.11980500.

Houghton, R. A., 2000: Interannual variability in the global carbon cycle. *J. Geophys. Res.*, **105**, 20121–20130, https://doi.org/10.1029/2000JD900041.

Hughes, J. K., P. J. Valdes, and R. Betts, 2006: Dynamics of a global-scale vegetation model. *Ecological Modelling*, **198**, 452–462, https://doi.org/10.1016/j.ecolmodel.2006.05.020.

Kalnay, E., and Coauthors, 1996: The NCEP/NCAR 40-year reanalysis project. *Bull. Amer. Meteor. Soc.*, **77**, 437–472, https://doi.org/10.1175/1520-0477(1996)077<0437:TNYRP>2.0.CO;2.

Kim, J.-S., J.-S. Kug, and S.-J. Jeong, 2017: Author Correction: Intensification of terrestrial carbon cycle related to El Niño–Southern Oscillation under greenhouse warming. *Nature Communications*, **8**, 207, https://doi.org/10.1038/s41467-017-02461-9.

Le Quéré, C., and Coauthors, 2018: Global carbon budget 2017. *Earth System Science Data*, **10**, 405–448, https://doi.org/10.5194/essd-10-405-2018.

Li, Y. Y., and Coauthors, 2021: Response of growing season gross primary production to El Niño in different phases of the pacific decadal oscillation over Eastern China based on Bayesian model averaging. *Adv. Atmos. Sci.*, **38**, 1580–1595, https://doi.org/10.1007/s00376-021-0265-1.

Lorenz, E. N., 1956: Empirical orthogonal functions and statistical weather prediction. Statistical Forecast Project Report 1, 49 pp.

Ma, J., X. M. Xiao, R. H. Miao, Y. Li, B. Q. Chen, Y. Zhang, and B. Zhao, 2019: Trends and controls of terrestrial gross primary productivity of China during 2000–2016. *Environmental Research Letters*, **14**, 084032, https://doi.org/10.1088/1748-9326/ab31e4.

Muller, W. A., C. Frankignoul, and N. Chouaib, 2008: Observed decadal tropical Pacific-North Atlantic teleconnections. *Geo-*

phys. Res. Lett., **35**, L24810, https://doi.org/10.1029/2008GL035901.

Nemani, R. R., C. D. Keeling, H. Hashimoto, W. M. Jolly, S. C. Piper, C. J. Tucker, R. B. Myneni, and S. W. Running, 2003: Climate-driven increases in global terrestrial net primary production from 1982 to 1999. *Science*, **300**, 1560–1563, https://doi.org/10.1126/science.1082750.

Nian, D., N. M. Yuan, K. R. Ying, G. Liu, Z. T. Fu, Y. J. Qi, and C. L. F. Franzke, 2020: Identifying the sources of seasonal predictability based on climate memory analysis and variance decomposition. *Climate Dyn.*, **55**, 3239–3252, https://doi.org/10.1007/s00382-020-05444-7.

Oleson, K. W., and Coauthors, 2010: Technical Description of version 4.0 of the Community Land Model (CLM) (No. NCAR/TN-478+STR). University Corporation for Atmospheric Research, https://doi.org/10.5065/D6FB50WZ.

Peng, J., L. Dan, and M. Huang, 2014: Sensitivity of global and regional terrestrial carbon storage to the direct CO_2 effect and climate change based on the CMIP5 model intercomparison. *PLoS One*, **9**, e95282, https://doi.org/10.1371/journal.pone.0095282.

Peng, J., and L. Dan, 2015: Impacts of CO_2 concentration and climate change on the terrestrial carbon flux using six global climate-carbon coupled models. *Ecological Modelling*, **304**, 69–83, https://doi.org/10.1016/j.ecolmodel.2015.02.016.

Peng, J., Y.-P. Wang, B. Z. Houlton, L. Dan, B. Pak, and X. B. Tang, 2020: Global carbon sequestration is highly sensitive to model-based formulations of nitrogen fixation. *Global Biogeochemical Cycles*, **34**, e2019GB006296, https://doi.org/10.1029/2019GB006296.

Peng, J., L. Dan, K. R. Ying, S. Yang, X. B. Tang, and F. Q. Yang, 2021: China's interannual variability of net primary production is dominated by the central china region. *J. Geophys. Res.*, **126**, e2020JD033362, https://doi.org/10.1029/2020JD033362.

Piao, S. L., J. Y. Fang, P. Ciais, P. Peylin, Y. Huang, S. Sitch, and T. Wang, 2009a: The carbon balance of terrestrial ecosystems in China. *Nature*, **458**, 1009–1013, https://doi.org/10.1038/nature07944.

Piao, S. L., P. Ciais, P. Friedlingstein, N. de Noblet-Ducoudré, P. Cadule, N. Viovy, and T. Wang, 2009b: Spatiotemporal patterns of terrestrial carbon cycle during the 20th century. *Global Biogeochemical Cycles*, **23**, GB4026, https://doi.org/10.1029/2008GB003339.

Piao, S. L., and Coauthors, 2013: Evaluation of terrestrial carbon cycle models for their response to climate variability and to CO_2 trends. *Global Change Biology*, **19**, 2117–2132, https://doi.org/10.1111/gcb.12187.

Piao, S. L., and Coauthors, 2020: Interannual variation of terrestrial carbon cycle: Issues and perspectives. *Global Change Biology*, **26**, 300–318, https://doi.org/10.1111/gcb.14884.

Rayner, N. A., D. E. Parker, E. B. Horton, C. K. Folland, L. V. Alexander, D. P. Rowell, E. C. Kent, and A. Kaplan, 2003: Global analyses of sea surface temperature, sea ice, and night marine air temperature since the late nineteenth century. *J. Geophys. Res.*, **108**, 4407, https://doi.org/10.1029/2002JD002670.

Reimer, J. J., R. Vargas, D. Rivas, G. Gaxiola-Castro, J. M. Hernandez-Ayon, and R. Lara-Lara, 2015: Sea surface temperature influence on terrestrial gross primary production along the southern California current. *PLoS One*, **10**, e0125177, https://doi.org/10.1371/journal.pone.0125177.

Richardson, A. D., D. Y. Hollinger, J. D. Aber, S. V. Ollinger, and B. H. Braswell, 2007: Environmental variation is directly responsible for short- but not long-term variation in forest-atmosphere carbon exchange. *Global Change Biology*, **13**, 788–803, https://doi.org/10.1111/j.1365-2486.2007.01330.x.

Schaefer, K., A. S. Denning, and O. Leonard, 2005: The winter Arctic Oscillation, the timing of spring, and carbon fluxes in the Northern Hemisphere. *Global Biogeochemical Cycles*, **19**, GB3017, https://doi.org/10.1029/2004GB002336.

Shen, B. Z., Z. D. Lin, R. Y. Lu, and Y. Lian, 2011: Circulation anomalies associated with interannual variation of early- and late-summer precipitation in Northeast China. *Science China Earth Sciences*, **54**, 1095–1104, https://doi.org/10.1007/s11430-011-4173-6.

Sitch, S., and Coauthors, 2003: Evaluation of ecosystem dynamics, plant geography and terrestrial carbon cycling in the LPJ dynamic global vegetation model. *Global Change Biology*, **9**, 161–185, https://doi.org/10.1046/j.1365-2486.2003.00569.x.

Smith, B., I. C. Prentice, and M. T. Sykes, 2001: Representation of vegetation dynamics in the modelling of terrestrial ecosystems: comparing two contrasting approaches within European climate space. *Global Ecology and Biogeography*, **10**, 621–637.

Tharammal, T., G. Bala, N. Devaraju, and R. Nemani, 2019: A review of the major drivers of the terrestrial carbon uptake: Model-based assessments, consensus, and uncertainties. *Environmental Research Letters*, **14**, 093005, https://doi.org/10.1088/1748-9326/ab3012.

Wang, B., J. Yang, T. J. Zhou, and B. Wang, 2008: Interdecadal changes in the major modes of Asian-Australian Monsoon variability: Strengthening relationship with ENSO since the late 1970s. *J. Climate*, **21**, 1771–1789, https://doi.org/10.1175/2007JCLI1981.1.

Wang, B., J.-Y. Lee, and B. Q. Xiang, 2015: Asian summer monsoon rainfall predictability: A predictable mode analysis. *Climate Dyn.*, **44**, 61–74, https://doi.org/10.1007/s00382-014-2218-1.

Wang, Y. P., and Coauthors, 2011: Diagnosing errors in a land surface model (CABLE) in the time and frequency domains. *Journal of Geophysical Research: Biogeosciences*, **116**, G01034.

Wieder, W. R., C. C. Cleveland, W. K. Smith, and K. Todd-Brown, 2015: Future productivity and carbon storage limited by terrestrial nutrient availability. *Nature Geoscience*, **8**, 441–444, https://doi.org/10.1038/ngeo2413.

Wilks, D. S., 1995: *Statistical Methods in the Atmospheric Sciences*. Academic Press, 467 pp.

Woodward, F. I., T. M. Smith, and W. R. Emanuel, 1995: A global land primary productivity and phytogeography model. *Global Biogeochemical Cycles*, **9**, 471–490, https://doi.org/10.1029/95GB02432.

Wu, R. G., and B. Wang, 2002: A contrast of the East Asian summer Monsoon-ENSO relationship between 1962-77 and 1978-93. *J. Climate*, **15**, 3266–3279, https://doi.org/10.1175/1520-0442(2002)015<3266:ACOTEA>2.0.CO;2.

Wu, Z. W., B. Wang, J. P. Li, and F.-F. Jin, 2009: An empirical seasonal prediction model of the east Asian summer monsoon using ENSO and NAO. *J. Geophys. Res.*, **114**, D18120, https://doi.org/10.1029/2009JD011733.

Yang, Q., Z. G. Ma, X. G. Fan, Z.-L. Yang, Z. F. Xu, and P. L. Wu, 2017: Decadal modulation of precipitation patterns over eastern China by sea surface temperature anomalies. *J. Cli-*

mate, **30**, 7017–7033, https://doi.org/10.1175/JCLI-D-16-0793.1.

Yao, Y. T., and Coauthors, 2018: Spatiotemporal pattern of gross primary productivity and its covariation with climate in China over the last thirty years. *Global Change Biology*, **24**, 184–196, https://doi.org/10.1111/gcb.13830.

Ying, K. R., T. B. Zhao, X.-W. Quan, X. G. Zheng, and C. S. Frederiksen, 2015: Interannual variability of autumn to spring seasonal precipitation in eastern China. *Climate Dyn.*, **45**, 253–271, https://doi.org/10.1007/s00382-014-2411-2.

Ying, K. R., T. B. Zhao, X. G. Zheng, X.-W. Quan, C. S. Frederiksen, and M. X. Li, 2016: Predictable signals in seasonal mean soil moisture simulated with observation-based atmospheric forcing over China. *Climate Dyn.*, **47**, 2373–2395, https://doi.org/10.1007/s00382-015-2969-3.

Ying, K. R., X. G. Zheng, T. B. Zhao, C. S. Frederiksen, and X.-W. Quan, 2017: Identifying the predictable and unpredictable patterns of spring-to-autumn precipitation over eastern China. *Climate Dyn.*, **48**, 3183–3206, https://doi.org/10.1007/s00382-016-3258-5.

Ying, K. R., C. S. Frederiksen, T. B. Zhao, X. G. Zheng, Z. Xiong, X. Yi, and C. X. Li, 2018: Predictable and unpredictable modes of seasonal mean precipitation over Northeast China. *Climate Dyn.*, **50**, 3081–3095, https://doi.org/10.1007/s00382-017-3795-6.

Zhang, X. Z., P. J. Rayner, Y.-P. Wang, J. D. Silver, X. J. Lu, B. Pak, and X. G. Zheng, 2016: Linear and nonlinear effects of dominant drivers on the trends in global and regional land carbon uptake: 1959 to 2013. *Geophys. Res. Lett.*, **43**, 1607–1614, https://doi.org/10.1002/2015GL067162.

Zhang, L., and Coauthors, 2019: Interannual variability of terrestrial net ecosystem productivity over China: Regional contributions and climate attribution. *Environmental Research Letters*, **14**, 014003, https://doi.org/10.1088/1748-9326/aaec95.

Zhang, A. Z., and G. S. Jia, 2020: ENSO-driven reverse coupling in interannual variability of pantropical water availability and global atmospheric CO_2 growth rate. *Environmental Research Letters*, **15**, 034006, https://doi.org/10.1088/1748-9326/ab66cc.

Zheng, X. G., and R. E. Basher, 1999: Structural time series models and trend detection in global and regional temperature series. *J. Climate*, **12**, 2347–2358, https://doi.org/10.1175/1520-0442(1999)012<2347:STSMAT>2.0.CO;2.

Zheng, X., D. M. Straus, and C. S. Frederiksen, 2008: Variance decomposition approach to the prediction of the seasonal mean circulation: Comparison with dynamical ensemble prediction using NCEP's CFS. *Quart. J. Roy. Meteor. Soc.*, **134**, 1997–2009, https://doi.org/10.1002/qj.330.

Zhu, Z. C., S. L. Piao, Y. Y. Xu, A. Bastos, P. Ciais, and S. S. Peng, 2017: The effects of teleconnections on carbon fluxes of global terrestrial ecosystems. *Geophys. Res. Lett.*, **44**, 3209–3218, https://doi.org/10.1002/2016GL071743.

ADVANCES IN ATMOSPHERIC SCIENCES, VOL. 39, AUGUST 2022, 1343–1359

• **Original Paper** •

Decadal Methane Emission Trend Inferred from Proxy GOSAT XCH_4 Retrievals: Impacts of Transport Model Spatial Resolution※

Sihong ZHU[1,4], Liang FENG[*2,3], Yi LIU[*1], Jing WANG[1], and Dongxu YANG[1]

[1]*Carbon Neutrality Research Center*, *Institute of Atmospheric Physics*, *Chinese Academy of Sciences*, *Beijing* 100029, *China*

[2]*National Centre for Earth Observation*, *University of Edinburgh*, *Edinburgh*, *EH*9 3*FF*, *UK*

[3]*University of Edinburgh*, *Edinburgh*, *EH*9 3*FF*, *UK*

[4]*University of Chinese Academy of Sciences*, *Beijing* 100049, *China*

(Received 19 December 2021; revised 22 April 2022; accepted 25 April 2022)

ABSTRACT

In recent studies, proxy XCH_4 retrievals from the Japanese Greenhouse gases Observing SATellite (GOSAT) have been used to constrain top-down estimation of CH_4 emissions. Still, the resulting interannual variations often show significant discrepancies over some of the most important CH_4 source regions, such as China and Tropical South America, by causes yet to be determined. This study compares monthly CH_4 flux estimates from two parallel assimilations of GOSAT XCH_4 retrievals from 2010 to 2019 based on the same Ensemble Kalman Filter (EnKF) framework but with the global chemistry transport model (GEOS-Chem v12.5) being run at two different spatial resolutions of 4° × 5° (R4, lon × lat) and 2° × 2.5° (R2, lon × lat) to investigate the effects of resolution-related model errors on the derived long-term global and regional CH_4 emission trends. We found that the mean annual global methane emission for the 2010s is 573.04 Tg yr^{-1} for the inversion using the R4 model, which becomes about 4.4 Tg yr^{-1} less (568.63 Tg yr^{-1}) when a finer R2 model is used, though both are well within the ensemble range of the 22 top-down results (2008–17) included in the current Global Carbon Project (from 550 Tg yr^{-1} to 594 Tg yr^{-1}). Compared to the R2 model, the inversion based on the R4 tends to overestimate tropical emissions (by 13.3 Tg yr^{-1}), which is accompanied by a general underestimation (by 8.9 Tg yr^{-1}) in the extratropics. Such a dipole reflects differences in tropical–mid-latitude air exchange in relation to the model's convective and advective schemes at different resolutions. The two inversions show a rather consistent long-term CH_4 emission trend at the global scale and over most of the continents, suggesting that the observed rapid increase in atmospheric methane can largely be attributed to the emission growth from North Africa (1.79 Tg yr^{-2} for R4 and 1.29 Tg yr^{-2} for R2) and South America Temperate (1.08 Tg yr^{-2} for R4 and 1.21 Tg yr^{-2} for R2) during the first half of the 2010s, and from Eurasia Boreal (1.46 Tg yr^{-2} for R4 and 1.63 Tg yr^{-2} for R2) and Tropical South America (1.72 Tg yr^{-2} for R4 and 1.43 Tg yr^{-2} for R2) over 2015–19. In the meantime, emissions in Europe have shown a consistent decrease over the past decade. However, the growth rates by the two parallel inversions show significant discrepancies over Eurasia Temperate, South America Temperate, and South Africa, which are also the places where recent GOSAT inversions usually disagree with one other.

Key words: methane emissions, long-term trend, horizontal resolution

Citation: Zhu, S. H., L. Feng, Y. Liu, J. Wang, and D. X. Yang, 2022: Decadal methane emission trend inferred from proxy GOSAT XCH4 retrievals: Impacts of transport model spatial resolution. *Adv. Atmos. Sci.*, **39**(8), 1343−1359, https://doi.org/10.1007/s00376-022-1434-6.

Article Highlights:

- Inversion modeling systems using CTMs with coarse horizontal resolutions can reliably estimate global total methane emissions and give a rather credible long-term trend in all TransCom-3 regions except for Eurasia Temperate, South America Temperate, and South Africa.
- Emission increases in North Africa and South American Temperate contributed the most strongly to global emission growth from 2010 to 2014. During the second half of the 2010s, accelerated methane increases in the atmosphere were mainly driven by Eurasia Boreal and Tropical South America emissions.

※ This paper is a contribution to the special issue on Carbon Neutrality: Important Roles of Renewable Energies, Carbon Sinks, NETs, and non-CO_2 GHGs.

* Corresponding authors: Yi LIU, Liang FENG
Emails: liuyi@mail.iap.ac.cn, liang.feng@ed.ac.uk

- There are large uncertainties and debates in methane emission from Eurasia Temperate. We discuss possible causes for different emission estimates, particularly over China, to highlight the adverse effects of the model transport error over regions that are poorly constrained by observations or a priori estimates.

1. Introduction

Methane concentrations in the atmosphere have more than doubled since the pre-industrial era, contributing about 20% to present-day human-induced global warming (Myhre et al., 2013; Etminan et al., 2016). Methane is also a chemical precursor to tropospheric ozone, which has adverse effects on both human and ecosystem health. Its lifetime in the atmosphere is about 8 to 11 years (Patra et al., 2011; Prather et al., 2012Canadell et al., 2021). Quantifying methane emission and understanding the factors driving its interannual variations are of both the public and scientific interest because CH_4 emission reduction is now considered to be an efficient strategy for combating global warming, which can improve air quality (Shindell et al., 2012; Schaefer et al., 2016; Schaefer, 2019).

Surface observations from the NOAA network (Dlugokencky, NOAA/GML (gml.noaa.gov/ccgg/trendsch4/) reveal significant interannual variability in the rate by which methane is increasing. This variability is caused by an imbalance of surface emissions and atmospheric sinks, mainly due to reactions with hydroxyl radicals (OH), chlorine atoms (Cl), and excited atomic oxygen (O(1D)) (Saunois et al., 2020). Emissions can be broadly divided into natural (e.g., wetlands, inland water systems, geological seeps, termites, oceans, terrestrial permafrost, and hydrates) (Bloom et al., 2010; Kirschke et al., 2013; Melton et al., 2013) and anthropogenic sources (e.g., from agriculture, fossil fuel combustion, and waste management) (Kirschke et al., 2013; Schaefer, 2019; Saunois et al., 2020). It is challenging to quantify the methane budget accurately and determine the drivers for the unstable methane trend due to large uncertainties in both sources (emissions) and sinks (Canadell et al., 2021). In the past several years, many studies focused on the reasons for the plateau in the trend and subsequent regrowth of CH_4 in the 2000s but reached no consensus, which is discussed in detail and concluded by Canadell et al. (2021). Based on sectoral a priori emission inventories derived from "Bottom-up" approaches, the "Top-down" method takes advantage of atmospheric measurements to optimize the total emissions and sinks (Jacob et al., 2016; Brasseur and Jacob, 2017). The quality of inferred emissions depends critically on the quality and density of measurements. In the 2010s, long-term satellite retrievals from GOSAT and TROPOMI, with improved precision and accuracy, provided worldwide measurements to cover spatial and temporal changes in the atmospheric column-averaged concentration of (XCH_4) to constrain and interpret the interannual variation of global and regional methane emissions and their trends (Fraser et al., 2013, 2014; Wecht et al., 2014; Turner et al., 2015; Feng et al., 2017; Lunt et al., 2019, 2021; Maasakkers et al., 2019; Miller et al., 2019). In the processes of "Top-down" inverse modeling, atmospheric transport and chemistry models (CTMs), driven by meteorological fields, act as a "bridge" to link methane sources and sinks to atmospheric concentrations and thus also impact the inversion results.

Several studies have investigated the influence of observations from different platforms such as in-situ measurements and remotely-sensed retrievals, uncertainties in prior emissions, and other inversion parameters in observationally-based system simulation experiments (OSSEs) (Meirink et al., 2008; Eraser et al., 2014; Bousserez et al., 2016; Turner et al., 2018; Zhang et al., 2018; Lu et al., 2021). However, errors in the atmospheric models used to simulate CH4 remain poorly characterized (Saito et al., 2013; Locatelli et al., 2015). These errors are mainly derived from transport errors and horizontal resolution-related representative or observation mismatch errors (Ganesan et al., 2019; Stanevich et al., 2020, 2021). Transport errors contain biases in numerical convective and advective schemes (Strahan and Polansky, 2006; Saito et al., 2013; Yu et al., 2018; Bisht et al., 2021), meteorological fields (Locatelli et al., 2013, Pandey et al., 2019), and parametrization of subgrid-scale processes (Locatelli et al., 2015). Saito et al. (2013) compared vertical profiles of twelve chemistry models in the TransCom-CH_4 intercomparison experiment with aircraft measurements. They concluded that transport uncertainties partly cause the disparity of the vertical gradients among models. Yu et al. (2018) investigated the impact of model resolution on transport in GEOS-Chem using ^{222}Rn, ^{210}Pb, and ^{7}Be tracers. They found that vertical transport is reduced in the model with coarse resolution. Bisht et al. (2021) suggested models at low resolution are probably transporting mass faster in the lower stratosphere, from the tropics to the mid-high latitudes. Influences of these transport errors on methane emissions inversion are also investigated. Locatelli et al. (2015) tested the sensitivity of methane budget to LMDz sub-grid-scale physical parameterizations. They found that the inversions using a coarser version of the transport model are actually masking a poor representation of the stratosphere–troposphere methane gradient in the model. Representative or observational mismatch errors due to model output in coarse grids have geographically broader average values than finer grids. These systematic uncertainties may cause an overestimation or underestimation of anthropogenic emissions related to geographically localized processes (such as oil and gas production and coal mining, biomass burning, livestock, and landfills) (Ganesan et al., 2019).

Stanevich et al. (2020, 2021) focused on short-term biases in the global GEOS-Chem chemical transport model at different model grids and assessed their effects on inversion results. Their simulations using two different spatial resolutions show large differences in the modeled CH_4 column abundances over major source regions such as China. They concluded that the simulation at a higher spatial resolution yielded a better agreement with observations.

To investigate the impacts of the horizontal resolution of CTMs on estimates of global and regional methane emission long-term trends, we report the first comparison of decadal methane emission trends (2010–19) obtained using the same Ensemble Kalman Filter (EnKF, Feng et al., 2017), but with the CTM (GEOS-Chem v12.5) being run at two different spatial resolutions: 4° (lat) × 5° (lon) (Referred to R4 hereafter) versus 2° × 2.5° (Referred to R2 hereafter). Here, a 10-year record of satellite column observations of methane from the Japanese Greenhouse gases Observing SATellite (GOSAT) retrievals was used to constrain the two parallel inversions.

We provide a detailed description of these data in section 2 and a description of the ensemble Kalman filter method and GEOS-Chem model. Validation results obtained using the Total Carbon Column Observing Network (TCCON) measurements are provided in section 3. We report our comparison results in section 4 and provide conclusions in section 5.

2. Data and Methods

2.1. *Ensemble Kalman Filter Inversion Method*

To constrain and optimize past methane fluxes, we utilized an existing Ensemble Kalman Filter (EnKF) framework developed by Feng et al. (2009, 2017) to assimilate space-based measurements of atmospheric concentrations from 2010 to 2019. As detailed by Feng et al. (2017), *a posteriori* methane flux estimates at a location x and time t are assumed to take the form of:

$$f_{\mathrm{p}}^{\mathrm{g}}(x,t) = f_0^{\mathrm{g}}(x,t) + \sum_{i=1}^{n} c_i^{\mathrm{g}} \mathrm{BF}_i^{\mathrm{g}}(x,t) \,, \tag{1}$$

where g denotes the methane tracer gas and $f_0^{\mathrm{g}}(x,t)$ describes a priori emission inventories. The coefficient c_i^{g} represents adjustment parameters for estimating methane fluxes from a joint state vector c through an optimized fitting of the model results to observations. The pulse-like basis function $\mathrm{BF}_i^{\mathrm{g}}(x,t)$ in (1) represents the methane flux perturbations from various sectors across predefined geographic regions. We divided a priori methane inventories into two source categories: anthropogenic and natural emissions. We defined 92 land sub-regions by dividing the 11 TransCom-3 (Gurney et al., 2002) land regions into almost four equal sub-regions, except for China, which was divided into 37 sub-regions due to its large emissions. The 11 oceanic regions defined in the TransCom-3 experiment were combined due to the insignificant exchange between the ocean and atmosphere. We selected state vectors as the monthly coefficients for scaling the pulse-like regional methane fluxes (basis functions) in 93 global regions. To achieve higher spatial resolution for assimilation, in this study, $\mathrm{BF}_i^{\mathrm{g}}(x,t)$ denotes the perturbation of total a priori estimates in various sub-regions for each month, rather than a priori fluxes from different emission sectors as described in Feng et al. (2017). Therefore, we estimated a total of 22 320 (i.e., 2 × (sub-sources) × 93 (sub-regions) × 120 (months)) coefficients through an optimal fitting of model concentrations with observations as follows:

$$\boldsymbol{c}_{\mathrm{a}} = \boldsymbol{c}_{\mathrm{f}} + \boldsymbol{K}\left[\boldsymbol{y} - \boldsymbol{H}(\boldsymbol{c}_{\mathrm{f}})\right] \,, \tag{2}$$

where $\boldsymbol{c}_{\mathrm{f}}$ and $\boldsymbol{c}_{\mathrm{a}}$ denote the a priori and *a posteriori* state vectors, respectively. $\boldsymbol{y}$ represents the XCH_4 observations retrievals by GOSAT in this study, and $\boldsymbol{H}(\boldsymbol{c}_{\mathrm{f}})$ represents a priori information, including the simulation process of the GEOS-Chem relating a priori inventories to concentration fields, as well as the sampling processes from fields to XCH_4 consistent with the format of the observations.

In the ensemble Kalman filter framework, we approximate the a priori error covariance $\boldsymbol{P}_{\mathrm{f}}$ by introducing an ensemble of perturbation states $\Delta\boldsymbol{C}_{\mathrm{f}} = \left[\Delta c_{\mathrm{f}_1}, \Delta c_{\mathrm{f}_2}, \ldots, \Delta c_{\mathrm{f}_{\mathrm{ne}}}\right]$, so that a priori covariance $\boldsymbol{P}_{\mathrm{f}}$ can be described as $\Delta\boldsymbol{C}_{\mathrm{f}}(\Delta\boldsymbol{C}_{\mathrm{f}})^{\mathrm{T}}$. The Kalman gain matrix $\boldsymbol{K}$ in (2) is given by:

$$\boldsymbol{K} \approx \Delta\boldsymbol{C}_{\mathrm{f}}\Delta\boldsymbol{Y}^{\mathrm{T}}\left[\Delta\boldsymbol{Y}(\Delta\boldsymbol{Y})^{\mathrm{T}} + \boldsymbol{R}\right]^{-1} \,, \tag{3}$$

where $\boldsymbol{R}$ is the observation error covariance, and $\Delta\boldsymbol{Y}$ denotes the projection of the flux perturbation ensemble $\Delta\boldsymbol{C}_{\mathrm{f}}$ to observation space $[\Delta\boldsymbol{Y} = \boldsymbol{H}(\Delta\boldsymbol{C}_{\mathrm{f}})]$. The *a posteriori* estimate uncertainties are also in the form of a perturbation ensemble, which can be obtained by introducing a transform matrix $\boldsymbol{T}$:

$$\Delta\boldsymbol{C}_{\mathrm{a}} = \Delta\boldsymbol{C}_{\mathrm{f}}\boldsymbol{T} \,, \tag{4}$$

$$\boldsymbol{T}(\boldsymbol{T})^{\mathrm{T}} = \boldsymbol{I} - (\Delta\boldsymbol{Y})^{\mathrm{T}}\left[\Delta\boldsymbol{Y}(\Delta\boldsymbol{Y})^{\mathrm{T}} + \boldsymbol{R}\right]^{-1}\Delta\boldsymbol{Y} \,. \tag{5}$$

For simplifying the calculation of $\boldsymbol{T}(\boldsymbol{T})^{\mathrm{T}}$, we used singular value decomposition (SVD) of the scaled model observation ensembles $\Delta\boldsymbol{Y}^{\mathrm{T}}\boldsymbol{R}^{-1/2}$ and an efficient numerical lower-upper solver to sequentially calculate the *a posteriori* estimates $\boldsymbol{c}_{\mathrm{a}}$ and the associated uncertainties $\Delta\boldsymbol{C}_{\mathrm{a}}$.

2.2. *GEOS-Chem Atmospheric Chemistry and Transport Model*

We used v12.5.0 of GEOS-Chem to describe the relationship between surface emissions and the atmospheric methane distributions, forming part of the forward model in our inversion system. The model is driven by MERRA-2 meteorological re-analysis fields from the Global Modeling and Assimilation Office (GMAO) of NASA (Bosilovich et al., 2016). In our experiments, GEOS-Chem model simulations are run at two horizontal resolutions, at R4 and R2, for comparison. We used 47 hybrid-sigma levels from the surface to 0.01 hPa, of which 30 lie below the dynamic troposphere. We used the non-local boundary layer mixing scheme imple-

mented by Lin and McElroy (2010). The initial CH_4 field on 1 January 2010 was obtained from Feng et al. (2017) with an additional 1-year spin-up period starting in 2009.

We used existing methane inventories for various source types. Specifically, we used the EDGAR v4.3.2 global emission inventory for 2012 [https://edgar.jrc.ec.europa.eu/, last access: 1 December 2017; (Janssens-Maenhout et al., 2019)] to represent anthropogenic emissions. This inventory includes various emission sources related to human activities (coal mining, oil and gas industry, livestock, and waste). We used the United States Environmental Protection Agency inventory (Maasakkers et al., 2016) for the United States and the oil and gas emissions from Sheng et al. (2017) for Canada and Mexico. Additionally, 10-year daily global open fire emissions were obtained from QFED (Darmenov and da Silva, 2013). Monthly wetland emissions from 2010 to 2019 were obtained from the WetCHARTS v1.0 extended ensemble mean (Bloom et al., 2017). For termite emissions, we used the results of Fung et al. (1991). Emissions from geological macro seeps were obtained from Etiope (2015) and Kvenvolden and Rogers (2005). In terms of areal seepage, we used sedimentary basins (micro seepage) and potential geothermal seepage maps from Kvenvolden and Rogers (2005) and emission factors from Lyon et al. (2015).

For the atmospheric sinks of methane, we used a 3-D global tropospheric OH fields based on a GEOS-Chem 1-year full-chemistry simulation to describe the main tropospheric removal process of CH_4 (Fraser et al., 2014). Another tropospheric oxidation sink from Cl atoms is based on fields from Sherwen et al. (2016). The soil uptake calculation uses fields from Fung et al. (1991) with temperature-based seasonality based on Murray et al. (2012). Other minor loss terms in stratospheric oxidation are described by Ridgwell et al. (1999).

2.3. *Data*

GOSAT was launched in 2009 by the Japanese Space Agency (JAXA) in collaboration with the Japanese National Institute for Environmental Studies and the Ministry of Environment. This satellite is equipped with a high-resolution Fourier-transform spectrometer (TANSO-FTS), which enables the measurement of concentrations of both CO_2 and CH_4. GOSAT is in a sun-synchronous orbit, with a local equator crossing time of 1300 LST. The instrument has a ground footprint diameter of 10.5 km with a pixel spacing of approximately 250 km. GOSAT achieves approximate global coverage in three days. We used the v9 GOSAT proxy column methane data from the University of Leicester, including nadir observations over land and glint observations over the ocean from 2009 to 2019 (Parker et al., 2015, 2020), with only the nadir measurements used for inversion. These data are routinely validated against ground-based remote sensing data (Parker et al., 2015) and occasionally with aircraft data (Webb et al., 2016). The proxy retrieval simultaneously provides CH_4 and CO_2 column estimates using absorption features around the wavelength of 1.6 μm, which is most sensitive to changes in these gases in the lower troposphere. In taking the ratio of these retrieved columns, CH_4/CO_2, CO_2 is assumed to be a proxy for modification along the light path (Frankenberg et al., 2011); this minimizes the influence of common factors affecting the retrieval of both gases, e.g., clouds and atmospheric scattering. As a result, this proxy retrieval method is less sensitive to scattering than the traditional full-physics retrieval approach and, therefore, yields greater data density over geographical regions with substantial aerosol loading, e.g., tropical areas during the dry season, when biomass burning is prevalent. Previous analyses have shown that these retrievals have a bias of 0.2% and a single-sounding precision of about 0.72% (Parker et al., 2011, 2015, 2020). We assume that GOSAT proxy column methane has an uncertainty of 1.2% to account for all possible errors, including observational errors, representative errors, and retrieval errors from the radiative transfer model.

3. Validation

3.1. *Comparison with GOSAT retrievals*

Figure 1 presents latitudinal differences between GOSAT-observed XCH_4 values, and simulated using GEOS-Chem with a priori emissions at R4 (a) and R2 (b) model grids, and values obtained using *a posteriori* emissions from (c) the R4 inversion and (d) R2 inversion. In the appendix, Fig. A2 presents the distribution of decadal mean differences. Before inversion, large gaps existed between GOSAT observations and model simulations at the two model grids, especially over mid-latitude and high-latitude areas of the northern hemisphere (NH). These gaps increase over time, reaching over 60 ppbv for the R4 simulation and almost 80 ppbv for the R2 simulation in 2019. After the assimilation of GOSAT measurements, differences between observations and model outputs were reduced to within ±2 ppbv in all latitudinal zones, except for high-latitude regions in the NH and southern hemisphere (SH). The R2 inversion performs better at high latitudes than the R4 experiment, narrowing differences to within ±2.5 ppbv throughout most time periods.

3.2. *Validation using TCCON measurements*

The TCCON is a global network of ground-based Fourier-transform spectrometers. It measures direct solar spectra in the near-infrared spectral region to collect information about atmospheric trace gases, including methane (Wunch et al., 2011). Currently, the TCCON consists of 26 operational stations. Due to their high precision and accuracy, TCCON datasets are commonly used to evaluate satellite retrievals (Karion et al., 2010). Therefore, these datasets provide essential information for comparison with *a posteriori* fields simulated by GEOS-Chem with R4 and R2 grids. The latest GGG2014 release (updated in August 2021) includes 35 long-term datasets of measurements, of which 34 datasets (Fig. A1 in the Appendix) representing the period from 2010 to 2019 were used for validation.

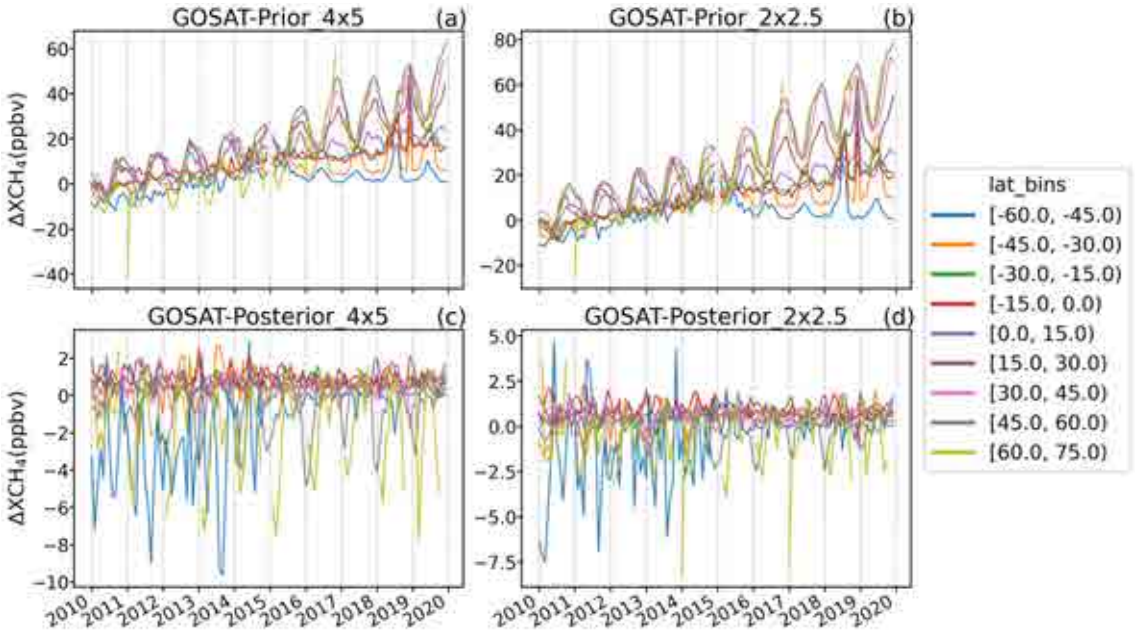

Fig. 1. Latitudinal difference between GOSAT-observed methane column concentrations (XCH_4) and those simulated using GEOS-Chem with a priori emissions at R4 (a) and R2 (b) and using *a posteriori* emissions after inversion at R4 (c) and R2 (d).

Figure 2 presents Taylor diagrams comparing TCCON measurements with GEOS-Chem outputs before and after inversion. Compared with R4 outputs using a priori emissions, we found a weaker correlation of R2 a priori model outputs with TCCON observations. Additionally, the root-mean-square deviation (RSMD) revealed that biases at most stations are larger at the R2 than at the R4 grid. However, the *a posteriori* model outputs of R2 performed better than R4 results, regardless of a correlation coefficient or RSMD. Moreover, compared with a priori outputs, seasonal variations (represented by the standard deviation) of *a posteriori* model results for both grids were closer to the average value of TCCON measurements. Emissions at high latitudes have larger seasonal variations and thus larger standard deviations. Thus, we confirmed that GOSAT retrievals provide useful constraints for a priori methane emissions, and the CTM with higher horizontal resolution performs better in inversion.

4. Results and Discussion

4.1. *Global methane emission trends*

Mean global annual methane emissions in R4 inversion is 573.04 Tg yr^{-1}, compared to 568.63 Tg yr^{-1} for R2 inversion (Table 1). The difference of about 4.4 Tg yr^{-1} is less than 1% of the mean annual emissions. Compared with other inversion results using GEOS-Chem runs at the R4 grid, we found that our results (561.10 Tg yr^{-1} for R4 and 559.91 Tg yr^{-1} for R2) are about 3% higher than the 2010–15 mean methane emission of 546 Tg yr^{-1} estimated by Maasakkers et al. (2019). Lu et al. (2021) also used GEOS-Chem simulations at the R4 grid to conduct GOSAT-only, in-situ-only, and joint GOSAT and in-situ inversions; our results are close to their joint inversion result (551 Tg yr^{-1}) for 2010–17 but much higher than their GOSAT-only inversion. Zhang et al. (2021) expanded the study period from 2017 to 2018 and concluded that the 9-year annual total emissions were 512 Tg yr^{-1} when only GOSAT retrievals were assimilated in inversion. Sensitivity tests (not included) show that the large differences are mainly due to different model OH concentrations. Zhao et al. (2020) studied the influence of the production and loss processes of OH on CH_4 lifetime and the global methane budget on decadal scales and found that interannual variation of OH has a significant impact on the top-down inversion of the methane budget, especially for tropical regions. However, Yin et al. (2021) compared six inversion results optimized by the inversion system PYVAR-LMDz based on the LMDz-INCA (1.9° × 3.75°) CTM (OH fields are from a full chemistry simulation by model LMDZ-INCA and the TransCom model intercomparison experiment). They suggested that the XCH_4 accelerated growth could be mostly induced by increased emissions. Our decadal mean emissions are close to the upper bound (510–570 Tg yr^{-1}) of the 8-year mean values for their six ensemble results. Janardanan et al. (2020) used GOSAT and surface measurements to optimize methane a priori estimates in the NIES-TM-FLEXPART-VAR (NTFVAR) inverse modeling system. They estimated the global annual mean methane emissions to be 573.4 Tg yr^{-1} from 2011 to 2017. Chandra et al. (2021) assimilated surface measurements from NOAA over three decades from 1988 to 2016 and reported global emissions over 2007–16

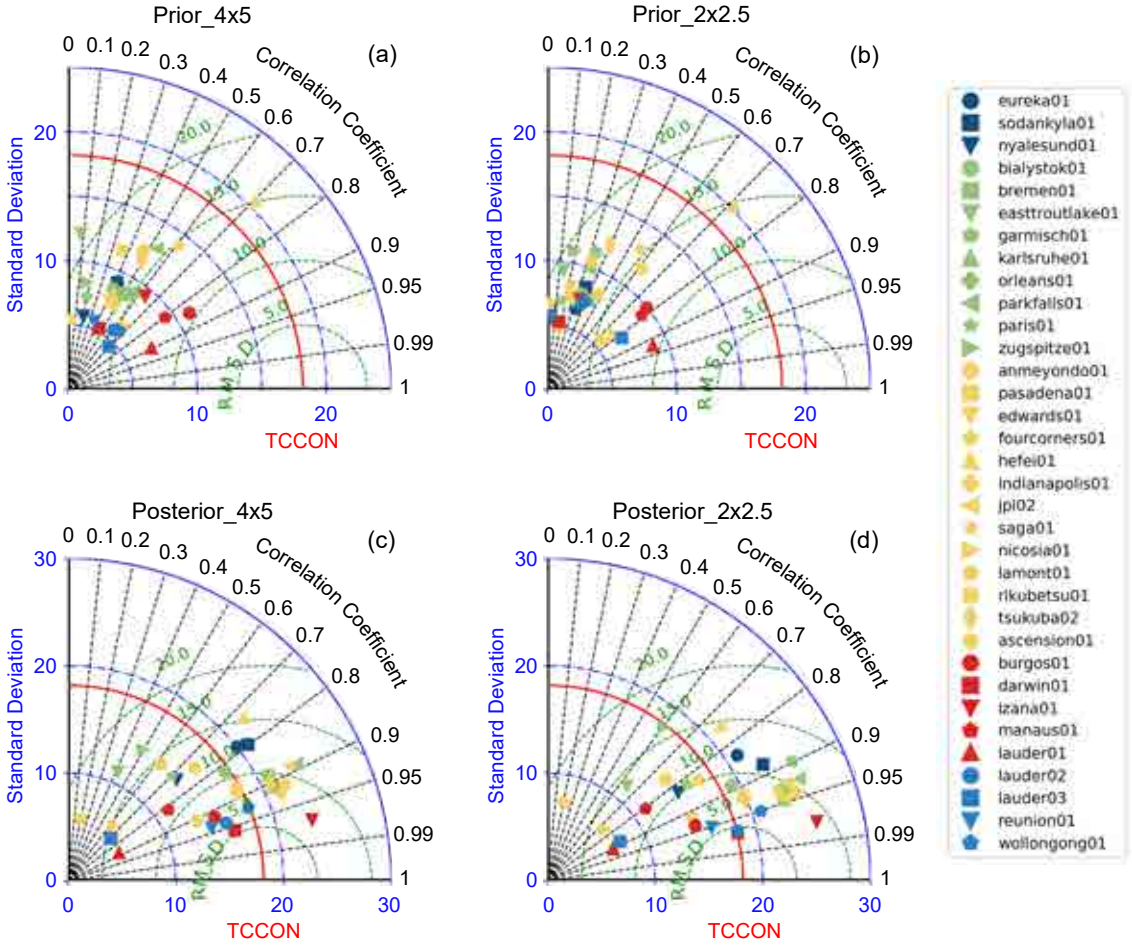

Fig. 2. Taylor diagrams of statistical results [correlation coefficient, standard deviation, and root-mean-square deviation (RMSD)] between surface-measured methane column concentrations (XCH_4) from the TCCON network and those simulated using GEOS-Chem with a priori emissions at R4 (a) and R2 (b), and using *a posteriori* emissions after inversion at R4 (c) and R2 (d) (Deep blue: latitudes of TCCON sites are larger than 60°N; Green: the latitudes of sites are within 45°–60°N; Yellow: the latitudes of sites are within 30°–45°N; Red: the latitudes of sites are within –15°S–45°N; Blue: The sites located in the mid-latitudes of SH).

(renewed growth of atmospheric methane) of 543± 16 Tg yr^{-1}.Based on an ensemble of 22 top-down methane budgets from 2008 to 2017, the Global Carbon Project (GCP) reports that the decadal mean emissions range from 550 to 594 Tg $yr^{-1,}$ with a mean value of 576 Tg yr^{-1}. Among the ensemble members, the 11 GOSAT-only or GOSAT and in-situ joint inversion results range from 564.1 to 594.1 Tg yr^{-1} with mean emissions of 579 Tg yr^{-1} (Saunois et al., 2020). Our results, using two different model grids, are comparable to these 11 GOSAT-related inversions. Several inversion results, including 9 surface CH_4 and 10 satellite XCH_4 inversions reported by Saunois et al. (2020), three decadal inversion results (1988–2016) using surface measurements from 19 sites given by Chandra et al. (2021) as well as global total emissions (Bousquet et al., 2006) were summarized in latest IPCC AR6 report (Canadell et al., 2021). Global total emissions in two inversions using surface CH_4 measurements show similar trends from 2000 to 2017 but large discrepancies in 2015. While continued methane growth occurred in 2015 with anomalies close to 25 Tg yr^{-1} [relative to 2010–16 as given by Chandra et al. (2021)], nine ensemble mean emissions from Saunois et al. (2020) show a plateau after the substantial increase in 2014. These two inversions both show declining trends after 2015, when the ensemble mean result from 10 satellite inversions differs greatly with ongoing increases. Two trends in our inversions are similar to the ensemble mean trend from satellite inversions with sustained growth from 2010 to 2017. The discrepancy between the surface inverted trends and satellite assimilated trends after 2015 still needs further investigation.

Figure 3a presents interannual variations of the global emissions from 2010 to 2019. Long-term increases can be found in both inversions, with the growth rate being 4.95 Tg yr^{-2} in R4 and 3.10 Tg yr^{-2} in the R2 model. The growth rate shows temporal fluctuations, with the largest increase in 2013 (25.51 Tg yr^{-2} in R4 and 13.00 Tg yr^{-2} in R2). Generally, most increases are derived from enhance-

Table 1. Global annual total emissions during the 2010s (Tg yr^{-1}).

Institution	CTM	Gridded (lon×lat)	Period	Observation used	Global total emissions	References
IAP	GEOS-Chem	4° × 5°	2010–19	GOSAT	573.04	this study
		2° × 2.5°			568.63	
University of Harvard	GEOS-Chem	4° × 5°	2010–15	GOSAT	546±2	(Maasakkers et al., 2019)
University of Harvard	GEOS-Chem	4° × 5°	2010–17	GOSAT	515	(Lu et al., 2021)
				In-situ	504	
				GOSAT & in-situ	551	
University of Harvard	GEOS-Chem	4° × 5°	2010–18	GOSAT	512	(Zhang et al., 2021)
JAMSTEC	MIROC4-ACTM	2.8125° × 2.8125°	2007–16	In-situ	543±16	(Chandra et al., 2021)
LSCE/CEA	LMDz-INCA	3.75°×1.875°	2010–17	GOSAT	510–570	(Yin et al., 2021)
NIES	NIES-TM v08.1i	2.5°	2011–17	GOSAT & in-situ	573.4	(Janardanan et al., 2020)
LSCE/IPSL	22 inversions ensemble mean		2008–17	In-situ or GOSAT or GOSAT &in-situ	576 (550–594)	(Saunois et al., 2020)
	11 inversions ensemble mean			GOSAT or GOSAT&in-situ	579 (564–594)	

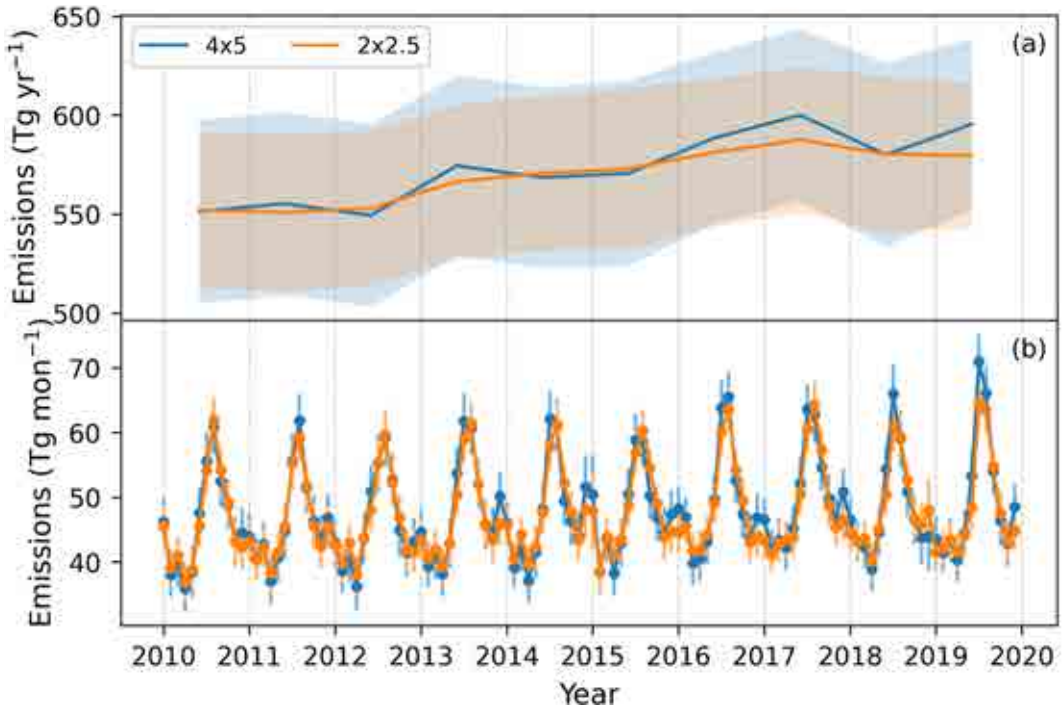

Fig. 3. Annual mean variations of global total methane emissions (a) in R4 (blue) and R2 (orange) versions of the GEOS-Chem model and their monthly variations (b) from 2010 to 2019.

ments over 2012–17, during which time the annual total emissions for both the R2 and R4 inversions increased by more than 35 Tg (49.25 Tg for R4 and 36.09 Tg for R2). Yin et al. (2021) also found the lowest annual total emission in 2012 and the highest in 2017 in the PYVAR-LMDz (1.9° × 3.75°) inversion system. Its 8-year increasing trend is about 4.1 Tg yr^{-2}, accounting for nearly 1% of the annual total emissions. On average, the first 8-year increase trends in our study are 7.04 Tg yr^{-2} and 5.15 Tg yr^{-2} in the R4 and R2, respectively, corresponding to annual increases of nearly 1.24% and 0.99%. Compared to R4 inversion, both the increasing trend and the percentage of total emissions in the R2 experiment are more consistent with the results of Yin et al. (2021).

Large discrepancies in annual total emissions between R4 and R2 can be observed in 2019. While *a posteriori* emissions in R2 continued to decrease after a peak in 2017, the emissions in R4 rebounded after decreasing in 2018. From

the monthly comparison shown in Fig. 3b, we found that the difference in 2019 arose mainly from the maximum emissions during summer. In addition to the large emissions gap in 2019, we found that emissions in summer (July in the NH and December in the SH) caused most of the difference in other years.

The latitudinal breakdown of emissions from 22 ensemble inversion results concluded by Saunois et al. (2020) reveals the dominance of tropical emissions at 368 Tg yr^{-1} [337–399], representing 64% of the global total over 2008–17. A total of 32% of the emissions are from the mid-latitudes (186 Tg yr^{-1} [166–204]), and 4% are from high latitudes (above 60°N). In this study, the dominant emissions over the tropics are 364.71 Tg yr^{-1} and 355.31 Tg yr^{-1} in R4 and R2, representing 63.64% and 62.48% of their global totals over 2010–19, respectively. Emissions from mid-latitudes account for 34.22% (196.12 Tg yr^{-1}) and 35.17% (200.02 Tg yr^{-1}). Those from high-latitude regions are 12.22 Tg yr^{-1} (2.13%) and 13.31 Tg yr^{-1} (2.34%) in R4 and R2, respectively. The emission distribution proportions in various latitudinal zonal are similar between R2 and R4 and are basically consistent with those given by Saunois et al. (2020). For the emission variation over various latitudinal zones, our results reveal global emission enhancements over 2015–19, compared to the first half of the 2010s, are derived mostly from tropical regions, representing 77.76% (21.57 Tg yr^{-1}) and 71.57% (15.85 Tg yr^{-1}) of their totals in R4 (27.74 Tg yr^{-1}) and R2 (22.11 Tg yr^{-1}). Compared to the R4 results, emission increases are more gradual in the R2 grid, with larger contributions coming from the mid-latitudes (9.28%) and high-latitudes (19.14%).

Considering the 1.16% larger proportion of tropical emissions to global totals, as well as the corresponding 6.19% greater contribution to the 5-year global increase in R4, we suggest explanations that may include a high-latitude bias in GEOS-Chem due to an imprecise description of convection across the tropopause (Bisht et al., 2021) and the inaccurate estimation of the vertical exchange between troposphere and stratosphere (Strahan and Polansky, 2006). Especially in R4, there is less methane in the troposphere and more methane in the lower stratosphere at high latitudes (shown in Fig. A3), which produces a latitudinal XCH_4 bias with large positive XCH_4 anomalies at high latitudes and small negative anomalies in the tropics (shown in Fig. A2). Bisht et al. (2021) attributed this bias to stronger quasi-horizontal mixing across the tropopause from the tropics to the mid-high latitudes in the model with a low resolution by comparing MIROC4-ACTM simulated CH_4 vertical profiles in the upper troposphere and lower stratosphere with the CONTRAIL (Comprehensive Observation Network for TRace gases by AIrLiner) aircraft observations. Stanevich et al. (2020) compared GEOS-Chem simulated XCH_4 in R4 and R2 with GOSAT, TCCON, and ACE-FTS (Atmospheric Chemistry Experiment Fourier Transform Spectrometer) observations and found that the R2 model produced a better simulation of CH_4, with smaller biases and a higher correlation to the independent data. They explained that the major reason for latitude-dependent errors is the excessive mixing in the upper troposphere and lower stratosphere at coarser resolutions. The larger model biases at R4 grid thus impact the distribution of *a posteriori* emissions and their long-term trends.

Detailed zonal mean *a posteriori* emissions variation by the R4 (a) and R2 (b) from 2010 to 2019 are presented in Fig. 4. We found the latitudinal distributions of the maximum values differ greatly in mid-latitude regions between R4 and R2. Compared with the single maximum around 35°N in R4, several additional high zonal mean values were obtained in R2, with the maximum near 30°N being the most apparent. Additionally, emissions around 25°N in R2 increased significantly in the 2010s, which was unclear in the R4 results. These results suggest that inversions using coarse models have difficulty reproducing hotspot emissions that are widely distributed over the mid-latitudes.

4.2. *Regional emissions comparison*

Decadal annual mean CH_4 emissions (shown in Fig. A5) are aggregated into the widely used 11 TransCom-3 land regions (Gurney et al., 2002), which are shown in Figure 5a. Among the eleven regions, the largest annual emissions from Eurasia Temperate are 123.28 Tg yr^{-1} and 135.70 Tg yr^{-1} in R4 and R2, accounting for 21.51% and 23.85% of their global totals, respectively. Annual emissions in R4 are underestimated by about 12.42 Tg yr^{-1} compared with those in R2, accounting for 9.15% of the regional totals. In the tropics, where wetlands are widely distributed, underestimations in annual emissions by R4 are about 5.85 Tg yr^{-1} in Tropical South America (58.97 Tg yr^{-1} for R4 and 64.81 Tg yr^{-1} for R2) and 8.70 Tg yr^{-1} in Tropical Asia (46.23 Tg yr^{-1} for R4 and 54.93 Tg yr^{-1} for R2), accounting for 9.02% and 15.84% of their annual totals. For North Africa, emissions in R4 are 3.46 Tg yr^{-1} higher than those in R2 (50.80 Tg yr^{-1} for R4 and 47.34 Tg yr^{-1}). For the high-latitude regions of Eurasia Boreal, North American Boreal, and Europe, the optimized emissions from R4 are smaller than emissions simulated by the R2 model. The differences between R4 and R2 are 2.19, 2.72, and 6.32 Tg yr^{-1}, accounting for 13.75%, 25.68%, and 15.67% of the totals in these regions, respectively.

In terms of differences in regional annual total emissions between the first half and the second half of the 2010s (shown in Fig. 5b), five-year annual total methane emissions in Eurasia Boreal, North Africa, and Tropical South America have shown significant growth (> 4 Tg yr^{-1}) compared to those over 2010–14. While the increase from Eurasia Boreal in the R4 inversion is smaller than that in R2, emission increases over North Africa and Tropical South America are overestimated in the R4. For emission growth inside the half-decade over the 2010s, we found increased emissions in North Africa (1.79 Tg yr^{-2} for R4 and 1.29 Tg yr^{-2} for R2, shown in Fig. 6f) and South American Temperate (1.08 Tg yr^{-2} for R4 and 1.21 Tg yr^{-2} for R2, shown in Fig. 6k) contribute the most (71.69% for R4 and 59.67% for R2) to global emissions growth (4.01 Tg yr^{-2} for R4 and

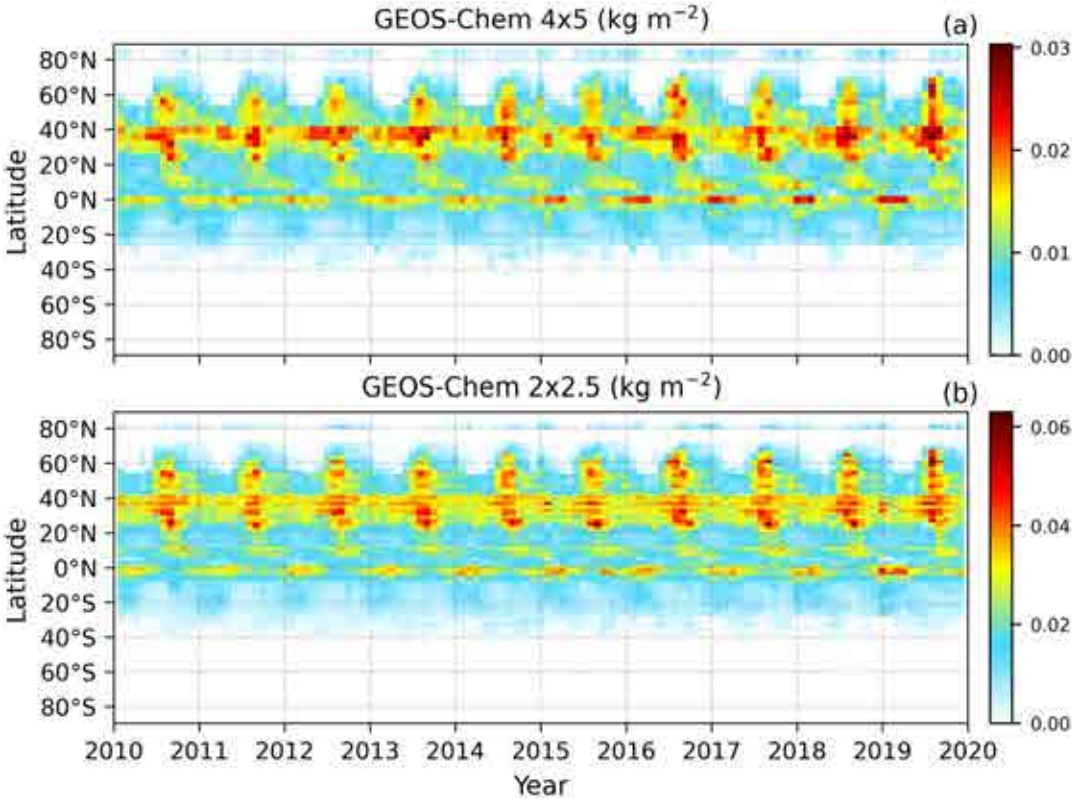

Fig. 4. Zonal mean monthly variations of methane emissions in the R4 (a) and R2 (b) versions of the GEOS-Chem model from 2010 to 2019.

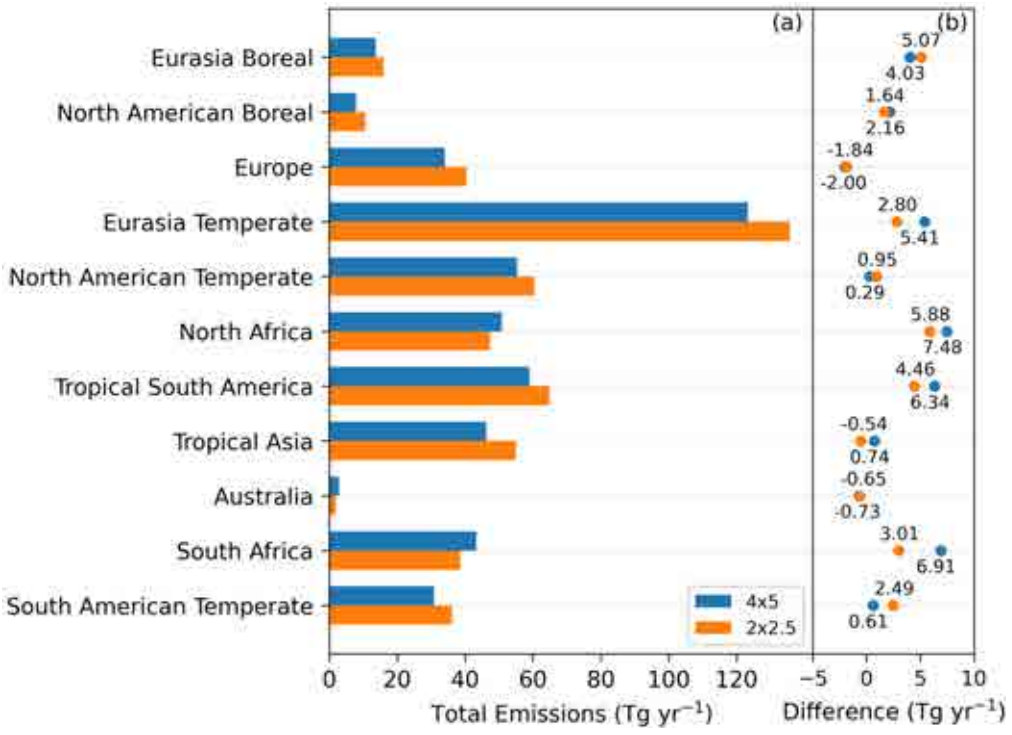

Fig. 5. Annual total methane emissions in the eleven TransCom-3 land regions from 2010 to 2019. Decadal annual mean optimized emissions obtained using the R4 (blue) and R2 (orange) versions of the GEOS-Chem model (a), and the differences in methane emissions between the second and the first half of the 2010s in R4 and R2 (b).

4.19 Tg yr $^{-2}$ for R2) before 2015. From six ensemble mean results over 2010–18, using the inversion system PYVAR-LMDz, Yin et al. (2021) also concluded that methane emissions from Tropical Africa (a large part of North Africa and a small part of South Africa in this study) and Eastern Brazil (basically located in South American Temperate) show an upward trend since 2012. However, several inversion results summarized by Canadell et al. (2021) show increases in the first half of the 2010s mainly from Eurasia Temperate (including West Asia, East Asia, and South Asia) and North America Temperate. In our study, the main contributions to emissions growth from 2010 to 2014 occurred in North Africa (including Northern Africa and part of Central Africa) and South American Temperate (South part of Tropical America and Temperate South America), while only a slight emission increase could be found from Central Africa and Temperate America with no trend in South Africa and large interannual variation in Tropical America. During the second half of the 2010s, accelerated methane growth in the atmosphere was mainly due to emissions from the Eurasia Boreal (1.46 Tg yr $^{-2}$ for R4 and 1.63 Tg yr $^{-2}$ for R2, shown in Fig. 6a) and Tropical South America (1.72 Tg yr $^{-2}$ for R4 and 1.43 Tg yr $^{-2}$ for R2, shown in Fig. 6g). The interannual variation in Eurasia Boreal (Russia) from Yin et al. (2021) is coincident with the increased emissions which occurred in 2014 and peaked in 2016. Chandra et al. (2021) also reported a similar increasing trend over Eurasia Boreal (North Asia), with emissions reaching a maximum in 2016. Our study additionally shows that in 2019, emissions from the Eurasia Boreal continued growing after a decline in 2017 and were nearly twice the emissions in 2010. In Europe (Fig. 6c), there are decadal declining trends, with the average rates of decrease of –0.58 Tg yr $^{-2}$ and –0.59 Tg yr $^{-2}$ in R4 and R2, respectively, accounting for about –1.7% of their totals. This result is consistent with an ongoing consensus (Saunois et al., 2020; Canadell et al., 2021; Chandra et al., 2021; Stavert et al., 2022). For Australia (Fig. 6i), annual emissions in both R2 and R4 show decreasing trends. However, these results incur large uncertainties as the relative difference in the 5-year decreases reached more than half of the total emissions.

Over the second half of the 2010s, methane variations in the South America Temperate and South Africa differ greatly between R4 and R2. The result in R2 shows no obvious decreasing trend in South America Temperate and no substantial increase in South Africa, which is similar to the results from Yin et al. (2021) and Stavert et al. (2022). Therefore, emission growth in South Africa in R4 may be overestimated, and emission trends in South America Temperate are insufficiently estimated over 2015–19.

The half-decadal variation in Fig. 5b shows large discrepancies for the Eurasia Temperate. The mean annual emission increase compared to those from the first half of the 2010s in R4 (5.41 Tg yr $^{-1}$) is nearly twice that in R2 (2.80 Tg yr $^{-1}$), with large discrepancies over 2015–19 (Fig. 6d). While emissions in R4 show remarkable growth after fluctuating between 2012 and 2015, those in the R2 inversion show no consistent growth with a continuous fluctu-

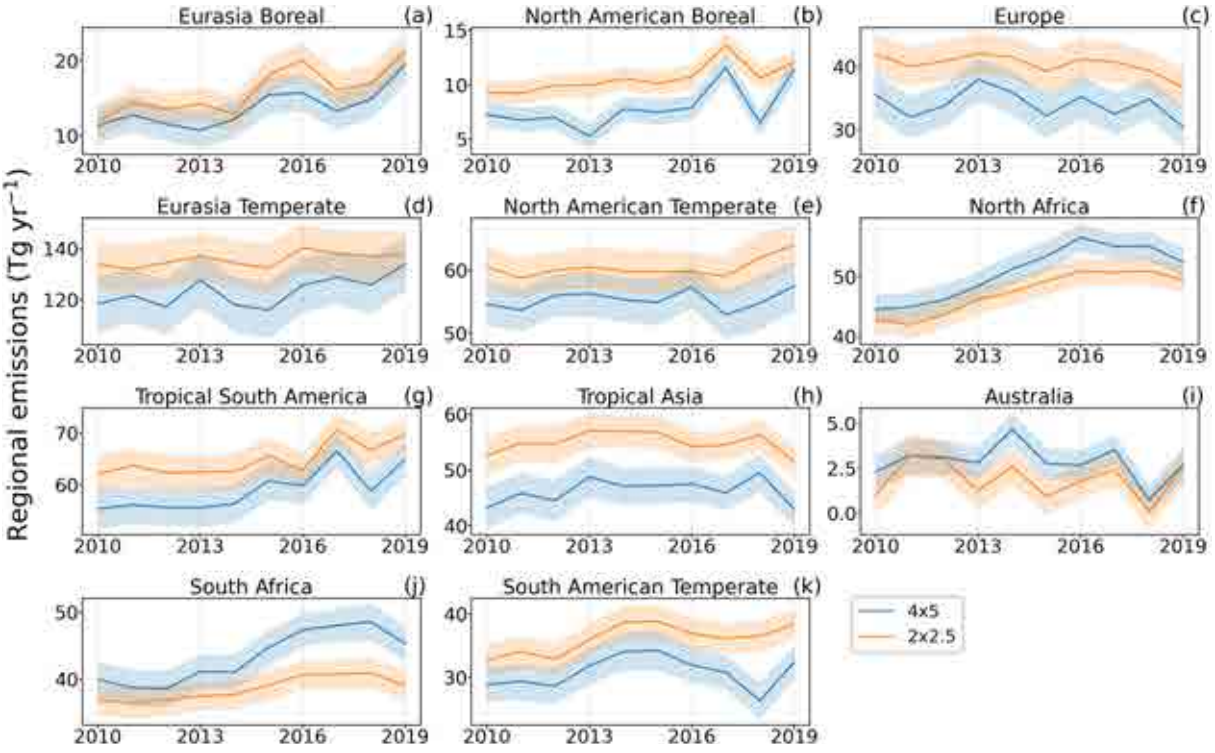

Fig. 6. Regional methane emission trends in the eleven TransCom-3 land regions (a–k) in R4 (blue) and R2 (orange) inversions and their monthly variations (b) from 2010 to 2019.

ation in the following years. There is also an ongoing debate about emissions from Eurasia Temperate among studies, which mainly focus on China, though all of them agree that coal emission has been overestimated by the widely used EDGAR (Maasakkers et al., 2019; Miller et al., 2019; Lu et al., 2021; Yin et al., 2021; Zhang et al., 2021; Stavert et al., 2022). Miller et al. (2019), Maasakkers et al. (2019), and Chandra et al. (2021) attributed atmospheric methane growth from 2010 to 2015 to increased emissions, partly from China, related to fossil fuel exploration. Stavert et al. (2022) and Yin et al. (2021) suggested a substantial increase in Chinese anthropogenic methane emissions from fossil fuels, agriculture, and waste from 2010 to 2017. However, Lu et al. (2021) compared inversion results using various observations, and found that anthropogenic emission trends in China for GOSAT-only (–0.6 Tg yr $^{-2}$) and for GOSAT and in situ joint inversion (–0.4 Tg yr $^{-2}$) over 2010–2017. Zhang et al. (2021) concluded that anthropogenic emission trends in China peaked midway within the 2010–18 record. One possible reason for the discrepancy in their inversion results may be the large uncertainties involved in the distribution of a priori estimates. While some studies suggest a decline in Chinese coal mining emissions since 2012 (Sheng et al., 2019, 2021; Gao et al., 2020, 2021), the trend reported by Lin et al. (2021) using national-level activity data from the National Bureau of Statistics of China and localized emission factors showed a slight increasing trend of 0.5 Tg yr $^{-2}$ for the period 2015–19. Additionally, the tropospheric transport bias involved in the coarser model may be another important reason (Stanevich et al., 2020). Stanevich et al. (2021) found that resolution-dependent model errors in the stratosphere can be traced back to biases in the uplift of CH_4 over the source regions in eastern China and North America. Regarding observational errors in GOSAT retrievals, Huang et al. (2020) found aerosols with a high single-scattering albedo and low asymmetry parameters (such as water-soluble aerosols, highly loaded in Northern China) induce large biases in the retrieval. Besides, there are very few retrievals over Southern China during the summer/monsoon season because of cloud cover (Chandra et al., 2017). Both the quality and the coverage of GOSAT XCH_4 retrievals may affect the convergence of posterior emissions in inversion.

To further study the systematic discrepancies in regional emissions, we used a box plot to show the difference between R4 and R2 on a finer monthly scale in Fig. 7. Despite similar long-term trends that can be found in most regions, there are large discrepancies between R4 and R2 on monthly timescales. Interquartile Range (IR = Q3 – Q1) relative to their monthly emissions is larger than 30% in Eura-

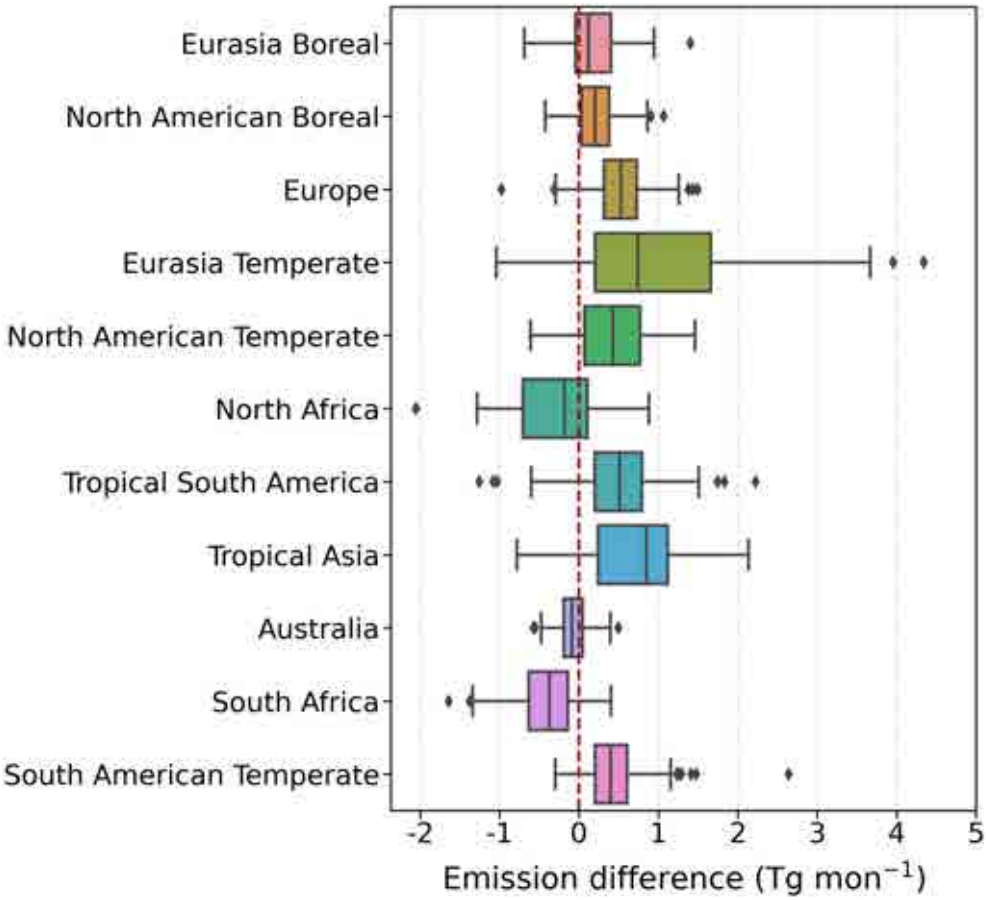

Fig. 7. Box diagram (minimum, maximum, median, first quartile, and third quartile) of regional monthly methane emissions difference (R2 minus R4) in the eleven TransCom-3 land regions.

sia, North American Boreal, and Australia, with the largest values in Australia at 105%. In other regions, IR values range from 10% to 20% of their monthly mean emissions, indicating that the horizontal resolution of CTMs can profoundly impact regional emission variation on monthly timescales. Therefore, monthly variations of regional methane emissions have large uncertainties and should be interpreted with caution.

5. Conclusions

To evaluate long-term methane emission trends using CTMs with coarse horizontal resolutions, we used the EnKF framework to optimize a priori methane emission inventories in the 4° × 5° (R4) and 2° × 2.5° (R2) versions of GEOS-Chem by assimilating GOSAT proxy v9.0 retrievals and compared the inverted emissions and their long-term trends from 2010 to 2019 on global, latitudinal, and regional scales.

Global annual total methane emissions in R4 and R2 during the 2010s are 573.04 Tg yr^{-1} and 568.63 Tg yr^{-1}, respectively, within the range of 22 top-down ensemble results (576 Tg yr^{-1} [550–594]) given by the Global Carbon Project (Saunois et al., 2020). Most increases were derived from enhancements over 2012–17, with the largest growth in 2013 (25.51 Tg yr^{-2} in R4 and 13.00 Tg yr^{-2} in R2). Compared to R4, the trend in R2 is closer to the ensemble mean trend (nearly 1%) inverted by Yin et al. (2021). Discrepancies between the two inversions mainly arise from different emissions during the boreal summer.

The latitudinal breakdown of emissions indicates that the dominant emissions over the tropics are 364.71 Tg yr^{-1} in R4 inversion and 355.31 Tg yr^{-1} in R2 inversion, representing 63.64% and 62.48% of their global totals over 2010–19, respectively. Both are well within the range of tropical emissions (368 Tg yr^{-1} [337–399]) reported by Saunois et al. (2020). Compared to the R2 model, the inversion based on R4 tends to overestimate tropical emissions (by 13.3 Tg yr^{-1}) and their contribution to the global half-decadal increase (by 6.19%), which is accompanied by a general underestimation (by 8.9 Tg yr^{-1}) in the extratropics. These differences may be caused by errors in modeling the vertical exchange between the troposphere and stratosphere in high latitudes (Strahan and Polansky, 2006; Stanevich et al., 2020) in the R4, and, to a lesser extent, in the R2 .

Among the eleven TransCom-3 land regions, similar trends with systematic discrepancies can be found in most regions for long-term variations, especially during the first half of the 2010s. Compared with mean emissions over the first five years of the 2010s, increases in mean emissions over 2015–19 mainly came from Eurasia Boreal, North Africa, South America Temperate, and Tropical South America, of which North Africa (1.79 Tg yr^{-2} for R4 and 1.29 Tg yr^{-2} for R2) and South America Temperate (1.08 Tg yr^{-2} for R4 and 1.21 Tg yr^{-2}) contributed the most (71.69% for R4 and 59.67% for R2) to the growth of global emissions from 2010 to 2014. During the second half of the 2010s, accelerated atmospheric increases in methane levels were mainly driven by Eurasia Boreal and Tropical South America emissions. Europe's annual methane emissions decreased by about –1.7% on both grids. Emission variations in Eurasia Temperate involve large uncertainties. The debate also exists among studies that mainly focus on China (Lu et al., 2021; Yin et al., 2021; Zhang et al., 2021; Stavert et al., 2022). The possible reasons may be large uncertainties involved in the distribution of a priori estimates (Gao et al., 2021; Lin et al., 2021), transport bias in the troposphere in CTMs (Stanevich et al., 2020, 2021), and sparse distribution of satellite retrievals (Chandra et al., 2017; Huang et al., 2020).

With ongoing and rapid increases in computing resources, atmospheric chemistry and transport models with higher resolution will be widely adopted; therefore, more atmospheric measurement data with consistent high spatial resolution will be needed. As several remote sensing retrieval products from various satellites are available (such as GOSAT, Tropomi, and MethaneSAT), methods to reasonably combine these products (such as taking advantage of the high accuracy of GOSAT retrievals and high spatial resolution of Tropomi retrievals) for inversion require further research.

Acknowledgements. This work is supported by the National Key R&D Plan of China (Grant No. SQ2019YFE013078), the Key Research Program of the Chinese Academy of Sciences (Grant No. ZDRW-ZS-2019-1), and the National Key R&D Program of China (Grant No. 2017YFB0504000). The support provided by the China Scholarship Council (CSC) and the University of Chinese Academy of Sciences during a visit of Sihong ZHU to the University of Edinburgh are also acknowledged. We thank Professor Paul Palmer for his useful comments. We thank the individual investigators who collected XCO_2 and XCH_4 data as part of the Total Carbon Column Observing Network (TCCON). We thank the broader GOSAT team, who provided their L1 data to develop the proxy CH_4 data product. We also thank the GEOS-Chem community, particularly the team at Harvard who helped maintain the GEOS-Chem model and the NASA Global Modeling and Assimilation Office (GMAO), who provided the MERRA 2 data product.

APPENDIX

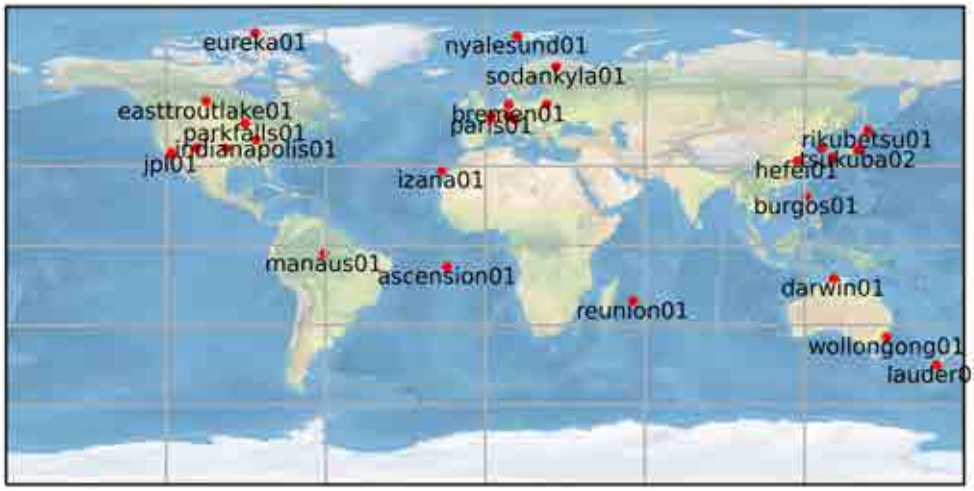

Fig. A1. Geographic locations of observation sites in the TCCON network.

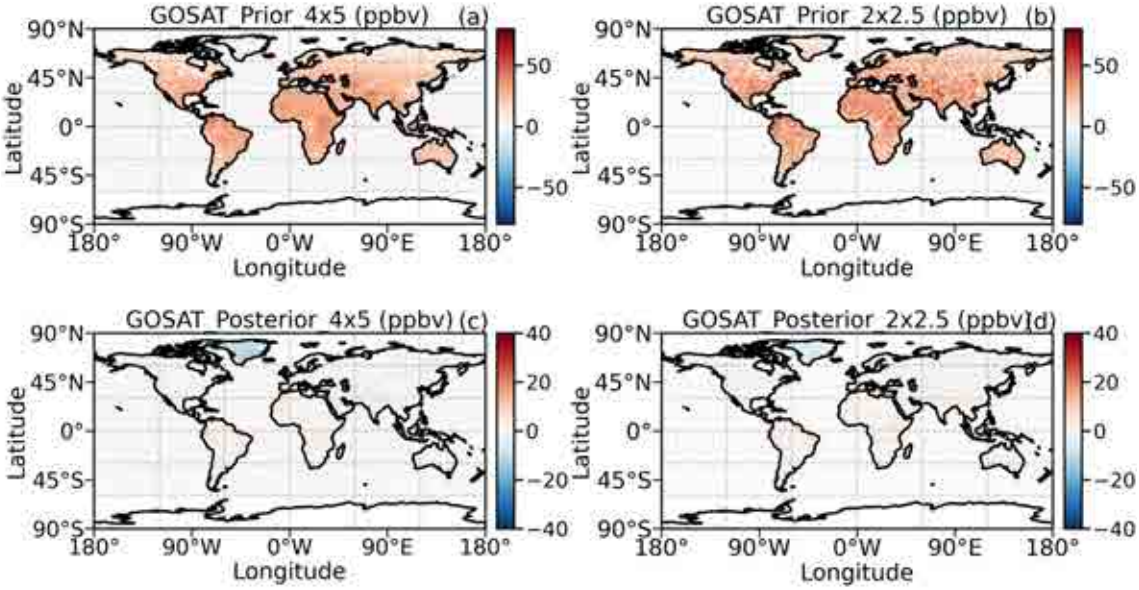

Fig. A2. The decadal mean difference between GOSAT-retrieved methane column concentrations (XCH_4) and those simulated using GEOS-Chem with a priori emissions at R4 (a) and R2 (b) scales and using *a posteriori* emissions after inversion at grid scales of R4 (c) and R2 (d).

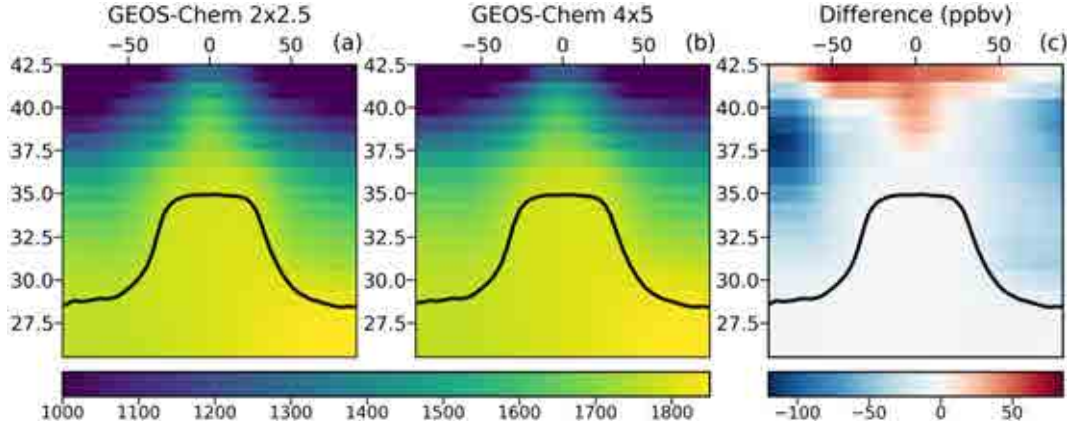

Fig. A3. The decadal zonal mean of the 3-D methane concentration field in R2 (a) and R4 (b) versions of the GEOS-Chem model and their difference (R2 minus R4) (c).

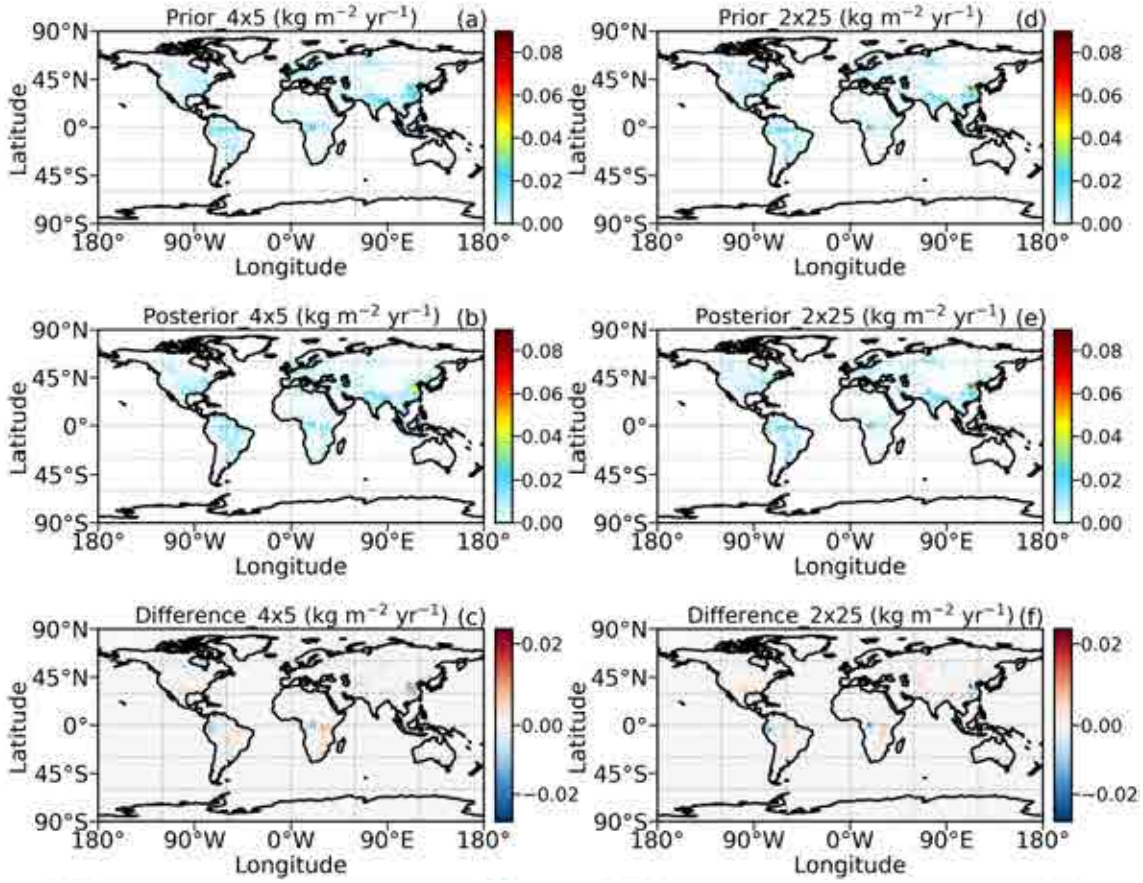

Fig. A4. Decadal mean distribution of a priori and a posteriori methane emissions in using R4 (a, d) and the R2 (b, e) inversions and their differences (a posteriori minus a priori) (c, f).

REFERENCES

Bisht, J. S. H., and Coauthors, 2021: Seasonal variations of SF_6, CO_2, CH_4, and N_2O in the UT/LS region due to emissions, transport, and chemistry. *J. Geophys. Res.*, **126**(4), e2020JD033541, https://doi.org/10.1029/2020JD033541.

Bloom, A. A., P. I. Palmer, A. Fraser, D. S. Reay, and C. Frankenberg, 2010: Large-scale controls of methanogenesis inferred from methane and gravity spaceborne data. *Science*, **327**, 322–325, https://doi.org/10.1126/science.1175176.

Bloom, A. A., and Coauthors, 2017: A global wetland methane emissions and uncertainty dataset for atmospheric chemical transport models (WetCHARTs version 1.0). *Geoscientific Model Development*, **10**, 2141–2156, https://doi.org/10.5194/gmd-10-2141-2017.

Bosilovich, M. G., R. Lucchesi, and M. Suarez, 2016: MERRA-2: File specification. GMAO Office Note No.9 (Version 1.1), 73 pp.

Bousquet, P., and Coauthors, 2006: Contribution of anthropogenic and natural sources to atmospheric methane variability. *Nature*, **443**, 439–443, https://doi.org/10.1038/nature05132.

Bousserez, N., D. K. Henze, B. Rooney, A. Perkins, K. J. Wecht, A. J. Turner, V. Natraj, and J. R. Worden, 2016: Constraints on methane emissions in North America from future geostationary remote-sensing measurements. *Atmospheric Chemistry and Physics*, **16**, 6175–6190, https://doi.org/10.5194/acp-16-6175-2016.

Brasseur, G. P., and D. J. Jacob, 2017: *Modeling of Atmospheric Chemistry*. Cambridge University Press.

Canadell, J. G., and Coauthors, 2021: Global carbon and other biogeochemical cycles and feedbacks. *Climate Change 2021: The Physical Science Basis. Contribution of Working Group I to the Sixth Assessment Report of the Intergovernmental Panel on Climate Change*, V. Masson-Delmotte et al., Eds., Cambridge University Press.

Chandra, N., S. Hayashida, T. Saeki, and P. K. Patra, 2017: What controls the seasonal cycle of columnar methane observed by GOSAT over different regions in India? *Atmospheric Chemistry and Physics*, **17**(20), 12 633–12 643, https://doi.org/10.5194/acp-17-12633-2017.

Chandra, N., and Coauthors, 2021: Emissions from the oil and gas sectors, coal mining and ruminant farming drive methane growth over the past three decades. *J. Meteor. Soc. Japan.*, **99**(2), 309–337, https://doi.org/10.2151/jmsj.2021-015.

Darmenov, A., and da Silva, A. M., 2013: The quick fire emissions dataset (QFED)—Documentation of versions 2.1, 2.2 and 2.4. NASA Tech. Rep. Series on Global Modeling and Data Assimilation, NASA TM-2013-104606.

Etiope, G., 2015: *Natural Gas Seepage*: *The Earth's Hydrocarbon Degassing*. Springer.

Etminan, M., G. Myhre, E. J. Highwood, and K. P. Shine, 2016: Radiative forcing of carbon dioxide, methane, and nitrous oxide: A significant revision of the methane radiative forcing. *Geophys. Res. Lett.*, **43**, 12 614–12 623, https://doi.org/10.1002/2016GL071930.

Feng, L., P. I. Palmer, H. Bösch, and S. Dance, 2009: Estimating surface CO_2 fluxes from space-borne CO_2 dry air mole fraction observations using an ensemble Kalman Filter. *Atmospheric Chemistry and Physics*, **9**(8), 2619–2633, https://doi.org/10.5194/acp-9-2619-2009.

Feng, L., and Coauthors, 2017: Consistent regional fluxes of CH_4 and CO_2 inferred from GOSAT proxy XCH_4: XCO_2 retrievals, 2010–2014. *Atmospheric Chemistry and Physics*, **17**, 4781–4797, https://doi.org/10.5194/acp-17-4781-2017.

Frankenberg, C., I. Aben, P. Bergamaschi, E. J. Dlugokencky, R. van Hees, S. Houweling, P. van der Meer, R. Snel, and P. Tol, 2011: Global column-averaged methane mixing ratios from 2003 to 2009 as derived from SCIAMACHY: Trends and variability. *J. Geophys. Res.*, **116**, D04302, https://doi.org/10.1029/2010JD014849.

Fraser, A., and Coauthors, 2013: Estimating regional methane surface fluxes: The relative importance of surface and GOSAT mole fraction measurements. *Atmospheric Chemistry and Physics*, **13**, 5697–5713, https://doi.org/10.5194/acp-13-5697-2013.

Fraser, A., P. I. Palmer, L. Feng, H. Bösch, R. Parker, E. J. Dlugokencky, P. B. Krummel, and R. L. Langenfelds, 2014: Estimating regional fluxes of CO_2 and CH_4 using space-borne observations of XCH_4:XCO_2. *Atmospheric Chemistry and Physics*, **14**, 12 883–12 895, https://doi.org/10.5194/acp-14-12883-2014.

Fung, I., J. John, J. Lerner, E. Matthews, M. Prather, L. P. Steele, and P. J. Fraser, 1991: Three-dimensional model synthesis of the global methane cycle. *J. Geophys. Res.*, **96**, 13 033–13 065, https://doi.org/10.1029/91JD01247.

Ganesan, A. L., and Coauthors, 2019: Advancing scientific understanding of the global methane budget in support of the Paris Agreement. *Global Biogeochemical Cycles*, **33**, 1475–1512, https://doi.org/10.1029/2018GB006065.

Gao, J. L., C. H. Guan, and B. Zhang, 2020: China's CH_4 emissions from coal mining: A review of current bottom-up inventories. *Science of the Total Environment*, **725**, 138295, https://doi.org/10.1016/j.scitotenv.2020.138295.

Gao, J. L., C. H. Guan, B. Zhang, and K. Li, 2021: Decreasing methane emissions from China's coal mining with rebounded coal production. *Environmental Research Letters*, **16**(12), 124037, https://doi.org/10.1088/1748-9326/ac38d8.

Gurney, K. R., and Coauthors, 2002: Towards robust regional estimates of CO_2 sources and sinks using atmospheric transport models. *Nature*, **415**(6872), 626–630, https://doi.org/10.1038/415626a.

Huang, Y. X., V. Natraj, Z.-C. Zeng, P. Kopparla, and Y. L. Yung, 2020: Quantifying the impact of aerosol scattering on the retrieval of methane from airborne remote sensing measurements. *Atmospheric Measurement Techniques*, **13**(12), 6755–6769, https://doi.org/10.5194/amt-13-6755-2020.

Jacob, D. J., and Coauthors, 2016: Satellite observations of atmospheric methane and their value for quantifying methane emissions. *Atmospheric Chemistry and Physics*, **16**, 14 371–14 396, https://doi.org/10.5194/acp-16-14371-2016.

Janardanan, R., and Coauthors, 2020: Country-scale analysis of methane emissions with a high-resolution inverse model using GOSAT and surface observations. *Remote Sensing*, **12**(3), 375, https://doi.org/10.3390/rs12030375.

Janssens-Maenhout, G., and Coauthors, 2019: EDGAR v4.3.2 global atlas of the three major greenhouse gas emissions for the period 1970–2012. *Earth System Science Data*, **11**, 959–1002, https://doi.org/10.5194/essd-11-959-2019.

Karion, A., C. Sweeney, P. Tans, and T. Newberger, 2010: AirCore: An innovative atmospheric sampling system. *J. Atmos. Oceanic Technol.*, **27**, 1839–1853, https://doi.org/10.1175/2010JTECHA1448.1.

Kirschke, S., and Coauthors, 2013: Three decades of global methane sources and sinks. *Nature Geoscience*, **6**, 813–823, https://doi.org/10.1038/ngeo1955.

Kvenvolden, K. A., and B. W. Rogers, 2005: Gaia's breath—global methane exhalations. *Marine and Petroleum Geology*, **22**, 579–590, https://doi.org/10.1016/j.marpetgeo.2004.08.004.

Lin, J.-T., and M. B. McElroy, 2010: Impacts of boundary layer mixing on pollutant vertical profiles in the lower troposphere: Implications to satellite remote sensing. *Atmos. Environ.*, **44**, 1726–1739, https://doi.org/10.1016/j.atmosenv.2010.02.009.

Lin, X. H., W. Zhang, M. Crippa, S. S. Peng, P. F. Han, N. Zeng, L. J. Yu, and G. C. Wang, 2021: A comparative study of anthropogenic CH_4 emissions over China based on the ensembles of bottom-up inventories. *Earth System Science Data*, **13**(3), 1073–1088, https://doi.org/10.5194/essd-13-1073-2021.

Locatelli, R., and Coauthors, 2013: Impact of transport model errors on the global and regional methane emissions estimated by inverse modelling. *Atmospheric Chemistry and Physics*, **13**(19), 9917–9937, https://doi.org/10.5194/acp-13-9917-2013.

Locatelli, R., P. Bousquet, M. Saunois, F. Chevallier, and C. Cressot, 2015: Sensitivity of the recent methane budget to LMDz sub-grid-scale physical parameterizations. *Atmospheric Chemistry and Physics*, **15**, 9765–9780, https://doi.org/10.5194/acp-15-9765-2015.

Lu, X., and Coauthors, 2021: Global methane budget and trend, 2010–2017: Complementarity of inverse analyses using in situ (GLOBALVIEWplus CH_4 ObsPack) and satellite (GOSAT) observations. *Atmospheric Chemistry and Physics*, **21**, 4637–4657, https://doi.org/10.5194/acp-21-4637-2021.

Lunt, M. F., P. I. Palmer, L. Feng, C. M. Taylor, H. Boesch, and R. J. Parker, 2019: An increase in methane emissions from tropical Africa between 2010 and 2016 inferred from satellite data. *Atmospheric Chemistry and Physics*, **19**, 14 721–14 740, https://doi.org/10.5194/acp-19-14721-2019.

Lunt, M. F., P. I. Palmer, A. Lorente, T. Borsdorff, J. Landgraf, R. J. Parker, and H. Boesch, 2021: Rain-fed pulses of methane from East Africa during 2018–2019 contributed to atmospheric growth rate. *Environmental Research Letters*, **16**(2), 024021, https://doi.org/10.1088/1748-9326/abd8fa.

Lyon, D. R., and Coauthors, 2015: Constructing a spatially resolved methane emission inventory for the Barnett Shale region. *Environ. Sci. Technol.*, **49**, 8147–8157, https://doi.org/10.1021/es506359c.

Maasakkers, J. D., and Coauthors, 2016: Gridded national inventory of U.S. methane emissions. *Environ. Sci. Technol.*, **50**, 13 123–13 133, https://doi.org/10.1021/acs.est.6b02878.

Maasakkers, J. D., and Coauthors, 2019: Global distribution of methane emissions, emission trends, and OH concentrations and trends inferred from an inversion of GOSAT satellite data for 2010–2015. *Atmospheric Chemistry and Physics*, **19**, 7859–7881, https://doi.org/10.5194/acp-19-7859-2019.

Meirink, J. F., P. Bergamaschi, and M. C. Krol, 2008: Four-dimensional variational data assimilation for inverse modelling of

atmospheric methane emissions: Method and comparison with synthesis inversion. *Atmospheric Chemistry and Physics*, **8**, 6341–6353, https://doi.org/10.5194/acp-8-6341-2008.

Melton, J. R., and Coauthors, 2013: Present state of global wetland extent and wetland methane modelling: Conclusions from a model inter-comparison project (WETCHIMP). *Biogeosciences*, **10**, 753–788, https://doi.org/10.5194/bg-10-753-2013.

Miller, S. M., A. M. Michalak, R. G. Detmers, O. P. Hasekamp, L. M. P. Bruhwiler, and S. Schwietzke, 2019: China's coal mine methane regulations have not curbed growing emissions. *Nature Communications*, **10**, 303, https://doi.org/10.1038/s41467-018-07891-7.

Murray, L. T., D. J. Jacob, J. A. Logan, R. C. Hudman, and W. J. Koshak, 2012: Optimized regional and interannual variability of lightning in a global chemical transport model constrained by LIS/OTD satellite data. *J. Geophys. Res.*, **117**, D20307, https://doi.org/10.1029/2012JD017934.

Myhre, G., and Coauthors, 2013: Radiative forcing of the direct aerosol effect from AeroCom Phase II simulations. *Atmospheric Chemistry and Physics*, **13**, 1853–1877, https://doi.org/10.5194/acp-13-1853-2013.

Pandey, S., and Coauthors, 2019: Influence of atmospheric transport on estimates of variability in the global methane burden. *Geophys. Res. Lett.*, **46**(4), 2302–2311, https://doi.org/10.1029/2018GL081092.

Parker, R., and Coauthors, 2011: Methane observations from the Greenhouse Gases Observing SATellite: Comparison to ground-based TCCON data and model calculations. *Geophys. Res. Lett.*, **38**(15), L15807, https://doi.org/10.1029/2011GL047871.

Parker, R. J., and Coauthors, 2015: Assessing 5 years of GOSAT Proxy XCH_4 data and associated uncertainties. *Atmospheric Measurement Techniques*, **8**(11), 4785–4801, https://doi.org/10.5194/amt-8-4785-2015.

Parker, R. J., and Coauthors, 2020: A decade of GOSAT proxy satellite CH_4 observations. *Earth System Science Data Discussions*, **2020**, 1–36, https://doi.org/10.5194/essd-2020-114.

Parker R J, and Coauthors., 2020: A decade of GOSAT Proxy satellite CH 4 observations. *Earth System Science Data*, **12**(4), 3383–3412, https://doi.org/10.5194/essd-12-3383-2020.

Patra, P. K., and Coauthors, 2011: TransCom model simulations of CH_4 and related species: Linking transport, surface flux and chemical loss with CH_4 variability in the troposphere and lower stratosphere. *Atmospheric Chemistry and Physics*, **11**, 12 813–12 837, https://doi.org/10.5194/acp-11-12813-2011.

Prather, M. J., C. D. Holmes, and J. Hsu, 2012: Reactive greenhouse gas scenarios: Systematic exploration of uncertainties and the role of atmospheric chemistry. *Geophys. Res. Lett.*, **39**(9), L09803, https://doi.org/10.1029/2012gl051440.

Ridgwell, A. J., S. J. Marshall, and K. Gregson, 1999: Consumption of atmospheric methane by soils: A process-based model. *Global Biogeochemical Cycles*, **13**, 59–70, https://doi.org/10.1029/1998GB900004.

Saito, R., and Coauthors, 2013: TransCom model simulations of methane: Comparison of vertical profiles with aircraft measurements. *J. Geophys. Res.*, **118**, 3891–3904, https://doi.org/10.1002/jgrd.50380.

Saunois, M., and Coauthors, 2020: The global methane budget: 2000–2017. *Earth System Science Data*, **12**(3), 1561–1623, https://doi.org/10.5194/essd-12-1561-2020.

Schaefer, H., 2019: On the causes and consequences of recent trends in atmospheric methane. *Current Climate Change Reports*, **5**, 259–274, https://doi.org/10.1007/s40641-019-00140-z.

Schaefer, H., and Coauthors, 2016: A 21st-century shift from fossil-fuel to biogenic methane emissions indicated by $^{13}CH_4$. *Science*, **352**, 80–84, https://doi.org/10.1126/science.aad2705.

Sheng, J.-X., D. J. Jacob, J. D. Maasakkers, M. P. Sulprizio, D. Zavala-Araiza, and S. P. Hamburg, 2017: A high-resolution (0.1°×0.1°) inventory of methane emissions from Canadian and Mexican oil and gas systems. *Atmos. Environ.*, **158**, 211–215, https://doi.org/10.1016/j.atmosenv.2017.02.036.

Sheng, J. X., S. J. Song, Y. Z. Zhang, R. G. Prinn, and G. Janssens-Maenhout, 2019: Bottom-up estimates of coal mine methane emissions in China: A gridded inventory, emission factors, and trends. *Environmental Science & Technology Letters*, **6**(8), 473–478, https://doi.org/10.1021/acs.estlett.9b00294.

Sheng, J. X., and Coauthors, 2021: Sustained methane emissions from China after 2012 despite declining coal production and rice-cultivated area. *Environmental Research Letters*, **16**(10), 104018, https://doi.org/10.1088/1748-9326/ac24d1.

Sherwen, T., and Coauthors, 2016: Global impacts of tropospheric halogens (Cl, Br, I) on oxidants and composition in GEOS-Chem. *Atmospheric Chemistry and Physics*, **16**(18), 12 239–12 271, https://doi.org/10.5194/acp-16-12239-2016.

Shindell, D., and Coauthors, 2012: Simultaneously mitigating near-term climate change and improving human health and food security. *Science*, **335**, 183–189, https://doi.org/10.1126/science.1210026.

Stanevich, I., and Coauthors, 2020: Characterizing model errors in chemical transport modeling of methane: Impact of model resolution in versions v9-02 of GEOS-Chem and v35j of its adjoint model. *Geoscientific Model Development*, **13**, 3839–3862, https://doi.org/10.5194/gmd-13-3839-2020.

Stanevich, I., and Coauthors, 2021: Characterizing model errors in chemical transport modeling of methane: Using GOSAT XCH_4 data with weak-constraint four-dimensional variational data assimilation. *Atmospheric Chemistry and Physics*, **21**, 9545–9572, https://doi.org/10.5194/acp-21-9545-2021.

Stavert, A. R., and Coauthors, 2022: Regional trends and drivers of the global methane budget. *Global Change Biology*, **28**(1), 182–200, https://doi.org/10.1111/gcb.15901.

Strahan, S. E., and B. C. Polansky, 2006: Meteorological implementation issues in chemistry and transport models. *Atmospheric Chemistry and Physics*, **6**(10), 2895–2910, https://doi.org/10.5194/acp-6-2895-2006.

Turner, A. J., and Coauthors, 2015: Estimating global and North American methane emissions with high spatial resolution using GOSAT satellite data. *Atmospheric Chemistry and Physics*, **15**, 7049–7069, https://doi.org/10.5194/acp-15-7049-2015.

Turner, A. J., D. J. Jacob, J. Benmergui, J. Brandman, L. White, and C. A. Randles, 2018: Assessing the capability of different satellite observing configurations to resolve the distribution of methane emissions at kilometer scales. *Atmospheric Chemistry and Physics*, **18**, 8265–8278, https://doi.org/10.5194/acp-18-8265-2018.

Webb, A. J., and Coauthors, 2016: CH_4 concentrations over the Amazon from GOSAT consistent with in situ vertical profile data. *J. Geophys. Res.*, **121**, 11 006–11 020, https://doi.org/

10.1002/2016JD025263.

Wecht, K. J., D. J. Jacob, M. P. Sulprizio, G. W. Santoni, S. C. Wofsy, R. Parker, H. Bösch, and J. Worden, 2014: Spatially resolving methane emissions in California: Constraints from the CalNex aircraft campaign and from present (GOSAT, TES) and future (TROPOMI, geostationary) satellite observations. *Atmospheric Chemistry and Physics*, **14**, 8173–8184, https://doi.org/10.5194/acp-14-8173-2014.

Wunch, D., and Coauthors, 2011: The total carbon column observing network. *Philosophical Transactions of the Royal Society A: Mathematical, Physical and Engineering Sciences*, **369**, 2087–2112, https://doi.org/10.1098/rsta.2010.0240.

Yin, Y., and Coauthors, 2021: Accelerating methane growth rate from 2010 to 2017: Leading contributions from the tropics and East Asia. *Atmospheric Chemistry and Physics*, **21**(16), 12 631–12 647, https://doi.org/10.5194/acp-21-12631-2021.

Yu, K. R., C. A. Keller, D. J. Jacob, A. M. Molod, S. D. Eastham, and M. S. Long, 2018: Errors and improvements in the use of archived meteorological data for chemical transport modeling: An analysis using GEOS-Chem v11-01 driven by GEOS-5 meteorology. *Geoscientific Model Development*, **11**(1), 305–319, https://doi.org/10.5194/gmd-11-305-2018.

Zhang, Y. Z., D. J. Jacob, J. D. Maasakkers, M. P. Sulprizio, J.-X. Sheng, R. Gautam, and J. Worden, 2018: Monitoring global tropospheric OH concentrations using satellite observations of atmospheric methane. *Atmospheric Chemistry and Physics*, **18**, 15 959–15 973, https://doi.org/10.5194/acp-18-15959-2018.

Zhang, Y. Z., and Coauthors, 2021: Attribution of the accelerating increase in atmospheric methane during 2010–2018 by inverse analysis of GOSAT observations. *Atmospheric Chemistry and Physics*, **21**, 3643–3666, https://doi.org/10.5194/acp-21-3643-2021.

Zhao Y. H., and Coauthors, 2020: Influences of hydroxyl radicals (OH) on top-down estimates of the global and regional methane budgets. *Atmospheric Chemistry and Physics*, **20**(15), 9525–9546, https://doi.org/10.5194/acp-20-9525-2020.

ADVANCES IN ATMOSPHERIC SCIENCES, VOL. 39, AUGUST 2022, 1360–1374

• **Original Paper** •

Effects of Plant Community Type on Soil Methane Flux in Semiarid Loess Hilly Region, Central Gansu Province, China※

Chuanjie YANG[1,2], Guang LI*[1,2], Lijuan YAN[3], Weiwei MA[1], Jiangqi WU[1], Yan TAN[1], Shuainan LIU[1], and Shikang ZHANG[3]

[1]*College of Forestry*, *Gansu Agricultural University*, *Lanzhou* 730070, *China*

[2]*Gansu Provincial Key Laboratory of Aridland Crop Science*, *Lanzhou* 730070, *China*

[3]*College of Agronomy*, *Gansu Agricultural University*, *Lanzhou* 730070, *China*

(Received 6 May 2021; revised 21 March 2022; accepted 25 April 2022)

ABSTRACT

Methane (CH_4) is an important greenhouse gas second only to CO_2 in terms of its greenhouse effect. Vegetation plays an important role in controlling soil CH_4 fluxes, but the spatial variability of soil CH_4 fluxes during vegetation restoration in Loess Hilly Region (LHR) is not fully understood. The effects of different plant community types [*Medicago sativa* grassland (MS); *Xanthoceras sorbifolium* forestland (XS); *Caragana korshinskii* bushland (CK); *Hippophae rhamnoides* shrubland (HR); and *Stipa bungeana* grassland (SB)] on soil CH_4 flux in LHR were studied via the static chamber technique. The results showed that the five plant community types were sinks of soil CH_4 in LHR, the plant community type significantly affected the soil CH_4 flux, and the average CH_4 uptake from high to low was in SB, HR, CK, MS, and XS. During the whole study period, the soil CH_4 flux showed similar interannual variation. The maximum absorption of soil CH_4 appeared in the growing season, while the minimum appeared in winter. Soil CH_4 uptake was positively correlated with soil temperature and soil moisture. Soil temperature and moisture are important controlling factors for the temporal variability of soil CH_4 flux. In LHR, the *Stipa bungeana* grassland is the more suitable plant community type for reducing soil CH_4 emissions. In the process of vegetation restoration in LHR, the soil CH_4 absorption potential of different plant community types should be considered, ecological benefits should be taken into account, and vegetation more suitable for mitigating the greenhouse effect should be selected.

Key words: plant community type, methane, temporal variation, Loess Hilly Region

Citation: Yang, C. J., G. Li, L. J. Yan, W. W. Ma, J. Q. Wu, Y. Tan, S. N. Liu, and S. K. Zhang, 2022: Effects of plant community type on soil methane flux in semiarid Loess Hilly Region, Central Gansu Province, China. *Adv. Atmos. Sci.*, **39**(8), 1360−1374, https://doi.org/10.1007/s00376-022-1169-4.

Article Highlights:

- The five plant community types studied are sinks of soil CH_4 in LHR.
- Plant community type significantly affects soil CH_4 flux, and the largest average soil CH_4 uptake flux is in *Stipa bungeana* grassland.
- Max (min) soil CH_4 uptake is in the growing season (winter); soil temperature and moisture control the temporal variation of soil CH_4 flux.
- *Stipa bungeana* grassland is the ideal plant community type to reduce soil CH_4 emissions in LHR.

1. Introduction

Methane (CH_4) is one of the main greenhouse gases with a strong absorption band in the infrared region, and its contribution to global warming accounts for about 20% (IPCC, 2013; Dutta et al., 2015). The global warming potential of CH_4 gas in 100 years is 25–32 times that of carbon dioxide (CO_2) (IPCC, 2007; Solomon, 2007; Neubauer and Megonigal, 2015). As of 2019, the global atmospheric concentration of CH_4 is 1.877 ± 0.002 μL L^{-1}, which is 2.6 times that of the preindustrial period, with an average growth rate of 0.43% in the last decade (WMO, 2020). The increase in anthropogenic CH_4 sources (Solomon, 2007; Barrie et al., 2009) and the decrease in natural CH_4 sinks (FAO, 2010)

※ This paper is a contribution to the special issue on Carbon Neutrality: Important Roles of Renewable Energies, Carbon Sinks, NETs, and non-CO_2 GHGs.

* Corresponding author: Guang LI
Email: lig@gsau.edu.cn

are the main reasons for the rapid increase in the CH_4 concentration in the atmosphere. If CH_4 emissions can be stabilized, the global temperature rise can be reduced by 25% (Thompson et al., 1992). Therefore, research on global CH_4 sources/sinks has attracted the attention of environmental scientists (Carmichael et al., 2014).

Vegetation is an important factor in global climate change and plays a key role in the complex interactions between the land surface and the atmosphere (Hong and Lakshmi, 2005). Studies have shown that different vegetation has different effects on soil CH_4 gas (Dalal and Allen, 2008; Kim et al., 2016; Oertel et al., 2016; Plain et al., 2019; Zhang et al., 2019; Chai et al., 2020; Ma et al., 2020), with production, oxidation, and transport being the three most important processes that control soil CH_4 fluxes (Bubier et al., 1993; Cao et al., 1996; Harazono et al., 2006; Lai, 2009; Von Fischer et al., 2010; Brummell et al., 2012). The composition and density of plant communities are extremely important in controlling soil CH_4 fluxes (Sebacher et al., 1985; Schimel, 1995; Shannon et al., 1996; Ding et al., 2004; Mills et al., 2013; Lai et al., 2014a, b). Vegetation affects soil CH_4 fluxes by changing the physicochemical properties of the soil (Bhandral et al., 2007; De La Bárcena et al., 2014), and a well-developed root system will loosen the compaction of the soil, thereby creating an aerobic environment that affects the flow of water and gases and influences the uptake and diffusion of soil CH_4 (Bhandral et al., 2007; Shi et al., 2013). Vegetation can have a key impact on soil CH_4 flux by providing organic substrate and increasing the transport of CH_4 (Jones et al., 1987; Schimel, 1995; Ström et al., 2003; Harazono et al., 2006; Von Fischer and Hedin, 2007; Bhullar et al., 2013a). After CH_4 production, the aeration tissues of herbaceous plants facilitate CH_4 transport by providing important pathways for CH_4 movement between soil and atmosphere (Joabsson et al., 1999; Ström et al., 2003; Whalen, 2005; Brummell et al., 2012; Bhullar et al., 2013a, b), allowing CH_4 to bypass the oxidation layer in the soil where it would otherwise be reoxidized (Whalen and Reeburgh, 1990; Jespersen et al., 1998; Frenzel and Karofeld, 2000; Heilman and Carlton, 2001; Inubushi et al., 2001; Joabsson and Christensen, 2001; Ström et al., 2005; Wilson and Humphreys, 2010). Also, the abundance of vegetation affects the growth and activity of aerobic microorganisms, and thus the ability of CH_4 to diffuse from soil to atmosphere (Schimel, 1995; Rusch and Rennenberg, 1998). Moreover, plants can also help the competitive process of CH_4 oxidation by transporting oxygen to their roots, which can support CH_4 reproduction when it is released into the surrounding soil (Sebacher et al., 1985; Conrad, 1996; Harazono et al., 2006). Therefore, it is crucial to understand the mechanisms by which vegetation affects soil CH_4 fluxes.

The processes controlling soil CH_4 fluxes are closely coupled to surrounding environmental conditions (Jones et al., 1987; Harriss and Frolking, 1992; Harazono et al., 2006; Von Fischer et al., 2010) and are community-wide (Billings, 1952). Therefore, the temporal variability of soil CH_4 fluxes under different vegetation is controlled by different factors. For example, in the Prince Albert National Park, Saskatchewan, soil CH_4 emissions are the highest in boreal aspen forest from late July to mid-September, and there are strong correlations between soil CH_4 fluxes and soil temperature (Simpson et al., 1997). The seasonal peak of soil CH_4 uptake in artificial grassland soils in the semi-arid region of Inner Mongolia occurs in the season when rainfall is more concentrated, and the factors affecting the seasonal variation of soil CH_4 uptake are mainly soil moisture and soil temperature (Wang, 2014). In a typical Mediterranean climate zone, soil CH_4 uptake fluxes reach a maximum in summer and a minimum in winter, and have a daily variation of small uptake fluxes during the day and large uptake fluxes at night (Fernández-Duque et al., 2020). Soil CH_4 is absorbed during the growing season and emitted during the non-growing season in the Huoditang Forest Region of the Qinling Mountains, with large seasonal fluctuations. Overly low temperatures inhibiting CH_4 oxidation is the main reason for the appearance of soil CH_4 emissions during the non-growing season (Liu et al., 2019). In the Abbey Lake area of the arid zone, the soil CH_4 emission from the abandoned land has a more obvious diurnal variation with a single or double-peaked curve, and moisture and temperature are the most important environmental factors affecting the variation of soil CH_4 emission from the abandoned land during the growing season (Sun et al., 2012). Therefore, it has become increasingly important to explore the main factors that play a decisive role in soil CH_4 fluxes.

Loess Hilly Region (LHR) is the most fragile and degraded area in China (Tang et al., 1993) and a key area of ecological restoration. In recent years, in order to control soil erosion effectively and realize ecological restoration and its virtuous cycle, a project known as "the Conversion of Farmland to Forests and Grasses Program" has been implemented in this area (Wu et al., 2018). This also allows the local vegetation to enter a relatively undisturbed recovery process. However, most studies on the vegetation in LHR have focused on soil physical properties (Wu et al., 2018), soil nutrients (An et al., 2006; Wang et al., 2020), enzyme activities (Yang et al., 2015; Wang et al., 2020), the soil organic carbon (SOC) pool, etc., with relatively few reports on the soil CH_4 flux under the different vegetation in this region. Therefore, it is very important, for regional and national carbon sink assessment in China, to increase understanding on the response of soil CH_4 flux to vegetation differences.

In this study, we investigated the effects of different plant community types (*Medicago sativa* grassland, *Xanthoceras sorbifolium* forestland, *Caragana korshinskii* bushland, *Hippophae rhamnoides* shrubland, and *Stipa bungeana* grassland) on soil CH_4 flux in LHR from November 2017 to October 2019 using a closed static chamber method. The main aims of the study were to: (1) determine the differences in soil CH_4 fluxes among different plant community types in LHR; and (2) identify the main environmental factors affecting soil CH_4 fluxes. We hypothesized that, among the

five plant community types in LHR, (1) there would be significant differences in soil CH_4 fluxes among plant community types; (2) the *Stipa bungeana* grassland, which is dominated by herbaceous plants with a clear numerical predominance, would be the strongest soil CH_4 sink among the five plant community types; and (3) soil temperature and soil moisture would influence the temporal variability of soil CH_4 fluxes.

2. Research area and methods

2.1. *Site description*

The study area was Anjiagou Watershed (35°33′02″–35°35′29″N, 104°38′13″–104°40′25″E), located in Anjiapo Village, Fengxiang Town, Dingxi City, Gansu Province, which belongs to the typical semi-arid loess hilly gully area of the fifth subregion (Fig. 1). The watershed covers an area of 8.54 ha (1 ha = 0.01 km^2), with elevation between 1900 m and 2250 m. The area has a temperate continental monsoon climate with an average annual temperature of 6.3°C, average annual precipitation of 427 mm, and evaporation level of 1500 mm, with concentrated and seasonal precipitation (more than 60%) occurring from May to September, mainly in the form of heavy rainfall (Fig. 2). The main soil types are loess and river saline soils (Gong et al., 2007). Before the 1990s, the area was deforested and cleared, and in 1999, the Conversion of Farmland to Forests and Grasses Program was officially launched to plant vegetation in the ratio of 1:2:7 with trees, shrubs, and herbs (Wang and Bennett, 2008). In the early stage of afforestation, the survival rate of the fallow forest and grass was improved by artificial irrigation and replanting measures. The artificially restored vegetation species in the watershed were *X. sorbifolium*, *C. korshinskii*, and *H. rhamnoides*. The herbaceous species were mainly *M. sativa* (Table 1). *Xanthoceras sorbifolium* (family: Sapindaceae) is a small- to medium-sized tree endemic to northern China and is an emerging oil crop used for advanced biofuels, functional foods, and pharmaceutical and cosmetic applications (Zhou and Cai, 2021). *Caragana korshinskii* (family: Leguminosae) is a perennial leguminous shrub widely distributed in arid and semi-arid regions of Eurasia, with important environmental benefits and economic value for sand fixation and water retention (Bai et al., 2017). *Hippophae rhamnoides* (family: Elaeagnaceae) is a tree species with drought, sand, and salt tolerance, which is planted in large quantities in northwestern China for desertification control and has a high ecological value (Wei et al., 2019). *Medicago sativa* (family: Leguminosae) is a perennial herbaceous plant with strong drought resistance and adaptation to poor soils, which is widely planted in the region (Ji et al., 2020).

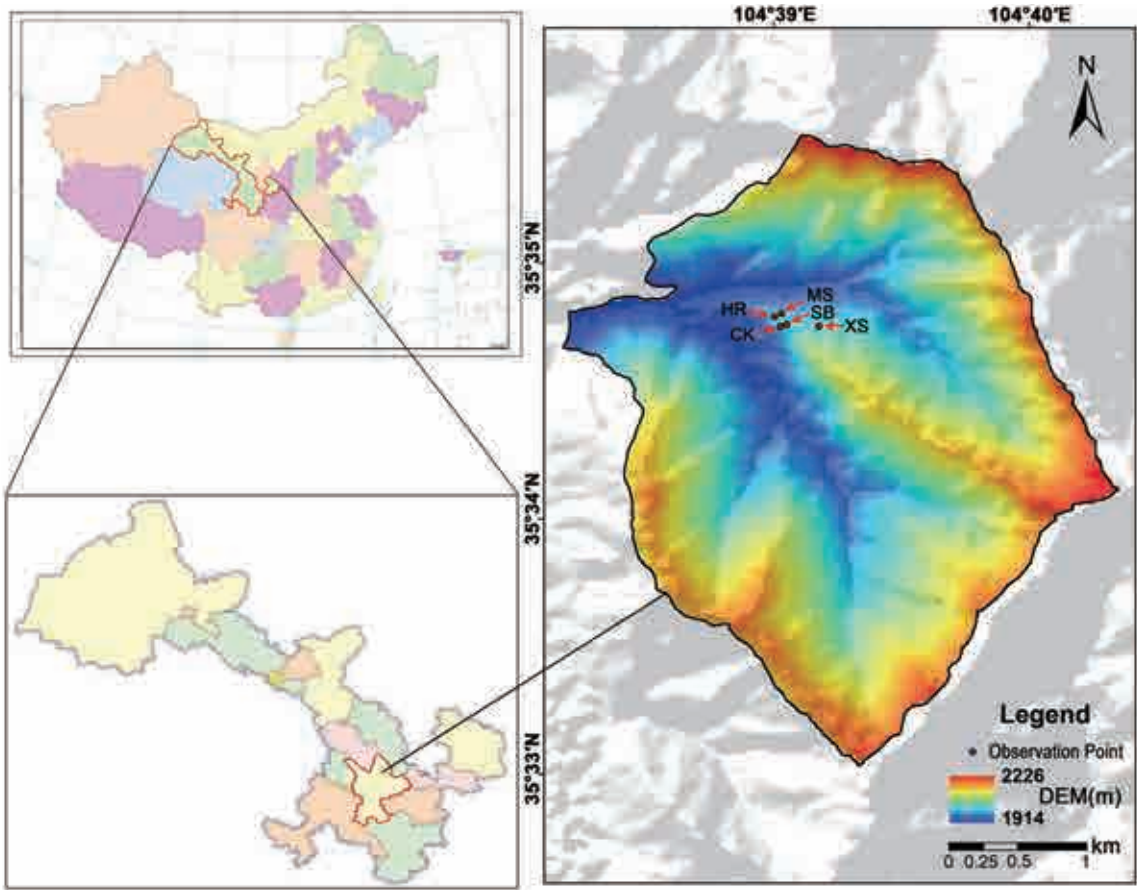

Fig. 1. Map of the study area: XS, *Xanthoceras sorbifolium* forestland; SB, *Stipa bungeana* grassland; CK, *Caragana korshinskii* bushland; HR, *Hippophae rhamnoides* shrubland; MS, *Medicago sativa* grassland.

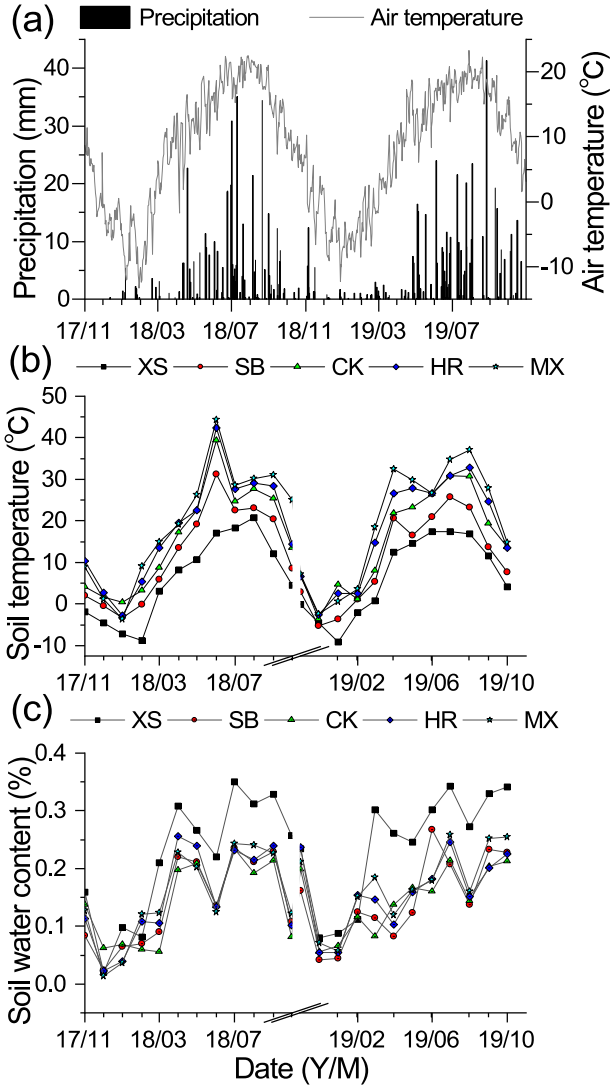

Fig. 2. Temporal patterns of (a) air temperature and precipitation of the study area, and (b) soil temperature and (c) soil water content in the top 10 cm of the five plant community types: XS, *Xanthoceras sorbifolium* forestland; SB, *Stipa bungeana* grassland; CK, *Caragana korshinskii* bushland; HR, *Hippophae rhamnoides* shrubland; MS, *Medicago sativa* grassland.

2.2. *Experimental design*

In September 2017, the ecosystems in the study area were classified into several types according to the different vegetation restoration types and the dominant species of the plant community, and five representative plant community types were selected as observations for the measurement of differences in soil CH_4 dynamics: *X. sorbifolium* forestland (XS), *Stipa bungeana* grassland (SB), *C. korshinskii* bushland (CK), *H. rhamnoides* shrubland (HR), and *M. sativa* grassland (MS). XS, CK, and HR were restored to woodland, mallow shrub community, and buckthorn shrub community, respectively, in 1999 through the implementation of the Conversion of Farmland to Forests and Grasses Program and manual management, without any further management measures. MS was abandoned in 2015 on the basis of cultivated land, planted with *M. sativa* and enclosed, and no further management measures were taken after survival. SB was abandoned in 1999 and naturally restored to an herbaceous community without any further management measures. Regarding the slope orientation, XS was located on the northeast slope, CK on the northwest slope, HR and MX on the north slope, and SB in the no-slope orientation zone. All sampling plots were set on sloping (but not significantly) arable land (except HR, which had a slope of about 5°). According to data from the local Hydrological and Water Resources Survey, the depth of the water table in the area during the experiment was about 100 m. Full details of the experimental sites are presented in Table 1 and Fig. 3. A completely randomized design was used, and three randomly selected sampling plots (7 m × 7 m) were taken from each plant community type, with a buffer zone of at least 5 m between each sampling plot, for a total of 15 sampling plots.

2.3. *Collection and analysis of CH_4 samples*

Stainless steel bases (50 cm × 50 cm × 15 cm, L × W × H) were laid out in September 2017 within the 15 selected sampling plots following the method in Ma et al. (2020) (Fig. 4). Soil CH_4 fluxes were sampled twice a month (biweekly) during the growing season (April to October) and once a month (mid-month) during the non-growing sea-

Table 1. Basic information on the different plant community types at the experimental sites.

Plot	Area (m^2)	Longitude and latitude	Elevation (m)	Main species	Coverage (%)	Height (cm)
MS	20 × 20	104°39′1.82″E 35°34′48.07″N	1990	*Medicago sativa* (90%), *Stipa bungeana, Artemisia lavandulifolia*	90.06±1.58^b	62.23±0.23^d
XS	20 × 20	104°39′10.62″E 35°34′45.08″N	2018	*Xanthoceras sorbifolium* (86%), *Bupleurum chinense, Gentiana macrophylla, Leontopodium leontopodioides*	95.32±2.35^c	76.45±2.54^e
CK	20 × 20	104°39′1.51″E 35°34′45.00″N	1999	*Caragana korshinskii* (42%), *Potentilla chinensis, Picris hieracioides*	50.43±5.45^a	16.00±0.79^a
HR	20 × 20	104°39′0.18″E 35°34′47.32″N	1998	*Hippophae rhamnoides* (81%), *Leontopodium leontopodioides, Artemisia annua*	89.26±0.78^b	54.89±1.23^c
SB	20 × 20	104°39′3.05″E 35°34′45.48″N	2008	*Stipa bungeana* (92%), *Plantago asiatica, Setaria viridis, Leymus secalinus*	98.23±0.63^c	35.93±0.44^b

Notes: XS, *Xanthoceras sorbifolium* forestland; SB, *Stipa bungeana* grassland; CK, *Caragana korshinskii* bushland; HR, *Hippophae rhamnoides* shrubland; MS, *Medicago sativa* grassland. The percentage of the main species is the coverage of the dominant species. Values are presented as mean ± standard error. Superscript letters indicate significant differences between plant community types ($P < 0.05$).

Fig. 3. Photographs of sampling plots with different plant community types: (a) *Medicago sativa* grassland; (b) *Xanthoceras sorbifolium* forestland; (c) *Caragana korshinskii* bushland; (d) *Hippophae rhamnoides* shrubland; (e) *Stipa bungeana* grassland.

son (November to March) from November 2017 to October 2019 (i.e., 24 months) (Xia et al., 2015). All samples were collected between 0900 local standard time (LST, LST=UTC+8 hours) and 1200 LST. The fluxes measured during this time are considered to be representative of the daily average fluxes (Wang and Wang, 2003; Lin et al., 2009; Ma et al., 2018). After the chamber was closed, air samples (five in total) were taken from inside the chamber at 10-min intervals (at minutes 0, 10, 20, 30, and 40) using a 100 mL polypropylene syringe equipped with a three-way plug valve (Ma et al., 2020). The air samples were transferred to pre-evacuated E-Switch aluminum foil composite film gas sampling bags (Shanghai Shenyuan Scientific Instruments Co., Ltd., Shanghai, China) via the three-way plug valve. Within 48 h, the samples were returned to the laboratory for analysis of CH_4 concentrations using a gas chromatograph (YiMeng A90, Changzhou Ban'nuo Instruments Co., Ltd., China). While collecting air samples, the temperature in the chamber and the soil temperature (T_{10}) and soil water content (SWC_{10}) at 10 cm above ground were measured using a portable digital thermometer (JM624, Jinming Instrument Co., Tianjing, China) and a temperature and humidity sensor (GS3,

Fig. 4. Photographs of the chamber: (a) top view and (b) side view of the sampling chamber; (c) side view and (d) top view of the stainless steel base.

METER Group, Pullman, WA, USA), respectively. Air temperature and precipitation data were obtained from a local weather station located in Anjiagou Watershed. The weather station was set up near the SB sampling plot (Fig. 1), and all sampling plots were within a 500 m radius. Thus, air temperature and precipitation were not subjected to any correction.

The CH_4 gas flux was calculated as

$$F = \frac{dC}{dt} \times \frac{M}{V_0} \times \frac{P}{P_0} \times \frac{T_0}{T} \times H\,, \tag{1}$$

where F is the gas flow rate (units: mg m^{-2} h^{-1}), dC/dt is the gradient of the time series of CH_4 concentration (units: ppmv h^{-1}) at the time of sampling, M is the molar mass (units: g mol^{-1}) of the measured gas, P is the pressure (units: hPa) at the sampling plot, and T is the temperature in the chamber (units: K) at the time of sampling. V_0, P_0, and T_0 are the molar volumes (L mol^{-1}) of the gas at standard conditions, air pressure (units: hPa), and absolute temperature (units: K), respectively, and H (units: m) is the height of the sampling box above the ground (Song et al., 2009). The data can be subjected to later calculations only if the goodness-of-fit (R^2) of the linear regression results for four or five samples is ⩾ 0.80 (Ma et al., 2020). Mean fluxes are expressed as the mean and standard deviation of three replicates.

The cumulative flux of CH_4 gas was estimated as follows:

$$\text{Sum} = \sum_{i=1}^{n} 24\left(\frac{F_i + F_{i+1}}{2}\right)(D_{i+1} - D_i)\,, \tag{2}$$

where i and $i + 1$ are the ith and ith + 1 observations, respectively; F_i is the CH_4 flux (units: mg m^{-2} h^{-1}) of the ith observation; and D_i is the Julian date of the ith observation.

2.4. *Auxiliary measurements*

In September 2017, the relative coverage, plant height, and dominant species were measured randomly in 15 sampling plots (50 cm × 50 cm) (Ma et al., 2018). At the same time, soil samples were taken from the 0–10 cm layer using a soil auger (diameter: 5 cm) following the diagonal five-point method (four points selected at each end of the "X" and one point at the intersection) (Wang et al., 2020). Five soil samples from the same soil layer in each plot were mixed to form one soil sample, for a total of 15 soil samples. After removing debris such as stones and residual roots, the samples were dried and put into self-sealing bags through 100-mesh soil sieves for determination of the soil pH value, SOC, and total nitrogen (TN).

The soil total porosity (STP) of the 0–10 cm layer was measured using the ring knife method (volume: 100 cm^3) (Wang et al., 2020). Soil pH was measured with a pH meter (PHS-3S, INESA Scientific Instrument Co., Shanghai, China), and the soil water ratio of suspension was 1:5 (Wu and Mu, 2019). SOC and TN were determined by referring to the method of Wu et al. (2020).

2.5. *Data analysis*

The data were organized using Microsoft Excel 2019, and all data were statistically analyzed using SPSS 22.0. One-way analysis of variance (Duncan's Multiple Range Test, $P < 0.05$) was used to determine the differences in vegetation properties (coverage, height), soil CH_4 fluxes, and soil characteristics [pH, STP, SOC, TN, ratio of carbon to nitrogen (C/N), T_{10}, SWC_{10}] among plant community types. General linear model (GLM) analysis and analysis of covariance (ANCOVA) were used to compare the interaction and effects of different plant community types (PCT) and soil temperature/soil water content on soil CH_4. The relationships between environmental variables (T_{10}, SWC_{10}) and soil CH_4 fluxes in the five plant community types were analyzed using Pearson correlation analysis (two-tailed). The interrelationships between T_{10}, SWC_{10}, and soil CH_4 fluxes in the five plant community types were analyzed using a linear regression method.

3. Results and analysis

3.1. *Environmental variables*

The vegetation properties (dominant species, vegetation cover, plant height) varied clearly at the five sites (Table 1). The plant community type significantly affected the physical properties of the soil (STP, T_{10}, SWC_{10}) throughout the experimental period ($P < 0.05$, Table 2). The STP of MS was significantly lower than that of the other four plant community types; the mean T_{10} of the five plant community types from 0 cm to 10 cm showed a trend of XS < SB < CK < HR < MS; and the variation in 10 cm soil SWC ranged from 14.0% to 24.3% (Table 2), showing a trend of CK < SB < HR < MS < XS (Table 2). The average T_{10} and SWC_{10} from 0 cm to 10 cm for all five plant community types showed a trend that the growing season was greater than the non-growing season (Figs. 2b and c). The SOC of MS was significantly higher than that of the other four plant community types ($P < 0.05$). The soil TN of XS was significantly higher than that of the other plant community types, and the soil C/N of XS, CK, and HR was significantly lower than that of the other two plant community types.

3.2. *Differences in soil CH_4 fluxes under different plant community types*

Throughout the observation period, soil CH_4 fluxes of the five different plant community types showed net uptake, with fluxes ranging from –0.061 mgC m^{-2} h^{-1} to –0.086 mgC m^{-2} h^{-1}. The soil CH_4 fluxes differed significantly ($P < 0.05$) among the different plant community types (Fig. 5), and the average soil CH_4 fluxes of SB were 1.29, 1.42, 1.20, and 1.08 times higher than those of MS, XS, CK, and HR, respectively. The cumulative soil CH_4 fluxes of the five different plant community types ranged from 14.986 kgC ha^{-1} to 19.796 kgC ha^{-1} throughout the observation period, showing a trend of XS < MS < CK < HR < SB (Table 3).

Throughout the observation period, there were significant seasonal variations in soil CH_4 fluxes among the five different plant community types (Fig. 6), with soil CH_4 uptake occurring mainly during the growing season [SB (–0.101 ± 0.007 mgC m^{-2} h^{-1}) > HR > CK > MS > XS (–0.073 ± 0.005 mgC m^{-2} h^{-1})]. In addition, soil CH_4 uptake began to decrease with fluctuation in November and reached its lowest value in February, after which the soil CH_4 flux gradually increased in volatility and reached a peak in April–June.

3.3. *Plant community control of soil CH_4 flux*

GLM analysis of plant community type and soil CH_4 flux showed that the interaction terms for PCT × T_{10} and

Table 2. Physicochemical properties of soil (0–10 cm depth) from sites with different plant community types.

Plot	STP (%)	T_{10} (°C)	SWC_{10} (%)	pH	SOC (g kg^{-1})	TN (g kg^{-1})	C/N
MS	49.45 ± 0.42^{a}	19.68 ± 2.08^{c}	0.17 ± 0.01^{a}	6.75 ± 0.16^{a}	11.08 ± 0.32^{d}	0.45 ± 0.05^{b}	25.73 ± 3.84^{b}
XS	73.39 ± 3.16^{c}	6.75 ± 1.46^{a}	0.24 ± 0.01^{b}	6.92 ± 0.22^{a}	10.58 ± 0.09^{cd}	0.77 ± 0.00^{c}	13.68 ± 0.11^{a}
CK	71.06 ± 2.24^{c}	15.80 ± 1.80^{bc}	0.14 ± 0.01^{a}	6.58 ± 0.34^{a}	5.45 ± 0.55^{a}	0.29 ± 0.01^{a}	18.86 ± 1.88^{a}
HR	62.85 ± 0.34^{b}	17.81 ± 1.88^{bc}	0.16 ± 0.01^{a}	6.67 ± 0.15^{a}	7.91 ± 0.21^{b}	0.45 ± 0.00^{b}	17.71 ± 0.54^{a}
SB	68.36 ± 1.03^{bc}	11.57 ± 1.62^{ab}	0.15 ± 0.01^{a}	7.00 ± 0.41^{a}	9.57 ± 0.30^{c}	0.32 ± 0.00^{a}	29.92 ± 0.86^{b}

Notes: STP, soil total porosity; SOC, soil organic carbon; TN, total nitrogen; C/N, carbon nitrogen ratio; T_{10}, soil temperature of top 10 cm; SWC_{10}, soil moisture of top 10 cm. Superscript letters indicate significant differences between plant community types ($P < 0.05$).

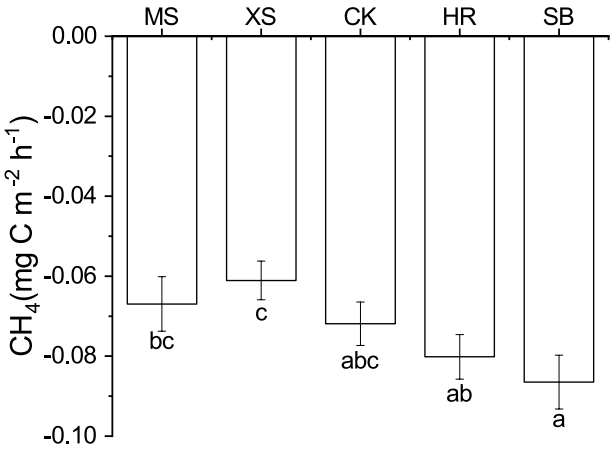

Fig. 5. Annual average soil CH_4 flux under different plant community types: MS, *Medicago sativa* grassland; XS, *Xanthoceras sorbifolium* forestland; CK, *Caragana korshinskii* bushland; HR, *Hippophae rhamnoides* shrubland; SB, *Stipa bungeana* grassland. Lowercase letters indicate statistically significant differences within observations among different plant community types ($P = 0.05$).

PCT × SWC_{10} were not significantly different for soil CH_4 fluxes ($P > 0.05$, Table 4), indicating that there were no interactive effects of plant community type and T_{10}/SWC_{10} on soil CH_4 flux. The ANCOVA of plant community type and soil CH_4 flux showed that excluding the effect of T_{10}, there was a significant effect of plant community type on soil CH_4 flux ($P < 0.05$); and excluding the effect of SWC_{10}, there was a significant effect of plant community type on soil CH_4 flux ($P < 0.05$) (Table 4).

There was a highly significant positive correlation (R^2 = 0.60–0.74, $P < 0.01$) between soil CH_4 flux and T_{10} under different plant community types (Table 5). There was also a significant positive correlation (R^2 = 0.44–0.57, $P < 0.05$) between soil CH_4 flux and SWC_{10} in MS, XS, and CK (Table 5). The results of linear regression analysis for the different environmental variables under different vegetation community types showed that the variations in T_{10} and SWC_{10} explained 36.0%–55.2% and 6.18%–33.3% of the temporal variation in soil CH_4, respectively ($P < 0.01$) (Fig. 7).

4. Discussion

4.1. *Effects of plant community type on soil CH_4 flux*

In this study, all five plant community types were sinks of soil CH_4 in LHR, with fluxes between –0.061 mgC m^{-2} h^{-1} and –0.086 mgC m^{-2} h^{-1} (Fig. 5), which is consistent with the finding of Zhao et al. (2018). The study by Wu and Mu (2019) in mountainous regions in Northeast China showed that soil CH_4 fluxes in planted forests ranged between –0.048 mgC m^{-2} h^{-1} and –0.077 mgC m^{-2} h^{-1}, which is significantly lower than the results of the present study and related to its lower mean annual temperature. Pihlatie et al. (2017), in boreal alpine forest, reported soil CH_4 fluxes of between –0.054 mgC m^{-2} h^{-1} and –0.096 mgC m^{-2} h^{-1}, which are higher than the results of this study owing to the fact that the mosses play an important role in the forest floor CH_4 exchange. There were significant differences in soil CH_4 flux among the five different plant community types ($P < 0.05$, Fig. 5), with the maximum value occurring in SB—a result similar to that of Pihlatie et al. (2017) and Zhao et al. (2018). Methane production tends to occur deep in the soil in anaerobic environments (Yang et al., 2014, 2019). In this study, the groundwater table was low, the soil envelope was thick (Chen, 2009), and most of the soils with different plant community types were well ventilated (Table 2), providing favorable oxygen conditions for the oxidation process of soil CH_4 (Lombardi et al., 1997). Therefore, soil CH_4 uptake dominated in this study area. In the present study, the vegetation cover of the grassland was much higher than that of the woodland, and the dense root system of the soil surface was conducive to the creation of an aerobic environment, thus increasing the uptake of soil CH_4 (Shi et al., 2013). Also, larger porosity affects the rate of CH_4 oxidation and methanotrophs abundance, which in turn affects the transport of CH_4 in the soil (De La Bárcena et al., 2014). Added to this, the diffusion of herbaceous aeration tissues is the main pathway for gas transport, and more oxygen diffuses into the soil through the aeration tissues, which can affect the growth and activity of aerobic microorganisms and increase the oxidation of methane (Schimel, 1995; Rusch and Rennenberg, 1998). This is consistent with the results of the present study, where the soil CH_4 flux of SB was significantly higher than that of other plant community types ($P < 0.05$, Fig. 5). This result is similar to previous findings (Schimel, 1995; Rusch and Rennenberg, 1998; Bhandral et al., 2007; Zhao et al., 2018). In SB, the number of herbaceous plants was significantly higher than that in other plant community types (Table 1), and their subsurface aeration tissues were also higher, resulting in significantly higher soil CH_4 uptake in SB than in other plant community types ($P < 0.05$, Fig. 3a). In contrast, the soil CH_4 uptake of XS was significantly lower than that of HR and SB ($P < 0.05$, Fig. 5) because of the higher leaf area and related shading of the

Table 3. Cumulative estimates of soil CH_4 uptake under different plant community types.

	MS (kgC ha^{-1})	XS (kgC ha^{-1})	CK (kgC ha^{-1})	HR (kgC ha^{-1})	SB (kgC ha^{-1})
Y1	−5.943 ± 0.743	−7.532 ± 0.500	−7.803 ± 0.499	−8.938 ± 0.956	−8.554 ± 1.450
Y2	−9.330 ± 0.475	−7.454 ± 0.524	−8.781 ± 0.728	−9.724 ± 0.426	−11.241 ± 0.449
Total	−15.273 ± 0.295	−14.986 ± 0.500	−16.585 ± 1.127	−18.662 ± 0.737	−19.796 ± 1.566

Notes: Values are presented as mean ± standard error. Y1, November 2017 to October 2018; Y2, November 2018 to October 2019.

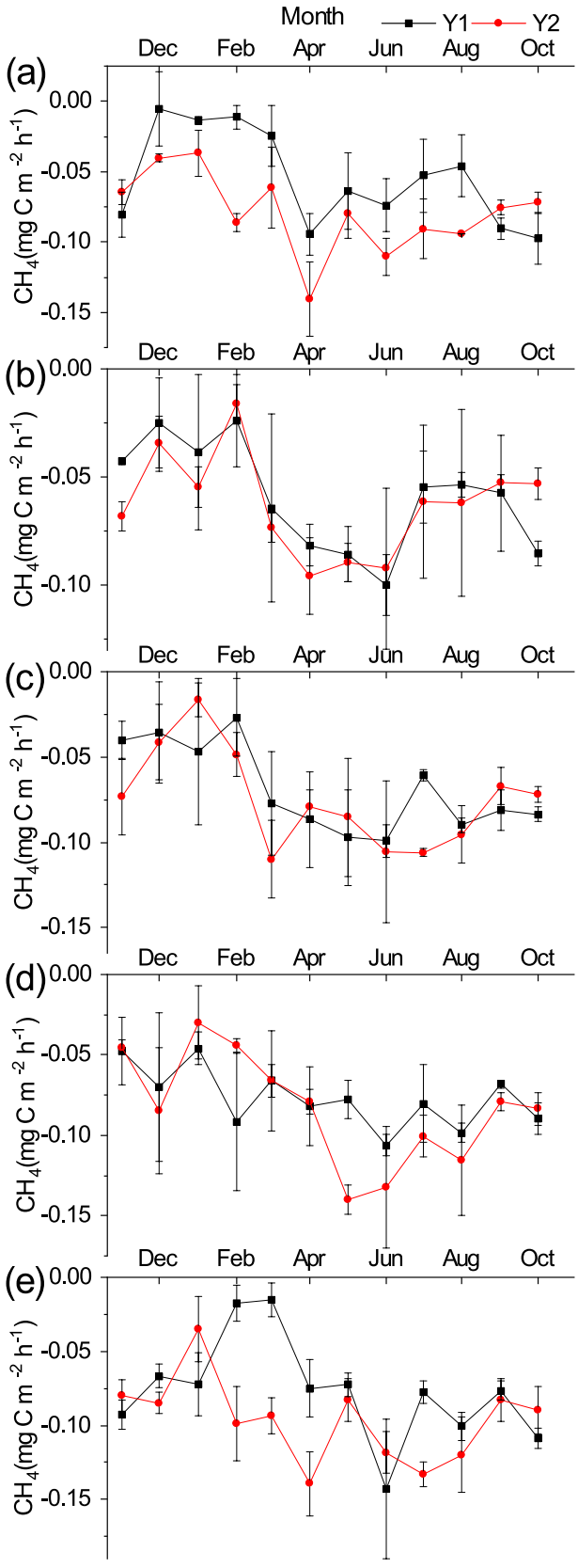

Fig. 6. Interannual variability of soil CH_4 flux under different plant community types during November 2017 to October 2019: (a) *Medicago sativa* grassland; (b) *Xanthoceras sorbifolium* forestland; (c) *Caragana korshinskii* bushland; (d) *Hippophae rhamnoides* shrubland; (e) *Stipa bungeana* grassland.

soil by tall vegetation (Kim, 2013; Oertel et al., 2016), which made the T_{10} in XS significantly lower than that of HR and SB (Table 2). The temperatures were significantly different under different vegetation coverages ($P < 0.05$, Table 2), which would have limited the growth and reproduction and activity of soil microorganisms and soil enzymes (Luan et al., 2016), in turn affecting soil CH_4 uptake. The decrease in temperature is accompanied by a decrease in evaporation and an increase in soil moisture, since the opening time of stomata can be reduced. Therefore, the conditions for soil CH_4 emissions are improved (Kim, 2013). However, the study by Wang et al. (2019) showed that the degradation of artificial clover meadow at a semi-arid loess hill site had a significant effect on the distribution and diversity of other herbaceous plants. This is the reason why the soil CH_4 uptake of CK in this study was not significantly different from that of other plant community types ($P > 0.05$, Fig. 5). Differences in plant community type may lead to differences in soil compaction (i.e., STP), which affects the movement of water and gases, and thus the gas diffusion conditions for CH_4 (Christiansen and Gundersen, 2011), with similar results presented in the current study (Table 2, Fig. 5).

In addition to proximal factors, there are a number of distal drivers that also influence soil CH_4 fluxes (Robertson, 1989). The distinct differences in morphology of different vegetation conditions affect the variation in soil temperature by influencing light, wind speed, rainfall, etc. Among them, arboreal vegetation (XS) has the greatest advantage in microclimate regulation. The main source of energy for soil temperature is radiant energy from the sun, and tall arboreal vegetation (XS) shades the soil because of its higher leaf area and associated height (Kim, 2013; Oertel et al., 2016), which made the T_{10} significantly lower in XS than in HR and SB (Table 2; Figs. 2b and c). The water content of the soil in the study area is very low, and there is almost no free water; plus, the heat exchange between the soil and the environment is mediated by the air, and the soil temperature is closely linked to the movement of soil water. Therefore, the SWC_{10} of XS is significantly higher than that of other plant community types (Table 2; Figs. 2b and c). Vegetation caused differences in soil temperature and moisture, which in turn influenced the changes in soil CH_4 flux. It has been shown that lower soil pH, which reduces the activity of soil microorganisms, leads to lower soil CH_4 uptake (Gatica et al., 2020). However, in this study, lower variation in soil pH among the plant community types did not significantly affect methanotrophic bacteria or archaea, which is consistent with the findings of Werner et al. (2007) and Ai et al. (2021). On the other hand, Nitrogen (nitrate, ammonia) may have a positive or neutral effect on soil CH_4 uptake in boreal temperate forest communities (Xia et al., 2020), which is similar to the results previously reported by our team in this region (Yan et al., 2019), albeit there is also no statistically significant relationship. It is well known that slope and slope orientation play a highly important role in regulating local temperature, radiation, and soil moisture. Among the five plant community types, XS, HR, and MX were located on shady slopes, CK

Table 4. Results of GLM analysis and ANCOVA.

GLM analysis			ANCOVA analysis		
Fixed factors	*F*	Sig.	Fixed factors	*F*	Sig.
PCT	1.353	0.251	PCT	60.392	**0.000**
T_{10}	55.539	**0.000**	T_{10}	4.841	**0.001**
PCT × T_{10}	0.803	0.524	–	–	–
PCT	1.579	0.181	PCT	4.121	**0.044**
SWC_{10}	3.844	0.051	SWC_{10}	3.153	**0.015**
PCT × SWC_{10}	0.324	0.862	–	–	–

Notes: Soil CH_4 fluxes were used as dependent variables, while the corresponding SWC_{10} or T_{10} were covariates. The fixed factor was plant community type (PCT). The *F*-value is the ratio of the two mean squares (effect term/error term). Significant values ($P < 0.05$) are indicated in bold.

Table 5. Pearson correlation coefficients and their two-tailed significance between environmental factors (T_{10} and SWC_{10}) and soil CH_4 flux under different plant community types during November 2017 to October 2019.

Plot		T_{10}	SWC_{10}
MS	Pearson	0.607**	0.444*
	Sig. (two-tailed)	0.002	0.030
XS	Pearson	0.600**	0.577**
	Sig. (two-tailed)	0.002	0.003
CK	Pearson	0.743**	0.491*
	Sig. (two-tailed)	0.000	0.015
HR	Pearson	0.660**	0.249
	Sig. (two-tailed)	0.000	0.241
SB	Pearson	0.606**	0.295
	Sig. (two-tailed)	0.002	0.162

Notes: A double asterisk (**) indicates significance at $p < 0.01$, while a single asterisk (*) indicates significance at $p < 0.05$. T_{10}, soil temperature of top 10 cm; SWC_{10}, soil water content of top 10 cm. Negative fluxes values indicating absorption (sinks) have been converted to positive values to facilitate the analysis.

on positive slopes, and SB in a no-slope orientation zone. The results showed that the soil CH_4 fluxes were not significantly correlated with slope orientation, which is consistent with the findings of Fang et al. (2009). This may have been caused by the fact that all sampling plots were laid out on almost flat cultivated land after land preparation and that the meteorological conditions were essentially the same.

4.2. *Effect of plant community type on the temporal variation in soil CH_4 flux*

Changes in vegetation and its microenvironment also make soil CH_4 fluxes show different temporal patterns of variation. In this study, the maximum values of soil CH_4 uptake under different plant community types in LHR occurred in the growing season, and the minimum values all occurred in winter. This is due to the freezing of the soil in winter, which decreases soil pore connectivity (Bhandral et al., 2007) and reduces microbial activity, resulting in lower uptake rates (Do Carmo et al., 2012). On the one hand, as solar radiation increases, the soil thaws and the soil temperature increases, allowing an increase in the rate of gas diffusion and the probability of microorganisms obtaining contact

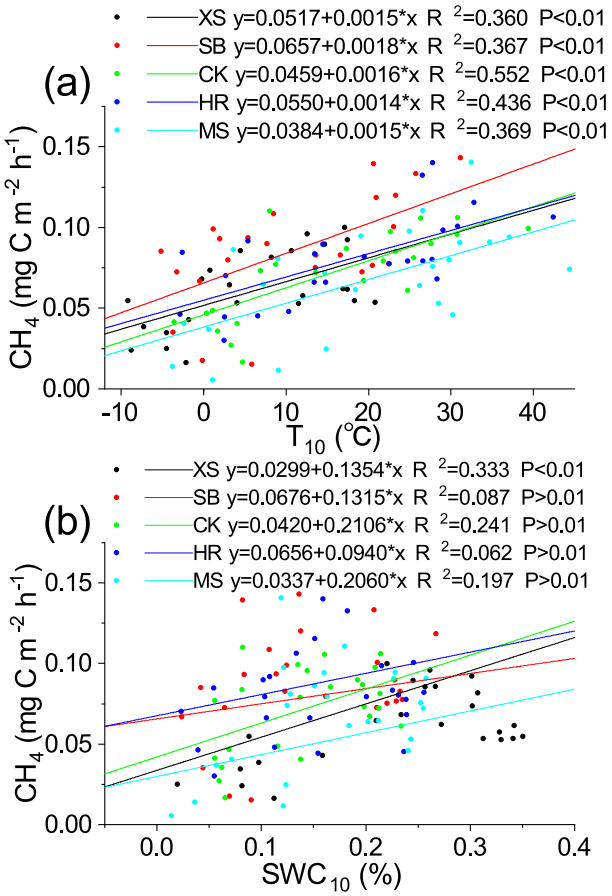

Fig. 7. Relationship between temporal variation of soil CH_4 flux and (a) T_{10} or (b) SWC_{10}: XS, *Xanthoceras sorbifolium* forestland; SB, *Stipa bungeana* grassland; CK, *Caragana korshinskii* bushland; HR, *Hippophae rhamnoides* shrubland; MS, *Medicago sativa* grassland.

with oxygen (Singh et al., 2010), which accelerates the rate of CH_4 oxidation and increases the uptake of CH_4 by the soil (Nesbit and Breitenbeck, 1992; Castro et al., 1995; Dou et al., 2015). Additionally, increased rainfall increases the soil water content, the CH_4 oxidizing bacteria are transformed from a dormant to active state, and increasing soil water content within a certain range is beneficial for CH_4 oxidative uptake (Chen et al., 2002). Due to the soil properties (Wu et al., 2018) and the climatic characteristics of low rainfall and

high evaporation in the study area, higher transpiration after rainfall accelerates the oxidation and transportation of CH_4 (Chen, 2003). However, it has also been shown that soil CH_4 fluxes are not simply linearly related to soil moisture (Ju et al., 2016; Zhang et al., 2019), and when soil water content continues to increase, it will cause an increase in soil water-filled pore space, which limits the rate and diffusion of atmospheric CH_4 oxidation (Werner et al., 2006; Curry, 2007; Wu et al., 2010). However, due to low rainfall and high evaporation in the study area, the SWC_{10} of the different plant community types could not be consistently increased to the saturated soil water content. Therefore, this idea could not be verified. Temperature and soil moisture are considered to be the main factors affecting the seasonal variation in soil CH_4 fluxes (Song et al., 2009; Zhu et al., 2015a, b), and the effects of both interact with each other and show different dominance depending on the characteristics of the ecosystem (Olefeldt et al., 2013). This reason is also evidenced by the linear regression relationship between T_{10}, SWC_{10}, and soil CH_4 fluxes in different plant community types in this study (Fig. 7), which is similar to the results of previous studies (Moore and Dalva, 1993; Glatzel et al., 2004; Cui et al., 2017; Ma et al., 2020). Furthermore, the fact that precipitation, as the main source of soil moisture in this area, is distributed in a pattern that is consistent with that of the temporal variation in soil CH_4 flux, also reiterates this view (Figs. 2 and 6). The results are similar to the findings of other studies (Ju et al., 2016; Ma et al., 2020). In contrast, the maximum uptake value at the MS site occurred in early spring; due to the enclosed setup of the MS site, the aboveground plants that had died out in the previous year's non-growing season increased the soil temperature (Li et al., 2018), thus increasing the uptake of CH_4 by the soil. With the growth of surface vegetation, the ground vegetation cover gradually increased, due to which the soil temperature gradually decreased, thus causing a change in soil CH_4 uptake in the form of an increase first, and then a decrease. Regarding the cumulative flux of soil CH_4, Wang et al. (2014) showed that the average rate of soil CH_4 uptake in Chinese forest and grassland was 49.43 μg m^{-2} h^{-1} and 59.62 μg m^{-2} h^{-1}, respectively, with annual cumulative fluxes of 4.22 kg ha^{-1} and 5.09 kg ha^{-1}. These data are comparable to the rate of soil CH_4 uptake in other forest and grassland sites worldwide (Wang et al., 2014). The average annual cumulative soil CH_4 uptake fluxes of the different plant community types in this study were 2.02 and 1.67 times higher than the annual cumulative uptake fluxes of Chinese forest and grassland, respectively, when only vegetation was considered. Therefore, it can be seen that the soil CH_4 uptake of different plant community types in this region is much higher than the average value in China, which is important for CH_4 reduction and mitigation of the greenhouse effect.

5. Conclusion

The results of the study showed that all five plant community types were sinks of soil CH_4 in LHR. Different plant community types significantly affected soil CH_4 fluxes in decreasing order as follows: SB > HR > CK > MS > XS. Throughout the study period, the maximum values of soil CH_4 uptake occurred in the growing season, while the minimum values all occurred in winter. Soil CH_4 fluxes were significantly and positively correlated with soil temperature and soil moisture. The combined effect of soil temperature and moisture is an important controlling factor for the temporal variability of soil CH_4 fluxes. In LHR, *Stipa bungeana* grassland is the plant community type with the highest capacity for soil CH_4 uptake among the five plant community types studied, and is a more desirable plant community type for mitigating soil CH_4 emissions. In the process of vegetation restoration in LHR, the soil CH_4 absorption potential of different plant community types should be considered, ecological benefits should be taken into account, and vegetation more suitable for mitigating the greenhouse effect should be selected. Therefore, when estimating the soil CH_4 exchange in LHR, it is necessary to consider the influence of the different plant community types.

Acknowledgements. We would like to thank all the people who were involved in the field and laboratory work. This study was financially supported by the Gansu Province Key Research and Development Program (Grant No. 20YF8NA135), the Gansu Province Financial Special Project (Grant No. GSCZZ 20160909), and the Industrial Support Program Project (Grant No. 2021CYZC-15, No.2022CYZC-41). The authors would like to thank Director Jin CHEN, Xiaoping WANG, and other staff from the Soil and Water Conservation Research Institute in Dingxi City, Gansu Province, for their support with the management of the experimental field, and Bin WU of the Ecological Research Center of Northeast Forestry University for his advice on the experimental data in this paper.

REFERENCES

Ai, J., Y. Lyu, Y.-C. Li, X. Zhong, and J. Li, 2021: Methanotrophs bacteria in special environment: A review. *Chinese Journal of Applied Ecology*, **32**, 1509–1517, https://doi.org/10.13287/j.1001-9332.202104.031. (in Chinese with English abstract)

An, S. S., Y. M. Huang, and B. C. Li, 2006: Characteristics of soil water stable aggregates and relationship with soil properties during vegetation rehablitation in a loess hilly region. *Chinese Journal of Soil Science*, **37**, 45–50, https://doi.org/10.19336/j.cnki.trtb.2006.01.010. (in Chinese with English abstract)

Barrie, L., G. Braathen, J. Butler, E. Dlugokencky, D. J. Hofmann, P. Tans, and Y. Tsutsumi, 2009: WMO Greenhouse Gas Bulletin. Eurpoean Geosciences Union General Assembly 2009,Vienna, Austria. [Available online from https://www.researchgate.net/publication/260797073_Annual_Greenhouse_Gas_Bulletin]

Bai, J., and Coauthors, 2017: Relative contribution of photorespiration and antioxidative mechanisms in *Caragana korshinskii* under drought conditions across the Loess Plateau. *Functional*

Plant Biology, **44**, 1111–1123, https://doi.org/10.1071/FP17060.

Bhandral, R., S. Saggar, N. S. Bolan, and M. J. Hedley, 2007: Transformation of nitrogen and nitrous oxide emission from grassland soils as affected by compaction. *Soil and Tillage Research*, **94**, 482–492, https://doi.org/10.1016/j.still.2006.10.006.

Bhullar, G. S., P. J. Edwards, and H. O. Venterink, 2013a: Variation in the plant-mediated methane transport and its importance for methane emission from intact wetland peat mesocosms. *Journal of Plant Ecology*, **6**(4), 298–304, https://doi.org/10.1093/jpe/rts045.

Bhullar, G. S., M. Iravani, P. J. Edwards, and H. O. Venterink, 2013b: Methane transport and emissions from soil as affected by water table and vascular plants. *BMC Ecology*, **13**, 32, https://doi.org/10.1186/1472-6785-13-32.

Billings, W. D., 1952: The environmental complex in relation to plant growth and distribution. *The Quarterly Review of Biology*, **27**, 251–265, https://doi.org/10.1086/399022.

Brummell, M. E., R. E. Farrell, and S. D. Siciliano, 2012: Greenhouse gas soil production and surface fluxes at a high arctic polar oasis. *Soil Biology and Biochemistry*, **52**, 1–12, https://doi.org/10.1016/j.soilbio.2012.03.019.

Bubier, J. L., T. R. Moore, and N. T. Roulet, 1993: Methane emissions from wetlands in the Midboreal region of Northern Ontario, Canada. *Ecology*, **74**, 2240–2254, https://doi.org/10.2307/1939577.

Cao, M. K., S. Marshall, and K. Gregson, 1996: Global carbon exchange and methane emissions from natural wetlands: Application of a process-based model. *J. Geophys. Res.*, **101**, 14 399–14 414, https://doi.org/10.1029/96JD00219.

Carmichael, M. J., E. S. Bernhardt, S. L. Bräuer, and W. K. Smith, 2014: The role of vegetation in methane flux to the atmosphere: Should vegetation be included as a distinct category in the global methane budget. *Biogeochemistry*, **119**, 1–24, https://doi.org/10.1007/s10533-014-9974-1.

Castro, M. S., P. A. Steudler, J. M. Melillo, J. D. Aber, and R. D. Bowden, 1995: Factors controlling atmospheric methane consumption by temperate forest soils. *Global Biogeochemical Cycles*, **9**, 1–10, https://doi.org/10.1029/94GB02651.

Chai, L. L., G. Hernandez-Ramirez, D. S. Hik, I. C. Barrio, C. M. Frost, C. C. Soto, and G. Esquivel-Hernández, 2020: A methane sink in the Central American high elevation páramo: Topographic, soil moisture and vegetation effects. *Geoderma*, **362**, 114092, https://doi.org/10.1016/j.geoderma.2019.114092.

Chen, H. S., 2003: Study on soil water movement and its cycling on a hillslope of the loess plateau. PhD dissertation, Northwest A&F University. (in Chinese with English abstract)

Chen, M. C., G. Y. Zhang, Y. B. Zou, and H. Min, 2002: Methane oxidation of green-house soils. *Journal of Zhejiang University* (*Agriculture & Life Sciences*), **28**, 501–506, https://doi.org/10.3321/j.issn:1008-9209.2002.05.008. (in Chinese with English abstract)

Chen, S. P., 2009: Full utilization of soil and water resources of the Loess Plateau in the middle and Eastern parts of Gansu Province. *Technical Supervision in Water Resources*, **17**, 22–23, https://doi.org/10.3969/j.issn.1008-1305.2009.05.010. (in Chinese with English abstract)

Christiansen, J. R., and P. Gundersen, 2011: Stand age and tree species affect N_2O and CH_4 exchange from afforested soils. *Biogeosciences*, **8**, 2535–2546, https://doi.org/10.5194/bg-8-2535-2011.

Conrad, R., 1996: Soil microorganisms as controllers of atmospheric trace gases (H_2, CO, CH_4, OCS, N_2O, and NO). *Microbiological Reviews*, **60**, 609–640, https://doi.org/10.1128/MR.60.4.609-640.1996.

Cui, L. J., and Coauthors, 2017: Rewetting decreases carbon emissions from the Zoige Alpine Peatland on the Tibetan Plateau. *Sustainability*, **9**, 948, https://doi.org/10.3390/su9060948.

Curry, C. L., 2007: Modeling the soil consumption of atmospheric methane at the global scale. *Global Biogeochemical Cycles*, **21**, GB4012, https://doi.org/10.1029/2006GB002818.

Dalal, R. C., and D. E. Allen, 2008: Greenhouse gas fluxes from natural ecosystems. *Australian Journal of Botany*, **56**, 396–407, https://doi.org/10.1071/BT07128.

De La Bárcena, T. G., L. D'Imperio, P. Gundersen, L. Vesterdal, A. Priemé, and J. R. Christiansen, 2014: Effects of the conversion of cropland to forest on the CH_4 oxidation capacity in soils. *Applied Soil Ecology*, **79**, 49–58, https://doi.org/10.1016/j.apsoil.2014.03.004.

Ding, W. X., Z. C. Cai, and H. Tsuruta, 2004: Methane concentration and emission as affected by methane transport capacity of plants in freshwater marsh. *Water, Air, and Soil Pollution*, **158**, 99–111, https://doi.org/10.1023/B:WATE.0000044836.71634.3d.

Do Carmo, J. B., E. R. De Sousa Neto, P. J. Duarte-Neto, J. P. H. B. Ometto, and L. A. Martinelli, 2012: Conversion of the coastal Atlantic forest to pasture: Consequences for the nitrogen cycle and soil greenhouse gas emissions. *Agriculture, Ecosystems & Environment*, **148**, 37–43, https://doi.org/10.1016/j.agee.2011.11.010.

Dou, X. L., W. Zhou, Q. F. Zhang, and X. L. Cheng, 2015: Greenhouse gas (CO_2, CH_4, N_2O) emissions from soils following afforestation in central China. *Atmos. Environ.*, **126**, 98–106, https://doi.org/10.1016/j.atmosenv.2015.11.054.

Dutta, M. K., R. Ray, R. Mukherjee, T. K. Jana, and S. K. Mukhopadhyay, 2015: Atmospheric fluxes and photo-oxidation of methane in the mangrove environment of the Sundarbans, NE coast of India; A case study from Lothian Island. *Agricultural and Forest Meteorology*, **213**, 33–41, https://doi.org/10.1016/j.agrformet.2015.06.010.

Fang, Y. T., P. Gundersen, W. Zhang, G. Y. Zhou, J. R. Christiansen, J. M. Mo, S. F. Dong, and T. Zhang, 2009: Soil–atmosphere exchange of N_2O, CO_2 and CH_4 along a slope of an evergreen broad-leaved forest in southern China. *Plant and Soil*, **319**, 37–48, https://doi.org/10.1007/s11104-008-9847-2.

FAO, 2010: *Global Forest Resources Assessment 2010.* FAO, 54 pp.

Fernández-Duque, B., I. A. Pérez, M. Á. García, N. Pardo, and M. L. Sánchez, 2020: Local regressions for decomposing CO_2 and CH_4 time-series in a semi-arid ecosystem. *Atmospheric Pollution Research*, **11**, 213–223, https://doi.org/10.1016/j.apr.2019.10.012.

Frenzel, P., and E. Karofeld, 2000: CH_4 emission from a hollow-ridge complex in a raised bog: The role of CH_4 production and oxidation. *Biogeochemistry*, **51**, 91–112, https://doi.org/10.1023/A:1006351118347.

Gatica, G., M. E. Fernández, M. P. Juliarena, and J. Gyenge, 2020: Environmental and anthropogenic drivers of soil methane fluxes in forests: Global patterns and among‐biomes differences. *Global Change Biology*, **26**, 6604–6615, https://doi.org/10.1111/gcb.15331.

Glatzel, S., N. Basiliko, and T. Moore, 2004: Carbon dioxide and methane production potentials of peats from natural, harvested and restored sites, Eastern Québec, Canada. *Wetlands*, **24**, 261–267,https://doi.org/10.1672/0277-5212(2004)024[0261:CDAMPP]2.0.CO;2.

Gong, Z. T., and Coauthors, 2007: Chinese soil taxonomy. *Bulletin of the Chinese Academy of Sciences*, **21**, 36–38.

Harazono, Y., and Coauthors, 2006: Temporal and spatial differences of methane flux at arctic tundra in Alaska. *Memoirs of National Institute of Polar Research*, **59**, 79–95.

Harriss, R. C., and S. E. Frolking, 1992: The sensitivity of methane emissions from Northern Freshwater wetlands to global warming. *Global Climate Change and Freshwater Ecosystems*, P. Firth and S. G. Fisher, Eds., Springer, 48–67, https://doi.org/10.1007/978-1-4612-2814-1_3.

Heilman, M. A., and R. G. Carlton, 2001: Methane oxidation associated with submersed vascular macrophytes and its impact on plant diffusive methane flux. *Biogeochemistry*, **52**, 207–224, https://doi.org/10.1023/A:1006427712846.

Hong, S., and V. Lakshmi, 2005: Relation between satellite-derived vegetation indices, surface temperature, and vegetation water content. *Proc. 2005 IEEE International Geoscience and Remote Sensing Symposium*, Seoul, IEEE, 1118–1122, https://doi.org/10.1109/IGARSS.2005.1525312.

Inubushi, K., H. Sugii, S. Nishino, and E. Nishino, 2001: Effect of aquatic weeds on methane emission from submerged paddy soil. *American Journal of Botany*, **88**, 975–979, https://doi.org/10.2307/2657078.

IPCC, 2007: *Contribution of Working Group I to the Fourth Assessment Report of the Intergovernmental Panel on Climate Change*. Cambridge University Press.

IPCC, 2013: *Climate Change 2013: The Physical Science Basis. Contribution of Working Group I to the Fifth Assessment Report of the Intergovernmental Panel on Climate Change*. Cambridge University Press.

Jespersen, D. N., B. K. Sorrell, and H. Brix, 1998: Growth and root oxygen release by *Typha latifolia* and its effects on sediment methanogenesis. *Aquatic Botany*, **61**, 165–180, https://doi.org/10.1016/S0304-3770(98)00071-0.

Ji, B., Z. J. Wang, Z. B. Pan, H. Xu, X.-S. Han, and Y. Z. Xie, 2020: Soil carbon storage characteristics of Alfalfa (*Medicago sativa*) Artificial grasslands in the semi-arid hilly gully region of the Loess Plateau, China. *Russian Journal of Ecology*, **51**, 466–476, https://doi.org/10.1134/S1067413620050045.

Joabsson, A., and T. R. Christensen, 2001: Methane emissions from wetlands and their relationship with vascular plants: An Arctic example. *Global Change Biology*, **7**, 919–932, https://doi.org/10.1046/j.1354-1013.2001.00044.x.

Joabsson, A., T. R. Christensen, and B. Wallén, 1999: Vascular plant controls on methane emissions from northern peatforming wetlands. *Trends in Ecology & Evolution*, **14**, 385–388, https://doi.org/10.1016/S0169-5347(99)01649-3.

Jones, W. J., D. P. Nagle Jr., and W. B. Whitman, 1987: Methanogens and the diversity of archaebacteria. *Microbiological Reviews*, **51**, 135–177, https://doi.org/10.1128/mr.51.1.135-177.1987.

Ju, H., G. Z. Shen, M. Z. Ma, J. L. Ge, W. T. Xu, C. M. Zhao, and Q. L. Zhang, 2016: Greenhouse gas fluxes of typical northern subtropical forest soils: Impacts of land use change and reduced precipitation. *Chinese Journal of Plant Ecology*, **40**, 1049–1063, https://doi.org/10.17521/cjpe.2016.0069. (in Chinese with English abstract)

Kim, S., S. Lee, M. McCormick, J. G. Kim, and H. Kang, 2016: Microbial community and greenhouse gas fluxes from abandoned rice paddies with different vegetation. *Microbial Ecology*, **72**, 692–703, https://doi.org/10.1007/s00248-016-0801-1.

Kim, Y. S., 2013: Soil-atmosphere exchange of CO_2, CH_4 and N_2O in Northern temperate forests: Effects of elevated CO_2 concentration, N deposition and forest fire. *European Journal of Forest Research*, **16**, 1–43.

Lai, D. Y. F., 2009: Methane dynamics in northern Peatlands: A review. *Pedosphere*, **19**, 409–421, https://doi.org/10.1016/S1002-0160(09)00003-4.

Lai, D. Y. F., N. T. Roulet, and T. R. Moore, 2014a: The spatial and temporal relationships between CO_2 and CH_4 exchange in a temperate ombrotrophic bog. *Atmos. Environ.*, **89**, 249–259, https://doi.org/10.1016/j.atmosenv.2014.02.034.

Lai, D. Y. F., T. R. Moore, and N. T. Roulet, 2014b: Spatial and temporal variations of methane flux measured by autochambers in a temperate ombrotrophic peatland. *J. Geophys. Res.*, **119**, 864–880, https://doi.org/10.1002/2013JG002410.

Li, W., J. L. Wang, X. J. Zhang, S. L. Shi, and W. X. Cao, 2018: Effect of degradation and rebuilding of artificial grasslands on soil respiration and carbon and nitrogen pools on an alpine meadow of the Qinghai-Tibetan Plateau. *Ecological Engineering*, **111**, 134–142, https://doi.org/10.1016/j.ecoleng.2017.10.013.

Lin, X. W., and Coauthors, 2009: Fluxes of CO_2, CH_4, and N_2O in an alpine meadow affected by yak excreta on the Qinghai-Tibetan plateau during summer grazing periods. *Soil Biology and Biochemistry*, **41**, 718–725, https://doi.org/10.1016/j.soilbio.2009.01.007.

Liu, Y. K., J.-Z. Pang, F. Yi, C.-H. Peng, S. X. Zhang, L. Hou, X. K. Wang, and H.-X. Zhang, 2019: Soil-atmosphere exchange of nitrous oxide, methane and carbon dioxide of different forest types at different elevations in Huoditang forest region of Qinling Mountains. *Journal of Northwest Forestry University*, **34**, 1–10, https://doi.org/10.3969/j.issn.1001-7461.2019.01.01.

Lombardi, J. E., M. A. Epp, and J. P. Chanton, 1997: Investigation of the methyl fluoride technique for determining rhizospheric methane oxidation. *Biogeochemistry*, **36**, 153–172, https://doi.org/10.1023/A:1005750201264.

Luan, J. W., H. T. Song, C. H. Xiang, D. Zhu, and D. Suolang, 2016: Soil moisture, species composition interact to regulate CO_2 and CH_4 fluxes in dry meadows on the Tibetan Plateau. *Ecological Engineering*, **91**, 101–112, https://doi.org/10.1016/j.ecoleng.2016.02.012.

Ma, W. W., A.-R. M. Alhassan, Y. S. Wang, G. Li, H. Wang, and J. M. Zhao, 2018: Greenhouse gas emissions as influenced by wetland vegetation degradation along a moisture gradient on the eastern Qinghai-Tibet Plateau of North-West China. *Nutrient Cycling in Agroecosystems*, **112**, 335–354, https://doi.org/10.1007/s10705-018-9950-6.

Ma, W. W., G. Li, J. H. Wu, G. R. Xu, and J. Q. Wu, 2020: Respiration and CH_4 fluxes in Tibetan peatlands are influenced by vegetation degradation. *CATENA*, **195**, 104789, https://doi.org/10.1016/j.catena.2020.104789.

Mills, R. T. E., N. Dewhirst, A. Sowerby, B. A. Emmett, and D. L. Jones, 2013: Interactive effects of depth and temperature on CH_4 and N_2O flux in a shallow podzol. *Soil Biology and Biochemistry*, **62**, 1–4, https://doi.org/10.1016/j.soilbio.2013.

03.003.

Moore, T. R., and M. Dalva, 1993: The influence of temperature and water table position on carbon dioxide and methane emissions from laboratory columns of peatland soils. *Journal of Soil Science*, **44**, 651–664, https://doi.org/10.1111/j.1365-2389.1993.tb02330.x.

Nesbit, S. P., and G. A. Breitenbeck, 1992: A laboratory study of factors influencing methane uptake by soils. *Agriculture, Ecosystems & Environment*, **41**, 39–54, https://doi.org/10.1016/0167-8809(92)90178-E.

Neubauer, S. C., and J. P. Megonigal, 2015: Moving beyond global warming potentials to quantify the climatic role of ecosystems. *Ecosystems*, **18**, 1000–1013, https://doi.org/10.1007/s10021-015-9879-4.

Oertel, C., J. Matschullat, K. Zurba, F. Zimmermann, and S. Erasmi, 2016: Greenhouse gas emissions from soils—A review. *Geochemistry*, **76**, 327–352, https://doi.org/10.1016/j.chemer.2016.04.002.

Olefeldt, D., M. R. Turetsky, P. M. Crill, and A. D. McGuire, 2013: Environmental and physical controls on northern terrestrial methane emissions across permafrost zones. *Global Change Biology*, **19**, 589–603, https://doi.org/10.1111/gcb.12071.

Pihlatie, M., A. J. Kieloaho, E. Halmeenmäki, K. Ryhti, and J. Heinonsalo, 2017: Ground vegetation reduces forest floor net CH_4 uptake in a boreal upland forest. Preprints, *Egu General Assembly Conf*, 4945, https://ui.adsabs.harvard.edu/abs/2017EGUGA..19.4945P.

Plain, C., F.-K. Ndiaye, P. Bonnaud, J. Ranger, and D. Epron, 2019: Impact of vegetation on the methane budget of a temperate forest. *The New Phytologist*, **221**, 1447–1546, https://doi.org/10.1111/nph.15452.

Robertson, G. P., 1989: Nitrification and denitrification in humid tropical ecosystems: potential controls on nitrogen retention. *Mineral nutrients in tropical forest and savanna ecosystems*, **9**, 55–69.

Rusch, H., and H. Rennenberg, 1998: Black alder (*Alnus glutinosa* (L.) Gaertn.) trees mediate methane and nitrous oxide emission from the soil to the atmosphere. *Plant and Soil*, **201**, 1–7, https://doi.org/10.1023/A:1004331521059.

Schimel, J. P., 1995: Plant transport and methane production as controls on methane flux from arctic wet meadow tundra. *Biogeochemistry*, **28**, 183–200, https://doi.org/10.1007/BF02186458.

Sebacher, D. I., R. C. Harriss, and K. B. Bartlett, 1985: Methane emissions to the atmosphere through aquatic plants. *Journal of Environmental Quality*, **14**, 40–46, https://doi.org/10.2134/jeq1985.00472425001400010008x.

Shannon, R. D., J. R. White, J. E. Lawson, and B. S. Gilmour, 1996: Methane efflux from emergent vegetation in peatlands. *Journal of Ecology*, **84**, 239–246, https://doi.org/10.2307/2261359.

Shi, R. A., L. J. Li, M. Y. You, J. Ding, S. Wang, and X. Z. Han, 2013: Impact of soil temperature and moisture on Soil N_2O emission from mollisols under different land-use types. *Journal of Agro-Environment Science*, **32**, 2286–2292, https://doi.org/10.11654/jaes.2013.11.026. (in Chinese with English abstract)

Simpson, I. J., G. C. Edwards, G. W. Thurtell, G. Den Hartog, H. H. Neumann, and R. M. Staebler, 1997: Micrometeorological measurements of methane and nitrous oxide exchange above a boreal aspen forest. *J. Geophys. Res.*, **102**, 29 331–29 341, https://doi.org/10.1029/97JD03181.

Singh, B. K., R. D. Bardgett, P. Smith, and D. S. Reay, 2010: Microorganisms and climate change: Terrestrial feedbacks and mitigation options. *Nature Reviews Microbiology*, **8**, 779–790, https://doi.org/10.1038/nrmicro2439.

Solomon, S., D. Qin, M. Manning, M. Marquis, K. Averyt, M. M. B. Tignor, and J. H. L. Miller, 2007: *Climate change 2007: The physical science basis. Contribution of Working Group I to the fourth assessment report of the Intergovernmental Panel on Climate Change.* ed. Cambridge University Press, Cambridge (United Kingdom).

Song, C. C., X. F. Xu, H. Q. Tian, and Y. Y. Wang, 2009: Ecosystem-atmosphere exchange of CH_4 and N_2O and ecosystem respiration in wetlands in the Sanjiang Plain, Northeastern China. *Global Change Biology*, **15**, 692–705, https://doi.org/10.1111/j.1365-2486.2008.01821.x.

Ström, L., A. Ekberg, M. Mastepanov, and T. R. Christensen, 2003: The effect of vascular plants on carbon turnover and methane emissions from a tundra wetland. *Global Change Biology*, **9**, 1185–1192, https://doi.org/10.1046/j.1365-2486.2003.00655.x.

Ström, L., M. Mastepanov, and T. R. Christensen, 2005: Species-specific effects of vascular plants on carbon turnover and methane emissions from wetlands. *Biogeochemistry*, **75**, 65–82, https://doi.org/10.1007/s10533-004-6124-1.

Sun, J. X., D. Liu, L. Qin, X. N. Zhang, X. M. He, and G. H. Lv, 2012: Research on Soil CH_4 flux of cotton fields and abandoned lands in Ebinur Lake Area. *Xinjiang Agricultural Sciences*, **49**, 1489–1496, https://doi.org/10.6048/j.issn.1001-4330.2012.08.019. (in Chinese with English abstract)

Tang, K. L., Q. C. Hou, B. K. Wang, and P. C. Zhang, 1993: The environment background and administration way of wind-water erosion crisscross region and Shenmu Experimental Area on the loess Plateau. *Memoir of NISWC, Academia Sinica and Ministry of Water Resources*, **18**, 2–15, http://stbcyj.paperonce.org/oa/darticle.aspx?id=19930202. (in Chinese with English abstract)

Thompson, A. M., K. B. Hogan, and J. S. Hoffman, 1992: Methane reductions: Implications for global warming and atmospheric chemical change. *Atmospheric Environment. Part A. General Topics*, **26**, 2665–2668, https://doi.org/10.1016/0960-1686(92)90118-5.

Von Fischer, J. C., and L. O. Hedin, 2007: Controls on soil methane fluxes: Tests of biophysical mechanisms using stable isotope tracers. *Global Biogeochemical Cycles*, **21**, GB2007, https://doi.org/10.1029/2006GB002687.

Von Fischer, J. C., R. C. Rhew, G. M. Ames, B. K. Fosdick, and P. E. Von Fischer, 2010: Vegetation height and other controls of spatial variability in methane emissions from the Arctic coastal tundra at Barrow, Alaska. *J. Geophys. Res.*, **115**, G00I03, https://doi.org/10.1029/2009JG001283.

Wang, H. X., 2014: Artificial grass grazing CH_4 fluxes characteristics of different semi-arid region of region of inner Mongolia. M.S. thesis, School of Resources and Environment. Inner Mongolia University. (in Chinese with English abstract)

Wang, H. Y., J. Q. Wu, G. Li, and L. J. Yan, 2020: Changes in soil carbon fractions and enzyme activities under different vegetation types of the northern Loess Plateau. *Ecology and Evolution*, **10**, 12 211–12 223, https://doi.org/10.1002/ece3.6852.

Wang, X. H., and J. Bennett, 2008: Policy analysis of the conver-

sion of cropland to forest and grassland program in China. *Environmental Economics and Policy Studies*, **9**, 119–143, https://doi.org/10.1007/BF03353986.

Wang, Y. F., and Coauthors, 2014: Soil methane uptake by grasslands and forests in China. *Soil Biology and Biochemistry*, **74**, 70–81, https://doi.org/10.1016/j.soilbio.2014.02.023.

Wang, Y. S., and Y. H. Wang, 2003: Quick measurement of CH_4, CO_2 and N_2O emissions from a short-plant ecosystem. *Adv. Atmos. Sci.*, **20**, 842–844, https://doi.org/10.1007/BF02915410.

Wang, Z. T., L. Yang, G. Li, C. S. Chai, Y. D. Zhang, R. Chen, and J. Q. Zhang, 2019: Effects of alfalfa (*Medicago sativa* L.) degradation on herbage distribution and diversity in the semi-arid Loess Plateau. *Acta Ecologica Sinica*, **39**, 3720–3729, https://doi.org/10.5846/stxb201805181099. (in Chinese with English abstract)

Wei, E. W., R. Yang, H. P. Zhao, P. H. Wang, S. Q. Zhao, W. C. Zhai, Y. Zhang, and H. L. Zhou, 2019: Microwave-assisted extraction releases the antioxidant polysaccharides from seabuckthorn (*Hippophae rhamnoides* L.) berries. *International Journal of Biological Macromolecules*, **123**, 280–290, https://doi.org/10.1016/j.ijbiomac.2018.11.074.

Werner, C., R. Kiese, and K. Butterbach-Bahl, 2007: Soil-atmosphere exchange of N_2O, CH_4, and CO_2 and controlling environmental factors for tropical rain forest sites in western Kenya. *J. Geophys. Res.*, **112**, D03308, https://doi.org/10.1029/2006JD007388.

Werner, C., X. H. Zheng, J. W. Tang, B. H. Xie, C. Y. Liu, R. Kiese, and K. Butterbach-Bahl, 2006: N_2O, CH_4 and CO_2 emissions from seasonal tropical rainforests and a rubber plantation in Southwest China. *Plant and Soil*, **289**, 335–353, https://doi.org/10.1007/s11104-006-9143-y.

Whalen, S. C., 2005: Biogeochemistry of methane exchange between natural wetlands and the atmosphere. *Environmental Engineering Science*, **22**, 73–94, https://doi.org/10.1089/ees.2005.22.73.

Whalen, S. C., and W. S. Reeburgh, 1990: Consumption of atmospheric methane by tundra soils. *Nature*, **346**, 160–162, https://doi.org/10.1038/346160a0.

Wilson, K. S., and E. R. Humphreys, 2010: Carbon dioxide and methane fluxes from Arctic mudboils. *Canadian Journal of Soil Science*, **90**, 441–449, https://doi.org/10.4141/CJSS09073.

WMO, 2020: WMO greenhouse gas bulletin: The state of greenhouse gases in the atmosphere based on global observations through 2019.

Wu, B., and C. C. Mu, 2019: Effects on greenhouse gas (CH_4, CO_2, N_2O) emissions of conversion from over-mature forest to secondary forest and Korean pine plantation in northeast China. *Forests*, **10**, 788, https://doi.org/10.3390/f10090788.

Wu, J. Q., H. Y. Wang, G. Li, W. W. Ma, J. H. Wu, Y. Gong, and G. R. Xu, 2020: Vegetation degradation impacts soil nutrients and enzyme activities in wet meadow on the Qinghai-Tibet Plateau. *Scientific Reports*, **10**, 21271, https://doi.org/10.1038/s41598-020-78182-9.

Wu, J. Q., W. W. Ma, G. Li, and G. P. Chen, 2018: Effects of four vegetation types on soil physical characteristics and permeability in Loess Plateau. *Journal of Soil and Water Conservation*, **32**, 133–138, https://doi.org/10.13870/j.cnki.stbcxb.2018.04.021. (in Chinese with English abstract)

Wu, X., Z. Yao, N. Brüggemann, Z. Y. Shen, B. Wolf, M. Dannenmann, X. Zheng, and K. Butterbach-Bahl, 2010: Effects of soil moisture and temperature on CO_2 and CH_4 soil–atmosphere exchange of various land use/cover types in a semi-arid grassland in Inner Mongolia, China. *Soil Biology and Biochemistry*, **42**, 773–787, https://doi.org/10.1016/j.soilbio.2010.01.013.

Xia, J. J., Z. W. Yan, G. S. Jia, H. Q. Zeng, P. D. Jones, W. Zhou, and A. Z. Zhang, 2015: Projections of the advance in the start of the growing season during the 21st century based on CMIP5 simulations. *Adv. Atmos. Sci.*, **32**, 831–838, https://doi.org/10.1007/s00376-014-4125-0.

Xia, N., E. Z. Du, X. H. Wu, Y. Tang, Y. Wang, and W. De Vries, 2020: Effects of nitrogen addition on soil methane uptake in global forest biomes. *Environmental Pollution*, **264**, 114751, https://doi.org/10.1016/j.envpol.2020.114751.

Yan, L. J., G. Li, J. Q. Wu, W. W. Ma, and H. Y. Wang, 2019: Effects of four typical vegetations on soil active organic carbon and soil carbon in Loess Plateau. *Acta Ecologica Sinica*, **39**, 5546–5554, https://doi.org/10.5846/stxb201805091031. (in Chinese with English abstract)

Yang, G., and Coauthors, 2014: Effects of soil warming, rainfall reduction and water table level on CH_4 emissions from the Zoige peatland in China. *Soil Biology and Biochemistry*, **78**, 83–89, https://doi.org/10.1016/j.soilbio.2014.07.013.

Yang, G., and Coauthors, 2019: Peatland degradation reduces methanogens and methane emissions from surface to deep soils. *Ecological Indicators*, **106**, 105488, https://doi.org/10.1016/j.ecolind.2019.105488.

Yang, J. J., S. S. An, H. Zhang, Y. N. Chen, T. H. Dang, and J. Y. Jiao, 2015: Effect of erosion on soil microbial biomass and enzyme activity in the loess hills. *Acta Ecologica Sinica*, **35**, 5666–5674, https://doi.org/10.5846/stxb201310302611. (in Chinese with English abstract)

Zhang, J., M. Y. Liu, M. M. Zhang, J. H. Yang, and R. S. Cao, 2019: Characteristics of soil greenhouse gas fluxes under different forest types in the Loess Plateau tableland, China. *Journal of Agro-Environment Science*, **38**, 944–956, https://doi.org/10.11654/jaes.2018-0826. (in Chinese with English abstract)

Zhao, G. Q., M. Y. Liu, J. H. Yang, H. Liu, J. Zhang, M. M. Zhang, and X. R. Li, 2018: Spatial variations and environmental interpretations of soil greenhouse gases fluxes under different land-use types in the tableland of the Loess Plateau. *Chinese Journal of Soil Science*, **49**, 461–468, https://doi.org/10.19336/j.cnki.trtb.2018.02.29. (in Chinese with English abstract)

Zhou, Q. Y., and Q. Cai, 2021: Role of ethylene in the regulatory mechanism underlying the abortion of ovules after fertilization in *Xanthoceras sorbifolium*. *Plant Molecular Biology*, **106**, 67–84, https://doi.org/10.1007/s11103-021-01130-2.

Zhu, X. X., and Coauthors, 2015b: Effects of warming, grazing/cutting and nitrogen fertilization on greenhouse gas fluxes during growing seasons in an alpine meadow on the Tibetan Plateau. *Agricultural and Forest Meteorology*, **214–215**, 506–514, https://doi.org/10.1016/j.agrformet.2015.09.008.

Zhu, X. Y., C. C. Song, C. M. Swarzenski, Y. D. Guo, X. H. Zhang, and J. Y. Wang, 2015a: Ecosystem-atmosphere exchange of CO_2 in a temperate herbaceous Peatland in the Sanjiang Plain of northeast China. *Ecological Engineering*, **75**, 16–23, https://doi.org/10.1016/j.ecoleng.2014.11.035.

ADVANCES IN ATMOSPHERIC SCIENCES, VOL. 39, AUGUST 2022, 1375–1385

• Original Paper •

The Synergism between Methanogens and Methanotrophs and the Nature of their Contributions to the Seasonal Variation of Methane Fluxes in a Wetland: The Case of Dajiuhu Subalpine Peatland※

Luwen WANG[1,2,3], Jiwen GE[*1,2,3], Liang FENG[2,3], Yaoyao LIU[1,2,3], Yu LI[1,2,3], Jiumei WANG[1,2,3], Xiang XIAO[1,2,3], and Zhiqi ZHANG[4]

[1]*Laboratory of Basin Hydrology and Wetland Eco-Restoration*, *China University of Geosciences*, *Wuhan* 430074, *China*

[2]*Hubei Key Laboratory of Wetland Evolution and Ecological Restoration*, *China University of Geosciences*, *Wuhan* 430074, *China*

[3]*Institution of Ecology and Environmental Sciences*, *China University of Geosciences*, *Wuhan* 430074, *China*

[4]*Shennongjia National Park Administration Bureau*, *Shennongjia Forestry District* 442417, *China*

(Received 3 July 2021; revised 24 September 2021; accepted 19 October 2021)

ABSTRACT

Wetland ecosystems are the most important natural methane (CH_4) sources, whose fluxes periodically fluctuate. Methanogens (methane producers) and methanotrophs (methane consumers) are considered key factors affecting CH_4 fluxes in wetlands. However, the symbiotic relationship between methanogens and methanotrophs remains unclear. To help close this research gap, we collected and analyzed samples from four soil depths in the Dajiuhu subalpine peatland in January, April, July, and October 2019 and acquired seasonal methane flux data from an eddy covariance (EC) system, and investigated relationships. A phylogenetic molecular ecological networks (pMENs) analysis was used to identify keystone species and the seasonal variations of the co-occurrence patterns of methanogenic and methanotrophic communities. The results indicate that the seasonal variations of the interactions between methanogenic and methanotrophic communities contributed to CH_4 emissions in wetlands. The keystone species discerned by the network analysis also showed their importance in mediating CH_4 fluxes. Methane (CH_4) emissions in wetlands were lowest in spring; during this period, the most complex interactions between microbes were observed, with intense competition among methanogens while methanotrophs demonstrated better cooperation. Reverse patterns manifested themselves in summer when the highest CH_4 flux was observed. *Methanoregula formicica* was negatively correlated with CH_4 fluxes and occupied the largest ecological niches in the spring network. In contrast, both *Methanocella arvoryzae* and Methylocystaceae demonstrated positive correlations with CH_4 fluxes and were better adapted to the microbial community in the summer. In addition, soil temperature and nitrogen were regarded as significant environmental factors to CH_4 fluxes. This study was successful in explaining the seasonal patterns and microbial driving mechanisms of CH_4 emissions in wetlands.

Key words: CH_4 fluxes, wetland, methanogens, methanotrophs, molecular ecological network

Citation: Wang, L. W., J. W. Ge, L. Feng, Y. Y. Liu, Y. Li, J. M. Wang, X. Xiao, and Z. Q. Zhang, 2022: The synergism between methanogens and methanotrophs and the nature of their contributions to the seasonal variation of methane fluxes in a wetland: The case of Dajiuhu subalpine peatland. *Adv. Atmos. Sci.*, **39**(8), 1375−1385, https://doi.org/10.1007/s00376-021-1255-z.

Article Highlights:

- The EC method was used to observe the dynamics of CH_4 fluxes, which were highest in summer and lowest in spring.
- The seasonal variations of interactions between methanogens and methanotrophs contributed to CH_4 emissions in wetlands.
- The keystone species discerned by network analysis showed their importance in mediating CH_4 fluxes.
- Soil temperature and nitrogen were regarded as important environmental factors to CH_4 fluxes.

※ This paper is a contribution to the special issue on Carbon Neutrality: Important Roles of Renewable Energies, Carbon Sinks, NETs, and non-CO_2 GHGs.

* Corresponding author: Jiwen GE
Email: gejiwen@cug.edu.cn

1. Introduction

Methane (CH_4) is a potent greenhouse gas in the atmosphere with a warming potential 26 times higher than that of carbon dioxide (CO_2) (IPCC, 2013). Since the pre-industrial period, global atmospheric CH_4 levels have increased threefold, reaching 1877 ±2 ppb in 2019 (WMO/GAW, 2020). Wetlands are considered the largest natural source of CH_4, which contribute about 20% to the global CH_4 emissions to the atmosphere (Saunois et al., 2020). Thus, exploring the CH_4 emission dynamics in wetlands could increase the understanding of global CH_4 emissions.

The dramatic seasonal changes of CH_4 fluxes in wetlands were observed in early studies. Overall, they were highest in summer and lowest in winter (Long et al., 2010; Hao et al., 2020). The production of CH_4 in wetlands is mainly due to the synergistic effect of methanogens and the other microbes within the anaerobic food chain, which gradually decompose soil organic carbon and generate CH_4 under anaerobic conditions (Wagner, 2017). At the same time, CH_4 is utilized by methanotrophs as an energy source (He et al., 2015). The influences of the methane metabolic microbial community succession on CH_4 fluxes have been discussed in previous research. The diversity (Yavitt et al., 2012), community structures (Liebner et al., 2015), and relative abundances (Peltoniemi et al., 2016) of methanogenic and methanotrophic communities have been proven to be closely related to the production and emissions of CH_4; nevertheless, some research suggests a more complicated relationship between CH_4 production and methanogenic and methanotrophic communities. Ramakrishnan et al. (2001) discovered that the compositions of methanogens were relatively similar despite a greater than 10-fold difference in CH_4 production rates across 11 rice field soils. Juottonen et al. (2008) observed large variations in CH_4 production but relatively little change in methanogenic composition and abundance across seasons in a boreal mire. Thus, the synergism between methanogens and methanotrophs should be considered, which could shed light upon the comprehensive interpretations of seasonal variations of CH_4 fluxes in wetlands.

The interactions among the methane metabolic microbial communities may have a greater impact on ecosystem functions than simply the community structure and abundance. The analysis of phylogenetic molecular ecological networks (pMENs) has been widely used in recent years because it can reveal the complex ecological interactions among microbes (Barberán et al., 2012) as well as the visual responses of microbes to environmental variations (Huang et al., 2019). Keystone species and other important microbes can be identified based on network topological parameters (Steele et al., 2011; Zhou et al., 2011). By employing a molecular ecological network analysis, Zhang et al. (2018) found a tight co-occurrence of methanogens in one module with some other species, indicating the potential for a tight co-occurrence with these kinds of microbes. Furthermore, Li et al. (2021) proposed that the methanogenic groups involved in commonly co-occurring links among networks contributed most to CH_4 emissions. However, both methanogens and methanotrophs are the dominant microbes that affect the CH_4 emissions in wetlands; therefore, the functions of methanotrophs should be considered. Hence, studies on the interactions between methanogens and methanotrophs can help us further comprehend the periodical variations of CH_4 fluxes in wetlands.

In this study, the eddy covariance (EC) system was used to observe the dynamics of CH_4 fluxes in the Dajiuhu subalpine peatland, the high-throughput sequencing technology and pMENs analysis methods were employed to explain the interactions of methanogenic and methanotrophic communities. The objectives of this study were to detect temporal patterns in CH_4 emissions and analyze the interactions between methanogenic and methanotrophic communities at seasonal scales.

The remainder of this paper is organized as follows. Section 2 discusses the data and methods, section 3 presents the results, section 4 discusses the results, and section 5 concludes.

2. Materials and methods

2.1. *Site description*

The study area (Fig. 1a), established in July 2015, was located in the Dajiuhu subalpine peatland of Shennongjia National Park, Shennongjia Forestry Administrative District, Hubei Province, China (31°28′44.45″ N, 110°00′14.61″ E, 1758 m). The Dajiuhu subalpine peatland is the best-preserved subalpine peatland in southern China, located in the north subtropical monsoon climate zone of the mid-latitudes. The annual average temperature in the study area is 7.4°C, and the annual average precipitation is 1560 mm. The total area of the wetland is 13.846 km^2, with soil types mainly consisting of bog soil, meadow marsh soil, and meadow soil. The dominant plant species is *Sphagnum palustre*, and the companion species include *Polytrichum commune*, *Juncus effusus*, *Carex argyi*, *Festuca rubra*, *Euphorbia esula*, *Sanguisorba officinalis,* and *Drosera rotundifolia,* etc.

2.2. *CH_4 fluxes measurement and data quality control*

Methane (CH_4) fluxes were measured from December 2018 to November 2019 using the open-path eddy covariance method at the height of 3 m. The EC system consists of a three-axis sonic anemometer (CSAT-3, Li-Cor, USA), an open-path CO_2/H_2O infrared gas analyzer (LI-7500, Li-Cor, USA), an open-path CH_4 analyzer (LI-7700, Li-Cor, USA), and a micrometeorological measurement system (Biomet100, LI-Cor, USA) (Fig. 1b). It can continuously measure CH_4 fluxes. The CR1000 data collector of the EC system automatically records data once every 30 minutes. The raw data was processed using the EddyPro 7.0.6 software (LI-COR). Low-quality data were removed, including those obtained under rainy and nonstationary conditions. CH_4 fluxes were also eliminated when the friction velocity was

lower than 0.15 m s^{-1} during nighttime. After quality control, the data availability was 42.70%. Data gaps in the half-hourly CH_4 fluxes were filled using the Mean Diurnal Variations and Gliding-window Method.

2.3. *Soil sample collection*

The footprint of the EC tower was shown in Fig. 1c, and the sample point was located in the main contribution area of the eddy covariance system. The samples collected in January, April, July, and October 2019, represented the seasons of winter, spring, summer, and autumn, respectively. To eliminate errors caused by soil depth, soil samples were collected at depths of 0, 10, 30, and 50 cm using a soil sampling rig. After removing roots, rocks, and other debris, a total of 48 soil samples were stored in a mobile refrigerator at 4°C in 50 ml centrifuge tubes and sterile bags. After transport back to the laboratory, the centrifuge tubes were stored at –80°C for high-throughput sequencing. The sterile bags were stored at –20°C for the determination of physical and chemical properties.

2.4. *Soil physicochemical analysis*

The soil's pH and Oxidation-Reduction Potential (Eh) were measured in situ using a portable pH meter (IQ Scientific Instruments, USA). Total organic carbon (TOC) and total nitrogen (TN) were calculated with an elemental analyzer (varioELcube, Germany). The presence of ammonium (NH_4^+-N), nitrate (NO_3^--N), and nitrite (NO_2^--N) were determined with an automated discrete analyzer (SmartChem200, AMS-Alliance).

2.5. *DNA extraction, PCR amplification, and high-throughput sequencing*

Deoxyribonucleic acid (DNA) was extracted from soil using the OMEGA Soil DNA Kit (OMEGA Bio-Tek, GA, United States). The quality of the DNA extracts was assessed via gel electrophoresis. The primer pairs used for PCR amplification of *mcrA* and *pomA* genes were MLr (5'-TTCATTGCRTAGTTWGGRTAGTT-3'), MLf (5'-GGTG-GTGTMGGATTCACACART AYGCWACAGC-3'), and A189 (GGNGACTGGGACTTCTGG), A650 (ACGTCCTT ACCGAAGGT), respectively. The PCR products were purified with a PCR purification kit (AXYGEN, AZ, United States) and quantified via a Microplate reader (BioTek, FLx800). The Illumina TruSeq Nano DNA LT Library Prep Kit was used to prepare libraries and sequenced on the Illumina MiSeq platform (Illumina, CA, United States). All steps were finished at Parsenor Biotechnology Co., Ltd, Shanghai.

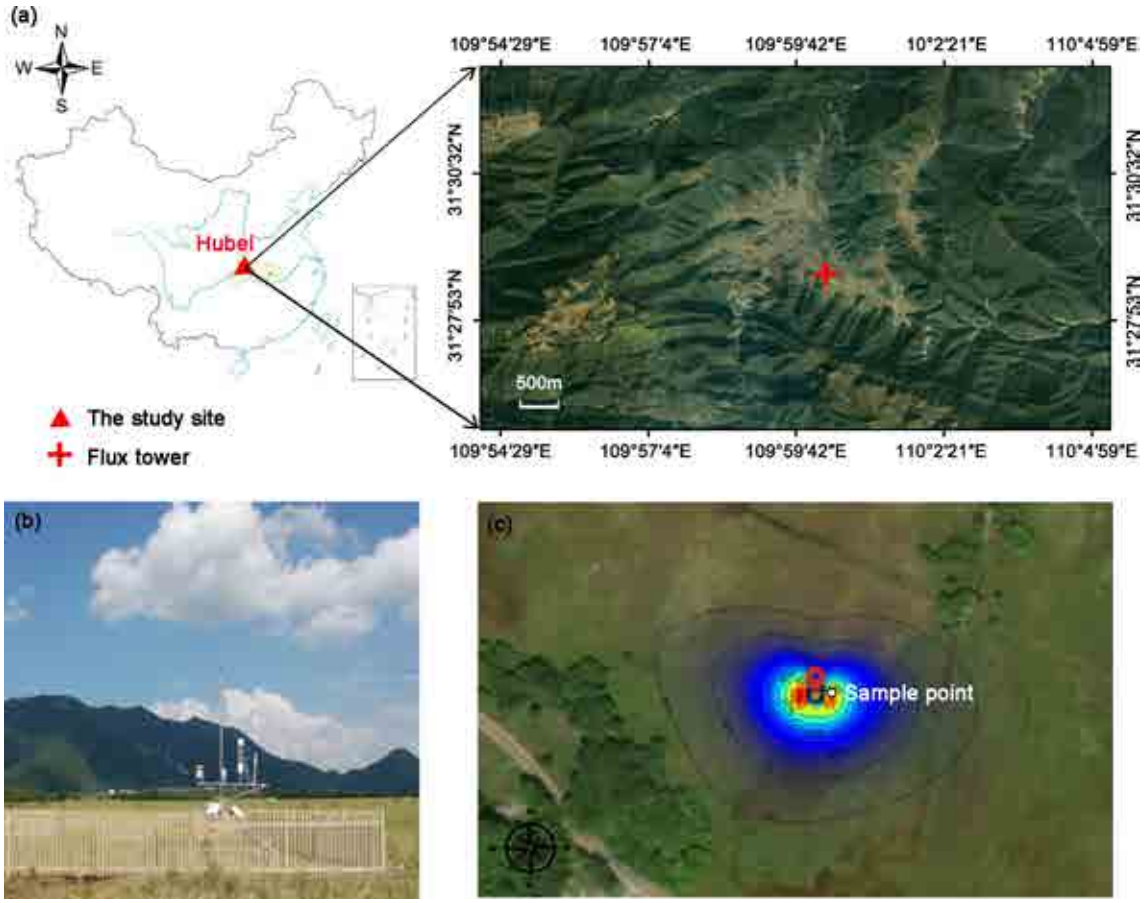

Fig. 1. Location map of the Dajiuhu subalpine peatland with the study site indicated (a), the image of the Eddy Covariance system (b), and the footprint of the Eddy Covariance tower with the sample point indicated (c).

2.6. *Molecular ecology networks construction and analysis*

Phylogenetic molecular ecological networks (pMENs) were constructed by sequencing of *mcrA* and *pomA* genes amplicons. The pMENs analysis was performed via a Random Matrix Theory (RMT)-based approach in a molecular ecological network analysis pipeline (MENA, http://ieg4.rccc.ou.edu/MENA/). Network visualization was completed using Gephi 0.9.2 (Zhao et al., 2021). Various network topological properties were characterized by similarity matrices. These included the average clustering coefficient, average degree, average path length, and modularity. Individual operational taxonomic units (OTUs) in the networks can be separated into four types of topological nodes in accordance with the values of the among-module connectivity (P_i) and within-module connectivity (Z_i) (Wang et al., 2018). The peripherals ($Z_i \leqslant 2.5$, $P_i \leqslant 0.62$), network hubs ($Z_i > 2.5$, $P_i > 0.62$), module hubs ($Z_i > 2.5$, $P_i \leqslant 0.62$), and connectors ($Z_i \leqslant 2.5$, $P_i > 0.62$) were considered as keystone OTUs.

3. Results

3.1. *Dynamics of CH_4 fluxes*

The remarkable seasonal variations of CH_4 fluxes are shown in Fig. 2. The Dajiuhu subalpine peatland was the source of CH_4 (Table 1), with an average CH_4 release rate of 18.50 nmol m^{-2} s^{-1}. The maximum monthly release rate

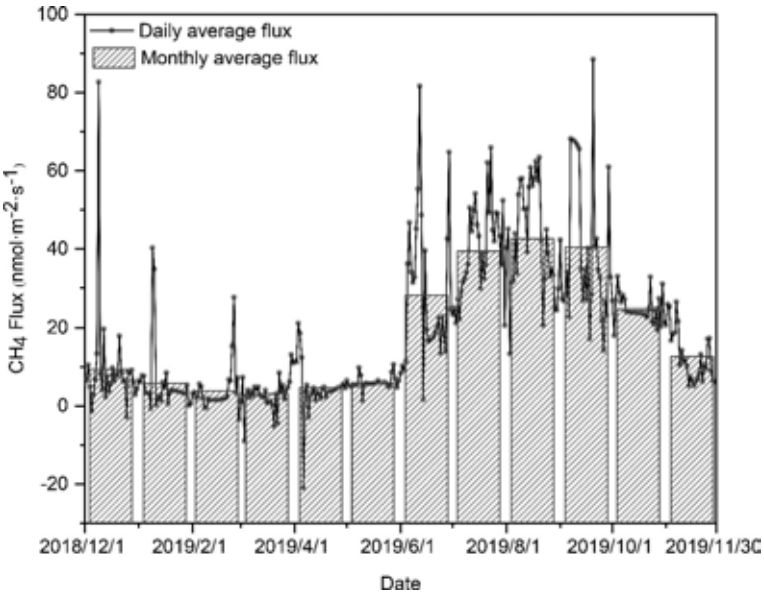

Fig. 2. Daily and monthly variations of CH_4 fluxes (nmol m^{-2} s^{-1}) from December 2018 to November 2019.

Table 1. CH_4 emissions in different time scales of Dajiuhu subalpine peatland.

Quarter	Month	Monthly average CH_4 fluxes (nmol m^{-2} s^{-1})	Quarterly average CH_4 fluxes (nmol m^{-2} s^{-1})	CH_4 quarterly cumulative emissions (mg m^{-2})	Proportion of annual cumulative emissions (%)	
Winter	2018.12	9.45	6.46	803.92	4.34	8.61
	2019.01	5.85			2.69	
	2019.02	3.83			1.59	
Spring	2019.03	3.09	4.62	587.02	1.42	6.29
	2019.04	4.71			2.09	
	2019.05	6.05			2.78	
Summer	2019.06	28.09	36.81	4681.16	12.48	50.16
	2019.07	39.41			18.10	
	2019.08	42.64			19.58	
Autumn	2019.09	40.40	25.92	3261.16	17.95	34.94
	2019.10	24.76			11.37	
	2019.11	12.65			5.62	
Mean value		18.50	18.50	2333.32	–	–
Total		–	–	9333.26	100	100

was 42.64 nmol m^{-2} s^{-1} in August, which was 13.8 times than that of in March (3.09 nmol m^{-2} s^{-1}). The monthly average release rate remained steady from December 2018 to May 2019 and then rose from May to August. The cumulative emissions of CH_4 were highest in summer (4681.16 mg m^{-2}) and lowest in spring (587.02 mg m^{-2}).

3.2. *Molecular ecological networks of methanogenic community*

The topological structure of the methanogenic networks in four seasons was different (Fig. 3a and Table S1 in the Electronic Supplementary Materials, ESM). The maximum number of nodes and edges appeared in spring (nodes: 621, edges: 32159). An obvious reduction occurred in summer (nodes: 512, edges: 8030) when the smallest average path length, average clustering coefficient, and the largest average degree of the spring network were observed. In the summer network, the average path length and the average clustering coefficient were both the largest. The tightest connections in spring could be inferred, while the lowest degree of connectivity occurred in summer. The modularity value of networks was larger in summer, and the smallest values occurred in spring. The proportion of negative edges to the total edges in the winter, spring, summer, and autumn networks were 29.90%, 73.26%, 47.19%, and 50.63%, respectively.

The topological roles of the OTUs in the four seasonal networks also showed seasonal changes (Fig. 3b and Table S2 in the ESM). Although network hubs are considered as super generalists (acting as both module hubs and connectors) (Olesen et al., 2007), no network hub was observed in the networks. There were 12, 3, 8, and 2 module hubs in the winter, spring, summer, and autumn networks, respectively. The nodes of connectors in the spring and summer networks were 17 and 1, respectively. Most of the module hubs and connectors of the winter, spring, and autumn networks belonged to *Methanoregula formicica*, whereas most in the summer networks were *Methanocella arvoryzae*.

3.3. *Molecular ecological networks of methanotrophic community*

The differences in the topological structure were shown in the four seasonal methanogenic networks (Fig. 4 and Table S1 in the ESM). The maximum number of nodes and edges appeared in spring (nodes: 811, edges: 377775), while minimum values emerged in summer (nodes: 589, edges: 2715). The average degree and network density of the summer network were the smallest, while there were larger values in the spring. There was also a decrease in the average path length and the average clustering coefficient in the spring network than in the summer. The highest degree of connectivity occurred in spring, and the lowest occurred in summer, which could be inferred by these topological parameters. The modularity value of networks was largest in summer and smaller in spring. The proportion of negative edges in the four networks was 47.79%, 7.70%, 28.18%, and 69.62%, respectively. We conclude that the competition among methanotrophs was weakest in spring.

The topological nodes varied in the four seasonal networks (Fig. 4b and Table S3 in the ESM). Only one network hub was found in the spring network, which belonged to Methylocystaceae. The nodes of module hubs in the winter, spring, summer, and autumn networks were 19, 9, 12, and 8, respectively, and there were 2, 2, and 8 connectors in the winter, spring, and summer networks, respectively. Most of the

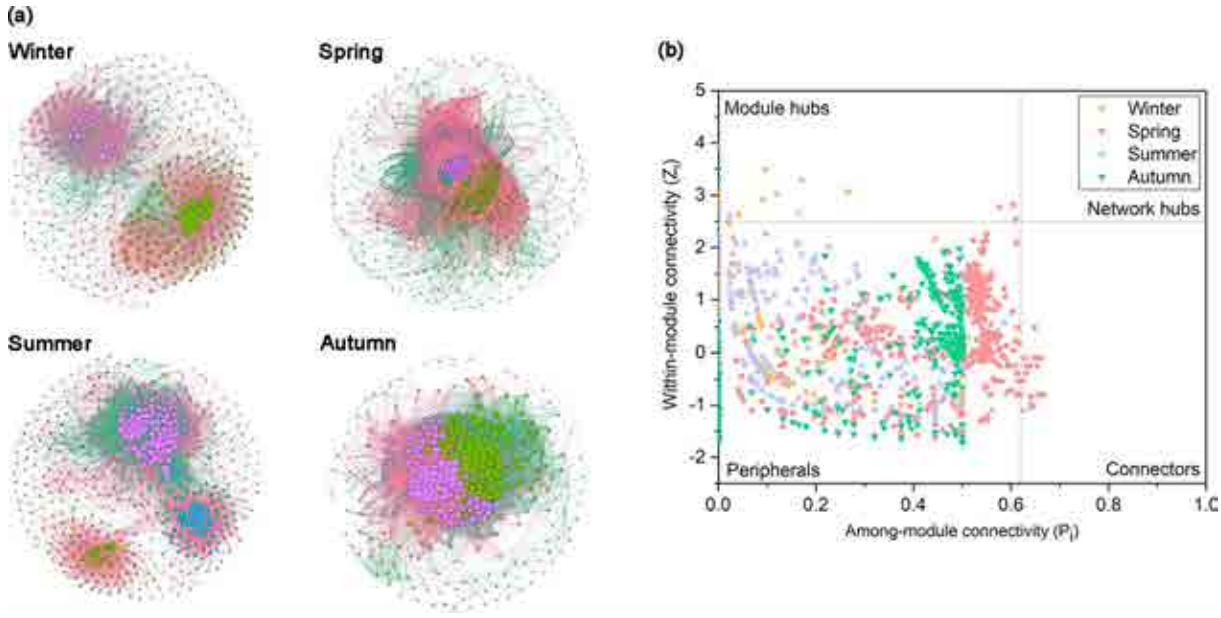

Fig. 3. Ecological molecular networks of the methanogenic community (a). Each node represents an OTU, sorted in color by modularity class, the size of each node is proportional to the number of connections, the red lines represent the positive (cooperative) interactions and the green lines represent the negative (competitive) interactions. The methanogenic Z_i-P_i plot of the topological role of each OTU (b).

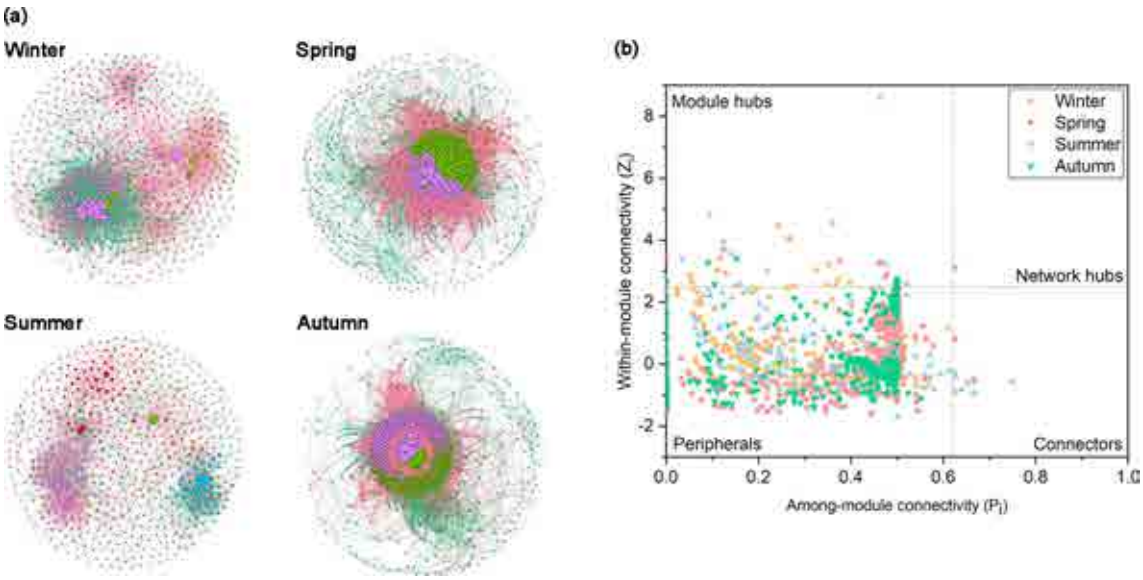

Fig. 4. Ecological molecular networks of the methanotrophic community (a) and the methanotrophic Z_i-P_i plot of the topological roles of OTU (b).

module hubs and connectors belong to Methylocystaceae, *Methylocapsa aurea*, and *Candidatus* Methyloumidiphilus alinensis. The module hubs and connectors in the spring and summer network were mainly attached to Methylocystaceae, while module hubs in the autumn network were affiliated with the *Methylocapsa aurea*.

3.4. *Co-occurrence patterns of methanogens and methanotrophs*

The interactions between the methanogenic and methanotrophic communities caused the seasonal variations (Fig. 5). The number of edges in the four networks was 252, 456, 185, 233 in sequence; the number of negative edges among them was 128, 225, 102, and 122 in sequence. These data imply that strong competition and cooperation existed between methanogens and methanotrophs in spring and summer, respectively. The majority of the methanogen connections were associated with *Methanoregula formicica* (winter: 178, spring: 228, summer: 128, autumn: 135), followed by *Methanocella arvoryzae* (winter: 48, spring: 103, summer: 50, autumn: 90). *Methanocella arvoryzae* played a pivotal role, evidenced by its numerous positive connections with other species; however, *Methanoregula formicica* was more competitive in summer. For the methanotrophs, Methylocystaceae accounted the majority of the connections (winter: 64, spring: 35, summer: 114, autumn: 64) in the networks. *Methylocapsa aurea* (winter: 27, spring: 22, summer: 35, autumn: 65) and *Candidatus* Methyloumidiphilus alinensis (winter: 66, spring: 64, summer: 7, autumn: 12) accounted for a large part otherwise. Numerous negative connections with the other species, *Methylocapsa aurea* and *Candidatus* Methyloumidiphilus alinensis, deemed them as competitors in spring, while Methylocystaceae contributed to maintaining community stability.

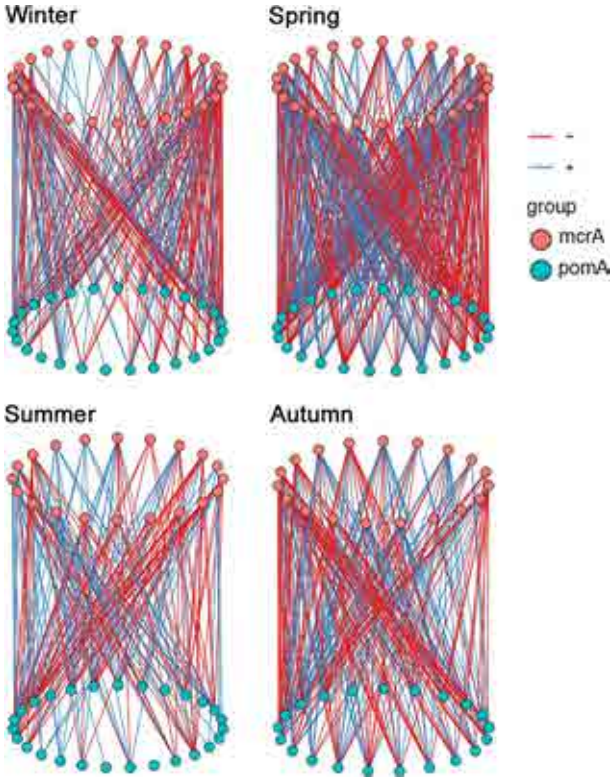

Fig. 5. The interactions between methanogens and methanotrophs. The red and blue nodes represent OTUs of the methanogens and methanotrophs, respectively; the red lines represent the positive (cooperative) interactions, the blue lines represent the negative (competitive) interactions.

3.5. *Correlations among environmental factors, methane metabolic microbial, and CH_4 fluxes*

The correlation analysis was carried out to demonstrate the correlations among environmental factors, methane

metabolic microbials, and CH_4 fluxes (Fig. 6, Table S4, and Table S5 in the ESM). Among the environmental factors measured, total nitrogen (TN) had the most significant influence on methanogens and methanotrophs, whereas the NH_4^+-N and NO_2^--N also exerted obvious effects. The CH_4 fluxes were positively correlated with soil temperature (r = 0.757) (r: Pearson correlation coefficient) but negatively correlated with the water table (r = –0.539), TN (r = –0.231), NH_4^+-N (r = –0.425), NO_2^--N (r = –0.336), and NO_3^--N (r = –0.202). The cumulative CH_4 emissions were positively correlated with the average clustering coefficient of the methanogenic community (r = 0.759), the diameter (r = 0.871) and average path length (r = 0.641) of the methanotrophic community, and the proportions of negative edges between methanogenic and methanotrophic communities (r = 0.961).

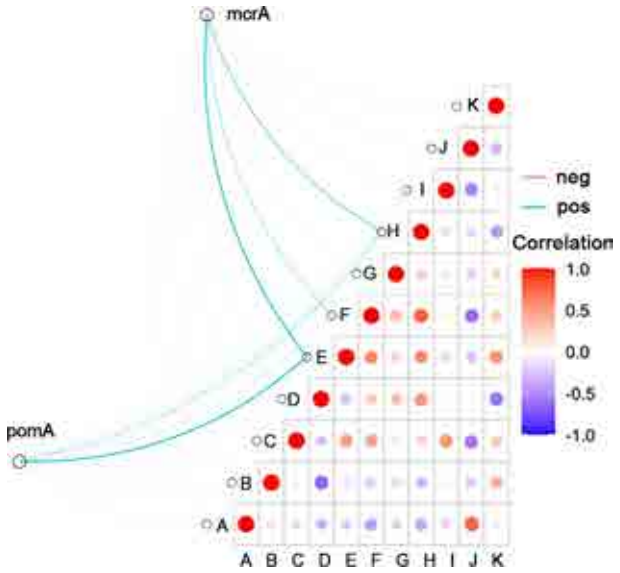

Fig. 6. Correlations among environmental factors, methane metabolic microbials, and methane fluxes. In order from A to K are: CH_4 fluxes, water table, pH, Oxidation-Reduction Potential (Eh), total nitrogen (TN), NH_4^+-N, NO_2^--N, NO_3^--N, total organic carbon (TOC), soil temperature (Ts), and soil water content (SWC).

4. Discussion

Methane emissions from the Dajiuhu subalpine peatland had obvious seasonal variations, CH_4 emissions were highest in summer and lowest in spring. The remarkable changes of CH_4 fluxes in wetlands were observed in previous studies, with the lowest emissions occurring in winter (Pypker et al., 2013; Zhang et al., 2016; Drollinger et al., 2019). However, in our study, there was a remarkable decrease in CH_4 fluxes during spring. It is clear that methanogens are important sources of CH_4 in wetlands (Thauer et al., 2008), and the biological activity of methanogens decreases in winter. Notably, CH_4 fluxes may fall to their minimum in spring. Some studies proposed that the abundances of methanogenic and methanotrophic communities underwent periodic variations (Chapman et al., 2017; Ren et al., 2018), but it was not a sufficient explanation for the changes of CH_4 fluxes.

In complex wetland ecosystems, interactions among methane metabolic microbial communities may have a greater influence on ecosystem functions. Using network analysis to explore the cooperative and/or competitive relationships between microbial taxa in complex communities could help us to understand the ecological laws and ascertain the functional roles of microbes comprehensively (Ma et al., 2016, 2020). In the present study, pMENs analysis was used to explore the variations of interactions between methanogenic and methanotrophic communities. The results demonstrated that the seasonal variations of the interactions between methanogens and methanotrophs were a crucial factor in CH_4 emissions. Moreover, some keystone species that were discerned by network analysis had correlational relationships with CH4 fluxes, reflecting their importance in mediating CH_4 fluxes.

Network modeling provides a great advantage in incorporating the complex relationships among microbes into an integrated pattern (Bascompte, 2007). The marked variations observed between the four seasonal networks indicated the variable interactions among methane metabolic microbial communities based on the season, which may affect the CH_4 fluxes. The largest number of nodes and edges was observed in the spring networks. Similarly, the high average degree and short average path length indicate that the spring networks had tight connectivity, conducive to the rapid and effective transmission of information (Zou et al., 2007). The edges in the network could be used to infer the interactive relationship between microbes. Positive correlations might reflect the same ecological niche or symbiotic relationship of the microbes allowing bacterial communities to potentially mitigate environmental stresses and expand their ecological niches through positive interactions (Zhang et al., 2019). In contrast, negative correlations suggest the presence of potential competition or a predation relationship (Layeghifard et al., 2017), which seemed more important when resources were relatively scarce (De Menezes et al., 2017). The largest and the smallest proportions of methanogenic negative edges and methanotrophic positive edges were presented in the spring networks, respectively. The intense competition among methanogens limited the production of CH_4, while better cooperation among methanotrophs was conducive to the consumption of CH_4. In summer, with the easing of competition between methanogens and the aggravation of competition between methanotrophs, a better realization of methanogenic community functions led to a general increase in the CH_4 emissions. In networks, nodes in the same module have similar ecological functions and niches (Newman, 2006), less modules could ensure a more efficient regulation and communication between modules when facing environmental stimuli. It follows that in summer, modules of the methanogenic and methanotrophic networks were the smallest and the largest, respectively, which helps to

explain that the centralized functions and niches in methanogenic communities were advantageous to CH_4 production, whereas methanotrophic communities could not efficienly respond to external disturbances and maintain functional stability.

In addition, the variations of topological roles in networks could also support our conclusions. Network hubs strongly support the structure of ecological networks, and are expected to create niches for other taxa (Toju et al., 2018). Only one network hub was found belonging to Methylocystaceae in the methanotrophic spring network. Module hubs and connectors are keystone species of the pMEN, which critically impact microbial community structures and their potential functions (Berry and Widder, 2014; Xie et al., 2020). For methanogens, growth in the number of module hubs in the winter and summer networks was observed, and connectors increased in the spring network. In terms of methanotrophs, there were more module hubs in the autumn and winter networks and more connectors in the summer network. Ninety-three percent of module hubs and connectors of the methanogenic networks, belonging to Methanomicrobiales and Methanocellales, were assigned to *Methanoregula formicic*a and *Methanocella arvoryzae*, respectively, and both were able to utilize H_2/CO_2 only to produce CH_4 (Horn et al., 2003). *Methanoregula formicica* had more negative than positive interactions with other OTUs, most of the time, which were liable to survive in the fierce competition; whereas, *Methanocella arvoryzae* only showed strong negative interactions with other OTUs in spring. Moreover, in agreement with previous studies, the results show that the presumptive keystone species differed as environmental conditions changed (Lu et al., 2013; Berry and Widder, 2014; Lupatini et al., 2014). *Methanocella arvoryzae* occupied the majority of module hubs in the summer network; on the other hand, most of the module hubs and connectors in other seasons were *Methanoregula formicica*.

Pearson's correlation analysis showed that *Methanoregula* was negatively correlated with CH_4 fluxes; nevertheless, *Methanocella* positively correlated with CH_4 fluxes (Table S6 in the ESM). Therefore, *Methanoregula formicica* inhibited CH_4 production when it occupied a large ecological niche in the spring. In contrast, *Methanocella arvoryzae* enhanced CH_4 production and emissions with a more favorable microbial community in the summer. Seventy-six percent of module hubs and connectors of the methanotrophic networks were assigned to *Methylocapsa aurea*, Methylocystaceae, and *Candidatus* Methyloumidiphilus. *Methylocapsa* aurea and Methylocystaceae belong to Rhizobiales and are type II methanotrophs. *Candidatus* Methyloumidiphilus belongs to *Methylococcales* and is a type I methanotroph. Type I methanotrophs adapt to the aerobic environment; however, the anaerobic environment is more suitable for type II methanotrophs (Amaral et al., 1995). Consistent with previous research, type II methanotrophs were the dominant flora in Dajiuhu subalpine peatland, characterized as an acidic, anaerobic wetland (Chen et al., 2008). *Methylocapsa aurea* had more negative than positive interactions with other OTUs most of the time. Methylocystaceae and Candidatus *Methyloumidiphilus alinensis* exhibited a similar change pattern, with more negative connections occurring in winter and summer with fewer in spring and autumn. Connectors and module hubs observed in the summer network were almost entirely Methylocystaceae, but the Methylocystaceae population plunged and even disappeared in the other seasons. Methylocystaceae showed positive correlations with CH_4 fluxes (Table S6), indicating that its roles in microbial communities have a critical impact on CH_4 emissions. Therefore, CH_4 oxidation was reduced and CH_4 emissions were increased when Methylocystaceae occupied a larger niche in summer.

Furthermore, CH_4 emissions in wetlands were also affected by many environmental factors. From the perspective of microbes, both methanogens and methanotrophs that were influenced by environmental factors could impact CH_4 fluxes. Pearson's correlation analysis showed that the CH_4 fluxes were significantly and positively correlated with soil temperature. The bioactivity of methanogens was relatively higher at 0°C–35°C. In a certain range, the diversity and quantity of methanogens increased with the rise of temperature, and the rate of CH_4 production grew accordingly (Kolton et al., 2019). In addition, summer was the growth period for *Sphagnum palustre*. During that time, the degradation rate of root exudates was accelerated, and the supply of methanogenic substrates was increased, which proved conducive to CH_4 production and emissions. The optimal temperature for methanotrophs was 25°C, but methanogens were much more sensitive to temperature than methanotrophs. Methane (CH_4) can be oxidized by methanotrophs at both low (–2°C) and high (30°C) temperatures (Chowdhury and Dick, 2013). In the study area, the soil temperature in spring was only 9°C–11°C, and the activity of methanogens decreased. At the same time, the methanotrophs maintained high activity under this condition which reduced the emissions because of steady CH_4 oxidation. The CH_4 fluxes were negatively correlated with soil NH_4^+-N, NO_2^--N, NO_3^--N, and TN, as well. Significant effects on methanogens and methanotrophs of TN, NH_4^+-N, and NO_2^--N were also shown by the correlation analysis. The results demonstrated that the contents of NH_4^+-N, NO_2^--N, NO_3^--N, and TN demonstrated a downward trend from winter to the next autumn. Microbes could use nitrates as electron acceptors in an anaerobic environment when oxidizing organic substrates (Bodelier et al., 2000), the gradual climb in nitrogen uptake by the growing plants could diminish the nitrogen available for CH_4 oxidation, which contributed to the high emission rates of CH_4 summer when plants matured (Bodelier and Laanbroek, 2004). Therefore, regulating the interactions between methanogens and methanotrophs through environmental factors may be an effective method to deal with excessive CH_4 emissions in wetlands.

The study provided a perspective to further reveal the impacts of microbes on CH_4 emissions in wetlands; how-

ever, it was not enough to consider the interactions between methanogenic and methanotrophic communities. In future research, the role of other relevant microbes in CH_4 emissions should be involved.

5. Conclusion

In conclusion, the seasonal co-occurrence patterns of methanogenic and methanotrophic communities and microbial driving mechanisms of CH_4 fluxes in Dajiuhu subalpine peatland were evaluated. The results implied that the methanogenic and methanotrophic co-occurrence patterns contributed to the seasonal variations of CH_4 fluxes. Specifically, the interactions, connectivity, and modularity of microbial networks were tied to CH_4 fluxes. The most complicated interactions among microbes and lowest CH_4 fluxes were observed in spring with the intense competition among methanogens. At the same time, methanotrophs demonstrated better cooperation, which was not conducive to the production of CH_4 and, instead, supported the consumption of CH_4. In contrast, the simplest networks and the highest CH_4 flux occurred in summer. Correspondingly, seasonal variations of topological roles and keystone species were closely related to CH_4 emissions, which suggested their importance in mediating CH_4 fluxes. *Methanoregula formicica* was negatively correlated with CH_4 fluxes and occupied larger ecological niches in the spring network. In contrast, *Methanocella arvoryzae* and Methylocystaceae positively correlated with CH_4 fluxes and adapted better to the microbial community in the summer. The results also indicated that soil temperature and nitrogen were crucial environmental factors that influenced CH_4 fluxes by indirectly affecting the biological activity of methanogens and methanotrophs.

Acknowledgements. This work was supported by the National Science Foundation of China (Grant No. 31971490). We thank the Institute of Shennongjia National Park Administration Bureau for data collecting assistance.

Electronic supplementary material: Supplementary material is available in the online version of this article at https://doi.org/10.1007/s00376-021-1255-z.

REFERENCES

Amaral, J. A., C. Archambault, S. R. Richards, and R. Knowles, 1995: Denitrification associated with groups I and II methanotrophs in a gradient enrichment system. *FEMS Microbiology Ecology*, **18**, 289–298, https://doi.org/10.1111/j.1574-6941.1995.tb00185.x.

Barberán, A., S. T. Bates, E. O. Casamayor, and N. Fierer, 2012: Using network analysis to explore co-occurrence patterns in soil microbial communities. *The ISME Journal*, **6**, 343–351, https://doi.org/10.1038/ismej.2011.119.

Bascompte, J., 2007: Networks in ecology. *Basic and Applied Ecology*, **8**, 485–490, https://doi.org/10.1016/j.baae.2007.06.003.

Berry, D., and S. Widder, 2014: Deciphering microbial interactions and detecting keystone species with co-occurrence networks. *Frontiers in Microbiology*, **5**, 219, https://doi.org/10.3389/fmicb.2014.00219.

Bodelier, P. L. E., and H. J. Laanbroek, 2004: Nitrogen as a regulatory factor of methane oxidation in soils and sediments. *FEMS Microbiology Ecology*, **47**, 265–277, https://doi.org/10.1016/S0168-6496(03)00304-0.

Bodelier, P. L. E., P. Roslev, T. Henckel, and P. Frenzel, 2000: Stimulation by ammonium-based fertilizers of methane oxidation in soil around rice roots. *Nature*, **403**, 421–424, https://doi.org/10.1038/35000193.

Chapman, E. J., H. Cadillo-Quiroz, D. L. Childers, M. R. Turetsky, and M. P. Waldrop, 2017: Soil microbial community composition is correlated to soil carbon processing along a boreal wetland formation gradient. *European Journal of Soil Biology*, **82**, 17–26, https://doi.org/10.1016/j.ejsobi.2017.08.001.

Chen, Y., M. G. Dumont, N. P. McNamara, P. M. Chamberlain, L. Bodrossy, N. Stralis-Pavese, and J. C. Murrell, 2008: Diversity of the active methanotrophic community in acidic peatlands as assessed by mRNA and SIP-PLFA analyses. *Environmental Microbiology*, **10**(2), 446–459, https://doi.org/10.1111/j.1462-2920.2007.01466.x.

Chowdhury, T. R., and R. P. Dick, 2013: Ecology of aerobic methanotrophs in controlling methane fluxes from wetlands. *Applied Soil Ecology*, **65**, 8–22, https://doi.org/10.1016/j.apsoil.2012.12.014.

De Menezes, A. B., A. E. Richardson, and P. H. Thrall, 2017: Linking fungal–bacterial co-occurrences to soil ecosystem function. *Current Opinion in Microbiology*, **37**, 135–141, https://doi.org/10.1016/j.mib.2017.06.006.

Drollinger, S., A. Maier, and S. Glatzel, 2019: Interannual and seasonal variability in carbon dioxide and methane fluxes of a pine peat bog in the Eastern Alps, Austria. *Agricultural and Forest Meteorology*, **275**, 69–78, https://doi.org/10.1016/j.agrformet.2019.05.015.

Hao, Q. Q., F. H. Liu, Y. C. Zhang, O. M. Wang, and L. L. Xiao, 2020: *Methylobacter* accounts for strong aerobic methane oxidation in the Yellow River Delta with characteristics of a methane sink during the dry season. *Science of the Total Environment*, **704**, 135383, https://doi.org/10.1016/j.scitotenv.2019.135383.

He, S. M., and Coauthors, 2015: Patterns in wetland microbial community composition and functional gene repertoire associated with methane emissions. *mBio*, **6**(3), e00066–15, https://doi.org/10.1128/mBio.00066-15.

Horn, M. A., C. Matthies, K. Kusel, A. Schramm, and H. L. Drake, 2003: Hydrogenotrophic methanogenesis by moderately acid-tolerant methanogens of a methane-emitting acidic peat. *Applied and Environmental Microbiology*, **69**(1), 74–83, https://doi.org/10.1128/AEM.69.1.74-83.2003.

Huang, R. L., Z. Y. Zhang, X. Xiao, N. Zhang, X. Y. Wang, Z. P. Yang, K. Q. Xu, and Y. T. Liang, 2019: Structural changes of soil organic matter and the linkage to rhizosphere bacterial communities with biochar amendment in manure fertilized soils. *Science of the Total Environment*, **692**, 333–343, https://doi.org/10.1016/j.scitotenv.2019.07.262.

IPCC, 2013: *Climate Change 2013*: *The Physical Science Basis*: *Working Group I Contribution to the Fifth Assessment Report of the Intergovernmental Panel on Climate Change*. Cambridge University Press, Cambridge, United Kingdom and New York, NY, USA.

Juottonen, H., E.-S. Tuittila, S. Juutinen, H. Fritze, and K. Yrjälä,

2008: Seasonality of rDNA-and rRNA-derived archaeal communities and methanogenic potential in a boreal mire. *The ISME Journal*, **2**(11), 1157–1168, https://doi.org/10.1038/ismej.2008.66.

Kolton, M., A. Marks, R. M. Wilson, J. P. Chanton, and J. E. Kostka, 2019: Impact of Warming on greenhouse gas production and microbial diversity in anoxic peat from a *Sphagnum*-dominated bog (Grand Rapids, Minnesota, United States). *Frontiers in Microbiology*, **10**, 870, https://doi.org/10.3389/fmicb.2019.00870.

Layeghifard, M., D. M. Hwang, and D. S. Guttman, 2017: Disentangling interactions in the microbiome: A network perspective. *Trends in Microbiology*, **25**(3), 217–228, https://doi.org/10.1016/j.tim.2016.11.008.

Li, D., H. W. Ni, S. Jiao, Y. H. Lu, J. Z. Zhou, B. Sun, and Y. T. Liang, 2021: Coexistence patterns of soil methanogens are closely tied to methane generation and community assembly in rice paddies. *Microbiome*, **9**(1), 20, https://doi.org/10.1186/s40168-020-00978-8.

Liebner, S., L. Ganzert, A. Kiss, S. Z. Yang, D. Wagner, and M. M. Svenning, 2015: Shifts in methanogenic community composition and methane fluxes along the degradation of discontinuous permafrost. *Frontiers in Microbiology*, **6**, 356, https://doi.org/10.3389/fmicb.2015.00356.

Long, K. D., L. B. Flanagan, and T. B. Cai, 2010: Diurnal and seasonal variation in methane emissions in a northern Canadian peatland measured by eddy covariance. *Global Change Biology*, **16**(9), 2420–2435, https://doi.org/10.1111/j.1365-2486.2009.02083.x.

Lu, L. H., S. X. Yin, X. Liu, W. M. Zhang, T. Y. Gu, Q. R. Shen, and H. Z. Qiu, 2013: Fungal networks in yield-invigorating and -debilitating soils induced by prolonged potato monoculture. *Soil Biology and Biochemistry*, **65**, 186–194, https://doi.org/10.1016/j.soilbio.2013.05.025.

Lupatini, M., A. K. A. Suleiman, R. J. S. Jacques, Z. I. Antoniolli, A. De Siqueira Ferreira, E. E. Kuramae, and L. F. W. Roesch, 2014: Network topology reveals high connectance levels and few key microbial genera within soils. *Frontiers in Environmental Science*, **2**, 10, https://doi.org/10.3389/fenvs.2014.00010.

Ma, B., and Coauthors, 2016: Geographic patterns of co-occurrence network topological features for soil microbiota at continental scale in eastern China. *The ISME Journal*, **10**(8), 1891–1901, https://doi.org/10.1038/ismej.2015.261.

Ma, B., and Coauthors, 2020: Earth microbial co-occurrence network reveals interconnection pattern across microbiomes. *Microbiome*, **8**(1), 82, https://doi.org/10.1186/s40168-020-00857-2.

Newman, M. E. J., 2006: Finding community structure in networks using the eigenvectors of matrices. *Phys. Rev. E*, **74**(3), 036104, https://doi.org/10.1103/PHYSREVE.74.036104.

Olesen, J. M., J. Bascompte, Y. L. Dupont, and P. Jordano, 2007: The modularity of pollination networks. *Proceedings of the National Academy of Sciences of the United States*, **104**(50), 19891–19896, https://doi.org/10.1073/pnas.0706375104.

Peltoniemi, K., and Coauthors, 2016: Responses of methanogenic and methanotrophic communities to warming in varying moisture regimes of two boreal fens. *Soil Biology and Biochemistry*, **97**, 144–156, https://doi.org/10.1016/j.soilbio.2016.03.007.

Pypker, T. G., P. A. Moore, J. M. Waddington, J. A. Hribljan, and R. C. Chimner, 2013: Shifting environmental controls on CH_4 fluxes in a sub-boreal peatland. *Biogeosciences*, **10**(12), 7971–7981, https://doi.org/10.5194/bg-10-7971-2013.

Ramakrishnan, B., T. Lueders, P. F. Dunfield, R. Conrad, and M. W. Friedrich, 2001: Archaeal community structures in rice soils from different geographical regions before and after initiation of methane production. *FEMS Microbiology Ecology*, **37**(2), 175–186, https://doi.org/10.1111/j.1574-6941.2001.tb00865.x.

Ren, J. S., C. C. Song, A. X. Hou, Y. Y. Song, X. Y. Zhu, and G. A. Cagle, 2018: Shifts in soil bacterial and archaeal communities during freeze-thaw cycles in a seasonal frozen marsh, Northeast China. *Science of the Total Environment*, **625**, 782–791, https://doi.org/10.1016/j.scitotenv.2017.12.309.

Saunois, M., and Coauthors, 2020: The global methane budget 2000–2017. *Earth System Science Data*, **12**(3), 1561–1623, https://doi.org/10.5194/essd-12-1561-2020.

Steele, J. A., and Coauthors, 2011: Marine bacterial, archaeal and protistan association networks reveal ecological linkages. *The ISME Journal*, **5**(9), 1414–1425, https://doi.org/10.1038/ismej.2011.24.

Thauer, R. K., A. K. Kaster, H. Seedorf, W. Buckel, and R. Hedderich, 2008: Methanogenic archaea: Ecologically relevant differences in energy conservation. *Nature Reviews Microbiology*, **6**(8), 579–591, https://doi.org/10.1038/nrmicro1931.

Toju, H., and Coauthors, 2018: Core microbiomes for sustainable agroecosystems. *Nature Plants*, **4**(5), 247–257, https://doi.org/10.1038/s41477-018-0139-4.

Wagner, D., 2017: Effect of varying soil water potentials on methanogenesis in aerated marshland soils. *Scientific Reports*, **7**, 14706, https://doi.org/10.1038/s41598-017-14980-y.

Wang, X. H., M. H. Zhu, N. K. Li, S. Du, J. D. Yang, and Y. Li, 2018: Effects of CeO_2 nanoparticles on bacterial community and molecular ecological network in activated sludge system. *Environmental Pollution*, **238**, 516–523, https://doi.org/10.1016/j.envpol.2018.03.034.

WMO/GAW, 2020: WMO greenhouse gas bulletin: The state of greenhouse gases in the atmosphere based on global observations through 2019, https://library.wmo.int/doc_num.php?explnum_id=10437.

Xie, F., A. Z. Ma, H. C. Zhou, Y. Liang, J. Yin, K. Ma, X. L. Zhuang, and G. Q. Zhuang, 2020: Niche differentiation of denitrifying anaerobic methane oxidizing bacteria and archaea leads to effective methane filtration in a Tibetan alpine wetland. *Environment International*, **140**, 105764, https://doi.org/10.1016/j.envint.2020.105764.

Yavitt, J. B., E. Yashiro, H. Cadillo-Quiroz, and S. H. Zinder, 2012: Methanogen diversity and community composition in peatlands of the central to northern Appalachian Mountain region, North America. *Biogeochemistry*, **109**, 117–131, https://doi.org/10.1007/s10533-011-9644-5.

Zhang, J., S. Jiao, and Y. H. Lu, 2018: Biogeographic distribution of bacterial, archaeal and methanogenic communities and their associations with methanogenic capacity in Chinese wetlands. *Science of the Total Environment*, **622–623**, 664–675, https://doi.org/10.1016/j.scitotenv.2017.11.279.

Zhang, Q., R. Sun, G. Q. Jiang, Z. W. Xu, and S. M. Liu, 2016: Carbon and energy flux from a *Phragmites australis* wetland in Zhangye oasis-desert area, China. *Agricultural and Forest Meteorology*, **230–231**, 45–57, https://doi.org/10.1016/j.agrformet.2016.02.019.

Zhang, Q. T., and Coauthors, 2019: High variations of methanogenic microorganisms drive full-scale anaerobic digestion process. *Environment International*, **126**, 543–551, https://doi.org/10.1016/j.envint.2019.03.005.

Zhao, Y. X., J. Q. Wang, Y. Liu, P. Zheng, and B. L. Hu, 2021: Microbial interaction promotes desulfurization efficiency under high pH condition. *Environ. Res.*, **200**, 111423, https://doi.org/10.1016/j.envres.2021.111423.

Zhou, J. Z., Y. Deng, F. Luo, Z. L. He, and Y. F. Yang, 2011: Phylogenetic molecular ecological network of soil microbial communities in response to elevated CO_2. *mBio*, **2**(4), e00122–11, https://doi.org/10.1128/mBio.00122-11.

Zou, L. H., W. J. Pei, T. Li, Z. Y. He, and Y. Cheung, 2007: Topological fractal networks introduced by mixed degree distribution. *Physica A: Statistical Mechanics and its Applications*, **380**, 592–600, https://doi.org/10.1016/j.physa.2007.02.060.